

METALLOENZYMES: POTENTIAL DRUG TARGETS

EDITED BY: Jamshed Iqbal, Jean Sévigny and Claus Jacob
PUBLISHED IN: Frontiers in Pharmacology





frontiers

Frontiers eBook Copyright Statement

The copyright in the text of individual articles in this eBook is the property of their respective authors or their respective institutions or funders. The copyright in graphics and images within each article may be subject to copyright of other parties. In both cases this is subject to a license granted to Frontiers.

The compilation of articles constituting this eBook is the property of Frontiers.

Each article within this eBook, and the eBook itself, are published under the most recent version of the Creative Commons CC-BY licence.

The version current at the date of publication of this eBook is CC-BY 4.0. If the CC-BY licence is updated, the licence granted by Frontiers is automatically updated to the new version.

When exercising any right under the CC-BY licence, Frontiers must be attributed as the original publisher of the article or eBook, as applicable.

Authors have the responsibility of ensuring that any graphics or other materials which are the property of others may be included in the CC-BY licence, but this should be checked before relying on the CC-BY licence to reproduce those materials. Any copyright notices relating to those materials must be complied with.

Copyright and source acknowledgement notices may not be removed and must be displayed in any copy, derivative work or partial copy which includes the elements in question.

All copyright, and all rights therein, are protected by national and international copyright laws. The above represents a summary only. For further information please read Frontiers' Conditions for Website Use and Copyright Statement, and the applicable CC-BY licence.

ISSN 1664-8714

ISBN 978-2-88971-627-2

DOI 10.3389/978-2-88971-627-2

About Frontiers

Frontiers is more than just an open-access publisher of scholarly articles: it is a pioneering approach to the world of academia, radically improving the way scholarly research is managed. The grand vision of Frontiers is a world where all people have an equal opportunity to seek, share and generate knowledge. Frontiers provides immediate and permanent online open access to all its publications, but this alone is not enough to realize our grand goals.

Frontiers Journal Series

The Frontiers Journal Series is a multi-tier and interdisciplinary set of open-access, online journals, promising a paradigm shift from the current review, selection and dissemination processes in academic publishing. All Frontiers journals are driven by researchers for researchers; therefore, they constitute a service to the scholarly community. At the same time, the Frontiers Journal Series operates on a revolutionary invention, the tiered publishing system, initially addressing specific communities of scholars, and gradually climbing up to broader public understanding, thus serving the interests of the lay society, too.

Dedication to Quality

Each Frontiers article is a landmark of the highest quality, thanks to genuinely collaborative interactions between authors and review editors, who include some of the world's best academicians. Research must be certified by peers before entering a stream of knowledge that may eventually reach the public - and shape society; therefore, Frontiers only applies the most rigorous and unbiased reviews.

Frontiers revolutionizes research publishing by freely delivering the most outstanding research, evaluated with no bias from both the academic and social point of view. By applying the most advanced information technologies, Frontiers is catapulting scholarly publishing into a new generation.

What are Frontiers Research Topics?

Frontiers Research Topics are very popular trademarks of the Frontiers Journals Series: they are collections of at least ten articles, all centered on a particular subject. With their unique mix of varied contributions from Original Research to Review Articles, Frontiers Research Topics unify the most influential researchers, the latest key findings and historical advances in a hot research area! Find out more on how to host your own Frontiers Research Topic or contribute to one as an author by contacting the Frontiers Editorial Office: frontiersin.org/about/contact

METALLOENZYMES: POTENTIAL DRUG TARGETS

Topic Editors:

Jamshed Iqbal, COMSATS University Islamabad, Pakistan

Jean Sévigny, Laval University, Canada

Claus Jacob, Saarland University, Germany

Citation: Iqbal, J., Sévigny, J., Jacob, C., eds. (2021). Metalloenzymes: Potential Drug Targets. Lausanne: Frontiers Media SA. doi: 10.3389/978-2-88971-627-2

Table of Contents

- 04 Editorial: Metalloenzymes: Potential Drug Targets**
Jamshed Iqbal, Claus Jacob and Jean Sévigny
- 07 Inhibition of Tyrosinase by Mercury Chloride: Spectroscopic and Docking Studies**
Jianmin Chen, Yaling Ye, Mengnan Ran, Qinglian Li, Zhipeng Ruan and Nan Jin
- 17 The Thyrotropin-Releasing Hormone-Degrading Ectoenzyme, a Therapeutic Target?**
Jean-Louis Charli, Adair Rodríguez-Rodríguez, Karina Hernández-Ortega, Antonieta Cote-Vélez, Rosa María Uribe, Lorraine Jaimes-Hoy and Patricia Joseph-Bravo
- 38 Development of Anthraquinone Derivatives as Ectonucleoside Triphosphate Diphosphohydrolase (NTPDase) Inhibitors With Selectivity for NTPDase2 and NTPDase3**
Younis Baqi, Mahmoud Rashed, Laura Schäkel, Enas M. Malik, Julie Pelletier, Jean Sévigny, Amelie Fiene and Christa E. Müller
- 53 Nucleotide Analog ARL67156 as a Lead Structure for the Development of CD39 and Dual CD39/CD73 Ectonucleotidase Inhibitors**
Laura Schäkel, Constanze C. Schmies, Riham M. Idris, Xihuan Luo, Sang-Yong Lee, Vittoria Lopez, Salahuddin Mirza, The Hung Vu, Julie Pelletier, Jean Sévigny, Vigneshwaran Namasivayam and Christa E. Müller
- 76 Sodium New Houttuynonate Affects Transcriptome and Virulence Factors of Pseudomonas aeruginosa Controlled by Quorum Sensing**
Yeye Zhao, Longfei Mei, Yuanqing Si, Jiadi Wu, Jing Shao, Tianming Wang, Guiming Yan, Changzhong Wang and Daqiang Wu
- 89 Discovery of a Novel Natural Allosteric Inhibitor That Targets NDM-1 Against Escherichia coli**
Yanan Yang, Yan Guo, Yonglin Zhou, Yawen Gao, Xiyan Wang, Jianfeng Wang and Xiaodi Niu
- 100 Functionalized Oxindolin Hydrazine Carbothioamide Derivatives as Highly Potent Inhibitors of Nucleoside Triphosphate Diphosphohydrolases**
Saira Afzal, Mariya al-Rashida, Abdul Hameed, Julie Pelletier, Jean Sévigny and Jamshed Iqbal
- 118 Biophysical Compatibility of a Heterotrimeric Tyrosinase-TYRP1-TYRP2 Metalloenzyme Complex**
Olga Lavinda, Prashiela Manga, Seth J. Orlow and Timothy Cardozo
- 129 Investigation of Angiogenesis and Wound Healing Potential Mechanisms of Zinc Oxide Nanorods**
Amr Hassan, Dalia Elebeedy, Emadeldin R. Matar, Aly Fahmy Mohamed Elsayed and Ahmed I. Abd El Maksoud



Editorial: Metalloenzymes: Potential Drug Targets

Jamshed Iqbal^{1*}, Claus Jacob² and Jean Sévigny^{3,4}

¹Centre for Advanced Drug Research, COMSATS University Islamabad, Abbottabad, Pakistan, ²Division of Bioorganic Chemistry, School of Pharmacy, University of Saarland, Saarbrücken, Germany, ³Centre de Recherche du CHU de Québec - Université Laval, Québec City, QC, Canada, ⁴Département de Microbiologie-Infectiologie et d'Immunologie, Faculté de Médecine, Université Laval, Québec City, QC, Canada

Keywords: metalloenzymes, ecto-5'-nucleotidase, nucleotide pyrophosphatase/phosphodiesterases, nucleoside triphosphate diphosphohydrolases, inhibitors

Editorial on the Research Topic

Metalloenzymes: Potential Drug Targets

Metalloenzymes have an important role in the regulation of many biological functions. Overexpressed and/or reduced secretion of such enzymes lead to different complications of clinical interest. The metal ions present in enzymes control the structure, folding, and functions of such proteins. The protein data bank (PDB) revealed that over 50% of proteins contain metal ions (Solomon et al., 1996). The development of metalloenzyme inhibitors are of interest in the treatment of various diseases. The interaction of ligands, i.e., compounds as inhibitors with target proteins via active sites provide a means of curing diseases. Most aptly, the inhibitors reported by academic or pharmaceutical usage of small molecules as inhibitors provide a rapid and viable way to treat diseases. Urease is a ubiquitous metalloenzyme, produced by various cell types from plants, fungi, and bacteria, etc., that bears a nickel atom in its active pocket. It hydrolyzes the urea into ammonia and carbamate which further decompose to ammonia and CO₂. The overexpression of urease was known to be linked with ulcers, hepatic coma, and formation of urinary stones (Upadhyay, 2012; Kappaun et al., 2018).

Carbonic anhydrase with zinc metal ion catalyze the hydration of CO₂ with water to produce hydrogen carbonate and H⁺ ions (Alvarez-Leefmans and Delpire, 2009). The hydration reaction involves the nucleophilic attack of the metal-bounded hydroxy (OH) group with the carbon (C) atom of carbon dioxide species (Silverman and Lindskog, 1988). The coordination of carbonic anhydrases (CAs) with metal ion occurs at active sites via binding with histidine, cysteine, and/or glutamine residues to form a tetrahedral shape (Steiner et al., 1975). The inhibitors of CAs have been employed as diuretic and antiglaucoma agents as well as anti-obesity and anticancer agents (Supuran, 2008).

Furthermore, ubiquitous ecto-nucleotidases such as 1) nucleoside triphosphate diphosphohydrolases (NTPDases), 2) nucleotide pyrophosphatase/phosphodiesterases (NPPs), 3) alkaline phosphatases (APs or ALPs), and 4) ecto-5'-nucleotidase (e5'NT) are all responsible for the integrity of proper cell functioning (Supuran, 2008). The NPPs possess zinc (Zn²⁺) metal ion at active sites while the e5'NT has additionally magnesium ion (Mg²⁺) at the active site. The overexpression of surface-located ecto-enzymes hydrolyzing nucleotides causes various complications which affect different functions such as cell proliferation, apoptosis as well as degenerative, neurological, and immunological responses. In the current issue, Baqi et al. reported the use of anthraquinone derivatives as NTPDase inhibitors which showed selectivity towards NTPDase2 and -3. The compound, 1-amino-4-(9-phenanthrylamino)-9,10-dioxo-9,10-dihydroanthracene-2-sulfonate, with an IC₅₀ value of 539 nM was found to be a potent inhibitor of NTPDase2, while the anthraquinone, 1-amino-4-[3-(4,6-dichlorotriazin-2-ylamino)-4-sulfophenylamino]-9,10-dioxo-

OPEN ACCESS

Edited and reviewed by:

Salvatore Salomone,
University of Catania, Italy

*Correspondence:

Jamshed Iqbal
drjamshed@cuiatd.edu.pk

Specialty section:

This article was submitted to
Experimental Pharmacology and Drug
Discovery,
a section of the journal
Frontiers in Pharmacology

Received: 25 July 2021

Accepted: 07 September 2021

Published: 24 September 2021

Citation:

Iqbal J, Jacob C and Sévigny J (2021)
Editorial: Metalloenzymes: Potential
Drug Targets.
Front. Pharmacol. 12:746925.
doi: 10.3389/fphar.2021.746925

9,10-dihydroanthracene-2-sulfonate, showed potency and selectivity towards NTPDase3 with an IC_{50} of 390 nM. The most potent compounds could serve as front-runners in the goal of treating different pathological complications (Baqi et al.). The inhibitors of NTPDase1 may serve as potential leads in cancer therapy. Adenosine derivatives were screened for CD39 and CD73. The biological assay results showed selective CD39 and dual CD39/CD73 inhibitors (Schäkel et al.). A docking study further showed putative binding of nucleotide analogs with target enzymes. Thus, the inhibition of metalloenzymes might be useful to cure different clinically important complications.

Prof. Iqbal's research group have made significant progress in the development and identification of different compounds as inhibitors of metalloenzymes. They have reported several inhibitors of carbonic anhydrase activity such as sulfonamides, sulfonates, and sulfamate derivatives (Zaraei et al., 2019; Saeed et al., 2021). Furthermore, many other types of molecules have also been reported as carbonic anhydrase inhibitors (Al-Rashida et al., 2014; Saeed et al., 2014; Zaib et al., 2014; Al-Rashida et al., 2015; Saeed et al., 2017; Abbas et al., 2018; Abbas A. et al., 2019). Supuran (2008) published an excellent review in *Nature Review Drug Discovery* to present carbonic anhydrase and its inhibitors. The presence of zinc metal provides a means of binding enzymes with several classes of compounds including sulphonamides, sulphamates, and sulphamides.

Urease is also a common target for treating ulcers which possesses two nickel atoms in its core structure. The inhibition of urease has been reported by using different heterocycles. In their studies, Iqbal et al. have reported 1,3-thiazoles (Channar et al., 2021), benzohydrazide derivatives (Abbas S. et al., 2019), acridine-based (thio)semicarbazones, hydrazones (Isaac et al., 2019), and semicarbazones derivatives (Qazi et al., 2018) as urease inhibitors. The copper metal ion containing tyrosinase has been known to be involved in melanin biosynthesis. Lavinda et al. developed a 3D model of the structure of human tyrosinase and TYRP2 on the basis of their crystallographic structure. The mechanism of mercury chloride ($HgCl_2$)-induced tyrosinase inactivation was investigated in this study (Chen et al.).

Iqbal et al. have also made progress on the inhibition of other biological targets which include other ecto-nucleotidases. Various

types of heterocyclic scaffolds such as the inhibitors of nucleotide pyrophosphatase/phosphodiesterases (NPPs) include substituted trifluoromethyl quinoline (Semreen et al., 2019), arylated thiadiazolopyrimidones (Jafari et al., 2016), and *p*-nitrophenyl thymidine 5'-monophosphate (Raza et al., 2011). Moreover, the development of ecto-5'-nucleotidase inhibitors may also serve to treat cancer (Iqbal et al., 2013). The heterocyclic compounds which have been synthesized and screened as NTPDases include oxoindolin phenylhydrazine carboxamides (Afzal et al., 2021), pyrrolo[2,3-*b*]pyridine derivatives (Ullah et al., 2021), spirooxindole derivatives (Ashraf et al., 2020), sulfonylhydrazones (Younus et al., 2020), 2-substituted-7-trifluoromethyl-thiadiazolopyrimidones (Afzal et al., 2020), pyrazolyl pyrimidinetrione, and thioxopyrimidinone conjugates as selective inhibitors of human ectonucleotidase (Andleeb et al., 2019), etc. Furthermore, the review articles of Iqbal (Iqbal, 2019) have also reported the importance of ectonucleotidase inhibitors in the treatment of various diseases. Though there are many other metal ions-containing proteins which have been targeted to treat clinically relevant conditions, Iqbal et al. have made a significant scientific contribution in finding good choices in the inhibition of urease, carbonic anhydrase, and ectonucleotidases.

In summary, metalloproteins present relevant targets for the development of modulators in order to treat various types of diseases. In this view, development of metalloprotein inhibitors with different structures, such as heterocyclic compounds, provide an excellent opportunity to treat such diseases. The presence of metal ions in these proteins help them bind with the inhibitor and play an important role in the inhibition process. Libraries of small heterocyclic molecules can be readily prepared to screen them against various target proteins to cure corresponding diseases.

AUTHOR CONTRIBUTIONS

All authors listed have made a substantial, direct, and intellectual contribution to the work and approved it for publication.

REFERENCES

- Abbas, A., Ali, B., Kanwal, K. M., Khan, K. M., Iqbal, J., Ur Rahman, S., et al. (2019a). Synthesis and *In Vitro* Urease Inhibitory Activity of Benzohydrazide Derivatives, *In Silico* and Kinetic Studies. *Bioorg. Chem.* 82, 163–177. doi:10.1016/j.bioorg.2018.09.036
- Abbas, S., Zaib, S., Rahman, S. U., Ali, S., Hameed, S., Tahir, M. N., et al. (2019b). Carbonic Anhydrase Inhibitory Potential of 1,2,4-Triazole-3-Thione Derivatives of Flurbiprofen, Ibuprofen and 4-Tert-Butylbenzoic Hydrazide: Design, Synthesis, Characterization, Biochemical Evaluation, Molecular Docking and Dynamic Simulation Studies. *Med. Chem.* 15 (3), 298–310. doi:10.2174/1573406414666181012165156
- Abbas, S., Nasir, H. H., Zaib, S., Ali, S., Mahmood, T., Ayub, K., et al. (2018). Carbonic Anhydrase Inhibition of Schiff Base Derivative of Imino-Methyl-Naphthalen-2-yl: Synthesis, Structure Elucidation, Molecular Docking, Dynamic Simulation and Density Functional Theory Calculations. *J. Mol. Struct.* 1156, 193–200. doi:10.1016/j.molstruc.2017.11.086
- Afzal, S., Al-Rashida, M., Hameed, A., Pelletier, J., Sévigny, J., and Iqbal, J. (2021). Synthesis, *In-Vitro* Evaluation and Molecular Docking Studies of Oxoindolin Phenylhydrazine Carboxamides as Potent and Selective Inhibitors of Ectonucleoside Triphosphate Diphosphohydrolase (NTPDase). *Bioorg. Chem.* 112, 104957. doi:10.1016/j.bioorg.2021.104957
- Afzal, S., Zaib, S., Jafari, B., Langer, P., Lecka, J., Sévigny, J., et al. (2020). Highly Potent and Selective Ectonucleoside Triphosphate Diphosphohydrolase (NTPDase1, 2, 3 and 8) Inhibitors Having 2-substituted-7-Trifluoromethyl-Thiadiazolopyrimidones Scaffold. *Med. Chem.* 16 (5), 689–702. doi:10.2174/1573406415666190614095821
- Al-Rashida, M., Ejaz, S. A., Ali, S., Shaukat, A., Hamayoun, M., Ahmed, M., et al. (2015). Diarylsulfonamides and Their Bioisosteres as Dual Inhibitors of Alkaline Phosphatase and Carbonic Anhydrase: Structure Activity Relationship and Molecular Modelling Studies. *Bioorg. Med. Chem.* 23 (10), 2435–2444. doi:10.1016/j.bmc.2015.03.054
- Al-Rashida, M., Hussain, S., Hamayoun, M., Altaf, A., and Iqbal, J. (2014). Sulfa Drugs as Inhibitors of Carbonic Anhydrase: New Targets for the Old Drugs. *Biomed. Res. Int.* 2014, 162928. doi:10.1155/2014/162928

- Alvarez-Leefmans, F. J., and Delpire, E. (2009). *Physiology and Pathology of Chloride Transporters and Channels in the Nervous System: From Molecules to Diseases*. Academic Press.
- Andleeb, H., Hameed, S., Ejaz, S. A., Khan, I., Zaib, S., Lecka, J., et al. (2019). Probing the High Potency of Pyrazolyl Pyrimidinetriones and Thioxopyrimidinediones as Selective and Efficient Non-nucleotide Inhibitors of Recombinant Human Ectonucleotidases. *Bioorg. Chem.* 88, 102893. doi:10.1016/j.bioorg.2019.03.067
- Ashraf, A., Shafiq, Z., Khan Jadoon, M. S., Tahir, M. N., Pelletier, J., Sevigny, J., et al. (2020). Synthesis, Characterization, and In Silico Studies of Novel Spirooxindole Derivatives as Ecto-5'-Nucleotidase Inhibitors. *ACS Med. Chem. Lett.* 11 (12), 2397–2405. doi:10.1021/acsmchemlett.0c00343
- Channar, P. A., Saeed, A., Afzal, S., Hussain, D., Kalesse, M., Shehzadi, S. A., et al. (2021). Hydrazine Clubbed 1,3-thiazoles as Potent Urease Inhibitors: Design, Synthesis and Molecular Docking Studies. *Mol. Divers.* 25 (2), 1–13. doi:10.1007/s11030-020-10057-7
- Iqbal, J., Saeed, A., Raza, R., Matin, A., Hameed, A., Furtmann, N., et al. (2013). Identification of Sulfonic Acids as Efficient Ecto-5'-Nucleotidase Inhibitors. *Eur. J. Med. Chem.* 70, 685–691. doi:10.1016/j.ejmech.2013.10.053
- Iqbal, J. (2019). Ectonucleotidases: Potential Target in Drug Discovery and Development. *Mrmc* 19 (11), 866–869. doi:10.2174/138955751911190517102116
- Isaac, I. O., Al-Rashida, M., Rahman, S. U., Alharthy, R. D., Asari, A., Hameed, A., et al. (2019). Acridine-based (Thio)semicarbazones and Hydrazones: Synthesis, In Vitro Urease Inhibition, Molecular Docking and In-Silico ADME Evaluation. *Bioorg. Chem.* 82, 6–16. doi:10.1016/j.bioorg.2018.09.032
- Jafari, B., Yelibayeva, N., Ospanov, M., Ejaz, S. A., Afzal, S., Khan, S. U., et al. (2016). Synthesis of 2-arylated Thiadiazolopyrimidones by Suzuki-Miyaura Cross-Coupling: a New Class of Nucleotide Pyrophosphatase (NPPs) Inhibitors. *RSC Adv.* 6 (109), 107556–107571. doi:10.1039/c6ra22750c
- Kappaun, K., Piovesan, A. R., Carlini, C. R., and Ligabue-Braun, R. (2018). Ureases: Historical Aspects, Catalytic, and Non-catalytic Properties - A Review. *J. Adv. Res.* 13, 3–17. doi:10.1016/j.jare.2018.05.010
- Qazi, S. U., Rahman, S. U., Awan, A. N., Al-Rashida, M., Alharthy, R. D., Asari, A., et al. (2018). Semicarbazone Derivatives as Urease Inhibitors: Synthesis, Biological Evaluation, Molecular Docking Studies and In-Silico ADME Evaluation. *Bioorg. Chem.* 79, 19–26. doi:10.1016/j.bioorg.2018.03.029
- Raza, R., Akhtar, T., Hameed, S., Lecka, J., Iqbal, J., and Sevigny, J. (2011). Identification of Potent and Selective Human Ecto-Nucleotide Pyrophosphatase/Phosphodiesterase-3 (hNPP3) Inhibitors. *Open Enzyme Inhib. J.* 4, 17–22. doi:10.2174/1874940201104010017
- Saeed, A., Al-Rashida, M., Hamayoun, M., Mumtaz, A., and Iqbal, J. (2014). Carbonic Anhydrase Inhibition by 1-Aroyl-3-(4-Aminosulfonylphenyl) thioureas. *J. Enzyme Inhib. Med. Chem.* 29 (6), 901–905. doi:10.3109/14756366.2013.866660
- Saeed, A., Khan, S. U., Mahesar, P. A., Channar, P. A., Shabir, G., and Iqbal, J. (2017). Substituted (E)-2-(2-benzylidenhydrazinyl)-4-methylthiazole-5-carboxylates as Dual Inhibitors of 15-lipoxygenase & Carbonic Anhydrase II: Synthesis, Biochemical Evaluation and Docking Studies. *Biochem. Biophys. Res. Commun.* 482 (1), 176–181. doi:10.1016/j.bbrc.2016.11.028
- Saeed, A., Ejaz, S. A., Ul-Hamid, A., El-Seedi, H. R., and Iqbal, J. (2021). Synthesis of and Molecular Docking Studies of Azomethine- Tethered Sulfonamides as Carbonic Anhydrase II & 15-lipoxygenase Inhibitors. *J. Mol. Struct.* 1243, 130821. doi:10.1016/j.molstruc.2021.130821
- Semreen, M. H., El-Gamal, M. I., Ullah, S., Jalil, S., Zaib, S., Anbar, H. S., et al. (2019). Synthesis, Biological Evaluation, and Molecular Docking Study of Sulfonate Derivatives as Nucleotide Pyrophosphatase/phosphodiesterase (NPP) Inhibitors. *Bioorg. Med. Chem.* 27 (13), 2741–2752. doi:10.1016/j.bmc.2019.04.031
- Silverman, D. N., and Lindskog, S. (1988). The Catalytic Mechanism of Carbonic Anhydrase: Implications of a Rate-Limiting Protolysis of Water. *Acc. Chem. Res.* 21 (1), 30–36. doi:10.1021/ar00145a005
- Solomon, E. I., Sundaram, U. M., and Machonkin, T. E. (1996). Multicopper Oxidases and Oxygenases. *Chem. Rev.* 96 (7), 2563–2606. doi:10.1021/cr950046o
- Steiner, H., Jonsson, B. H., and Lindskog, S. (1975). The Catalytic Mechanism of Carbonic Anhydrase. Hydrogen-Isotope Effects on the Kinetic Parameters of the Human C Isoenzyme. *Eur. J. Biochem.* 59 (1), 253–259. doi:10.1111/j.1432-1033.1975.tb02449.x
- Supuran, C. T. (2008). Carbonic Anhydrases: Novel Therapeutic Applications for Inhibitors and Activators. *Nat. Rev. Drug Discov.* 7 (2), 168–181. doi:10.1038/nrd2467
- Ullah, S., El-Gamal, M. I., El-Gamal, R., Pelletier, J., Sévigny, J., Shehata, M. K., et al. (2021). Synthesis, Biological Evaluation, and Docking Studies of Novel Pyrrolo [2, 3-b] Pyridine Derivatives as Both Ectonucleotide Pyrophosphatase/phosphodiesterase Inhibitors and Antiproliferative Agents. *Eur. J. Med. Chem.* 217, 113339. doi:10.1016/j.ejmech.2021.113339
- Upadhyay, L. S. B. (2012). *Urease Inhibitors*. New Delhi, India: A review.
- Younus, H. A., Hameed, A., Mahmood, A., Khan, M. S., Saeed, M., Batool, F., et al. (2020). Sulfonylhydrazones: Design, synthesis and investigation of ectonucleotidase (ALP & e5'NT) inhibition activities. *Bioorg. Chem.* 100, 103827. doi:10.1016/j.bioorg.2020.103827
- Zaib, S., Saeed, A., Stolte, K., Flörke, U., Shahid, M., and Iqbal, J. (2014). New Aminobenzenesulfonamide-Thiourea Conjugates: Synthesis and Carbonic Anhydrase Inhibition and Docking Studies. *Eur. J. Med. Chem.* 78, 140–150. doi:10.1016/j.ejmech.2014.03.023
- Zaraei, S. O., El-Gamal, M. I., Shafique, Z., Amjad, S. T., Afridi, S., Zaib, S., et al. (2019). Sulfonate and Sulfamate Derivatives Possessing Benzofuran or Benzothiophene Nucleus as Potent Carbonic Anhydrase II/IX/XII Inhibitors. *Bioorg. Med. Chem.* 27 (17), 3889–3901. doi:10.1016/j.bmc.2019.07.026

Conflict of Interest: The authors declare that the research was conducted in the absence of any commercial or financial relationships that could be construed as a potential conflict of interest.

Publisher's Note: All claims expressed in this article are solely those of the authors and do not necessarily represent those of their affiliated organizations, or those of the publisher, the editors and the reviewers. Any product that may be evaluated in this article, or claim that may be made by its manufacturer, is not guaranteed or endorsed by the publisher.

Copyright © 2021 Iqbal, Jacob and Sévigny. This is an open-access article distributed under the terms of the Creative Commons Attribution License (CC BY). The use, distribution or reproduction in other forums is permitted, provided the original author(s) and the copyright owner(s) are credited and that the original publication in this journal is cited, in accordance with accepted academic practice. No use, distribution or reproduction is permitted which does not comply with these terms.



Inhibition of Tyrosinase by Mercury Chloride: Spectroscopic and Docking Studies

Jianmin Chen^{1,2*}, Yaling Ye¹, Mengnan Ran¹, Qinglian Li¹, Zhipeng Ruan^{1,2}
and Nan Jin^{1,2}

¹ School of Pharmacy and Medical Technology, Putian University, Fujian, China, ² Key Laboratory of Pharmaceutical Analysis and Laboratory Medicine, Putian University, Fujian Province University, Fujian, China

OPEN ACCESS

Edited by:

Jamshed Iqbal,
COMSATS University Islamabad,
Pakistan

Reviewed by:

Cláudia Sirlene Oliveira,
Pelé Petit Prince Research Institute,
Brazil
Mohamed A. Abdelgawad,
Al Jouf University,
Saudi Arabia

*Correspondence:

Jianmin Chen
chenjianmin1985@sina.com

Specialty section:

This article was submitted to
Experimental Pharmacology
and Drug Discovery,
a section of the journal
Frontiers in Pharmacology

Received: 29 October 2019

Accepted: 27 January 2020

Published: 06 March 2020

Citation:

Chen J, Ye Y, Ran M, Li Q, Ruan Z and
Jin N (2020) Inhibition of Tyrosinase by
Mercury Chloride: Spectroscopic and
Docking Studies.
Front. Pharmacol. 11:81.
doi: 10.3389/fphar.2020.00081

Inorganic mercury compounds have been used in skin-lightening products since ancient times. Although a previous study demonstrated that mercury impeded the transfer of Cu^{2+} to the apotyrasinase, the effect of mercury on tyrosinase is still unclear. In the present study, the mechanism of mercury chloride (HgCl_2) induced inactivation of tyrosinase was investigated for the first time. The IC_{50} values were 29.97 and 77.93 $\mu\text{mol/L}$ for monophenolase and diphenolase, respectively. A kinetic analysis revealed that HgCl_2 inhibited tyrosinase activity in an irreversible non-competitive manner. The strong intrinsic fluorescence quenching suggested that the formation of the HgCl_2 -tyrosinase complex induced conformational changes of the enzyme, and HgCl_2 had only one single binding site or a single class of binding site on tyrosinase. The molecular docking and further experiments demonstrated that HgCl_2 bound to the amino residuals (His) in the catalytic center of tyrosinase. To our knowledge, these findings presented in this paper were the first evidence of the direct interactions between HgCl_2 and tyrosinase, which provided a deep understanding of the inhibition mechanism of mercury on tyrosinase.

Keywords: mercury chloride, tyrosinase, spectroscopic measurements, molecular docking, inhibition mechanism

INTRODUCTION

Tyrosinase (EC 1.14.18.1), a type III copper protein, is ubiquitously distributed in bacteria, fungi, plants, insects, crustaceans, and mammals (Yoon et al., 2009). It is able to perform two successive reactions: the hydroxylation of tyrosine to dopa (monophenolase activity) and also the subsequent oxidation of dopa to dopaquinone (diphenolase activity) (Körner and Pawelek, 1982; Tan et al., 2016). Dopaquinone, also known as o-dopaquinone, is of high reactivity and its derivatives spontaneously polymerize to form melanin through a series of chemical reactions (Seo et al., 2003). Consequently, tyrosinase plays a pivotal role in melanin formation, which is an important component responsible for skin pigmentation in humans. Although melanin produced in skin melanocytes provides protection from UV radiation, excessive accumulation of melanin may cause cosmetic flaws such as age spots, freckles, senile lentigines, solar lentigo, and melasma in humans (Germanò et al., 2012; Hridya et al., 2016; Soares et al., 2017).

To decrease the abnormal accumulation of melanin, the use of skin-lightening (also known as skin bleaching and skin whitening) products has been prevalent among women all over the world

for decades (Olumide et al., 2008). The active ingredients known to be effective for skin lightening include various corticosteroids, hydroquinone, and mercury (Barry et al., 2011). Mercury exists primarily in three forms: inorganic, organic, and metallic (or elemental) (Boyd et al., 2000). Inorganic mercury compounds, including mercuric chloride, mercurous chloride, and mercurous oxide, have been used in skin-lightening products since ancient times (Kibukamusoke et al., 1974). These compounds occur in a mercuric (Hg II) or mercurous (Hg I) form and have toxic effects on humans (Clarkson et al., 2003). It has been discovered that the use of skin-lightening products is one of the causes of mercury toxicity (Agrawal and Mazhar, 2015). More specifically, the use of skin-lightening products containing inorganic mercury may lead to central nervous system, gastrointestinal and renal toxicity (Chan, 2011). For this reason, the sale of skin-lightening products containing inorganic mercury was prohibited in many countries (Al-Saleh, 2016). Despite repeated warnings of mercury poisoning by health authorities and the ban against the sale of skin-lightening products containing inorganic mercury, these products are widely available for sale in pharmacies, beauty aid stores and on the internet (Hamann et al., 2014).

The failure in the prohibition of adding inorganic mercury to skin-lightening products is an interesting question worthy of consideration. We believe that the main reason may be the good performance of inorganic mercury compounds in skin-lightening and anti-freckle effects. So now comes the question, why do these compounds exhibit such strong inhibition ability of melanin production. It is well known that mercury can replace the copper needed for tyrosinase activity, thereby deactivating enzymes and producing skin-lightening effects (Lerner, 1952a). Specifically, mercury ions can compete with copper ions for active centers on apotyrasinase to produce an inactive preparation; it is worth noting that once copper becomes attached to the enzyme it is replaced by ion of mercury with difficulty (Lerner, 1952b). That is to say, the previous literature (Lerner, 1952b) has demonstrated that mercury only displayed an effect on apotyrasinase as opposed to tyrosinase. Therefore, the direct interaction between mercury and tyrosinase is still unknown. In this study, we used kinetics measurements, spectral investigation, and molecular docking to study the effects of mercury on tyrosinase and tried to elucidate the intrinsic mechanism of the interaction at the molecular level.

MATERIALS AND METHODS

Materials

Tyrosine (98%), dopa (98%), and mushroom tyrosinase (1000U/mg, EC 1.14.18.1) were purchased from Sigma-Aldrich (St. Louis, MO, USA). Mercuric chloride (HgCl₂, 99.5%) and kojic acid (99%) was obtained from Aladdin Bio-technology (Shanghai, China). Histidine (His), valine (Val), glutamate (Glu), and alanine (Ala) were of analytical grade and bought from Xiya Chemical Industry (Shandong, China). All other chemicals and reagents used were of analytical grade or pharmaceutical grade. A Milli-Q-Plus ultra-pure water system

from Millipore (Sartorius 611, Germany) was used throughout the study to obtain water used during the experiments.

The Effects on the Monophenolase Activity of Tyrosinase

The method was modified based on the previous description (Chen et al., 2016). In brief, the assays were carried out by using 3 mL of reaction system containing 0.5 mmol/L substrate (tyrosine) in 50 mmol/L Na₂HPO₄-NaH₂PO₄ buffer solution (PBS, pH = 6.8) at 305 K. A 100 µL aliquot of HgCl₂ solutions with various concentrations (0, 1.25, 5 and 10 mmol/L) was added to the reaction system to give concentrations ranged from 0 to 333.33 µmol/L. The final concentration of tyrosinase was 33.33 U/mL. The optical densities (OD) at wavelength of 475 nm were recorded using UV spectrophotometer (UV 2550, SHIMADZU) every 30 s in the first 2 mins and then every 1 min until 30 mins. Kojic acid was used as a positive control. The appropriate blanks (containing both tyrosine and HgCl₂ but without tyrosinase) were tested and subtracted to correct the absorbance.

The Effects on the Diphenolase Activity of Tyrosinase

The method was performed as previously described (Chen et al., 2017). The assays were carried out by using 3 mL of reaction system containing 0.5 mmol/L substrate (dopa) in 50 mmol/L PBS (pH = 6.8) at 305 K. The final concentration of tyrosinase was 13.33 U/mL. A 100 µL aliquot of HgCl₂ solutions with various concentrations (0.15, 0.31, 0.625, 1.25, 5, 10, and 20mmol/L) was added to the reaction system to give concentrations ranged from 10.42 to 666.67 µmol/L. The OD values of the reaction system in the presence of HgCl₂ solutions (A₁) were recorded at the wavelength of 475 nm using the UV spectrophotometer. The OD values of the reaction system in the absence of HgCl₂ and tyrosinase were used as a positive (A₂) and a negative (A₃) control, respectively. Relative enzymatic activity (%) = (A₁-A₃)/A₂×100%. The experiment was repeated three times. The IC₅₀ value was calculated as the concentration (leading to achieve 50% inhibition) according to the equation, which is obtained by curve fitting of the enzyme activity versus the concentrations of inhibitor.

Immobilized Tyrosinase for Analysis of Inhibitory Mechanism

Experiments were conducted to confirm the inhibitory mechanism of HgCl₂ on tyrosinase furtherly by using immobilized tyrosinase. In brief, we added 200 µL of diluted tyrosinase (2500 U/mL) to each well of a 24-well polystyrene plate and then covered the plate and incubated it at 4°C overnight to produce immobilized tyrosinase. The plate was brought to room temperature, and we thoroughly decanted the solution from wells and washed the wells two times with PBS to remove the unfixed enzyme. We added 3 mL of inhibitor solution to each well and incubated them at room temperature for 30 mins to assure the fully reaction between the inhibitor and

the enzyme, discarding the liquid following by washing the wells two times with PBS to remove the excess inhibitor. Then, 3 mL of PBS was added to each well, and they stood for 10 mins to make the dissociation of inhibitor-tyrosinase complex. WE thoroughly decanted the solution from wells to remove the dissociated inhibitor (the procedure was repeated three times). Finally, 3 mL of substrate (dopa) was added to each well and react at room temperature for 30 mins to test the residual activity of tyrosinase. The tested samples included PBS (negative control), 95% ethanol (positive control of irreversible inhibitor), kojic acid (positive control of reversible inhibitor), and HgCl₂, and each sample was tested three times. The concentration of Kojic acid and HgCl₂ was both 666.67 μmol/L.

Kinetic Analysis for Non-Competitive Inhibition

The non-competitive inhibition type of tyrosinase was assayed by a Lineweaver–Burk plot, which can be described as the following equation:

$$\frac{1}{v} = \frac{K_m}{V_{\max}} \left(1 + \frac{[I]}{K_i} \right) \frac{1}{[S]} + \frac{1 + \frac{[I]}{K_i}}{V_{\max}} \quad (1)$$

and a secondary plot is presented below

$$\text{In.} = \frac{[I]}{K_i V_{\max}} + \frac{1}{V_{\max}} \quad (2)$$

where v is velocity of the enzyme reaction calculated by a change in absorbance at the wavelength of 475 nm per minute in the absence and presence of HgCl₂. K_m and K_i are the Michaelis–Menten constant and inhibition constant, respectively. The values of K_m can be calculated from the equation (1). $[I]$ and $[S]$ are the concentrations of inhibitor and substrate, respectively. In. is the intercept value of the Lineweaver–Burk curve. K_i should be calculated by the secondary plot of In. vs. $[I]$.

Intrinsic Fluorescence Quenching

The fluorescence emission spectra were obtained using Spectrofluorometer FS5 (Edinburgh Instruments, England) equipped with a 150 W xenon lamp and a thermostat bath. We added a 2.0 mL aliquot of tyrosinase solution (400 U/mL) to the quartz cuvette (1 cm path length) and gradually added 2 mmol/L solution of HgCl₂ to give concentrations ranged from 0 to 400 μmol/L. After five-minute incubation periods, fluorescence in the range of 290–500 nm was measured while the excitation wavelength was fixed at 280 nm. All the fluorescence data collected from these experiments were corrected for absorption of excitation light and re-absorption of emitted light according to the following equation: (Wang et al., 2015)

$$F_c = F_m e^{(A_1 + A_2)/2} \quad (3)$$

where F_c and F_m represent the corrected and measured fluorescence, respectively. A_1 and A_2 are the absorbance of HgCl₂ at excitation and emission wavelengths, respectively.

Molecular Docking Study

Molecular docking study was performed by using AutoDock 4.2.6. The X-ray crystal structure of *Agaricus bisporus* tyrosinase (PDB ID: 2Y9W) and the 3D structure of HgCl₂ were both retrieved from the RCSB Protein Data Bank (Ismaya et al., 2011). All input files were prepared using an AutoDockTools (ADT) 1.5.4 package, and a charge of +2 was assigned for copper ions. In order to carry out the docking simulation, a 60 Å × 60 Å × 60 Å -point grid with a spacing of 0.375 Å centered at 4.827, 28.489, 92.878 Å was defined, which fully enclosed the catalytic center of tyrosinase. The AutoGrid program was used to construct the grid maps for energy scoring. The three-dimensional location and orientation of the HgCl₂ was explored using the Lamarckian genetic algorithm (LGA). The docking results generated 100 conformations of HgCl₂, which were grouped into clusters by a root mean square (RMS) deviation tolerance of 2.0. The lowest energy (optimal conformation) and the largest number cluster (suboptimal conformation) were chosen for further analyses with the PyMOL molecular graphics system.

The Interactions Between HgCl₂ and Amino Acid

According to the results of docking study, we furtherly checked the interactions between HgCl₂ and amino acid. We assumed that if HgCl₂ indeed binds to the amino acid residues of the enzyme, such as His, Val, Glu, and Ala, premixing the amino acid with HgCl₂ would affect the inhibitory effects. Thus, the monophenolase and diphenolase activity of tyrosinase both were determined by adding the mixture of HgCl₂ and amino acid. The mixture was prepared just before use by adding an aliquot of 200 μL HgCl₂ solution to the equal volume of amino acid solution, and which was allowed to react for 10 mins at room temperature. Furtherly, to prove the interaction between His and HgCl₂, the UV-Vis spectra of His, HgCl₂, and the mixture of both were measured. In brief, 5 and 10 mmol/L solutions of His, HgCl₂ were prepared beforehand, and the mixture was produced by mixing the His and HgCl₂ solutions (10 mmol/L) in the volume ratio of 1:1. The spectra of the samples at the wavelengths between 200 and 800 nm were scanned by using UV spectrophotometer (UV 2550, SHIMADZU). The experiment was repeated three times.

Statistical Analysis

Each data point of the experimental results, including tyrosinase activity assay, kinetic analysis for non-competitive type inhibition, fluorescence quenching test, and interactions between amino acid and HgCl₂, was repeated at least three times. The data are presented as the mean ± SD (standard deviation). The statistical significance was determined at the level of P-value (< 0.05) by one-way analysis of variance.

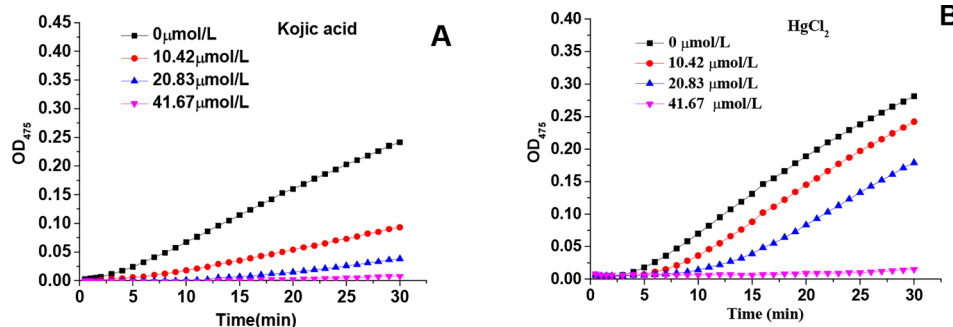


FIGURE 1 | Effects of various concentrations of kojic acid and HgCl_2 on monophenolase: progression of tyrosine oxidation by tyrosinase in the presence of various concentrations of kojic acid (A) and HgCl_2 (B).

RESULTS AND DISCUSSION

Effects of HgCl_2 on the Monophenolase Activity of Tyrosinase

Figures 1A, B showed the kinetic progression of tyrosine oxidation by tyrosinase in the presence of various concentrations of kojic acid and HgCl_2 , respectively. With the increase of kojic acid concentration, the lag time was prolonged from 1.44 min to approximately 10.33 min. Similarly, HgCl_2 also exhibited a marked inhibitory effect with significant prolongation of the lag period from 2.00 to 13.4 mins. The inhibitory effects of HgCl_2 on monophenolase were activity dependent on the concentrations because the steady rate (the slope of linear part of the kinetic equation) decreased with the increasing concentration of the inhibitors (Park et al., 2005). The IC_{50} values of kojic acid and HgCl_2 were 13.10 and 29.97 $\mu\text{mol/L}$, respectively, suggesting that HgCl_2 had less inhibitory capability than kojic acid on monophenolase activity.

Effect of HgCl_2 on the Diphenolase Activity of Tyrosinase

Both kojic acid and HgCl_2 significantly inhibited the diphenolase activity in a dose-dependent manner, as shown in Figure 2. With an increase in the concentration of kojic acid and HgCl_2 , the diphenolase activities decreased rapidly with IC_{50} values of 73.05 and 77.93 $\mu\text{mol/L}$, respectively. HgCl_2 exhibited significant inhibitory effect on the monophenolase activity also showed the same inhibitory effect on diphenolase activity, indicating it could inhibit the melanin synthesis in the early enzymatic stages. It is well-known that mercury replaces the copper required for tyrosinase activity, but once copper becomes attached to the enzyme it is replaced by ions of mercury with difficulty (Lerner, 1952b). That is to say, mercury was commonly considered to inhibit the melanin production by preventing the formation of the activated tyrosinase *via* replacement of copper ions. However, in this study, we found that mercury could inhibit both the monophenolase and diphenolase activity of tyrosinase by binding to the enzyme directly instead of replacing the copper ions required for tyrosinase.

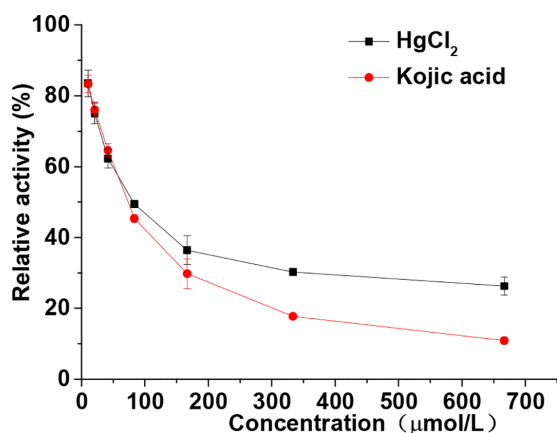


FIGURE 2 | Relative activity of tyrosinase through diphenolase reactions with dopa in the presence of various concentrations (from 10.42–666.67 $\mu\text{mol/L}$) of HgCl_2 and kojic acid. The final concentrations of dopa were 0.5 mmol/L. Data are presented as mean \pm standard deviation ($n = 3$).

Inhibition Mechanism of HgCl_2 on Tyrosinase

The relationship between enzyme activity (expressed as the rate of the oxidation reaction) and its concentration (6.67, 13.33, 20, 26.67, and 33.33 U/mL) in the presence of different concentrations of HgCl_2 (0, 4.17, 16.67, 33.33, and 66.67 $\mu\text{mol/L}$) was investigated. A series of parallel (or roughly parallel) lines with the same slope and different abscissa intercepts (Figure 3A) were observed from the plots of tyrosinase activity versus the concentrations of enzyme in the presence of various concentrations of HgCl_2 , suggesting the inhibition of HgCl_2 on tyrosinase was irreversible (Qiu et al., 2005). The increase of abscissa intercept indicated that the number of effective enzyme molecules decreased due to the irreversible inhibition.

In order to prove the irreversible inhibition furtherly, immobilized tyrosinase was used to study the effects of HgCl_2 on tyrosinase, the results of which were shown in Figure 3B. As a negative control, the activity of tyrosinase treated by PBS was

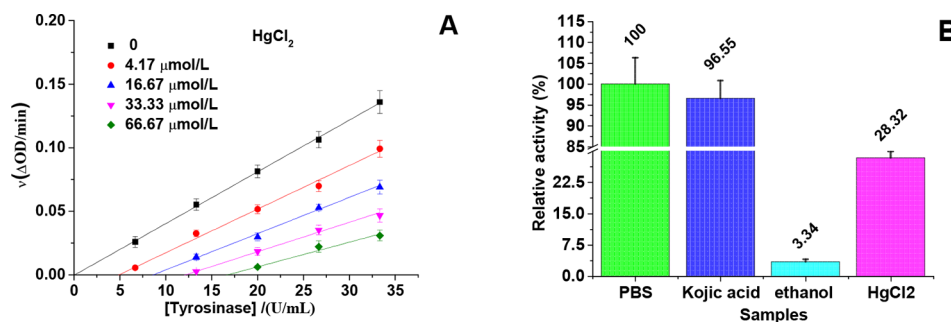


FIGURE 3 | Inhibition mechanism of HgCl_2 on tyrosinase. **(A)** An irreversible inhibition of the enzyme on a kinetic basis: the concentrations of HgCl_2 were 0, 4.17, 16.67, 33.33, and 66.67 $\mu\text{mol/L}$ for curves, and the concentrations of tyrosinase were 6.67, 13.33, 20, 26.67, and 33.33 U/mL. **(B)** Immobilized tyrosinase for analysis of inhibitory mechanism: As a negative control, the activity of tyrosinase with PBS treatment was defined as 100%, and the concentration of kojic acid and HgCl_2 were both 666.67 $\mu\text{mol/L}$. The experiment was repeated three times ($n = 3$).

defined as 100%. The activity of tyrosinase treated by kojic acid returned to 96.55% because of the reversible inhibition, whilst treated by 95% ethanol only returned to 3.34% because of the irreversible inhibition. The activity of tyrosinase treated by HgCl_2 returned to 28.32%, indicating HgCl_2 indeed inhibits the tyrosinase in an irreversible way compared to kojic acid. However, the enzyme activity is much higher than the one treated by 95% ethanol, which may be due to the fact that the amount of the inhibitor (HgCl_2) is not enough to inactivate the whole enzyme molecules coated on the plate.

Inhibition Type of HgCl_2 on the Tyrosinase

The inhibitory effect of HgCl_2 on the diphenolase activity was studied by the Lineweaver-Burk double reciprocal plots. As shown in **Figure 4A**, the horizontal axis intercept ($-1/K_m$) keeps the value unchanged and the vertical axis intercept ($1/V_{max}$) increases with the increasing inhibitor concentration, indicating that HgCl_2 induced a non-competitive inhibition (Chen et al., 2005). Therefore, HgCl_2 could bind both free enzyme and the enzyme-substrate complex with the same inhibition constants (K_i). The value of K_i (29.41 $\mu\text{mol/L}$) was

obtained from a plot of the vertical axis intercept (intercept of Lineweaver-Burk double reciprocal plots) versus the inhibitor concentration (Mu et al., 2013), as shown in **Figure 4B**.

Effects of HgCl_2 on Tyrosinase Conformational Change

From the result of the intrinsic fluorescence spectra, we observed that HgCl_2 bound to the tyrosinase resulted in conformational changes of tyrosinase: the spectra were gradually decreased in a dose-dependent manner (**Figures 5A, B**). The concentrations of HgCl_2 for the curves (a–f) were 0, 95.24, 181.82, 260.87, 333.33, and 400.00 $\mu\text{mol/L}$, respectively. Although the decrease in the fluorescence intensity were caused by quenching, there were no significant wavelength shift with the accumulation of HgCl_2 , indicating that tyrosinase does not undergo conspicuous overall structural changes. Moreover, the fluorescence intensity decreased with the increasing concentration of the inhibitor because of the tryptophan-masking properties of HgCl_2 , which implied that the tyrosinase became disagglomerated, and its structure was loosened (Donghyun et al., 2006).

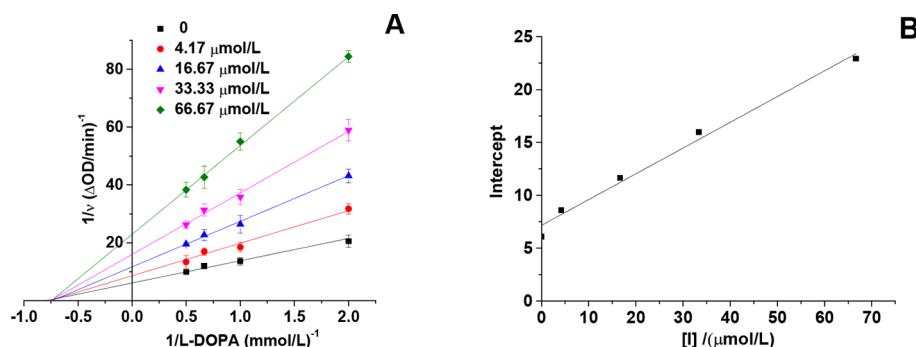


FIGURE 4 | Lineweaver-Burk plot of mushroom tyrosinase in the presence of HgCl_2 : $c(\text{tyrosinase}) = 13.33$ U/mL, $c(\text{HgCl}_2) = 0, 4.17, 16.67, 33.33$, and 66.67 $\mu\text{mol/L}$ for curves, respectively. The experiment was repeated three times ($n = 3$).

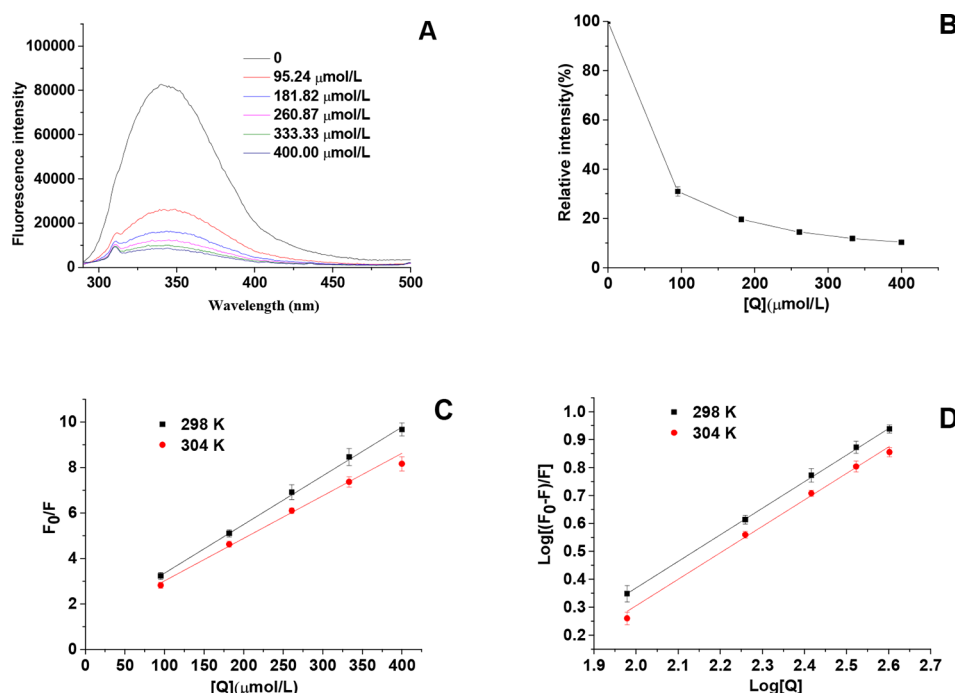


FIGURE 5 | (A) Intrinsic fluorescence spectra of tyrosinase in the presence of HgCl₂ at various concentrations, which were 0, 95.24, 181.82, 260.87, 333.33, and 400.00 μmol/L for curves, respectively. **(B)** Relative intensity (%) of tyrosinase at various concentrations of HgCl₂ (298K). **(C)** The Stern–Volmer plots for the fluorescence quenching of tyrosinase at various temperatures (298 and 304 K). **(D)** Plots of log [(F₀-F)/F] against log [Q] at various temperatures (298 and 304 K). F₀ and F are the fluorescence intensities of tyrosinase in the absence and presence of HgCl₂, and [Q] represents the concentration of HgCl₂. The experiment was repeated three times (n = 3).

To identify the interaction mechanism of HgCl₂ on tyrosinase, the data of fluorescence quenching were presented in the form of a Stern–Volmer plot, using the following equation:

$$F_0/F = 1 + K_q \tau_0 [Q] = 1 + K_{sv} [Q] \quad (4)$$

where, F_0 and F represent the steady-state fluorescence intensities in the absence and presence of HgCl₂ (quencher), respectively, $[Q]$ denotes the concentration of HgCl₂, K_q is the quenching rate constant of the biomolecule ($K_q = K_{sv}/\tau_0$), K_{sv} is the Stern–Volmer dynamic quenching constant, and τ_0 is the average lifetime of the fluorophore in the absence of quencher ($\tau_0 = 10^{-8}$ s). The value of K_{sv} determined by the linear regression plot of F_0/F vs. $[Q]$ at 298 and 304 K were $(2.14 \pm 0.05) \times 10^4$ and $1.83 \pm 0.03 \times 10^4$ L/mol, respectively. The plot (**Figure 5C**) showed a good linear relationship, indicating that a single type of quenching process (static or dynamic quenching) occurred during the formation of HgCl₂-tyrosinase complex. K_{sv} values decreased gradually with the increase of the temperatures, which manifested that the fluorescence quenching of tyrosinase by HgCl₂ was a static quenching process (Lin et al., 2018). The corresponding K_q values of $(2.14 \pm 0.05) \times 10^{12}$ and $(1.83 \pm 0.03) \times 10^{12}$ L/mol/s at 298 and 304 K were much higher than the maximum scattering collision quenching constant (2.0×10^{10} L/mol/s) (Abouzied and Alshihi, 2008), suggesting that

static quenching is dominant in the HgCl₂-tyrosinase interaction (Wang et al., 2014).

For static quenching interactions, if there are similar and independent sites in biological molecules, the apparent binding constants (K_a) and the number of binding sites (n) can be obtained from the following equation:

$$\log \frac{F_0 - F}{F} = \log K_a + n \log [Q] \quad (5)$$

According to the intercept and slope value of the regression curve (**Figure 5D**), the values of K_a and n for metal-tyrosinase interaction were calculated based on equation (5). The K_a value of $(2.87 \pm 0.02) \times 10^4$ L/mol achieved the order of magnitude of 10^4 L/mol, indicating the moderate binding of HgCl₂ to tyrosinase (Fan et al., 2017). The results of the section (INHIBITION MECHANISM OF HgCl₂ ON TYROSINASE) showed that HgCl₂ had a significant inhibitory effect on tyrosinase that was irreversible. We suggested that HgCl₂ might be irreversibly coordinated with the amino acid residues of tyrosinase to form the HgCl₂-tyrosinase complexes, resulting in the conformation change of the catalytic center of tyrosinase. Furthermore, the n values (0.96 ± 0.01) were close to one, suggesting that there was a single binding site or a single class of binding sites in tyrosinase for HgCl₂.

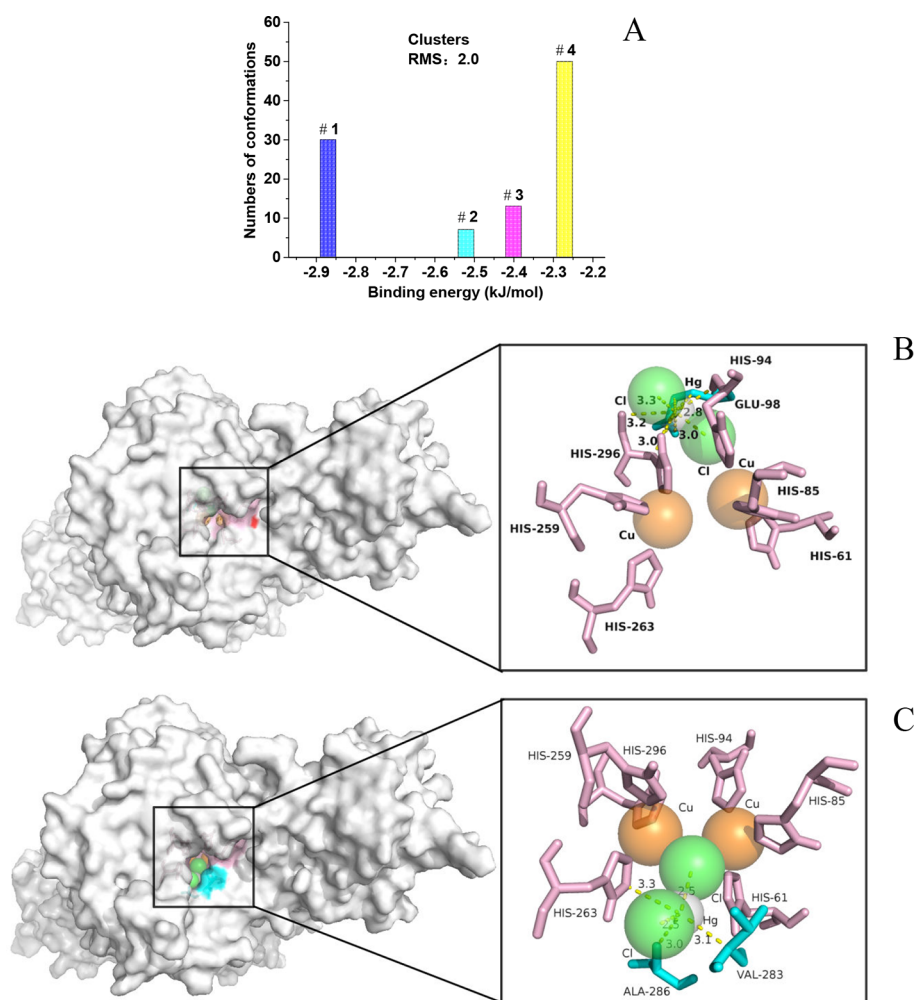


FIGURE 6 | (A) Group the conformations into clusters at the specified RMS deviation tolerance of 2.0; **(B)** details of the optimal conformation; **(C)** details of the suboptimal conformation.

Docked Conformations

Molecular docking was further performed to explore the interaction between HgCl_2 and tyrosinase. We cluster all the conformations (100) with ADT by a root mean square (RMS) deviation tolerance of 2.0, resulting in four clusters, as shown in **Figure 6A**. The X position of each bar is plotted by the energy of the lowest energy conformation in the cluster, and the height of the bar represents the number of docked conformations in each cluster. The best docking result (optimal conformation) can be recognized as the lowest energy conformation, and can also be selected according to the RMS deviation from the reference structure (usually the crystallographic bonding mode) (Morris et al., 2008). Thus, a lowest energy (-2.87 kJ/mol) conformation in the first cluster is recognized as the optimal conformation, as shown in **Figure 6B**. A lowest energy (-2.27 kJ/mol) conformation in the fourth cluster was recognized as the suboptimal conformation because the conformation-like one with the ligand (tropolone) binds to the catalytic center of tyrosinase (Ismaya

TABLE 1 | Information between the amino acid residues and HgCl_2 .

Conformations	Binding energy (kJ/mol)	Residue	Atom of the residue ^a	Distance(Å)
Optimal	-2.87	His 94	O	2.8
		His 296	O	3.2
		His 296	CB	3.0
		His 296	HD	3.0
		Glu 98	OE	2.7
		Glu 98	ND	3.6
		Glu 98	CD	3.3
		Glu 98	CG	3.3
		Glu 98	CB	2.8
Suboptimal	-2.27	His 263	CE	3.3
		His 263	ND	3.5
		His 263	NE	3.9
		Ala 286	CB	3.0
		Val 283	CA	3.1

^aThe first character of the atom name consists of the chemical symbol for the atom type. All the atom names beginning with "C" are carbon atoms; "N" indicates a nitrogen and "O" indicates oxygen. The next character is the remoteness indicator code, which is transliterated according to: "B" stands for (-) "β"; "G" ~ "γ"; "D" ~ "δ"; "E" ~ "ε"; "Z" ~ "ζ"; and "H" ~ "η".

et al., 2011), as shown in **Figure 6C**. For the optimal conformation, HgCl_2 is surrounded by amino acid residues (His 94, His 296, and Glu 98), whilst the suboptimal conformation is located adjacent to amino acid residues (His 263, Ala 286, and Val 283). The detailed information of interaction between the amino acid residues and HgCl_2 is summarized in **Table 1**. As we all know, the catalytic center of tyrosinase is like a pocket, which consists of two Cu ions and six histidine residues, including His 61, His 85, His 94, His 259, His 263, and His 296 (Ismaya et al., 2011). Therefore, it can be inferred that the HgCl_2 may change the morphology of catalytic center by binding with the amino acid residues, such as His 94, His 296, and His 263. Some experiments (in next section) were furtherly designed to support this point.

Further Exploration of Binding Sites

Amino acids, including His, Val, Glu, and Ala, were checked to see whether they have any impact on the inhibitory effect of HgCl_2 on tyrosinase. It was found that only His exhibited the significant effect on protecting the diphenolase activity in the presence of HgCl_2 , as shown in **Figure 7A**. We also found that His took effects in a concentration-dependent manner, and the protecting capability increased from $48.83 \pm 1.89\%$ to $83.43 \pm 2.56\%$ with the increasing concentrations ranged from 10.42 to 666.67 $\mu\text{mol/L}$, which is illustrated in **Figure 7B**. The effects of His on monophenolase activity in the presence of HgCl_2 were shown in **Figure 7C**, which demonstrated that His also protect the monophenolase activity when compared to **Figure 1B**. Val, Glu, and Ala still exhibited no effects on protecting the monophenolase activity (Data no shown).

The results demonstrated that HgCl_2 preferred to bind with His rather than other amino acid residues, such as Val, Glu, and Ala. Once HgCl_2 bound to free His, it was difficult to bind it to the residual His, which resulted in the protective effects. In order to further prove the interaction between His and HgCl_2 , the UV-Vis spectra of His, HgCl_2 , and the mixture of both is presented in **Figure 7D**; this shows the significant difference between the mixture and His (or HgCl_2), suggesting the formation of His- HgCl_2 complexes. Thus, based on this indirect and direct evidence (results of docking study), we believe that HgCl_2 exhibits inhibitory effects on tyrosinase by binding to the amino residual (His) of the catalytic center of tyrosinase.

CONCLUSIONS

In this paper, kinetics studies, different spectroscopic measurements, and molecular docking studies were employed to explore the inhibitory effects and mechanism of HgCl_2 on tyrosinase. For monophenolase, HgCl_2 could obviously prolong its lag time and decrease its steady-state rate with the IC_{50} value of 29.97 $\mu\text{mol/L}$. A kinetic study showed that HgCl_2 could also significantly inhibit the diphenolase activity with the IC_{50} value of 77.93 $\mu\text{mol/L}$ in an irreversible non-competitive manner. HgCl_2 quenched the fluorescence of tyrosinase by a static procedure and formed an irreversible complex with K_i value of 29.41 $\mu\text{mol/L}$. The molecular docking study suggested that HgCl_2 bound to the His residual of the catalytic center of tyrosinase and might change the morphology, leading to the inhibitory effects. Our studies firstly demonstrated that

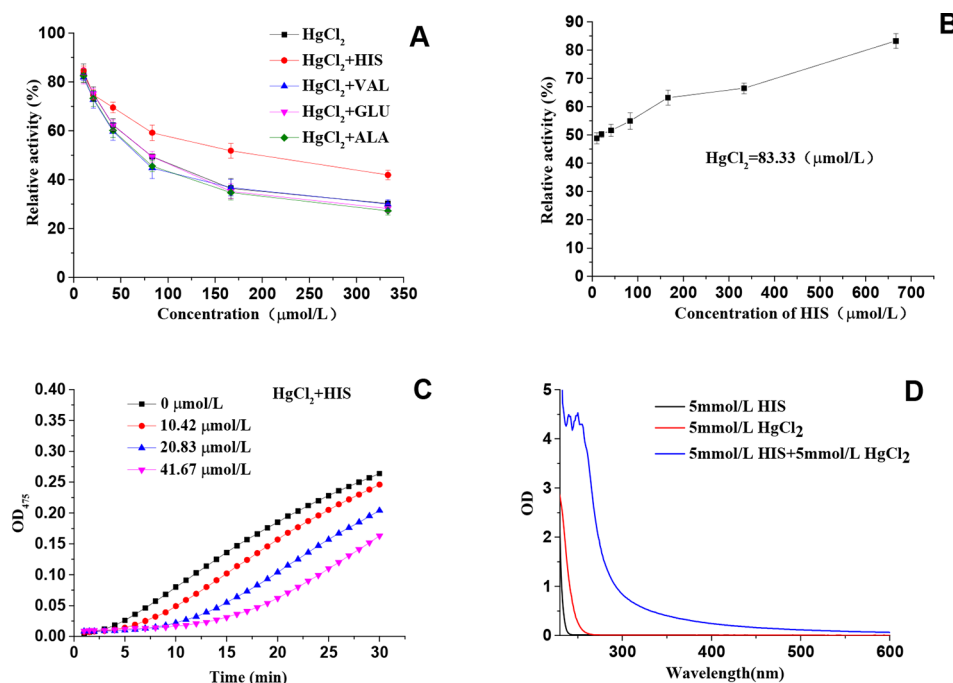


FIGURE 7 | (A) Effects of amino acids on protecting the diphenolase activity in the presence of HgCl_2 ; **(B)** The relationship between the protecting effects and the concentration of His; **(C)** Effects of His on protecting the monophenolase activity in the presence of HgCl_2 ; **(D)** The UV-Vis spectra of His, HgCl_2 , and a mixture of both. The experiment was repeated three times ($n = 3$).

HgCl₂ has the capability to inhibit tyrosinase directly, which is helpful to further our understanding of the inhibition mechanism of mercury on tyrosinase and to expand the scientific understanding of the toxicity of mercury in organisms.

DATA AVAILABILITY STATEMENT

The datasets generated for this study are available on request to the corresponding author.

AUTHOR CONTRIBUTIONS

JC, ZR, and NJ contributed conception and design of the study and performed the docking study. YY, MR, and QL designed and

performed the inhibitory effects of HgCl₂ on tyrosinase. All authors contributed to manuscript revisions and read and approved the submitted version.

FUNDING

This work was supported by the Natural Science Foundation of Fujian Province (grant number 2019J01806), the Education Department of Fujian Province (grant number JZ160470), the Putian Science and Technology Bureau (grant number 2018SP3004), and the Training Program of Innovation and Entrepreneurship for Undergraduates (grant number 201811498003, 201811498027, and 201911498055).

REFERENCES

- Abouzied, O. K., and Alshihi, O. I. K. (2008). Characterization of subdomain IIA binding site of human serum albumin in its native, unfolded, and refolded states using small molecular probes. *J. Am. Chem. Soc.* 130, 10793–10801. doi: 10.1021/ja8031289
- Agrawal, S. S., and Mazhar, M. (2015). Adulteration of mercury in skin whitening creams – a nephrotoxic agent. *Curr. Med. Res. Pract.* 5, 172–175. doi: 10.1016/j.cmrp.2015.07.007
- Al-Saleh, I. (2016). Potential health consequences of applying mercury-containing skin-lightening creams during pregnancy and lactation periods. *Int. J. Hyg. Environ. Health* 219, 468–474. doi: 10.1016/j.ijheh.2016.03.002
- Barry, L., Nisha, M., and Kundu, R. V. (2011). Widespread use of toxic skin lightening compounds: medical and psychosocial aspects. *Dermatol. Clinics* 29, 111–123. doi: 10.1016/j.det.2010.08.010
- Boyd, A. S., Seger, D., Vannucci, S., Langley, M., Abraham, J. L., and King, L. E. (2000). Mercury exposure and cutaneous disease. *J. Am. Acad. Dermatol.* 43, 81–90. doi: 10.1067/mjd.2000.106360
- Chan, T. Y. K. (2011). Inorganic mercury poisoning associated with skin-lightening cosmetic products. *Clin. Toxicol.* 49, 886–891. doi: 10.3109/15563650.2011.626425
- Chen, Q.-X., Song, K.-K., Qiu, L., Liu, X.-D., Huang, H., and Guo, H.-Y. (2005). Inhibitory effects on mushroom tyrosinase by p-alkoxybenzoic acids. *Food Chem.* 91, 269–274. doi: 10.1016/j.foodchem.2004.01.078
- Chen, J., Yu, X., and Huang, Y. (2016). Inhibitory mechanisms of glabridin on tyrosinase. *Spectrochim. Acta A Mol. Biomol. Spectrosc.* 168, 111–117. doi: 10.1016/j.saa.2016.06.008
- Chen, J., Liu, S., Huang, Z., Huang, W., Li, Q., and Ye, Y. (2017). Molecular inhibitory mechanism of dihydromyricetin on mushroom tyrosinase. *J. Biomol. Struct. Dyn.* 36, 3740–3752. doi: 10.1080/07391102.2017.1397059
- Clarkson, T. W., Magos, L., and Myers, G. J. (2003). The toxicology of mercury – current exposures and clinical manifestations. *New Engl. J. Med.* 349, 1731–1737. doi: 10.1056/NEJMra022471
- Donghyun, K., Jiyeoun, P., Jinhee, K., Cheolkyu, H., Jeonghyeok, Y., Namdoo, K., et al. (2006). Flavonoids as mushroom tyrosinase inhibitors: a fluorescence quenching study. *J. Agric. Food Chem.* 54, 935–941. doi: 10.1021/jf0521855
- Fan, M., Zhang, G., Hu, X., Xu, X., and Gong, D. (2017). Quercetin as a tyrosinase inhibitor: inhibitory activity, conformational change and mechanism. *Food Res. Int.* 100, 226–233. doi: 10.1016/j.foodres.2017.07.010
- Germanò, M. P., Cacciola, F., Donato, P., Dugo, P., Certo, G., D'angelo, V., et al. (2012). Betula pendula leaves: polyphenolic characterization and potential innovative use in skin whitening products. *Fitoterapia* 83, 877–882. doi: 10.1016/j.fitote.2012.03.021
- Hamann, C. R., Boonchai, W., Wen, L., Sakanashi, E. N., Chu, C.-Y., Hamann, K., et al. (2014). Spectrometric analysis of mercury content in 549 skin-lightening products: is mercury toxicity a hidden global health hazard? *J. Am. Acad. Dermatol.* 70, 281–287.e283. doi: 10.1016/j.jaad.2013.09.050
- Hridya, H., Amrita, A., Mohan, S., Gopalakrishnan, M., Dakshinamurthy, T. K., Doss, G. P., et al. (2016). Functionality study of santalin as tyrosinase inhibitor: a potential depigmentation agent. *Int. J. Biol. Macromol.* 86, 383–389. doi: 10.1016/j.ijbiomac.2016.01.098
- Ismaya, W. T., Rozeboom, H. J., Weijn, A., Mes, J. J., Fusetti, F., Wichers, H. J., et al. (2011). Crystal structure of Agaricus bisporus mushroom tyrosinase: identity of the tetramer subunits and interaction with tropolone. *Biochemistry* 50, 5477–5486. doi: 10.1021/bi200395t
- Kibukamusoke, J. W., Davies, D. R., and Hutt, M. S. (1974). Membranous nephropathy due to skin-lightening cream. *Br. Med. J.* 2, 646–647. doi: 10.1136/bmj.2.5920.646
- Körner, A. M., and Pawelek, J. M. (1982). Mammalian tyrosinase catalyzes three reactions in the biosynthesis of melanin. *Science* 217, 1163–1165. doi: 10.1126/science.6810464
- Lerner, A. B. (1952a). Effect of ions on melanin formation. *J. Invest. Dermatol.* 18, 47–52. doi: 10.1038/jid.1952.6
- Lerner, A. B. (1952b). Mammalian tyrosinase: effect of ions on enzyme action. *Arch. Biochem. Biophys.* 36, 473–481. doi: 10.1016/0003-9861(52)90435-9
- Lin, M. Z., Chai, W. M., Chong, O. Y., Huang, Q., Xu, X. H., and Peng, Y. Y. (2018). Antityrosinase mechanism of omeprazole and its application on the preservation of fresh-cut Fuji apple. *Int. J. Biol. Macromol.* 117, 538–545. doi: 10.1016/j.ijbiomac.2018.05.172
- Morris, G. M., Huey, R., and Olson, A. J. (2008). Using AutoDock for ligand-receptor docking. *Curr. Protoc. Bioinf.* Chapter 8, Unit 8.14. 24 (1), 1–40. doi: 10.1002/0471250953.bi0814s24
- Mu, Y., Li, L., and Hu, S.-Q. (2013). Molecular inhibitory mechanism of triclin on tyrosinase. *Spectrochim. Acta A Mol. Biomol. Spectrosc.* 107, 235–240. doi: 10.1016/j.saa.2013.01.058
- Olumide, Y. M., Akinkugbe, A. O., Dan, A., Tahir, M., Ngozi, A., Shola, A., et al. (2008). Complications of chronic use of skin lightening cosmetics. *Int. J. Dermatol.* 47, 344–353. doi: 10.1111/j.1365-4632.2008.02719.x
- Park, K., Park, Y., Lee, J., Hahn, H., Lee, S., Bae, C., et al. (2005). Inhibition kinetics of mushroom tyrosinase by copper-chelating ammonium tetrathiomolybdate. *Biochim. Et Biophys. Acta Gen. Subj.* 1726, 115–120. doi: 10.1016/j.bbagen.2005.06.010
- Qiu, L., Chen, Q. Q., Huang, H., and Song, K. K. (2005). Irreversibly inhibitory kinetics of 3,5-dihydroxyphenyl decanoate on mushroom (Agaricus bisporus) tyrosinase. *Bioorganic Med. Chem.* 13, 6206–6211. doi: 10.1016/j.bmc.2005.06.034
- Seo, S. Y., And, V. K. S., and Sharma, N. (2003). Mushroom Tyrosinase: Recent Prospects. *J. Agric. Food Chem.* 51, 2837–2853. doi: 10.1021/jf020826f
- Soares, M. A., Almeida, M. A., Marins-Goulart, C., Chaves, O. A., Echevarria, A., and Mcc, D. O. (2017). Thiosemicarbazones as inhibitors of tyrosinase enzyme. *Bioorganic Med. Chem. Lett.* 27, 3546–3550. doi: 10.1016/j.bmcl.2017.05.057
- Tan, X., Song, Y. H., Park, C., Lee, K. W., Kim, J. Y., Kim, D. W., et al. (2016). Highly potent tyrosinase inhibitor, neorauflavane from *Campylotropis hirtella* and inhibitory mechanism with molecular docking. *Bioorganic Med. Chem.* 24, 153–159. doi: 10.1016/j.bmc.2015.11.040

- Wang, Y., Zhang, G., Yan, J., and Gong, D. (2014). Inhibitory effect of morin on tyrosinase: insights from spectroscopic and molecular docking studies. *Food Chem.* 163, 226–233. doi: 10.1016/j.foodchem.2014.04.106
- Wang, Y., Zhang, G., Pan, J., and Gong, D. (2015). Novel insights into the inhibitory mechanism of kaempferol on xanthine oxidase. *J. Agric. Food Chem.* 63, 526–534. doi: 10.1021/jf505584m
- Yoon, J., Fujii, S., and Solomon, E. I. (2009). Geometric and electronic structure differences between the type 3 copper sites of the multicopper oxidases and hemocyanin/tyrosinase. *Proc. Natl. Acad. Sci. U. S. A.* 106, 6585–6590. doi: 10.1073/pnas.0902127106

Conflict of Interest: The authors declare that the research was conducted in the absence of any commercial or financial relationships that could be construed as a potential conflict of interest.

Copyright © 2020 Chen, Ye, Ran, Li, Ruan and Jin. This is an open-access article distributed under the terms of the Creative Commons Attribution License (CC BY). The use, distribution or reproduction in other forums is permitted, provided the original author(s) and the copyright owner(s) are credited and that the original publication in this journal is cited, in accordance with accepted academic practice. No use, distribution or reproduction is permitted which does not comply with these terms.



The Thyrotropin-Releasing Hormone-Degrading Ectoenzyme, a Therapeutic Target?

Jean-Louis Charli*, Adair Rodríguez-Rodríguez, Karina Hernández-Ortega, Antonieta Cote-Vélez, Rosa María Uribe, Lorraine Jaimes-Hoy and Patricia Joseph-Bravo

Departamento de Genética del Desarrollo y Fisiología Molecular, Instituto de Biotecnología, Universidad Nacional Autónoma de México (UNAM), Cuernavaca, Mexico

OPEN ACCESS

Edited by:

Jean Sévigny,
Laval University, Canada

Reviewed by:

Gabor Wittmann,
Tufts Medical Center, United States
Albert Eugene Pekary,
VA Greater Los Angeles Healthcare
System, United States

*Correspondence:

Jean-Louis Charli
charli@ibt.unam.mx

Specialty section:

This article was submitted to
Experimental Pharmacology
and Drug Discovery,
a section of the journal
Frontiers in Pharmacology

Received: 04 February 2020

Accepted: 21 April 2020

Published: 08 May 2020

Citation:

Charli J-L, Rodríguez-Rodríguez A, Hernández-Ortega K, Cote-Vélez A, Uribe RM, Jaimes-Hoy L and Joseph-Bravo P (2020) The Thyrotropin-Releasing Hormone-Degrading Ectoenzyme, a Therapeutic Target? *Front. Pharmacol.* 11:640. doi: 10.3389/fphar.2020.00640

Thyrotropin releasing hormone (TRH: Glp-His-Pro-NH₂) is a peptide mainly produced by brain neurons. In mammals, hypophysiotropic TRH neurons of the paraventricular nucleus of the hypothalamus integrate metabolic information and drive the secretion of thyrotropin from the anterior pituitary, and thus the activity of the thyroid axis. Other hypothalamic or extrahypothalamic TRH neurons have less understood functions although pharmacological studies have shown that TRH has multiple central effects, such as promoting arousal, anorexia and anxiolysis, as well as controlling gastric, cardiac and respiratory autonomic functions. Two G-protein-coupled TRH receptors (TRH-R1 and TRH-R2) transduce TRH effects in some mammals although humans lack TRH-R2. TRH effects are of short duration, in part because the peptide is hydrolyzed in blood and extracellular space by a M1 family metallopeptidase, the TRH-degrading ectoenzyme (TRH-DE), also called pyroglutamyl peptidase II. TRH-DE is enriched in various brain regions but is also expressed in peripheral tissues including the anterior pituitary and the liver, which secretes a soluble form into blood. Among the M1 metallopeptidases, TRH-DE is the only member with a very narrow specificity; its best characterized biological substrate is TRH, making it a target for the specific manipulation of TRH activity. Two other substrates of TRH-DE, Glp-Phe-Pro-NH₂ and Glp-Tyr-Pro-NH₂, are also present in many tissues. Analogs of TRH resistant to hydrolysis by TRH-DE have prolonged central efficiency. Structure-activity studies allowed the identification of residues critical for activity and specificity. Research with specific inhibitors has confirmed that TRH-DE controls TRH actions. TRH-DE expression by β 2-tanycytes of the median eminence of the hypothalamus allows the control of TRH flux into the hypothalamus-pituitary portal vessels and may regulate serum thyrotropin secretion. In this review we describe the critical evidences that suggest that modification of TRH-DE activity in tanycytes, and/or in other brain regions, may generate beneficial consequences in some central and metabolic disorders and identify potential drawbacks and missing information needed to test these hypotheses.

Keywords: thyroid hormone, thyrotropin, thyrotropin-releasing hormone, thyrotropin-releasing hormone-degrading ectoenzyme, anxiety, depression, mood

INTRODUCTION

Thyrotropin releasing hormone (TRH; Glp-His-Pro-NH₂) is a small peptide expressed mainly in the brain, secreted by neurons. TRH interacts with plasma membrane G-protein-coupled receptors; one TRH receptor (TRH-R1) is detected in humans, whereas an additional one (TRH-R2) in rodents (Sun et al., 2003) and a total of three in teleosts and frogs (Bidaud et al., 2004; Saito et al., 2011). In mammals, TRH-R1 and TRH-R2 arise from different genes (Sun et al., 2003); the maps of their brain expression do not coincide (Heuer et al., 2000); they possess distinct ligand-independent activities, with TRH-R2 showing a stronger constitutive activity (Wang and Gershengorn, 1999). These distinct characteristics and the differential behaviors of KO mice for each receptor (Rabeler et al., 2004; Zeng et al., 2007; Sun et al., 2009) suggest that each type of receptor fulfills distinct functions in response to TRH. However, data in mice indicate that central TRH effects may depend mainly on TRH-R1 expression (Thirunarayanan et al., 2013).

The best-known function of TRH is the control of the hypothalamus–pituitary–thyroid (HPT) axis; TRH is synthesized by processing of a protein precursor in neurons of the paraventricular nucleus of the hypothalamus (PVN) that project their terminal boutons into the median eminence (hypophysiotropic neurons). Once released into the extracellular space TRH diffuses into the hypothalamic–pituitary portal vessels from where it controls secretion of thyrotropin (TSH) from the anterior pituitary. In turn, TSH controls the synthesis and secretion of thyroid hormones (TH) in the thyroid. This link adjusts TH secretion according to energy balance information, which is integrated by the hypophysiotropic PVN TRH neurons. TRH may also control prolactin secretion from the anterior pituitary (Martinez de la Escalera and Weiner, 1992; Joseph-Bravo et al., 2015b), although hypophysiotropic PVN TRH neurons regulating prolactin may differ from those controlling TSH secretion (Sánchez et al., 2001).

Various additional hypothalamic and extrahypothalamic neuronal populations express *Trh* (Lechan et al., 1986; Segerson et al., 1987; Hökfelt et al., 1989; Heuer et al., 2000), but their physiological role is not well understood. Soon after the discovery of extrahypothalamic TRH, several studies revealed central pharmacological effects of TRH that were independent of HPT axis control in laboratory animals, including increased locomotion, arousal, improvement of depression-like behaviors, reduction of epileptic seizures, and neuroprotection (Horita, 1998; Gary et al., 2003; Daimon et al., 2013; Fröhlich and Wahl, 2019). These observations led to attempts to use TRH in therapeutic contexts, for example in some neurodegenerative diseases (Gary et al., 2003; Daimon et al., 2013; Fröhlich and Wahl, 2019). Moreover, TRH is also present in selected loci outside the central nervous system whose importance is still poorly appreciated.

Early evidence that the half-life of TRH in rodent blood or in tissue extracts is 3–5 min (Redding and Schally, 1969; Prasad and Peterkofsky, 1976; Taylor and Dixon, 1976), and that TRH pharmacological effects are of short duration led to the

synthesis of TRH analogues with improved stability, agonist potency and/or brain accessibility (Horita, 1998; Gary et al., 2003; Daimon et al., 2013; Fröhlich and Wahl, 2019). Other efforts were directed to elucidate the mechanism contributing to the rapid extracellular disappearance of TRH. TRH can be removed from the brain extracellular space by transport into brain cells; nevertheless, this event has a small V_{\max} and may have a very limited quantitative importance (Charli et al., 1984). The molecular entity that contributes to this transport has not been characterized; it may reflect TRH-R mediated endocytosis (Ashworth et al., 1995), or the action of a TRH transporter (Bagul et al., 2014).

Alternatively, TRH may be hydrolyzed by peptidases. Pyroglutamyl peptidase I (PPI; EC 3.4.19.3) is a soluble cysteine aminopeptidase with a wide specificity, that hydrolyses almost any Glp-X peptide, except if X is a proline (Awadé et al., 1994). This enzyme is present in all life kingdoms, and found in many tissues, including brain. Although PPI hydrolyses TRH *in vitro* (Morier et al., 1979; O'Leary and O'Connor, 1995; Charli et al., 1998), the only evidence that it contributes to TRH turnover *in situ* is that an inhibitor of PPI (and PE) enhances TRH levels and release in primary cultures of hypothalamic cells (Faivre-Bauman et al., 1986). Since PPI action is probably restricted to the cytoplasm, it may contribute to the intracellular turnover of TRH leaking from intracellular granules, but its subcellular localization is not compatible with a post-secretory role. In support of this idea, the specific inhibition of PPI activity in brain slices does not change TRH release and the intraperitoneal injection of a specific inhibitor of PPI that inhibits brain PPI activity does not change brain TRH levels (Charli et al., 1987). Furthermore, inhibition of enzyme activity does not protect TRH from degradation in rat serum (Friedman and Wilk, 1985).

Prolyl endopeptidase (PE; EC 3.4.21.26) is a serine endopeptidase with a wide specificity; it hydrolyses internal Pro-X peptide bonds, except if X is a proline. This enzyme is soluble, present in all life kingdoms, and many tissues, including the mammalian brain, albeit a membrane-bound isoform has also been identified. PE hydrolyzes the Pro-NH₂ bond of TRH *in vitro* (Wilk, 1983; O'Leary and O'Connor, 1995; Charli et al., 1998; Tenorio-Laranga et al., 2008). PE role in TRH turnover *in vivo* is controversial; inhibition of PE enhances TRH levels and release in primary cultures of hypothalamic cells (Faivre-Bauman et al., 1986), the intraperitoneal injection of a PE inhibitor enhances TRH concentration in the cerebral cortex (Bellemere et al., 2005), and PE or a similar enzyme degrades TRH in rabbit seminal plasma (Siviter and Cockle, 1995). However, other experiments showed that PE inhibition in brain slices does not change TRH release into the medium and that the intraperitoneal injection of a specific inhibitor of PE does not change brain TRH levels *in vivo* (Charli et al., 1987). Furthermore, the intraseptal injection of a PE inhibitor does not change the effect of TRH on time of arousal from ethanol-induced narcosis in rats (Lazcano et al., 2012). Since PE regulates inositol polyphosphate phosphatase activities (Williams et al., 1999), the effect of PE inhibition on TRH levels may result from

an alteration of the intracellular turnover of the secretory granules that contain TRH. Likewise, inhibition of PE does not protect TRH from degradation in rat serum (Friedman and Wilk, 1985). Thus, in general, PE may not control the extracellular turnover of TRH.

Another peptidase that may hydrolyze TRH is prolyl carboxypeptidase (PCP; EC 3.4.16.2) (Jeong et al., 2012), but there is no evidence that PCP coincides with TRH or alters TRH biological actions *in vivo*. Therefore, the quantitative importance of the previously described mechanisms of inactivation of TRH may be very limited *in vivo*, in particular for its extracellular inactivation, due in most cases to incompatible subcellular localizations of peptide and enzymes (Charli et al., 1998). In sum, contrary to what is sometimes mentioned in the literature, neither uptake nor soluble peptidases constitute relevant mechanisms for the extracellular inactivation of TRH.

The discovery of the thyrotropin-releasing hormone-degrading ectoenzyme (TRH-DE; EC 3.4.19.6) stems from the identification of an enzymatic activity that hydrolyses the Glp-His bond of TRH, initially in serum and called thyroliberinase, to underpin its narrow specificity (Bauer et al., 1981), and later in brain (Garat et al., 1985). The most striking property of this pyroglutamyl peptidase is a very narrow specificity (Lanzara et al., 1989; Wilk and Wilk, 1989; Elmore et al., 1990; Gallagher and O'Connor, 1998; Heuer et al., 1998a), a compelling argument in favor of looking at this peptidase as a therapeutic target, for example when enhancement of TRH action may be beneficial. TRH-DE was initially named pyroglutamyl peptidase II (PPII), to stress its clear biochemical difference with PPI; in contrast to PPI, TRH-DE/PPII is a metallopeptidase (Czekay and Bauer, 1993). A review describing the major biochemical characteristics of TRH-DE was previously published (Sánchez et al., 2013).

In the next sections, we briefly review the structure and proposed physiological roles of TRH-DE, focusing on recent advances, and we identify major challenges to translate this knowledge to clinical applications. Although the biochemical, topological and functional properties of the enzyme strongly argue in favor of its implication in the extracellular inactivation of TRH, its role may vary with cellular context, and might extend beyond hydrolysis of TRH. Contexts in which an intervention on TRH-DE may have therapeutic potential are delineated, and limitations are identified.

TRHDE GENE, TRANSCRIPTS, PROTEIN STRUCTURE, ISOFORMS AND SPECIFICITY

The sequence and genomic locus of the *Trhde* gene (we use the rodent abbreviations for gene names throughout the review) was initially described in humans (Schomburg et al., 1999); there is only one gene localized on chromosome 12. In mammals, the *Trhde* gene is adjacent to the tryptophan hydroxylase 2 gene (<https://www.ensembl.org>). In mouse, the gene localizes to chromosome 10 (<http://www.informatics.jax.org/marker/MGI:2384311>) while in rats, to chromosome 7. *Trhde* gene

sequences and enzymatic activities have been detected in mammals, including activity in human serum and cerebrospinal fluid (Prasad and Jayaraman, 1986; Bundgaard and Møss, 1990; Charli et al., 1998). The gene is also detected in other vertebrate classes (Schomburg et al., 1999; Chávez-Gutiérrez et al., 2006). TRH-DE is not an essential gene in mice as TRH-DE KO animals are healthy, reproduce normally and their metabolic parameters are normal when bred in standard conditions (Tang et al., 2010).

Trhde transcription initiation sites have not been formally mapped. In mouse, three transcription start sites have been proposed (<http://www.informatics.jax.org/marker/MGI:2384311>); two are conserved in rat for which various transcripts differing widely in size have been detected (Schauder et al., 1994). Apart from alternative transcription start sites, there is little information about the mechanisms that lead to transcript diversity, except for a potential alternative splicing event in rats at exon 14-intron 14 boundary that leads to a truncated TRH-DE isoform (Chavez-Gutierrez et al., 2005). In mice three alternative splicing events may generate various TRH-DE isoforms (<http://www.informatics.jax.org/>). Bioinformatic approaches suggest that in mice response elements for multiple transcription factors exist along the 2 Kb region upstream from the most upstream of the predicted transcriptional start sites (Figure 1). However, promoter structure and genomic regulatory elements have not been experimentally mapped.

Another transcript derived from the human *Trhde* locus is *Trhde* antisense RNA 1 (*Trhde-as1*) (https://www.ncbi.nlm.nih.gov/nucleotide/NR_026837). This long non-coding RNA is found in the cytoplasm and binds directly to miR-103 in samples of human lung, inhibiting parameters of human lung cancer progression (Zhuan et al., 2019). Individuals challenged with

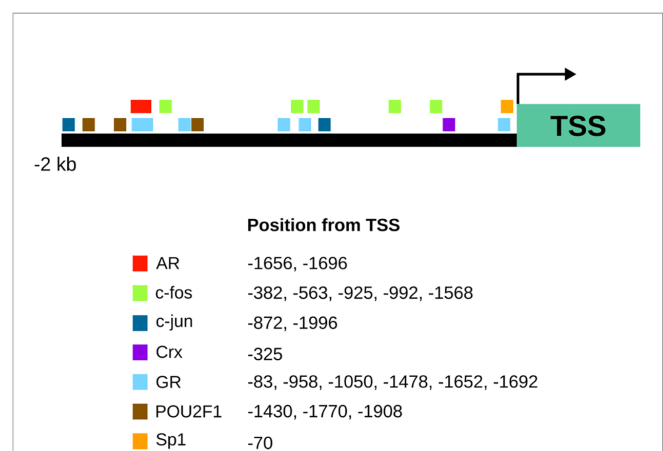


FIGURE 1 | A map of candidates for transcriptional regulation of *Trhde* expression predicted by bioinformatic analysis. Transcription factor binding sites were identified 2 kb upstream of the most upstream of the 3 predicted transcriptional start sites (TSSR99301) of the mouse with PROMO (Messegueur et al., 2002; Farre, 2003). This site is conserved in rats. AR, androgen receptor; Crx, Cone-rod homeobox protein; GR, glucocorticoid receptor; NF-kappaB, nuclear factor kappa-light-chain-enhancer of activated B cells; POU2F1, POU domain, class 2, transcription factor 1; Sp1, specificity protein 1.

an injection of LPS show a significant drop of *Trhde-as1* expression in adipose tissue samples (Ferguson et al., 2016). The relevance of *Trhde-as1* expression for *Trhde* function is unknown.

The purification and cloning of the rat brain/pituitary isoform revealed that TRH-DE is 1,025 amino acids long (1,024 in human) (Bauer, 1994; Schauder et al., 1994). TRH-DE is a member of the M1 family of zinc-aminopeptidases, a family of 12 members (in humans) that includes aminopeptidases that have a wider specificity than TRH-DE, including aminopeptidase N (the closest relative of TRH-DE), which preferentially hydrolyses neutral aminoacids from the N-terminus (Sjöström et al., 2002). Although TRH-DE 3D structure is still unknown, analogy with other members of the family suggests it is a type II cell surface peptidase with a small intracellular domain, a single transmembrane domain, and a large extracellular part with a flexible stem followed by a catalytic domain, and an additional domain separated by a flexible loop (Chávez-Gutiérrez et al., 2006). Topology of the domains is consistent with biochemical evidence that demonstrated TRH-DE is an ectoenzyme (Charli et al., 1988), making it a prime candidate for primary hydrolysis of TRH in the extracellular space.

A large set of TRH derivatives has been tested to define TRH-DE specificity; TRH analogues modified on the C- or N-terminal residues are poor substrates of TRH-DE (Lanzara et al., 1989; Wilk and Wilk, 1989; Heuer et al., 1998a; Kelly et al., 2000). For example, gonadotropin-releasing hormone (GnRH), a decapeptide with a N-terminal Glp-His is not a substrate of TRH-DE (O'Connor and O'Cuinn, 1985; Elmore et al., 1990; Gallagher and O'Connor, 1998). Substitution of the histidyl residue of TRH by a series of amino acids influences the ability of porcine TRH-DE to catalyze the hydrolysis of the Glp-X bond in TRH-like peptides; thus, TRH-like peptides substituted with Gly, Asn, Gln, Trp, Glu, Asp, Pro or Cys are not substrates of TRH-DE, while low turnover rates are observed with Ala, Ser, Thr, Ile, Leu, Val. In contrast, TRH-like peptides substituted with Tyr or Phe have turnover rates approaching that of TRH (Kelly et al., 2000). This agrees with evidence that Glp-Phe-Pro-NH₂ is a substrate of bovine brain TRH-DE (Kelly et al., 1997; Gallagher and O'Connor, 1998). The structural determinants of TRH-DE narrow specificity have been partially clarified; two amino-acid substitutions in the catalytic domain are critical and form a conserved signature that distinguishes it from other M1 family members (Chávez-Gutiérrez et al., 2006).

One of the two TRH-like peptides that are relatively good substrates of the enzyme *in vitro*, Gln-Phe-Pro-NH₂, has been detected in peripheral organs including pancreas and thyroid gland (Khan et al., 1992; Gkonos et al., 1994; Kulkarni et al., 1995). Although it was initially suggested that TRH-like peptides, other than TRH, were not detectable in brain (Rondeel et al., 1995a; Rondeel et al., 1995b), it was later shown that, among other, Gln-Tyr-Pro-NH₂, and Gln-Phe-Pro-NH₂ are present in brain (Pekary et al., 2004; Pekary et al., 2005). To our knowledge, although these peptides are likely the product of posttranslational processing of precursor peptides (Linden et al., 1996), the precursors are still unknown. However, they

may act as intercellular messengers, including in the brain, since their concentrations can vary rapidly in response to some stimuli, suggesting changes in synthesis and/or release (Pekary and Sattin, 2012; Pekary et al., 2015), and there is direct evidence that a peptide similar to Gln-Phe-Pro-NH₂ can be released into hypothalamic extracellular space *in vitro* (Méndez et al., 1999). *Bona fide* receptors for Gln-Phe-Pro-NH₂ and Gln-Tyr-Pro-NH₂ have not been detected; they are weak agonists of TRH receptors (Hinkle et al., 2002).

Information about TRH-DE biosynthesis, transport and turnover is scant. The membrane isoform is a N-glycosylated protein; within its large extracellular domain, 12 putative N-glycosylation sites are found (Schauder et al., 1994). In its native form, TRH-DE can be partially deglycosylated (by about 50%) without affecting its activity (Bauer, 1994). The relevance of remaining glycosyl residues is not yet known. N-linked protein glycosylation starts in the endoplasmic reticulum and is a conserved process in eukaryotic cells. The subsequent details of processing that occur in Golgi compartments, according to protein-, cell- and species-specific clues (Aebi, 2013), have not been described for TRH-DE. Thyroliberinase, the soluble isoform secreted into blood, may be a product of alternative splicing or proteolysis (Schmitmeier et al., 2002). A membrane-bound truncated TRH-DE (TRH-DE*) is detected in many tissues, formed probably through an alternative splicing event; TRH-DE* does not hydrolyze TRH but it inhibits TRH-DE activity when it dimerizes with the full-length TRH-DE (Chavez-Gutierrez et al., 2005). In line with these results, correlative evidence suggests that the tissue-specific pattern of TRH-DE activity is defined in part by the *Trhde/Trhde** expression ratio (Chavez-Gutierrez et al., 2005). Finally, little is known about TRH-DE interactions with other proteins. TRH-DE* may interact physically with Akt1 in mesenchymal-derived soft tissue sarcoma (STS) cell lines (Zhu et al., 2011) but an interpretation of the physiological relevance of this interaction awaits resolution.

SPECIFIC INHIBITORS OF TRH-DE

To investigate the biological functions of TRH-DE, TRH-DE inhibitors have been synthesized. Protease inhibitors frequently include structural features that enable their interaction with the active site of the enzyme (Cushman et al., 1977; Kaysser, 2019). TRH-DE is weakly inhibited by the products of hydrolysis of TRH, Glp and His-Pro-NH₂; combination of these molecules with zinc-binding groups results in poor TRH-DE inhibitors (Bauer et al., 1997). In general, TRH derivatives with modifications to the C- or N-terminal residues of TRH do not inhibit TRH-DE activity (Lanzara et al., 1989; Wilk and Wilk, 1989; Elmore et al., 1990; Gallagher and O'Connor, 1998; Kelly et al., 2000). However, GnRH, a Glp-His peptide C-terminally extended with hydrophobic residues does inhibit TRH-DE activity (O'Connor & O'Cuinn, 1985; Elmore et al., 1990; Gallagher and O'Connor, 1998). Furthermore, some analogues modified on the histidine residue have also shown some

potential. Thus, the first specific inhibitor described was N-[1-carboxy-2-phenylethyl]N-imidazole benzyl histidyl- β -naphthylamide (CPHNA). With a K_i of 8 μ M, CPHNA has no effect on TRH receptors and does not inhibit PE activity (Charli et al., 1989).

The systematic screening of a directed peptide library led to the finding that Glp-Asn-Pro-7-amido-4-methyl coumarin (Glp-Asn-Pro-AMC) has a K_i of 0.97 μ M, making this peptide a relatively potent reversible TRH-DE inhibitor (Kelly et al., 2000). Improved potency was achieved by extension of Glp-Asn-ProNH₂ with hydrophobic amino acids at the C-terminus. Thus, Glp-Asn-Pro-Tyr-Trp-Trp-AMC displays a K_i of 1 nM, which makes it the most potent competitive TRH-DE inhibitor described to date. Unfortunately, the *in vivo* potency of this peptide is poor (Kelly et al., 2005).

Another potent synthetic inhibitor of TRH-DE is the phosphinic analogue of TRH, Glp Ψ [P(O)(OH)]HisProNH₂ (Ψ -TRH) with a K_i of 170 nM, in which the scissile peptide bond of TRH has been replaced by the chemically stable phosphinic bond (Matziari et al., 2008).

Finally, a natural TRH-DE inhibitor named *Hermodice carunculata* protease inhibitor (HcPI) was isolated from the marine annelide *H. carunculata*. HcPI inhibits rat TRH-DE (a brain membrane extract with 7.5 mg protein/ml) with an IC_{50} of 4.8 μ g/ml (Pascual et al., 2004). It is a small hydrophilic molecule very specific for TRH-DE, since it is at least 100 fold less potent at inhibiting the activity of the nearest homologue in the M1 family, aminopeptidase N (Cruz et al., 2008), and it is brain permeant (Pascual et al., 2004). HcPI structure is still unknown; solving it may lead to new tools.

TRH ANALOGUES RESISTANT TO HYDROLYSIS

TRH is a poor drug candidate. Although TRH is stable in the gastrointestinal tract, it has low intestinal permeability (Yokohama et al., 1984). The intranasal route of delivery presents a possible alternative route to access the brain (Veronesi et al., 2007; Zada et al., 2019). Furthermore, TRH has also a short plasma half-life, being rapidly hydrolyzed by peptidases (Redding and Schally, 1969; Prasad and Peterkofsky, 1976; Taylor and Dixon, 1976), and its cerebral absorption is low (Cornford et al., 1978). Finally, TRH has extensive neuroendocrine, central and autonomic/cardiac effects that may limit its therapeutic use (Gary et al., 2013; Khomane et al., 2011; Joseph-Bravo et al., 2015b).

Thus, TRH analogues have been developed to increase stability, delivery, specificity and potency. The properties of these analogs have been previously described extensively (Colson and Gershengorn, 2006; Monga et al., 2008; Khomane et al., 2011; Gary et al., 2003). Their stability in the presence of TRH-DE has seldom been directly tested or was tested against

tissue homogenates that contain irrelevant peptidases. However, their stability in serum is a relatively good measure of their resistance to TRH-DE, since thyroliberinase is the main activity degrading TRH in serum. In this section, we describe TRH analogues that are resistant to TRH-DE.

TRH-like peptides in which the N-terminal Glp residue is replaced with a non-natural amino acid have promising pharmacological properties. Taltirelin ([1-methyl-(S)-4,5-dihydroorotyl]-L-His-L-ProNH₂) was synthesized by replacing the Glp residue of TRH with (S)-4,5-dihydroorotic acid (Suzuki et al., 1990). Taltirelin produces central nervous system (CNS) effects at about 100 times lower doses than TRH and has eight times longer duration of antagonistic action on pentobarbital-induced sleep than TRH (Yamamura et al., 1990; Yamamura et al., 1991a; Kinoshita et al., 1998). The differences in the activities of Taltirelin and TRH in the CNS have been attributed to the higher stability of Taltirelin in blood against thyroliberinase, and its higher lipophilicity than TRH that account for its increased penetration across the blood-brain barrier. Taltirelin resistance to hydrolysis by TRH-DE has been questioned, as Taltirelin was rapidly degraded in rat cerebral and pituitary homogenates (Kodama et al., 1997; Kobayashi et al., 2019a), but it is likely that in these homogenates enzymes distinct from TRH-DE were actively degrading Taltirelin.

Montirelin (6-methyl-5-oxothiomorpholinyl-3-carbonyl-His-Pro-NH₂, CG-3703) is a derivative of the Gln moiety of TRH, which is an efficient CNS-stimulating agent (Horita, 1998). This TRH analog readily penetrates into the brain after its systemic administration in rats (Itoh et al., 1995) and inhibits specific Gln-[3methyl-His]-Pro-NH₂ binding (K_i = 35 nM) to rat brain receptors as efficiently as TRH (K_i = 39.7 nM) (Urayama et al., 2001). Montirelin exhibits high stability in the blood (Sugimoto et al., 1996) and shows strong resistance to enzymatic degradation by pyroglutamyl aminopeptidase from brain or other related pyroglutamate aminopeptidases from liver and pituitary (Bauer, 1979; Griffiths et al., 1982).

Azetirelin (N ^{α} -[(5)-4-oxo2-azetidiny]carbonyl]-His-Pro-NH₂ dehydrate) has arousal actions 10–40 fold more potent and 8–36 times longer lasting than TRH (Yamamoto and Shimizu, 1987). This longer duration of action is probably because Azetirelin has a longer half-life in dogs and humans than TRH. However, Azetirelin has low oral bioavailability (Sasaki et al., 1994) and methods to improve its absorption have been evaluated (Sasaki et al., 1999).

Posatirelin (L-6-ketopiperidine-2-carbonyl-L-leucyl-proline amide) is a neutral analog with improved CNS activity and with cholinergic, catecholaminergic and neurotrophic properties (Oka et al., 1989; Amenta et al., 1997; Monga et al., 2008). Posatirelin has a stronger anticataleptic effect than TRH (Szirtes et al., 1986), and improves cognitive and motor disturbances in rats (Drago et al., 1996), while having poor influence on TSH

release (Szirtes et al., 1984). Several human studies have also suggested beneficial effects in subjects with cognitive impairments (Cucinotta et al., 1994; Parnetti et al., 1995). Posatiorelin is stable in human and rabbit serum, while it is slowly degraded in rat and mouse plasma (Terauchi et al., 1988).

Rovatiorelin (1-{N-[(4S,5S)-(5-methyl-2-oxooxazolidin-4-yl)-carbonyl]-3-(thiazol-4-yl)-L-alanyl}-(2R)-2-methylpyrrolidine trihydrate) has a higher affinity for TRH-R1 ($K_i = 702$ nM) than Taltirelin ($K_i = 3,880$ nM) but still lower than TRH ($K_i = 128$ nM) in cell membrane preparation from CHO-K1 cells overexpressing the human TRH receptor (Ijro et al., 2015). Rovatiorelin is resistant to thyroliberinase in rat plasma and also to TRH-DE in pituitary (Kobayashi et al., 2018; Kobayashi et al., 2019a; Kobayashi et al., 2019b).

TRH-like peptides with simultaneous replacement of Glp by a panel of hetero ring-containing carboxylic acids and central histidine by 1-alkyl-L-histidines activate TRH-R2 with higher potencies than TRH-R1. One of these, with simultaneous substitution of Glp by pyrazine-2-carboxylic acid (2-Pyz) and central His with C_3H_7 (2-Pyz-L-His(1-alkyl)-L-Pro-NH₂), exhibits high selectivity towards TRH-R2 but poor potency compared to TRH, high stability in rat blood plasma, antagonizes pentobarbital-induced sleeping time with a higher potency than TRH, and is devoid of adverse cardiovascular and CNS effects (Meena et al., 2015).

Another class of TRH derivative corresponds to those that have dual pharmacological activity, acting both as inhibitor of TRH-DE and as receptor agonist. Glp-Asn-Pro-AMC reversibly inhibits TRH-DE activity and binds preferentially to central TRH receptors (Kelly et al., 2000). The replacement of the hydrophobic L-amino acid residues with their D-isomers in C-terminally extended analogs of Glp-Asn-Pro-NH₂ led to Glp-Asn-Pro-D-Tyr-D-Trp-NH₂ (named JAK4D), which is effective at producing and potentiating some central actions of TRH without evoking TSH release *in vivo*. This peptide has high plasma stability and combined potent inhibition of TRH-DE (K_i 151 nM) with high affinity binding to central TRH receptors (K_i 6.8 nM). In addition, JAK4D has a high ability to cross the blood-brain barrier and shows a clean preliminary toxicology profile (Scalabrino et al., 2007; Kelly et al., 2015).

To conclude, TRH analogs incorporating resistance to hydrolysis by TRH-DE and/or inhibition of TRH-DE activity associate with enhanced pharmacological activity, compared to TRH.

TRH-DE IS CRITICAL FOR THE EXTRACELLULAR CATABOLISM OF TRH IN THE CENTRAL NERVOUS SYSTEM

Trhde expression is detected at relatively late phases of brain development. TRH-DE activity appears in the male rat brain a few days before birth, and peaks at post-natal day 8 in hypothalamus and posterior cerebral cortex, while it decreases afterwards to adult values. The pattern differs in the olfactory bulb, two peaks of specific activity being observed at the 3th and 22nd day (Vargas et al., 1992b). *Trhde* expression is at least 10-fold higher in brain than in nine other organs of male or female Fisher 344 rats and this ratio is stable from 2 to 104 weeks (Yu et al., 2014) (Figure 2). Thus, the brain is the region with the highest TRH-DE specific activity in adult animals (Vargas et al., 1992a; Lin and Wilk, 1998).

Trhde transcript levels and activity vary widely among brain regions, with highest values detected in cerebral cortex and hippocampus, as well as in cerebellar hemispheres, regions with limited *Trh* expression (Vargas et al., 1987; Vargas et al., 1992a; Heuer et al., 1998b; Lin and Wilk, 1998). In the adult rat brain, the map of *Trhde* transcript distribution is generally consistent with the proposal that it is expressed by neurons (Heuer et al., 1998b). This is congruent with evidence that TRH-DE activity is enriched in synaptosomes (Torres et al., 1986) and that in primary culture of E17 hypothalamic cells, neurons are the major cell type expressing TRH-DE activity (Cruz et al., 1991). Furthermore, many rat cortical *Trhde* mRNA positive cells are *Slc17a7* mRNA positive (express vesicular glutamate transporter 1), and some *Gad* mRNA positive (express glutamic acid decarboxylase), which directly confirms that neurons express *Trhde* (Rodríguez-Molina et al., 2014). Finally, single cell transcriptomic data of mouse CNS and peripheral nervous system (Zeisel et al., 2018) (Table 1) indicate that apart from

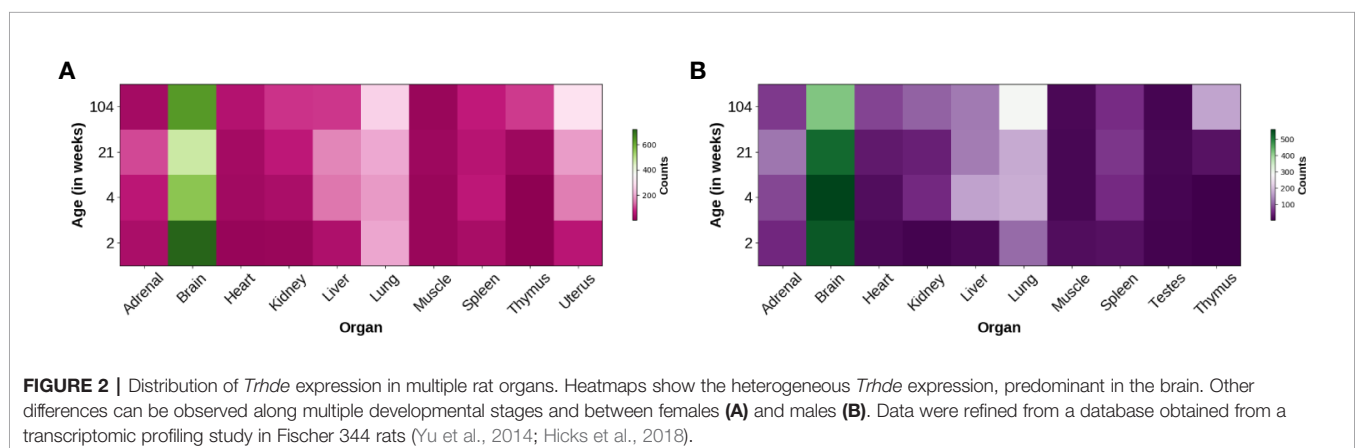


TABLE 1 | Cells types along the mouse central and peripheral nervous system with the highest expression of *Trhde*, and relative expression of *Trhr* and *Trhr2*.

Region	Phenotype	<i>Trhde</i>	<i>Trhr</i>	<i>Trhr2</i>
Hippocamposeptal projection, cortex/hippocampus	GABA/Sst	+++++	–	++
Nucleus of the solitary tract	GABA/Gly/Ach	+++++	+	–
Myenteric plexus of small intestine	Ach	++++	–	–
Subiculum/Cortex	Glu	++++	+	++++
Hippocampus CA3	Glu	+++	+	–
Lateral cortex layer 6: gustatory, barrel field, auditory	Glu	+++	–	–
Superior Coliculus	Glu	++	–	–
Cortical pyramidal layer 4	Glu	++	–	–
Hippocampus interneurons	GABA	++	–	–
Interneuron-selective interneurons, cortex/hippocampus	GABA	++	–	–
Cortical pyramidal layer 6b	Glu	++	–	–
Cortical pyramidal layer 6	Glu	++	–	–
Entorhinal superficial layers	Glu	++	–	–
Spinal cord, Dorsal cord lamina 2-5	Glu	++	–	–
Inhibitory neurons, hindbrain	GABA/Gly	++	+	++
Septal nucleus, Meissnert and diagonal band	GABA/ACh	+	+	–
Cerebral cortex	Glu	+	–	++
Cortical pyramidal layer 6	Glu	+	–	++
Paragigantocellular reticular nucleus	GABA/Gly	+	++	+++++
Neuroblasts, olfactory bulb	Glu	+	–	–
Striatum/Amygdala	GABA/ACh	+	+	–
Inhibitory neurons, midbrain	GABA	+	–	–
Spinal cord, Dorsal cord lamina 2-5	Glu	+	–	–
Lateral hypothalamus	Glu/TRH	+	+	–
Piriform cortex	Glu	+	+++++	–
Septal nucleus	Glu	+	–	–
Inhibitory neurons, spinal cord	GABA	+	++	–
Basket and bistratified cells, cortex/hippocampus	GABA	+	–	++
Cingulate/retrosplenial area, layer 5	Glu	+	–	–
Dorsal root ganglion	Glu	+	–	–
Sleep-active interneurons, cortex/hippocampus	GABA/Sst/NO/NPY	+	–	–
Interneuron-selective interneurons, cortex/hippocampus	GABA/VIP	+	–	–
Cortical pyramidal layer 5	Glu	+	–	+
Cortical pyramidal layer 2/3	Glu	+	–	++
Piriform cortex, pyramidal neurons	Glu	+	–	–
Interneuron-selective interneurons, hippocampus	GABA/VIP	+	–	–
Nucleus of the solitary tract	Glu	+	+	–
Hippocampus CA1	Glu	+	–	–
Cingulate/retrosplenial area, layer 2	Glu	+	–	–
Arcuate nucleus of the hypothalamus	GABA/AgRP/NPY	+	–	–
Inner horizontal cell, olfactory bulb	GABA	+	–	+
Superior olivary complex	GABA/Gly	+	–	–

(Continued)

TABLE 1 | Continued

Region	Phenotype	<i>Trhde</i>	<i>Trhr</i>	<i>Trhr2</i>
Pons	GABA/NO	+	–	–
Ventromedial hypothalamus	Glu	+	–	–
Olfactory bulb	GABA	+	–	–
Anterior olfactory nucleus and ventral striatum	Glu	+	–	–
Superior Coliculus	GABA	+	+	–
Granule neurons, cerebellum	Glu	+	–	–
Interneuron-selective interneurons, cortex/hippocampus	GABA/VIP/CRH	+	–	–
Pallidum	GABA	+	–	–
A1-2 Noradrenergic cell groups	Glu/Nor/PrIRH	+	–	–
Superior colliculus superficial grey layer	GABA	+	+	–

Data obtained from single cell transcriptomic analysis (Zeisel et al., 2018). Expression level: –, undetected; +, very low; ++, low; +++, medium; +++++, high; ++++++, very high. Ach, acetylcholine; AgRP, Agouti related peptide; CRH, corticotropin releasing hormone; Glu, Glutamate; Gly, glycine; NO, nitric oxide; Nor, norepinephrine; NPY, neuropeptide Y; PrIRH, prolactin releasing hormone; Sst, somatostatin; VIP, vasoactive intestinal peptide.

many neuron types, the majority of non-neuronal cells have undetectable levels of *Trhde* mRNA.

Many TRH neurons are glutamatergic (Zeisel et al., 2018). Although *Trhde* is expressed by multiple types of glutamatergic neurons, the regional distributions of *Trh* and *Trhde* mRNAs do not match (Heuer et al., 2000); in contrast, destruction of serotonin (5HT) neurons of the raphe nucleus, where TRH colocalizes with 5HT, decreases TRH content, but not TRH-DE activity, in their projections to the spinal cord (Joseph-Bravo et al., 1994), suggesting *Trhde* is not co-expressed with *Trh* in this pathway. However, the single cell transcriptomic map of the mouse brain (Zeisel et al., 2018) shows that while many *Trhde* neurons do not express *Trh*, most *Trh* cell types do express low levels of *Trhde*, while two hypothalamic *Trh* cell types are clearly positive for *Trhde*. An independent single-cell mouse transcriptomic study showed that in the medial hypothalamus there are 5 predominant clusters of *Trh* neurons, one being clearly positive for *Trhde* (Campbell et al., 2017).

Some TRH-DE neurons may be TRH-R1 or TRH-R2 positive, because the maps of the distribution of *Trhde*, *Trhr* and *Trhr2* mRNAs in the brain reveal a partial co-expression of *Trhde* and one of its receptors (Heuer et al., 2000). Data at single cell level are consistent with coexpression in some neurons, but also indicate many mismatches (Zeisel et al., 2018). An example of a site of co-expression is the medial hypothalamus, where three of the five clusters of *Trhde* neurons do express *Trhr* (Campbell et al., 2017). Furthermore, in the medial septum a large fraction of the *Trhde* cells does not express *Trhr* (Lazcano et al., 2012). We have no clues about the relationship between the subcellular localizations of TRH-DE and TRH-Rs in the cells that do express both *Trhde* and *Trhr* or *Trhr2*, in part because of the lack of TRH-DE antibodies suitable for immunocytochemistry. Existing data thus suggest no systematic association of TRH-DE with TRH receptors. What is thus the relevance of TRH-DE for TRH communication?

In brain slices, exogenous TRH is rapidly hydrolyzed, a major product being His-Pro-NH₂, one of the two catabolites of TRH hydrolysis by TRH-DE *in vitro*, suggesting indeed that TRH-DE hydrolyzes TRH in the brain extracellular fluid (Méndez et al., 1999). In brain slices, inhibition of TRH-DE activity with CPHNA increases TRH levels recovered in the extracellular medium, with a stronger effect in regions with higher TRH-DE activity (Charli et al., 1989). Gln-Asn-Pro-Tyr-Trp-Trp-AMC also enhanced recovery of TRH released from rat brain slices (Kelly et al., 2005). Furthermore, perfusion of cortical slices with a TRH-DE inhibitor mimics the effect of TRH on the shape of action potentials generated by pyramidal neurons, suggesting that endogenous TRH released in the extracellular fluid is hydrolyzed by TRH-DE (Rodríguez-Molina et al., 2014). Thus, extracellular turnover of TRH (either exogenous or endogenous) in brain slices is relatively rapid and occurs at least in part through hydrolysis by TRH-DE.

Besides these *in vitro* studies, there is indirect evidence that TRH may be hydrolyzed through TRH-DE activity in brain *in vivo*. If TRH is hydrolyzed by TRH-DE in the brain extracellular space, the reaction product His-Pro-NH₂ could be degraded to His-Pro by dipeptidyl peptidase IV, a widely expressed ectoenzyme (Mentlein, 1999), and/or cyclize spontaneously to His-Pro-diketopiperazine (HPDKP), which may be metabolically stable and accumulate in the brain (Prasad, 1989). HPDKP is indeed found in the brain and although diet may be an external source, part of HPDKP most likely comes from TRH hydrolysis since its concentration is reduced in the hypothalamus and cortex of TRH knockout mice (Yamada et al., 1999).

A more direct evidence for the importance of TRH-DE in controlling the effects of TRH in the brain comes from a study on the effect of TRH on ethanol-induced narcosis. One of the pharmacological effects of TRH is its capacity to enhance alertness, and reverse narcosis, and one of the brain regions that mediate this last effect is the lateral septum. An intra-medial septum injection of the TRH-DE inhibitors pGlu-Asn-Pro-AMC, or Ψ-TRH which is not an agonist of TRH-R1, enhances the effect of exogenous TRH on the duration of ethanol-induced loss of righting reflex; the time of loss of the reflex is also decreased by the injection of Ψ-TRH alone (Lazcano et al., 2012). These data give further support to the proposal that TRH-DE regulates TRH turnover *in vivo*.

Although the relevance of TRH-DE for TRH inactivation in brain requires more extensive studies, it seems reasonable to conclude that its activity may at least in some anatomical contexts be present in neuron targets of TRH or adjacent neurons, and control the turnover of TRH, and thus duration and/or intensity of TRH effect. Although the primary products of TRH-DE activity (Gln and His-Pro-NH₂) are inactive against TRH receptors, supporting an inactivation role, the product of His-Pro-NH₂ cyclization, HPDKP, may mimic or oppose some TRH effects, making it possible to argue that TRH-DE biotransforms TRH (Prasad, 1995). At pharmacological doses HPDKP may be neuroprotective and improve glucose metabolism in obese and/or diabetic animals (Minelli et al.,

2008). However, the physiological relevance of TRH biotransformation to HPDKP in brain is currently unknown. Thus, it seems pertinent to conclude that a major function of TRH-DE is TRH inactivation in the brain. In contrast, it remains to be determined whether Gln-Phe-Pro-NH₂ and Gln-Tyr-Pro-NH₂ actions are indeed terminated by TRH-DE activity *in vivo*.

POTENTIAL THERAPEUTIC TARGETING OF TRH-DE IN THE CNS

This section covers some of the major pharmacological properties of TRH, and of the two TRH-like peptides that are potential *in vivo* substrates of TRH-DE in the CNS, to illustrate the contexts in which TRH-DE targeting may be considered therapeutically beneficial.

Except for TRH neurons controlling the HPT axis, few experimental studies have addressed the *in vivo* physiological role of other TRH neurons. This is because of the absence of useful TRH-R antagonists *in vivo*, of the difficulty to manipulate the activity of specific TRH subtypes, and to limited information about the projections of various TRH neuron types. Some studies used strategies that correlate behavior with markers of TRH neuron activity, such as evaluation of the expression of *Trh* or cFOS, or region-specific manipulation of *Trh* expression. Along with tracing experiments, this research laid the ground to insert some TRH neurons in physiological contexts. Many studies have rather evaluated the impact of TRH or analogues on behavior and/or biochemical markers of neuronal activity. Peripheral or central (intracerebroventricular or nucleus-specific) administration of TRH or analogues produces in laboratory animals multiple behavioral changes, besides activation of the HPT axis. The mechanisms of TRH action are not fully understood, although advances have been made to characterize the electrophysiological/biochemical effects of TRH, and to identify target cells and circuits involved. Initial results led to early attempts to use TRH and analogues with improved stability, agonist potency and/or brain accessibility for experimental treatment of psychiatric or neurological diseases. A comprehensive analysis of TRH effects is beyond the scope of this review; the reader is referred to excellent reviews (Kelly, 1995; Horita, 1998; Gary et al., 2003; Daimon et al., 2013; Fröhlich and Wahl, 2019). As for other receptors, TRH or analogue action is not only limited by access and stability, but also by ligand-induced desensitization and down regulation (Sun et al., 2003; Hinkle et al., 2012). Reduced TRH receptor binding and behavioral tolerance is observed after repeated administration of TRH (Ogawa et al., 1983; Simasko and Horita, 1985), a fact that stresses one of the limits of the therapeutic use of any analogue. We will restrict the following paragraphs to some well-established effects of TRH or analogues, and whenever knowledge permits to discuss the targeting of TRH-DE.

TRH administration acutely increases arousal and locomotion; these effects are reproduced by direct injection of TRH into nucleus accumbens and septum (Horita, 1998). Other

central regions are likely involved; for example, TRH increases the activity of lateral hypothalamus orexin neurons, which project to several areas involved in arousal (González et al., 2009; Hara et al., 2009). TRH-induced dopamine release has been observed in different paradigms and was proposed to be involved in TRH-induced motor activity (Kalivas et al., 1987; Yamamura et al., 1991b). The effect of TRH on arousal is also related with TRH-induced awakening from ethanol narcosis and coincides with the stimulatory effect of acute ethanol administration on *Trh* mRNA levels, accompanied with decreased *Trhde* mRNA levels and TRH-DE activity, and TRH tissue content, suggesting increased release of TRH in nucleus accumbens (de Gortari et al., 2005). In the septum, there is evidence that inhibition of TRH-DE activity promotes arousal from ethanol narcosis (Lazcano et al., 2012). Contrary to TRH, Gln-Phe-Pro-NH₂ and Gln-Tyr-Pro-NH₂ are not analeptic (Hinkle et al., 2002). Amplification of TRH action on arousal by TRH-DE inhibition may be therapeutically useful in niche applications.

TRH or analogue administration has generally a strong anorexic effect. The anorexic effect of TRH is probably mediated through multiple target regions; one of them is the nucleus accumbens, where TRH may interact with dopaminergic communication (Puga et al., 2016). Other regions potentially involved in the anorexic effect of TRH are various hypothalamic nuclei, such as the tuberomammillary nucleus, where TRH containing axons innervate histamine neurons (Gotoh et al., 2007; Sárvari et al., 2012), or the perifornical area/bed nucleus of stria terminalis region, from where TRH neurons may control the activity of proopiomelanocortin neurons of the arcuate nucleus (Péterfi et al., 2018). However, it was also noted that TRH injection into the brainstem promotes food intake through TRH-R1 activation (Ao et al., 2006), suggesting that control of food intake through TRH manipulation may require the optimization of the access route. There is not yet any experimental evidence showing that TRH-DE may regulate the anorexic (or orexigenic) effect of TRH.

TRH improves cognitive function (Bennett et al., 1997). TRH analogs administered to animals prevent the memory impairment caused by chronic ethanol administration or brain lesions (Bennett et al., 1997; Gary et al., 2003; Daimon et al., 2013; Meena et al., 2015). *In vivo*, TRH, or some analogs, activate the septo-hippocampal and basalis cortical cholinergic systems, eliciting acetylcholine release onto the hippocampus and cortex and restore cognitive deficits of animals with lesions in the medial septum (Itoh et al., 1994; Bennett et al., 1997; Horita, 1998; Prokai-Tatrai and Prokai, 2009; Daimon et al., 2013). The TRH analogue 2-Pyz-L-His (1-alkyl)-L-Pro-NH₂, which exhibits high selectivity towards TRH-R2, and is more stable in rat blood plasma than TRH, possesses cognitive-enhancing activity when administered intravenously in the scopolamine-induced cognition impairment mice model, evaluated with the Morris water maze and the passive avoidance tests (Meena et al., 2015).

The hippocampus is critical in learning and memory. TRH immunoreactivity is detected in pyramidal and granular layers of CA1 and CA3, and in ventral dentate gyrus coincident with TRH binding (Hökfelt et al., 1989; Sharif et al., 1989) and with

expression of *Trhr* (Calzá et al., 1992; Heuer et al., 2000). In support of the relevance of hippocampal TRH communication in learning, the status of TRH transmission is modified in the hippocampus of rats trained for 5 days in the water maze. TRH release is reduced, whereas expression of *Trh* and *Trhr* is upregulated in CA3, supporting plastic changes induced by the process of learning (Aguilar-Valles et al., 2007). TRH produces a time-dependent biphasic effect on NMDA receptor responses (Zarif et al., 2016), whereas it increases the excitability of GABA interneurons (Deng et al., 2006) in the hippocampus. Interestingly, pyramidal cells of the Ammon's horn express *Trhde* mRNA in abundance (Heuer et al., 1998b); *Trhde* may be expressed on the cell body and/or dendrites of the CA neurons. Blockade of NMDA receptors by MK801 decreases relatively rapidly TRH-DE activity in hippocampal slices, while blockade of AMPA or GABA-A receptors does not (Rodríguez-Molina et al., 2009). Additional cognitive effects of TRH may be direct onto cerebral cortex, where *Trhde* mRNA expression is also high (Heuer et al., 1998b) and TRH-DE regulates TRH action on pyramidal neurons action potential shape (Rodríguez-Molina et al., 2014). Thus, cognitive actions of TRH may be amplified by inhibition of TRH-DE activity.

Several reports show that endogenous or exogenous TRH is an anticonvulsant (Kubek et al., 1989; Sattin, 1999; Sah et al., 2011). In man, TRH is efficient for treatment of West syndrome, Lennox-Gastaut syndrome, and early infantile epileptic encephalopathy (Takeuchi et al., 2001). The electrical subthreshold stimulation produced during kindling in the amygdala or the hippocampus increases *Trh* expression or TRH content (Rosen et al., 1992; Kubek et al., 1993; de Gortari et al., 1995). Amygdala kindling increases *Trh* expression, but decreases that of *Trhr*, *Trhr2*, and *Trhde* in amygdala, and hippocampus, while only that of *Trhr2* and *Trhde* in frontal cortex (de Gortari et al., 2006). TRH content increases as kindling progresses whereas the activity of TRH-DE increases in the initial stages and decreases once kindling is established (de Gortari et al., 1995). Decreased *Trhde* expression may facilitate the protective effects of TRH. These data suggest that inhibition of TRH-DE may be protective in some forms of epilepsy.

The peripheral or central administration of TRH produces an anxiolytic effect in several animal tests (Vogel et al., 1980; Thompson and Rosen, 2000; Gutiérrez-Mariscal et al., 2008). There is evidence that endogenous TRH can perform a similar function. Thus, in animals subjected to the defensive burying test, there is a specific inhibition of TRH release and *Trh* mRNA levels in amygdala but not in other limbic areas (Gutiérrez-Mariscal et al., 2008). Furthermore, amygdalar *Trh* expression and anxiety behavior are inversely correlated in the elevated plus maze and in the open field test (Gutiérrez-Mariscal et al., 2012). In adult male rats, exposure to an open field test during the inactive phase increases *Trh* expression in the cortical nucleus of the amygdala, an area involved in processing fear stimuli (Gutiérrez-Mariscal et al., 2008). *Trhr* KO mice are more anxious than wild type relatives (Zeng et al., 2007) while those deficient in *Trhr2* exhibit reduced anxiety (Sun et al., 2009). It is warranted to test the status of *Trhde* KO mice.

Experimental evidence for an antidepressant effect of TRH in animal models and humans is controversial, although *Trhr*-deficient mice are euthyroid and exhibit a depressive behavior (Sun et al., 2009). As an example of controversy, the injection of TRH into rats decreases the immobility time in the Porsolt test (Drago et al., 1990) whereas the injection of Taltirelin into the amygdala increases the immobility time in chronic-stress-induced depressed mice. In the depressed mice, *Trh* and *Trhr* expression in the basolateral amygdala is increased after 14 days of 2 h of daily restraint (Choi et al., 2015). This result seems to contradict the reported anxiolytic effect of TRH. Species and strain differences in stress responses and the previous stress history of the animal (Joseph-Bravo et al., 2015a) may explain some of these discrepant results. Finally, Gln-Tyr-Pro-NH₂ is active in the Porsolt Swim Test (Pekary et al., 2005). Since mood stabilizing valproate acutely enhances, among other TRH-like peptides, Gln-Tyr-Pro-NH₂ concentration in brain regions and most notably in pyriform cortex (Pekary et al., 2004), it will be relevant to take Gln-Tyr-Pro-NH₂ into account if TRH-DE is targeted for an anti-depressant effect.

Several neurologic disorders improve with treatment with TRH and some of its stable analogs. This has been shown for scopolamine-induced memory loss, prolonged impaired consciousness (Horita, 1998; Meena et al., 2015), and neuronal death occurring after a transient ischemic attack (TIA) (Shishido et al., 1999). In rats, *Trh* expression increases in peri-ischemic tissue, while that of *Trhde* drops drastically. The response is independent of age of induction of TIA, and post-ischemia time. This may be a TRH protective effect, amplified by *Trhde* down regulation (Buga et al., 2012). Neuroprotective actions of TRH analogs include protection against neuronal injury induced by excitotoxicity and oxidative stress, and inflammation (Gary et al., 2003; Daimon et al., 2013; Fröhlich and Wahl, 2019). In the spinal cord, TRH may be involved in motor activity control and pain modulation; its administration promotes the recovery from acute spinal cord injury and has been used clinically with promising results (Fehlins and Baptiste, 2005). Taltirelin, which is degradation resistant, has been accepted in the treatment of spinocerebellar degeneration (SCD) (Kinoshita et al., 1994; Kinoshita et al., 1998). Taltirelin has anti-ataxic and neuroprotective actions (Urayama et al., 2002; Nakamura et al., 2005; Veronesi et al., 2007). Finally, JAK4D elicits large neuroprotective effects in neurodegenerative animal models. Systemic administration of JAK4D reduces cognitive deficits in a kainate (KA)-induced rat model of neurodegeneration, protects against free radical release and neuronal damage evoked by KA in rat, and reduces motor decline and lumbar spinal cord neuronal loss in a transgenic Amyotrophic Lateral Sclerosis mice model (Kelly et al., 2015). These data point to the importance of targeting TRH-DE to improve treatment of neurodegenerative diseases with TRH derivatives.

TRH analogs resistant to degradation by TRH-DE are promising for treating some neurological disorders. However, autonomic effects of these analogs need to be considered. Central TRH application has effects on the respiratory, cardiac and gastric systems. Most of these actions are due to targets of the

TRH neurons present in brain stem. TRH is synthesized in raphe pallidus, obscurus, and para-pyramidal neurons that project to sympathetic preganglionic neurons of the intermediolateral (IML) cell column of the spinal cord and to vagal motor neurons located in the dorsal vagal complex (Taché et al., 2006). Some of TRH neurons that project to the IML use serotonin and substance P as co-transmitters; depending on the complement of receptors in target neurons, TRH participates in several aspects of respiratory network control (Hodges and Richerson, 2008).

In the vagal complex TRH activates neurons of the dorsal motor nucleus of the vagus that project to visceral organs such as pancreas regulating insulin secretion (Yang et al., 2002), or as stomach, stimulating gastric secretion (Tache, 2012). TRH-TRH-R1 signaling in brain stem, or TRH administered in low doses, have protective action against damaging agents in the gastric mucosa, whereas this is not the case in high doses as injections into the cisterna magna induce a dose-related activation of gastric vagal efferent discharges in rats. TRH applied in the hindbrain modulates gastric secretion and motility, blood pressure, hepatic blood flow, stimulates brown adipose tissue thermogenesis and respiratory output (Taché et al., 2006; Hou et al., 2012; Yang et al., 2012; Pilowsky, 2014). Although TRH-DE activity is lower in the brain stem than in other regions of the brain (Vargas et al., 1992a), the potential to alter autonomic functions if TRH-DE is affected cannot be underestimated.

In conclusion, at CNS level, many TRH effects, and some Gln-Phe-Pro-NH₂ and Gln-Tyr-Pro-NH₂ actions, may have a therapeutic potential (i.e. antiepilepsy, anxiolysis, improvement of learning, neuroprotection). The presence of TRH-DE in many of the sites of action of TRH suggests that inhibition of TRH-DE activity should increase the action of endogenous TRH. This may produce results that are better suited than those sought with TRH analogues.

TRH-DE AND THE THYROID AXIS

This topic has been recently reviewed (Rodríguez-Rodríguez et al., 2019) and will only be briefly discussed here. Although a large part of CNS *Trhde* is expressed in neurons, a few years ago it was discovered that *Trhde* is expressed in tanycytes of the hypothalamus, a glial cell type localized at the base and ventrolateral walls of the third ventricle of the hypothalamus (Sánchez et al., 2009). All sub-types of tanycytes express *Trhde*; the β 2 tanycytes, which send cytoplasmic extensions into the external layer of the median eminence where they are close to TRH terminals of the parvocellular TRHergic neurons of the PVN, in proximity of the portal capillaries that transport TRH to the anterior pituitary have the highest expression of *Trhde* (Sánchez et al., 2009). In median eminence explants, TRH-DE inhibition enhances TRH recovered from the incubation medium, suggesting that the enzyme actively hydrolyses TRH in the median eminence extracellular space (Sánchez et al., 2009). Thus, after release TRH may be partially hydrolyzed by TRH-DE before entry into the portal vessels. A physiological consequence would be that the amount of TRH reaching the anterior pituitary

would not only depend on the activity of the TRH neurons, but also on median eminence TRH-DE activity, which would regulate the intensity of TRH-induced TSH secretion according to clues detected at median eminence level. Consistent with this idea, it was shown that although the intraperitoneal injection of HcPI in control animals does not change serum concentration of TSH, it does increase it in cold stressed animals (Sánchez et al., 2009). Although HcPI inhibits TRH-DE activity inside the blood–brain barrier, as well in the anterior pituitary and serum, *Trhde* expression is not detected in thyrotropes, and inhibition of TRH-DE expression or activity does not enhance TRH-induced TSH release (Bauer et al., 1990; Cruz et al., 2008); this evidence strongly suggests that anterior pituitary TRH-DE is not critical for the control of TSH release. Finally, the role of the serum enzyme, that is produced by the liver (Schmitmeier et al., 2002) cannot be discarded, since this isoform likely circulates through the portal vessels. Although a definitive demonstration for control of TRH entry into the portal capillaries by tanyocyte TRH-DE is required, evidence about regulation of TRH-DE activity is also consistent with this proposal.

A major mode of control of the activity of the HPT axis is negative feedback at various levels, including inhibition of *Trh* mRNA synthesis in the hypophysiotropic neurons of the PVN (Fekete and Lechan, 2014). At the level of the tanyocytes, *Trhde* expression and activity are rapidly (in a few hours) stimulated by peripheral injection of T4, thus putatively contributing to the negative feedback (Sánchez et al., 2009). The effect of T4 on *Trhde* depends on the local conversion of T4 to T3 by deiodinase 2 (*Dio2*) also expressed in tanyocytes (Marsili et al., 2011). The mechanism by which TH induces *Trhde* expression is not known; thyroid hormone response elements have not been detected in the vicinity of the putative transcription initiation of *Trhde* (Figure 1), although many genes regulated by TH do not contain them (Chatonnet et al., 2013).

The HPT axis is regulated by energy balance (Fekete and Lechan, 2014; Joseph-Bravo et al., 2015b). Apart from down regulation of TRH neurons activity, a prolonged fast enhances *Dio2* and *Trhde* expression and activity in the male rat median eminence (Diano et al., 1998; Lazcano et al., 2015). The transient induction of *Trhde* expression may contribute to prolong the downward adjustment of the HPT axis, along with an increase in thyroliberinase activity, in spite of a partial reactivation of *Trh* synthesis by the PVN at 72 h fasting (Lazcano et al., 2015). Other data show that diet-induced obesity (with unsaturated fat) enhances median eminence *Trhde* expression in male rats (Jaimes-Hoy et al., 2019), suggesting that the relationship between energy balance and activity of TRH-DE is complex. Finally, *Trhde* expression in the median eminence is programed by neonatal stress, along with other aspects of HPT axis function (Jaimes-Hoy et al., 2016). It is thus evident that long-term events shape median eminence TRH-DE activity.

In these models, there are few clues about the immediate regulators of *Trhde* expression/activity, and it has not been shown that *Trhde* adjustments are critical for HPT axis activity. The local thyroid status is probably involved (Lazcano et al., 2015) and besides hormonal signals, tanyocytes are responsive to neuronal inputs. Recently it was shown that the release of TRH

in the median eminence activates the TRH-R1 receptor on the surface of tanyocytes, resulting in two rapid events: an increase of the surface of tanyocyte end-feets covering the portal capillaries, and an increase in TRH-DE activity in the median eminence, both of which may reduce TRH access to the capillary bed. Furthermore, a long term (days) blockade of Gq transduction decreased TRH-DE activity. Thus, the firing of TRH neurons likely regulates TRH-DE activity and localization. This coordinated mechanism may help to shape the pulses of TRH that reach the anterior pituitary (Müller-Fielitz et al., 2017).

An intriguing question is the relevance of TRH-like peptides sensitive to hydrolysis by TRH-DE in the control of the HPT axis. Gln-Phe-Pro-NH₂ is released from hypothalamic slices (Méndez et al., 1999), Gln-Phe-Pro-NH₂, as well as TRH, is detected in rat thyroid (Rausell et al., 1999; Smyth et al., 1999) and Gln-Phe-Pro-NH₂ enhances serum T3 concentration (Cremades et al., 1998). Thus, median eminence and thyroid gland may be sites where the functional relationship between Gln-Phe-Pro-NH₂ and TRH-DE warrants further investigation.

TARGETING MEDIAN EMINENCE TRH-DE TO CONTROL THYROID STATUS?

Thyroid diseases are very common and a major one is sub-clinical or clinical hypothyroidism, which is mainly treated with T4 (and T3). Although this therapeutic option is successful, it is not perfect and there is room for improvement. Among the major problems of the therapeutic use of TH is the risk of producing unattended hyperthyroidism and thus cardiovascular or skeletal consequences. These problems have led to significant avenues of research, to limit unintended effects. One of these approaches has been the development of specific agonists of TH receptor β (Runfola et al., 2020). Another focus has been on the development of thyroid hormone-peptide complexes, to direct TH to the tissues that express the peptide receptor (Finan et al., 2016).

Peripheral inhibition of peptidase activity has been quite successful in various contexts (hypertension, type 2 diabetes). Although requiring confirmatory experiments, the weight of evidence strongly suggests that in rats median eminence TRH-DE activity controls the output of TRH and thus TSH secretion, at least during bouts of TRH neurons activity. This suggests that inhibition of this enzyme may transiently increase TRH-induced TSH secretion, enhancing the hypothalamic signal that promotes TSH secretion in conditions of insufficient drive. Because $\beta 2$ tanyocyte TRH-DE activity is outside the blood brain barrier, it should be possible to target this compartment and enhance the extracellular concentration of TRH in the portal vessels, without affecting TRH communication in the rest of the CNS. Furthermore, the narrow specificity of TRH-DE should facilitate the development of agents that have no impact on other peptides turnover. The final purpose of this manipulation would be to enhance thyroid hormone secretion without changing the natural pattern of control of the HPT axis and to produce self-regulated and small effects on TH concentration,

reducing cardiovascular and bone effects.

Various milestones should be reached to target peripheral TRH-DE activity to improve thyroid status in hypothyroidism. One is to characterize the long-term impact of TRH-DE inhibition on HPT axis parameters, since the axis can self-regulate efficiently; for example, the long-term ablation of tanycytes does not change serum TSH concentration (Yoo et al., 2019). Another consideration is that changes in serum TSH concentration may have non thyroidal effects. Likewise, prolactin secretion would have to be monitored, to exclude alteration of this critical hormone. Finally, the distribution and role of TRH-DE activity in the periphery requires clarification.

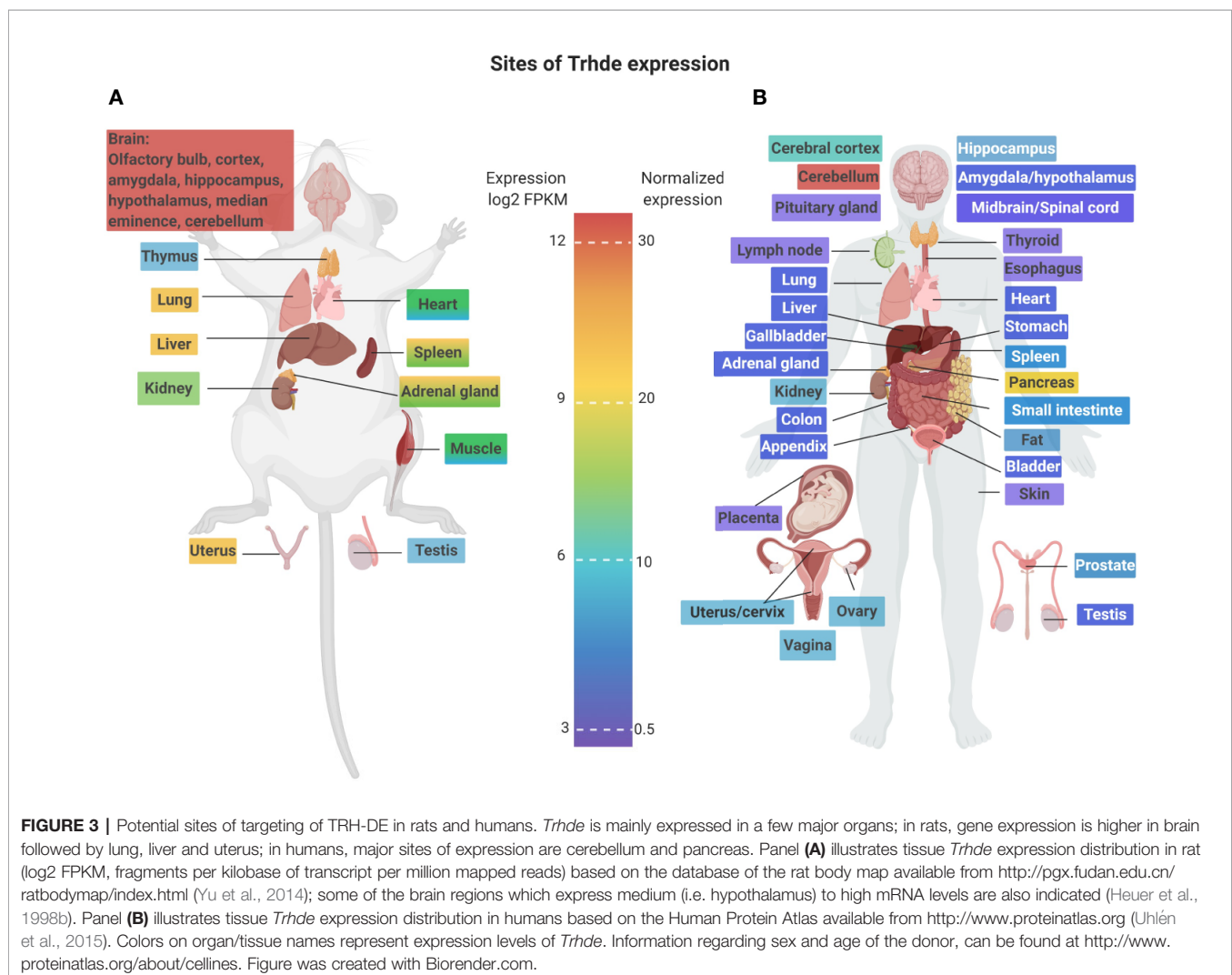
TRH-DE AND PROLACTIN SECRETION

In mammals, apart from the negative control of prolactin secretion by hypothalamic tuberoinfundibular dopamine neurons, hypothalamic prolactin releasing factors are also important (Grattan, 2015). TRH is not only a thyrotropin

releasing factor but also a prolactin releasing factor. TRH is necessary to maintain maximal prolactin output in lactating mice (Yamada et al., 2006). In primary cultures of female rat anterior pituitary cells, *Trhde* expression is detected in some lactotropes, and inhibition of TRH-DE expression or activity enhances TRH-induced prolactin secretion (Bauer et al., 1990; Cruz et al., 2008). If the importance of *Trhde* for the control of prolactin secretion, which is contingent on many factors, is confirmed in relevant *in vivo* models, inhibition of anterior pituitary TRH-DE activity might increase prolactin secretion.

TRH-DE IN PERIPHERAL TISSUES

Although targeting of CNS and/or median eminence/pituitary TRH-DE activity has experimental support, a much less understood aspect is the function of *Trhde* expressed in the periphery. This must be fully assessed for establishing the safety profile of the peripheral inhibition of TRH-DE activity or expression. **Figures 2 and 3** illustrate that although the brain is



a major source of *Trhde* expression, developmentally regulated expression of *Trhde* is also detected in multiple rat tissues, of both sexes. However, it should be noted that in rats and rabbits, the peripheral tissues have low levels of TRH-DE activity (Vargas et al., 1992a). Human transcriptomic data indicate baseline expression of *Trhde* in various peripheral organs, being more abundant in kidney, spleen, ovaries, uterus, adipose tissue, small intestine Peyer's patch, duodenum, pancreas, and lung, and lower in colon, prostate, stomach and testis. In these tissues, *Trhde* expression is detected in adults. For kidney, lung, stomach and testis, *Trhde* expression has also been reported at early stages of embryonic development ("ensembl.org: TRHDE—ENSG00000072657," n.d. and "bgee.org: TRH-DE—ENSG00000072657") (Figure 3). We review below the state of knowledge about TRH-DE in the best-studied tissues.

Thyroliberinase is a liver specific isoform of TRH-DE (Schmitmeier et al., 2002) that is secreted into the general circulation. It is the only enzyme that degrades TRH in rat serum (Friedman and Wilk, 1985). Its role is puzzling; it probably reaches the hypothalamic-pituitary portal vessels, but its specific relevance for anterior pituitary control is untested. Thyroliberinase may also reduce the buildup of TRH concentration in the peripheral tissues where TRH may act as a paracrine effector (Morley, 1979). Finally, it should contribute significantly to the limited efficiency of the parenteral injection of TRH, being an interesting target to enhance the efficacy of parenteral TRH analogues.

One of the peripheral tissues in which TRH presence was noticed early is the rat pancreas, where it is concentrated in the islets of Langerhans (Martino et al., 1978). A transient prenatal expression of *Trh* is detected in pancreatic β -cells, which coincides with development of insulin secretory activity (Yamaoka and Itakura, 1999; Basmaciogullari et al., 2000; Štrbák, 2018). In rodents, *Trhr* is expressed in the pancreas, including in β -cells (Yamada et al., 2000; Luo and Yano, 2004); a potential effect of TRH-TRH-R1 is the promotion of programmed cell death during development (Mulla et al., 2009). *Trh* KO mice have an increased glycemia, which may be the result of reduced secretion of insulin in response to high glucose concentration (Yamada et al., 1997). On the other hand, *Trhr* KO mice are hypothyroid and hyperglycemic (Zeng et al., 2007), while *Trhr2* KO mice are euthyroid and normoglycemic (Sun et al., 2009). Gln-Phe-Pro-NH₂ is detected in pancreas, where it attenuates TRH effect on insulin secretion in perfused islets (Kulkarni et al., 1995). Although pancreatic *Trhde* expression is significant in human (Figure 3), there is no evidence for TRH-DE activity in developing or adult rat (Vargas et al., 1992b). *Trhde* KO mice are normoglycemic (Tang et al., 2010). The relevance of TRH-DE in human pancreatic function requires an urgent investigation; is expression leading to TRH-DE activity, or to non-active isoforms?

Trh, and *Trhr* are expressed in the heart, in fibroblasts and in cardiomyocytes (Carnell et al., 1992; Shi et al., 1996); TRH, as well as Gln-Phe-Pro-NH₂ and Gln-Tyr-Pro-NH₂, are detected in heart tissue, where values vary along the circadian cycle (Pekary

and Sattin, 2017). Various evidences suggest that heart TRH might be relevant in cardiovascular disease. TRH induces hypertrophic and fibrotic markers in heart cells (Schuman et al., 2014). Overexpression of *Trh* in left ventricular cells promotes heart hypertrophy in rats (Jin et al., 2004). Spontaneously hypertensive rats overexpress *Trh* in the left ventricle, and reduction of *Trh* expression inhibits fibrosis and cardiomyocyte enlargement (Schuman et al., 2011). Furthermore, angiotensin II-induced heart hypertrophy depends on *Trh* expression (Peres Diaz et al., 2018). Thus, TRH may have a substantial role in cardiac hypertrophy. *Trhde* is expressed in the heart of Fischer-344 male and female rats, with noticeable developmental increases (Figure 2) (Yu et al., 2014). In the human heart, *Trhde* transcripts can be detected at 10 weeks (Szabo et al., 2015). It will be important to clarify whether TRH-DE activity is present in heart and controls local TRH and/or Gln-Phe-Pro-NH₂ and Gln-Tyr-Pro-NH₂ actions.

TRH-like immunoreactivity is detected in various organs of the digestive system (Leppäluoto et al., 1978). TRH levels are high in gastric juice and mucosa (Nishio et al., 1999). In the digestive system, while TRH-R1 presence in the stomach is scarce (Nishio et al., 1990), TRH-R1 has been detected by immunohistochemistry in the small intestine (Mitsuma et al., 1995), where TRH excites submucous neurons and enhances heat shock protein 60 expression (Zafirov et al., 1991; Sasahara et al., 1998). One subtype of cholinergic neuron, in the myenteric plexus of the mouse small intestine, is characterized by a very high expression of *Trhde* (Zeisel et al., 2018) (Table 1), but these neurons, which may receive vagal afferents, do not express *Trhr* or *Trhr2*. In this system, TRH-DE may inactivate TRH produced and released locally. However, as for the heart, there is yet no evidence that TRH-DE activity is present in the intestinal mucosa. Because of the high relative expression of *Trhde* in neurons of the enteric system, potential adverse effects of TRH-DE manipulation should be considered. In humans, intestinal *Trhde* expression initiates around 10–20 weeks of age (Szabo et al., 2015), being significant in adults. An accumulation of neuropeptides, including TRH, in the lumen of the colon of patients with inflammatory bowel disease (Yamamoto et al., 1996) is noticeable; animal models of the disease might shed light about TRH-DE role in this pathology, if any.

TRH has significant effects over the function of immune system, some of which dependent on pituitary control (Kamath et al., 2009). Hypophysiotropic TRH neurons are involved in inflammation responses dependent and independent of T-cell activation. LPS administration doesn't induce T-cell activation and is linked with an initial reduction of *Trh* expression in the PVN (Kamath et al., 2009). However, T-cell dependent inflammation induces the opposite, with the response dependent on hypophysiotropic TRH neurons and prolactin secretion from the pituitary (Perez Castro et al., 1999). Although the site of TRH production acting directly on immune cells is unknown, TRH-R1 can be detected in lymphoid tissues, including the thymus (Montagne et al., 1999) and bone marrow (Matre et al., 2003). Administration of TRH in rats

increases the proliferation of cells of the thymus (Pawlikowski et al., 1992) and protects against its involution and reduction of the count of lymphocytes in peripheral blood, induced by lateral hypothalamus lesion (Lesnikov et al., 1992). TRH may thus be of therapeutic value in diseases dependent on immune system activation. Administration of TRH protects against pathogens such as encephalomyelitis virus (Pierpaoli and Yi, 1990), and candidiasis (Błaszowska et al., 2004). Transcriptomic analysis reveals that *Trhde* is expressed in thymus, with a significant drop of expression in aging rats (**Figure 2**) (Yu et al., 2014). Although TRH-DE activity and function have not been determined in lymphoid organs, TRH-DE inhibitors could be interesting alternatives to TRH treatment in inflammatory diseases.

In the reproductive system, Leydig cells express both *Trh* and *Trhr* (Pekary and Sattin, 2017). Repeated administration of TRH counters aging-induced alteration of rat testicular structure and function (Pierpaoli, 2013). Gln-Phe-Pro-NH₂ is also expressed by the prostate and detected in seminal fluid (Bilek et al., 1992; Khan et al., 1992; Gkonos et al., 1994); however, its local effect is unknown. In females, TRH increases the contractility of urethral and vaginal muscle (Zacur et al., 1985) and Gln-Phe-Pro-NH₂ is detected in the mammary gland (Ghilchik et al., 2000). Since low levels of expression of *Trhde* occur in various reproductive organs (**Figure 3**), its relevance for TRH or Gln-Phe-Pro-NH₂ actions may not be important but should nevertheless be investigated.

In conclusion, there is little evidence that, apart from pituitary and liver, other peripheral tissues which express *Trhde* give rise to significant TRH-DE activity. It remains possible that in some tissues expression might be mainly attributed to the mRNA coding for the truncated version of TRH-DE (Chavez-Gutierrez et al., 2005) and that TRH-DE* is not only a dominant negative isoform of TRH-DE but is also a non-catalytic protein. However, *Trhde* KO mice do not show any obvious problem in standard conditions, except for a small decrease of body weight (Tang et al., 2010). Finally, it will be critical to clarify the extent of TRH-DE activity in human tissues.

CONCLUSIONS AND CHALLENGES

With the available information of the wide distribution of TRH receptors, and the multiple functions TRH displays, the pharmacological use of agonists of the TRH-R1 receptors that resist degradation by TRH-DE might impact on many functions.

Albeit alternatives are not completely excluded yet, it appears that hydrolysis by the TRH degrading ectoenzyme in the serum and the extracellular space of the brain, including the median eminence, is a critical pathway for TRH inactivation. The relevance of this enzyme for Gln-Phe-Pro-NH₂ and Gln-Tyr-Pro-NH₂ inactivation remains to be investigated. Since most central pharmacological effects of peptidase resistant analogues of TRH are beneficial in rodents, and there is some consistent evidence in humans, targeting central TRH-DE with specific inhibitors may have significant advantages over TRH agonists in some central diseases, in particular to produce more focused effects according to the natural activity of the TRH neurons. On

the other hand, the limited span of the distribution of TRH-DE activity in the periphery opens the possibility that inhibition of median eminence TRH-DE activity may be an interesting target for treatment of hypothyroidism and may have few non-intended targets, if a compound that does not pass the blood-brain barrier is chosen. However, it will be necessary to understand the full extent of the distribution of peripheral TRH-DE activity and function in humans before this idea proceeds further.

Targeting the inactivation process in the brain will increase ligand concentration in the synaptic space and increase TRH effect, alike the mechanism of action of drugs that inhibit neurotransmitter uptake. However, an intrinsic problem lies on the stringent specificity of TRH-DE for the TRH structure. Thus, it is not surprising that some of the TRH-DE inhibitors function also as TRH-R agonists (Scalabrino et al., 2007) and may thus promote receptor down regulation or, undesirable side effects. For example, even for a more stable analog of TRH as Taltirelin, hyperprolactinemia is induced (Kanasaki et al., 2011). Even if the analog does not produce endocrine effects in humans, other peripheral effects such as induction of gastric erosion and hypermotility of the intestine may occur. The challenge to design a specific inhibitor to TRH-DE not recognized by TRH-R1 has been overcome with Ψ-TRH design, although better chemistries and affinities are required. In theory, this should be possible, as has been done for other proteases (Patchett and Cordes, 1985; Traube et al., 2014; Lai et al., 2015).

Even if better inhibitors are found, unknowns remain. Are Gln-Phe-Pro-NH₂ and Gln-Tyr-Pro-NH₂ physiologically relevant substrates of TRH-DE? Does inhibition of TRH-DE activity has concrete effects in preclinical models? These, and other milestones, need to be passed to determine if manipulation of TRH-DE expression or activity has therapeutic potential.

AUTHOR CONTRIBUTIONS

J-LC conceived and wrote the manuscript. PJ-B conceived and wrote the manuscript. AR-R generated figures and table and edited the manuscript. KH-O, AC-V, RU, and LJ-H wrote specific parts of the manuscript.

FUNDING

Supported by grants from DGAPA-UNAM to J-LC (PAPITT IN206712), and AC-V (PAPITT IN 206416 and 212719), and from CONACYT to JLC (PN562; CB254960).

ACKNOWLEDGMENTS

This manuscript is dedicated to the memory of Dr. Milagros Méndez who was our first PhD student and contributed to delineate the *in vivo* role of the multiple peptidases that hydrolyze TRH. The research described in this paper has

benefited from the talented help of many. Besides the individuals that are included in the reference list, we thank Elizabeth Mata, Sergio González and Graciela Cabeza Pérez, for providing animals, to Shirley Elizabeth Ainsworth Gore, Jesús Omar Arriaga Pérez, Arturo Ocadiz Ramírez, Juan Manuel Hurtado

REFERENCES

- Aebi, M. (2013). N-linked protein glycosylation in the ER. *Biochim. Biophys. Acta (BBA) Mol. Cell Res.* 1833, 2430–2437. doi: 10.1016/j.bbamcr.2013.04.001
- Aguilar-Valles, A., Sánchez, E., de Gortari, P., García-Vazquez, A. I., Ramírez-Amaya, V., Bermúdez-Rattoni, F., et al. (2007). The expression of TRH, its receptors and degrading enzyme is differentially modulated in the rat limbic system during training in the Morris water maze. *Neurochem. Int.* 50, 404–417. doi: 10.1016/j.neuint.2006.09.009
- Amenta, F., Sabbatini, M., Coppi, G., Maggioni, A., Olgiati, V., and Panocka, I. (1997). Effect of treatment with the neuroactive peptide posatirelin on microanatomical changes of frontal cortex and hippocampus caused by lesions of the locus coeruleus. *Drugs Exp. Clin. Res.* 23, 77–88.
- Ao, Y., Go, V. L. W., Toy, N., Li, T., Wang, Y., Song, M. K., et al. (2006). Brainstem Thyrotropin-Releasing Hormone regulates food intake through vagal-dependent cholinergic stimulation of ghrelin Secretion. *Endocrinology* 147, 6004–6010. doi: 10.1210/en.2006-0820
- Ashworth, R., Yu, R., Nelson, E. J., Dermer, S., Gershengorn, M. C., and Hinkle, P. M. (1995). Visualization of the thyrotropin-releasing hormone receptor and its ligand during endocytosis and recycling. *Proc. Natl. Acad. Sci.* 92, 512–516. doi: 10.1073/pnas.92.2.512
- Awadé, A. C., Cleuziat, P. H., Gonzalès, T. H., and Robert-Baudouy, J. (1994). Pyrrolidone carboxyl peptidase (Pcp): An enzyme that removes pyroglutamic acid (pGlu) from pGlu-peptides and pGlu-proteins. *Proteins* 20, 34–51. doi: 10.1002/prot.340200106
- Bagul, P., Khomane, K. S., Kesharwani, S. S., Pragyani, P., Nandekar, P. P., Meena, C. L., et al. (2014). Intestinal transport of TRH analogs through PepT1: the role of *in silico* and *in vitro* modeling: role of structural modifications on PepT1-mediated transport. *J. Mol. Recognit.* 27, 609–617. doi: 10.1002/jmr.2385
- Basmaciogullari, A., Cras-Meneur, C., Czernichow, P., and Scharfmann, R. (2000). Pancreatic pattern of expression of thyrotropin-releasing hormone during rat embryonic development. *J. Endocrinol.* 166, 481–488. doi: 10.1677/joe.0.1660481
- Bauer, K., Nowak, P., and Kleinkauf, H. (1981). Specificity of a serum peptidase hydrolyzing thyroliberin at the pyroglutamyl-histidine bond. *Eur. J. Biochem.* 118, 173–176. doi: 10.1111/j.1432-1033.1981.tb05501.x
- Bauer, K., Carmeliet, P., Schulz, M., Baes, M., and Deneef, C. (1990). Regulation and cellular localization of the membrane bound Thyrotropin-Releasing Hormone-degrading enzyme in primary cultures of neuronal, glial and adenohipophyseal cells. *Endocrinology* 127, 1224–1233. doi: 10.1210/endo-127-3-1224
- Bauer, K., Heuer, H., Ifflander, F., Peters, A., Schmitmeier, S., Shomburg, L., et al. (1997). “Inactivation of thyrotropin-releasing hormone (TRH) by a TRH-specific ectoenzyme,” in *Cell-Surface Peptidases in Health and Disease*. Eds. B. Kenny and C. M. AJ (UK: Oxford: BIOS Scientific Publishers), 239–248.
- Bauer, K. (1979). Thyroliberin analogues as competitive inhibitors of thyroliberin degradation by brain enzymes. *Hoppe-Seyler's Z Physiol. Chem.* 360, 1126.
- Bauer, K. (1994). Purification and Characterization of the Thyrotropin-releasing-hormone-degrading Ectoenzyme. *Eur. J. Biochem.* 224, 387–396. doi: 10.1111/j.1432-1033.1994.00387.x
- Bellemere, G., Vaudry, H., Morain, P., and Jegou, S. (2005). Effect of prolyl endopeptidase inhibition on arginine-vasopressin and Thyrotrophin-Releasing Hormone catabolism in the rat brain. *J. Neuroendocrinol.* 17, 306–313. doi: 10.1111/j.1365-2826.2005.01308.x
- Bennett, G. W., Ballard, T. M., Watson, C. D., and Fone, K. C. F. (1997). Effect of neuropeptides on cognitive function. *Exp. Gerontol.* 32, 451–469. doi: 10.1016/S0531-5565(96)00159-3
- Bidaud, I., Galas, L., Bulant, M., Jenks, B. G., Ouwers, D. T. W. M., Jégou, S., et al. (2004). Distribution of the mRNAs encoding the thyrotropin-releasing hormone (TRH) precursor and three TRH receptors in the brain and pituitary of *Xenopus laevis*: Effect of background color adaptation on TRH and TRH receptor gene expression: proTRH and α TRHR mRNAs in Brain and Pituitary of *Xenopus*. *J. Comp. Neurol.* 477, 11–28. doi: 10.1002/cne.20235
- Bilek, R., Gkonos, P. J., Tavianini, M. A., Smyth, D. G., and Roos, B. A. (1992). The thyrotrophin-releasing hormone (TRH)-like peptides in rat prostate are not formed by expression of the TRH gene but are suppressed by thyroid hormone. *J. Endocrinol.* 132, 177–184. doi: 10.1677/joe.0.1320177
- Blaszowska, J., Pawlikowski, M., Komorowski, J., and Kurnatowski, P. (2004). Effect of thyroliberin on the course of experimental candidosis in mice. Thyroliberin-Wirkung auf den Verlauf der experimentellen Candidose der Maus. *Mycoses* 47, 115–120. doi: 10.1111/j.1439-0507.2004.00961.x
- Buga, A.-M., Scholz, C. J., Kumar, S., Herndon, J. G., Alexandru, D., Cojocaru, G. R., et al. (2012). Identification of new therapeutic targets by genome-wide analysis of gene expression in the ipsilateral cortex of aged rats after stroke. *PLoS One* 7, e50985. doi: 10.1371/journal.pone.0050985
- Bundgaard, H., and Moss, J. (1990). Effect of thyroliberin on the course of experimental candidosis in mice. *Pharmaceut. Res.* 07, 885–892. doi: 10.1023/A:1015933504191
- Calzá, L., Giardino, L., Ceccatelli, S., Zanni, M., Elde, R., and Hökfelt, T. (1992). Distribution of thyrotropin-releasing hormone receptor messenger RNA in the rat brain: An *in situ* hybridization study. *Neuroscience* 51, 891–909. doi: 10.1016/0306-4522(92)90528-A
- Campbell, J. N., Macosko, E. Z., Fenselau, H., Pers, T. H., Lyubetskaya, A., Tenen, D., et al. (2017). A molecular census of arcuate hypothalamus and median eminence cell types. *Nat. Neurosci.* 20, 484–496. doi: 10.1038/nn.4495
- Carnell, N. E., Feng, P., Kim, U. J., and Wilber, J. F. (1992). Preprothyrotropin-releasing hormone mRNA and TRH are present in the rat heart. *Neuropeptides* 22, 209–212. doi: 10.1016/0143-4179(92)90047-Z
- Chávez-Gutiérrez, L., Matta-Camacho, E., Osuna, J., Horjales, E., Joseph-Bravo, P., Maigret, B., et al. (2006). Homology modeling and site-directed mutagenesis of pyroglutamyl peptidase II. Insights into omega-versus aminopeptidase specificity in the M1 family. *J. Biol. Chem.* 281, 18581–18590. doi: 10.1074/jbc.M601392200
- Charli, J.-L., Ponce, G., McKelvy, J. F., and Joseph-Bravo, P. (1984). Accumulation of Thyrotropin Releasing Hormone by rat hypothalamic slices. *J. Neurochem.* 42, 981–986. doi: 10.1111/j.1471-4159.1984.tb12700.x
- Charli, J. L., Mendez, M., Joseph-Bravo, P., and Wilk, S. (1987). Specific inhibitors of pyroglutamyl peptidase I and prolyl endopeptidase do not change the *in vitro* release of TRH or its content in rodent brain. *Neuropeptides* 9, 373–378. doi: 10.1016/0143-4179(87)90010-2
- Charli, J.-L., Cruz, C., Vargas, M.-A., and Joseph-Bravo, P. (1988). The narrow specificity pyroglutamate amino peptidase degrading TRH in rat brain is an ectoenzyme. *Neurochem. Int.* 13, 237–242. doi: 10.1016/0197-0186(88)90060-5
- Charli, J.-L., Mendez, M., Vargas, M.-A., Cisneros, M., Assai, M., Joseph-Bravo, P., et al. (1989). Pyroglutamyl peptidase II inhibition specifically increases recovery of TRH released from rat brain slices. *Neuropeptides* 14, 191–196. doi: 10.1016/0143-4179(89)90044-9
- Charli, J. L., Vargas, M. A., Cisneros, M., de Gortari, P., Baeza, M. A., Jasso, P., et al. (1998). TRH inactivation in the extracellular compartment: role of pyroglutamyl peptidase II. *Neurobiol. (Bp)* 6, 45–57.
- Chatonnet, F., Guyot, R., Benoit, G., and Flamant, F. (2013). Genome-wide analysis of thyroid hormone receptors shared and specific functions in neural cells. *Proc. Natl. Acad. Sci.* 110, E766–E775. doi: 10.1073/pnas.1210626110
- Chavez-Gutierrez, L., Bourdais, J., Aranda, G., Vargas, M. A., Matta-Camacho, E., Ducancel, F., et al. (2005). A truncated isoform of pyroglutamyl aminopeptidase II produced by exon extension has dominant-negative activity. *J. Neurochem.* 92, 807–817. doi: 10.1111/j.1471-4159.2004.02916.x
- Choi, J., Kim, J., Kim, T.-K., Park, J.-Y., Lee, J.-E., Kim, H., et al. (2015). TRH and TRH receptor system in the basolateral amygdala mediate stress-induced

- depression-like behaviors. *Neuropharmacology* 97, 346–356. doi: 10.1016/j.neuropharm.2015.03.030
- Colson, A., and Gershengorn, M. (2006). Thyrotropin-Releasing Hormone analogs. *MRC* 6, 221–226. doi: 10.2174/138955706775476019
- Cornford, E. M., Braun, L. D., Crane, P. D., and Oldendorf, W. H. (1978). Blood-brain barrier restriction of peptides and the low uptake of enkephalins. *Endocrinology* 103, 1297–1303. doi: 10.1210/endo-103-4-1297
- Cremades, A., Peñañiel, R., Rausell, V., Del Río-García, J., and Smyth, D. G. (1998). The thyrotropin-releasing hormone-like peptides pGlu-Phe-Pro amide and pGlu-Glu-Pro amide increase plasma triiodothyronine levels in the mouse; the activity is sensitive to testosterone. *Eur. J. Pharmacol.* 358, 63–67. doi: 10.1016/S0014-2999(98)00593-7
- Cruz, C., Charli, J.-L., Vargas, M. A., and Joseph-Bravo, P. (1991). Neuronal localization of pyroglutamate aminopeptidase II in primary cultures of fetal mouse brain. *J. Neurochem.* 56, 1594–1601. doi: 10.1111/j.1471-4159.1991.tb02056.x
- Cruz, R., Vargas, M. A., Uribe, R. M., Pascual, I., Lazcano, I., Yiotakis, A., et al. (2008). Anterior pituitary pyroglutamyl peptidase II activity controls TRH-induced prolactin release. *Peptides* 29, 1953–1964. doi: 10.1016/j.peptides.2008.07.011
- Cucinotta, D., Senin, U., Girardello, R., and Crepaldi, G. (1994). Positron emission tomography with ¹⁸F-fluorodeoxyglucose (FDG) in patients with senile dementia of Alzheimer type (SDAT): a double-blind multicentre trial with ascorbic acid and citicoline. *J. Neurol.* 241, S129.
- Cushman, D. W., Cheung, H. S., Sabo, E. F., and Ondetti, M. A. (1977). Design of potent competitive inhibitors of angiotensin-converting enzyme. Carboxyalkanoyl and mercaptoalkanoyl amino acids. *Biochemistry* 16, 5484–5491. doi: 10.1021/bi00644a014
- Czekay, G., and Bauer, K. (1993). Identification of the thyrotropin-releasing-hormone-degrading ectoenzyme as a metallopeptidase. *Biochem. J.* 290, 921–926. doi: 10.1042/bj2900921
- Daimon, C., Chiridon, P., Maudsley, S., and Martin, B. (2013). The role of Thyrotropin Releasing Hormone in aging and neurodegenerative diseases. *AJAD* 29–59. doi: 10.7726/ajad.2013.1003
- de Gortari, P., Fernández-Guardiola, A., Martínez, A., Cisneros, M., and Joseph-Bravo, P. (1995). Changes in TRH and its degrading enzyme pyroglutamyl peptidase II, during the development of amygdaloid kindling. *Brain Res.* 679, 144–150. doi: 10.1016/0006-8993(95)00237-K
- de Gortari, P., Romero, F., Cisneros, M., and Joseph-bravo, P. (2005). Acute administration of alcohol modulates pyroglutamyl amino peptidase II activity and mRNA levels in rat limbic regions. *Neurochem. Int.* 46, 347–356. doi: 10.1016/j.neuint.2004.11.002
- de Gortari, P., Uribe, R. M., García-Vázquez, A., Aguilar-Valles, A., Martínez, A., Valdés, A., et al. (2006). Amygdala kindling differentially regulates the expression of the elements involved in TRH transmission. *Neurochem. Int.* 48, 31–42. doi: 10.1016/j.neuint.2005.08.003
- Deng, P.-Y., Porter, J. E., Shin, H.-S., and Lei, S. (2006). Thyrotropin-releasing hormone increases GABA release in rat hippocampus: TRH modulation of hippocampal GABAergic transmission. *J. Physiol.* 577, 497–511. doi: 10.1113/jphysiol.2006.118141
- Diano, S., Naftolin, F., Goglia, F., and Horvath, T. L. (1998). Fasting-induced increase in type II iodothyronine deiodinase activity and messenger ribonucleic acid levels is not reversed by thyroxine in the rat hypothalamus. *Endocrinology* 139, 2879–2884. doi: 10.1210/endo.139.6.6062
- Drago, F., Pulvirenti, L., Spadaro, F., and Pennisi, G. (1990). Effects of TRH and prolactin in the behavioral despair (swim) model of depression in rats. *Psychoneuroendocrinology* 15, 349–356. doi: 10.1016/0306-4530(90)90060-M
- Drago, F., Coppi, G., Antonuzzo, P. A., Valerio, C., Genazzani, A. A., Grassi, M., et al. (1996). Effects of RGH 2202 on cognitive and motor behavior of the rat. *Neurobiol. Aging* 17, 67–71. doi: 10.1016/0197-4580(95)02006-3
- Elmore, M. A., Griffiths, E. C., O'Connor, B., and O'Cuinn, G. (1990). Further characterization of the substrate specificity of a TRH hydrolysing pyroglutamate aminopeptidase from guinea-pig brain. *Neuropeptides* 15, 31–36. doi: 10.1016/0143-4179(90)90157-T
- Ensemble release 99. - January 2020. EMBL-EBI. http://Jan2020.archive.ensembl.org/Homo_sapiens/Gene/ExpressionAtlas?g=ENSG00000072657;r=12:72087266-72670758 [accessed march 21, 2020].
- Faivre-Bauman, A., Loudes, C., Barret, A., Tixier-Vidal, A., and Bauer, K. (1986). Possible role of neuropeptide degrading enzymes on thyroliberin secretion in fetal hypothalamic cultures grown in serum free medium. *Neuropeptides* 7, 125–138. doi: 10.1016/0143-4179(86)90088-0
- Farre, D. (2003). Identification of patterns in biological sequences at the ALGGEN server: PROMO and MALGEN. *Nucleic Acids Res.* 31, 3651–3653. doi: 10.1093/nar/gkg605
- Fehlings, M. G., and Baptiste, D. C. (2005). Current status of clinical trials for acute spinal cord injury. *Injury* 36, S113–S122. doi: 10.1016/j.injury.2005.06.022
- Fekete, C., and Lechan, R. M. (2014). Central regulation of hypothalamic-pituitary-thyroid axis under physiological and pathophysiological conditions. *Endocrine Rev.* 35, 159–194. doi: 10.1210/er.2013-1087
- Ferguson, J. F., Xue, C., Hu, Y., Li, M., and Reilly, M. P. (2016). Adipose tissue RNASeq reveals novel gene–nutrient interactions following n-3 PUFA supplementation and evoked inflammation in humans. *J. Nutr. Biochem.* 30, 126–132. doi: 10.1016/j.jnutbio.2015.12.010
- Finan, B., Clemmensen, C., Zhu, Z., Stemmer, K., Gauthier, K., Müller, L., et al. (2016). Chemical hybridization of glucagon and thyroid hormone optimizes therapeutic impact for metabolic disease. *Cell* 167, 843–857.e14. doi: 10.1016/j.cell.2016.09.014
- Fröhlich, E., and Wahl, R. (2019). The forgotten effects of thyrotropin-releasing hormone: Metabolic functions and medical applications. *Front. Neuroendocrinol.* 52, 29–43. doi: 10.1016/j.yfrne.2018.06.006
- Friedman, T. C., and Wilk, S. (1985). The effect of inhibitors of prolyl endopeptidase and pyroglutamyl peptide hydrolase on TRH degradation in rat serum. *Biochem. Biophys. Res. Commun.* 132, 787–794. doi: 10.1016/0006-291X(85)91201-X
- Gallagher, S. P., and O'Connor, B. (1998). A study of a highly specific pyroglutamyl aminopeptidase type-II from the membrane fraction of bovine brain. *Int. J. Biochem. Cell Biol.* 30, 115–133. doi: 10.1016/S1357-2725(97)00074-5
- Garat, B., Miranda, J., Charli, J.-L., and Ioseph-Bravo, P. (1985). Presence of a membrane bound pyroglutamyl amino peptidase degrading thyrotropin releasing hormone in rat brain. *Neuropeptides* 6, 27–40. doi: 10.1016/0143-4179(85)90128-3
- Gary, K. A., Sevarino, K. A., Yarbrough, G. G., Prange, A. J., and Winokur, A. (2003). The Thyrotropin-Releasing Hormone (TRH) hypothesis of homeostatic regulation: implications for TRH-based therapeutics. *J. Pharmacol. Exp. Ther.* 305, 410–416. doi: 10.1124/jpet.102.044040
- Ghilchik, M. W., Tobaruella, M., del Río-García, J., and Smyth, D. G. (2000). Characterization of neutral TRH-like peptides in mammary gland, mammary tumors and milk. *Biochim. Biophys. Acta (BBA) Gen. Subj.* 1475, 55–60. doi: 10.1016/S0304-4165(00)00043-X
- Gkonos, P. J., Kwok, C. K., Block, N. L., and Roos, B. A. (1994). Identification of the human seminal TRH-like peptide pGlu-Phe-Pro-NH₂ in normal human prostate. *Peptides* 15, 1281–1283. doi: 10.1016/0196-9781(94)90154-6
- González, J. A., Horjales-Araujo, E., Fugger, L., Broberger, C., and Burdakov, D. (2009). Stimulation of orexin/hypocretin neurones by thyrotropin-releasing hormone: TRH activates central orexin neurones. *J. Physiol.* 587, 1179–1186. doi: 10.1113/jphysiol.2008.167940
- Gotoh, K., Fukagawa, K., Fukagawa, T., Noguchi, H., Kakuma, T., Sakata, T., et al. (2007). Hypothalamic neuronal histamine mediates the thyrotropin-releasing hormone-induced suppression of food intake. *J. Neurochem.* 103, 1102–1110. doi: 10.1111/j.1471-4159.2007.04802.x
- Grattan, D. R. (2015). 60 YEARS OF NEUROENDOCRINOLOGY: The hypothalamo-prolactin axis. *J. Endocrinol.* 226, T101–T122. doi: 10.1530/JOE-15-0213
- Griffiths, E. C., McDermott, J. R., and Smith, A. I. (1982). Mechanisms of brain inactivation of centrally-acting thyrotrophin-releasing hormone (TRH) analogues: a high-performance liquid chromatography study. *Regul. Peptides* 5, 1–11. doi: 10.1016/0167-0115(82)90070-2
- Gutiérrez-Mariscal, M., de Gortari, P., López-Rubalcava, C., Martínez, A., and Joseph-Bravo, P. (2008). Analysis of the anxiolytic-like effect of TRH and the response of amygdalar TRHergic neurons in anxiety. *Psychoneuroendocrinology* 33, 198–213. doi: 10.1016/j.psyneuen.2007.11.002
- Gutiérrez-Mariscal, M., Sánchez, E., Rebolledo-Solleiro, D., García-Vázquez, A. I., Cote-Vélez, A., Acasuso-Rivero, C., et al. (2012). The acute response of the amygdalar TRH system to psychogenic stressors varies dependent on the paradigm and circadian condition. *Brain Res.* 1452, 73–84. doi: 10.1016/j.brainres.2012.02.071

- Hökfelt, T., Tsuruo, Y., Ulfhake, B., Cullheim, S., Arvidsson, U., Foster, G. A., et al. (1989). SECTION II. SYNAPTIC ROLE OF TRH: Distribution of TRH-like immunoreactivity with special reference to coexistence with other neuroactive compounds. *Ann. NY Acad. Sci.* 553, 76–105. doi: 10.1111/j.1749-6632.1989.tb46633.x
- Hara, J., Gerashchenko, D., Wisor, J. P., Sakurai, T., Xie, X., and Kilduff, T. S. (2009). Thyrotropin-Releasing Hormone increases behavioral arousal through modulation of hypocretin/orexin neurons. *J. Neurosci.* 29, 3705–3714. doi: 10.1523/JNEUROSCI.0431-09.2009
- Heuer, H., Ehrchen, J., Bauer, K., and Schäfer, M. K. H. (1998a). Region-specific expression of thyrotrophin-releasing hormone-degrading ectoenzyme in the rat central nervous system and pituitary gland: Distribution of the TRH-degrading ectoenzyme. *Eur. J. Neurosci.* 10, 1465–1478. doi: 10.1046/j.1460-9568.1998.00158.x
- Heuer, H., Schäfer, M. K.-H., and Bauer, K. (1998b). The Thyrotropin-Releasing Hormone-degrading ectoenzyme: the third element of the Thyrotropin-Releasing Hormone-signaling system. *Thyroid* 8, 915–920. doi: 10.1089/thy.1998.8.915
- Heuer, H., Schäfer, M. K. H., O'Donnell, D., Walker, P., and Bauer, K. (2000). Expression of thyrotropin-releasing hormone receptor 2 (TRH-R2) in the central nervous system of rats. *J. Comp. Neurol.* 428, 319–336. doi: 10.1002/1096-9861(20001211)428:2<319::AID-CNE10>3.0.CO;2-9
- Hicks, S. C., Okrah, K., Paulson, J. N., Quackenbush, J., Irizarry, R. A., and Bravo, H. C. (2018). Smooth quantile normalization. *Biostatistics* 19, 185–198. doi: 10.1093/biostatistics/kxx028
- Hinkle, P. M., Pekary, A. E., Senanayaki, S., and Sattin, A. (2002). Role of TRH receptors as possible mediators of analeptic actions of TRH-like peptides. *Brain Res.* 935, 59–64. doi: 10.1016/S0006-8993(02)02454-X
- Hinkle, P. M., Gehret, A. U., and Jones, B. W. (2012). Desensitization, trafficking, and resensitization of the pituitary Thyrotropin-Releasing Hormone receptor. *Front. Neurosci.* 6, 180. doi: 10.3389/fnins.2012.00180
- Hodges, M. R., and Richerson, G. B. (2008). Contributions of 5-HT neurons to respiratory control: Neuromodulatory and trophic effects. *Respiratory Physiol. Neurobiol.* 164, 222–232. doi: 10.1016/j.resp.2008.05.014
- Horita, A. (1998). An update on the CNS actions of TRH and its analogs. *Life Sci.* 62, 1443–1448. doi: 10.1016/S0024-3205(98)00087-3
- Hou, L., Zhou, X., Chen, Y., Qiu, D., Zhu, L., and Wang, J. (2012). Thyrotropin-releasing hormone causes a tonic excitatory postsynaptic current and inhibits the phasic inspiratory inhibitory inputs in inspiratory-inhibited airway vagal preganglionic neurons. *Neuroscience* 202, 184–191. doi: 10.1016/j.neuroscience.2011.12.003
- Ijio, T., Nakamura, K., Ogata, M., Inada, H., Kiguchi, S., Maruyama, K., et al. (2015). Effect of rovatirelin, a novel thyrotropin-releasing hormone analog, on the central noradrenergic system. *Eur. J. Pharmacol.* 761, 413–422. doi: 10.1016/j.ejphar.2015.05.047
- Itoh, Y., Ogasawara, T., Mushiroy, T., Yamazaki, A., Ukai, Y., and Kimura, K. (1994). Effect of NS-3, a thyrotropin-releasing hormone analog, on in vivo acetylcholine release in rat brain: regional differences and its sites of action. *J. Pharmacol. Exp. Ther.* 271, 884–890.
- Itoh, Y., Sugimoto, T., Ukai, Y., Morino, A., and Kimura, K. (1995). Permeability of NS-3, a Thyrotropin-releasing Hormone analogue, into the brain after its systemic administration in rats: a microdialysis study. *J. Pharm. Pharmacol.* 47, 833–836. doi: 10.1111/j.2042-7158.1995.tb05750.x
- Jaimes-Hoy, L., Gutiérrez-Mariscal, M., Vargas, Y., Pérez-Maldonado, A., Romero, F., Sánchez-Jaramillo, E., et al. (2016). Neonatal maternal separation alters, in a sex-specific manner, the expression of TRH, of TRH-degrading ectoenzyme in the rat hypothalamus, and the response of the thyroid axis to starvation. *Endocrinology* 157, 3253–3265. doi: 10.1210/en.2016-1239
- Jaimes-Hoy, L., Romero, F., Charli, J.-L., and Joseph-Bravo, P. (2019). Sex dimorphic responses of the hypothalamus–pituitary–thyroid axis to maternal separation and palatable diet. *Front. Endocrinol.* 10, 445. doi: 10.3389/fendo.2019.00445
- Jeong, J. K., Szabo, G., Kelly, K., and Diano, S. (2012). Prolyl carboxypeptidase regulates energy expenditure and the thyroid axis. *Endocrinology* 153, 683–689. doi: 10.1210/en.2011-1399
- Jin, H., Fedorowicz, G., Yang, R., Ogasawara, A., Peale, F., Pham, T., et al. (2004). Thyrotropin-Releasing Hormone is induced in the left ventricle of rats with heart failure and can provide inotropic support to the failing heart. *Circulation* 109, 2240–2245. doi: 10.1161/01.CIR.0000127951.13380.B4
- Joseph-Bravo, P., Fresán, M. E., Cisneros, M., Vargas, M. A., and Charli, J.-L. (1994). Pyroglutamyl peptidase II activity is not in the processes of bulbospinal TRHergic neurons. *Neurosci. Lett.* 178, 243–246. doi: 10.1016/0304-3940(94)90769-2
- Joseph-Bravo, P., Jaimes-Hoy, L., and Charli, J.-L. (2015a). Regulation of TRH neurons and energy homeostasis-related signals under stress. *J. Endocrinol.* 224, R139–R159. doi: 10.1530/JOE-14-0593
- Joseph-Bravo, P., Jaimes-Hoy, L., Uribe, R.-M., and Charli, J.-L. (2015b). 60 YEARS OF NEUROENDOCRINOLOGY: TRH, the first hypophysiotropic releasing hormone isolated: control of the pituitary–thyroid axis. *J. Endocrinol.* 226, T85–T100. doi: 10.1530/JOE-15-0124
- Kalivas, P. W., Stanley, D., and Prange, A. J. (1987). Interaction between thyrotropin-releasing hormone and the mesolimbic dopamine system. *Neuropharmacology* 26, 33–38. doi: 10.1016/0028-3908(87)90041-4
- Kamath, J., Yarbrough, G. G., Prange, A. J., and Winokur, A. (2009). The thyrotropin-releasing hormone (TRH)–immune system homeostatic hypothesis. *Pharmacol. Ther.* 121, 20–28. doi: 10.1016/j.pharmthera.2008.09.004
- Kanasaki, H., Oride, A., Mijiddorj, T., Purwana, I., and Miyazaki, K. (2011). Secondary amenorrhea in a woman with spinocerebellar degeneration treated with thyrotropin-releasing hormone: a case report and in vitro analysis. *J. Med. Case Rep.* 5, 567. doi: 10.1186/1752-1947-5-567
- Kayser, L. (2019). Built to bind: biosynthetic strategies for the formation of small-molecule protease inhibitors. *Nat. Prod. Rep.* 36, 1654–1686. doi: 10.1039/C8NP00095F
- Kelly, J. A., Loscher, C. E., Gallagher, S., and O'Connor, B. (1997). Degradation of pyroglutamyl-phenylalanyl-proline amide by a pyroglutamyl aminopeptidase purified from membrane fractions of bovine brain. *Biochem. Soc. Trans.* 25, 114S–114S. doi: 10.1042/bst025114s
- Kelly, J. A., Slatore, G. R., Tipton, K. F., Williams, C. H., and Bauer, K. (2000). Kinetic investigation of the specificity of porcine brain Thyrotropin-releasing Hormone-degrading ectoenzyme for Thyrotropin-releasing Hormone-like peptides. *J. Biol. Chem.* 275, 16746–16751. doi: 10.1074/jbc.M910386199
- Kelly, J. A., Scalabrino, G. A., Slatore, G. R., Cullen, A. A., Gilmer, J. F., Lloyd, D. G., et al. (2005). Structure–activity studies with high-affinity inhibitors of pyroglutamyl-peptidase II. *Biochem. J.* 389, 569–576. doi: 10.1042/BJ20041722
- Kelly, J. A., Boyle, N. T., Cole, N., Slatore, G. R., Colivicchi, M. A., Stefanini, C., et al. (2015). First-in-class thyrotropin-releasing hormone (TRH)-based compound binds to a pharmacologically distinct TRH receptor subtype in human brain and is effective in neurodegenerative models. *Neuropharmacology* 89, 193–203. doi: 10.1016/j.neuropharm.2014.09.024
- Kelly, J. A. (1995). Thyrotropin-releasing hormone: basis and potential for its therapeutic use. *Essays Biochem.* 30, 133–149.
- Khan, Z., Aitken, A., Garcia, J. R., and Smyth, D. G. (1992). Isolation and identification of two neutral thyrotropin releasing hormone-like peptides, pyroglutamylphenylalanineproline amide and pyroglutamylglutamineproline amide, from human seminal fluid. *J. Biol. Chem.* 267, 7464–7469.
- Khomane, K. S., Meena, C. L., Jain, R., and Bansal, A. K. (2011). Novel thyrotropin-releasing hormone analogs: a patent review. *Expert Opin. Ther. Patents* 21, 1673–1691. doi: 10.1517/13543776.2011.623127
- Kinoshita, K., Nagao, T., and Ono, H. (1994). Effects of TA-0910, an orally active TRH analog, on the spinal reflex in spinal rats. *Neuropharmacology* 33, 1183–1188. doi: 10.1016/S0028-3908(05)80008-5
- Kinoshita, K., Yamamura, M., Sugihara, J., Suzuki, M., and Matsuoka, Y. (1998). Taltirelin Hydrate (TA-0910): an orally active Thyrotropin-Releasing Hormone mimetic agent with multiple actions. *CNS Drug Rev.* 4, 25–41. doi: 10.1111/j.1527-3458.1998.tb00039.x
- Kobayashi, N., Sato, N., Fujimura, Y., Kihara, T., Sugita, K., Takahashi, K., et al. (2018). Discovery of the orally effective Thyrotropin-Releasing Hormone mimetic: 1-[(4 S, 5 S)-(5-Methyl-2-oxooxazolidine-4-yl)carbonyl]-3-(thiazol-4-yl)-L-alanyl-(2 R)-2-methylpyrrolidine Trihydrate (Rovatiorelin Hydrate). *ACS Omega* 3, 13647–13666. doi: 10.1021/acsomega.8b01481
- Kobayashi, K., Abe, Y., Harada, H., Oota, E., Endo, T., and Takeda, H. (2019a). Non-clinical pharmacokinetic profiles of rovatirelin, an orally available thyrotropin-releasing hormone analogue. *Xenobiotica* 49, 106–119. doi: 10.1080/00498254.2017.1423130

- Kobayashi, K., Abe, Y., Kawai, A., Furihata, T., Harada, H., Endo, T., et al. (2019b). Human mass balance, pharmacokinetics and metabolism of rovatirelin and identification of its metabolic enzymes *in vitro*. *Xenobiotica* 49, 1434–1446. doi: 10.1080/00498254.2019.1580796
- Kodama, H., Furuuchi, S., Takahashi, M., Sugihara, J., and Yoshikawa, M. (1997). Disposition of Taltirelin. (1): absorption, distribution, metabolism and excretion in rats and dogs. *Drug Metab. Pharmacokinet.* 12, 460–474. doi: 10.2133/dmpk.12.460
- Kubek, M. J., Low, W. C., Sattin, A., Morzorati, S. L., Meyerhoff, J. L., and Larsen, S. H. (1989). Role of TRH in seizure modulation. *Ann. N. Y. Acad. Sci.* 553, 286–303. doi: 10.1111/j.1749-6632.1989.tb46650.x
- Kubek, M. J., Knobloch, S. M., Sharif, N. A., Burt, D. R., Buterbaugh, G. G., and Fuson, K. S. (1993). Thyrotropin-Releasing hormone gene expression and receptors are differentially modified in limbic foci by seizures. *Ann. Neurol.* 33, 70–76. doi: 10.1002/ana.41030112
- Kulkarni, R. N., Wang, Z. L., Akinsanya, K. O., Bennet, W. M., Wang, R. M., Smith, D. M., et al. (1995). Pyroglutamyl-phenylalanyl-proline amide attenuates thyrotropin-releasing hormone-stimulated insulin secretion in perfused rat islets and insulin-secreting clonal beta-cell lines. *Endocrinology* 136, 5155–5164. doi: 10.1210/endo.136.11.7588254
- Lai, C.-T., Li, H.-J., Yu, W., Shah, S., Bommineni, G. R., Perrone, V., et al. (2015). Rational modulation of the induced-fit conformational change for slow-onset inhibition in *Mycobacterium tuberculosis* InhA. *Biochemistry* 54, 4683–4691. doi: 10.1021/acs.biochem.5b00284
- Lanzara, R., Liebman, M., and Wilk, S. (1989). The use of analogues of TRH to probe the specificity of pyroglutamyl peptidase II. *Ann. NY Acad. Sci.* 553, 559–562. doi: 10.1111/j.1749-6632.1989.tb46696.x
- Lazcano, I., Uribe, R. M., Martínez-Chávez, E., Vargas, M. A., Matziari, M., Joseph-Bravo, P., et al. (2012). Pyroglutamyl peptidase II inhibition enhances the analeptic effect of Thyrotropin-Releasing Hormone in the rat medial septum. *J. Pharmacol. Exp. Ther.* 342, 222–231. doi: 10.1124/jpet.112.192278
- Lazcano, I., Cabral, A., Uribe, R. M., Jaimes-Hoy, L., Perello, M., Joseph-Bravo, P., et al. (2015). Fasting enhances pyroglutamyl peptidase II activity in tanyocytes of the mediobasal hypothalamus of male adult rats. *Endocrinology* 156, 2713–2723. doi: 10.1210/en.2014-1885
- Lechan, R. M., Wu, P., and Jackson, I. M. D. (1986). Immunolocalization of the Thyrotropin-Releasing Hormone prohormone in the rat central nervous system. *Endocrinology* 119, 1210–1216. doi: 10.1210/endo-119-3-1210
- Leppäluoto, J., Koivusalo, F., and Kraama, R. (1978). Thyrotropin-releasing factor: Distribution in neural and gastrointestinal tissues. *Acta Physiol. Scandinavica* 104, 175–179. doi: 10.1111/j.1748-1716.1978.tb06264.x
- Lesnikov, V. A., Korneva, E. A., Dall'ara, A., and Pierpaoli, W. (1992). The involvement of pineal gland and melatonin in immunity and aging: II. Thyrotropin-Releasing Hormone and melatonin forestall involution and promote reconstitution of the thymus in anterior hypothalamic area (Aha)-lesioned mice. *Int. J. Neurosci.* 62, 141–153. doi: 10.3109/00207459108999767
- Lin, J., and Wilk, S. (1998). Quantitation and regulation of pyroglutamyl peptidase II messenger RNA levels in rat tissues and GH3 cells. *Neuroendocrinology* 67, 197–208. doi: 10.1159/000054315
- Linden, H., del Rio Garcia, J., Huber, A., Kreil, G., and Smyth, D. (1996). The TRH-like peptides in rabbit testis are different from the TRH-like peptide in the prostate. *FEBS Lett.* 379, 11–14. doi: 10.1016/0014-5793(95)01468-3
- Luo, L., and Yano, N. (2004). Expression of thyrotropin-releasing hormone receptor in immortalized beta-cell lines and rat pancreas. *J. Endocrinol.* 181, 401–412. doi: 10.1677/joe.0.1810401
- Méndez, M., Cisneros, M., Baez, A., Joseph-Bravo, P., and Charli, J. L. (1999). Three TRH-like molecules are released from rat hypothalamus *in vitro*. *Neurochem. Res.* 24, 815–823. doi: 10.1023/a:1020993527602
- Müller-Fielitz, H., Stahr, M., Bernau, M., Richter, M., Abele, S., Krajka, V., et al. (2017). Tanyocytes control the hormonal output of the hypothalamic-pituitary-thyroid axis. *Nat. Commun.* 8, 484. doi: 10.1038/s41467-017-00604-6
- Marsili, A., Sanchez, E., Singru, P., Harney, J. W., Zavacki, A. M., Lechan, R. M., et al. (2011). Thyroxine-induced expression of pyroglutamyl peptidase II and inhibition of TSH release precedes suppression of TRH mRNA and requires type 2 deiodinase. *J. Endocrinol.* 211, 73–78. doi: 10.1530/JOE-11-0248
- Martinez de la Escalera, G., and Weiner, R. I. (1992). Dissociation of dopamine from its receptor as a signal in the pleiotropic hypothalamic regulation of prolactin secretion. *Endocr. Rev.* 13, 241–255. doi: 10.1210/edrv-13-2-241
- Martino, E., Lernmark, A., Seo, H., Steiner, D. F., and Refetoff, S. (1978). High concentration of thyrotropin-releasing hormone in pancreatic islets. *Proc. Natl. Acad. Sci.* 75, 4265–4267. doi: 10.1073/pnas.75.9.4265
- Matre, V., Hovring, P. I., Fjeldheim, Å.-K., Helgeland, L., Orvain, C., Andersson, K. B., et al. (2003). The human neuroendocrine thyrotropin-releasing hormone receptor promoter is activated by the haematopoietic transcription factor c-Myb. *Biochem. J.* 372, 851–859. doi: 10.1042/bj20030057
- Matziari, M., Bauer, K., Dive, V., and Yiotakis, A. (2008). Synthesis of the phosphinic analogue of Thyrotropin Releasing Hormone. *J. Org. Chem.* 73, 8591–8593. doi: 10.1021/jo8014215
- Meena, C. L., Ingole, S., Rajpoot, S., Thakur, A., Nandekar, P. P., Sangamwar, A. T., et al. (2015). Discovery of a low affinity thyrotropin-releasing hormone (TRH)-like peptide that exhibits potent inhibition of scopolamine-induced memory impairment in mice. *RSC Adv.* 5, 56872–56884. doi: 10.1039/C5RA06935A
- Mentlein, R. (1999). Dipeptidyl-peptidase IV (CD26)-role in the inactivation of regulatory peptides. *Regul. Peptides* 85, 9–24. doi: 10.1016/S0167-0115(99)00089-0
- Messeguer, X., Escudero, R., Farre, D., Nunez, O., Martinez, J., and Alba, M. M. (2002). PROMO: detection of known transcription regulatory elements using species-tailored searches. *Bioinformatics* 18, 333–334. doi: 10.1093/bioinformatics/18.2.333
- Minelli, A., Bellezza, I., Grottelli, S., and Galli, F. (2008). Focus on cyclo(His-Pro): history and perspectives as antioxidant peptide. *Amino Acids* 35, 283–289. doi: 10.1007/s00726-007-0629-6
- Mitsuma, T., Rhue, N., Sobue, G., Hirooka, Y., Kayama, M., Yokoi, Y., et al. (1995). Distribution of thyrotropin releasing hormone receptor in rats: an immunohistochemical study. *Endocr. Regul.* 29, 129–134.
- Monga, V., Meena, C., Kaur, N., and Jain, R. (2008). Chemistry and biology of Thyrotropin-Releasing Hormone (TRH) and its analogs. *CMC* 15, 2718–2733. doi: 10.2174/092986708786242912
- Montagne, J.-J., Ladram, A., Nicolas, P., and Bulant, M. (1999). Cloning of Thyrotropin-Releasing Hormone precursor and receptor in rat thymus, adrenal gland, and testis. *Endocrinology* 140, 1054–1059. doi: 10.1210/endo.140.3.6558
- Morier, E., Moreau, O., Masson, M. A., Han, K.-K., and Rips, R. (1979). Evidence for the enzymic degradation of thyrotropin-releasing-hormone (trh) and pseudo-hormone (pyroglutamyl-histidyl-amphetamine) by calf liver pyroglutamine-amino-peptidase. *Int. J. Biochem.* 10, 769–783. doi: 10.1016/0020-711X(79)90155-1
- Morley, J. E. (1979). Extrahypothalamic Thyrotropin Releasing Hormone (TRH) — Its distribution and its functions. *Life Sci.* 25, 1539–1550. doi: 10.1016/0024-3205(79)90435-1
- Mulla, C. M., Geras-Raaka, E., Raaka, B. M., and Gershengorn, M. C. (2009). High levels of Thyrotropin-Releasing Hormone receptors activate programmed cell death in human pancreatic precursors. *Pancreas* 38, 197–202. doi: 10.1097/MPA.0b013e31818d14a8
- Nakamura, T., Honda, M., Kimura, S., Tanabe, M., Oda, S., and Ono, H. (2005). Taltirelin improves motor ataxia independently of monoamine levels in rolling mouse Nagoya, a model of spinocerebellar atrophy. *Biol. Pharm. Bull.* 28, 2244–2247. doi: 10.1248/bpb.28.2244
- Nishio, Y., Kusugami, K., Kaneko, H., Yamamoto, H., Konagaya, T., Nagai, H., et al. (1999). Intraluminal thyrotropin-releasing hormone affects gastric somatostatin and acid secretion through its specific receptor in rats. *Scand. J. Gastroenterol.* 34, 270–275. doi: 10.1080/00365529950173672
- O'Connor, B., and O'Cuinn, G. (1985). Purification of amino and kinetic studies on a narrow specificity synaptosomal membrane pyroglutamate aminopeptidase from guinea-pig brain. *Eur. J. Biochem.* 150, 47–52. doi: 10.1111/j.1432-1033.1985.tb08986.x
- O'Leary, R., and O'Connor, B. (1995). Thyrotropin-releasing hormone. *J. Neurochem.* 65, 953–963. doi: 10.1046/j.1471-4159.1995.65030953.x
- Ogawa, N., Mizuno, S., Nukina, I., Tsukamoto, S., and Mori, A. (1983). Chronic thyrotropin releasing hormone (TRH) administration on TRH receptors and muscarinic cholinergic receptors in CNS. *Brain Res.* 263, 348–350. doi: 10.1016/0006-8993(83)90328-1
- Oka, M., Ochi, Y., Furukawa, K., Ito, T., Miura, Y., Karasawa, T., et al. (1989). L-6-ketopiperidine-2-carbonyl-L-leucyl-L-proline amide as a novel thyrotropin releasing hormone analogue with improving effects on impaired central nervous systems functions. *Arzneimittelforschung* 39, 297–303.

- Péterfi, Z., Farkas, E., Nagyunyomi-Sényi, K., Kádár, A., Ottó, S., Horváth, A., et al. (2018). Role of TRH/UCN3 neurons of the perifornical area/bed nucleus of stria terminalis region in the regulation of the anorexigenic POMC neurons of the arcuate nucleus in male mice and rats. *Brain Struct. Funct.* 223, 1329–1341. doi: 10.1007/s00429-017-1553-5
- Parnetti, L., Ambrosoli, L., Abate, G., Azzini, C., Balestreri, R., Bartorelli, L., et al. (1995). Positirelin for the treatment of late-onset Alzheimer's disease: a double-blind multicentre study vs citicoline and ascorbic acid. *Acta Neurol. Scand.* 92, 135–140. doi: 10.1111/j.1600-0404.1995.tb01027.x
- Pascual, I., Gil-Parrado, S., Cisneros, M., Joseph-Bravo, P., Díaz, J., Possani, L. D., et al. (2004). Purification of a specific inhibitor of pyroglutamate aminopeptidase II from the marine annelide *Hermodice carunculata*. *Int. J. Biochem. Cell Biol.* 36, 138–152. doi: 10.1016/S1357-2725(03)00175-4
- Patchett, A. A., and Cordes, E. H. (1985). "The design and properties of N-Carboxyalkyl dipeptide inhibitors of angiotensin-converting Enzyme," in *Advances in Enzymology - and Related Areas of Molecular Biology*. Ed. A. Meister (Hoboken, NJ, USA: John Wiley & Sons, Inc.), 1–84. doi: 10.1002/9780470123034.ch1
- Pawlikowski, M., Żerek-Meleń, G., and Winczyk, K. (1992). Thyroliberin (TRH) increases thymus cell proliferation in rats. *Neuropeptides* 23, 199–202. doi: 10.1016/0143-4179(92)90123-E
- Pekary, A. E., and Sattin, A. (2012). Rapid modulation of TRH and TRH-like peptide release in rat brain and peripheral tissues by ghrelin and 3-TRP-ghrelin. *Peptides* 36, 157–167. doi: 10.1016/j.peptides.2012.04.021
- Pekary, A. E., and Sattin, A. (2017). TRH and TRH-Like peptide levels co-vary with reproductive and metabolic rhythms. *Horm. Metab. Res.* 49, 86–94. doi: 10.1055/s-0042-111012
- Pekary, A. E., Sattin, A., Meyerhoff, J. L., and Chilingar, M. (2004). Valproate modulates TRH receptor, TRH and TRH-like peptide levels in rat brain. *Peptides* 25, 647–658. doi: 10.1016/j.peptides.2004.01.016
- Pekary, A. E., Faull, K. F., Paulson, M., Lloyd, R. L., and Sattin, A. (2005). TRH-like antidepressant peptide, pyroglutamyltyrosylprolineamide, occurs in rat brain. *J. Mass Spectrom* 40, 1232–1236. doi: 10.1002/jms.904
- Pekary, A. E., Sattin, A., and Lloyd, R. L. (2015). Ketamine modulates TRH and TRH-like peptide turnover in brain and peripheral tissues of male rats. *Peptides* 69, 66–76. doi: 10.1016/j.peptides.2015.04.003
- Peres Diaz, L. S., Schuman, M. L., Aisicovich, M., Toblli, J. E., Pirola, C. J., Landa, M. S., et al. (2018). Angiotensin II requires an intact cardiac thyrotropin-releasing hormone (TRH) system to induce cardiac hypertrophy in mouse. *J. Mol. Cell. Cardiol.* 124, 1–11. doi: 10.1016/j.jmcc.2018.09.009
- Perez Castro, C., Peñalva, R., Páez Pereda, M., Renner, U., Reul, J. M., Stalla, G. K., et al. (1999). Early activation of thyrotropin-releasing-hormone and prolactin plays a critical role during a T cell-dependent immune response. *Endocrinology* 140, 690–697. doi: 10.1210/endo.140.2.6482
- Pierpaoli, W., and Yi, C. (1990). The involvement of pineal gland and melatonin in immunity and aging I. Thymus-mediated, immunoreconstituting and antiviral activity of thyrotropin-releasing hormone. *J. Neuroimmunol.* 27, 99–109. doi: 10.1016/0165-5728(90)90059-V
- Pierpaoli, W. (2013). Aging-reversing properties of Thyrotropin-Releasing Hormone. *CAS* 6, 92–98. doi: 10.2174/1874609811306010012
- Pilowsky, P. M. (2014). "Peptides, serotonin, and breathing," in *Progress in Brain Research* (Oxford, UK:Elsevier), 169–189. doi: 10.1016/B978-0-444-63274-6.00009-6
- Prasad, C., and Jayaraman, A. (1986). Metabolism of thyrotropin-releasing hormone in human cerebrospinal fluid. Isolation and characterization of pyroglutamate aminopeptidase activity. *Brain Res.* 364, 331–337. doi: 10.1016/0006-8993(86)90845-0
- Prasad, C., and Peterkofsky, A. (1976). Demonstration of pyroglutamylpeptidase and amidase activities toward thyrotropin-releasing hormone in hamster hypothalamus extracts. *J. Biol. Chem.* 251, 3229–3234.
- Prasad, C. (1989). Neurobiology of Cyclo(His-Pro). *Ann. NY Acad. Sci.* 553, 232–251. doi: 10.1111/j.1749-6632.1989.tb46646.x
- Prasad, C. (1995). Bioactive cyclic dipeptides. *Peptides* 16, 151–164. doi: 10.1016/0196-9781(94)00017-Z
- Prokai-Tatrai, K., and Prokai, L. (2009). Prodrugs of Thyrotropin-Releasing Hormone and related peptides as central nervous system agents. *Molecules* 14, 633–654. doi: 10.3390/molecules14020633
- Puga, L., Alcántara-Alonso, V., Coffeen, U., Jaimes, O., and de Gortari, P. (2016). TRH injected into the nucleus accumbens shell releases dopamine and reduces feeding motivation in rats. *Behav. Brain Res.* 306, 128–136. doi: 10.1016/j.bbr.2016.03.031
- Rabeler, R., Mittag, J., Geffers, L., Rütger, U., Leitges, M., Parlow, A. F., et al. (2004). Generation of Thyrotropin-Releasing Hormone receptor 1-deficient mice as an animal model of central hypothyroidism. *Mol. Endocrinol.* 18, 1450–1460. doi: 10.1210/me.2004-0017
- Rausell, V., Fraser, H. M., Tobaruela, M., del Rio-García, J., and Smyth, D. G. (1999). Identification of the TRH-like peptides pGlu-Glu-Pro amide and pGlu-Phe-Pro amide in rat thyroid: regulation by thyroid status. *Regul. Peptides* 81, 55–60. doi: 10.1016/S0167-0115(99)00017-8
- Redding, T. W., and Schally, A. V. (1969). Studies on the Thyrotropin-Releasing Hormone (TRH) activity in peripheral blood. *Exp. Biol. Med.* 131, 420–425. doi: 10.3181/00379727-131-33892
- Rodríguez-Molina, V., Vargas, M.Á., Joseph-Bravo, P., and Charli, J.-L. (2009). NMDA receptor up-regulates pyroglutamyl peptidase II activity in the rat hippocampus. *Neurosci. Lett.* 449, 211–214. doi: 10.1016/j.neulet.2008.11.005
- Rodríguez-Molina, V., Patiño, J., Vargas, Y., Sánchez-Jaramillo, E., Joseph-Bravo, P., and Charli, J.-L. (2014). TRH regulates action potential shape in cerebral cortex pyramidal neurons. *Brain Res.* 1571, 1–11. doi: 10.1016/j.brainres.2014.05.015
- Rodríguez-Rodríguez, A., Lazcano, I., Sánchez-Jaramillo, E., Uribe, R. M., Jaimes-Hoy, L., Joseph-Bravo, P., et al. (2019). Tanycytes and the control of Thyrotropin-Releasing Hormone flux into portal capillaries. *Front. Endocrinol.* 10, 401. doi: 10.3389/fendo.2019.00401
- Rondeel, J. M. M., Klootwijk, W., Linkels, E., Jeucken, W., H. M. P., Hofland, L. J., et al. (1995a). Further studies on the regulation, localization and function of the TRH-like peptide pyroglutamyl-glutamyl-prolineamide in the rat anterior pituitary gland. *J. Endocrinol.* 146, 293–300. doi: 10.1677/joe.0.1460293
- Rondeel, J. M. M., Klootwijk, W., Linkels, E., van Haasteren, G. A. C., de Greef, W. J., and Visser, T. J. (1995b). Regulation of the TRH-like peptide pyroglutamyl-glutamyl-prolineamide in the rat anterior pituitary gland. *J. Endocrinol.* 145, 43–49. doi: 10.1677/joe.0.1450043
- Rosen, J. B., Cain, C. J., Weiss, S. R. B., and Post, R. M. (1992). Alterations in mRNA of enkephalin, dynorphin and thyrotropin releasing hormone during amygdala kindling: an in situ hybridization study. *Mol. Brain Res.* 15, 247–255. doi: 10.1016/0169-328X(92)90115-R
- Runfola, M., Sestito, S., Bellusci, L., La Pietra, V., D'Amore, V. M., Kowalik, M. A., et al. (2020). Design, synthesis and biological evaluation of novel TR β selective agonists sustained by ADME-toxicity analysis. *Eur. J. Med. Chem.* 188, 112006. doi: 10.1016/j.ejmech.2019.112006
- Sánchez, E., Uribe, R. M., Corkidi, G., Zoeller, R. T., Cisneros, M., Zacarias, M., et al. (2001). Differential responses of Thyrotropin-Releasing Hormone (TRH) neurons to cold exposure or suckling indicate functional heterogeneity of the TRH system in the paraventricular nucleus of the rat hypothalamus. *Neuroendocrinology* 74, 407–422. doi: 10.1159/000054707
- Sánchez, E., Vargas, M. A., Singru, P. S., Pascual, I., Romero, F., Fekete, C., et al. (2009). Tanycyte Pyroglutamyl Peptidase II contributes to regulation of the hypothalamic-pituitary-thyroid axis through glial-axonal associations in the median eminence. *Endocrinology* 150, 2283–2291. doi: 10.1210/en.2008-1643
- Sánchez, E., Charli, J.-L., and Lechan, R. M. (2013). "Pyroglutamyl-Peptidase II," in *Handbook of Proteolytic Enzymes* (Oxford, UK:Elsevier), 414–419. doi: 10.1016/B978-0-12-382219-2.00083-1
- Sárvári, A., Farkas, E., Kádár, A., Zséli, G., Füzesi, T., Lechan, R. M., et al. (2012). Thyrotropin-releasing hormone-containing axons innervate histaminergic neurons in the tuberomammillary nucleus. *Brain Res.* 1488, 72–80. doi: 10.1016/j.brainres.2012.10.010
- Sah, N., Rajput, S. K., Singh, J. N., Meena, C. L., Jain, R., Sikdar, S. K., et al. (2011). l-pGlu-(2-propyl)-l-His-l-ProNH₂ attenuates 4-aminopyridine-induced epileptiform activity and sodium current: a possible action of new thyrotropin-releasing hormone analog for its anticonvulsant potential. *Neuroscience* 199, 74–85. doi: 10.1016/j.neuroscience.2011.10.008
- Saito, Y., Mekuchi, M., Kobayashi, N., Kimura, M., Aoki, Y., Masuda, T., et al. (2011). Molecular cloning, molecular evolution and gene expression of cDNAs encoding thyrotropin-releasing hormone receptor subtypes in a teleost, the sockeye salmon (*Oncorhynchus nerka*). *Gen. Comp. Endocrinol.* 174, 80–88. doi: 10.1016/j.ygcen.2011.07.011

- Sasahara, H., Otaka, M., Itoh, S., Iwabuchi, A., Odashima, M., Wada, I., et al. (1998). Effect of preinduction of heat-shock proteins on acetic acid-induced small intestinal lesions in rats. *Dig. Dis. Sci.* 43, 2117–2130. doi: 10.1023/a:1018827802462
- Sasaki, I., Fujita, T., Murakami, M., Yamamoto, A., Nakamura, E., Imasaki, H., et al. (1994). Intestinal absorption of azetirelin, a new Thyrotropin-Releasing Hormone (TRH) analogue. I. Possible factors for the low oral bioavailability in rats. *Biol. Pharm. Bull.* 17, 1256–1261. doi: 10.1248/bpb.17.1256
- Sasaki, I., Tozaki, H., Matsumoto, K., Ito, Y., Fujita, T., Murakami, M., et al. (1999). Development of an oral formulation of azetirelin, a new thyrotropin-releasing hormone (TRH) analogue, using n-lauryl-beta-D-maltopyranoside as an absorption enhancer. *Biol. Pharm. Bull.* 22, 611–615. doi: 10.1248/bpb.22.611
- Sattin, A. (1999). The role of TRH and related peptides in the mechanism of action of ECT. *J. ECT* 15, 76–92. doi: 10.1097/00124509-199903000-00007
- Scalabrino, G. A., Hogan, N., O'Boyle, K. M., Slator, G. R., Gregg, D. J., Fitchett, C. M., et al. (2007). Discovery of a dual action first-in-class peptide that mimics and enhances CNS-mediated actions of thyrotropin-releasing hormone. *Neuropharmacology* 52, 1472–1481. doi: 10.1016/j.neuropharm.2007.02.003
- Schäuder, B., Schomburg, L., Kohrle, J., and Bauer, K. (1994). Cloning of a cDNA encoding an ectoenzyme that degrades thyrotropin-releasing hormone. *Proc. Natl. Acad. Sci.* 91, 9534–9538. doi: 10.1073/pnas.91.20.9534
- Schmitmeier, S., Thole, H., Bader, A., and Bauer, K. (2002). Purification and characterization of the thyrotropin-releasing hormone (TRH)-degrading serum enzyme and its identification as a product of liver origin. *Eur. J. Biochem.* 269, 1278–1286. doi: 10.1046/j.1432-1033.2002.02768.x
- Schomburg, L., Turwitt, S., Prescher, G., Lohmann, D., Horsthemke, B., and Bauer, K. (1999). Human TRH-degrading ectoenzyme cDNA cloning, functional expression, genomic structure and chromosomal assignment. *Eur. J. Biochem.* 265, 415–422. doi: 10.1046/j.1432-1327.1999.00753.x
- Schuman, M. L., Landa, M. S., Toblli, J. E., Peres Diaz, L. S., Alvarez, A. L., Finkielman, S., et al. (2011). Cardiac Thyrotropin-Releasing Hormone mediates left ventricular hypertrophy in spontaneously hypertensive rats. *Hypertension* 57, 103–109. doi: 10.1161/HYPERTENSIONAHA.110.161265
- Schuman, M. L., Peres Diaz, L. S., Landa, M. S., Toblli, J. E., Cao, G., Alvarez, A. L., et al. (2014). Thyrotropin-releasing hormone overexpression induces structural changes of the left ventricle in the normal rat heart. *Am. J. Physiol. Heart Circ. Physiol.* 307, H1667–H1674. doi: 10.1152/ajpheart.00494.2014
- Segerson, T. P., Hoefler, H., Childers, H., Wolfe, H. J., Wu, P., Jackson, I. M. D., et al. (1987). Localization of Thyrotropin-Releasing Hormone prohormone messenger ribonucleic acid in rat brain by in situ hybridization. *Endocrinology* 121, 98–107. doi: 10.1210/endo-121-1-98
- Sharif, N. A., Towle, A. C., Burt, D. R., Mueller, R. A., and Breese, G. R. (1989). Contrasmitters: differential effects of serotonin (5-HT)-depleting drugs on levels of 5-HT and TRH and their receptors in rat brain and spinal cord. *Brain Res.* 480, 365–371. doi: 10.1016/0006-8993(89)90209-6
- Shi, Z.-X., Xu, W., Mergner, W. J., Li, Q.-L., Cole, K. H., and Wilber, J. F. (1996). Localization of Thyrotropin-Releasing Hormone mRNA expression in the rat heart by in situ hybridization histochemistry. *Pathobiology* 64, 314–319. doi: 10.1159/000164066
- Shishido, Y., Furushiro, M., Tanabe, S., Shibata, S., Hashimoto, S., and Yokokura, T. (1999). Effects of prolyl endopeptidase inhibitors and neuropeptides on delayed neuronal death in rats. *Eur. J. Pharmacol.* 372, 135–142. doi: 10.1016/S0014-2999(99)00185-5
- Simasko, S. M., and Horita, A. (1985). Treatment of rats with the TRH analog MK-771. *Neuropharmacology* 24, 157–165. doi: 10.1016/0028-3908(85)90175-3
- Siviter, R. J., and Cockle, S. M. (1995). Peptides related to thyrotrophin-releasing hormone are degraded in seminal plasma by an enzyme similar to prolyl endopeptidase. *J. Endocrinol.* 144, 61–66. doi: 10.1677/joe.0.1440061
- Sjöström, H., Norén, O., and Olsen, J. (2002). “Structure and function of aminopeptidase N,” in *Cellular Peptidases in Immune Functions and Diseases 2*. Eds. J. Langner and S. Ansoorge ((Boston, MA: Springer US)), 25–34. doi: 10.1007/0-306-46826-3_2
- Smyth, D. G., del Rio-Garcia, J., Wallnöfer, H., Gogl, H., Simma, W., Huber, A., et al. (1999). Protirelin (thyrotropin-releasing hormone) in thyroid gland: possible involvement in regulation of thyroid status. *Zhongguo Yao Li Xue Bao* 20, 289–291.
- Štrbák, V. (2018). Pancreatic Thyrotropin Releasing Hormone and Mechanism of Insulin Secretion. *Cell Physiol. Biochem.* 50, 378–384. doi: 10.1159/000494013
- Sugimoto, T., Hayashi, T., Okita, A., and Morino, A. (1996). Pharmacokinetics of the new thyrotropin releasing hormone analogue montirelin hydrate. 1st communication: plasma concentrations, metabolism and excretion after a single intravenous administration to rats, dogs and monkeys. *Arzneimittelforschung* 46, 106–113.
- Sun, Y., Lu, X., and Gershengorn, M. (2003). Thyrotropin-releasing hormone receptors – similarities and differences. *J. Mol. Endocrinol.* 30, 87–97. doi: 10.1677/jme.0.0300087
- Sun, Y., Zupan, B., Raaka, B. M., Toth, M., and Gershengorn, M. C. (2009). TRH-receptor-type-2-deficient mice are euthyroid and exhibit increased depression and reduced anxiety phenotypes. *Neuropsychopharmacol.* 34, 1601–1608. doi: 10.1038/npp.2008.217
- Suzuki, M., Sugano, H., Matsumoto, K., Yamamura, M., and Ishida, R. (1990). Synthesis and central nervous system actions of thyrotropin-releasing hormone analog containing a dihydroorotic acid moiety. *J. Med. Chem.* 33, 2130–2137. doi: 10.1021/jm00170a014
- Szabo, L., Morey, R., Palpant, N. J., Wang, P. L., Afari, N., Jiang, C., et al. (2015). Statistically based splicing detection reveals neural enrichment and tissue-specific induction of circular RNA during human fetal development. *Genome Biol.* 16, 126. doi: 10.1186/s13059-015-0690-5
- Szirtes, T., Kisfaludy, L., Palosi, E., and Szporny, L. (1984). Synthesis of thyrotropin-releasing hormone analogs. 1. Complete dissociation of central nervous system effects from thyrotropin-releasing activity. *J. Med. Chem.* 27, 741–745. doi: 10.1021/jm00372a006
- Szirtes, T., Kisfaludy, L., Palosi, E., and Szporny, L. (1986). Synthesis of thyrotropin-releasing hormone analogs. 2. Tripeptides structurally greatly different from TRH with high central nervous system activity. *J. Med. Chem.* 29, 1654–1658. doi: 10.1021/jm00159a015
- Taché, Y., Yang, H., Miampamba, M., Martinez, V., and Yuan, P. Q. (2006). Role of brainstem TRH/TRH-R1 receptors in the vagal gastric cholinergic response to various stimuli including sham-feeding. *Autonomic Neurosci.* 125, 42–52. doi: 10.1016/j.autneu.2006.01.014
- Tache, Y. (2012). Brainstem neuropeptides and vagal protection of the gastric mucosal against injury: role of prostaglandins, nitric oxide and calcitonin-gene related peptide in capsaicin afferents. *CMC* 19, 35–42. doi: 10.2174/092986712803414097
- Takeuchi, Y., Takano, T., Abe, J., Takikita, S., and Ohno, M. (2001). Thyrotropin-releasing hormone: role in the treatment of West syndrome and related epileptic encephalopathies. *Brain Dev.* 23, 662–667. doi: 10.1016/S0387-7604(01)00303-5
- Tang, T., Li, L., Tang, J., Li, Y., Lin, W. Y., Martin, F., et al. (2010). A mouse knockout library for secreted and transmembrane proteins. *Nat. Biotechnol.* 28, 749–755. doi: 10.1038/nbt.1644
- Taylor, W. L., and Dixon, J. E. (1976). The inhibition of thyrotropin-releasing hormone deamidation in porcine hypothalamic tissues. *Biochim. Biophys. Acta (BBA) Gen. Subj.* 444, 428–434. doi: 10.1016/0304-4165(76)90386-X
- Tenorio-Laranga, J., Venäläinen, J. I., Männistö, P. T., and García-Horsman, J. A. (2008). Characterization of membrane-bound prolyl endopeptidase from brain: Membrane-bound prolyl oligopeptidase: mPOP. *FEBS J.* 275, 4415–4427. doi: 10.1111/j.1742-4658.2008.06587.x
- Terauchi, Y., Ishikawa, S., Oida, S., Negoro, T., Kagemoto, A., and Sekine, Y. (1988). Determination of L-6-keto-piperidine-2-carbonyl-L-leucyl-L-proline amide (RGH-2202), a new analog of thyrotropin-releasing hormone, in plasma by radioimmunoassay. *J. Pharmacobio. Dynamics* 11, 459–464. doi: 10.1248/bpb1978.11.459
- Thirunarayanan, N., Nir, E. A., Raaka, B. M., and Gershengorn, M. C. (2013). Thyrotropin-Releasing Hormone Receptor Type 1 (TRH-R1), not TRH-R2, Primarily Mediates Taltirelin Actions in the CNS of Mice. *Neuropsychopharmacol.* 38, 950–956. doi: 10.1038/npp.2012.256
- Thompson, B. L., and Rosen, J. B. (2000). Effects of TRH on acoustic startle, conditioned fear and active avoidance in rats. *Neuropeptides* 34, 38–44. doi: 10.1054/npep.1999.0785
- Torres, H., Charli, J., Gonzaleznoriega, A., Vargas, M., and Joseph-Bravo, P. (1986). Subcellular distribution of the enzymes degrading thyrotropin releasing hormone and metabolites in rat brain. *Neurochem. Int.* 9, 103–110. doi: 10.1016/0197-0186(86)90038-0
- Traube, T., Shokhen, M., and Albeck, A. (2014). A new method for filtering of reactive “warheads” of transition-state analog protease inhibitors. *Eur. J. Med. Chem.* 77, 134–138. doi: 10.1016/j.ejmech.2014.02.059

- Uhlén, M., Fagerberg, L., Hallström, B. M., Lindskog, C., Oksvold, P., Mardinoglu, A., et al. (2015). Tissue-based map of the human proteome. *Science* 347, 1260419–1260419. doi: 10.1126/science.1260419
- Urayama, A., Yamada, S., Hirano, K., Deguchi, Y., and Kimura, R. (2001). Brain receptor binding characteristics and pharmacokinetic-pharmacodynamic analysis of thyrotropin-releasing hormone analogues. *Life Sci.* 70, 647–657. doi: 10.1016/S0024-3205(01)01445-X
- Urayama, A., Yamada, S., Kimura, R., Zhang, J., and Watanabe, Y. (2002). Neuroprotective effect and brain receptor binding of taltirelin, a novel thyrotropin-releasing hormone (TRH) analogue, in transient forebrain ischemia of C57BL/6J mice. *Life Sci.* 72, 601–607. doi: 10.1016/S0024-3205(02)02268-3
- Vargas, M., Mendez, M., Cisneros, M., Joseph-Bravo, P., and Charli, J. L. (1987). Regional distribution of the membrane-bound pyroglutamate amino peptidase-degrading thyrotropin-releasing hormone in rat brain. *Neurosci. Lett.* 79, 311–314. doi: 10.1016/0304-3940(87)90450-2
- Vargas, M. A., Cisneros, M., Herrera, J., Joseph-Bravo, P., and Charli, J.-L. (1992a). Regional distribution of pyroglutamyl peptidase II in rabbit brain, spinal cord, and organs. *Peptides* 13, 255–260. doi: 10.1016/0196-9781(92)90105-C
- Vargas, M. A., Herrera, J., Uribe, R. M., Charli, J.-L., and Joseph-Bravo, P. (1992b). Ontogenesis of pyroglutamyl peptidase II activity in rat brain, adenohippophysis and pancreas. *Dev. Brain Res.* 66, 251–256. doi: 10.1016/0165-3806(92)90087-D
- Veronesi, M. C., Kubek, D. J., and Kubek, M. J. (2007). Intranasal delivery of a Thyrotropin-Releasing Hormone analog attenuates seizures in the amygdala-kindled rat. *Epilepsia* 48, 2280–2286. doi: 10.1111/j.1528-1167.2007.01218.x
- Vogel, R. A., Frye, G. D., Wilson, J. H., Kuhn, C. M., Mailman, R. B., Mueller, R. A., et al. (1980). Attenuation of the effect of punishment by thyrotropin-releasing hormone: comparisons with chlórdiazepoxide. *J. Pharmacol. Exp. Ther.* 212, 153–161.
- Wang, W., and Gershengorn, M. C. (1999). Rat TRH receptor type 2 exhibits higher basal signaling activity than TRH receptor type 1. *Endocrinology* 140, 4916–4919. doi: 10.1210/endo.140.10.7159
- Wilk, S., and Wilk, E. (1989). Pyroglutamyl peptidase II, a thyrotropin releasing hormone degrading enzyme: purification and specificity studies of the rabbit brain enzyme. *Neurochem. Int.* 15, 81–89. doi: 10.1016/0197-0186(89)90079-X
- Wilk, S. (1983). Prolyl endopeptidase. *Life Sci.* 33, 2149–2157. doi: 10.1016/0024-3205(83)90285-0
- Williams, R. S. B., Eames, M., Ryves, W. J., Viggars, J., and Harwood, A. J. (1999). Loss of a prolyl oligopeptidase confers resistance to lithium by elevation of inositol (1,4,5) trisphosphate. *EMBO J.* 18, 2734–2745. doi: 10.1093/emboj/18.10.2734
- Yamada, M., Saga, Y., Shibusawa, N., Hirato, J., Murakami, M., Iwasaki, T., et al. (1997). Tertiary hypothyroidism and hyperglycemia in mice with targeted disruption of the thyrotropin-releasing hormone gene. *Proc. Natl. Acad. Sci.* 94, 10862–10867. doi: 10.1073/pnas.94.20.10862
- Yamada, M., Shibusawa, N., Hashida, T., Satoh, T., Monden, T., Prasad, C., et al. (1999). Abundance of Cyclo (His-Pro)-like immunoreactivity in the brain of TRH-deficient mice. *Endocrinology* 140, 538–541. doi: 10.1210/endo.140.1.6607
- Yamada, M., Shibusawa, N., Hashida, T., Ozawa, A., Monden, T., Satoh, T., et al. (2000). Expression of Thyrotropin-Releasing Hormone (TRH) receptor subtype 1 in mouse pancreatic islets and HIT-T15, an insulin-secreting clonal β cell line. *Life Sci.* 66, 1119–1125. doi: 10.1016/S0024-3205(00)00415-X
- Yamada, M., Shibusawa, N., Ishii, S., Horiguchi, K., Umezawa, R., Hashimoto, K., et al. (2006). Prolactin secretion in mice with Thyrotropin-Releasing Hormone deficiency. *Endocrinology* 147, 2591–2596. doi: 10.1210/en.2005-1326
- Yamamoto, M., and Shimizu, M. (1987). Effects of a new TRH analogue, YM-14673 on the central nervous system. *Naunyn-Schmiedeberg's Arch. Pharmacol.* 336, 561–565. doi: 10.1007/BF00169314
- Yamamoto, H., Morise, K., Kusugami, K., Furusawa, A., Konagaya, T., Nishio, Y., et al. (1996). Abnormal neuropeptide concentration in rectal mucosa of patients with inflammatory bowel disease. *J. Gastroenterol.* 31, 525–532. doi: 10.1007/BF02355052
- Yamamura, M., Kinoshita, K., Nakagawa, H., Tanaka, T., Maeda, K., and Ishida, R. (1990). Pharmacological study of TA-0910, a new thyrotropin-releasing hormone (TRH) analog. (I). Effects on the central nervous system by oral administration. *Jpn. J. Pharmacol.* 53, 451–461. doi: 10.1254/jjp.53.451
- Yamamura, M., Kinoshita, K., Nakagawa, H., and Ishida, R. (1991a). Pharmacological study of TA-0910, a new thyrotropin-releasing hormone (TRH) analog (II): Involvement of the DA system in the locomotor stimulating action of TA-0910. *Jpn. J. Pharmacol.* 55, 57–68. doi: 10.1254/jjp.55.57
- Yamamura, M., Kinoshita, K., Nakagawa, H., and Ishida, R. (1991b). Pharmacological study of TA-0910, a new thyrotropin-releasing hormone (TRH) analog (III): Inhibition of pentobarbital anesthesia. *Jpn. J. Pharmacol.* 55, 69–80. doi: 10.1254/jjp.55.69
- Yamaoka, T., and Itakura, M. (1999). Development of pancreatic islets (review). *Int. J. Mol. Med.* 247–261. doi: 10.3892/ijmm.3.3.247
- Yang, H., Taché, Y., Ohning, G., and Go, V. L. W. (2002). Activation of raphe pallidus neurons increases insulin through medullary Thyrotropin-Releasing Hormone (TRH)-vagal pathways. *Pancreas* 25, 301–307. doi: 10.1097/00006676-200210000-00014
- Yang, H., Nyby, M. D., Ao, Y., Chen, A., Adelson, D. W., Smutko, V., et al. (2012). Role of brainstem thyrotropin-releasing hormone-triggered sympathetic overactivation in cardiovascular mortality in type 2 diabetic Goto-Kakizaki rats. *Hypertens. Res.* 35, 157–165. doi: 10.1038/hr.2011.154
- Yokohama, S., Yoshioka, T., Yamashita, K., and Kitamori, N. (1984). Intestinal absorption mechanisms of thyrotropin-releasing hormone. *J. Pharmacobio. Dynamics* 7, 445–451. doi: 10.1248/bpb1978.7.445
- Yoo, S., Cha, D., Kim, S., Jiang, L., Adebesin, M., Wolfe, A., et al. (2019). Ablation of tanycytes of the arcuate nucleus and median eminence increases visceral adiposity and decreases insulin sensitivity in male mice. *bioRxiv*. doi: 10.1101/637587
- Yu, Y., Zhao, C., Su, Z., Wang, C., Fuscoe, J. C., Tong, W., et al. (2014). Comprehensive RNA-Seq transcriptomic profiling across 11 organs, 4 ages, and 2 sexes of Fischer 344 rats. *Sci. Data* 1, 140013. doi: 10.1038/sdata.2014.13
- Zacur, H. A., Genadry, R., Rock, J. A., King, T. M., Smith, B. R., and Foster, G. V. (1985). Thyrotropin-Releasing Hormone-Induced contraction of urethral and vaginal muscle. *J. Clin. Endocrinol. Metab.* 61, 787–789. doi: 10.1210/jcem-61-4-787
- Zada, M. H., Kubek, M., Khan, W., Kumar, A., and Domb, A. (2019). Dispersible hydrolytically sensitive nanoparticles for nasal delivery of thyrotropin releasing hormone (TRH). *J. Control Release* 295, 278–289. doi: 10.1016/j.jconrel.2018.12.050
- Zafirov, D. H., Cooke, H. J., and Wood, J. D. (1991). Thyrotropin-releasing hormone excites submucous neurons an guinea-pig ileum. *Eur. J. Pharmacol.* 204, 109–112. doi: 10.1016/0014-2999(91)90843-F
- Zarif, H., Petit-Paillet, A., Heurteaux, C., Chabry, J., and Guyon, A. (2016). TRH modulates glutamatergic synaptic inputs on CA1 neurons of the mouse hippocampus in a biphasic manner. *Neuropharmacology* 110, 69–81. doi: 10.1016/j.neuropharm.2016.04.004
- Zeisel, A., Hochgerner, H., Lönnerberg, P., Johnsson, A., Memic, F., van der Zwan, J., et al. (2018). Molecular architecture of the mouse nervous system. *Cell* 174, 999–1014.e22. doi: 10.1016/j.cell.2018.06.021
- Zeng, H., Schimpf, B. A., Rohde, A. D., Pavlova, M. N., Gragerov, A., and Bergmann, J. E. (2007). Thyrotropin-Releasing Hormone receptor 1-deficient mice display increased depression and anxiety-like behavior. *Mol. Endocrinol.* 21, 2795–2804. doi: 10.1210/me.2007-0048
- Zhu, Q.-S., Rosenblatt, K., Huang, K.-L., Lahat, G., Brobey, R., Bolshakov, S., et al. (2011). Vimentin is a novel AKT1 target mediating motility and invasion. *Oncogene* 30, 457–470. doi: 10.1038/onc.2010.421
- Zhuan, B., Lu, Y., Chen, Q., Zhao, X., Li, P., Yuan, Q., et al. (2019). Overexpression of the long noncoding RNA TRHDE-AS1 inhibits the progression of lung cancer via the miRNA-103/KLF4 axis. *J. Cell Biochem.* 120, 17616–17624. doi: 10.1002/jcb.29029

Conflict of Interest: The authors declare that the research was conducted in the absence of any commercial or financial relationships that could be construed as a potential conflict of interest.

Copyright © 2020 Charli, Rodríguez-Rodríguez, Hernández-Ortega, Cote-Vélez, Uribe, Jaimes-Hoy and Joseph-Bravo. This is an open-access article distributed under the terms of the Creative Commons Attribution License (CC BY). The use, distribution or reproduction in other forums is permitted, provided the original author(s) and the copyright owner(s) are credited and that the original publication in this journal is cited, in accordance with accepted academic practice. No use, distribution or reproduction is permitted which does not comply with these terms.



OPEN ACCESS

Edited by:

Salvatore Salomone,
University of Catania, Italy

Reviewed by:

Carla Denise Bonan,
Pontifical Catholic University of Rio
Grande do Sul, Brazil
Holger Stephan,
Helmholtz-Gemeinschaft Deutscher
Forschungszentren (HZ), Germany

*Correspondence:

Younis Baqi
baqi@squ.edu.om
Christa E. Müller
christa.mueller@uni-bonn.de

[†]On leave from the Department of
Pharmaceutical and Medicinal
Chemistry, Faculty of Pharmacy,
Al-Azhar University, Cairo, Egypt

Specialty section:

This article was submitted to
Experimental Pharmacology
and Drug Discovery,
a section of the journal
Frontiers in Pharmacology

Received: 05 June 2020

Accepted: 03 August 2020

Published: 27 August 2020

Citation:

Baqi Y, Rashed M, Schäkel L,
Malik EM, Pelletier J, Sévigny J,
Fiene A and Müller CE (2020)
Development of Anthraquinone
Derivatives as Ectonucleoside
Triphosphate Diphosphohydrolase
(NTPDase) Inhibitors With Selectivity
for NTPDase2 and NTPDase3.
Front. Pharmacol. 11:1282.
doi: 10.3389/fphar.2020.01282

Development of Anthraquinone Derivatives as Ectonucleoside Triphosphate Diphosphohydrolase (NTPDase) Inhibitors With Selectivity for NTPDase2 and NTPDase3

Younis Baqi^{1*}, Mahmoud Rashed^{2†}, Laura Schäkel², Enas M. Malik², Julie Pelletier³, Jean Sévigny^{3,4}, Amelie Fiene² and Christa E. Müller^{2*}

¹ Department of Chemistry, Faculty of Science, Sultan Qaboos University, Muscat, Oman, ² PharmaCenter Bonn, Pharmaceutical Institute, Pharmaceutical & Medicinal Chemistry, University of Bonn, Bonn, Germany, ³ Centre de Recherche du CHU de Québec–Université Laval, Québec, QC, Canada, ⁴ Département de Microbiologie-Infectiologie et d'Immunologie, Faculté de Médecine, Université Laval, Québec, QC, Canada

Ectonucleoside triphosphate diphosphohydrolases (NTPDases) catalyze the hydrolysis of nucleoside tri- and di-phosphates to mono-phosphates. The products are subsequently hydrolyzed by ecto-5'-nucleotidase (ecto-5'-NT) to nucleosides. NTPDase inhibitors have potential as novel drugs, e.g., for the treatment of inflammation, neurodegenerative diseases, and cancer. In this context, a series of anthraquinone derivatives structurally related to the anthraquinone dye reactive blue-2 (RB-2) was synthesized and evaluated as inhibitors of human NTPDases utilizing a malachite green assay. We identified several potent and selective inhibitors of human NTPDase2 and -3. Among the most potent NTPDase2 inhibitors were 1-amino-4-(9-phenanthrylamino)-9,10-dioxo-9,10-dihydroanthracene-2-sulfonate (20, PSB-16131, IC₅₀ of 539 nM) and 1-amino-4-(3-chloro-4-phenylsulfanyl)phenylamino-9,10-dioxo-9,10-dihydroanthracene-2-sulfonate (48, PSB-2020, IC₅₀ of 551 nM). The most potent NTPDase3 inhibitors were 1-amino-4-[3-(4,6-dichlorotriazin-2-ylamino)-4-sulfophenylamino]-9,10-dioxo-9,10-dihydroanthracene-2-sulfonate (42, PSB-1011, IC₅₀ of 390 nM) and 1-amino-4-(3-carboxy-4-hydroxyphenylamino)-9,10-dioxo-9,10-dihydroanthracene-2-sulfonate (33, PSB-2046, IC₅₀ of 723 nM). The best NTPDase2 inhibitor 20 showed a non-competitive inhibition type, while the NTPDase3 inhibitor 42 behaved as a mixed-type inhibitor. These potent compounds were found to be selective vs. other NTPDases. They will be useful tools for studying the roles of NTPDase2 and -3 in physiology and under pathological conditions.

Keywords: anthraquinone, CD39, inhibitor, metalloenzymes, neuroinflammation, NTPDase2, NTPDase3, synthesis

INTRODUCTION

Ectonucleotidases are membrane-bound metalloenzymes that affect extracellular nucleotide and nucleoside levels by catalyzing the hydrolysis of nucleotides to the corresponding nucleosides releasing inorganic phosphate or diphosphate (Dou et al., 2018; Le et al., 2019; Vuerich et al., 2019). There are four major subfamilies of ectonucleotidases: the ecto-nucleoside triphosphate diphosphohydrolases (NTPDases), the ecto-nucleotide pyrophosphatases/phosphodiesterases (NPPs), the alkaline phosphatases (APs), and the ecto-5'-nucleotidase (ecto-5'-NT, CD73) (Bonan, 2012; Al-Rashida and Iqbal, 2015; Baqi, 2015; Fiene et al., 2016; Le et al., 2019). In inflammatory processes, there may be a massive increase in extracellular ATP concentrations causing proinflammatory immune responses *via* P2X and P2Y receptors. ATP can be hydrolyzed by NTPDases, or at very high concentrations also by APs, *via* ADP to AMP. Alternatively, ATP can be cleaved directly to AMP and diphosphate (pyrophosphate) by NPPs (Lee and Müller, 2017). The resulting AMP can eventually be hydrolyzed by ecto-5'-NT yielding adenosine, which induces antiinflammatory effects *via* activation of P1 (adenosine) receptors (King et al., 2006; Burnstock, 2018; Antonioli et al., 2019; Müller et al., 2020).

Several studies reported that NTPDase2 is localized in specialized astrocytes in rodent brain, such as laminar astrocytes associated with fiber tracts in the brain stem and cerebrum (Braun et al., 2003; Braun et al., 2004), tanycytes, non-stellate astrocytes in

the gray matter of discrete regions, like habenula (Gampe et al., 2012), satellite astrocytes in the dorsal root ganglion (Braun et al., 2003), and astrocyte-like progenitor cells of the subventricular zone (SVZ) of the lateral ventricle (Shukla et al., 2005; Mishra et al., 2006; Gampe et al., 2015). NTPDase3 is localized in the midline regions: in the thalamus, hypothalamus, and the medulla oblongata (Belcher et al., 2006; Grković et al., 2016). Both enzymes, NTPDase2, and to a lesser extent also NTPDase3, preferentially catalyze the dephosphorylation of ATP to ADP, generating the physiological ligand for P2Y₁, P2Y₁₂, and P2Y₁₃ receptors (Kukulski et al., 2005; Zimmermann et al., 2012; Burnstock, 2020; Müller et al., 2020). Therefore, NTPDase2 and -3 may modulate inflammatory reactions within the CNS and could represent useful therapeutic targets in neuroinflammatory and neurodegenerative diseases.

So far only few, moderately potent, NTPDase inhibitors have been described (**Figure 1**), which can be divided into nucleotide derivatives and non-nucleotides. ARL67156 (**1**, **Figure 1**) is a weak, competitive inhibitor of human NTPDase1 ($K_i = 11 \mu\text{M}$) and -3 ($K_i = 18 \mu\text{M}$) but does not inhibit human NTPDase2 and -8 (Lévesque et al., 2007). 8-BuS-ATP (**2**, **Figure 1**) was shown to inhibit NTPDase1 ($K_i = 0.8 \mu\text{M}$) but being a substrate of NTPDase2, -3, and -8 it is of limited use (Lecka et al., 2013). The corresponding 8-BuS-ADP and especially 8-BuS-AMP also inhibited NTPDase1 but appeared to be more stable towards hydrolysis (Lévesque et al., 2007). PSB-6426 (**3**, **Figure 1**) is a metabolically stable, uncharged compound derived from uridine-5'-carboxylate. It was identified as a moderately potent,

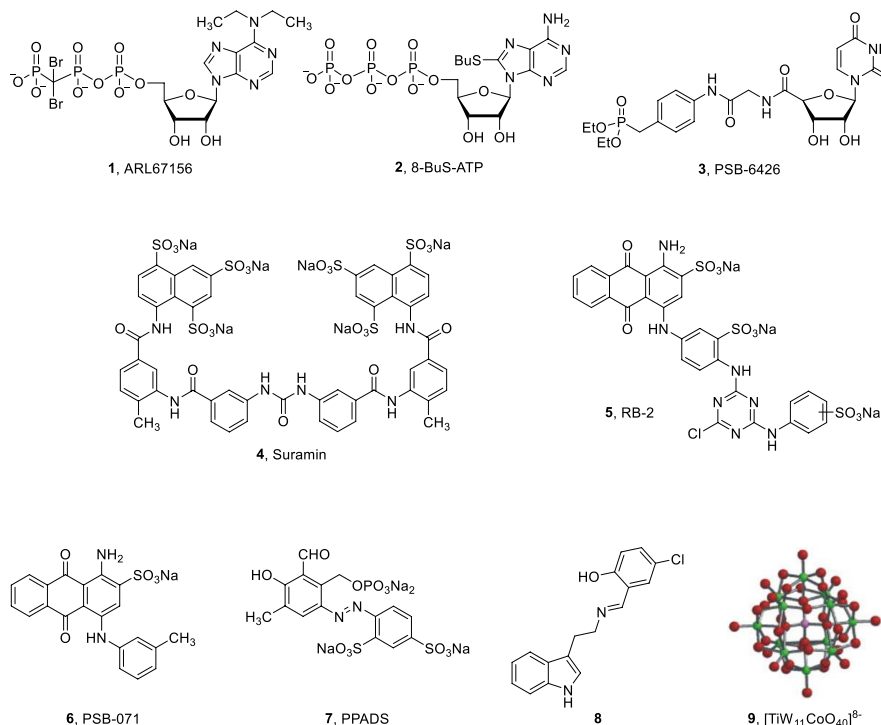


FIGURE 1 | Structures of selected NTPDase inhibitors (Iqbal et al., 2005; Müller et al., 2006; Brunschweiler et al., 2008; Baqi et al., 2009b; Zebisch et al., 2014; Kanwal et al., 2019).

selective competitive inhibitor of human NTPDase2 ($K_i = 8.2 \mu\text{M}$) (Brunschweiler et al., 2008). Non-nucleotide-derived compounds have also been developed as NTPDase inhibitors (compounds 4–7, **Figure 1**). These include suramin (4), reactive blue-2 (RB-2, 5), and its derivative PSB-071 (6), PPADS (7), and tryptamine-derived imine 8 (Iqbal et al., 2005; Baqi et al., 2009b; Zebisch et al., 2014; Kanwal et al., 2019). However, these compounds are non-selective and showed only moderate inhibitory activity in the low micromolar range and/or limited stability (Iqbal et al., 2005; Baqi et al., 2009b; Zebisch et al., 2014; Kanwal et al., 2019). Another class of NTPDase inhibitors are the polyoxometalates (POMs) such as $[\text{TiW}_{11}\text{CoO}_{40}]^{8-}$ (9), which are inorganic, negatively charged metal complexes. POM derivative 9 inhibited rat NTPDase1, -2, and -3 in the submicromolar concentration range, but this highly negatively charged compound displays limited stability (Müller et al., 2006). Moreover, specific antibodies have been reported that inhibit NTPDase2 and -3 activities; however, the inhibition is not complete (Munkonda et al., 2009; Pelletier et al., 2017). Previously, we evaluated anthraquinone derivatives at rat NTPDase1, -2, and -3, and one of the most potent but non-selective compounds was PSB-071 (6) (Baqi et al., 2009b). In the present study, we investigated the structure-activity relationships (SARs) of this class of NTPDase inhibitors with the goal to improve their inhibitory potency and subtype-selectivity, in particular with the aim to obtain potent NTPDase2- (and NTPDase3-) selective inhibitors. Such compounds are required for biological studies since they are expected to lead to an accumulation of ADP thereby acting as indirect P2Y₁, P2Y₁₂ and P2Y₁₃ receptor agonists.

EXPERIMENTAL SECTION

Chemistry

Material and Methods

All materials were used as purchased (Acros, Alfa Aesar, Merck, or Sigma-Aldrich, Germany). Thin-layer chromatography was performed using TLC aluminum sheets silica gel 60 F₂₅₄ or TLC aluminum sheets reversed phase (RP) silica gel 18 F₂₅₄ (Merck, Darmstadt, Germany). Colored compounds were visible at daylight; other compounds were visualized under UV light (254 nm). Flash chromatography was performed on a Büchi system using silica gel RP-18 (Merck, Darmstadt, Germany). ¹H and ¹³C NMR data were collected on either a Bruker Avance 500 MHz NMR spectrometer at 500 MHz (¹H) or 126 MHz (¹³C), respectively or a 600 MHz NMR spectrometer at 600 MHz (¹H) or 151 MHz (¹³C), respectively. Deuterated dimethyl sulfoxide (DMSO-*d*₆) or chloroform-*d* (CDCl₃) were used as a solvent. Chemical shifts are reported in parts per million (ppm) relative to the deuterated solvent, i.e., DMSO, δ ¹H 2.49 ppm; ¹³C 39.7 ppm, coupling constants *J* are given in Hertz, and spin multiplicities are given as s (singlet), d (doublet), t (triplet), q (quartet), sext (sextet), m (multiplet), and br (broad).

The purities of isolated products were determined by high performance liquid chromatography (HPLC) coupled with

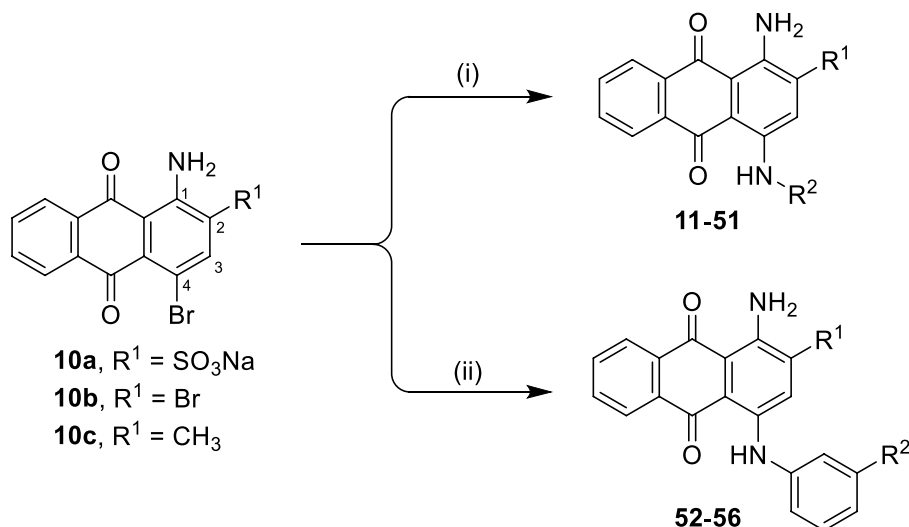
electrospray ionization mass spectrometry (ESI-MS) and ultraviolet (UV) detector using the following procedure: the compounds were dissolved at a concentration of 0.5 mg/mL in H₂O/MeOH = 1:1, containing 2 mM NH₄CH₃COO. Then, 10 μL of the sample was injected into an HPLC column (Phenomenex Luna 3 μm C18, 50 mm \times 2.00 mm). Elution was performed with a gradient of water:methanol (containing 2 mM NH₄CH₃COO) from 90:10 to 0:100 starting the gradient immediately at a flow rate of 250 $\mu\text{L}/\text{min}$ for 15 min, followed by washing with 100% methanol for another 15 min. The purity of the compounds proved to be $\geq 95\%$. For microwave reactions, a CEM Focused Microwave Synthesis Type Discover apparatus was employed. A freeze-dryer (CHRIST ALPHA 1-4 LSC) was used for lyophilization.

The synthesis and analysis of compounds 11–22, 24–26, 31–33, 36, 38–40, 42–44, 46, 49–52, 54–56, and 58 was previously described (Baqi and Müller, 2007; Weyler et al., 2008; Baqi et al., 2009b; Baqi et al., 2010; Baqi and Müller, 2010; Baqi et al., 2011; Baqi and Müller, 2012; Fiene et al., 2016; Malik et al., 2016). All other compounds (23, 27–30, 34, 35, 37, 41, 45, 47, 48, 53, and 57) were newly prepared in analogy to described methods (Baqi and Müller, 2010; Baqi and Müller, 2012; Malik et al., 2016; Pelletier et al., 2017) with modifications as described below.

General Procedure A: Preparation of 4-Substituted

1-Aminoanthraquinone-2-sulfonate Derivatives (11–51)

To a 5 mL microwave reaction vial, equipped with a magnetic stirring bar, were added 1-amino-4-bromo substituted anthraquinone compounds [bromaminic acid sodium salt (10a) or 1-amino-2,4-dibromoanthraquinone (10b)] (0.1–0.3 mmol) and the appropriate aniline or amine derivative (1.5–9.0 equiv), followed by a buffer solution of Na₂HPO₄ (pH 9.6) (5.0 mL) and NaH₂PO₄ (pH 4.2) (1.0 mL) and a finely powdered elemental copper (0.002–0.003 g, 5–10 mol%). The mixture was capped and irradiated in the microwave oven (80–100 W) for 5–24 min at 100–120°C. The reaction mixture was cooled down to room temperature (rt), and the product was purified using the following procedure. The contents of the vial were filtered to remove the elemental copper. Then, ca. 200 mL of water was added to the filtrate, and the aqueous solution was extracted with dichloromethane (200 mL). The extraction procedure was repeated until the dichloromethane layer became colorless (two to three times). The aqueous layer was reduced by rotary evaporation to a volume of 10–20 mL, which was subsequently submitted to flash column chromatography using RP-18 silica gel and water as an eluent. The polarity of the eluent was then gradually decreased by the addition of acetone in the following steps: 5, 10, 20, 40, and 60%. Fractions containing blue product were collected. For some compounds the last step of purification (RP-18 flash chromatography) had to be repeated two to three times to obtain pure product ($\geq 95\%$ purity as determined by HPLC-UV-MS). The pooled product-containing fractions were evaporated under vacuum to remove the acetone and reduce the water volume. The remaining water was subsequently removed by lyophilization to yield up to 80% of the product as blue powder (**Scheme 1** and **Table 1**).



SCHEME 1 | General synthesis of 4-substituted anthraquinone derivatives 11–56^a. ^aReagents and conditions: (i) $R^2\text{-NH}_2$, phosphate buffer (pH 6–7), Cu^0 , microwave, 80–120°C, 5–24 min; (ii) m -substituted aniline, CuOAc , KOAc , 110°C, argon, 2–15 h; for R^1 and R^2 , see **Table 1**.

General Procedure B: Preparation of 2-Substituted 1-Amino-4-anilinoanthraquinone Derivatives (52–56)

A round bottom flask (25 mL) equipped with a magnetic stirring bar was charged with one equivalent of starting material (10b or 1-amino-4-bromo-2-methylantraquinone (10c)), an excess of appropriate aniline derivative (15 equiv.) and copper(I) acetate (10 mol%) in the presence of 2.25 equiv. of potassium acetate (**Scheme 1**). The resulting mixture was heated at 110°C under an argon atmosphere for 2–15 h, and the progress of the reaction was monitored by TLC using 10% dichloromethane/cyclohexane as eluent. The reaction mixture was then let to cool down to room temperature, followed by the addition of ethanol (5 mL), and the blue-colored precipitate was filtered off and washed successively with ethanol, 0.1 M HCl, and water (ca. 15 mL each), and then the solid material was dried at 70°C in the oven for 16 h. The product was then purified by silica gel column chromatography using dichloromethane/cyclohexane (9:1) as eluent. The desired products (52–56) were obtained in high yields (**Scheme 1** and **Table 1**).

General Procedure C: Preparation of 4-Substituted Anthraquinone-2-sulfonate Derivatives (57 and 58)

To a 50 mL round bottom flask equipped with a magnetic stirring bar, 0.1 mmol of 1-aminoanthraquinone derivative (21 or 33) was added, followed by 5 mL of 1 M hydrochloric acid. The solution was cooled to 0–5°C in an ice bath, and a previously cooled solution of NaNO_2 (13.8 mg, 0.2 mmol, 2 equiv) in 0.5 mL of distilled water was added dropwise. After 5 min, the mixture was allowed to warm up to rt, followed by addition of 30 mg of zinc powder (1.0 mmol, 10 equiv) and 5 mL of ethanol. The resulting mixture was then allowed to stir at rt for ca. 30 s. The mixture was filtered off, and the purple-colored filtrate was then

purified by flash column chromatography on a reversed phase silica gel (RP-18) using a gradient of acetone in water (5 and 20%) as the eluent. Fractions containing the purple product were collected and evaporated in vacuum to remove acetone and decrease the volume of water to ca. 10–20 mL. Complete drying was achieved with a freeze-dryer, affording purple-colored products in excellent yields (**Scheme 2** and **Table 1**).

Sodium 1-amino-4-(3-iodophenylamino)-9,10-dioxo-9,10-dihydroanthracene-2-sulfonate (23)

Reaction conditions according to general procedure A: Compound 10a (0.1213 g, 0.3 mmol), 3-iodoaniline (0.1314 g, 0.6 mmol), a buffer solution of Na_2HPO_4 (pH 9.6) (5.0 mL) and NaH_2PO_4 (pH 4.2) (1.0 mL), and copper metal (0.003–0.005 g, 0.05–0.08 mmol). MW conditions: 100 W, 120°C, 10 min. Analytical data: blue powder (34% yield), mp >300°C. ^1H NMR (500 MHz, $\text{DMSO}-d_6$): δ 7.20 (t, $J = 7.9$ Hz, 1H, 2'-H), 7.29 (m, 1H, 5'-H or 6'-H), 7.51 (m, 1H, 5'-H or 6'-H), 7.65 (t, $J = 1.9$ Hz, 1H, 4'-H), 7.85 (m, 2H, 6-H, 7-H), 7.98 (s, 1H, 3-H), 8.25 (m, 2H, 5-H, 8-H), 11.79 (s, 1H, 4-NH). ^{13}C NMR (126 MHz, $\text{DMSO}-d_6$): δ 95.55, 109.51, 112.66, 121.91, 122.99, 126.12, 126.20, 130.91, 131.53, 132.70, 133.00, 133.51, 133.58, 134.26, 139.56, 141.38, 142.66, 144.66, 182.12, 183.07. LC-MS (m/z): 519.2 [$\text{M} - \text{Na}$][−], 521.4 [$\text{M} - \text{Na}$]⁺. Purity by HPLC-UV (254 nm)-ESI-MS: 100%.

Sodium 1-amino-4-(2-(hydroxymethyl)phenylamino)-9,10-dioxo-9,10-dihydroanthracene-2-sulfonate (27)

Reaction conditions according to general procedure A: Compound 10a (0.1213 g, 0.3 mmol), 2-aminobenzyl alcohol (0.0738 g, 0.6 mmol), a buffer solution of Na_2HPO_4 (pH 9.6) (5.0 mL) and NaH_2PO_4 (pH 4.2) (1.0 mL), and copper metal

TABLE 1 | Inhibitory activity of anthraquinone derivatives at human ecto-NTPDases.

				IC ₅₀ ± SEM (μM) ^a (or % inhibition at 2 μM concentration)			
				NTPDase1	NTPDase2	NTPDase3	NTPDase8
Compd.	R ¹	R ²	R ³				
5 RB-2		For structure see Figure 1		(17)	(42)	0.942 ± 0.024	(-8)
6 PSB-071		For structure see Figure 1		(-4)	(22)	(1)	(-21)
				51.5 (rat) ^b	12.8 (rat) ^b	19.1 (rat) ^b	
Structure A							
11		-	-	(-3)	(0)	(6)	(-4)
12		-	-	(-10)	(11)	(6)	(3)
13		-	-	(-12)	(12)	(-3)	(-3)
14		-	-	(-13)	(15)	(-10)	(-15)
15		-	-	(-19)	(31)	(-4)	(9)
				>100 (rat) ^b	>100 (rat) ^b	1.5 (rat) _b	
16		-	-	(3)	5.62 ± 0.72	(-21)	(3)
17		-	-	(-1)	(15)	1.64 ± 0.26	(-11)
18		-	-	(-8)	(34)	(-9)	(3)
				0.328 (rat) ^b	19.1 (rat) ^b	2.22 (rat) ^b	
19		-	-	(0)	(13)	4.72 ± 0.40	(-35)
20		-	-	(-7)	0.539 ± 0.290	(-5)	(6)
PSB-16131							
Structure B							
21	H	F	H	(-8)	(15)	(0)	(-1)
22	H	Br	H	(-4)	(12)	8.96 ± 1.08	(-26)
23	H	I	H	(0)	(21)	(2)	(4)
24	H	NO ₂	H	(-32)	(19)	15.3 ± 2.5	(3)
25	H	H	NH ₂	(-19)	(17)	(-25)	(-12)
26	H	CO ₂ H	H	(-17)	(2)	3.10 ± 0.45	(-17)
27		H	H	(-1)	(12)	(11)	(4)
28	H		H	(-2)	(7)	(-9)	(1)
29	H	H		(-4)	(5)	(-3)	(-4)

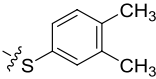
(Continued)

TABLE 1 | Continued

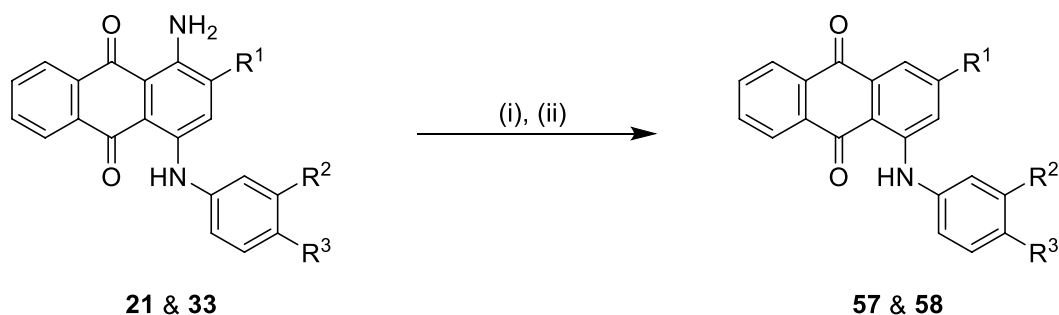
				IC ₅₀ ± SEM (μM) ^a (or % inhibition at 2 μM concentration)			
Compd.	R ¹	R ²	R ³	NTPDase1	NTPDase2	NTPDase3	NTPDase8
30	H		H	(-6)	(7)	1.52 ± 0.28	(-11)
31	H	NH ₂	SO ₃ H	(-15)	(1)	4.26 ± 0.54	(-19)
32	H	SO ₃ H	NH ₂	(10)	(5)	1.73 ± 0.55	(-20)
33	H	CO ₂ H	OH	(-12)	(12)	0.723 ± 0.032	(-9)
PSB-2046							
34	Cl	Cl	H	(1)	(16)	(-2)	(7)
35	CO ₂ H	F	H	(-21)	(-3)	(32)	(-10)
36	CO ₂ H	H	Cl	(-20)	(-2)	4.04 ± 0.47	(-17)
37	F	H	OH	(-8)	(5)	(-12)	(-6)
38	CH ₃	H	Cl	(2)	5.45 ± 0.70	(9)	(-1)
39	H		H	(36)	3.59 ± 0.85	13.1 ± 1.65	(28)
40	H		H	(12)	1.11 ± 0.06	(18)	(9)
41	H		H	(1)	0.984 ± 0.327	(10)	(6)
42	H		SO ₃ H	(-2)	(10)	0.390 ± 0.041	(-7)
PSB-1011							
43	H	H		(7)	1.32 ± 0.05	(3)	(3)
44	H	H		(15)	0.934 ± 0.136	(7)	(6)
45	H	H		(52)	1.08 ± 0.08	(42)	(21)
46	H	H		(33)	1.73 ± 0.29	(21)	(10)
47	H	H		(34)	0.951 ± 0.225	(16)	(4)
48	H	Cl		(29)	0.551 ± 0.195	(20)	(14)
PSB-2020							
49	H	H		(46)	1.28 ± 0.34	(36)	(27)
50	H	H		(38)	1.13 ± 0.27	(34)	(17)

(Continued)

TABLE 1 | Continued

				IC ₅₀ ± SEM (μM) ^a (or % inhibition at 2 μM concentration)			
				NTPDase1	NTPDase2	NTPDase3	NTPDase8
Compd.	R ¹	R ²	R ³				
51	H	H		(51)	0.832 ± 0.053	(44)	(27)
Structure C							
52	Br	CO ₂ H	—	(-2)	(-5)	(1)	(3)
53	Br	C ₂ H ₅	—	(-4)	(5)	(-2)	(-4)
54	CH ₃	F	—	(-4)	(7)	(-2)	(-2)
55	CH ₃	OCH ₃	—	(-6)	(3)	(0)	(-2)
56	CH ₃	C ₂ H ₅	—	(-3)	(6)	(-1)	(-3)
Structure D							
57	SO ₃ H	F	H	(14)	(-6)	(9)	(-1)
58	SO ₃ H	CO ₂ H	OH	(1)	(5)	(32)	(5)

^aIC₅₀ values for potent inhibitors are highlighted in bold. ^bBaqi et al., 2009b. Data are from at least three separate experiments.



SCHEME 2 | Synthesis of deaminated anilinoanthraquinone derivatives 57 and 58^a. ^aReagents and conditions: (i) NaNO₂, HCl (1 M), 0–5°C, 5 min; (ii) Zn (10 equiv.), ethanol, rt, 30 s; for R¹, R², and R³, see **Table 1**.

(0.003–0.005 g, 0.05–0.08 mmol). MW conditions: 100 W, 120°C, 10 min. Analytical data: blue powder (44.3% yield), mp >300°C. ¹H NMR (500 MHz, DMSO-*d*₆): δ 4.52 (d, *J* = 4.1 Hz, 2H, -CH₂OH), 5.30 (t, *J* = 5.0 Hz, 1H, -CH₂OH), 7.23 (m, 3H, 3'-H, 5'-H, 6'-H), 7.34 (td, *J* = 7.7, 1.6 Hz, 1H, 4'-H), 7.50 (dd, *J* = 7.6, 1.5 Hz, 1H, 3-H), 7.84 (m, 2H, 6-H, 7-H), 8.26 (m, 2H, 5-H, 8-H), 11.94 (s, 1H, 4-NH). ¹³C NMR (126 MHz, DMSO-*d*₆): δ 60.59, 109.31, 111.72, 123.37, 123.96, 124.69, 126.07, 126.15, 128.10, 129.15, 132.85, 133.19, 133.80, 134.31, 135.79, 137.78, 141.26, 142.65, 144.41, 181.95, 182.34. LCMS (*m/z*): 423.1 [M - Na]⁺. Purity by HPLC-UV(220–700 nm)-ESI-MS 100%.

Sodium 1-amino-4-(3-(hydroxymethyl)phenylamino)-9,10-dioxo-9,10-dihydroanthracene-2-sulfonate (28)

Reaction conditions according to general procedure A: Compound 10a (0.1213 g, 0.3 mmol), 3-aminobenzyl alcohol (0.0738 g, 0.6 mmol), a buffer solution of Na₂HPO₄ (pH 9.6) (5.0 mL) and NaH₂PO₄ (pH 4.2) (1.0 mL), and copper metal (0.003–0.005 g, 0.05–0.08 mmol). MW conditions: 100 W, 120°C, 10 min. Analytical data: blue powder (67.7% yield), mp >300°C. ¹H NMR (500 MHz, DMSO-*d*₆): δ 4.52 (d, *J* = 3.7 Hz, 2H, -CH₂OH), 5.24 (t, *J* = 5.7 Hz, 1H, -CH₂OH), 7.15 (m, 2H, 5'-H, 6'-H), 7.21 (s, 1H, 2'-H), 7.39 (t, *J* = 7.7 Hz, 1H, 3'-H), 7.85 (m,

2H, 6-H, 7-H), 7.99 (s, 1H, 3-H), 8.27 (m, 2H, 5-H, 8-H), 12.06 (s, 1H, 4-NH). ^{13}C NMR (126 MHz, DMSO- d_6): δ 62.73, 109.23, 111.39, 121.37, 121.55, 122.74, 122.92, 126.08, 126.16, 129.46, 132.88, 133.27, 133.73, 134.29, 139.19, 141.21, 142.97, 144.46, 144.71, 181.90, 182.53. LCMS (m/z): 423.1 $[\text{M} - \text{Na}]^-$. Purity by HPLC-UV(220–700 nm)-ESI-MS 100%.

Sodium 1-amino-4-(4-(hydroxymethyl)phenylamino)-9,10-dioxo-9,10-dihydroanthracene-2-sulfonate (29)

Reaction conditions according to general procedure A: Compound 10a (0.1213 g, 0.3 mmol), 4-aminobenzyl alcohol (0.0738 g, 0.6 mmol), a buffer solution of Na_2HPO_4 (pH 9.6) (5.0 mL) and NaH_2PO_4 (pH 4.2) (1.0 mL), and copper metal (0.003–0.005 g, 0.05–0.08 mmol). MW conditions: 100 W, 120°C, 10 min. Analytical data: blue powder (50.9% yield), mp >300°C. ^1H NMR (500 MHz, DMSO- d_6): δ 4.51 (d, $J = 5.2$ Hz, 2H, $-\text{CH}_2\text{OH}$), 5.19 (t, $J = 5.8$ Hz, 1H, $-\text{CH}_2\text{OH}$), 7.24 (m, 2H, 3'-H, 5'-H), 7.39 (m, 2H, 2'-H, 6'-H), 7.84 (m, 2H, 6-H, 7-H), 7.98 (s, 1H, 3-H), 8.27 (m, 2H, 5-H, 8-H), 12.06 (s, 1H, 4-NH). ^{13}C NMR (126 MHz, DMSO- d_6): δ 62.73, 109.21, 111.20, 122.78, 123.34, 126.06, 126.16, 128.03, 132.87, 133.23, 133.75, 134.29, 137.77, 139.24, 141.43, 143.00, 144.43, 181.87, 182.40. LCMS (m/z): 423.1 $[\text{M} - \text{Na}]^-$. Purity by HPLC-UV(220–900 nm)-ESI-MS 98%.

Sodium 1-amino-4-(3-(carboxymethyl)phenylamino)-9,10-dioxo-9,10-dihydroanthracene-2-sulfonate (30)

Reaction conditions according to general procedure A: Compound 10a (0.1213 g, 0.3 mmol), 3-aminophenylacetic acid (0.0906 g, 0.6 mmol), a buffer solution of Na_2HPO_4 (pH 9.6) (5.0 mL) and NaH_2PO_4 (pH 4.2) (1.0 mL), copper metal (0.003–0.005 g, and 0.05–0.08 mmol). MW conditions: 100 W, 120°C, 10 min. Analytical data: blue powder (73% yield), mp >300°C. ^1H NMR (500 MHz, DMSO- d_6): δ 3.40 (s, 2H, $-\text{CH}_2\text{CO}_2\text{H}$), 7.07 (m, 2H, 4'-H, 6'-H), 7.18 (s, 1H, 2'-H), 7.31 (t, $J = 7.8$ Hz, 1H, 5'-H), 7.83 (m, 2H, 6-H, 7-H), 8.02 (s, 1H, 3-H), 8.27 (m, 2H, 5-H, 8-H), 10.11 (s, 1H, $-\text{CH}_2\text{CO}_2\text{H}$), 12.08 (s, 1H, 4-NH). ^{13}C NMR (126 MHz, DMSO- d_6): δ 43.74, 109.23, 111.29, 120.49, 122.96, 124.25, 125.76, 126.09, 126.16, 129.11, 132.87, 133.24, 133.76, 134.28, 138.84, 141.24, 142.93, 144.44, 150.43, 173.43, 181.89, 182.46. LCMS (m/z): 451.4 $[\text{M} - \text{Na}]^-$, 453.3 $[\text{M} - \text{Na}]^+$. Purity by HPLC-UV(220–700 nm)-ESI-MS 100%.

Sodium 1-amino-4-(2,3-dichlorophenylamino)-9,10-dioxo-9,10-dihydroanthracene-2-sulfonate (34)

Reaction conditions according to general procedure A: Compound 10a (0.3639 g, 0.9 mmol), 2,3-dichloroaniline (0.4374 g, 2.7 mmol), a buffer solution of Na_2HPO_4 (pH 9.6) (5.0 mL) and NaH_2PO_4 (pH 4.2) (1.0 mL), and copper metal (0.003–0.005 g, 0.05–0.08 mmol). MW conditions: 100 W, 120°C, 10 min. Analytical data: blue powder (20% yield), mp >300°C. ^1H NMR (500 MHz, DMSO- d_6): δ 7.40 (m, 3H, 4'-H, 5'-H, 6'-H), 7.86 (m, 2H, 6-H, 7-H), 7.93 (s, 1H, 3-H), 8.27 (m, 2H, 5-H, 8-H), 11.90 (s, 1H, 4-NH). ^{13}C NMR (126 MHz, DMSO- d_6): δ 109.75, 113.86, 121.13, 123.01, 124.14, 125.11, 126.22, 126.25, 128.64, 132.84, 133.10, 133.40, 133.79, 134.26, 138.08,

139.08, 142.39, 144.85, 182.30, 183.86. LCMS (m/z): 461.1 $[\text{M} - \text{Na}]^-$, 463.1 $[\text{M} - \text{Na}]^+$. Purity by HPLC-UV(220–700 nm)-ESI-MS 100%.

Sodium 1-amino-4-(2-carboxy-3-fluorophenylamino)-9,10-dioxo-9,10-dihydroanthracene-2-sulfonate (35)

Reaction conditions according to general procedure A: Compound 10a (0.1213 g, 0.3 mmol), 2-amino-6-fluorobenzoic acid (0.0930 g, 0.6 mmol), a buffer solution of Na_2HPO_4 (pH 9.6) (5.0 mL) and NaH_2PO_4 (pH 4.2) (1.0 mL), and copper metal (0.003–0.005 g, 0.05–0.08 mmol). MW conditions: 100 W, 120°C, 10 min. Analytical data: blue powder (40.1% yield), mp >300°C. ^1H NMR (500 MHz, DMSO- d_6): δ 6.78 (t, $J = 8.6$ Hz, 1H, 6'-H), 6.94 (d, $J = 8.0$ Hz, 1H, 4'-H), 7.15 (m, 1H, 5'-H), 7.81 (m, 2H, 6-H, 7-H), 8.10 (s, 1H, 3-H), 8.26 (m, 2H, 5-H, 8-H), 12.07 (s, 1H, 4-NH). ^{13}C NMR (126 MHz, DMSO- d_6): δ 109.66, 109.89, 110.08, 113.17, 116.81, 124.44, 126.03, 126.25, 127.21, 132.80, 133.11, 133.84, 134.20, 138.60, 139.02, 141.95, 144.57, 158.56, 160.49, 166.00, 181.84, 182.19. LCMS (m/z): 455.2 $[\text{M} - \text{Na}]^-$, 457.3 $[\text{M} - \text{Na}]^+$. Purity by HPLC-UV(220–700 nm)-ESI-MS 98%.

Sodium 1-amino-4-(2-fluoro-4-hydroxyphenylamino)-9,10-dioxo-9,10-dihydroanthracene-2-sulfonate (37)

Reaction conditions according to general procedure A: Compound 10a (0.1213 g, 0.3 mmol), 4-amino-3-fluorophenol (0.0762 g, 0.6 mmol), a buffer solution of Na_2HPO_4 (pH 9.6) (5.0 mL) and NaH_2PO_4 (pH 4.2) (1.0 mL), and copper metal (0.003–0.005 g, 0.05–0.08 mmol). MW conditions: 100 W, 120°C, 10 min. Analytical data: blue powder (38.4% yield), mp >300°C. ^1H NMR (500 MHz, DMSO- d_6): δ 6.72 (m, 2H, 4'-H, 5'-H), 7.23 (s, 1H, 3'-H), 7.58 (d, $J = 1.7$ Hz, 1H, 3-H), 7.84 (m, 2H, 6-H, 7-H), 8.27 (m, 2H, 5-H, 8-H), 11.68 (s, 1H, 4-NH). ^{13}C NMR (126 MHz, DMSO- d_6): δ 103.65, 103.82, 110.51, 112.18, 117.38, 122.18, 126.06, 126.16, 128.64, 132.85, 133.21, 133.71, 134.30, 142.94, 143.25, 144.12, 157.03, 158.34, 181.86, 182.50. LCMS (m/z): 427.3 $[\text{M} - \text{Na}]^-$, 429.2 $[\text{M} - \text{Na}]^+$. Purity by HPLC-UV(220–900 nm)-ESI-MS 97%.

Sodium 1-amino-4-(3-(phenylsulfanyl)phenylamino)-9,10-dioxo-9,10-dihydroanthracene-2-sulfonate (41)

Reaction conditions according to general procedure A: Compound 10a (0.1213 g, 0.3 mmol), 3-(phenylsulfanyl)aniline (0.0664 g, 0.33 mmol), a buffer solution of Na_2HPO_4 (pH 9.6) (5.0 mL) and NaH_2PO_4 (pH 4.2) (1.0 mL), and copper metal (0.003–0.005 g, 0.05–0.08 mmol). MW conditions: 100 W, 120°C, 7 min. Analytical data: blue powder (14.7% yield), mp >300°C. ^1H NMR (500 MHz, DMSO- d_6): δ 7.07 (m, 1H, 6'-H), 7.12 (t, $J = 1.9$ Hz, 1H, 2'-H), 7.18 (dd, $J = 7.8, 1.9$ Hz, 1H, 4'-H), 7.34 (m, 1H, 5'-H), 7.45 (m, 5H, 2''-H, 3''-H, 4''-H, 5''-H, 6''-H), 7.85 (m, 2H, 6-H, 7-H), 8.01 (s, 1H, 3-H), 8.25 (m, 2H, 5-H, 8-H), 11.84 (s, 1H, 4-NH). ^{13}C NMR (126 MHz, DMSO- d_6): δ 109.24, 112.04, 121.11, 122.70, 123.10, 125.00, 125.92, 126.00, 127.94, 129.79, 130.59, 131.82, 132.78, 133.13, 133.25, 133.43, 134.08, 137.12, 139.86, 140.44, 142.58, 144.41, 181.88, 182.72.

LCMS (m/z): 501.0 $[M - Na]^-$, 503.2 $[M - Na]^+$. Purity by HPLC-UV(220–700 nm)-ESI-MS 99.4%.

Sodium 1-amino-4-[4-(4-chlorophenylthio)phenylamino]-9,10-dioxo-9,10-dihydroanthracene-2-sulfonate (45)

Reaction conditions according to general procedure A: Compound 10a (0.1213 g, 0.3 mmol), 4-(4-chlorophenylsulfanyl)aniline (0.0778 g, 0.33 mmol), a buffer solution of Na_2HPO_4 (pH 9.6) (5.0 mL) and NaH_2PO_4 (pH 4.2) (1.0 mL), and copper metal (0.003–0.005 g, 0.05–0.08 mmol). MW conditions: 100 W, 120°C, 8 min. Analytical data: blue powder (6% yield), mp >300°C. 1H NMR (500 MHz, DMSO- d_6): δ 7.30 (m, 2H, 2'-H, 6'-H), 7.32 (m, 2H, 3''-H, 5''-H), 7.42 (m, 2H, 3'-H, 5'-H), 7.46 (m, 2H, 2''-H, 6''-H), 7.86 (m, 2H, 6-H, 7-H), 8.07 (s, 1H, 3-H), 8.27 (m, 2H, 5-H, 8-H), 11.91 (s, 1H, 4-NH). ^{13}C NMR (126 MHz, DMSO- d_6): δ 109.40, 112.62, 123.00, 125.96, 126.03, 127.22, 129.36, 130.82, 131.44, 132.84, 133.34, 133.42, 133.83, 134.08, 135.46, 139.19, 139.95, 142.45, 144.55, 181.96, 182.92. LCMS (m/z): 535.0 $[M - Na]^-$, 536.1 $[M - Na]^+$. Purity by HPLC-UV(220–400 nm)-ESI-MS 99%.

Sodium 1-amino-4-[4-(4-methoxyphenylthio)phenylamino]-9,10-dioxo-9,10-dihydroanthracene-2-sulfonate (47)

Reaction conditions according to general procedure A: Compound 10a (0.1213 g, 0.3 mmol), 4-(4-methoxyphenylsulfanyl)aniline (0.0763 g, 0.33 mmol), a buffer solution of Na_2HPO_4 (pH 9.6) (5.0 mL) and NaH_2PO_4 (pH 4.2) (1.0 mL), and copper metal (0.003–0.005 g, 0.05–0.08 mmol). MW conditions: 100 W, 120°C, 10 min. Analytical data: blue powder (14.2% yield), mp >300°C. 1H NMR (500 MHz, DMSO- d_6): δ 3.79 (s, 3H, $-OCH_3$), 7.01 (m, 2H, 2'-H, 6'-H), 7.23 (s, 4H, 2''-H, 3''-H, 5''-H, 6''-H), 7.44 (m, 2H, 3'-H, 5'-H), 7.85 (m, 2H, 6-H, 7-H), 7.99 (s, 1H, 3-H), 8.26 (m, 2H, 5-H, 8-H), 11.95 (s, 1H, 4-NH). ^{13}C NMR (126 MHz, DMSO- d_6): δ 55.26, 109.21, 111.78, 115.36, 122.71, 123.54, 123.77, 125.92, 126.01, 129.91, 132.43, 132.77, 133.20, 133.48, 134.08, 134.70, 137.83, 140.16, 142.62, 144.39, 159.55, 181.82, 182.55. LCMS (m/z): 531.1 $[M - Na]^-$, 532.2 $[M - Na]^+$. Purity by HPLC-UV(220–400 nm)-ESI-MS 98.9%.

Sodium 1-amino-4-(3-chloro-4-phenylsulfanyl)-phenylamino-9,10-dioxo-9,10-dihydroanthracene-2-sulfonate (48)

Reaction conditions according to general procedure A: Compound 10a (0.1213 g, 0.3 mmol), 3-chloro-4-(phenylsulfanyl)aniline (0.0778 g, 0.33 mmol), a buffer solution of Na_2HPO_4 (pH 9.6) (5.0 mL) and NaH_2PO_4 (pH 4.2) (1.0 mL), and copper metal (0.003–0.005 g, 0.05–0.08 mmol). MW conditions: 100 W, 120°C, 8 min. Analytical data: blue powder (6.5% yield), mp >300°C. 1H NMR (500 MHz, DMSO- d_6): δ 7.21 (dd, J = 8.5, 2.3 Hz, 1H, 6'-H), 7.25 (d, J = 8.5 Hz, 1H, 5'-H), 7.34 (m, 3H, 3''-H, 4''-H, 5''-H), 7.42 (m, 2H, 2''-H, 6''-H), 7.51 (d, J = 2.2 Hz, 1H, 2'-H), 7.86 (m, 2H, 6-H, 7-H), 8.03 (s, 1H, 3-H), 8.25 (m, 2H, 5-H, 8-H), 11.68 (s, 1H, 4-NH). ^{13}C NMR (126 MHz, DMSO- d_6): δ 109.60, 113.55, 121.02, 122.52, 123.29, 125.99, 126.05, 126.99, 127.60, 129.71, 130.51, 132.92, 133.33, 133.49, 133.64, 133.69, 134.06, 135.28, 138.17, 140.95, 142.21, 144.71, 182.12, 183.21. LCMS (m/z): 535.0 $[M - Na]^-$,

536.1 $[M - Na]^+$. Purity by HPLC-UV(220–700 nm)-ESI-MS 97.7%.

1-Amino-2-bromo-4-(3-ethylphenylamino)anthracene-9,10-dione (53)

Reaction conditions according to general procedure B: Compound 10b (0.1143 mg, 0.3 mmol, 1 equiv.), 3-ethylaniline (0.5453 mg, 4.5 mmol, 15 equiv.), copper(I) acetate (0.0037 mg, 10 mol%) and potassium acetate (0.066 mg, 0.68 mmol) at 110°C for 2 h. Analytical data: dark blue powder (57.6% yield), mp = 229–230°C. 1H NMR (500 MHz, Chloroform- d): δ 1.29 (t, J = 7.6 Hz, 3H, $-CH_2-CH_3$), 2.68 (q, J = 7.6 Hz, 2H, $-CH_2-CH_3$), 7.05 (d, 1H, 4'-H), 7.10 (m, 2H, 2'-H, 6'-H), 7.33 (m, 1H, 5'-H), 7.76 (m, 2H, 6-H, 7-H), 7.88 (s, 1H, 3-H), 8.35 (m, 2H, 5-H, 8-H), 11.90 (s, 1H, 4-NH). ^{13}C NMR (126 MHz, Chloroform- d): δ 15.65, 28.94, 111.50, 111.73, 121.23, 122.93, 123.61, 124.79, 126.51, 126.76, 127.74, 129.68, 133.09, 133.15, 133.90, 134.45, 139.47, 142.81, 143.07, 146.32, 183.77, 183.88. LC-MS (m/z): 419.2 $[M - H]^-$, 421.2 $[M + H]^+$. Purity by HPLC-UV(254 nm)-ESI-MS 95%.

4-(3-Fluorophenylamino)-9,10-dioxo-9,10-dihydroanthracene-2-sulfonic acid (57)

Reaction conditions according to general procedure C: Compound 21 (0.0434, 0.1 mmol) was dissolved in 5 mL of 1 M HCl then cooled down to 0–5°C in an ice bath. Subsequently $NaNO_2$ (14 mg, 0.2 mmol) dissolved in water (0.5 mL) was added portion-wise, and the mixture was stirred for 5 min. It was then warmed up to rt followed by the addition of ethanol (5 mL) and zinc (65 mg, 1 mmol, 10 equiv.) and left stirring at rt for 30 s. Analytical data: dark violet powder (75% yield), mp >300°C. 1H NMR (600 MHz, DMSO- d_6): δ 7.06 (td, J = 8.6, 2.5 Hz, 1H, 5'-H), 7.22 (m, 2H, 4'-H, 6'-H), 7.50 (m, 1H, 2'-H), 7.79, 7.85 (2 d, J = 1.5 Hz, each 1H, 1-H, 3-H), 7.89, 7.93 (2 td, J = 7.5, 1.5 Hz, each 1H, 6-H, 7-H), 8.19, 8.24 (2 dd, J = 7.7, 1.3 Hz, 1H, each 1H, 5-H, 8-H), 11.20 (s, 1H, 4-NH). ^{13}C NMR (151 MHz, DMSO- d_6): δ 110.34, 110.50, 111.64, 111.78, 114.12, 115.71, 116.23, 119.36, 119.38, 126.69, 126.84, 131.44, 131.51, 132.67, 134.16, 134.35, 134.47, 134.86, 141.12, 141.19, 147.90, 154.52, 162.16, 163.78, 182.48, 184.68. LCMS (m/z): 396.0 $[M - H]^-$, 398.1 $[M + H]^+$. Purity by HPLC-UV(220–800 nm)-ESI-MS 99%.

Malachite Green Assay to Investigate NTPDase Inhibitors

Membrane preparations expressing human NTPDase1, -2, -3, or -8, respectively, were obtained as previously described (Sévigny et al., 1997; Cogan et al., 1999; Kukulski et al., 2005; Lecka et al., 2013; Lee et al., 2018). Enzyme inhibition assays were performed using the malachite green assay in analogy to published procedures with some modifications (Dou et al., 2018). The reaction buffer contained 10 mM HEPES, 2 mM $CaCl_2$, and 1 mM $MgCl_2$ (pH 7.4) in a final volume of 50 μ L in transparent 96-well half-area plates. The compounds were initially tested at a final concentration of 2 μ M using a COS-7-cell membrane preparation expressing the appropriate NTPDase isoenzyme (protein amount: 143 ng for NTPDase1, 175 ng for NTPDase2,

152 ng for NTPDase3, and 175 ng for NTPDase8). Preincubated of the enzyme preparations was performed at 37°C in the presence or absence of test compounds with gentle shaking (Eppendorf Thermomixer comfort at 500 rpm) for 5 min. The reaction was initiated by the addition of 50 μ M ATP [K_m (CD39) = 17 μ M] for NTPDase1 or 100 μ M ATP for NTPDase2, -3, and -8 [K_m (NTPDase2) = 70 μ M; K_m (NTPDase3) = 75 μ M; K_m (NTPDase8) = 46 μ M] (Kukulski et al., 2005). After 15 min of incubation at 37°C with gentle shaking, the reaction was stopped by the addition of the detection reagents (20 μ L malachite green solution, 0.6 mM, and 30 μ L of ammonium molybdate solution, 20 mM, in 1.5 M sulfuric acid). The released inorganic phosphate was quantified after 20 min of gentle shaking at 25°C by measuring the absorption of the malachite green-phosphomolybdate complex at 600 nm using a BMG PheraStar FS plate reader (BMG Labtech GmbH, Ortenberg, Germany). The corrected absorption was calculated by subtracting the absorption of the negative control samples, which were incubated with previously denatured enzyme (90°C, 15 min). Full concentration-inhibition curves were determined with inhibitor concentrations ranging from 0.03 to 30 μ M in the presence of 2% DMSO. Inhibition-type experiments were performed with 25, 50, 100, 150 and 200 μ M ATP as substrate for NTPDase2 in the presence of inhibitor 20 (0, 0.25, 0.5, and 1 μ M) and 25, 50, 100 and 150 μ M ATP substrate for NTPDase3 and compound 42 (0.25, 0.5, and 1 μ M). For all of the presented data, at least three independent experiments were performed, and IC_{50} values were calculated by GraphPad Prism 8 software.

RESULTS AND DISCUSSION

A library of 48 anthraquinone derivatives was synthesized and tested at human NTPDase1, -2, -3, and -8, which are ectoenzymes hydrolyzing extracellular nucleotides, using the malachite green assay. Subsequently, inhibition curves for compounds showing above 50% inhibition at 2 μ M test concentration were determined.

Chemistry

The target compounds (11–58) were synthesized as depicted in **Schemes 1** and **2**. The syntheses of compounds 11–22, 24–26, 31–33, 36, 38–40, 42–44, 46, 49–52, 54–56, and 58 had been previously described (Baqi and Müller, 2007; Weyler et al., 2008; Baqi et al., 2009b; Baqi et al., 2010; Baqi and Müller, 2010; Baqi et al., 2011; Baqi and Müller, 2012; Fiene et al., 2016; Malik et al., 2016). In addition to previously reported AQ derivatives, a series of 14 new compounds (23, 27–30, 34, 35, 37, 41, 45, 47, 48, 53, and 57) was prepared. Condensation of sodium 1-amino-4-bromo-9,10-dioxo-9,10-dihydroanthracene-2-sulfonate (R^1 = SO_3Na , 10a, **Scheme 1**), 1-amino-2,4-dibromo-9,10-dioxo-9,10-dihydroanthracene (R^1 = Br, 10b, **Scheme 1**), or 1-amino-4-bromo-2-methyl-9,10-dioxo-9,10-dihydroanthracene (R^1 = CH_3 , 10c, **Scheme 1**) with the appropriate (ar)alkylamine or aniline derivatives yielded the target compounds in satisfactory

to excellent isolated yields. Anthraquinones 11–51 bearing a sulfonate substitution at the 2-position were synthesized starting from compound 10a in sodium phosphate buffer (pH 6–7) in the presence of a catalytic amount of elemental copper (Cu^0) under microwave reaction conditions at 80–120°C for 5–24 min (Baqi and Müller, 2007; Baqi and Müller, 2010).

Compounds 52–56, bearing a bromo or methyl residue at the 2-position, were synthesized starting from 10b or 10c, respectively, with excess of the appropriate aniline derivatives (15 eq.) under argon in the presence of potassium acetate and copper(I) acetate ($CuOAc$) as a catalyst, upon heating at 110°C for 2–15 h (**Scheme 1**).

In order to investigate the role of the amino group at the 1-position of the anthraquinone moiety, two anilinoanthraquinone derivatives (21 and 33) were treated with sodium nitrite in hydrochloric acid solution (1 M) at 0–5°C for 5 min, then allowed to warm up to room temperature, followed by the addition of ethanol and an excess of zinc powder (10 equiv.) to achieve deamination within 30 seconds (Baqi and Müller, 2012), affording the desired products 57 and 58 in excellent yields (**Scheme 2**).

Biological Studies

Inhibition of human NTPDases was performed using the malachite green assay, which was established on a robotic system (Z' factors > 0.70) (Baykov et al., 1988; Fiene et al., 2015). The malachite green assay enables the detection of the phosphate produced by the enzymatic hydrolysis of nucleotides. A fixed substrate concentration of 50 μ M ATP for NTPDase1 and 100 μ M for NTPDase2, -3, and -8 was employed. Test compounds were initially screened at a concentration of 2 μ M. For compounds that showed about 50% inhibition or more, concentration-dependent inhibition curves were determined, and IC_{50} values were calculated. A total of 48 synthesized anthraquinone derivatives including 14 new compounds not previously described in the literature were evaluated for their inhibitory activity at human NTPDase1, -2, -3, and -8 (for results see **Table 1**).

Structure-Activity Relationships (SARs)

The anthraquinone derivative reactive blue-2 (RB-2 (5), **Figure 1** and **Table 1**) showed the highest potency at NTPDase3 (IC_{50} of 0.942 μ M) followed by NTPDase2 and was inactive at NTPDase8 (**Table 1**). RB-2 is a relatively large molecule (molecular weight of >800 g/mol) with high polarity bearing three negatively charged sulfonate (SO_3Na) groups. Therefore, smaller and less polar anthraquinone derivatives were designed, synthesized, and evaluated as NTPDases inhibitors (see **Table S1** in **Supplementary Materials** for clogD values of all anthraquinone derivatives discussed in the present study).

In our previous study, we had investigated a smaller series of anthraquinone derivatives at ecto-NTPDases of rat, which had led to the identification of PSB-071 (6) bearing a *m*-methyl substituent on the 4-anilino group. This inhibitor was slightly

selective for rat NTPDase2 (12.8 μM) (Baqi et al., 2009b; Zebisch et al., 2014) vs. rat NTPDase1 and -3, while in the present study, it showed no significant inhibitory activity on all tested human NTPDases (compound 6, **Table 1**), except for NTPDase2, at which it displayed very moderate potency.

Introducing of an (ar)alkyl group, such as propyl (11), benzyl (12) and phenethyl (13) at the 4-amino group of 1-amino-2-sulfoanthraquinone abolished the inhibitory activity on all tested NTPDases (entry 3–5, **Table 1**). Moreover, unsubstituted aromatic rings, such as phenyl, 1-naphthyl and 2-naphthyl, 14, 15, and 18 (**Table 1**), all showed no inhibitory activity as well. The naphthylamino-substituted anthraquinone derivatives 15 and 18 had shown good potency in our previous study at rat NTPDase3 (both) and at rat NTPDase1 (compound 18) indicating considerable species differences between rat and human NTPDases.

Interestingly, a combination between structures of 1-naphthyl and 2-naphthyl resulting in phenanthryl derivative 20, yielded a potent inhibitor of NTPDase2 which displayed no activity vs. NTPDase1, -3, and -8 at the tested concentration. This is probably due to the presence of a large lipophilic pocket present in human NTPDase2. This presence of a lipophilic pocket in NTPDase2 was confirmed with compound 16 (IC_{50} of 5.62 μM , **Table 1**), which is bearing an extra lipophilic methyl group in the 2-position of the 1-naphthyl moiety; again, this compound was found to be selective vs. the other investigated human NTPDases (-1, -3, and -8). Introduction of polar and negatively charged groups, SO_3H (17) or CO_2H (19) on the naphthyl moiety shifted the inhibitory activity towards human NTPDase3.

In the next step, we introduced different substituents on phenyl ring D (compounds 21–38, **Table 1**). Mono-substitution of the aromatic ring D with Br (22), NO_2 (24), CO_2H (26), or $\text{CH}_2\text{CO}_2\text{H}$ (30) in the *meta*-position led to selective inhibition of NTPDase3, while other mono-substitutions including *m*-F, *p*- NH_2 , *o*- CH_2OH , *m*- CH_2OH , and *p*- CH_2OH resulted in no inhibition at all tested NTPDases. On the other hand, di-substitution with polar functions, e.g., NH_2 , SO_3H , and OH, on the *meta*- and

para-position of the phenyl ring restored the inhibitory potency towards NTPDase2, especially compound 33 showing inhibitory potency at submicromolar concentration. Any polar substituent in the *ortho*-position and in combination with a substituent in the *meta*- or *para*-position led to inactive derivatives. The introduction of lipophilic substituents in the *ortho*- and *para*-position shifted the inhibitory potency towards NTPDase2, see compound 38 (**Table 1**).

Next, we introduced an additional aromatic residue, ring E. Lipophilic substitution in the *meta*- and *para*-position resulted in moderate to good potency at NTPDase2 (39–41 and 43–51, **Table 1**), with potencies reaching the submicromolar range (IC_{50} of 0.551 μM , 48), while a *m*-dichlorotriazinyl moiety in combination with a *p*- SO_3H group furnished the most potent compound of the present anthraquinone series at NTPDase3 (42, IC_{50} of 0.390 μM , **Table 1**).

Any modification on the anthraquinone moiety, such as removal of the amino group in position 1 or replacement of the sulfonate function in position 2 of the anthraquinone core by bromo or methyl abolished the inhibitory activity (see compounds 52–58, **Table 1**).

Concentration–response curves for selected potent anthraquinone derivatives 20, 44, 48, and 51 on NTPDase2 and for 17, 30, 33, and 42 on NTPDase3 are depicted in **Figure 2**.

The most potent inhibitors were found to be selective vs. other tested human NTPDases. For examples, the NTPDase2 inhibitors 20 and 44 were found to be selective vs. NTPDase1, -3, and -8, while the other two most potent NTPDase2 inhibitors 48 and 51 showed lower selectivity (**Figure 3**). The identified NTPDase3 inhibitors 17, 30, 33 and 42 were selective vs. NTPDase1, -2, and -8 (**Figure 3**).

The SARs for human NTPDase2 and -3 are summarized in **Figure 4**. Large and lipophilic substituents have led to selectivity for NTPDase2 (**Figure 4A**), while smaller and polar substituent have provided selectivity for NTPDase3 (**Figure 4B**).

We previously published articles highlighting the fact that the anthraquinone scaffold represents a privileged scaffold in

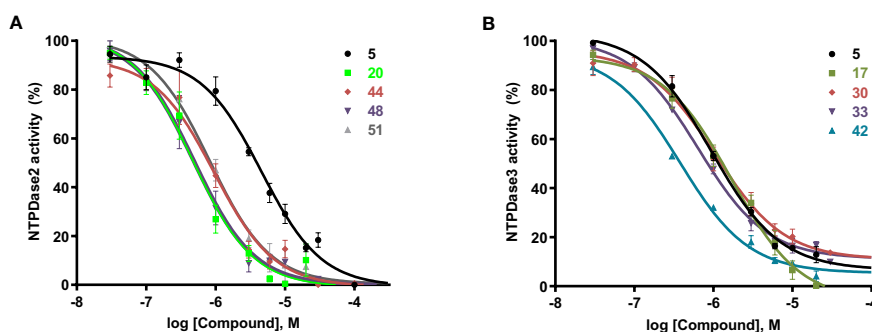


FIGURE 2 | Concentration-inhibition curves of selected anthraquinone derivatives **(A)** determined using the malachite green assay on recombinant human NTPDase2 expressed in COS7 cell membrane preparations. ATP at a concentration of 100 μM ($K_m = 70 \mu\text{M}$) was used as substrate and **(B)** determined using the malachite green assay on recombinant human NTPDase3 expressed in COS7 cell membrane preparations. ATP at a concentration of 100 μM ($K_m = 75 \mu\text{M}$) was used as substrate. Data points shown are mean values of at least three independent experiments. IC_{50} values are collected in **Table 1**.

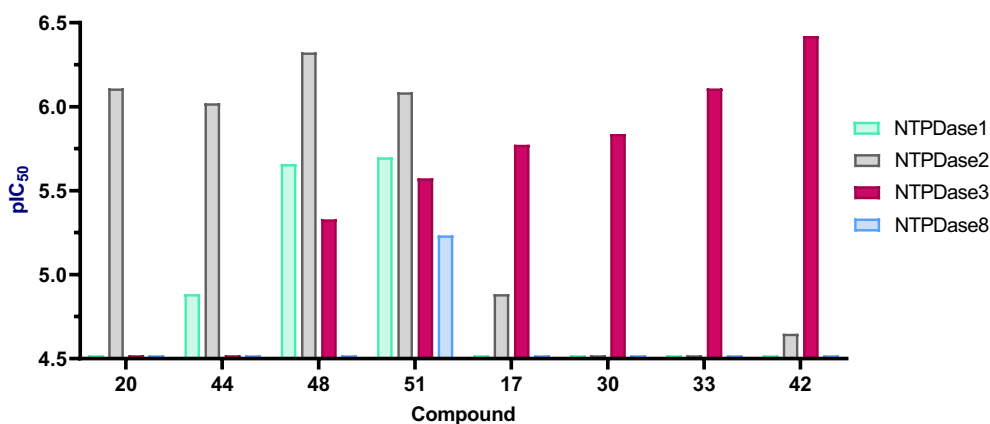


FIGURE 3 | Selectivity of selected anthraquinone derivatives on different human NTPDase ecto-enzymes determined using the malachite green assay. Shown are the pIC₅₀ values of compounds 20, 44, 48 and 51, active on NTPDase 2 and compounds 17, 30, 33 and 42 active on NTPDase3.

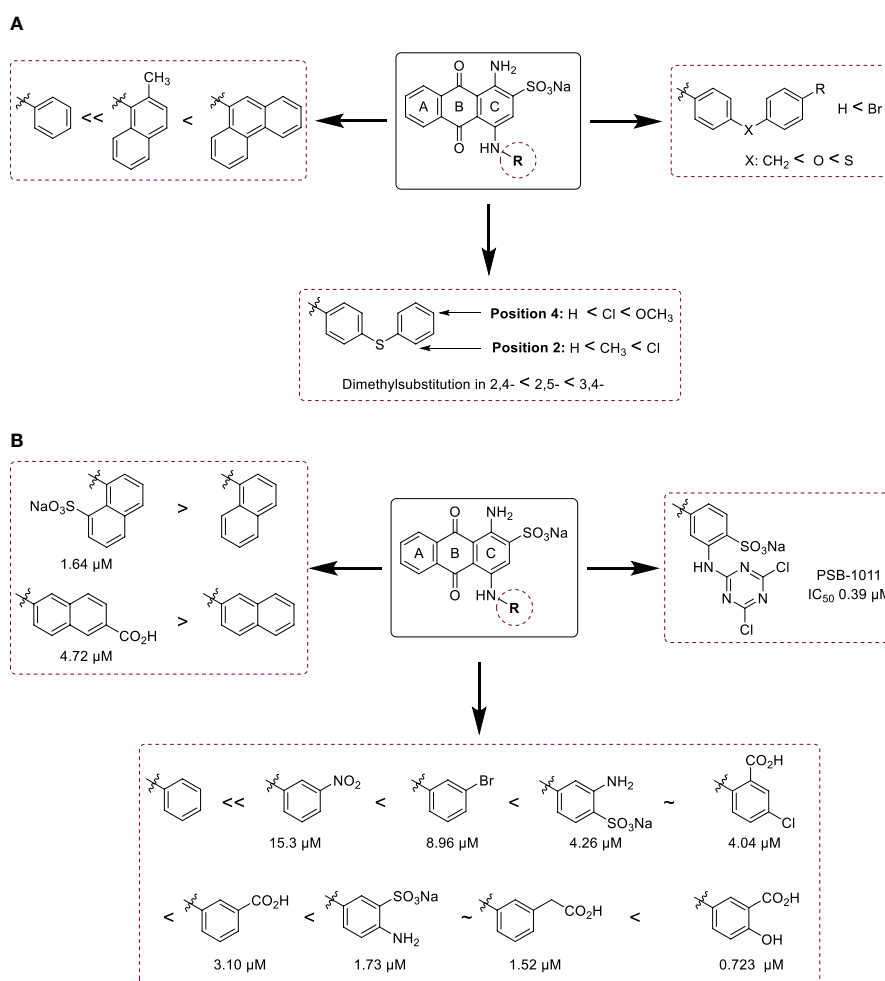


FIGURE 4 | Summary of SARs of anthraquinone derivatives **(A)** at human NTPDase2 and **(B)** at human NTPDase3.

medicinal chemistry targeting different nucleotide-binding proteins including ecto-5'-nucleotidase, P2Y₁₂ and P2X₂ receptors (Baqi, 2016; Malik and Müller, 2016). However, this does not mean that potent compounds are non-selective. In fact, selectivity for specific targets has been achievable (Baqi et al., 2009a; Baqi, 2016; Malik and Müller, 2016; Rafehi et al., 2017a; Rafehi et al., 2017b). Compounds that are highly potent at a specific target typically also have shown selectivity. In a study published in 2010, we reported the first SARs of anthraquinone derivatives as inhibitors of rat ecto-5'-nucleotidase (CD73) (Baqi et al., 2010). The observed SARs were clearly different from the SARs of anthraquinone derivatives as NTPDase inhibitors. For example, compound 15 displayed an IC₅₀ of 0.53 μ M at rat CD73 but was virtually inactive at NTPDases, while compound 20, found to be a potent inhibitor of human NTPDase2 in the present study, was shown to be only weakly active against CD73 (58% inhibition at 1 mM concentration) (Baqi et al., 2010). The compounds have not yet been tested at alkaline phosphatase, but this enzyme has a very high K_m value for adenine nucleotides, and its significance in the context of extracellular nucleotide metabolism and signaling in inflammation is therefore questionable. Nevertheless, ancillary activities of NTPDase inhibitors as blockers of CD73 or alkaline phosphatase would not be detrimental, but might even enhance their over-all effects leading to an accumulation of immunostimulatory, pro-inflammatory nucleotides while inhibiting the final production of immunosuppressive adenosine. Future studies might therefore be directed at multi-target drugs inhibiting more than one single ectonucleotidase.

Mechanism of Enzyme Inhibition

In previous studies at rat NTPDase2 and -3, selected small 1-amino-4-anilino-2-sulfoanthraquinone derivatives were found to display a competitive inhibition mechanism (Baqi et al., 2009b; Zebisch et al., 2014). In the present study at human NTPDases, the most potent inhibitors at NTPDase2, compound

20, and at NTPDase3, compound 42, were investigated with regard to their inhibition mechanism (see Figure 5).

NTPDase2 inhibitor 20 displayed non-competitive inhibition, while the larger NTPDase3 inhibitor 42 showed a mixed inhibition type. Together with previous results (Baqi et al., 2009b; Zebisch et al., 2014), these data show that anthraquinone derivatives may inhibit NTPDase isoenzymes with different inhibition mechanisms depending on the compound's substitution pattern and perhaps also the NTPDase subtype and the species.

CONCLUSIONS

Ectonucleoside triphosphate diphosphohydrolase (E-NTPDase) plays a major role in controlling extracellular nucleotide levels. NTPDase inhibitors have potential as novel drugs, for example, for the treatment of inflammation, neurodegenerative diseases and cancer. In the present study, we synthesized and investigated a series of 48 anthraquinone derivatives as potential inhibitors of NTPDases, 14 of which are novel compounds. The synthesized compounds showed no inhibitory activity on NTPDase1 (CD39) or NTPDase8, while potent inhibitors for NTPDase2 or -3 were identified. The most potent inhibitors exhibited selectivity for either NTPDase2 or -3. It was noticed that human NTPDase2 features a lipophilic pocket that accommodates polynuclear-aromatic rings such as phenanthryl or naphthyl bearing lipophilic substituents such as chloro or methyl. In contrast, NTPDase3 was found to accommodate smaller hydrophilic functions such as hydroxyl, carboxyl or sulfonate. These NTPDase3-inhibitors were selective (>10-fold) vs. other NTPDases. Although inhibitors bearing polar sulfonate functions cannot be expected to be brain-penetrant, they will be useful tools for studying peripheral effects, or maybe even used to study central effects after direct application to the brain.

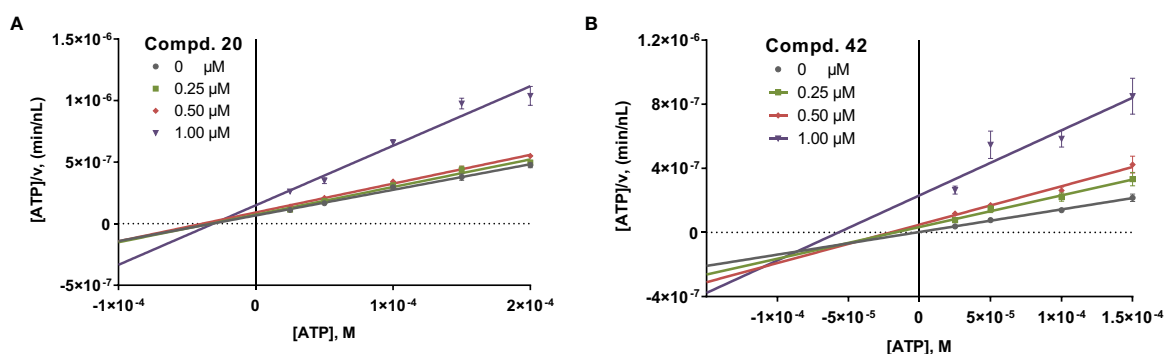


FIGURE 5 | (A) Hanes-Woolf plot for NTPDase2 inhibition by 20, determined using the malachite green assay and recombinant human NTPDase2 expressed in COS7 cell membranes. ATP at concentrations of 25, 50, 100, 150 and 200 μ M (K_m = 70 μ M) was used as a substrate. Data points shown are the mean values \pm SEM of at least three independent experiments, each performed in triplicates (n = 3). **(B)** Hanes-Woolf plot for NTPDase3 inhibition by 42, determined using the malachite green assay and recombinant human NTPDase3 expressed in COS7 cell membranes. ATP at concentrations of 25, 50, 100, and 150 μ M (K_m = 75 μ M) was used as a substrate. Data points shown are the mean values \pm SEM of at least three independent experiments, each performed in triplicates (n = 3).

DATA AVAILABILITY STATEMENT

The original contributions presented in the study are included in the article/**Supplementary Material**. Further inquiries can be directed to the corresponding authors.

AUTHOR CONTRIBUTIONS

CM and YB designed the study. YB, MR, and EM synthesized the compounds. LS and AF performed the biological assays. JS and JP expressed the NTPDases and produced the enzyme-containing membrane preparations. YB, CM, and MR wrote the manuscript with contributions from all coauthors. All authors contributed to the article and approved the submitted version.

FUNDING

This study was supported by the DFG (SFB 1328, ID 335447717), the BMBF (BIGS DrugS), and the Arab-German Young

Academy of Sciences and Humanities (AGYA) (01DL16002 & 01DL20003). EM is grateful to the Deutscher Akademischer Austauschdienst (DAAD) for a PhD scholarship. JS received support from the Natural Sciences and Engineering Research Council of Canada (NSERC; RGPIN-2016-05867) and was the recipient of a “Chercheur National” Scholarship from the Fonds de Recherche du Québec—Santé (FRQS).

ACKNOWLEDGMENTS

We thank Marion Schneider for LCMS analyses and Sabine Terhart-Krabbe and Annette Reiner for NMR spectra.

SUPPLEMENTARY MATERIAL

The Supplementary Material for this article can be found online at: <https://www.frontiersin.org/articles/10.3389/fphar.2020.01282/full#supplementary-material>

REFERENCES

- Al-Rashida, M., and Iqbal, J. (2015). Inhibition of alkaline phosphatase: an emerging new drug target. *Mini Rev. Med. Chem.* 15, 41–51. doi: 10.2174/1389557515666150219113205
- Antonoli, L., Blandizzi, C., Pacher, P., and Haskó, G. (2019). The purinergic system as a pharmacological target for the treatment of immune-mediated inflammatory diseases. *Pharmacol. Rev.* 71, 345–382. doi: 10.1124/pr.117.014878
- Baqi, Y., and Müller, C. E. (2007). Rapid and efficient microwave-assisted copper (0)-catalyzed ullmann coupling reaction: general access to anilinoanthraquinone derivatives. *Org. Lett.* 9, 1271–1274. doi: 10.1021/ol070102v
- Baqi, Y., and Müller, C. E. (2010). Synthesis of alkyl- and aryl-aminosubstituted anthraquinone derivatives by microwave-assisted copper(0)-catalyzed Ullmann coupling reactions. *Nat. Protoc.* 5, 945–953. doi: 10.1038/nprot.2010.63
- Baqi, Y., and Müller, C. E. (2012). Efficient and mild deamination procedure for 1-aminoanthraquinones yielding a diverse library of novel derivatives with potential biological activity. *Tetrahedron Lett.* 53, 6739–6742. doi: 10.1016/j.tetlet.2012.09.011
- Baqi, Y., Atzler, K., Köse, M., Glänzel, M., and Müller, C. E. (2009a). High-affinity, non-nucleotide-derived competitive antagonists of platelet P2Y₁₂ receptors. *J. Med. Chem.* 52, 3784–3793. doi: 10.1021/jm9003297
- Baqi, Y., Weyler, S., Iqbal, J., Zimmermann, H., and Müller, C. E. (2009b). Structure-activity relationships of anthraquinone derivatives derived from bromaminic acid as inhibitors of ectonucleoside triphosphate diphosphohydrolases (E-NTPDases). *Purinerg. Signal.* 5, 91–106. doi: 10.1007/s11302-008-9103-5
- Baqi, Y., Lee, S.-Y., Iqbal, J., Ripphausen, P., Lehr, A., Scheiff, A. B., et al. (2010). Development of potent and selective inhibitors of ecto-5'-nucleotidase based on an anthraquinone scaffold. *J. Med. Chem.* 53, 2076–2086. doi: 10.1021/jm901851t
- Baqi, Y., Hausmann, R., Rosefort, C., Rettinger, J., Schmalzing, G., and Müller, C. E. (2011). Discovery of potent competitive antagonists and positive modulators of the P2X₂ receptor. *J. Med. Chem.* 54, 817–830. doi: 10.1021/jm1012193
- Baqi, Y. (2015). Ecto-nucleotidase inhibitors: recent developments in drug discovery. *Mini Rev. Med. Chem.* 15, 21–33. doi: 10.2174/1389557515666150219115141
- Baqi, Y. (2016). Anthraquinones as a privileged scaffold in drug discovery targeting nucleotide-binding proteins. *Drug Discovery Today* 21, 1571–1577. doi: 10.1016/j.drudis.2016.06.027
- Baykov, A. A., Evtushenko, O. A., and Avaeva, S. M. (1988). A malachite green procedure for orthophosphate determination and its use in alkaline phosphatase-based enzyme immunoassay. *Anal. Biochem.* 171, 266–270. doi: 10.1016/0003-2697(88)90484-8
- Belcher, S. M., Zsarnovszky, A., Crawford, P. A., Hemani, H., Spurling, L., and Kirley, T. L. (2006). Immunolocalization of ecto-nucleoside triphosphate diphosphohydrolase 3 in rat brain: implications for modulation of multiple homeostatic systems including feeding and sleep-wake behaviors. *Neuroscience* 137, 1331–1346. doi: 10.1016/j.neuroscience.2005.08.086
- Bonan, C. D. (2012). Ectonucleotidases and nucleotide/nucleoside transporters as pharmacological targets for neurological disorders. *CNS Neurol. Disord. Drug Targets* 11, 739–750. doi: 10.2174/187152712803581092
- Braun, N., Sévigny, J., Mishra, S. K., Robson, S. C., Barth, S. W., Gerstberger, R., et al. (2003). Expression of the ecto-ATPase NTPDase2 in the germinal zones of the developing and adult rat brain. *Eur. J. Neurosci.* 17, 1355–1364. doi: 10.1046/j.1460-9568.2003.02567.x
- Braun, N., Sévigny, J., Robson, S. C., Hammer, K., Hanani, M., and Zimmermann, H. (2004). Association of the ecto-ATPase NTPDase2 with glial cells of the peripheral nervous system. *Glia* 45, 124–132. doi: 10.1002/glia.10309
- Brunschweiler, A., Iqbal, J., Umbach, F., Scheiff, A. B., Munkonda, M. N., Sévigny, J., et al. (2008). Selective nucleoside triphosphate diphosphohydrolase-2 (NTPDase2) inhibitors: nucleotide mimetics derived from uridine-5'-carboxamide. *J. Med. Chem.* 51, 4518–4528. doi: 10.1021/jm800175e
- Burnstock, G. (2018). The therapeutic potential of purinergic signalling. *Biochem. Pharmacol.* 151, 157–165. doi: 10.1016/j.bcp.2017.07.016
- Burnstock, G. (2020). Introduction to purinergic signaling. *Methods Mol. Biol.* 2041, 1–15. doi: 10.1007/978-1-4939-9717-6_1
- Cogan, E. B., Birrell, G. B., and Griffith, O. H. A. (1999). Robotics-based automated assay for inorganic and organic phosphates. *Anal. Biochem.* 271, 29–35. doi: 10.1006/abio.1999.4100
- Dou, L., Chen, Y. F., Cowan, P. J., and Chen, X. P. (2018). Extracellular ATP signaling and clinical relevance. *Clin. Immunol.* 188, 67–73. doi: 10.1016/j.clim.2017.12.006
- Fiene, A., Baqi, Y., Lecka, J., Sévigny, J., and Müller, C. E. (2015). Fluorescence polarization immunoassays for monitoring nucleoside triphosphate diphosphohydrolase (NTPDase) activity. *Analyst* 140, 140–148. doi: 10.1039/c4an01694g
- Fiene, A., Baqi, Y., Malik, E. M., Newton, P., Li, W., Lee, S. Y., et al. (2016). Inhibitors for the bacterial ectonucleotidase LpNTPDase from *Legionella pneumophila*. *Bioorg. Med. Chem.* 24, 4363–4371. doi: 10.1016/j.bmc.2016.07.027

- Gampe, K., Hammer, K., Kittel, Á., and Zimmermann, H. (2012). The medial habenula contains a specific nonstellate subtype of astrocyte expressing the ectonucleotidase NTPDase2. *Glia* 60, 1860–1870. doi: 10.1002/glia.22402
- Gampe, K., Stefani, J., Hammer, K., Brendel, P., Pöttsch, A., Enikolopov, G., et al. (2015). NTPDase2 and purinergic signaling control progenitor cell proliferation in neurogenic niches of the adult mouse brain. *Stem Cells* 33, 253–264. doi: 10.1002/stem.1846
- Grković, I., Bjelobaba, I., Mitrović, N., Lavrnja, I., Drakulić, D., Martinović, J., et al. (2016). Expression of ecto-nucleoside triphosphate diphosphohydrolase3 (NTPDase3) in the female rat brain during postnatal development. *J. Chem. Neuroanat.* 77, 10–18. doi: 10.1016/j.jchemneu.2016.04.001
- Iqbal, J., Vollmayer, P., Braun, N., Zimmermann, H., and Müller, C. E. (2005). A capillary electrophoresis method for the characterization of ecto-nucleoside triphosphate diphosphohydrolases (NTPDases) and the analysis of inhibitors by in-capillary enzymatic microreaction. *Purinerg. Signal.* 1, 349–358. doi: 10.1007/s11302-005-8076-x
- Kanwal, Khan, K. M., Salar, U., Afzal, S., Wadood, A., Taha, M., et al. (2019). Schiff bases of tryptamine as potent inhibitors of nucleoside triphosphate diphosphohydrolases (NTPDases): Structure-activity relationship. *Bioorg. Chem.* 82, 253–266. doi: 10.1016/j.bioorg.2018.10.046
- King, A. E., Ackley, M. A., Cass, C. E., Young, J. D., and Baldwin, S. A. (2006). Nucleoside transporters: from scavengers to novel therapeutic targets. *Trends. Pharm. Sci.* 27, 416–425. doi: 10.1016/j.tips.2006.06.004
- Kukulski, F., Lévesque, S. A., Lavoie, É. G., Lecka, J., Bigonnesse, F., Knowles, A. F., et al. (2005). Comparative hydrolysis of P2 receptor agonists by NTPDases 1, 2, 3 and 8. *Purinerg. Signal.* 1, 193. doi: 10.1007/s11302-005-6217-x
- Le, T. T., Berg, N. K., Harting, M. T., Li, X., Eltzschig, H. K., and Yuan, X. (2019). Purinergic Signaling in Pulmonary Inflammation. *Front. Immunol.* 10:1633:1633. doi: 10.3389/fimmu.2019.01633
- Lecka, J., Gillerman, I., Fausther, M., Salem, M., Munkonda, M. N., Brosseau, J.-P., et al. (2013). 8-BuS-ATP derivatives as specific NTPDase1 inhibitors. *Br. J. Pharmacol.* 169, 179–196. doi: 10.1111/bph.12135
- Lee, S.-Y., and Müller, C. E. (2017). Nucleotide pyrophosphatase/phosphodiesterase 1 (NPP1) and its inhibitors. *MedChemComm* 8, 823–840. doi: 10.1039/c7md00015d
- Lee, S. Y., Luo, X., Namasivayam, V., Geiss, J., Mirza, S., Pelletier, J., et al. (2018). Development of a selective and highly sensitive fluorescence assay for nucleoside triphosphate diphosphohydrolase1 (NTPDase1, CD39). *Analyst* 143, 5417–5430. doi: 10.1039/c8an01108g
- Lévesque, S. A., Lavoie, E. G., Lecka, J., Bigonnesse, F., and Sévigny, J. (2007). Specificity of the ecto-ATPase inhibitor ARL67156 on human and mouse ectonucleotidases. *Br. J. Pharmacol.* 152, 141–150. doi: 10.1038/sj.bjp.0707361
- Malik, E., and Müller, C. E. (2016). Anthraquinones as pharmacological tools and drugs. *Med. Res. Rev.* 36, 705–748. doi: 10.1002/med.21391
- Malik, E. M., Rashed, M., Wingen, L., Baqi, Y., and Müller, C. E. (2016). Ullmann reactions of 1-amino-4-bromoanthraquinones bearing various 2-substituents furnishing novel dyes. *Dyes. Pigm.* 131, 33–40. doi: 10.1016/j.dyepig.2016.03.023
- Mishra, S. K., Braun, N., Shukla, V., Füllgrabe, M., Schomerus, C., Korf, H. W., et al. (2006). Extracellular nucleotide signaling in adult neural stem cells: synergism with growth factor-mediated cellular proliferation. *Development* 133, 675–684. doi: 10.1242/dev.02233
- Müller, C. E., Iqbal, J., Baqi, Y., Zimmermann, H., Röllich, A., and Stephan, H. (2006). Polyoxometalates – a new class of potent ecto-nucleoside triphosphate diphosphohydrolase (NTPDase) inhibitors. *Bioorg. Med. Chem. Lett.* 16, 5943–5947. doi: 10.1016/j.bmcl.2006.09.003
- Müller, C. E., Baqi, Y., and Namasivayam, V. (2020). Agonists and antagonists for purinergic receptors. *Methods Mol. Biol.* 2041, 45–64. doi: 10.1007/978-1-4939-9717-6_3
- Munkonda, M. N., Pelletier, J., Ivanenkov, V. V., Fausther, M., Tremblay, A., Künzli, B., et al. (2009). Characterization of a monoclonal antibody as the first specific inhibitor of human NTP diphosphohydrolase-3 - Partial characterization of the inhibitory epitope and potential applications. *FEBS J.* 276, 479–496. doi: 10.1111/j.1742-4658.2008.06797.x
- Pelletier, J., Agonsanou, H., Delvalle, N., Fausther, M., Salem, M., Gulbransen, B., et al. (2017). Generation and characterization of polyclonal and monoclonal antibodies to human NTPDase2 including a blocking antibody. *Purinerg. Signal.* 13, 293–304. doi: 10.1007/s11302-017-9561-8
- Rafehi, M., Malik, E. M., Neumann, A., Abdelrahman, A., Hanck, T., Namasivayam, V., et al. (2017a). Development of potent and selective antagonists for the UTP-activated P2Y4 receptor. *J. Med. Chem.* 60, 3020–3038. doi: 10.1021/acs.jmedchem.7b00030
- Rafehi, M., Neumann, A., Baqi, Y., Malik, E. M., Wiese, M., Namasivayam, V., et al. (2017b). Molecular recognition of agonists and antagonists by the nucleotide-activated G protein-coupled P2Y2 receptor. *J. Med. Chem.* 60, 8425–8440. doi: 10.1021/acs.jmedchem.7b00854
- Sévigny, J., Levesque, F. P., Grondin, G., and Beaudoin, A. R. (1997). Purification of the blood vessel ATP diphosphohydrolase, identification and localisation by immunological techniques. *Biochim. Biophys. Acta* 1334, 73–88. doi: 10.1016/S0304-4165(96)00079-7
- Shukla, V., Zimmermann, H., Wang, L., Kettenmann, H., Raab, S., Hammer, K., et al. (2005). Functional expression of the ecto-ATPase NTPDase2 and of nucleotide receptors by neuronal progenitor cells in the adult murine hippocampus. *J. Neurosci. Res.* 80, 600–610. doi: 10.1002/jnr.20508
- Vuerich, M., Robson, S. C., and Longhi, M. S. (2019). Ectonucleotidases in Intestinal and Hepatic Inflammation. *Front. Immunol.* 10, 507. doi: 10.3389/fimmu.2019.00507
- Weyler, S., Baqi, Y., Hillmann, P., Kaulich, M., Hunder, A. M., Müller, I. A., et al. (2008). Combinatorial synthesis of anilinoanthraquinone derivatives and evaluation as non-nucleotide-derived P2Y₂ receptor antagonists. *Bioorg. Med. Chem. Lett.* 18, 223–227. doi: 10.1016/j.bmcl.2007.10.082
- Zebisch, M., Baqi, Y., Schäfer, P., Müller, C. E., and Sträter, N. (2014). Crystal structure of NTPDase2 in complex with the sulfoanthraquinone inhibitor PSB-071. *J. Struct. Biol.* 185, 336–341. doi: 10.1016/j.jsb.2014.01.005
- Zimmermann, H., Zebisch, M., and Sträter, N. (2012). Cellular function and molecular structure of ecto-nucleotidases. *Purinerg. Signal.* 8, 3, 437–502. doi: 10.1007/s11302-012-9309-4

Conflict of Interest: The authors declare that the research was conducted in the absence of any commercial or financial relationships that could be construed as a potential conflict of interest.

Copyright © 2020 Baqi, Rashed, Schäkel, Malik, Pelletier, Sévigny, Fiene and Müller. This is an open-access article distributed under the terms of the Creative Commons Attribution License (CC BY). The use, distribution or reproduction in other forums is permitted, provided the original author(s) and the copyright owner(s) are credited and that the original publication in this journal is cited, in accordance with accepted academic practice. No use, distribution or reproduction is permitted which does not comply with these terms.



Nucleotide Analog ARL67156 as a Lead Structure for the Development of CD39 and Dual CD39/CD73 Ectonucleotidase Inhibitors

OPEN ACCESS

Edited by:

Elena Adinolfi,
University of Ferrara, Italy

Reviewed by:

Fernanda Bueno Morrone,
Pontifical Catholic University of Rio
Grande do Sul, Brazil
Stephanie Federico,
University of Trieste, Italy

*Correspondence:

Christa E. Müller
christa.mueller@uni-bonn.de

[†]These authors have contributed
equally to this work

Specialty section:

This article was submitted to
Experimental Pharmacology
and Drug Discovery,
a section of the journal
Frontiers in Pharmacology

Received: 07 June 2020

Accepted: 04 August 2020

Published: 08 September 2020

Citation:

Schäkel L, Schmies CC, Idris RM,
Luo X, Lee S-Y, Lopez V, Mirza S,
Vu TH, Pelletier J, Sévigny J,
Namasivayam V and Müller CE (2020)
Nucleotide Analog ARL67156 as a
Lead Structure for the Development of
CD39 and Dual CD39/CD73
Ectonucleotidase Inhibitors.
Front. Pharmacol. 11:1294.
doi: 10.3389/fphar.2020.01294

Laura Schäkel^{1†}, Constanze C. Schmies^{1†}, Riham M. Idris¹, Xihuan Luo¹,
Sang-Yong Lee¹, Vittoria Lopez¹, Salahuddin Mirza¹, The Hung Vu¹, Julie Pelletier²,
Jean Sévigny^{2,3}, Vigneshwaran Namasivayam¹ and Christa E. Müller^{1*}

¹ PharmaCenter Bonn, Pharmaceutical Institute, Pharmaceutical Sciences Bonn (PSB), Pharmaceutical & Medicinal
Chemistry, University of Bonn, Bonn, Germany, ² Centre de Recherche du CHU de Québec – Université Laval, Québec City,
QC, Canada, ³ Département de Microbiologie-Infectiologie et d'Immunologie, Faculté de Médecine, Université Laval, Québec
City, QC, Canada

Nucleoside triphosphate diphosphohydrolase1 (NTPDase1, CD39) inhibitors have potential as novel drugs for the (immuno)therapy of cancer. They increase the extracellular concentration of immunostimulatory ATP and reduce the formation of AMP, which can be further hydrolyzed by ecto-5'-nucleotidase (CD73) to immunosuppressive, cancer-promoting adenosine. In the present study, we synthesized analogs and derivatives of the standard CD39 inhibitor ARL67156, a nucleotide analog which displays a competitive mechanism of inhibition. Structure-activity relationships were analyzed at the human enzyme with respect to substituents in the *N*⁶- and C8-position of the adenine core, and modifications of the triphosph(on)ate chain. Capillary electrophoresis coupled to laser-induced fluorescence detection employing a fluorescent-labeled ATP derivative was employed to determine the compounds' potency. Selected inhibitors were additionally evaluated in an orthogonal, malachite green assay versus the natural substrate ATP. The most potent CD39 inhibitors of the present series were ARL67156 and its derivatives 31 and 33 with *K_i* values of around 1 μM. Selectivity studies showed that all three nucleotide analogs additionally blocked CD73 acting as dual-target inhibitors. Docking studies provided plausible binding modes to both targets. The present study provides a full characterization of the frequently applied CD39 inhibitor ARL67156, presents structure-activity relationships, and provides a basis for future optimization towards selective CD39 and dual CD39/CD73 inhibitors.

Keywords: ARL67156, CD39, CD73, docking, dual-target inhibitors, ecto-5'-nucleotidase, nucleoside triphosphate diphosphohydrolase1 (NTPDase1), nucleotides

INTRODUCTION

Nucleoside triphosphate diphosphohydrolase1 (NTPDase1, CD39, EC 3.6.1.5) catalyzes the hydrolysis of extracellular nucleoside tri- and diphosphates producing the corresponding monophosphates (Zimmermann et al., 2012). CD39 is membrane-bound and often co-localized with ecto-5'-nucleotidase (CD73), another ectonucleotidase that further hydrolyzes the nucleoside monophosphates to the corresponding nucleosides (Flögel et al., 2012; Augusto et al., 2013; Bastid et al., 2015). The main substrate of CD39 is ATP which is cleaved *via* ADP to AMP, while AMP acts as the main substrate of CD73 which catalyzes its hydrolysis to adenosine (see **Figure 1**).

Many tumor cells overexpress ectonucleotidases (De Marchi et al., 2019; Horenstein et al., 2019) which metabolize proinflammatory ATP to immunosuppressive, angiogenic, prometastatic, and tumor growth-promoting adenosine (Vitiello et al., 2012). Inhibition of CD39 could reduce the production of cancer-promoting adenosine, e.g. in the tumor micro-environment, and increase the concentration of immunostimulatory ATP. Due to its pathophysiological role, CD39 represents a promising potential drug target that requires, however, further validation. For this purpose, potent, selective, and metabolically stable inhibitors need to be identified. Besides selective CD39 inhibitors, dual inhibition of CD39 and CD73 is of interest and may be synergistic since the substrate of CD73, extracellular AMP, may additionally be formed by alternative ectonucleotidases, such as nucleotide pyrophosphatase/phosphodiesterase1 (NPP1) (Lee and Müller, 2017; Lee et al., 2017a).

Up to now, only moderately potent and/or non-selective CD39 inhibitors are available. These can be divided into (i) nucleotide derivatives and analogs, e.g. *N*⁶-diethyl- β , γ -dibromomethylene-ATP (ARL67156, I) and 8-butylthio-AMP (8-BuS-AMP, II), and (ii) non-nucleotides, including the sulfonate dyes reactive blue 2 (RB-2) and related anthraquinone derivatives (e.g. III), polyoxometalates (e.g. PSB-POM-142, IV), and tryptamine-derived imines (e.g. V) (Crack et al., 1995; Müller et al., 2006; Lévesque et al., 2007; Baqi et al., 2009; Lecka et al., 2013; Lee et al., 2015; Kanwal et al., 2019). A selection of the most potent CD39 inhibitors described so far is depicted in **Figure 2**.

The nucleotide-based competitive CD39 inhibitor *N*⁶-diethyl- β , γ -dibromomethylene-ATP (ARL67156) was developed by Fisons Laboratories (now AstraZeneca, Loughborough, UK) as

a probe to study ecto-nucleotidases and purinoceptors (Crack et al., 1995). The nucleotide analog was proposed to be relatively stable towards hydrolysis by ectonucleotidases (CD39; NTPDase2,-3,-8; CD73; NPP1; NPP3) because the cleavage site is blocked by replacement of the β , γ -oxygen atom of the ATP triphosphate chain by a dibromomethylene moiety yielding a phosphonate linkage (Lévesque et al., 2007). ARL67156 (I) was shown to competitively inhibit the mouse and human forms of CD39 [*K_i* (human) 11 μ M], NTPDase3 [*K_i* (human) 18 μ M], and NPP1 [*K_i* (human) 12 μ M], but was reported to have a weaker effect on NTPDase2, NTPDase8, NPP3, and CD73 (Lévesque et al., 2007). Furthermore, in contrast to other NTPDase inhibitors, ARL67156 had no significant effect on P2 receptors due to di-substitution of the exocyclic amino group (Robson et al., 2006). ARL67156 is currently the only commercially available CD39 inhibitor, claimed to be metabolically stable and CD39-selective, and it is therefore frequently used for *in vitro* as well as *in vivo* studies despite its moderate potency (Mandapathil et al., 2010; Zhou et al., 2014; Li et al., 2015). Metabolic stability of ARL67156 has not been sufficiently studied to date, and structure-activity relationships (SARs) are largely unknown.

In this study, we characterized the CD39 inhibitor ARL67156 (I) and used it as a lead structure for studying the SARs of ATP analogs and derivatives as inhibitors of CD39 and other ectonucleotidases. Derivatization in the *N*⁶- and 8-position of the adenine ring, as well as replacement of the di-bromomethylene bridge were performed. Selectivity versus a broad range of ectonucleotidases and metabolic stability were determined for ARL67156 and selected potent inhibitors. Finally, we performed docking studies to facilitate future drug design efforts.

MATERIALS AND METHODS

Syntheses

Materials and Instruments

All reagents were commercially obtained from various producers (Acros, Fluorochem, Merck, Carbosynth, Santa Cruz, Sigma Aldrich, and TCI) and used without further purification, unless otherwise stated. Commercial solvents of reagent grade were used without additional purification or drying. 8-Bromoadenosine was synthesized according to a published procedure (Bhattarai et al., 2015). Reactions were monitored by thin layer chromatography (TLC) using Merck silica gel 60 F254 aluminum sheets and dichloromethane (DCM)/methanol (9:1 or 3:1) as the mobile phase. The TLC plates were analyzed by ultraviolet (UV) light at a wavelength (λ) of 254 nm. Column chromatography was carried out on silica gel 0.040–0.060 mm, pore diameter ca. 6 nm. Anion exchange chromatography was performed on a fast protein liquid chromatography (FPLC) instrument (ÄKTA FPLC, from Amersham Biosciences) with a HiPrep Q Fast Flow sepharose column, 16 x 100 mm (GE Healthcare Life Sciences). Elution of the nucleoside triphosphate analogs was achieved with a linear gradient (5–100%, 0.5 M aqueous ammonium bicarbonate buffer in water, 8 column volumes, flow 1 ml/min). The neutral

Abbreviations: ADT, AutoDockTools; CE, capillary electrophoresis; DCM, dichloromethane; DMSO, dimethyl sulfoxide; DAD, diode array detector; CD39, nucleoside triphosphate diphosphohydrolase1; CD73, ecto-5'-nucleotidase; ESI, electrospray ionization; FPLC, fast protein liquid chromatography; HEPES, 4-(2-hydroxyethyl)piperazine-1-ethanesulfonic acid; HPLC, high performance liquid chromatography; LIF, laser-induced fluorescence; MS, mass spectrometry; MGL, Molecular Graphics Laboratory; DMF, *N,N*-dimethylformamide; NMR, nuclear magnetic resonance; NTPDase1, nucleoside triphosphate diphosphohydrolase1; NPP1, nucleotide pyrophosphatase/phosphodiesterase1; SAR(s), structure-activity relationship(s); TEAC, triethylammonium hydrogencarbonate; TLC, thin layer chromatography.

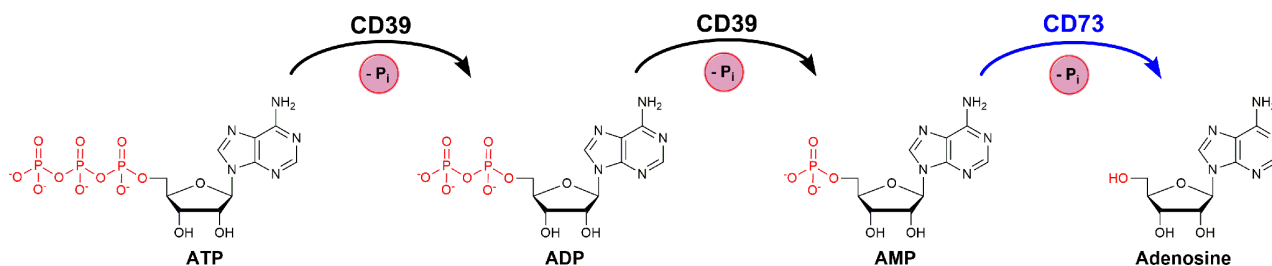
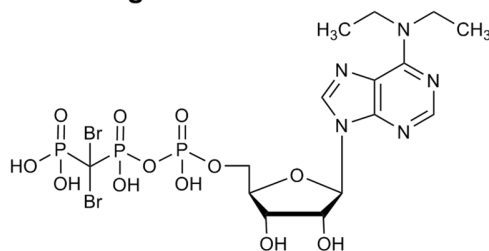
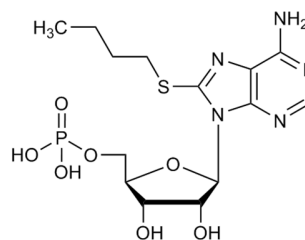


FIGURE 1 | Consecutive hydrolysis of ATP to adenosine by cleaving the terminal phosphate group and releasing inorganic phosphate (P_i), catalyzed by the enzymes CD39 and CD73.

Nucleotide analogs or derivatives

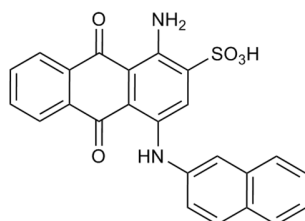


ARL-67156 (I)
human CD39: $K_i = 11 \mu\text{M}$
(Lévesque et al., 2007)
(Crack et al., 1995)

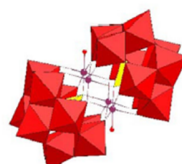


8-BuS-AMP (II)
human CD39: $K_i = 0.8 \mu\text{M}$
(Lecka et al., 2013)

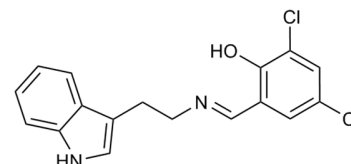
Non-nucleotides



1-Amino-2-sulfo-4-(2-naphthylamino)-anthraquinone (III)
rat CD39: $K_i = 0.33 \mu\text{M}$
(Baqi et al., 2009)



PSB-POM142 (IV)
[Co₄(H₂O)₂(PW₉O₃₄)₂]¹⁰⁻
human CD39: $K_i = 0.00388 \mu\text{M}$
(Lee et al., 2015)



Tryptamine derivative (V)
human CD39: $K_i = 0.021 \mu\text{M}$
(Kanwal et al., 2019)

FIGURE 2 | Chemical structures and reported potencies of selected CD39 inhibitors.

impurities (e.g. nucleosides) eluted first, followed by charged species (mono-, and finally triphosphate analogs). Semi-preparative high performance liquid chromatography (HPLC) was performed on a Knauer Smartline 1050 HPLC system equipped with a Eurospher-100 C18 column, 250 x 20 mm, particle size 10 μm . The UV absorption was detected at 254 nm. Fractions were collected, and appropriate fractions were pooled, diluted with water, and lyophilized several times, using a CHRIST

ALPHA 1-4 LSC freeze dryer, to remove the NH₄HCO₃ buffer, yielding the nucleotides as white powders. Mass spectra were recorded on an API 2000 mass spectrometer (Applied Biosystems, Darmstadt, Germany) with a turbo ion spray ion source coupled with an Agilent 1100 HPLC system (Agilent, Böblingen, Germany) using an EC50/2 Nucleodur C18 Gravity 3 μm column (Macherey-Nagel, Düren, Germany), or on a micrOTOF-Q mass spectrometer (Bruker, Köln, Germany) with

an ESI-source coupled with an HPLC Dionex Ultimate 3000 (Thermo Scientific, Braunschweig, Germany) using an EC50/2 Nucleodur C18 Gravity 3 μm column (Macherey-Nagel, Düren, Germany). All compounds containing Br atoms (14–16 and 24–38) showed the expected typical isotope distribution pattern (see **Figures S6 and S7**). UV absorption was detected from 220 to 400 nm using a diode array detector (DAD). Nuclear magnetic resonance (NMR) spectra were recorded on Bruker Avance 500 and Ascend 600 MHz spectrometers. DMSO- d_6 , CD $_3$ OD, or D $_2$ O were used as solvents. ^{31}P -NMR spectra were recorded at 25°C, and phosphoric acid was used as an external standard. For spectra recorded in D $_2$ O, 3-(trimethylsilyl)propionic acid sodium salt- d_4 was used as an external standard. When DMSO- d_6 was used, spectra were recorded at 30°C. Shifts are given in ppm relative to the external standard (in ^{31}P -NMR) or relative to the remaining protons of the deuterated solvent used as internal standard (^1H -, ^{13}C -NMR). Coupling constants are given in Hertz (Hz). The designation used to assign the peaks in the spectra is as follows: singlet (s), doublet (d), triplet (t), quartet (q), multiplet (m), broad (br). Melting points were determined on a Büchi 530 melting point apparatus and are uncorrected.

Synthetic Procedures

General Procedure for the Synthesis of Compounds 2–7

To 6-chloro-9-(β -D-ribofuranosyl)purine (1, 0.5 g, 1.7 mmol, 1.0 eq) in absolute ethanol (15 ml) the appropriate alkylamine and Et $_3\text{N}$ (0.1 ml, 1.6 mmol, 0.9 eq) were added. The reaction mixture was refluxed for 6–36 h followed by evaporation of the solvent. Yields for intermediate products **3–6** were estimated to be above 70%; however exact yields were not determined because they were used without drying and desalting for the subsequent step; only a small amount was purified for analytical purposes.

(2R,3R,4S,5R)-2-(6-(Diethylamino)-9H-purin-9-yl)-5-(hydroxymethyl)tetrahydrofuran-3,4-diol (2)

The compound was synthesized using *N,N*-diethylamine (0.3 ml, 3.4 mmol, 2.0 eq) and purified by silica gel column chromatography (CH $_3$ OH/DCM 2:23) yielding a white powder (0.50 g, 100%). ^1H -NMR (500 MHz, DMSO- d_6) δ 8.34 (s, 1H, N=CHN) 8.19 (s, 1H, N=CHN) 5.89 (d, 1H, J = 6.04 Hz, CHN) 5.39 (d, 1H, J = 6.19 Hz, CHOH) 5.33 (dd, 1H, J = 4.59, 7.02 Hz, CH $_2$ OH) 5.13 (d, 1H, J = 4.61 Hz, CHOH) 4.58 (q, 1H, J = 6.04 Hz, CHOH) 4.14 (td, 1H, J = 3.36, 4.82 Hz, CHOH) 4.03 [br s, 4H, N(CH $_2$ CH $_3$) $_2$] 3.95 (q, 1H, J = 3.54 Hz, CHCH $_2$) 3.66–3.54 (d m, 2H, CHCH $_2$) 1.19 [t, 6H, J = 6.95 Hz, N(CH $_2$ CH $_3$) $_2$]. ^{13}C -NMR (125 MHz, DMSO- d_6) δ 153.27, 151.95, 150.06, 138.96, 119.47, 87.94, 85.91, 73.57, 70.70, 61.73, 42.56, 13.48. LC/ESI-MS (m/z): positive mode 324.1 [M+H] $^+$. Purity determined by HPLC-UV (254 nm)-ESI-MS: 99.2%. mp: 180°C.

(2R,3R,4S,5R)-2-(6-(Dimethylamino)-9H-purin-9-yl)-5-(hydroxymethyl)tetrahydrofuran-3,4-diol (3)

The compound was synthesized using *N,N*-dimethylamine (0.1 ml, 1.75 mmol, 1.0 eq) and purified by silica gel column chromatography (CH $_3$ OH/DCM 1:49) yielding a white powder (0.52 g). ^1H -NMR (500 MHz, DMSO- d_6) δ 8.35 (s, 1H, N=CHN) 8.20 (s, 1H, N=CHN) 5.90 (d, 1H, J = 5.97 Hz, CHN) 5.39 (d, 1H,

J = 6.17 Hz, CHOH) 5.32 (dd, 1H, J = 4.62, 6.95 Hz, CH $_2$ OH) 5.13 (d, 1H, J = 4.78 Hz, CHOH) 4.56 (q, 1H, J = 5.99 Hz, CHOH) 4.14 (m, 1H, CHCH $_2$) 3.95 (q, 1H, J = 3.55 Hz, CHOH) 3.66–3.55 (d m, 2H, CHCH $_2$) 3.45 [br s, 6H, N(CH $_3$) $_2$]. ^{13}C -NMR (125 MHz, DMSO- d_6) δ 154.46, 151.82, 150.05, 138.69, 119.94, 87.94, 85.88, 73.64, 70.65, 61.68, 11.57. LC/ESI-MS (m/z): positive mode 296.0 [M+H] $^+$. Purity determined by HPLC-UV (254 nm)-ESI-MS: 98%. mp: 186°C (lit. 184°C) (Čechová et al., 2011).

(2R,3R,4S,5R)-2-(6-(Ethyl(methyl)amino)-9H-purin-9-yl)-5-(hydroxymethyl)tetrahydrofuran-3,4-diol (4)

The compound was synthesized using *N*-ethylmethylamine (0.2 ml, 1.75 mmol, 1.0 eq) yielding a white powder (0.93 g). ^1H -NMR (500 MHz, DMSO- d_6) δ 8.35 (s, 1H, N=CHN) 8.20 (s, 1H, N=CHN) 5.90 (d, 1H, J = 6.00 Hz, CHN) 5.39 (d, 1H, J = 6.19 Hz, CHOH) 5.32 (dd, 1H, J = 4.61, 6.96 Hz, CH $_2$ OH) 5.13 (d, 1H, J = 4.76 Hz, CHOH) 4.57 (q, 1H, J = 5.99 Hz, CHOH) 4.14 (m, 1H, CHCH $_2$) 4.04 (br s, 2H, NCH $_2$) 3.95 (q, 1H, J = 3.51 Hz, CHOH) 3.66–3.54 (d m, 2H, CHCH $_2$) 3.39 (br s, 3H, NCH $_3$) 1.17 (t, 3H, J = 7.00 Hz, CH $_3$). ^{13}C -NMR (125 MHz, DMSO- d_6) δ 153.82, 151.89, 150.02, 138.82, 119.69, 87.91, 85.88, 73.59, 70.66, 61.69, 44.78, 35.47, 12.56. LC/ESI-MS (m/z): positive mode 310.0 [M+H] $^+$. Purity determined by HPLC-UV (254 nm)-ESI-MS: 98.0%. mp: 101°C.

2R,3S,4R,5R)-2-(Hydroxymethyl)-5-(6-(methyl(propyl)amino)-9H-purin-9-yl)tetrahydrofuran-3,4-diol (5)

The compound was synthesized using *N*-methylpropylamine (0.18 ml, 1.75 mmol, 1.0 eq) and purified by silica gel column chromatography (CH $_3$ OH/DCM 1:9) yielding a white powder (0.66 g). ^1H -NMR (500 MHz, DMSO- d_6) δ 8.35 (s, 1H, N=CHN) 8.19 (s, 1H, N=CHN) 5.89 (d, 1H, J = 5.97 Hz, CHN) 5.41 (d, 1H, J = 6.16 Hz, CHOH) 5.33 (m, 1H, CH $_2$ OH) 5.14 (d, 1H, J = 4.64 Hz, CHOH) 4.57 (q, 1H, J = 5.76 Hz, CHOH) 4.14 (d, 1H, J = 3.62 Hz, CHOH) 3.95 (d, 1H, J = 3.13 Hz, CHCH $_2$) 3.66–3.54 (d m, 2H, CHCH $_2$) 3.16 (br s, 2H, NCH $_2$) [signals underneath previous peaks: (NCH $_3$)] 1.64 (q, 2H, J = 7.30 Hz, CH $_2$) 0.87 (t, 3H, J = 7.34 Hz, CH $_3$). ^{13}C -NMR (125 MHz, DMSO- d_6) δ 154.16, 151.88, 150.10, 138.79, 119.71, 87.92, 85.92, 73.62, 70.71, 61.74, 51.32, 48.75, 21.58, 11.06. LC/ESI-MS (m/z): positive mode 324.1 [M+H] $^+$. Purity determined by HPLC-UV (254 nm)-ESI-MS: 97.7%. mp: 178°C.

(2R,3R,4S,5R)-2-(6-(Dipropylamino)-9H-purin-9-yl)-5-(hydroxymethyl)tetrahydrofuran-3,4-diol (6)

The compound was synthesized using *N,N*-dipropylamine (0.25 ml, 1.75 mmol, 1.0 eq) and purified by silica gel column chromatography (CH $_3$ OH/DCM 1:19) yielding a white powder (0.65 g). ^1H -NMR (500 MHz, DMSO- d_6) δ 8.35 (s, 1H, N=CHN) 8.18 (br s, 1H, N=CHN) 5.89 (d, 1H, J = 6.05 Hz, CHN) 5.40 (d, 1H, J = 5.91 Hz, CHOH) 5.33 (dd, 1H, J = 4.63, 6.97 Hz, CH $_2$ OH) 5.14 (d, 1H, J = 4.60 Hz, CHOH) 4.58 (q, 1H, J = 5.66 Hz, CHOH) 4.13 (q, 1H, J = 4.53 Hz, CHOH) 4.06 [m, 4H, N(CH $_2$) $_2$] 3.95 (q, 1H, J = 3.50 Hz, CHCH $_2$) 3.65–3.54 (d m, 2H, CHCH $_2$) 1.64 [m, 4H, (CH $_2$) $_2$] 0.89 [t, 6H, J = 7.37 Hz, (CH $_3$) $_2$]. ^{13}C -NMR (125 MHz, DMSO- d_6) δ 153.80, 151.88, 150.10, 138.89, 119.50, 87.92, 85.92, 73.56, 70.73, 61.92, 56.17, 48.74, 18.70, 11.18. LC/

ESI-MS (m/z): positive mode 352.1 [M+H]⁺. Purity determined by HPLC-UV (254 nm)-ESI-MS: 98.3%. mp: 145°C.

(2R,3R,4S,5R)-2-(6-(Ethyl(propyl)amino)-9H-purin-9-yl)-5-(hydroxymethyl)tetrahydrofuran-3,4-diol (7)

The compound was synthesized using *N*-ethylpropylamine (0.2 ml, 1.75 mmol, 1.0 eq) and purified by silica gel column chromatography (CH₃OH/DCM 1:9) yielding a white powder (0.38 g, 65%). ¹H-NMR (500 MHz, CD₃OD) δ 8.15 (d, 2H, *J* = 2.01 Hz, 2x N=CHN) 5.93 (d, 1H, *J* = 6.55 Hz, CHN) 4.74 (dd, 1H, *J* = 5.15, 6.48 Hz, CHOH) 4.30 (dd, 1H, *J* = 2.45, 5.09 Hz, CHCH₂) 4.16 (q, 1H, *J* = 2.40 Hz, CHOH) 3.88–3.72 (d m, 2H, CHCH₂) overlapping with 4.10–3.72 (br s, 4H, 2x NCH₂) 1.73 (m, 2H, CH₂CH₂CH₃) 1.25 (t, 3H, *J* = 7.04 Hz, CH₂CH₃) 0.95 [t, 3H, *J* = 7.39 Hz, (CH₂)₂CH₃]. ¹³C-NMR (151 MHz, CD₃OD) δ 155.40, 152.72, 150.70, 140.17, 121.60, 91.21, 88.17, 75.17, 72.77, 63.58, 51.25, 44.72, 22.52, 13.90, 11.36. LC/ESI-MS (m/z): positive mode 310.0 [M+H]⁺. Purity determined by HPLC-UV (254 nm)-ESI-MS: 97.2%. mp: 160°C.

(2R,3R,4S,5R)-2-(6-(Benzylamino)-9H-purin-9-yl)-5-(hydroxymethyl)tetrahydrofuran-3,4-diol (8)

The compound was synthesized according to a published procedure (Shimazaki et al., 1987) and purified by silica gel column chromatography (CH₃OH/DCM 1:9) yielding a white powder (3.45 g, 96%). ¹H-NMR (500 MHz, DMSO-*d*₆) δ: 8.36 (s, 1H, H-8), 8.19 (s, 1H, H-2), 7.33–7.17 (m, 5H, H_{arom.}), 5.88 (d, *J* = 6.1 Hz, 1H, H-1'), 5.39 (d, *J* = 6.2 Hz, 1H, OH-2'), 5.33 (dd, *J* = 7.1, 4.6 Hz, 1H, OH-5'), 5.13 (d, *J* = 4.7 Hz, 1H, OH-3'), 4.71 [s (br), 2H, N-CH₂], 4.61 (dd, *J* = 11.3, 6.0 Hz, 1H, H-2'), 4.14 (dd, *J* = 8.2, 4.8 Hz, 1H, H-3'), 3.96 (dd, *J* = 3.5 Hz, 1H, H-4'), 3.68–3.64 (m, 1H, H-5'a), 3.57–3.52 (m, 1H, H-5'b), (1H, NH not visible). ¹³C-NMR (125 MHz, DMSO-*d*₆) δ: 154.7 (C-6, C_{quat.}), 152.5 (C-2, CH), 148.6 (C-4, C_{quat.}), 140.1 (C_{arom.}, C_{quat.}), 140.0 (C-8, CH), 128.3 (2 x C_{arom.}, CH), 127.2 (2 x C_{arom.}, CH), 126.7 (C_{arom.}, CH), 119.9 (C-5, C_{quat.}), 88.1 (C-1', CH), 86.0 (C-4', CH), 73.6 (C-2', CH), 70.8 (C-3', CH), 61.8 (C-5', CH₂), 43.0 (C_{benzyl}, CH₂). LC-ESI-MS (m/z): positive mode 358 [M+H]⁺. Purity determined by HPLC-UV (254 nm)-ESI-MS: 98%. mp: 178–180°C. (Lit. 184–186°C) (Shimazaki et al., 1987).

Synthesis of (2R,3S,4R,5R)-2-(Hydroxymethyl)-5-(6-phenethylamino)-9H-purin-9-yl)tetrahydrofuran-3,4-diol (9)

The compound was synthesized according to a published procedure (Shimazaki et al., 1987) and purified by silica gel column chromatography (CH₃OH/DCM 1:9) yielding a white powder (3.21 g, 86%). ¹H-NMR (500 MHz, DMSO-*d*₆) δ: 8.33 (s, 1H, H-8), 8.23 (s, 1H, H-2), 7.87 [s (br), 1H, NH], 7.29–7.16 (m, 5H, H_{arom.}), 5.88 (d, *J* = 6.1 Hz, 1H, H-1'), 5.40 (d, *J* = 6.2 Hz, 1H, OH-2'), 5.36 (dd, *J* = 7.2, 4.5 Hz, 1H, OH-5'), 5.14 (d, *J* = 4.6 Hz, 1H, OH-3'), 4.61 (dd, *J* = 6.2, 4.9 Hz, 1H, H-2'), 4.15 (dd, *J* = 4.8, 3.0 Hz, 1H, H-3'), 3.96 (dd, *J* = 3.5 Hz, 1H, H-4'), 3.71 [s (br), 2H, N-CH₂], 3.69–3.65 (m, 1H, H-5'a), 3.57–3.53 (m, 1H, H-5'b), 2.92 (t, *J* = 9.0 Hz, 2H, CH₂-Ph). ¹³C-NMR (125 MHz, DMSO-*d*₆) δ: 154.7 (C-6, C_{quat.}), 152.5 (C-2, CH), 148.5 (C-4, C_{quat.}), 139.9 (C-8, CH), 139.6 (C_{arom.}, C_{quat.}), 128.8 (2 x C_{arom.}, CH), 128.4 (2 x C_{arom.}, CH), 126.2 (C_{arom.}, CH), 119.9 (C-5, C_{quat.}),

88.1 (C-1', CH), 86.0 (C-4', CH), 73.6 (C-2', CH), 70.8 (C-3', CH), 61.8 (C-5', CH₂), 41.4 (N-CH₂), 35.1 (CH₂-Ph). LC-ESI-MS (m/z): positive mode 372 [M+H]⁺. Purity determined by HPLC-UV (254 nm)-ESI-MS: 96%. mp: 183–185°C. (Lit. 166–168°C) (Shimazaki et al., 1987).

Synthesis of (2R,3R,4S,5R)-2-(6-amino-8-(butylthio)-9H-purin-9-yl)-5-(hydroxymethyl)tetrahydrofuran-3,4-diol (12)

To a solution of 8-bromoadenosine (10, 0.5 g, 1.44 mmol, 1.0 eq) in absolute ethanol, thiourea (0.2 g, 2.63 mmol, 1.8 eq) was added. After 7 h of refluxing the solution was allowed to cool down and the resulting precipitate was filtered off. The remaining filtrate was evaporated yielding a yellow oil that was resuspended in a mixture of H₂O/EtOH 1:1. The solution was adjusted to basic pH with 2 M NaOH. Butyl iodide (0.5 mL, 4.32 mmol, 3.0 eq) was added and the reaction was stirred at rt for 2 h. After extraction with ethylacetate (3 x 100 ml), the organic phase was evaporated. Purification by column chromatography (8% MeOH in DCM) afforded the product as a white solid (0.39 g, 76%). ¹H-NMR (500 MHz, DMSO-*d*₆) δ 8.04 (s, 1H, NCH=N) 7.23 (s, 2H, NH₂) 5.77 (d, 1H, *J* = 7.21 Hz, CHN) 5.59 (dd, 1H, *J* = 3.47, 8.81 Hz, CHOH) 5.36 (d, 1H, *J* = 6.14 Hz, CHOH) 5.14 (d, 1H, *J* = 4.54 Hz, CH₂OH) 4.98 (dd, 1H, *J* = 6.14, 11.88 Hz, CHCH₂) 4.16 (m, 1H, CHOH) 3.96 (m, 1H, CHOH) 3.68–3.50 (d m, 2H, CHCH₂) 3.32–3.27 (d m, 2H overlapping with H₂O peak, SCH₂) 1.68 (m, 2H, CH₂) 1.41 (m, 2H, CH₂) 0.90 (t, 3H, *J* = 7.27 Hz, CH₂CH₃). ¹³C-NMR (126 MHz, DMSO-*d*₆) δ 184.05, 154.67, 151.39, 150.56, 148.83, 119.74, 89.01, 86.72, 71.40, 71.12, 62.36, 32.22, 31.03, 21.32, 13.56. LC/ESI-MS (m/z): positive mode 356.2 [M+H]⁺. Purity determined by HPLC-UV (254 nm)-ESI-MS: 99.0%. mp: 105°C (lit. 171.5°C) (Halbfinger et al., 1999).

Synthesis of (2R,3S,4R,5R)-2-(Hydroxymethyl)-5-(6-(methylamino)-9H-purin-9-yl)tetrahydrofuran-3,4-diol (13)

To 6-chloro-9-(β-D-ribofuranosyl)purine (1, 2.0 g, 7.0 mmol) in absolute ethanol (40 ml), 33 wt % methylamine in absolute ethanol (0.9 ml, 21 mmol, 3 eq) and Et₃N (2 ml, 14 mmol, 2 eq) were added. After 4 h of refluxing, the solvent was evaporated. Column chromatography (CH₃OH/DCM 1:9) yielded the product as a white powder (2.0 g, 100%). ¹H-NMR (500 MHz, DMSO-*d*₆) δ 8.32 (s, 1H, NCH=N) 8.21 (br s, 1H, NCH=N) 7.77 (br s, 1H, NHCH₃) 5.87 (d, 1H, *J* = 6.17 Hz, CHN) 5.40 (br s, 1H, CHOH) 5.14 (br s, 1H, CHOH) 4.59 (t, 1H, *J* = 5.33 Hz, CHOH) 4.14 (dd, 1H, *J* = 3.21, 4.75 Hz, CHOH) 3.95 (q, 1H, *J* = 3.51 Hz, CHCH₂) 3.66–3.54 (d m, 2H, CHCH₂) 3.05 (m, 3H, NHCH₃). ¹³C-NMR (125 MHz, DMSO-*d*₆) δ 156.52, 152.46, 148.22, 139.74, 119.98, 88.05, 86.02, 73.65, 70.77, 61.79, 24.44. LC/ESI-MS (m/z): positive mode 282.3 [M+H]⁺. Purity determined by HPLC-UV (254 nm)-ESI-MS: 99.3%. mp: 132°C (lit. 130–132°C) (Čechová et al., 2011).

General Procedure for the Synthesis of 14–16

To a solution of N⁶-substituted adenosine (2, 3, or 13, 1.0 eq) in 0.1 M sodium acetate buffer pH 4.0 (15 ml) bromine (5.0 eq) was added. The reaction was stirred at rt overnight and monitored by TLC. The solution was decolorized by the addition of a 40% solution of NaHSO₃, and the pH of the solution was then adjusted to 7 with 4-N aq. NaOH. The precipitate was filtered off and washed with water.

(2R,3R,4S,5R)-2-(8-Bromo-6-(methylamino)-9H-purin-9-yl)-5-(hydroxymethyl)tetrahydrofuran-3,4-diol (14)

The compound was synthesized starting from 13 (1.96 g, 7.0 mmol, 1.0 eq) and afforded a white solid (0.60 g, 25%). ¹H-NMR (500 MHz, DMSO-*d*₆) δ 8.20 (s, 1H, NCH=N) 8.02 (s, 1H, NH) 5.84 (d, 1H, *J* = 7.08 Hz, CHN) 5.45 (q, 1H, *J* = 4.07 Hz, CHOH) 5.41 (d, 1H, *J* = 6.77 Hz, CHOH) 5.19 (d, 1H, *J* = 4.60 Hz, CH₂OH) 5.07 (dd, 1H, *J* = 6.55, 11.33 Hz, CHCH₂) 4.20 (m, 1H, CHOH) 3.97 (dd, 1H, *J* = 4.07, 5.66 Hz, CHOH) 3.69–3.49 (d m, 2H, CHCH₂) 2.94 (s, 3H, NHCH₃). ¹³C-NMR (125 MHz, DMSO-*d*₆) δ 154.12, 152.58, 149.04, 126.87, 120.40, 90.57, 86.84, 71.34, 70.99, 62.24, 27.10. LC/ESI-MS (*m/z*): positive mode 346.1 [M+H]⁺. Purity determined by HPLC-UV (254 nm)-ESI-MS: 95.6%. mp: 228°C.

(2R,3R,4S,5R)-2-(8-Bromo-6-(dimethylamino)-9H-purin-9-yl)-5-(hydroxymethyl)tetrahydrofuran-3,4-diol (15)

The compound was synthesized starting from 3 (2.0 g, 7.0 mmol, 1.0 eq) and afforded a white solid (0.60 g, 21%). ¹H-NMR (500 MHz, DMSO-*d*₆) δ 8.18 (s, 1H, NCH=N) 5.84 (d, 1H, *J* = 6.47 Hz, CHN) 5.41 (overlapping q and d, 2H, 2x CHOH) 5.19 (d, 1H, *J* = 4.68 Hz, CH₂OH) 5.08 (dd, 1H, *J* = 6.48, 11.80 Hz, CHCH₂) 4.21 (m, 1H, CHOH) 3.97 (m, 1H, CHOH) 3.70–3.49 (d m, 2H, CHCH₂) 3.41 [br s, 6H, N(CH₃)₂]. ¹³C-NMR (125 MHz, DMSO-*d*₆) δ 153.29, 151.72, 150.88, 126.06, 120.37, 90.68, 86.80, 71.12, 70.96, 62.25, 56.16, 18.68. LC/ESI-MS (*m/z*): positive mode 374.2 [M+H]⁺. Purity determined by HPLC-UV (254 nm)-ESI-MS: 96.6%. mp: 152°C.

(2R,3R,4S,5R)-2-(8-Bromo-6-(diethylamino)-9H-purin-9-yl)-5-(hydroxymethyl)tetrahydrofuran-3,4-diol (16)

The compound was synthesized starting from 2 (1.919 g, 5.9 mmol, 1.0 eq) and afforded a white solid (0.52 g, 23%). ¹H-NMR (500 MHz, DMSO-*d*₆) δ 8.17 (s, 1H, N=CHN) 5.84 (d, 1H, *J* = 6.75 Hz, CHN) 5.45 (dd, 1H, *J* = 3.87, 8.57 Hz, CHOH) 5.42 (d, 1H, *J* = 5.89 Hz, CHOH) 5.20 (d, 1H, *J* = 4.40 Hz, CH₂OH) 5.09 (q, 1H, *J* = 5.92 Hz, CHCH₂) 4.19 (td, 1H, *J* = 2.45, 4.76 Hz, CHOH) 3.97 (td, 1H, *J* = 2.97, 4.04 Hz, CHOH) 4.19–3.7 [br s, 4H, overlapping with previous peaks N(CH₂CH₃)₂] 3.67–3.51 (d m, 2H, CHCH₂) 1.18 [t, 6H, *J* = 6.89 Hz, N(CH₂CH₃)₂]. ¹³C-NMR (125 MHz, DMSO-*d*₆) δ 152.14, 151.88, 150.94, 126.35, 119.92, 90.70, 86.85, 71.08, 62.29, 56.19, 42.87, 18.70, 13.65. LC/ESI-MS (*m/z*): positive mode 402.0 [M+H]⁺. Purity determined by HPLC-UV (254 nm)-ESI-MS: 97.6%.

General Procedure for the Synthesis of Compounds 17–20

To the 8-bromo-*N*⁶-substituted adenosine derivatives 14–16 in absolute ethanol (15 ml) the corresponding alkylamine and Et₃N (0.1 ml, 1.6 mmol, 0.9 eq) were added. The reaction mixture was refluxed for 6–36 h followed by evaporation of the solvent.

(2R,3R,4S,5R)-2-(8-(Cyclopropylamino)-6-(methylamino)-9H-purin-9-yl)-5-(hydroxymethyl)tetrahydrofuran-3,4-diol (17)

The compound was synthesized starting from 14 (0.5 g, 1.4 mmol, 1.0 eq), using cyclopropylamine (0.3 ml, 4.2 mmol, 3.0 eq). Purification by column chromatography (CH₃OH/DCM 1:49) afforded the desired product as a yellow waxy residue

(0.18 g, 37%). ¹H-NMR (500 MHz, DMSO-*d*₆) δ 7.98 (s, 1H, N=CHN) 7.05 (d, 1H, *J* = 2.63 Hz, NHCH₃) 6.86 (q, 1H, *J* = 4.66 Hz, NHCH) 5.87 (d, 1H, *J* = 7.29 Hz, CHN) 5.82 (dd, 1H, *J* = 4.35, 6.07 Hz, NHCH) 5.15 (d, 1H, *J* = 6.68 Hz, CHOH) 5.08 (d, 1H, *J* = 4.35 Hz, CHOH) 4.58 (q, 1H, *J* = 6.98, 12.55 Hz, CH₂OH) 4.32 (t, 1H, *J* = 4.96 Hz, CHCH₂) 4.09 (m, 1H, CHOH) 3.94 (q, 1H, *J* = 2.52 Hz, CHOH) 3.61 (m, 2H, CHCH₂) 2.93 (d, 3H, *J* = 4.66 Hz, NHCH₃) 0.66 (m, 2H, CH₂) 0.45 (m, 2H, CH₂). ¹³C-NMR (125 MHz, DMSO-*d*₆) δ 152.26, 151.58, 148.87, 137.05, 117.62, 86.49, 85.75, 71.03, 70.84, 61.75, 25.01, 18.67, 6.83, 6.19. LC-MS (*m/z*): positive mode 337.1 [M+H]⁺. Purity determined by HPLC-UV (254 nm)-ESI-MS: 89.4%. mp: 219°C.

(2R,3R,4S,5R)-2-(8-(Butylamino)-6-(methylamino)-9H-purin-9-yl)-5-(hydroxymethyl)tetrahydrofuran-3,4-diol (18)

The compound was synthesized starting from 14 (0.4 g, 1.1 mmol, 1.0 eq) using *N*-butylamine (0.3 ml, 4.2 mmol, 3.0 eq). Purification by column chromatography (CH₃OH/DCM 1:9) afforded the desired product as a slightly yellow solid (0.36 g, 93%). ¹H-NMR (500 MHz, DMSO-*d*₆) δ 7.95 (s, 1H, N=CHN) 6.83 (t, 1H, *J* = 5.51 Hz, NHCH₂) 6.77 (q, 1H, *J* = 4.74 Hz, NHCH₃) 5.89 (d, 1H, *J* = 7.69 Hz, CHN) 5.84 (br s, 1H, CH₂OH) 5.19 (br s, 1H, CHOH) 5.11 (br s, 1H, CHOH) 4.62 (br s, 1H, CHCH₂) 4.11 (br s, 1H, CHOH) 3.95 (br d, 1H, *J* = 1.98 Hz, CHOH) 3.62 (br s, 2H, CHCH₂) 3.36 (m overlapping with H₂O, 2H, NHCH₂) 2.92 (d, 3H, *J* = 4.78 Hz, NHCH₃) 1.56 (m, 2H, CH₂) 1.33 (m, 2H, CH₂) 0.89 (t, 3H, *J* = 7.38 Hz, CH₂CH₃). ¹³C-NMR (125 MHz, DMSO-*d*₆) δ 152.01, 151.35, 148.86, 148.59, 117.62, 86.45, 85.78, 71.09, 70.87, 61.79, 42.17, 31.00, 29.44, 27.44, 19.78, 13.19. LC/ESI-MS (*m/z*): positive mode 353.0 [M+H]⁺. Purity determined by HPLC-UV (254 nm)-ESI-MS: 91.4%. mp: 202°C.

(2R,3R,4S,5R)-2-(8-(Butylamino)-6-(dimethylamino)-9H-purin-9-yl)-5-(hydroxymethyl)tetrahydrofuran-3,4-diol (19)

The compound was synthesized starting from 15 (0.5 g, 1.3 mmol, 1.0 eq) using butylamine (0.4 ml, 4.3 mmol, 3.2 eq). Purification by column chromatography (CH₃OH/DCM 1:24) afforded the desired product as a slightly yellow solid (0.16 g, 33%). ¹H-NMR (500 MHz, CD₃OD) δ 8.00 (s, 1H, NCH=N) 6.04 (d, 1H, *J* = 8.08 Hz, CHN) 4.76 (dd, 1H, *J* = 5.57, 7.43 Hz, CHCH₂) 4.32 (dd, 1H, *J* = 1.80, 5.60 Hz, CHOH) 4.16 (br d, 1H, *J* = 1.80 Hz, CHOH) 3.88–3.81 (m, 2H, CHCH₂) 3.47 [s, 6H, N(CH₃)₂] 2.97 (t, 2H, *J* = 7.47 Hz, NHCH₂) 1.71 (m, 2H, CH₂) 1.46 (m, 2H, CH₂) 1.02 (m, 3H, CH₃). ¹³C-NMR (125 MHz, CD₃OD) δ 152.09, 150.65, 150.06, 147.41, 118.20, 87.05, 86.16, 71.42, 71.36, 61.69, 42.00, 37.40, 31.16, 19.78, 12.79. LC-MS (*m/z*): positive mode 235.2, 366.9 [M+H]⁺. Purity determined by HPLC-UV (254 nm)-ESI-MS: 85.9%. mp: 119°C.

(2R,3R,4S,5R)-2-(6-(Diethylamino)-8-(methylamino)-9H-purin-9-yl)-5-(hydroxymethyl)tetrahydrofuran-3,4-diol (20)

The compound was synthesized starting from 16 (0.52 g, 1.30 mmol, 1.0 eq) using methylamine (8 M, 33% (w/w) in ethanol, 0.06 ml, 1.31 mmol, 1.0 eq). Purification by column chromatography (CH₃OH/DCM 2:23) afforded the desired product as a white powder (0.30 g, 67%). ¹H-NMR (500 MHz,

DMSO- d_6) δ 7.94 (d, 1H, J = 0.97 Hz, N=CHN) 6.81 (q, 1H, J = 4.38 Hz, NHCH₃) 5.87 (d, 1H, J = 7.23 Hz, CHN) 5.85 (m, 1H, CH₂OH) 5.17 (d, 1H, J = 6.63 Hz, CHOH) 5.05 (m, 1H, CHOH) 4.65 (q, 1H, J = 6.71 Hz, CHCH₂) 4.11 (br s, 1H, CHOH) 3.95 (d, 1H, J = 1.96 Hz, CHOH) 3.87 [q, 4H, J = 6.09 Hz, N(CH₂)₂] 3.62 (m, 2H, CHCH₂) 3.08 (q, 3H, J = 7.26 Hz, NCH₃) 1.16 [m, 6H, N(CH₂CH₃)₂]. ¹³C-NMR (125 MHz, DMSO- d_6) δ 151.00, 150.62, 150.51, 148.30, 117.27, 86.55, 85.77, 71.08, 70.81, 61.78, 45.90, 42.07, 28.98, 14.04, 8.74. LC/ESI-MS (m/z): positive mode 352.9 [M+H]⁺. Purity determined by HPLC-UV (254 nm)-ESI-MS: 98%. mp: 115°C.

Synthesis of (2R,3R,4S,5R)-2-(8-(Butylthio)-6-(methylamino)-9H-purin-9-yl)-5-(hydroxymethyl)tetrahydrofuran-3,4-diol (21)

To a solution of 14 (0.5 g, 1.4 mmol, 1.0 eq) in absolute ethanol, thiourea (0.2 g, 2.49 mmol, 1.8 eq) was added. After 7 h of refluxing the solution was evaporated yielding a yellow oil that was resuspended in a mixture of H₂O/EtOH 1:1. The solution was brought to basic pH with 2 M NaOH. 1-Iodobutane (0.5 ml, 4.32 mmol, 3.0 eq) was added and the reaction was stirred at rt for 5 h. After extraction with ethyl acetate (3 x 100 ml), the organic phase was evaporated. Purification by column chromatography (CH₃OH/DCM 1:24) afforded a white solid. (0.21 g, 42%). ¹H-NMR (500 MHz, DMSO- d_6) δ 8.13 (br s, 1H, NCH=N) 7.63 (br s, 1H, NHCH₃) 5.77 (d, 1H, J = 6.89 Hz, CHN) 5.62 (dd, 1H, J = 3.61, 8.93 Hz, CH₂OH) 5.37 (d, 1H, J = 6.42 Hz, CHOH) 5.16 (d, 1H, J = 4.29 Hz, CHOH) 4.98 (q, 1H, J = 6.50 Hz, CHCH₂) 4.15 (m, 1H, CHOH) 3.96 (q, 1H, J = 3.70 Hz, CHOH) 3.68–3.49 (d m, 2H, CHCH₂) 3.26 (m, 2H, SCH₂) 2.96 (br s, 3H, NHCH₃) 1.67 (m, 2H, CH₂) 1.40 (m, 2H, CH₂) 0.89 (t, 3H, J = 7.38 Hz, CH₂CH₃). ¹³C-NMR (125 MHz, DMSO- d_6) δ 153.80, 151.47, 148.49, 128.29, 127.32, 89.04, 86.79, 71.54, 71.17, 62.41, 32.27, 31.11, 27.17, 21.37, 13.59. LC/ESI-MS (m/z): positive mode 370.1 [M+H]⁺. Purity determined by HPLC-UV (254 nm)-ESI-MS: 90.1%. mp: 144°C.

Synthesis of (2R,3R,4S,5R)-2-(8-(Butylthio)-6-(diethylamino)-9H-purin-9-yl)-5-(hydroxymethyl)tetrahydrofuran-3,4-diol (22)

Compound 16 (0.74 g, 1.83 mmol, 1.0 eq) was suspended in absolute ethanol (5 ml) and the solution was alkalized with 2 M NaOH. Butanethiol (0.4 ml, 3.7 mmol, 2.0 eq) was added and the reaction mixture was stirred at rt for 5 days. After evaporation, the crude product was subjected to silica gel chromatography. However, separation of starting material and product was not possible. Therefore, the mixture was purified by RP-HPLC (20–100% CH₃OH in H₂O in 15 min, 20 ml/min) yielding the desired product as a white powder (0.09 g, 12%). ¹H-NMR (500 MHz, DMSO- d_6) δ 8.10 (s, 1H, N=CHN) 5.72 (t, 1H, J = 6.89 Hz, CHN) 5.60 (dd, 1H, J = 3.43, 8.71 Hz, CH₂OH) 5.36 (d, 1H, J = 5.22 Hz, CHOH) 5.16 (m, 1H, CHOH) 4.98 (d, 1H, J = 5.24 Hz, CHCH₂) 4.15 (s, 1H, CHOH) 3.95 (m, 1H, CHOH) 4.15–3.65 [large bulb, 4H, underneath other peaks, N(CH₂)₂] 3.65–3.51 (d m, 2H, CHCH₂) 3.25 (m, 2H, SCH₂) 1.72 (m, 2H, CH₂) 1.40 (m, 2H, CH₂) 1.19 [t, 6H, J = 6.69 Hz, N(CH₂CH₃)₂] 0.89 [t, 3H, J =

7.39 Hz, S(CH₂)₃CH₃]. ¹³C-NMR (125 MHz, DMSO- d_6) δ 151.78, 151.54, 150.81, 147.96, 119.80, 88.99, 86.78, 71.31, 71.16, 62.44, 42.61, 31.88, 31.39, 21.56, 13.60 [missing: N(CH₂CH₃)₂]. LC/ESI-MS (m/z): positive mode 412.0 [M+H]⁺. Purity determined by HPLC-UV (254 nm)-ESI-MS: 98.5%. mp: 147°C.

Preparation of Triethylammonium Hydrogencarbonate (TEAC) Buffer

A 1 M solution of TEAC was prepared by adding dry ice slowly to a 1 M triethylamine solution in water for several hours until a pH of approximately 7.4–7.6 was indicated using a pH meter.

General Procedure for the Synthesis of I and 24–38

Lyophilized adenosine derivatives and proton sponge (1.5 eq) were dissolved in 5 ml of trimethyl phosphate under an argon atmosphere at room temperature. The mixture was cooled to 0°C, and phosphoryl chloride (0.1 ml, 1.3 mmol) was added dropwise. After 5 h of stirring at 0°C, tributylamine (4 eq) and 0.5 M tri-*N*-butylammonium dibromomethylenebisphosphonate solution in DMF (2.5 eq) were added to the mixture simultaneously. After 30 min, a cold 0.5 M aqueous TEAC solution (20 ml, pH 7.4–7.6) was added to the mixture and stirring was continued at room temperature for 1 h. Trimethyl phosphate was extracted with *tert*-butylmethylether (3 x 200 ml) and the aqueous solution was lyophilized. The crude nucleoside triphosphate analogs were purified by fast protein liquid chromatography (FPLC). After equilibration of the column with deionized water, the crude product was dissolved in deionized water and injected into the column. The column was first washed with 5% 0.5 M NH₄HCO₃ buffer to remove unbound components. Elution started with a solvent gradient of 5–80% 0.5 M NH₄HCO₃ buffer over 8 column volumes followed by an isocratic phase at 80% of 0.5 M NH₄HCO₃ buffer. Fractions were collected, and appropriate fractions were pooled and lyophilized several times. The monophosphate and the triphosphate analogs were each purified by preparative HPLC (0–30% acetonitrile in 50 mM NH₄HCO₃ buffer within 15 min, 20 ml/min). Fractions were collected and appropriate fractions pooled and lyophilized.

(Dibromo((((((2R,3S,4R,5R)-5-(6-(diethylamino)-9H-purin-9-yl)-3,4-dihydroxytetrahydrofuran-2-yl)methoxy)-(hydroxy)-phosphoryl)oxy)(hydroxy)phosphoryl)methyl)-phosphonic Acid (I)

The compound was synthesized starting from 2 (0.32 g, 1.0 mmol, 1.0 eq) affording a white solid (0.03 g, 4%). ¹H-NMR (500 MHz, D₂O) δ 8.43 (s, 1H, N=CHN) 8.14 (s, 1H, N=CHN) 6.11 (d, 1H, J = 5.83 Hz, CHN) 4.76 (d, 1H, J = 5.53 Hz, CHOH) 4.63 (m, 1H, CHOH) 4.40 (m, 1H, CHCH₂) 4.33 (m, 2H, CHCH₂) 3.85 [br s, 4H, N(CH₂CH₃)₂] 1.24 [t, 6H, J = 7.07 Hz, N(CH₃)₂]. ¹³C-NMR (125 MHz, D₂O) δ 156.09, 155.13, 152.30, 140.63, 121.34, 89.38, 86.70, 77.05, 73.12, 68.09, 57.61, 46.64, 15.47. ³¹P-NMR (202 MHz, D₂O) δ 7.61 (d, 1P, J = 13.94 Hz, P_γ) 0.40 (dd, 1P, J = 13.66, 29.09 Hz, P_β) -10.61 (d, 1P, J = 29.33 Hz, P_α). LC/ESI-MS (m/z): positive mode 719.9052 [M+H]⁺ (calcd.

719.9054), and negative mode 717.8904 $[M-H]^-$. Purity determined by HPLC-UV (254 nm)-ESI-MS: 97.5%. mp: 127°C.

(Dibromo((((2R,3S,4R,5R)-5-(6-(dimethylamino)-9H-purin-9-yl)-3,4-dihydroxytetrahydro-furan-2-yl)methoxy)-(hydroxy)phosphoryl)oxy)(hydroxy)phosphoryl)methyl-phosphonic Acid (24)

The compound was synthesized starting from 3 (0.29 g, 1.0 mmol, 1.0 eq) affording a white solid (0.01 g, 1%). 1H -NMR (500 MHz, D_2O) δ 8.45 (s, 1H, N=CHN) 8.17 (s, 1H, N=CHN) 6.12 (d, 1H, J = 5.92 Hz, CHN) 4.78 (m, 1H overlapping with H_2O , CHCH₂) 4.61 (dd, 1H, J = 3.60, 4.99 Hz, CHOH) 4.41 (m, 1H, CHOH) 4.31 (m, 2H, CHCH₂) 3.42 (br s, 6H, N(CH₃)₂). ^{13}C -NMR (125 MHz, D_2O) δ 156.66, 154.25, 152.05, 140.97, 121.92, 89.56, 86.89, 77.12, 73.26, 68.16, 51.04, 48.52, 41.92. ^{31}P -NMR (202 MHz, D_2O) δ 7.48 (d, 1P, J = 14.23 Hz, P _{γ}) -0.73 (dd, 1P, J = 14.24, 27.90 Hz, P _{β}) -10.65 (d, 1P, J = 28.38 Hz, P _{α}). LC/ESI-MS (m/z): positive mode 691.8745 $[M+H]^+$ (calcd. 691.8742), and negative mode 689.8587 $[M-H]^-$. Purity determined by HPLC-UV (254 nm)-ESI-MS: 99.7%. mp: 184°C.

(Dibromo((((2R,3S,4R,5R)-5-(6-(ethyl(methyl)amino)-9H-purin-9-yl)-3,4-dihydroxytetra-hydrofuran-2-yl)methoxy)-(hydroxy)phosphoryl)oxy)(hydroxy)phosphoryl)methyl-phosphonic Acid (25)

The compound was synthesized starting from 4 (0.3 g, 1.0 mmol, 1.0 eq) affording a white solid (0.08 g, 12%). 1H -NMR (500 MHz, D_2O) δ 8.41 (s, 1H, N=CHN) 8.11 (s, 1H, N=CHN) 6.10 (d, 1H, J = 5.79 Hz, CHN) 4.76 (t, 1H, J = 4.99 Hz, CHOH) 4.61 (t, 1H, J = 3.49 Hz, CHOH) 4.40 (br s, 1H, CHCH₂) 4.31 (m, 2H, CHCH₂) 3.88 (br s, 2H, NCH₂) 3.30 (br s, 3H, NCH₃) 1.20 (t, 3H, J = 7.10 Hz, NCH₂CH₃). ^{13}C -NMR (125 MHz, D_2O) δ 156.57, 155.00, 152.16, 140.60, 121.57, 89.49, 86.73, 77.08, 73.13, 68.11, 59.78, 48.81, 39.25, 14.75. ^{31}P -NMR (202 MHz, D_2O) δ 7.58 (d, 1P, J = 14.50 Hz, P _{γ}) 0.22 (q, 1P, J = 14.29, 29.14 Hz, P _{β}) -10.62 (d, 1P, J = 29.27 Hz, P _{α}). LC/ESI-MS (m/z): positive mode 705.8896 $[M+H]^+$ (calcd. 705.8898), and negative mode 703.8737 $[M-H]^-$. Purity determined by HPLC-UV (254 nm)-ESI-MS: 100%. mp: 199°C.

(Dibromo((((2R,3S,4R,5R)-3,4-dihydroxy-5-(6-(methyl(propyl)amino)-9H-purin-9-yl)tetra-hydrofuran-2-yl)-methoxy)-(hydroxy)phosphoryl)oxy)(hydroxy)phosphoryl)-methylphosphonic Acid (26)

The compound was synthesized starting from 5 (0.32 g, 1.0 mmol, 1.0 eq) affording a white solid (0.06 g, 9%). 1H -NMR (500 MHz, D_2O) δ 8.43 (s, 1H, N=CHN) 8.15 (s, 1H, N=CHN) 6.12 (d, 1H, J = 5.96 Hz, CHN) 4.77 (d, 1H, J = 5.58 Hz, CHOH) 4.63 (t, 1H, J = 4.23 Hz, CHOH) 4.41 (br s, 1H, CHCH₂) 4.36–4.24 (d m, 2H, CHCH₂) 3.90 (br s, 2H, NCH₂) 3.55 (br s, 3H, NCH₃) 1.69 (m, 2H, NCH₂CH₂) 0.89 (t, 3H, J = 7.40 Hz, CH₂CH₃). ^{13}C -NMR (125 MHz, D_2O) δ 157.07, 155.07, 152.33, 140.55, 121.69, 89.60, 86.82, 77.06, 73.22, 68.19, 58.70, 55.17, 39.98, 23.18, 12.99. ^{31}P -NMR (202 MHz, D_2O) δ 7.56 (d, 1P, J = 13.84 Hz, P _{γ}) -0.23 (dd, 1P, J = 14.43, 29.03 Hz, P _{β}) -10.62 (d, 1P, J = 28.61 Hz, P _{α}). LC/ESI-MS (m/z): positive mode 719.9050 $[M+H]^+$ (calcd. 719.9055), and negative mode 717.8896 $[M-H]^-$. Purity determined by HPLC-UV (254 nm)-ESI-MS: 95.6%. mp: 101°C.

(Dibromo((((2R,3S,4R,5R)-5-(6-(dipropylamino)-9H-purin-9-yl)-3,4-dihydroxytetrahydro-furan-2-yl)methoxy)-(hydroxy)phosphoryl)oxy)(hydroxy)phosphoryl)methyl-phosphonic Acid (27)

The compound was synthesized starting from 6 (0.35 g, 1.0 mmol, 1.0 eq) affording a white solid (0.06 g, 8%). 1H -NMR (500 MHz, D_2O) δ 8.43 (s, 1H, N=CHN) 8.15 (s, 1H, N=CHN) 6.12 (d, 1H, J = 5.88 Hz, CHN) 4.76 (d, 1H, J = 5.53 Hz, CHOH) 4.64 (m, 1H, CHOH) 4.40 (m, 1H, CHCH₂) 4.36–4.26 (d m, 2H, CHCH₂) 3.81 [br s, 4H, N(CH₂CH₂CH₃)₂] 1.68 [m, 4H, N(CH₂CH₂CH₃)₂] 0.91 [t, 6H, J = 7.40 Hz, N(CH₂CH₂CH₃)₂]. ^{13}C -NMR (125 MHz, D_2O) δ 156.76, 155.12, 152.44, 140.49, 121.54, 89.36, 86.77, 77.06, 73.10, 68.12, 53.51, 50.89, 23.47, 13.12. ^{31}P -NMR (202 MHz, D_2O) δ 7.64 (d, 1P, J = 13.87 Hz, P _{γ}) 0.78 (q, 1P, J = 13.82, 29.45 Hz, P _{β}) -10.59 (d, 1P, J = 29.59 Hz, P _{α}). LC/ESI-MS (m/z): positive mode 747.9349 $[M+H]^+$ (calcd. 747.9368), and negative mode 745.9222 $[M-H]^-$. Purity determined by HPLC-UV(254 nm)-ESI-MS: 97%. mp: 189°C.

(Dibromo((((2R,3S,4R,5R)-5-(6-(ethyl(propyl)amino)-9H-purin-9-yl)-3,4-dihydroxytetra-hydrofuran-2-yl)methoxy)-(hydroxy)phosphoryl)oxy)(hydroxy)phosphoryl)methyl-phosphonic Acid (28)

The compound was synthesized starting from 7 (0.33 g, 1.0 mmol, 1.0 eq) affording a white solid (0.05 g, 6%). 1H -NMR (500 MHz, D_2O) δ 8.42 (s, 1H, N=CHN) 8.14 (s, 1H, N=CHN) 6.10 (d, 1H, J = 5.70 Hz, CHN) 4.75 (t, 1H, J = 5.41 Hz, CHOH) 4.63 (m, 1H, CHOH) 4.39 (s, 1H, CHCH₂) 4.33 (m, 2H, CHCH₂) 3.78 (br d, 4H, J = 56.7 Hz, N(CH₂)₂) 1.68 (m, 2H, NCH₂CH₂CH₃) 1.20 (t, 3H, J = 7.05 Hz, CH₃) 0.91 (t, 3H, J = 7.39 Hz, CH₃). ^{13}C -NMR (125 MHz, D_2O) δ 156.41, 155.11, 152.37, 140.54, 121.41, 89.36, 86.32, 77.05, 73.16, 68.13, 61.65, 53.08, 47.05, 23.53, 15.39, 13.13. ^{31}P -NMR (202 MHz, D_2O) δ 7.68 (d, 1P, J = 7.68 Hz, P _{γ}) 1.10 (dd, 1P, J = 13.61, 29.77 Hz, P _{β}) -10.59 (d, 1P, J = 29.75 Hz, P _{α}). LC/ESI-MS (m/z): positive mode 734.1371 $[M+H]^+$ (calcd. 734.1373), and negative mode 731.9086 $[M-H]^-$. Purity determined by HPLC-UV (254 nm)-ESI-MS: 97.1%. mp: 128°C.

(((((2R,3S,4R,5R)-5-(6-(Benzylamino)-9H-purin-9-yl)-3,4-dihydroxytetrahydrofuran-2-yl)methoxy)-(hydroxy)phosphoryl)oxy)(hydroxy)phosphoryl)dibromomethyl-phosphonic Acid (29)

The compound was synthesized starting from 8 (0.36 g, 1.0 mmol, 1.0 eq) affording a white solid (0.001 g, recovered from NMR). 1H -NMR (600 MHz, D_2O) δ : 8.52 (s, 1H, H-8), 8.24 (s, 1H, H-2), 7.44–7.33 (m, 5H, H_{arom.}), 6.15 (d, J = 6.6 Hz, 1H, H-1'), 4.84 (s (br), 2H, N-CH₂), 4.81 (t, J = 5.4 Hz, 1H, H-2'), 4.63 (dd, J = 5.4, 3.6 Hz, 1H, H-3'), 4.42 (m, 1H, H-4'), 4.36–4.32 (m, 1H, H-5'a), 4.28 – 4.24 (m, 1H, H-5'b), (OHs and NH are not visible). ^{13}C -NMR (125 MHz, D_2O) δ : 157.5 (C-6, C_{quat.}), 155.7 (C-2, CH), 142.3 (C-8, CH), 141.3 (C-4, C_{quat.}), 131.6 (2 x C_{arom.}, CH), 130.2 (C_{arom.}, CH), 129.7 (2 x C_{arom.}, CH), 124.7 (C_{arom.}, C_{quat.}), 121.8 (C-5, C_{quat.}), 117.8 (Br-C-Br), 89.5 (C-1', CH), 87.0 (C-4', CH), 77.2 (C-2', CH), 73.3 (C-3', CH), 68.2 (C-5', CH₂), 46.8 (C_{benzyl}, CH₂). ^{31}P -NMR (243 MHz, D_2O) δ : 7.67 (d, J = 14.34 Hz, 1P, P _{γ}), -0.45 (dd, J = 14.34, 28.43 Hz, 1P, P _{β}), -10.52 (d, J = 28.43 Hz, 1P,

P_{α}). LC-ESI-MS (m/z): positive mode 753.7 [M+H]⁺. Purity determined by HPLC-UV (254 nm)-ESI-MS: 99.9%.

(Dibromo((((((2R,3S,4R,5R)-3,4-dihydroxy-5-(6-(phenethylamino)-9H-purin-9-yl)tetrahydrofuran-2-yl)methoxy)(hydroxy)phosphoryl)oxy)(hydroxy)phosphoryl)methyl)phosphonic Acid (30)

The compound was synthesized starting from **9** (0.37 g, 1.0 mmol, 1.0 eq) affording a white solid (0.018 g, 4.8%). ¹H-NMR (600 MHz, D₂O) δ 8.51 (s, 1H, C8-H), 8.22 (s, 1H, C2-H), 7.28 (s, 5H, aryl), 7.21 (s, 1H, NH), 6.09 (d, J = 5.7 Hz, 1H, C1'-H), 4.59 (t, J = 4.1 Hz, 1H, C3'-H), 4.41 (t, 1H, C4'-H), 4.35–4.28 (m, 2H, C5'-H), 3.87 (s, 2H, CH₂), 3.01 (s, 2H, CH₂), ¹³C-NMR (151 MHz, D₂O) δ 143.24 (1C, Cq-aryl), 131.95 (2C, CH-aryl), 131.41 (1C, CH-aryl), 129.48 (1C, CH-aryl), 90.06 (1C, C1'), 86.95 (1C, C2'), 77.35 (1C, C3'), 73.18 (1C, C4'), 68.08 (1C, C5'). ³¹P-NMR (243 MHz, D₂O) δ 7.59 (d, J = 14.7 Hz, P_γ), -0.60 (dd, J = 28.7, 14.8 Hz, P_β), -10.50 (d, J = 28.2 Hz, P_α). LC-ESI-MS (m/z): positive mode 766.9 [M+H]⁺. Purity determined by HPLC-UV (254 nm)-ESI-MS: 99.9%.

(((((((2R,3S,4R,5R)-5-(6-Amino-8-(butylthio)-9H-purin-9-yl)-3,4-dihydroxytetrahydrofuran-2-yl)methoxy)(hydroxy)phosphoryl)oxy)(hydroxy)phosphoryl)dibromomethyl)phosphonic Acid (31)

The compound was synthesized starting from **12** (0.27 g, 0.76 mmol, 1.0 eq) affording a white solid (0.014 g, 2.5%). ¹H-NMR (500 MHz, D₂O) δ 8.17 (s, 1H, N=CHN) 6.10 (d, 1H, J = 6.23 Hz, CHN) 5.19 (t, 1H, J = 6.19 Hz, CHOH) 4.61 (m, 1H, CHOH) 4.39 (dd, 1H, J = 6.34, 10.22 Hz, CHCH₂) 4.33 (m, 2H, CHCH₂) 3.29 (m, 2H, SCH₂) 1.73 (m, 2H, CH₂) 1.44 (m, 2H, CH₂) 0.90 (t, 3H, J = 7.39 Hz, CH₃). ¹³C-NMR (125 MHz, D₂O) δ 155.14, 154.91, 153.42, 152.48, 121.74, 90.88, 86.35, 79.70, 72.54, 68.28, 57.53, 35.40, 33.48, 24.09, 15.69. ³¹P-NMR (202 MHz, D₂O) δ 7.46 (d, 1P, J = 14.53 Hz, P_γ), -0.69 (dd, 1P, J = 14.69, 29.01 Hz, P_β), -10.62 (d, 1P, J = 28.16 Hz, P_α). LC/ESI-MS (m/z): positive mode 751.8752 [M+H]⁺ (calcd. 751.8775), and negative mode 749.8619 [M-H]⁻. Purity determined by HPLC-UV (254 nm)-ESI-MS: 100%. mp: 167°C.

(Dibromo((((((2R,3S,4R,5R)-5-(8-(cyclopropylamino)-6-(methylamino)-9H-purin-9-yl)-3,4-dihydroxytetrahydrofuran-2-yl)methoxy)(hydroxy)phosphoryl)oxy)(hydroxy)phosphoryl)methyl)phosphonic Acid (32)

The compound was synthesized starting from **17** (0.14 g, 0.41 mmol, 1.0 eq) affording a white solid (7.0 mg, 2%). ¹H-NMR (500 MHz, D₂O) δ 8.16 (s, 1H, N=CHN) 5.96 (d, 1H, J = 7.36 Hz, CHN) 4.63 (dd, 1H, J = 2.7, 5.7 Hz, CHCH₂) 4.41 (m, 1H, CHOH) 4.35 (br s, 1H, CHOH) 4.24 (d, 2H, J = 11.92 Hz, CHCH₂) 3.10 (s, 3H, NHCH₃) 2.76 (m, 1H, NHCH) 0.88 (m, 2H, CHCH₂) 0.8–0.72 (d m, 2H, CHCH₂). ¹³C-NMR (125 MHz, D₂O) δ 155.34, 152.79, 150.67, 150.23, 117.66, 89.45, 87.11, 73.81, 72.65, 63.36, 50.90, 30.49, 27.18, 9.67. ³¹P-NMR (202 MHz, D₂O) δ 7.51 (d, 1P, J = 14.60 Hz, P_γ), -0.84 (dd, 1P, J = 14.74, 27.48 Hz, P_β), -11.16 (d, 1P, J = 27.67 Hz, P_α). LC/ESI-MS (m/z): positive mode 732.8970 [M+H]⁺ (calcd. 732.9007), and

negative mode 730.8852 [M-H]⁻. Purity determined by HPLC-UV (254 nm)-ESI-MS: 100%. mp: 232°C.

(Dibromo((((((2R,3S,4R,5R)-5-(8-(butylamino)-6-(methylamino)-9H-purin-9-yl)-3,4-dihydroxytetrahydrofuran-2-yl)methoxy)(hydroxy)phosphoryl)oxy)(hydroxy)phosphoryl)methyl)-phosphonic Acid (33)

The compound was synthesized starting from **18** (0.32 g, 1.0 mmol, 1.0 eq) affording a white solid (0.017 g, 2.3%). ¹H-NMR (500 MHz, D₂O) δ 8.13 (s, 1H, N=CHN) 6.04 (d, 1H, J = 7.76 Hz, CHN) 4.78 (t, 1H, J = 7.82 Hz, CHOH) 4.66 (dd, 1H, J = 2.16, 5.70 Hz, CHOH) 4.45 (m, 1H, 1x CHCH₂) 4.38 (br s, 1H, CHCH₂) 4.24 (m, 1H, 1x CHCH₂) 3.50 (m, 2H, NHCH₂) 3.04 (s, 3H, NHCH₃) 1.67 (m, 2H, CH₂) 1.39 (q, 2H, J = 7.48 Hz, CH₂) 0.93 (t, 3H, J = 7.40 Hz, CH₃). ¹³C-NMR (125 MHz, D₂O) δ 154.90, 152.87, 150.47, 150.25, 118.58, 89.15, 87.28, 73.33, 72.84, 68.44, 57.70, 45.31, 33.43, 30.46, 22.31, 16.07. ³¹P-NMR (202 MHz, D₂O) δ 7.48 (d, 1P, J = 16.02 Hz, P_γ), -0.87 (dd, 1P, J = 14.47, 26.89 Hz, P_β), -11.26 (d, 1P, J = 27.48 Hz, P_α). LC/ESI-MS (m/z): positive mode 748.9324 [M+H]⁺ (calcd. 748.9320), and negative mode 746.9163 [M-H]⁻. Purity determined by HPLC-UV (254 nm)-ESI-MS: 99.0%. mp: 178°C.

(Dibromo((((((2R,3S,4R,5R)-5-(8-(butylamino)-6-(dimethylamino)-9H-purin-9-yl)-3,4-dihydroxytetrahydrofuran-2-yl)methoxy)(hydroxy)phosphoryl)oxy)(hydroxy)phosphoryl)methyl)-phosphonic Acid (34)

The compound was synthesized starting from **19** (0.1 g, 0.27 mmol, 1.0 eq) affording a white solid (6.0 mg, 1.8%). ¹H-NMR (500 MHz, D₂O) δ 8.07 (s, 1H, N=CHN) 6.06 (d, 1H, J = 7.83 Hz, CHN) 4.71 (m, 2H, NCH₂) 4.45 (m, 1H, CHOH) 4.38 (br s, 1H, CHOH) 4.24 (d, 1H, J = 11.78 Hz, CHCH₂) 3.54 (d m, 2H, CHCH₂) 3.42 (s, 6H, N(CH₃)₂) 1.68 (m, 2H, CH₂) 1.38 (m, 2H, CH₂) 0.93 (t, 3H, J = 7.40 Hz, CH₃). ¹³C-NMR (125 MHz, D₂O) δ 163.50, 154.52, 152.23, 149.19, 119.98, 89.00, 87.24, 73.35, 72.84, 68.47, 56.93, 45.12, 41.61, 33.75, 22.88, 16.03. ³¹P-NMR (202 MHz, D₂O) δ 6.15 (d, 1P, J = 14.67 Hz, P_γ), -2.22 (dd, 1P, J = 14.72, 27.57 Hz, P_β), -12.61 (d, 1P, J = 27.71 Hz, P_α). LC/ESI-MS (m/z): positive mode 762.9478 [M+H]⁺ (calcd. 762.9477), and negative mode 760.9331 [M-H]⁻. Purity determined by HPLC-UV (254 nm)-ESI-MS: 98%. mp: 193°C.

(Dibromo((((((2R,3S,4R,5R)-5-(6-(diethylamino)-8-(methylamino)-9H-purin-9-yl)-3,4-dihydroxytetrahydrofuran-2-yl)methoxy)(hydroxy)phosphoryl)oxy)(hydroxy)phosphoryl)methyl)phosphonic Acid (35)

The compound was synthesized starting from **20** (0.08 g, 0.23 mmol, 1.0 eq) affording a white solid (9.0 mg, 4%). ¹H-NMR (500 MHz, D₂O) δ 8.04 (s, 1H, N=CHN) 6.06 (d, 1H, J = 7.82 Hz, CHN) 4.72 (m, 1H, CHOH) 4.60 (dd, 1H, J = 1.99, 5.68 Hz, CHOH) 4.45 (dd, 1H, J = 6.43, 10.55 Hz, CHCH₂) 4.33 (d m, 2H, CHCH₂) 3.88 (m, 4H, N(CH₂CH₃)₂) 3.09 (s, 3H, NHCH₃) 1.24 (t, 6H, J = 7.06 Hz, N(CH₂CH₃)₂). ¹³C-NMR (125 MHz, D₂O) δ 155.08, 152.57, 151.93, 149.89, 119.72, 89.05, 87.04, 73.36, 72.91, 68.66, 57.89, 46.34, 31.89, 15.61. ³¹P-NMR (202 MHz, D₂O) δ

7.14 (s, 1P, P_γ) 0.27 (br s, 1P, P_β) -10.77 (d, 1P, J = 26.2 Hz, P_α). LC/ESI-MS (m/z): positive mode 748.9295 $[M+H]^+$ (calcd. 748.9320), and negative mode 746.9181 $[M+H]^-$. Purity determined by HPLC-UV (254 nm)-ESI-MS: 93.7%. mp: 249°C.

(Dibromo((((2R,3S,4R,5R)-5-(8-(butylthio)-6-(methylamino)-9H-purin-9-yl)-3,4-dihydroxy-tetrahydrofuran-2-yl)methoxy)(hydroxy)phosphoryl)oxy)-(hydroxy)phosphoryl)methyl)phosphonic Acid (36)

The compound was synthesized starting from 21 (0.2 g, 0.54 mmol, 1.0 eq) affording a white solid (13.0 mg, 3%). $^1\text{H-NMR}$ (500 MHz, D_2O) δ 8.19 (s, 1H, $\text{N}=\text{CHN}$) 6.11 (d, 1H, J = 6.70 Hz, CHN) 5.20 (q, 1H, J = 6.30 Hz, CHOH) 4.62 (dd, 1H, J = 4.10, 6.09 Hz, CHOH) 4.37 (m, 1H, CHCH_2) 4.32 (d m, 2H, CHCH_2) 3.26 (m, 2H, SCH_2) 3.08 (s, 3H, NCH_3) 1.71 (m, 2H, CH_2) 1.44 (m, 2H, CH_2) 0.91 (t, 3H, J = 7.40 Hz, CH_3). $^{13}\text{C-NMR}$ (125 MHz, D_2O) δ 156.01, 154.39, 153.99, 152.30, 122.21, 90.78, 86.17, 73.53, 72.52, 68.30, 50.37, 35.76, 33.60, 30.30, 24.06, 15.69. $^{31}\text{P-NMR}$ (202 MHz, D_2O) δ 7.49 (d, 1P, J = 14.51 Hz, P_γ) 0.70 (dd, 1P, J = 14.28, 27.73 Hz, P_β) -10.64 (d, 1P, J = 28.37 Hz, P_α). LC/ESI-MS (m/z): positive mode 765.8919 $[M+H]^+$ (calcd. 765.8931), and negative mode 763.8787 $[M+H]^-$. Purity determined by HPLC-UV (254 nm)-ESI-MS: 95.4%. mp: 172°C.

(Dibromo((((2R,3S,4R,5R)-5-(8-(butylthio)-6-(diethylamino)-9H-purin-9-yl)-3,4-dihydroxy-tetrahydrofuran-2-yl)methoxy)(hydroxy)phosphoryl)oxy)-(hydroxy)phosphoryl)methyl)phosphonic Acid (37)

The compound was synthesized starting from 22 (0.1 g, 0.24 mmol, 1.0 eq) affording a white solid (7.0 mg, 4%). $^1\text{H-NMR}$ (500 MHz, D_2O) δ 8.18 (s, 1H, $\text{N}=\text{CHN}$) 6.13 (d, 1H, J = 6.41 Hz, CHN) 5.16 (t, 1H, J = 6.26 Hz, CHCH_2) 4.63 (m, 1H, CHOH) 4.38 (dd, 1H, J = 4.92, 10.90 Hz, CHOH) 4.32 (m, 2H, CHCH_2) 3.92 [br s, 4H, $\text{N}(\text{CH}_2)_2$] 3.30–3.22 (d m, 2H, SCH_2) 1.72 (m, 2H, CH_2) 1.42 (m, 2H, CH_2) 1.26 (t, 6H, J = 7.03 Hz, $\text{N}(\text{CH}_2\text{CH}_3)_2$) 0.89 (t, 3H, J = 7.39 Hz, CH_3). $^{13}\text{C-NMR}$ (125 MHz, D_2O) δ 153.66, 153.37, 152.57, 151.90, 122.31, 90.78, 86.33, 73.72, 72.61, 68.29, 50.92, 47.16, 36.19, 34.10, 24.22, 15.75, 15.38. $^{31}\text{P-NMR}$ (202 MHz, D_2O) δ 7.48 (d, 1P, J = 13.83 Hz, P_γ) -0.74 (dd, 1P, J = 12.88, 25.51 Hz, P_β) -10.64 (d, 1P, J = 28.45 Hz, P_α). LC/ESI-MS (m/z): positive mode 807.9381 $[M+H]^+$ (calcd. 807.9401), and negative mode 805.9304 $[M+H]^-$. Purity determined by HPLC-UV (254 nm)-ESI-MS: 92%. mp: 190°C.

(((((2R,3S,4R,5R)-5-(6-amino-9H-purin-9-yl)-3,4-dihydroxytetrahydrofuran-2-yl)methoxy)-(hydroxy)-phosphoryl)oxy)(hydroxy)phosphoryl)dibromomethyl)-phosphonic Acid (38)

The compound was synthesized starting from 23 (0.2 g, 0.75 mmol, 1.0 eq) affording a white powder (0.12 g, 24%). $^1\text{H-NMR}$ (500 MHz, D_2O) δ 8.53 (s, 1H, $\text{N}=\text{CHN}$) 8.25 (s, 1H, $\text{N}=\text{CHN}$) 6.14 (d, 1H, J = 6.0 Hz, CHN) 4.79 (s, 1H, CHOH) 4.62 (m, 1H, CHOH) 4.41 (m, 1H, CHCH_2) 4.30 (d m, 2H, CHCH_2). $^{13}\text{C-NMR}$ (125 MHz, D_2O) δ 158.49, 155.69, 152.04, 142.81, 121.51, 89.63, 86.95, 77.21, 73.33, 68.20, 57.26. $^{31}\text{P-NMR}$ (202 MHz, D_2O) δ 7.56 (d, 1P, J = 14.45 Hz, P_γ) -0.50 (dd, 1P, J = 14.40, 28.55 Hz, P_β) -10.58 (d, 1P, J = 28.56 Hz, P_α). LC/ESI-MS (m/z):

positive mode 663.8407 $[M+H]^+$ (calcd. 663.8406), and negative mode 661.8256 $[M+H]^-$. Purity determined by HPLC-UV (254 nm)-ESI-MS: 100%. mp: degradation >250°C.

Synthesis of (((((((2R,3S,4R,5R)-5-(6-Amino-9H-purin-9-yl)-3,4-dihydroxytetrahydrofuran-2-yl)methoxy)-(hydroxy)-phosphoryl)oxy)(hydroxy)phosphoryl)dichloromethyl)-phosphonic Acid (39)

Adenosine (23, 0.2 g, 0.75 mmol, 1.0 eq) and proton sponge (0.24 g, 1.13 mmol, 1.5 eq) were dissolved in 5.0 ml of trimethyl phosphate under an argon atmosphere at room temperature. The mixture was cooled to 0°C and phosphoryl chloride (0.1 ml, 1.3 mmol, 1.7 eq) was added dropwise. After 5 h of stirring at 0°C, tributylamine (4.0 eq) and 0.5 M tri-*N*-butylammonium dichloromethylenebisphosphonate solution in DMF (2.5 eq) were added to the mixture simultaneously. After 30 min, cold 0.5 M aqueous TEAC solution (20 ml, pH 7.4–7.6) was added to the mixture and stirring was continued at room temperature for 1 h. Trimethyl phosphate was extracted with *tert*-butylmethylether (3 x 200 ml), and the aqueous solution was lyophilized. The crude nucleoside triphosphate analogs were purified by FPLC. After equilibration of the column with deionized water, the crude product was dissolved in deionized water and injected into the column. The column was first washed with 5% 0.5 M NH_4HCO_3 buffer to remove unbound components. Elution started with a solvent gradient of 5–80% of 0.5 M NH_4HCO_3 buffer over 8 column volumes followed by an isocratic phase of 80% of 0.5 M NH_4HCO_3 buffer. Fractions were collected, appropriate fractions were pooled and lyophilized several times. The nucleotide analog was further purified by preparative HPLC (0–30% acetonitrile in 50 mM NH_4HCO_3 buffer within 15 min, 20 ml/min). Fractions were collected and appropriate fractions were pooled and lyophilized yielding a white solid (0.05 g, 8%). $^1\text{H-NMR}$ (500 MHz, D_2O) δ 8.53 (s, 1H, $\text{N}=\text{CHN}$) 8.25 (s, 1H, $\text{N}=\text{CHN}$) 6.14 (d, 1H, J = 5.95 Hz, CHN) 4.78 (s, 1H, CHOH) 4.61 (m, 1H, CHOH) 4.41 (br s, 1H, CHCH_2) 4.28 (d m, 2H, CHCH_2). $^{13}\text{C-NMR}$ (125 MHz, D_2O) δ 158.54, 155.74, 152.05, 142.79, 121.52, 89.62, 86.99, 77.21, 73.26, 68.16, 37.53. $^{31}\text{P-NMR}$ (202 MHz, D_2O) δ 7.83 (d, 1P, J = 18.36 Hz, P_γ) 0.16 (dd, 1P, J = 18.58, 29.06 Hz, P_β) -10.55 (d, 1P, J = 29.64 Hz, P_α). LC/ESI-MS (m/z): positive mode 573.9446 $[M+H]^+$ (calcd. 573.9445), and negative mode 571.9304 $[M+H]^-$. Purity determined by HPLC-UV (254 nm)-ESI-MS: 98.1%. mp: 205°C.

Synthesis of (((((((2R,3S,4R,5R)-5-(6-Amino-9H-purin-9-yl)-3,4-dihydroxytetrahydrofuran-2-yl)methoxy)-(hydroxy)-phosphoryl)oxy)(hydroxy)phosphoryl)difluoromethyl)-phosphonic Acid (40)

Adenosine (23, 0.2 g, 0.75 mmol, 1.0 eq) and proton sponge (0.24 g, 1.13 mmol, 1.5 eq) were dissolved in 5.0 ml of trimethyl phosphate under an argon atmosphere at room temperature. The mixture was cooled to 0°C and phosphoryl chloride (0.1 ml, 1.3 mmol, 1.7 eq) was added dropwise. After 5 h of stirring at 0°C, tributylamine (4.0 eq) and 0.5 M tri-*N*-butylammonium difluoromethylenebisphosphonate solution in DMF (2.5 eq) were added to the mixture simultaneously. After 30 min, cold

0.5 M aqueous TEAC solution (20 ml, pH 7.4 - 7.6) was added to the mixture and stirring was continued at room temperature for one hour. Trimethyl phosphate was extracted with *tert*-butylmethylether (3 x 200 ml) and the aqueous solution was lyophilized. The crude nucleoside triphosphate analog was purified by FPLC. After equilibration of the column with deionized water, the crude product was dissolved in deionized water and injected into the column. The column was washed with 5% 0.5 M NH_4HCO_3 buffer to remove unbound components. Elution started with a solvent gradient of 5–80% of 0.5 M NH_4HCO_3 buffer over 8 column volumes followed by an isocratic phase of 80% of 0.5 M NH_4HCO_3 buffer. Fractions were collected, appropriate fractions were pooled and lyophilized several times. The product was further purified by preparative HPLC (0–30% acetonitrile in 50 mM NH_4HCO_3 buffer within 15 min, 20 ml/min). Fractions were collected and appropriate fractions pooled and lyophilized yielding a white solid (0.025 g, 6%). ^1H -NMR (500 MHz, D_2O) δ 8.52 (s, 1H, N=CHN) 8.25 (s, 1H, N=CHN) 6.14 (d, 1H, J = 6.02 Hz, CHN) 4.78 (d, 1H, J = 5.60 Hz, CHCH_2) 4.57 (m, 1H, CHOH) 4.41 (br s, 1H, CHOH) 4.25 (d m, 2H, CHCH_2). ^{13}C -NMR (125 MHz, D_2O) δ 158.39, 155.55, 152.01, 142.77, 121.48, 89.58, 86.87, 71.17, 73.24, 68.07. ^{31}P -NMR (202 MHz, D_2O) δ 3.40 (td, 1P, J = 58.87, 79.05 Hz, P_γ) -4.56 (tdd, 1P, J = 28.07, 56.21, 84.20 Hz, P_β) -10.68 (d, 1P, J = 30.49 Hz, P_α). ^{19}F -NMR (202 MHz, D_2O) δ -19.76 (t, 2F, J = 82.12 Hz). LC/ESI-MS (m/z): positive mode 542.0017 $[\text{M}+\text{H}]^+$ (calcd. 542.0049), and negative mode 539.9888 $[\text{M}+\text{H}]^-$. Purity determined by HPLC-UV (254 nm)-ESI-MS: 100%. mp: >231°C (decomposition).

Biological Assays

Chemicals and Materials

ATP, calcium chloride, magnesium chloride, 4-(2-hydroxyethyl)-piperazine-1-ethanesulfonic acid (HEPES), ammonium heptamolybdate, dimethyl sulfoxide (DMSO), malachite green, α,β -methylene-ATP (**41**), α,β -methylene-ADP (**42**), β,γ -methylene-ATP (**43**), and polyvinylalcohol were obtained from Sigma (Steinheim, Germany). Disodium hydrogenphosphate and sulfuric acid were purchased from Carl Roth (Karlsruhe, Germany). N^6 -[6-(Fluoresceinyl-5'-carboxamido)hexyl]-ATP (PSB-170621A) was obtained from Jena Bioscience (Jena, Germany). The polyacrylamide-coated capillary [30 cm (10 cm effective length) \times 50 μm (id), \times 360 μm (od)] was purchased from Chromatographie Service GmbH (Langerwehe, Germany).

Expression of the Enzymes

The cDNAs of the human enzymes NPP1, NPP3, NPP5, CD38 and CD73 (Genbank accession no. NM_006258, NM_005021, NM_021572, NM_001775, and NM_002526, respectively) were obtained from Origene (Rockville, USA). Soluble enzymes were produced as previously reported with some modifications (Lee et al., 2015; Junker et al., 2019). Briefly, the catalytic domains of the enzymes were amplified and sub-cloned into the expression vector pACGP67 A/B modified with the addition of 9 x histidine tag (His-tag) at the C-terminus (except for NPP1). The plasmids were transfected in Sf9 insect cells using CellfectinTM II Reagent (Thermo Fisher Scientific, MA, USA) and ProEasyTM baculovirus

linearized DNA (Cat.#A10S, AB Vector, LLC). Protein expression was conducted for 48 h at 27°C. The signal peptide sequence of the expression vector shuttled the proteins into the supernatant. The supernatant medium was collected, and the enzymes were purified using HisPurTM Ni²⁺-NTA spin columns according to the manufacturer's protocol. The protein concentration was determined by the method previously described by Lowry et al. (1951).

Human CD39 Preparation

Human umbilical cords were obtained under approved institutional review board protocol (Comité d'Éthique de la Recherche du CHU de Québec – Université Laval) following written consent as previously described (Sévinny et al., 1997). They were minced and homogenized with a polytron in 95 mM NaCl, 0.1 mM phenylmethylsulfonyl fluoride (PMSF), and 45 mM Tris solution, pH 7.6. The homogenates were then filtered through a cheese cloth, centrifuged for 15 min at 600 g, and the supernatants were subsequently centrifuged for 1 h at 100,000 g. The pellets were resuspended in 5 mM Tris buffer solution, pH 8.0 and 10% glycerol. All purification steps were performed at 4°C. The preparations were kept at -80°C.

Fluorescence Capillary Electrophoresis Assay for CD39

The enzyme activity assay was performed as previously described (Lee et al., 2018). For inhibition screening, three independent experiments were performed. The concentration of the fluorescent substrate PSB-017621A was 0.5 μM (K_m = 19.6 μM); the assay is highly sensitive and therefore allows the use of low substrate concentrations below the K_m value which facilitates the identification and characterization of moderately potent competitive inhibitors. Test compounds were initially investigated at a concentration of 10 μM , and 40 ng protein from human umbilical cord membrane preparations containing CD39 were added to initiate the reaction. The reaction buffer contained 10 mM HEPES, 2 mM CaCl_2 , 1 mM MgCl_2 , pH 7.4. The samples were incubated at 37°C for 4 min, and the enzymatic reaction was terminated by heating at 90°C for 5 min. The solution was then diluted 1:20 with reaction buffer to perform separation of nucleotides by capillary electrophoresis (CE) followed by laser-induced fluorescence (LIF) detection. For compounds showing $\geq 70\%$ inhibition of enzymatic activity, compared to the positive control without inhibitor, concentration-inhibition curves were generated at concentrations ranging from 0.01 to 300 μM . Three independent experiments were performed, and curves were calculated by GraphPad Prism 8 software (GraphPad software, San Diego, CA, USA).

Analysis was carried out using a P/ACE MDQ capillary electrophoresis system (Beckman Instruments, Fullerton, CA, USA). The separation was performed in a polyacrylamide-coated capillary [30 cm (10 cm effective length) \times 50 μm (id), \times 360 μm (od)]. Before each run, the capillary was rinsed with the background electrolyte [50 mM phosphate buffer (pH 6.5)] for 1 min at 30 psi. Samples were electrokinetically injected by applying a voltage of -6 kV for 30 s at the capillary outlet, and the fluorescent nucleotide derivatives were separated by voltage

application of -15 kV. Detection was performed at an excitation wavelength of 488 nm and an emission wavelength of 520 nm. Data collection and peak area analysis were performed by the P/ACE MDQ software 32 KARAT obtained from Beckman Coulter (Fullerton, CA, USA).

Malachite Green Assay for CD39 and NTPDases2, -3, and -8

The enzymatic activity assay was determined essentially as previously described (Cogan et al., 1999) with a few adaptations. The reaction buffer contained 10 mM HEPES, 2 mM CaCl₂, 1 mM MgCl₂, pH 7.4 in a final volume of 50 µl in transparent 96-well half area plates. For CD39 (NTPDase1), we made use of human umbilical cord membranes preparations which express high levels of the enzyme. For the other human NTPDase isoenzymes, we had to resort to recombinant expression. Human umbilical cord membrane preparations (250 ng) natively expressing high amounts of CD39, or the respective recombinant COS-7 cell membrane preparations expressing the appropriate NTPDase isoenzyme (ca. 100 ng of protein depending on enzyme activity) (Sévigny et al., 1997; Lecka et al., 2013) with or without inhibitor were preincubated at 37°C and gentle shaking (Eppendorf Thermomixer comfort at 500 rpm) for 5 min. The amount of enzyme preparation was adjusted to ensure 10–20% of substrate conversion. The reaction was initiated by the addition of 50 µM ATP [K_m (CD39) = 17 µM; K_m (NTPDase2) = 70 µM; K_m (NTPDase3) = 75 µM; K_m (NTPDase8) = 46 µM] (Kukulski et al., 2005). After 15 min of incubation at 37°C with gentle shaking, the reaction was stopped by adding the detection reagents (20 µl malachite green solution, 0.6 mM, and 30 µl ammonium molybdate solution, 20 mM, in sulfuric acid, 1.5 M). The released (inorganic) phosphate was quantified after 20 min of gentle shaking at 25°C by measuring the absorption of the malachite green-phosphomolybdate complex at 600 nm using a BMG PheraStar FS plate reader (BMG Labtech GmbH, Ortenberg, Germany). The corrected absorption was calculated by subtracting the absorption of the negative control samples, which were incubated with denatured enzyme (90°C, 15 min), and the inhibition was calculated as follows:

$$\% \text{ Inhibition} = \frac{(B - T)}{B} \times 100 \%$$

where B is the average corrected absorption of the positive control without inhibitor and T the corrected absorption in the presence of test compound.

Full concentration-inhibition curves were determined with inhibitor concentrations ranging from 0.1 to 300 µM in the presence of 2% DMSO. Three independent experiments were performed (n = 3) and curves were calculated by the GraphPad Prism 8 software. The K_i value was calculated using the Cheng-Prusoff equation for competitive inhibitors:

$$K_i = \frac{IC_{50}}{1 + \frac{[S]}{K_m}}$$

CD73 Assay

The assay was performed as previously described (Freundlieb et al., 2014). Briefly, it contained with 0.09 µg/ml of soluble human CD73 recombinantly expressed in Sf9 insect cells as described (Junker et al., 2019), the respective test compound, and 5.0 µM [2,8-³H]AMP (specific activity 7.4 x 10⁸ Bq/mmol, 20 mCi/mmol) as radioactive substrate in assay buffer consisting of 25 mM Tris buffer, 140 mM NaCl, 25 mM NaH₂PO₄ pH 7.4. The enzymatic reaction was performed for 25 min at 37°C in a shaking water bath. Then, 500 µl of cold precipitation buffer (100 mM LaCl₃, 100 mM sodium acetate, pH 4.0) were added to precipitate free phosphate and unconverted [2,8-³H]AMP. After 30 min on ice, filtration through GF/B glass fiber filters using a cell harvester was used to separate AMP from adenosine. After washing each reaction vial three times with 400 µl of cold (4°C) demineralized water, aliquots of the filtrate were taken, and 5 ml of scintillation cocktail (ULTIMA Gold XR9) was added. The amount of formed adenosine was quantified by liquid scintillation counting (TRICARB 2900 TR, Packard/PerkinElmer).

NPP1 Assay

Inhibition of NPP1 was determined as previously described (Lee et al., 2017b). *p*-Nitrophenyl-5'-thymidine monophosphate (*p*-Nph-5'-TMP) was used as an artificial substrate which results in the formation of the *p*-nitrophenolate anion with an absorption maximum of 400 nm. Purified soluble NPP1 [0.36 µg, expressed in Sf9 insect cells as previously described (Lee et al., 2015)] was mixed with test compound (20 µM final concentration for initial screening, 0.1–200 µM for determining concentration-dependent inhibition curves), 2% DMSO and 400 µM of *p*-Nph-5'-TMP as a substrate in a final volume of 100 µl. The mixture was incubated for 30 min at 37°C with gentle shaking, and the enzyme reaction was terminated by the addition of 20 µl of 1 M NaOH. The absorption was measured at 405 nm using a BMG PheraStar FS plate reader (BMG Labtech GmbH, Ortenberg, Germany).

NPP4 Assay

Soluble NPP4 was expressed in Sf9 insect cells as recently described in detail (Lopez et al., 2020). Diadenosine tetraphosphate (AP₄A) was employed as a substrate which is cleaved by NPP4 to ATP and AMP. The reaction product ATP was quantified by luciferin-luciferase reaction (Lopez et al., 2020). A mixture of 1.4 µg of NPP4 (soluble form expressed in insect cells and purified) (Lopez et al., 2020), 10 µM of test compound, 2 % DMSO, and 20 µM of AP₄A as a substrate were incubated for 60 min at 37°C with gentle shaking. The reaction was terminated by heating at 90°C for 5 min, and after cooling down on ice, 50 µl of D-luciferin dissolved in buffer (300 mM Tris-HCl, 15 mM MgCl₂, 100 ng D-luciferin, pH 7.8) and 50 µl of luciferase (50 ng dissolved in H₂O) were added. The firefly luciferase reacts with D-luciferin in the presence of ATP produced by NPP4. The resulting luminescence was measured between 10–14 min at 560 nm using a BMG PheraStar FS plate reader (BMG Labtech GmbH, Ortenberg, Germany).

NPP3 and NPP5 Assays

The assays were performed in analogy to published procedures (Blacher et al., 2015). The enzymatic activity of human NPP3 and NPP5 (soluble forms expressed in insect cells and purified as previously described (Lee et al., 2015; Lopez et al., 2020) was measured using 1,*N*⁶-etheno-nicotinamide adenine dinucleotide (ϵ -NAD⁺) as a substrate, which is hydrolyzed to fluorescent 1,*N*⁶-etheno-AMP (ϵ -AMP). The enzymatic reactions were performed in reaction buffer [10 mM *N*-cyclohexyl-2-aminoethanesulfonic acid (CHES), 2 mM CaCl₂, and 1 mM MgCl₂, pH 9.0 in H₂O]. Purified NPP3 (90 ng) or NPP5 (400 ng), 20 μ M of ϵ -NAD⁺ and 10 μ M of the test compound were incubated for 30 min at 37°C. The relative fluorescence at 270 nm excitation and 420 nm emission was detected by a fluorescence microplate reader (Flexstation, Medical Devices LLC, USA, Softmax Pro software to collect the data).

CD38 Assay

The assay operation was analogous to the NPP3 and NPP5 assays. The enzymatic reactions were performed in 10 mM HEPES reaction buffer (pH 7.2) using 8 ng of human CD38 (expressed in Sf9 insect cells) in analogy to a published procedure (Blacher et al., 2015).

Metabolic Stability

The experiments were performed by Pharmacelsus, Saarbrücken, Germany (<https://www.pharmacelsus.com/services/in-vitro-adme/>) using human and mouse liver microsomes (0.5 mg/mL, mixed gender, pooled). Compounds were tested at a concentration of 1 μ M. Data points represent means of two separate experiments performed in duplicates.

Molecular Modeling and Docking Studies

Recently, we reported a homology model of the human CD39 generated based on rat CD39 (PDB ID: 3ZX3, 1.70 Å) to understand the binding mode of the natural substrate ATP and the fluorescent-labeled ATP derivative, PSB-170621A (Lee et al., 2018). The generated homology model of human CD39 was used for the docking procedure using AutoDock 4.2 (Morris et al., 2009). For docking studies on human CD73 we used the recently published X-ray structure of human CD73 (PDB ID: 6S7F, 2.05 Å) co-crystallized with the inhibitor PSB-12379 (Bhattarai et al., 2019). The AutoDockTools (ADT) from Molecular Graphics Laboratory (MGL) were employed to generate the input files for both CD39 and CD73 and to analyze the docking results obtained from AutoDock 4.2 (Sanner, 1999). Prior to docking, the three-dimensional energy scoring grids for a box of 60 × 60 × 60 points with a spacing of 0.375 Å were computed. The grids were centered based on the substrate binding site of the enzyme. For each ligand, 50 independent docking calculations using the *varCPSO*-ls algorithm from PSO@Autodock implemented in AutoDock4.2 were performed and terminated after 500,000 evaluation steps (Namasivayam and Günther, 2007). The parameters of *varCPSO*-ls algorithm, the cognitive and social coefficients *c*₁ and *c*₂, were set at 6.05 with 60 individual particles as a swarm size. Default values were applied for all the other

available parameters for the grid generation and docking calculation. The top-scoring binding poses with the lowest energy and highly populated poses were visually analyzed and selected the final binding pose.

RESULTS AND DISCUSSION

Chemistry

The ATP analog ARL67156 (I), which is known as a standard inhibitor of CD39, was selected as a lead structure, and different substitutions of the adenine base and modifications of the phosphate chain were performed. The appropriate adenosine derivatives were synthesized and subsequently submitted to phosphorylation according to the Ludwig procedure (Ludwig, 1981) with small modifications.

Synthesis of Nucleosides

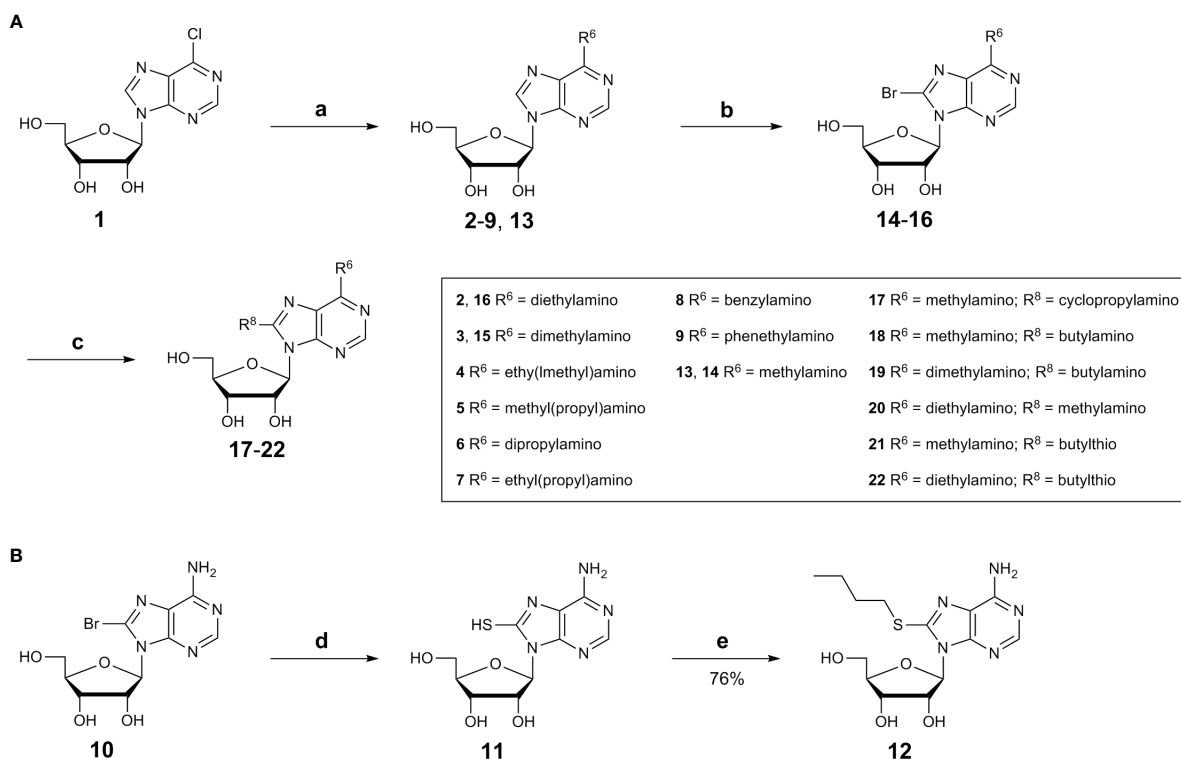
Adenosine derivatives were synthesized starting with substitutions of the *N*⁶-position. Commercially available 6-chloropurine riboside (1) was reacted with dialkylamine derivatives in the presence of a base in ethanol (**Scheme 1**) (Bhattarai et al., 2015). Purification by silica gel chromatography yielded the desired *N*⁶-disubstituted adenosine derivatives (2–9, 13).

Since 8-BuS-AMP (II), 8-BuS-ADP and 8-Bu-ATP were described as CD39 inhibitors (Lecka et al., 2013), we introduced an 8-butyl substituent to study its effect on the ATP analogs as well. For this purpose, 8-bromoadenosine (10) was reacted with thiourea in ethanol yielding the intermediate 8-thioadenosine (11), which was subsequently alkylated using 1-iodobutane in a mixture of water and ethanol (1:1) in the presence of sodium hydroxide (**Scheme 1**) (Fox et al., 1958; Kikugawa et al., 1973; El-Tayeb et al., 2009). Purification by silica gel chromatography yielded the desired adenosine derivative 12.

In order to investigate whether 8- and *N*⁶-substitution could be additive, combinations of both were synthesized. For this purpose, *N*⁶-substituted adenosine derivatives (2, 3, and 13) were prepared as described above in **Scheme 1** (Bhattarai et al., 2015). Then, the 8-position was brominated under acidic conditions (Ikehara and Uesugi, 1969; Bhattarai et al., 2015). The pH value of the reaction was maintained by adding 0.1 M sodium acetate buffer (pH 4.0). Excess bromine was subsequently removed by sodium hydrogen sulfite, and neutralization with aqueous NaOH solution followed by filtration affording the desired compounds 14–16 (**Scheme 1**). The bromine atom was subsequently substituted by an alkylamine to obtain compounds 17–22 (**Scheme 1**) (Long et al., 1967; Chattopadhyaya and Reese, 1977; Bhattarai et al., 2015).

Synthesis of Nucleotides

The adenosine derivatives were submitted to phosphorylation according to the Ludwig procedure with small modifications (Ludwig, 1981). The lyophilized nucleosides were dissolved in trimethylphosphate and reacted with phosphoryl chloride (POCl₃) in the presence of proton sponge [1,8-bis-(dimethylamino)]

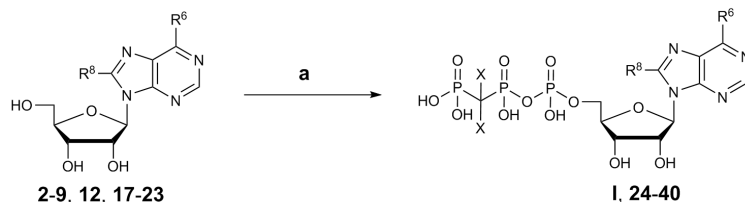


SCHEME 1 | (A) Synthesis *N*⁶,8-disubstituted adenosine derivatives (see **Table 1**), Reagents and conditions: a) dialkylamine, Et₃N, absolute EtOH, reflux, 2–48h; b) bromine, sodium acetate buffer, pH 4.0, room temperature, overnight; c) alkylamine, Et₃N, absolute EtOH, reflux, 18–48 h; **(B)** Synthesis of 8-substituted adenosine derivatives 11 and 12. Reagents and conditions: d) thiourea, EtOH, 1h, reflux; e) 1-iodobutane, H₂O/EtOH (1:1), 2 M aq.NaOH.

naphthalene] to yield the reactive 5'-dichlorophosphates as intermediates (Yoshikawa et al., 1967; El-Tayeb et al., 2009). Reaction with tris-*N*-butylammonium-dibromomethylene-bisphosphonate in anhydrous *N,N*-dimethylformamide (DMF) followed by hydrolysis with triethylammonium hydrogencarbonate (TEAC) buffer led to the desired nucleotide analogs (**Scheme 2**).

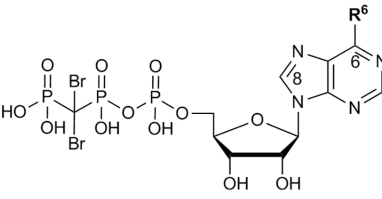
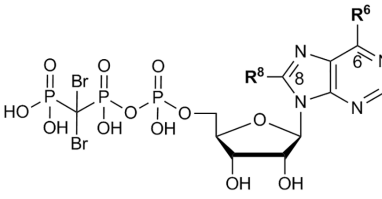
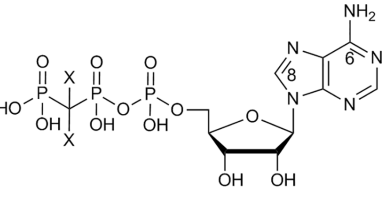
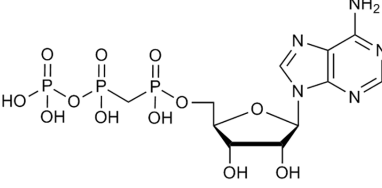
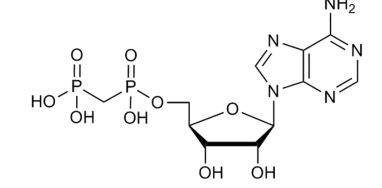
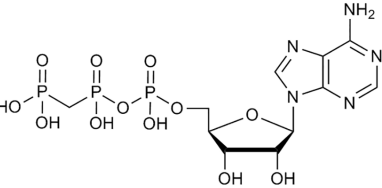
Dibromomethylenebisphosphonate was synthesized from tetraisopropyl-methylenebisphosphonate according to published

procedures (Mohamady and Jakeman, 2005; McKenna et al., 2007; Oertell et al., 2014). After completion of the phosphorylation reaction, trimethylphosphate was removed from the crude reaction mixture by extraction with *tert*-butylmethylether followed by lyophilization of the water layer. The nucleotides were purified by anion exchange chromatography on a sepharose column using a fast protein liquid chromatography (FPLC) apparatus by applying a linear gradient (5–80%,



SCHEME 2 | General synthesis of nucleotides I and 24–40 by triphosphorylation. Reagents and conditions: a) three steps: (i) trimethylphosphate, phosphoryl chloride, proton sponge [1,8-bis-(dimethylamino)naphthalene], 0–4°C, 4–5 h, argon; (ii) For 24–38: 0.5 M tris-*N*-butylammonium-dibromomethylene-bisphosphonate [Bu₃N CBr₂(PO₃H)₂] solution in anhydrous DMF, Bu₃N, 0–4°C, 5 min. For 39: 0.5 M Bu₃N-CCl₂(PO₃H)₂ solution in anhydrous DMF, Bu₃N, 0–4°C, 5 min. For 40: 0.5 M Bu₃N CF₂(PO₃H)₂ solution in anhydrous DMF, Bu₃N, 0–4°C, 5 min.; (iii) 0.5 M TEAC buffer pH 7.4–7.6, room temperature, 1 h. For R⁶ and R⁸ see (**Scheme 1**) (2–9, 12, 17–22) and **Table 1** (I, 24–40); compound 23 is adenosine R⁶, R⁸ = H).

TABLE 1 | Potency of nucleotides as inhibitors of human CD39.

 I, 24-30	 31-37	 38-40
 41	 42	 43
Compound	Structure	$K_i \pm \text{SEM}$ (μM) ^{a,b} (or % inhibition at 10 μM)
N⁶-Substituted β,γ-dibromomethylene-ATP derivatives I, 24-30		
I, ARL67156	R⁶ -N(CH ₂ CH ₃) ₂	0.973 \pm 0.239
24	-N(CH ₃) ₂	3.45 \pm 0.56 ^c
25	-N(CH ₂ CH ₃)CH ₃	40.1 \pm 7.0
26	-N((CH ₂) ₂ CH ₃)CH ₃	6.48 \pm 2.6
27	-N((CH ₂) ₂ CH ₃) ₂	4.04 \pm 2.12
28	-N((CH ₂) ₂ CH ₃)(CH ₂ CH ₃)	2.68 \pm 1.11
29	-NH-benzyl	2.22 \pm 0.02
30	-NH((CH ₂) ₂ Ph)	>> 10 (4%)
30	-NH((CH ₂) ₂ Ph)	4.82 \pm 0.21
N⁶,8-Disubstituted β,γ-dibromomethylene-ATP derivatives 31-37		
31	R⁶ -NH ₂ R⁸ S(CH ₂) ₃ CH ₃	1.13 \pm 0.23
32	-NHCH ₃ -NH-cyclopropyl	4.11 \pm 0.86 ^c
33	-NHCH ₃ -NH(CH ₂) ₃ CH ₃	5.72 \pm 0.86
34	-N(CH ₃) ₂ -NH(CH ₂) ₃ CH ₃	1.51 \pm 0.40
35	-N(CH ₂ CH ₃) ₂ -NHCH ₃	3.35 \pm 1.63 ^c
36	-NHCH ₃ -S(CH ₂) ₃ CH ₃	\approx 10 (54%)
37	-N(CH ₂ CH ₃) ₂ -S(CH ₂) ₃ CH ₃	\approx 10 (59%)
		> 10 (39%)
		7.48 \pm 1.29
		5.98 \pm 5.26 ^c
β,γ-Dihalogenomethylene-ATP analogs 38-40		
38	X -Br	5.26 \pm 0.22
39	-Cl	9.53 \pm 1.46
40	-F	10.6 \pm 0.4
		4.55 \pm 0.49 ^c
Methylene-ATP and -ADP analogs 41-43		
41 α,β -Methylene-ATP	see structure above	0.632 \pm 0.024
42 α,β -Methylene-ADP (AOPCP)	see structure above	7.20 \pm 0.64 ^c
43 β,γ -Methylene-ATP	see structure above	>> 10 (14%)
		>> 10 (23%)

^aFluorescence capillary electrophoresis assay: screening at 10 μM was performed, or concentration-inhibition curves ($n = 3$) were determined using the fluorescent substrate PSB-017621A (0.5 μM).

^b K_i values are depicted in bold.

^cMalachite green assay: concentration-inhibition curves ($n = 3$) were determined using the natural substrate ATP (50 μM).

0.5 M aqueous ammonium hydrogencarbonate buffer in water) (McCoy et al., 2014). The neutral impurities (e.g. nucleosides) eluted first, followed by charged species [mono-, di-, and finally triphosphates]. The products were further purified by HPLC

on reverse-phase C18 material to remove inorganic phosphates and buffer components to yield the desired nucleoside triphosphate analogs I and 24–40 in high purity of $\geq 92\%$ (Table 1).

For investigating structure-activity relationships regarding the triphosphate moiety, variants of the β,γ -dibromomethylene group are of interest. The naked β,γ -methylene-ATP (43), without any substituents attached to the methylene group, was commercially available. β,γ -Dibromomethylene-ATP (38) was synthesized starting from adenosine (23) according to the procedure described above. Additionally, β,γ -dichloro- and β,γ -difluorobisphosphonic acid were synthesized according to published procedures (McKenna et al., 1988; Boyle, 2006). The bisphosphonic acids were converted to the corresponding tri-*N*-butylammonium salts by dissolution of the acids in 50% aqueous ethanol and subsequent drop-wise addition of tri-*N*-butylamine until a pH of 7.8–8.0 was reached followed by evaporation and lyophilization (McKenna et al., 1988; Oertell et al., 2014). Triphosphorylation reaction with adenosine (23) and subsequent purification was carried out as described above to yield the desired ATP analogs 39 and 40 (Table 1). For reference purposes, the lead structure ARL67156 (I) was also synthesized. The structures of the obtained synthesized nucleotide analogs were confirmed by ^1H -, ^{13}C -, and ^{31}P -NMR spectroscopy, in addition to LC/ESI-MS analysis performed in both positive and negative mode. Purity was determined by high-performance liquid chromatography (HPLC)-UV (254 nm)-electrospray ionization mass spectrometry (ESI)-MS. NMR and LCMS data of selected final products are depicted in Figures S1–S5 (see Supplementary Material).

Biological Evaluation

CD39 Inhibition

Inhibition of human CD39 was determined using the previously developed fluorescence-based capillary electrophoresis method utilizing a fluorescent ATP derivative as a substrate (Lee et al., 2018). For compounds showing high inhibition (>60% at 10 μM concentration) concentration-inhibition curves were determined using the same assay. Selected compounds were additionally investigated using the malachite green assay in order to confirm the results using the natural substrate ATP (Table 1). ARL67156 had been shown to be a competitive inhibitor (Lévesque et al., 2007), and the same inhibition type can be assumed for its derivatives and analogs, which bear structural resemblance to the CD39 substrate ATP. K_i values were calculated using the Cheng-Prusoff equation (Cheng and Prusoff, 1973).

The lead structure ARL67156 displayed a K_i value of 0.973 μM in our fluorescence-based CE assay, being somewhat more potent than previously reported (Lévesque et al., 2007). In the malachite green assay versus ATP as a substrate, it showed a K_i value of 3.45 μM , which is in the same range. Replacement of one ethyl group by a methyl group at the N^6 -nitrogen atom of ARL67156 (I) reduced potency by about 7-fold (compound 25, K_i 6.48 μM), while replacement of both N^6 -ethyl groups by methyl in 24 had an even more dramatic effect (K_i 40.1 μM), 41-fold decrease compared to I. Introduction of propyl substitution was better tolerated, see 27 (N^6 -dipropyl) and 28 (N^6 -ethyl, N^6 -propyl-substituted) with K_i values of 2.68 and 2.22 μM , respectively. The N^6 -methyl, N^6 -propyl derivative 26 was also in the same range as the N^6 -methyl, N^6 -ethyl derivative 25,

indicating that the enzyme accommodates lipophilic substituents in that position. While an N^6 -benzyl residue (in 29) led to abolishment of the CD39-inhibiting activity, N^6 -phenylethyl-substitution (derivative 30) restored inhibitory activity (K_i 4.82 μM). This might be explained by the higher flexibility of the phenethyl group and its increased lipophilicity, while the benzyl group may produce clashes with the hydrophobic amino acid residues in the binding pocket.

As a next step we investigated 8-substituted analogs of ARL67156 with optional N^6 -mono- or disubstitution (compounds 31–37). These compounds were inspired by 8-butylthio-AMP (II) which had been reported as a similarly potent CD39 inhibitor as ARL67156 (Lecka et al., 2013). These nucleotides can be regarded as hybrid molecules derived from I and II, containing features of both CD39 inhibitors. In fact, 2-butylthio-substitution of N^6 -unsubstituted I was equally potent as ARL67156 (I) as confirmed in both assays, against fluorescent (K_i 1.13 μM) and natural substrate (K_i 4.11 μM) (compound 31, Table 1). However, combination with the N^6 -diethyl substitution of I led to significantly reduced potency (37, K_i 7.48 and 5.98 μM in the two employed assays), while the 8-butylthio- N^6 -monomethyl-substituted derivative 36 was even less potent (K_i > 10 μM). This indicates that both substituents, at C8 and N^6 , have interdependent effects on potency and are not simply additive.

We subsequently replaced the 8-butylthio residue by other 8-substituents connected *via* an amino rather than a thio linker (32–35). The smaller methylamino residue in the 8-position in combination with the N^6 -diethyl substitution of I led to reduced potency (compound 35, K_i \approx 10 μM). However, 8-butylamino substitution in combination with a small N^6 -monomethyl residue in 33 again led to a similarly potent CD39 inhibitor as lead structure I and N^6 -unsubstituted 8-butylthio derivative 31 (see compound 33, K_i 1.51 and 3.35 μM in the two employed assays). A cyclopropylamino residue in the 8-position was not superior but resulted in a slight reduction in potency (compare 32 and 33). Introduction of a second N^6 -methyl group into 33 reduced the potency (34, K_i \approx 10 μM).

With a further set of compounds, we investigated the replacement of the dibromo-substitution on the triphosphate-analogous linker of lead structure I. For simplification, we prepared the corresponding N^6 -unsubstituted analogs. The direct N^6 -unsubstituted analog of I, compound 38, with dibromomethylene modification of the triphosphate chain, was about 5-fold less potent than the lead compound I (K_i 5.26 μM vs. 0.973 μM). Its dichloro- (39) and difluoro-substituted (40) analogs were only about 2-fold less potent than the more lipophilic dibromo-derivative 38, while the unsubstituted β,γ -methylene-ATP (43) was virtually inactive. These results indicate that an electron-withdrawing substituent on the β,γ -methylene-ATP derivatives was required. In the CD39 substrate ATP and in the inhibitor α,β -methylene-ATP (41), which is a poor substrate of CD39, the β,γ -oxygen bridge exerts electron withdrawing effects. In fact, 41 was found to be as potent as ARL67156 (I) in blocking CD39 (K_i 0.632 μM vs. the fluorescent substrate). It was less potent in the malachite green assay, perhaps due to partial hydrolysis

during the longer incubation time in that assay (3 vs. 15 min). The structure-activity relationships of all ARL67156 (I) derivatives and analogs are represented in **Figure 3**.

Selectivity

ARL67156 was previously described as a competitive inhibitor of CD39 ($K_i = 11 \pm 3 \mu\text{M}$), NTPDase3 ($K_i = 18 \pm 4 \mu\text{M}$), and NPP1 ($K_i = 12 \pm 3 \mu\text{M}$) (Lévesque et al., 2007). In the present study, the selectivity of ARL67156 (I) and its analogs was assessed by testing lead structure I and the two most potent derivatives 31 and 33 in a large array of human ectonucleotidases, namely NTPDases1 (CD39), -2, -3, and -8, NPP1, -3, -4, and -5, CD73 (ecto-5'-nucleotidase) and CD38 (for results see **Table 2** and **Figure 4**). The experiments were performed by established procedures (Freundlieb et al., 2014; Lee et al., 2015; Blacher et al., 2015; Lopez et al., 2020). All of the compounds inhibited also NTPDase3, CD73 and NPP1, but they showed lower potency at NTPDase3 and NPP1 than at CD39. The inhibition of CD73 was equal to that of CD39, with the exception of compound 33, which inhibited CD73 with an even 8-fold higher potency compared to CD39. Compound 31 was found to also weakly inhibit NTPDase2.

The selectivity data clearly shows that the reported CD39 inhibitor ARL67156 (I), which is commercially available and broadly used in biological studies, is in fact a dual CD39/CD73 inhibitor showing ancillary inhibition of NPP1 and NTPDase3 at higher concentrations. 8-Butylthio- β,γ -bromomethylene-ATP (31) displays a similar profile with comparable potency at CD39. Both compounds could, in fact, be characterized as multi-target ectonucleotidase inhibitors. Compound 33 with an N^6 -methyl residue and 8-butylamino-substitution is even significantly more

TABLE 2 | Inhibition of selected ecto-nucleotidases by ARL67156 (I) and analogs 31 and 33^a.

Enzyme	$K_i \pm \text{SEM } (\mu\text{M})$ (or % inhibition)		
	ARL67156 (I)	31	33
CD39	0.973 \pm 0.239	1.13 \pm 0.23	1.51 \pm 0.40
NTPDase2	> 50 (18%)	22.2 \pm 0.5	78.0 \pm 0.6
NTPDase3	7.94 \pm 1.36	1.54 \pm 0.34	7.80 \pm 1.34
NTPDase8	> 50 (2%)	> 50 (2%)	> 50 (-11%)
CD73	0.451 \pm 0.121	0.831 \pm 0.274	0.185 \pm 0.074
NPP1	4.41 \pm 3.53	5.17 \pm 1.75	7.68 \pm 5.40
NPP3	> 10 (13%)	> 10 (8%)	> 10 (8%)
NPP4	> 10 (-1%)	> 10 (2%)	> 10 (4%)
NPP5	> 10 (-3%)	> 10 (2%)	> 10 (1%)
CD38	> 10 (0%)	> 10 (7%)	> 10 (6%)

^a K_i values of potent compounds are shown in bold.

potent as inhibitor of ecto-5'-nucleotidase (CD73, K_i 0.185 μM , 8-fold difference) than of CD39. All three inhibitors could serve as novel lead structures for developing dual CD39/CD73 inhibitors or triple CD39/CD73/NPP1 inhibitors which might be advantageous for the immunotherapy of cancer as compared to selective inhibitors that block only a single ectonucleotidase.

Metabolic Stability

The most potent CD39 inhibitors I, 31, and 33 were further studied for metabolic stability in human and mouse liver microsomes which are mainly responsible for drug metabolism (see **Figure S8**). Surprisingly, all three compounds appeared to be metabolically highly unstable with half-lives of less than 1 min. To ensure that degradation was caused by microsomal enzymes and not due to chemical instability, stock solutions were

Combination of C8- and N^6 -substitution

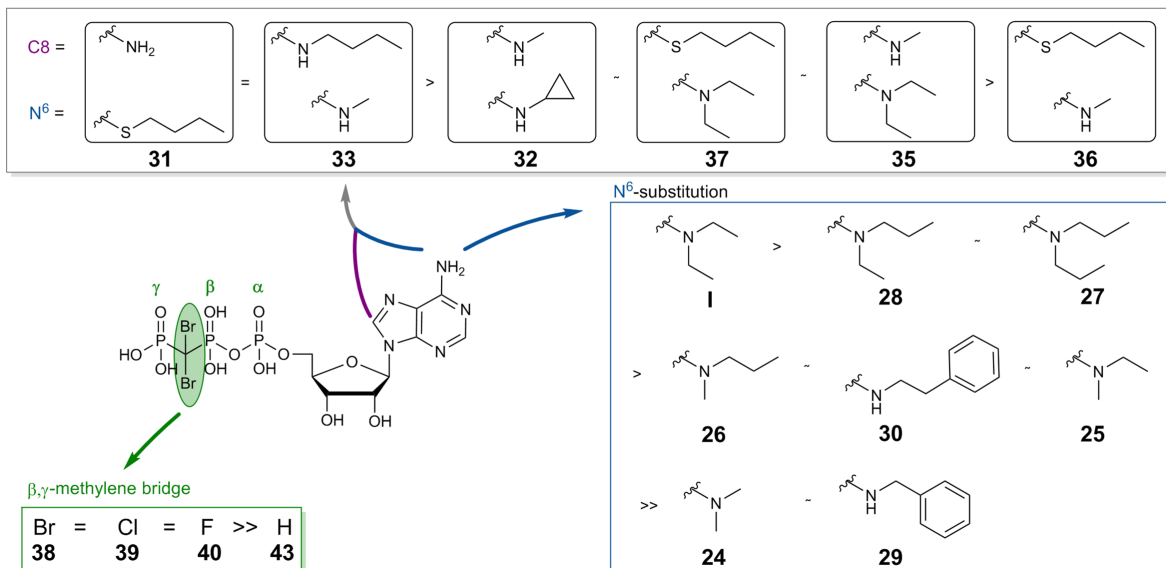


FIGURE 3 | Structure-activity relationships of ARL67156 (I) derivatives and analogs as CD39 inhibitors.

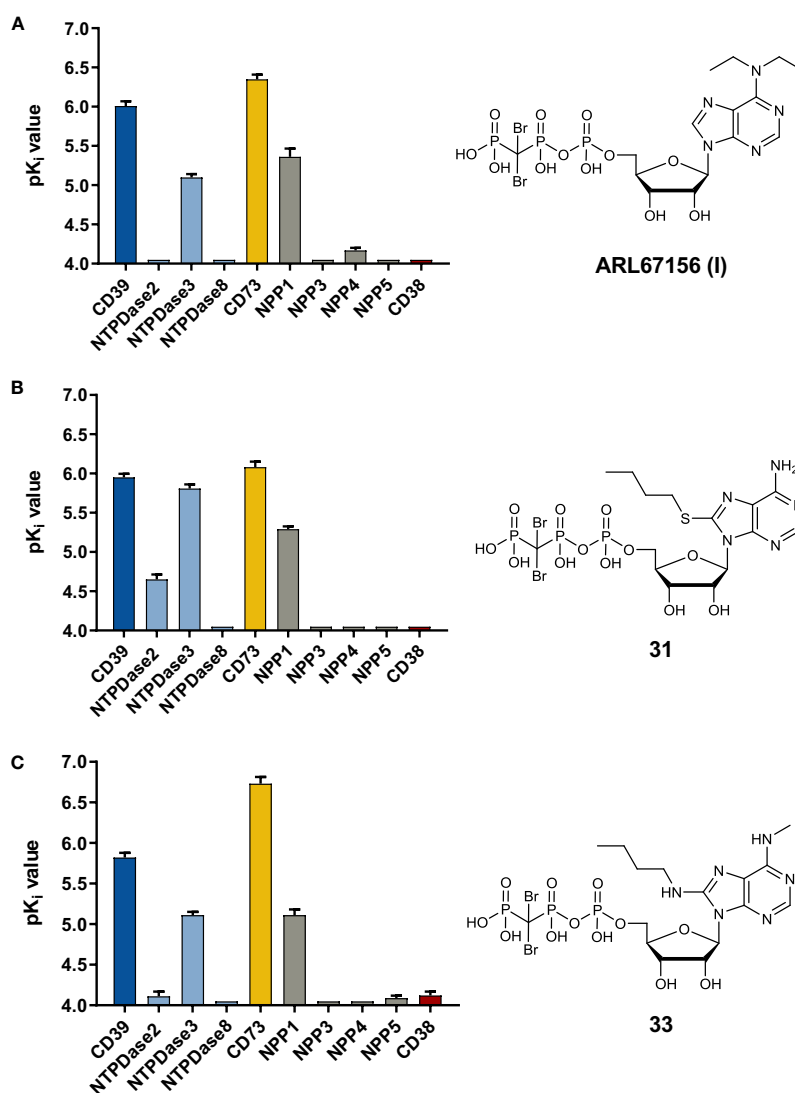


FIGURE 4 | Selectivity profile of selected CD39 inhibitors (A) Effect of ARL67156 (I), (B) compound 31 and (C) compound 33 at human ecto-nucleotidases. pK_i values for CD39, as determined in the fluorescence capillary electrophoresis assay, are compared to those at other ecto-nucleotidases. Assay procedures are described in the method section.

analyzed by LC/ESI-MS analysis, and were in all cases found to be stable. ARL67156 (I) is commonly used as a “selective” CD39 inhibitor, and the compound had been assumed to be metabolically stable in biological studies because of its β,γ -dibromomethylene bridge (Crack et al., 1995; Lévesque et al., 2007). However, the present results show that ARL67156 and its derivatives are not suitable for *in vivo* application. Nevertheless, they represent useful tool compounds for *in vitro* studies.

Molecular Modelling Studies

NTPDase1 (CD39)

Recently, we published a homology model of human CD39 based on the crystal structures of rat CD39 and human NTPDase2 (Lee

et al., 2018). In the present study, we utilized this model for docking studies to rationalize the observed SARs. As a competitive inhibitor, ARL67156 (I) binds to the catalytic site of the enzyme and is predicted to possess virtually the same orientation and similar interactions as the natural substrate ATP. The key interactions of ATP with the amino acid residues in the binding site of CD39 had previously been verified by mutagenesis studies as discussed by Lee et al. (2018).

In brief, the α -phosphate group of ATP (Figure 5A and Figure S9A) interacts with H59, the β -phosphate group with G56, S57, and S58, while T131, G216, A217, and S218 form interactions with the γ -phosphate, either directly, or mediated by water. The calcium cation forms an octahedral complex and

stabilizes the phosphate groups in the binding pocket *via* interactions with the β - and γ -phosphates. The 3'-hydroxy-group of the ribose interacts with D259, while the adenine ring is sandwiched between F365 and Y408 and stabilized by π - π -interactions.

ARL67156 (**I**, **Figure 5B**) was docked and found to have a similar orientation in the binding site of the enzyme as ATP. The key residue interactions of the phosphate groups, the hydroxy groups of the ribose and the adenine ring are identical for ATP and ARL67156. The dibromomethylene substitution prevents hydrolysis by the enzyme and additionally ensures full deprotonation of the γ -phosphate due to its electron-withdrawing properties. Unsubstituted β,γ -methylene-ATP (**43**) shows no significant inhibition, while the halogen-substituted ATP analogs **38**, **39**, and **40** inhibit the enzyme with IC_{50} values in the low micromolar range. Full deprotonation of the γ -phosphate likely favors interactions with the amino acid residues, the main chain of G216, A217, S218 and the side chain of Q220 in the binding pocket, and their interaction with the calcium ion (see **Figure S9**).

The putative binding pose of the natural substrate ATP (**Figure 5A**) shows that the amino group in the C6-position does not appear to directly interact with amino acid residues of the enzyme; it is oriented towards the surface of the enzyme. This surface of the binding pocket is lined by a large number of hydrophobic residues, F365, V366, V404, Y408, and Y412. The docked pose of **I** (ARL67156, **Figure 5B**) suggests that the diethyl substitution at N^6 possibly forms hydrophobic interactions with

these residues and stabilizes the adenine ring and the phosph(on)ate groups in the binding pocket. This was supported by comparing the biological activity of **I** ($K_i = 0.973 \mu\text{M}$) with the analogous compound with an unsubstituted amino group (**38**, $K_i = 5.26 \mu\text{M}$). However, substitution with shorter (**24**) or larger (**25–28**) alkyl chains resulted in a decrease in inhibitory potency in comparison to **I**. A phenethyl residue was tolerated (compound **30**, $K_i = 4.82 \mu\text{M}$) while a benzyl group (**29**) was not. This may be due to the lower flexibility of the benzyl compared to the phenethyl moiety, which may result in clashes with hydrophobic residues such as V404 and others in the binding sub-pocket. This shows that the surface of the binding pocket requires an optimal substitution, a diethyl group as in **I**, to form hydrophobic interactions.

The putative binding poses of **31** and **37** (**Figures 5C, D**) observed in the docking studies show that the butylthio-substitution at position 8 is oriented towards the amino acid residues H59, R85, F365, and Y408. The combination of butylthio at position 8 with an unsubstituted amino group at position 6 (**31**, $K_i = 1.13 \mu\text{M}$) gave a similarly potent inhibitor as lead structure **I** (ARL67156, $K_i = 0.973 \mu\text{M}$). The docked pose of **31** (**Figure 5C**) shows the butylthio to be flexible and positioned within the limited available space in the binding pocket. The potency was maintained with a methylamino-substitution at C6 and butylthio replaced with a butylamino residue at the 8-position. However, the potency was decreased upon N^6 -diethylamino substitution in **37**. Although the docked pose of **37** displayed only minor differences in the orientation in

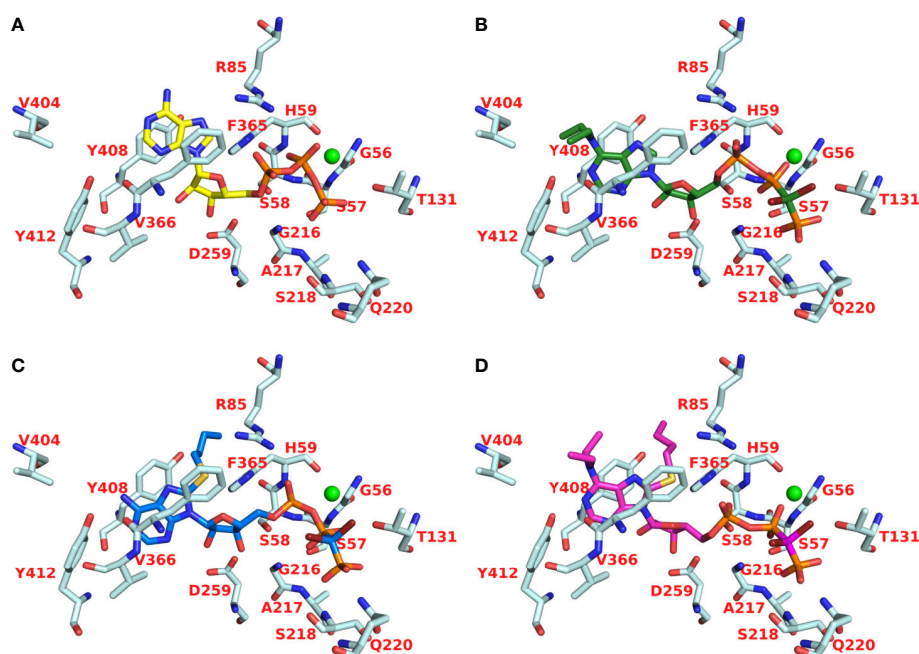


FIGURE 5 | Docked poses nucleotides in the substrate binding pocket of the human CD39 homology model. Binding poses of the natural substrate ATP (yellow) (**A**), of **I** (green) (**B**), of **31** (marine blue) (**C**), and of **37** (magenta) (**D**) are shown; the important amino acids are colored in pale cyan and shown in stick representation. The cofactor Ca^{2+} is represented as a green sphere. Oxygen atoms are colored in red and nitrogen atoms in blue.

comparison to those of I and 31 in the binding pocket, the two larger substituents might introduce significant differences in the compounds' conformations and their interaction with amino acid residues in the binding pocket (**Figure 5D**). These results were supported by compounds 34 and 35 in which both positions, N^6 and C8, were substituted with larger alkyl residues leading to significantly reduced inhibitory potency at CD39. 2D-interaction diagrams are depicted in **Figure S9** of Supplementary Material.

Ecto-5'-Nucleotidase (CD73)

Recently, a high resolution X-ray structure of human CD73 in complex with a subnanomolar inhibitor, the nucleotide analog PSB-12379, derived from the ADP analog AOPCP (or α,β -methylene-ADP) was obtained (Bhattarai et al., 2019). Compared to the human CD39 sequence which consists of 428 amino acids, human CD73 is larger consisting of 574 amino acid residues. The number of positively and negatively charged amino

acid residues in the binding pocket are similar in both CD39 and CD73 with six and five, respectively (**Figure 6**). This suggests that the potency of the nucleotide analogs depends on their orientation and interaction with these amino acid residues in the binding pocket. At human CD73, N^6 -substituted adenine nucleotide analogs show higher inhibitory potency compared to their N^6 -unsubstituted derivatives. PSB-12379 occupies the binding site of the CD73 substrate. The diphosphonate chain (PCP) is bound between the two zinc ions and form electrostatic interactions, the α -phosphonate forms hydrogen bond interactions with N245, R354, and R395, the β -phosphonate group with N117, H118, and R395, and the ribose hydroxyl groups with R354, R395, and D506. The adenine ring is stacked between F417 and F500 (**Figure 7A** and **Figure S10**).

In our selectivity studies, ARL67156 (I) and its derivatives 31 and 33 were found to be similarly or even more potent inhibitors of CD73 as compared to CD39. In order to gain insights into the binding mode of the selected compounds I, 31, and 37, we docked

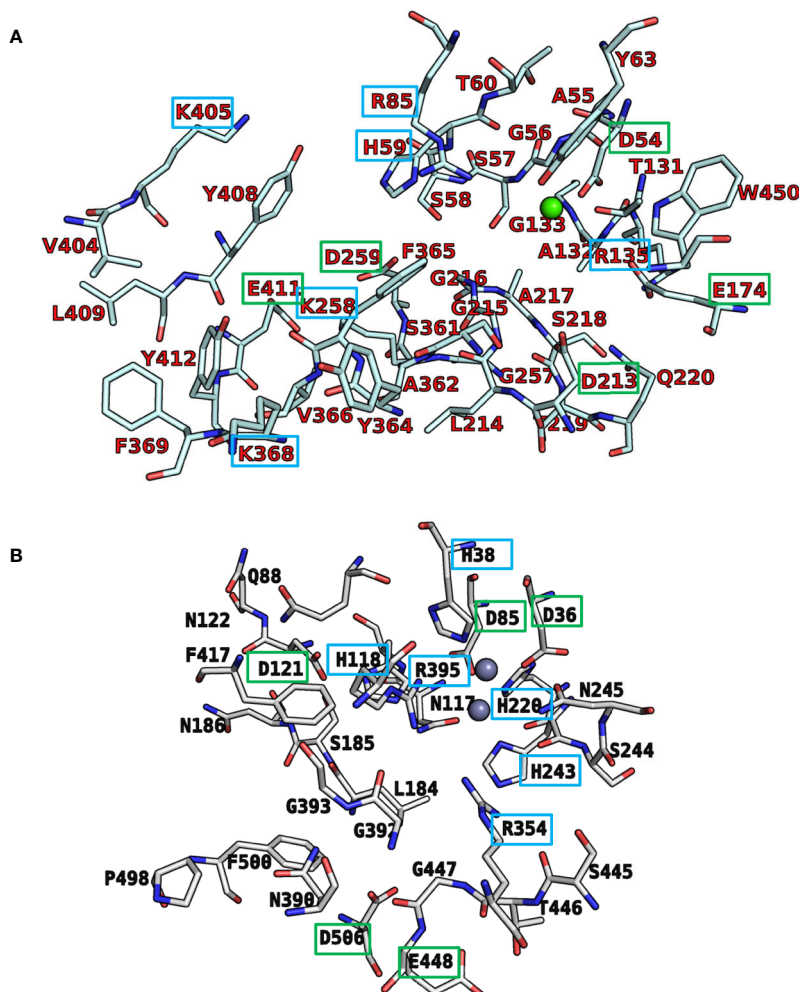


FIGURE 6 | Comparison of (A) the putative substrate binding site of human CD39 (pale cyan) and (B) the substrate binding site of human CD73 (gray). Important amino acids are shown; positively and negatively charged amino acids are highlighted by blue and green boxes, respectively. Oxygen atoms are colored in red, nitrogen atoms in blue, sulfur atoms in yellow, calcium atom in green, and zinc atoms in dark gray.

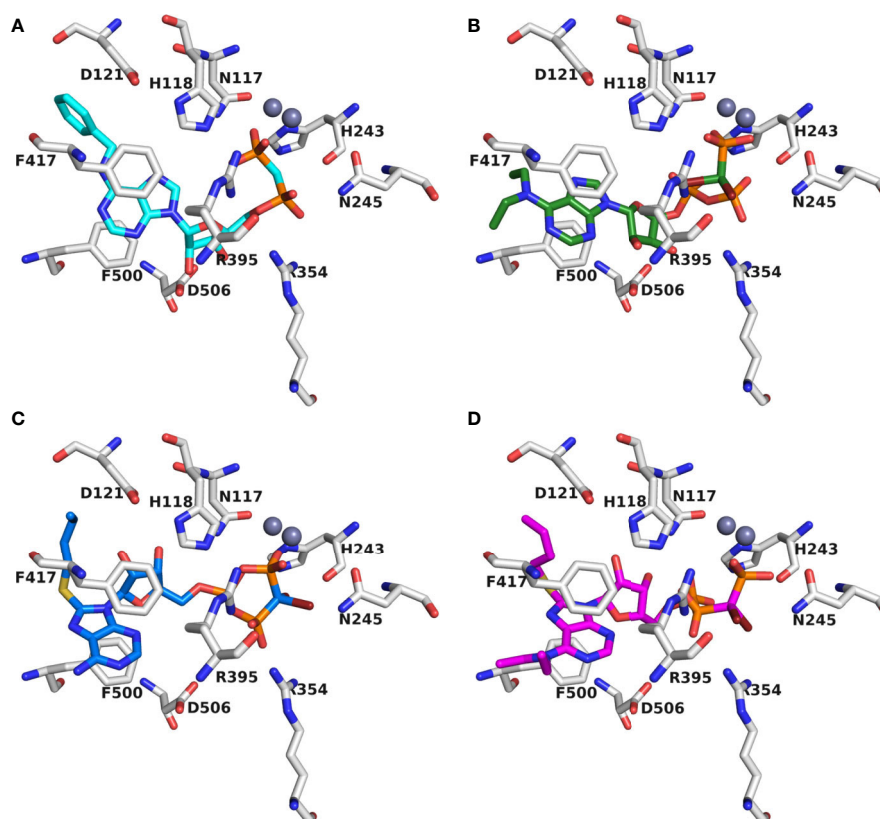


FIGURE 7 | Docked poses of ARL67156 (I) and derivatives in the substrate binding pocket of human CD73 based on an X-ray structure (PDB ID: 6s7f). **(A)** Binding pose of the co-crystallized inhibitor PSB-12379 (orange); **(B)** binding pose of I (green); **(C)** binding pose of 31 (marine blue), and **(D)** binding pose of 37 (magenta). Important amino acids are colored in orange and shown in line representation. The two zinc ions in the substrate binding site are represented as blue spheres. Oxygen atoms are colored in red and nitrogen atoms in blue.

these three inhibitors into the binding site of human CD73. The docked poses of ARL67156 and its derivatives (31 and 37) indicate that the phosphate groups are directing the compounds into the binding pocket and are likely bound between the two zinc ions. Compared to the diphosphonate PSB-12379, the β,γ -methylene triphosphate chain of ARL67156 and its derivatives was observed to be folded inside the binding pocket. In the pocket of CD73, the γ -phosphonate group likely interacts with N117, H118, and R395, the β -phosphonate group with R354 and the α -phosphate with H243 (**Figure 7B**). The hydroxyl groups of the ribose moiety interact with D506 and the adenine ring is likely sandwiched between F417 and F500. The diethylamino substitution at position 6 is extended towards the surface. Interestingly, the butylthio-substituent at position 8 of the adenine ring in compound 31 induces a conformational rotation along the nucleosidic bond shifting the adenine riboside conformation from anti to syn (**Figure 7C**). The hydroxyl groups are predicted to form an interaction with D121. The butylthio group is oriented towards the surface of the enzyme. As shown in **Figure 7D**, the rotation of the ribose is altered and shifted when a large lipophilic alkyl group is introduced as in 37 together with the butylthio group at position 8. 2D-interaction diagrams are depicted in **Figure S10** of Supplementary Material.

CONCLUSIONS

ARL67156 is so far the only commercially available “selective” inhibitor of CD39. Apart from reports describing it as a competitive inhibitor, its characterization has been limited. In the present study we synthesized ARL67156 analogs and derivatives to get insights into the structure-activity relationships of this class of CD39 inhibitors. The presence of electron-withdrawing groups adjacent to the terminal phos-ph(on)ate was found to be crucial indicating that full deprotonation is required for interactions within the orthosteric binding site. The size and polarity of substituents on the adenine ring are required to position it within the apolar substrate binding site of the enzyme. ARL67156 and two of the most potent analogs, 31 and 33, were extensively characterized. Surprisingly, all three CD39 inhibitors were found to be similarly potent or even more potent in inhibiting CD73 and can therefore be envisaged as dual- or multi-target drugs. Dual inhibition of these enzymes, both of which have been proposed as novel targets for cancer immunotherapy, might result in synergistic effects. Both enzymes are cooperating leading to the conversion of proinflammatory ATP to antiinflammatory adenosine. If both,

CD39 and CD73, are inhibited at the same time, the concentration of ATP will be increased (by CD39 inhibition), while the concentration of adenosine will be decreased (by CD73 inhibition). This is expected to result in a dramatic enhancement of immunostimulatory, anti-metastatic, and cytotoxic effects (Allard et al., 2017).

However, metabolic stability investigated in human and mouse liver microsomal preparations, was found to be extremely poor, prohibiting their use for *in vivo* studies. Nevertheless, these ectonucleotidase inhibitors should be useful as pharmacological tool compounds for simultaneous inhibition of the CD39/CD73 catalysis cascade *in vitro*. The presented results provide a solid basis for future optimization of nucleotide analogs as CD39 and dual CD39/CD73 inhibitors.

DATA AVAILABILITY STATEMENT

The raw data supporting the conclusions of this article will be made available by the authors, without undue reservation, to any qualified researcher.

AUTHOR CONTRIBUTIONS

LS and CM wrote the manuscript with contributions from all coauthors. CS synthesized most of the compounds. TV synthesized some of the compounds. LS, RI, XL, S-YL, VL, and

SM tested the compounds at ectonucleotidases. JP and JS produced the preparations of CD39 and other recombinant NTPDases. VN and LS performed the molecular modeling studies. CM designed and supervised the project.

FUNDING

Funded by the Deutsche Forschungsgemeinschaft (DFG, German Research Foundation) - Project-ID: 335447717 - SFB 1328. JS received support from the Natural Sciences and Engineering Research Council of Canada (NSERC; RGPIN-2016-05867) and was the recipient of a “Chercheur National” Scholarship from the Fonds de Recherche du Québec – Santé (FRQS).

ACKNOWLEDGMENTS

The authors thank Marion Schneider for LCMS analyses, and Sabine Terhart-Krabbe and Annette Reiner for NMR spectra.

SUPPLEMENTARY MATERIAL

The Supplementary Material for this article can be found online at: <https://www.frontiersin.org/articles/10.3389/fphar.2020.01294/full#supplementary-material>

REFERENCES

- Allard, B., Longhi, M. S., Robson, S. C., and Stagg, J. (2017). The ectonucleotidases CD39 and CD73: Novel checkpoint inhibitor targets. *Immunol. Rev.* 276, 121–144. doi: 10.1111/immr.12528
- Augusto, E., Matos, M., Sévigny, J., El-Tayeb, A., Bynoe, M. S., Müller, C. E., et al. (2013). Ecto-5'-nucleotidase (CD73)-mediated formation of adenosine is critical for the striatal adenosine A_{2A} receptor functions. *J. Neurosci.* 33, 11390–11399. doi: 10.1523/JNEUROSCI.5817-12.2013
- Baqi, Y., Weyler, S., Iqbal, J., Zimmermann, H., and Müller, C. E. (2009). Structure-activity relationships of anthraquinone derivatives derived from bromaminic acid as inhibitors of ectonucleoside triphosphate diphosphohydrolases (E-NTPDases). *Purinergic Signal.* 5, 91–106. doi: 10.1007/s11302-008-9103-5
- Bastid, J., Regairaz, A., Bonnefoy, N., Dejous, C., Giustiniani, J., Laheurte, C., et al. (2015). Inhibition of CD39 enzymatic function at the surface of tumor cells alleviates their immunosuppressive activity. *Cancer Immunol. Res.* 3, 254–265. doi: 10.1158/2326-6066.CIR-14-0018
- Bhattarai, S., Freundlieb, M., Pippel, J., Meyer, A., Abdelrahman, A., Fiene, A., et al. (2015). α,β -Methylene-ADP (AOPCP) derivatives and analogues: development of potent and selective ecto-5'-nucleotidase (CD73) inhibitors. *J. Med. Chem.* 58, 6248–6263. doi: 10.1021/acs.jmedchem.5b00802
- Bhattarai, S., Pippel, J., Meyer, A., Freundlieb, M., Schmies, C., Abdelrahman, A., et al. (2019). X-Ray co-crystal structure guides the way to subnanomolar competitive ecto-5'-nucleotidase (CD73) inhibitors for cancer immunotherapy. *Adv. Ther.* 2, 1900075. doi: 10.1002/adtp.201900075
- Blacher, E., Baruch, B. B., Levy, A., Geva, N., Green, K. D., Garneau-Tsodikova, S., et al. (2015). Inhibition of glioma progression by a newly discovered CD38 inhibitor. *Int. J. Cancer* 136, 1422–1433. doi: 10.1002/ijc.29095
- Boyle, N. A. (2006). Difluoromethylenediphosphonate: a convenient, scalable, and high-yielding synthesis. *Org. Lett.* 8, 187–189. doi: 10.1021/ol052288r
- Čechová, L., Jansa, P., Šála, M., Dračinský, M., Holý, A., and Janeba, Z. (2011). The optimized microwave-assisted decomposition of formamides and its synthetic utility in the amination reactions of purines. *Tetrahedron* 67, 866–871. doi: 10.1016/j.tet.2010.12.040
- Chattopadhyaya, J. B., and Reese, C. B. (1977). Reaction between 8-bromoadenosine and amines. Chemistry of 8-hydrazinoadenosine. *Synthesis* 10, 725–726. doi: 10.1055/s-1977-24555
- Cheng, Y. C., and Prusoff, W. H. (1973). Relation between the inhibition constant K_i and the concentration of inhibitor which causes fifty percent inhibition (IC₅₀) of an enzymatic reaction. *Biochem. Pharmacol.* 22, 3099–3108. doi: 10.1016/0006-2952(73)90196-2
- Cogan, E. B., Birrell, G. B., and Griffith, O. H. (1999). A robotics-based automated assay for inorganic and organic phosphates. *Anal. Biochem.* 271, 29–35. doi: 10.1006/abio.1999.4100
- Crack, B. E., Pollard, C. E., Beukers, M. W., Roberts, S. M., Hunt, S. F., Ingall, A. H., et al. (1995). Pharmacological and biochemical analysis of FPL 67156, a novel, selective inhibitor of ecto-ATPase. *Br. J. Pharmacol.* 114, 475–481. doi: 10.1111/j.1476-5381.1995.tb13251.x
- De Marchi, E., Orioli, E., Pegoraro, A., Sangaletti, S., Portararo, P., Curti, A., et al. (2019). The P2X7 receptor modulates immune cells infiltration, ectonucleotidases expression and extracellular ATP levels in the tumor microenvironment. *Oncogene* 38, 3636–3650. doi: 10.1038/s41388-019-0684-y
- El-Tayeb, A., Iqbal, J., Behrens, A., Romio, M., Schneider, M., Zimmermann, H., et al. (2009). Nucleoside-5'-monophosphates as prodrugs of adenosine A_{2A} receptor agonists activated by ecto-5'-nucleotidase. *J. Med. Chem.* 52, 7669–7677. doi: 10.1021/jm900538v
- Flögel, U., Burghoff, S., van Lent, P. L. E. M., Temme, S., Galbarz, L., Ding, Z., et al. (2012). Selective activation of adenosine A_{2A} receptors on immune cells by a CD73-dependent prodrug suppresses joint inflammation in experimental rheumatoid arthritis. *Sci. Transl. Med.* 4, 1–8. doi: 10.1126/scitranslmed.3003717

- Fox, J. J., Wempen, I., Hampton, A., and Doerr, I. L. (1958). Thiation of nucleosides. I. Synthesis of 2-amino-6-mercapto-9- β -D-ribofuranosylpurine ("Thioguanosine") and related purine nucleosides. *J. Am. Chem. Soc.* 80, 1669–1675. doi: 10.1021/ja01540a041
- Freundlieb, M., Zimmermann, H., and Müller, C. E. (2014). A new, sensitive ecto-5'-nucleotidase assay for compound screening. *Anal. Biochem.* 446, 53–58. doi: 10.1016/j.ab.2013.10.012
- Halbinger, E., Major, D. T., Ritzman, M., Ubl, J., Reiser, G., Boyer, J. L., et al. (1999). Molecular recognition of modified adenine nucleotides by the P2Y₁-Receptor. 1. A synthetic, biochemical, and NMR approach. *J. Med. Chem.* 42, 5325–5337. doi: 10.1021/jm990156d
- Horenstein, A. L., Morandi, F., Bracci, C., Pistoia, V., and Malavasi, F. (2019). Functional insights into nucleotide-metabolizing ectoenzymes expressed by bone marrow-resident cells in patients with multiple myeloma. *Immunol. Lett.* 205, 40–50. doi: 10.1016/j.imlet.2018.11.007
- Ikehara, M., and Uesugi, S. (1969). Studies of nucleosides and nucleotides. XXXVIII. Synthesis of 8-bromoadenosine nucleotides. *Chem. Pharm. Bull. (Tokyo)*. 17, 348–354. doi: 10.1248/cpb.17.348
- Junker, A., Renn, C., Döbelmann, C., Namasivayam, V., Jain, S., Losenkova, K., et al. (2019). Structure-activity relationship of purine and pyrimidine nucleotides as ecto-5'-nucleotidase (CD73) inhibitors. *J. Med. Chem.* 62, 3677–3695. doi: 10.1021/acs.jmedchem.9b00164
- Kanwal, M. K., Salar, U., Afzal, S., Wadood, A., Taha, M., Perveen, S., et al. (2019). Schiff bases of tryptamine as potent inhibitors of nucleoside triphosphate diphosphohydrolases (NTPDases): Structure-activity relationship. *Bioorg. Chem.* 82, 253–266. doi: 10.1016/j.bioorg.2018.10.046
- Kikugawa, K., Suehiro, H., and Ichino, M. (1973). Platelet aggregation inhibitors. VI. 2-Thioadenosine derivatives. *J. Med. Chem.* 16, 1381–1388. doi: 10.1021/jm00270a014
- Kukulski, F., Lévesque, S. A., Lavoie, É. G., Lecka, J., Bigonnesse, F., Knowles, A. F., et al. (2005). Comparative hydrolysis of P2 receptor agonists by NTPDases 1, 2, 3 and 8. *Purinergic Signal.* 1, 193–204. doi: 10.1007/s11302-005-6217-x
- Lecka, J., Gillerman, I., Fausther, M., and Sevigny, J. (2013). 8-BuS-ATP derivatives as specific NTPDase1 inhibitors. *Br. J. Pharmacol.* 169, 179–196. doi: 10.1111/bph.12135
- Lee, S. Y., Fiene, A., Li, W., Hanck, T., Brylev, K. A., Fedorov, V. E., et al. (2015). Polyoxometalates - potent and selective ecto-nucleotidase inhibitors. *Biochem. Pharmacol.* 93, 171–181. doi: 10.1016/j.bcp.2014.11.002
- Lee, S.-Y., and Müller, C. E. (2017). Nucleotide pyrophosphatase/phosphodiesterase 1 (NPP1) and its inhibitors. *MedChemComm.* 8 (5), 823–840. doi: 10.1039/c7md00015d
- Lee, S. Y., Namasivayam, V., and Müller, C. E. (2017a). The promiscuous ectonucleotidase NPP1: molecular insights into substrate binding and hydrolysis. *Biochim. Biophys. Acta* 1861, 603–614. doi: 10.1016/j.bbagen.2016.12.019
- Lee, S. Y., Sarkar, S., Bhattarai, S., Namasivayam, V., De Jonghe, S., Stephan, H., et al. (2017b). Substrate-dependence of competitive nucleotide pyrophosphatase/phosphodiesterase1 (NPP1) inhibitors. *Front. Pharmacol.* 8, 54. doi: 10.3389/fphar.2017.00054
- Lee, S.-Y., Luo, X., Namasivayam, V., Geiss, J., Mirza, S., Pelletier, J., et al. (2018). Development of a selective and highly sensitive fluorescence assay for nucleoside triphosphate diphosphohydrolase1 (NTPDase1, CD39). *Analyst* 143, 5417–5430. doi: 10.1039/C8AN01108G
- Lévesque, S. A., Lavoie, É. G., Lecka, J., Bigonnesse, F., and Sévigny, J. (2007). Specificity of the ecto-ATPase inhibitor ARL 67156 on human and mouse ectonucleotidases. *Br. J. Pharmacol.* 152, 141–150. doi: 10.1038/sj.bjp.0707361
- Li, P., Gao, Y., Cao, J., Wang, W., Chen, Y., Zhang, G., et al. (2015). CD39+ regulatory T cells attenuate allergic airway inflammation. *Clin. Exp. Allergy* 45, 1126–1137. doi: 10.1111/cea.12521
- Long, R. A., Robins, R. K., and Townsend, L. B. (1967). Purine nucleosides. XV. The synthesis of 8-amino- and 8- substituted aminopurine nucleosides. *J. Org. Chem.* 32, 2751–2756. doi: 10.1021/jo01284a024
- Lopez, V., Lee, S. Y., Stephan, H., and Müller, C. E. (2020). Recombinant expression of ecto-nucleotide pyrophosphatase/phosphodiesterase 4 (NPP4) and development of a luminescence-based assay to identify inhibitors. *Anal. Biochem.* 603, 113774. 131–3. doi: 10.1016/j.ab.2020.113774
- Ludwig, J. (1981). A new route to nucleoside 5'-triphosphates. *Acta Biochim. Biophys. Acad. Sci. Hung.* 16, 131–133.
- Mandapathil, M., Hildorfer, B., Szczepanski, M. J., Czystowska, M., Szajnik, M., Ren, J., et al. (2010). Generation and accumulation of immunosuppressive adenosine by human CD4⁺CD25^{high}FOXP3⁺ regulatory T Cells. *J. Biol. Chem.* 285, 7176–7186. doi: 10.1074/jbc.M109.047423
- McCoy, L. S., Shin, D., and Tor, Y. (2014). Isomorphous emissive GTP surrogate facilitates initiation and elongation of in vitro transcription reactions. *J. Am. Chem. Soc.* 136, 15176–15184. doi: 10.1021/ja5039227
- McKenna, C. E., Khawli, L. A., Ahmad, W.-Y., Pham, P., and Bongartz, J.-P. (1988). Synthesis of α -halogenated methanodiphosphonates. *Phosphorous Sulfur Relat. Elem.* 37, 1–12. doi: 10.1080/03086648808074346
- McKenna, C. E., Kashemirov, B., Upton, T. G., Batra, V. K., Goodman, M. F., Pedersen, L. C., et al. (2007). (R)- β , γ -Fluoromethylene-dGTP-DNA ternary complex with DNA polymerase β . *J. Med. Chem.* 129, 15412–15413. doi: 10.1021/ja072127v
- Mohamady, S., and Jakeman, D. L. (2005). An improved method for the synthesis of nucleoside triphosphate analogues. *J. Org. Chem.* 70, 10588–10591. doi: 10.1021/jo0518598
- Morris, G. M., Huey, R., Lindstrom, W., Sanner, M., Belew, R. K., Goodsell, D. S., et al. (2009). AutoDock4 and AutoDockTools4: Automated docking with selective receptor flexibility. *J. Comput. Chem.* 30, 2785–2791. doi: 10.1002/jcc
- Müller, C. E., Iqbal, J., Baqi, Y., Zimmermann, H., Röllich, A., and Stephan, H. (2006). Polyoxometalates-a new class of potent ecto-nucleoside triphosphate diphosphohydrolase (NTPDase) inhibitors. *Bioorg. Med. Chem. Lett.* 16, 5943–5947. doi: 10.1016/j.bmcl.2006.09.003
- Namasivayam, V., and Günther, R. (2007). PSO@AUTODOCK: A fast flexible molecular docking program based on swarm intelligence. *Chem. Biol. Drug Des.* 70, 475–484. doi: 10.1111/j.1747-0285.2007.00588.x
- Oertel, K., Chamberlain, B. T., Wu, Y., Ferri, E., Kashemirov, B. A., Beard, W. A., et al. (2014). Transition state in DNA polymerase β catalysis: rate-limiting chemistry altered by base-pair configuration. *Biochemistry* 53, 1842–1848. doi: 10.1021/bi500101z
- Randall, R. J., and Lewis, A. (1951). Protein measurement with the Folin phenol reagent. *J. Biol. Chem.* 193, 265–275.
- Robson, S. C., Sévigny, J., and Zimmermann, H. (2006). The E-NTPDase family of ectonucleotidases: structure function relationships and pathophysiological significance. *Purinergic Signal.* 2, 409–430. doi: 10.1007/s11302-006-9003-5
- Sanner, M. F. (1999). Python: A programming language for software integration and development. *J. Mol. Graph. Model.* 17, 57–61.
- Sévigny, J., Lévesque, F. P., Grondin, G., and Beaudoin, A. R. (1997). Purification of the blood vessel ATP diphosphohydrolase, identification and localisation by immunological techniques. *Biochim. Biophys. Acta* 1334, 73–88. doi: 10.1016/S0304-4165(96)00079-7
- Shimazaki, N., Shima, I., Hemmi, K., and Hashimoto, M. (1987). N6-(2,2-Diphenylethyl)adenosine, a novel adenosine receptor agonist with antipsychotic-like activity. *J. Med. Chem.* 30, 1709–1711. doi: 10.1021/jm00393a003
- Vitello, L., Gorini, S., Rosano, G., and La Sala, A. (2012). Immunoregulation through extracellular nucleotides. *Blood* 120, 511–518. doi: 10.1182/blood-2012-01-406496
- Yoshikawa, M., Kato, T., and Takenishi, T. (1967). A novel method for phosphorylation of nucleosides to 5'-nucleotides. *Tetrahedron Lett.* 50, 5065–5068. doi: 10.1016/S0040-4039(01)89915-9
- Zhou, J. Z., Riquelme, M. A., Gao, X., Ellies, L. G., Sun, L. Z., and Jiang, J. X. (2014). Differential impact of adenosine nucleotides released by osteocytes on breast cancer growth and bone metastasis. *Oncogene* 34, 1831–1842. doi: 10.1038/onc.2014.113
- Zimmermann, H., Zebisch, M., and Sträter, N. (2012). Cellular function and molecular structure of ecto-nucleotidases. *Purinergic Signal.* 8, 437–502. doi: 10.1007/s11302-012-9309-4

Conflict of Interest: The authors declare that the research was conducted in the absence of any commercial or financial relationships that could be construed as a potential conflict of interest.

Copyright © 2020 Schäkel, Schmies, Idris, Luo, Lee, Lopez, Mirza, Vu, Pelletier, Sévigny, Namasivayam and Müller. This is an open-access article distributed under the terms of the Creative Commons Attribution License (CC BY). The use, distribution or reproduction in other forums is permitted, provided the original author(s) and the copyright owner(s) are credited and that the original publication in this journal is cited, in accordance with accepted academic practice. No use, distribution or reproduction is permitted which does not comply with these terms.



Sodium New Houttuynia Affects Transcriptome and Virulence Factors of *Pseudomonas aeruginosa* Controlled by Quorum Sensing

Yeye Zhao^{1†}, Longfei Mei^{1†}, Yuanqing Si¹, Jiadi Wu¹, Jing Shao^{1,2}, Tianming Wang², Guiming Yan³, Changzhong Wang^{1,2} and Daqiang Wu^{1,2,3*}

¹ Department of Pathogenic Biology and Immunology, College of Integrated Chinese and Western Medicine, Anhui University of Chinese Medicine, Hefei, China, ² Key Laboratory of Chinese Herbal Compound Formula in Anhui Province, Anhui University of Chinese Medicine, Hefei, China, ³ Division of Molecular and Cell Biophysics, Hefei National Science Center for Physical Sciences, University of Science and Technology of China, Hefei, China

OPEN ACCESS

Edited by:

Jean Sévigny,
Laval University, Canada

Reviewed by:

Rodolfo García-Contreras,
National Autonomous University of
Mexico, Mexico
Jintae Lee,
Yeungnam University, South Korea

*Correspondence:

Daqiang Wu
daqwu@126.com

[†]These authors have contributed
equally to this work

Specialty section:

This article was submitted to
Experimental Pharmacology
and Drug Discovery,
a section of the journal
Frontiers in Pharmacology

Received: 14 June 2020

Accepted: 14 September 2020

Published: 02 October 2020

Citation:

Zhao Y, Mei L, Si Y, Wu J, Shao J,
Wang T, Yan G, Wang C and Wu D
(2020) Sodium New Houttuynia
Affects Transcriptome and Virulence
Factors of *Pseudomonas aeruginosa*
Controlled by Quorum Sensing.
Front. Pharmacol. 11:572375.
doi: 10.3389/fphar.2020.572375

As a major opportunistic pathogen, *Pseudomonas aeruginosa* can produce various virulence factors and form biofilms. These processes are controlled by the quorum sensing (QS) system. Sodium new houttuynia (SNH) is an adduct of houttuynia, the main component of the common Chinese medicine plant *Houttuynia cordata*, which has antibacterial and anti-inflammatory effects. We evaluated the effect of SNH on *P. aeruginosa* biofilms, virulence factors, and transcription. Transcriptome analysis showed that the key *rhII* and *pqsA* genes of the *P. aeruginosa* QS system were down-regulated after SNH treatment. SNH reduces proteases and pyocyanin production and inhibits biofilm formation by regulating the *P. aeruginosa* QS system. SNH also changes the expression of genes related to virulence factors and biofilms (*lasA*, *lasB*, *lecA*, *phzM*, *pqsA*, and *pilG*). These results suggested that the mechanism of SNH against *P. aeruginosa* by affecting the expression of biofilm and virulence factors controlled by quorum sensing.

Keywords: *Pseudomonas aeruginosa*, virulence factors, biofilm, quorum sensing, sodium new houttuynia, transcriptome

INTRODUCTION

Pseudomonas aeruginosa is a common clinical opportunistic pathogen (Denning et al., 2003; Xiaoming et al., 2012; Gurunathan et al., 2014). Patients with severe burns (Ramsey and Wozniak, 2005; Bentzmann and Patrick, 2011) or metabolic diseases are sensitive to infection when the body resistance decreases. *P. aeruginosa* infections has a high morbidity and mortality in the clinic because of its secretion of a large number of virulence factors and increasing antibiotic resistance (Breidenstein et al., 2011). Therefore, there is an urgent need to develop new drugs against *P. aeruginosa* infection.

Bacterial quorum sensing (QS) is a cellular communication mechanism that depends on the concentration of signal molecules (Ma et al., 2012; Asfahl and Schuster, 2017). There are main three QS regulation systems in *P. aeruginosa* (Kim et al., 2015), the Las, Rhl, and PQS systems (Schuster

et al., 2013; Kalia et al., 2015; Rajkumari et al., 2018), whose transcription regulators are LasR, RhlR, and PqsR respectively. The *P. aeruginosa* QS system is involved in regulating the expression of virulence factors and biofilms (Van Delden and Igleski, 1998; Williams and Camara, 2009). At an appropriate concentration, these receptor proteins bind to their respective signal molecules and induce transcription encoding different virulence products such as elastase, rhamnolipid, and pyocyanin. The LasI/Rhl system contains the synthase LasI/RhlI and the transcription activator LasR/RhlR. The Las system can synthesize and recognize N-3-oxo-C12-HSL through LasI synthetase and transcription regulator *LasR*. The second AHL system is the Rhl system, which can synthesize C4-HSL. The combination of RhlR and C4-HSL activates the expression of antibiotics, rhamnolipids, alkaline proteases, elastase, lectin LecA, cyanide, and genes produced by mass movement. Therefore, it is important to understand the relationship between antibacterial drugs and the *P. aeruginosa* QS system.

Houttuynia cordata is a traditional Chinese medicine, which is derived from Saururaceae. *H. cordata* has the functions of antibacterial, antiviral, improving immunity, diuresis and so on. And it is one of the varieties officially identified medicine and food by the Ministry of Health (Figure 1). Sodium new houttuynfonate (SNH) is a sodium bisulfite adduct of the active ingredient of the Chinese herbal medicine *H. cordata* (Shao et al., 2012) and dodecanoyl acetaldehyde. SNH has spectrum wide antibacterial activity, few adverse reactions, and improves immunity (Juanjuan, 2009; Yumei et al., 2012; Yang et al., 2016). Previously, we confirmed that sodium houttuynfonate (SH) has a certain inhibitory effect on *P. aeruginosa* (Shao et al., 2013; Wu et al., 2014; Wu et al., 2015). SNH and SH structures are highly similar, but SNH is more chemically stable than does SH (Yumei et al., 2012). Therefore, it is important to understand the inhibitory effects and mechanisms of SNH on *P. aeruginosa*. We speculate that SNH may also inhibit the activity of *P. aeruginosa* by regulating the QS system.

MATERIALS AND METHODS

Chemicals, Bacteria, and Culture Medium

SNH was purchased from Shanghai Yuanye Biological Technology Co., Ltd. (Shanghai, China), with the content $\geq 98\%$. Azithromycin (AZM) was acquired from the Northeast Pharmaceutical Group Shenyang No. 1 Pharmaceutical Co., Ltd. (Shenyang, China). *P. aeruginosa* strain ATCC 27853 was purchased from the China National Institute for the Control of Pharmaceutical and Biological Products (Beijing, China). PDP medium was acquired from Qingdao Hi-Tech Park Haibo Biotechnology Co., Ltd. (Qingdao, China). A single ATCC 27853 colony was selected from Luria-Bertani (LB) solid medium (Hangzhou, China) and cultured in 5 ml LB liquid media (Hangzhou, China) at 37°C, with shaking at 220 r/min for 24 h, then by centrifugation at 10,800 g for 1 min. The supernatant was discarded and the pellet was resuspended in sterile saline solution for optic density detection at 600 nm (OD600) in a UV spectrophotometer. The absorbance of cell suspensions was adjusted to 0.08–0.1, and diluted to 10^7 times for later use for further experiments.

Measurement of Minimum Inhibitory Concentration and Minimum Bactericidal Concentration

The minimum inhibitory concentration (MIC) (Wiegand et al., 2008) and minimum bactericidal concentration (MBC) of SNH were determined using the microdilution method. Different concentrations of SNH solution (100 μ l; 2,048, 1,024, 512, 256, 128, 64, 32, 16, 8, and 4 μ g/ml) were added with an equal volume of diluted bacterial solution to a 96-well plate. AZM treatment was used as a positive control and culture medium and bacterial solution were used as a blank control group. Plates were incubated at 37°C for 24 h, and the minimum drug concentration with aseptic growth was taken as the MIC. An aliquot (100 μ l) was transferred from the sterile growth well to

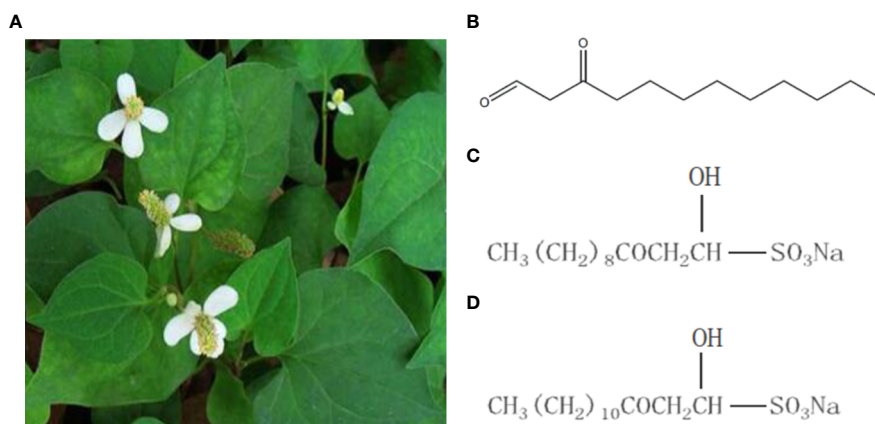


FIGURE 1 | *Houttuynia cordata* Thunb and related compounds. **(A)** *Houttuynia cordata* Thunb (www.cqcqfn.com). **(B)** Houttuynin. **(C)** Sodium houttuynfonate and **(D)** Sodium new houttuynfonate.

the nutrient agar plate, and cultured at 37°C. After 24 h, MBC was determined as less than 5 colonies on the plate. The experiment was repeated three times.

Growth Curve

SNH solutions (100 µl) were prepared to final concentrations of 2,048, 1,024, and 512 µg/ml. Equal volumes of SNH and bacterial solutions were added to 96-well plates, and the control groups established. Plates were incubated at 37°C, the OD₆₀₀ (Nalca et al., 2006) measured at different time points, and the growth curves were drawn.

Drug Treatment and Sample Collection

SNH (2 ml) and an equal volume of bacterial solution was added to the test tube to obtain a concentration of 1 x MIC SNH and the bacteria was cultured at 37°C for 24 h. The blank control group was the SNH treatment control group and no drugs were added. Centrifuge to remove supernatant, and rinsed three times with sterile water. The collected bacterial sample was placed in a centrifuge tube, sealed with sealing film, and placed directly onto dry ice to perform RNA-seq (Poluri et al., 2019). For each group, four samples were prepared under the same experimental conditions.

Transcriptome Sequencing

SNH-induced sequencing of *P. aeruginosa* transcription was performed using the BGISEQ-500 platform (Huada Gene Technology). First, total RNA was processed and purified, and reverse transcription performed to synthesize cDNA which was then used to produce double-stranded DNA. The end of the synthesized double-stranded DNA was flattened and phosphorescence added to the 5' end. The 3' end then forms a sticky end protruding from an "a", and a bubbly joint with a protruding "t" at the 3' end is connected. PCR amplification is then performed using specific primers, PCR products thermally denatured into single strands, and the single-stranded DNA is circularized to obtain a single-stranded circular DNA library.

Data are obtained by transcription sequencing was counted using the SOAPnue (Yuxin et al., 2018) filtering software and filtered using trimmomatic (Bolger et al., 2014). First, reads containing the linker, with unknown base N content greater than 5%, and those of low-quality were removed. NC_002516.2 was used as reference genome. Bowtie2 software was used to align clean reads to the reference gene sequence, and RSEM (Dewey and Bo, 2011; Langmead and Salzberg, 2012) was used to calculate expression levels.

Differential Gene Expression Analysis

Differentially expressed genes (DEGs) were detected based in the method described by Wang et al. (2010). For comparison, the *P*-values calibrated for multiple tests were performed according to the Benjamini and Hochberg method. False discovery rate (FDR) threshold ≤ 0.05 and $|\log_2 \text{fold change (FC)}| > 1$ were defined as significant DEGs (Sun et al., 2015).

Gene Ontology and Kyoto Encyclopedia of Genes and Genomes Enrichment Analysis

DEGs were subjected to Gene Ontology (GO) enrichment analysis and Kyoto Encyclopedia of Genes and Genomes (KEGG) pathway analysis (Sun et al., 2017). In general, DEGs are annotated into GO entries, and the number of genes under each entry is counted to analyze GO and KEGG pathway enrichment. GO entries and KEGG pathways are corrected for *P*-value by FDR, and the *Q*-value ≤ 0.05 is considered significantly enriched. The major biological functions that DEGs perform can be evaluated by analysis of significant GO and KEGG pathway enrichment.

Determination of Total Protease, LasA Staphylococcal Protease, LasB Elastase, LecA Lectin, Pyocyanin, and Floating Swimming Ability

Bacterial supernatants (500 µl) extracted following treatment with different SNH concentrations were incubated with 1 ml of skim milk (1.25%) at 37°C for 20 min, and their OD₆₀₀ measured (El-Mowafy et al., 2014). The overnight *Staphylococcus aureus* culture was boiled for 10 min, centrifuged for 10 min at 10,000 g, and the precipitate was resuspended in 10 mM with Na₂HPO₄ (pH4.5) to an OD₆₀₀ of 0.8. The supernatants with different SNH concentrations and *S. aureus* suspensions were mixed at a ratio of 1:9, and OD₆₀₀ was measured at different time points to calculate the activity of LasA *Staphylococcus* protease (Kessler et al., 1993). Bacterial supernatants with different SNH concentrations were used to measure the amounts of secreted elastase LasB and lectin LecA using ELISA kits (Shanghai, China). Different concentrations of pyocyanin assay medium, PAO1, cultured at 37°C for 24 h at 220 r/min were removed from the shaker and centrifuged for 1 min at 10,800 g to remove the supernatant, diluted with sterile water to 0.5 M colorimetric tube, and diluted to 10⁴ times for later use, inoculated on the slant of the medium, and cultured at 37°C for 24 h. Chloroform (3 ml) was added to the test tube, mixed thoroughly and allowed to stand for 15 min. When the chloroform layer turned green they were transferred to another test tube. Then 1 ml of 1 mol/L HCL was added, mixed, and left to stand for 5 min. The OD₅₂₀ was measured when the solution turned pink. The pyocyanin content was determined by: OD₅₂₀ * 17.072 (Kong et al., 2005). In a word, the supernatant samples were tested for virulence factors 24 h after co-incubation with bacteria and drugs, the expression was standardized by growth OD₆₀₀. Flootation exercise plates with different drug concentrations (10 g/L tryptone, 10 g/L NaCl, 0.3% agar) were prepared. The strain cultured for 24 h at 37°C and 220 r/min was taken from the shaker and the supernatant was centrifuged at 12,000 r/min, diluted to 0.5 M, and serially diluted 100 times. Using a pipette gun, 2 µl of bacterial liquid was inoculated onto the surface of the floating motion medium, and was placed at 37°C for 24 h to measure colony diameter (Rashid and Kornberg, 2000).

Biofilm Formation

SNH solution (2 ml) with final concentrations of 2,048, 1,024, and 512 µg/ml and an equal volume of diluted bacterial solution were added to a 6-well plate and placed a sterile cover glass. The positive control AZM and blank control group were set up simultaneously. Plates were incubated at 37°C for 24 h, then the planktonic bacteria were washed 3 times on the slide with PBS. The samples were then placed in pre-cooled 2.5% glutaraldehyde solution at least 2 hours in the dark at 4°C, and placed in 30%, 50%, 70%, 90% and 100% ethanol for gradient dehydration for 10 minutes. After drying at room temperature, the biofilm samples were sprayed gold after vacuum drying, and observed and imaged (×5000) with Scanning Electron Microscope (GeminiSEM 500, Germany). Crystal violet (0.4%) was used for staining, 30% acetic acid was used for dissolution, and absorbance was measured at 540 nm as previously described (Corral-Lugo et al., 2016).

RT-PCR and qRT-PCR

Expression of *rhlI*, *pqsA*, *lasA*, *lasB*, *lecA*, *phzM*, and *pilG* genes in the QS system was evaluated using PCR. Preparations of different concentrations of bacteria and drugs were used for coculture. In the control group, Mueller-Hinton Broth (MH (B)) medium was added instead of SNH. After culturing at 37°C for 24 h, the supernatant was removed and total RNA extracted from the bacteria using TIANGEN's RNAprep Pure Cell/Bacteria Kit and following the manufacturer's instructions. cDNA was reverse transcribed using TIANGEN's FastQuant RT Kit. RT-PCR was performed using 2 × EasyTaq PCR SuperMix (TransGen Biotech, Beijing, China) and a GENETEST Series Gene Amplifier (Hangzhou, China). The reaction involved 35 amplification cycles of: 94°C 5 min, 94°C 30 s, 56°C 30 s, 72°C 30 s, and 72°C 10 min. The synthesized DNA was electrophoresed on a 1.5% agarose gel, and then imaged on a gel imager. SYBR dye was used for qRT-PCR experiments and the 25 µl reaction system included 12.5 µl SYBR dye, 1 µl upstream primer and 1 µl downstream primer (10 µM), 0.5 µl cDNA, and 11 µl DEPC water. The reaction was performed on an Applied Biosystems 7,500 real-time PCR system (USA) and the reaction steps were: 95°C 15 s, 56°C 30 s, 72°C 30 s, for 40 amplification cycles. Reactions were gradient cooled at 95°C–60°C and the dissolution curve detected. *rpoD* was used as an internal reference, and the gene expression determined by $2^{-\Delta\Delta CT}$. Primer sequences are shown in Table 1.

In Vivo Evaluation of Efficacy of SNH Against *P. aeruginosa*

Galleria mellonella larvae were obtained from Tianjin Huiyude Biological Technology Co., Ltd., with size of 2–3 cm and weight of 0.2–0.3 g. The larvae were stored at 4°C for later use. SNH and AZM were dissolved in PBS without any cosolvent to avoid the possible toxic effects of cosolvent against larvae. The treatment groups of larvae were set as follows: PBS group (without any drugs and infection, infection (*P. aeruginosa* 10⁴ CFU per one larvae, the rest of infection groups were treated with same concentration of *P. aeruginosa*) + PBS group, infection + SNH

TABLE 1 | Sequences of primers used in this study.

Primer name	DNA chain	Sequence (5'-3')
<i>lasR</i> (Wu et al.,2014)	Forward	CATCGTCGCAACTACCC
	Reverse	GCGCACCACCTGCAACACT
<i>lasI</i> (Wu et al.,2014)	Forward	TTGCTCGCCGCACATC
	Reverse	GGCACGGATCATCATCTT
<i>rhlI</i> (Wu et al.,2014)	Forward	ATCCGCAAACCCGCTAC
	Reverse	GCAGGCTGGACCAGAATAT
<i>lasA</i> (Wu et al.,2014)	Forward	CTACAGCATCAACCCGAAAG
	Reverse	TAGCGCCGCGACAACT
<i>lasB</i> (Wu et al.,2014)	Forward	GTTCTATCCGCTGGTGTCTG
<i>lecA</i> (Hickey et al.,2018)	Reverse	CGCTGCCCTTCTTGATG
<i>phzM</i> (Wu et al.,2014)	Forward	TGCGCTGGTCATGAAGAT TG
	Reverse	GAACGAGCCGGAGTTATTGC
	Forward	GACATGGTGCTGTTCTACGG
	Reverse	TGGAATGCCAGGTTGCTC
<i>pilG</i> (Wu et al.,2014)	Forward	ACGGTTTGAAAGTGATGGTG
<i>pqsA</i> (Wu et al.,2014)	Reverse	AAATGATGTTCCGATGGGT
<i>rpoD</i> (Wu et al.,2014)	Forward	TGGTGGTGCGTGAAGCC
	Reverse	GGAACCCGAGGTGTATTGC
	Forward	AGGCCGTGAGCAGGGAT
	Reverse	GGTGGTGCGACCGATGT

2048 µg/ml group, infection + SNH 1024 µg/ml group, infection + SNH 512 µg/ml group, infection + AZM 64 µg/ml group. The vivo assays were carried as previously described (Wu et al., 2020).

Statistical Analysis

SPSS 23.0 statistical software was used for analysis, and the results are reported as mean ± standard deviation. All procedures were performed in triplicate.

RESULTS

Effect of SNH on *P. aeruginosa* Growth

We evaluated the antibacterial potential of SNH against *P. aeruginosa* and determined its MIC and MBC. At a concentration of 2048 µg/ml, aseptic growth is visible to the naked eye, indicating that the MIC of SNH to *P. aeruginosa* is 2048 µg/ml. These results show that SNH has certain antibacterial potential against *P. aeruginosa*. MBC was evaluated based on MIC results, and the bactericidal activity of SNH under MIC was observed. By counting observing plated ATCC 27853 bacteria, it was found that all long bacteria were long and that the number of colonies was > 5. The MBC results suggested that SNH had a bacteriostatic effect on ATCC 27853 and not a bactericidal effect. Therefore, the antibacterial effect of SNH is suitable for use against infections caused by *P. aeruginosa*.

SNH had no effect on the growth of *P. aeruginosa* below the MIC (Figure 2). Compared with the untreated blank control, the OD value decreased in the presence of SNH before 24 h, but there was no statistical difference (Data not shown), and OD₆₀₀ decreased slightly after 30 h, but compared with AZM group, the data showed significant difference, and AZM group

decreased significantly from 36 h to 42 h indicating that SNH did not affect the growth of *P. aeruginosa*, and the change of biofilm formation was not caused by the change of growth.

Transcriptome Sequencing and Clustering DEGs

To further understand the antibacterial mechanism of SNH, we performed transcriptome sequencing. Totally 170.44 MB of transcriptome sequencing data was obtained after RNA-seq applying BGISEQ-500 platform. The original sequencing sequence data has been deposited into the NCBI SRA database (SRA accession: PRJNA542020) (<http://identifiers.org/ncbi/insdc.sra:SRP197195>). In total, 5940 reference genes (<https://www.ncbi.nlm.nih.gov/geo/query/acc.cgi?acc=GSE133428>) were assembled from sequencing data, with 5,937 (99.95%) known genes in the control group and 5,934 (99.9%) in the SNH treated group. Principal component analysis was based on FDR threshold ≤ 0.05 and $|\log_2 \text{fold change (FC)}| > 1$, and 1,674 significant DEGs were identified. Of these DEGs, 1,454 were down-regulated and the remaining 220 were up-regulated (Figure 3).

Analysis of GO and KEGG Pathway of DEGs

GO analysis provides reliable gene product descriptions from various databases and offers a set of dynamic, controlled, and structured terminologies to describe gene functions and products in organism. According to GO functions, all DEGs were classified into: biological process, cellular component, and molecular function. The most annotated functions were “catalytic activity” (GO: 0003824), “membrane” (GO: 0016020), “binding” (GO: 0005488), “cellular process” (GO: 0009987), “membrane part” (GO: 0044425), “metabolic process” (GO: 0008152), and “cell” (GO: 0005623). There were 664 genes in “catalytic activity”, 445 genes in “membrane”, 442 in “binding”, 396 in “membrane part”, 415 in “cell process”, and 294 in “metabolic process” (Figure 4A). DEGs were also

enriched in KEGG pathways, which provide data on biological systems and their relationships at molecular, cellular, and organism levels. The KEGG pathways were annotated using the assembled *P. aeruginosa* transcriptome, and the results were mapped with GO terms. The first three functions that were most significantly enriched in KEGG pathway analysis were the QS system, biofilm formation, and bacterial secretion system Type I, Type II, Type III, and Type VI was changed under SNH treatment (Supplementary Material Figure 2). Among them, 39 genes were enriched in the QS system, 37 genes were enriched in biofilm formation, and 34 genes were enriched in the secretion system. In addition, degradation of fluorobenzoic acid, degradation of chlorocyclohexane and chlorobenzene, degradation of benzoic acid, and biosynthesis of non-ribosomal peptides containing iron carriers are the most significantly abundant signal pathways (Figure 4B). These results show that *P. aeruginosa* gene expression was up-regulated or down-regulated after SNH treatment compared with the control group. These results indicate that there are certain interactions between SNH and *P. aeruginosa*, and suggest that SNH may further inhibit the expression of virulence factors and the biofilm formation by influencing the QS system and bacterial metabolic pathways.

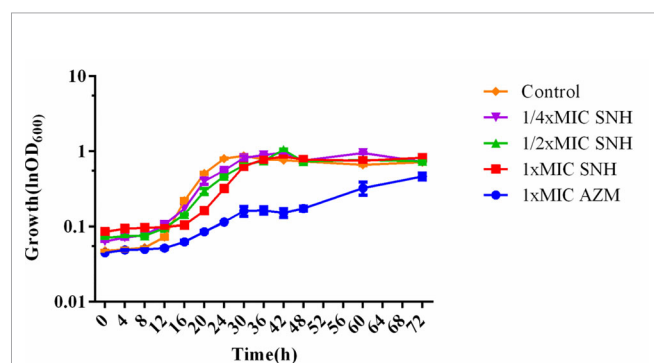


FIGURE 2 | Growth curves of *P. aeruginosa* treated with different concentrations SNH. The drug concentration of treatments was as follows: Control (without any drugs), 512 $\mu\text{g/ml}$ (1/4xMIC) SNH, 1,024 $\mu\text{g/ml}$ (1/2xMIC) SNH, 2,048 $\mu\text{g/ml}$ (1xMIC) sodium new houtuyfonate (SNH), and 64 $\mu\text{g/ml}$ (1xMIC) azithromycin (AZM).

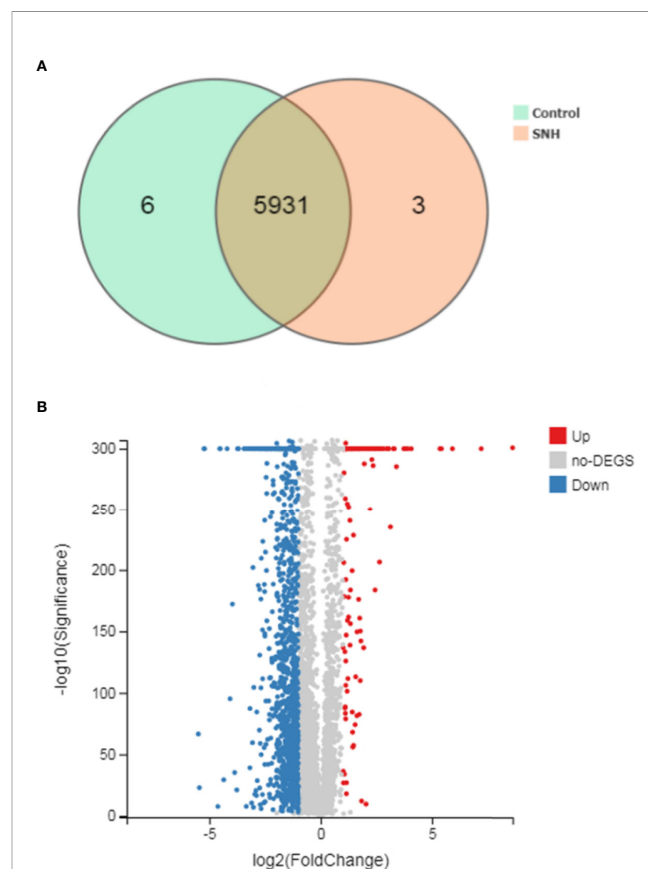


FIGURE 3 | (A) Venn picture of differentially expressed genes (DEGs) and (B) Volcano graph between sodium new houtuyfonate (SNH) treated group and control group.

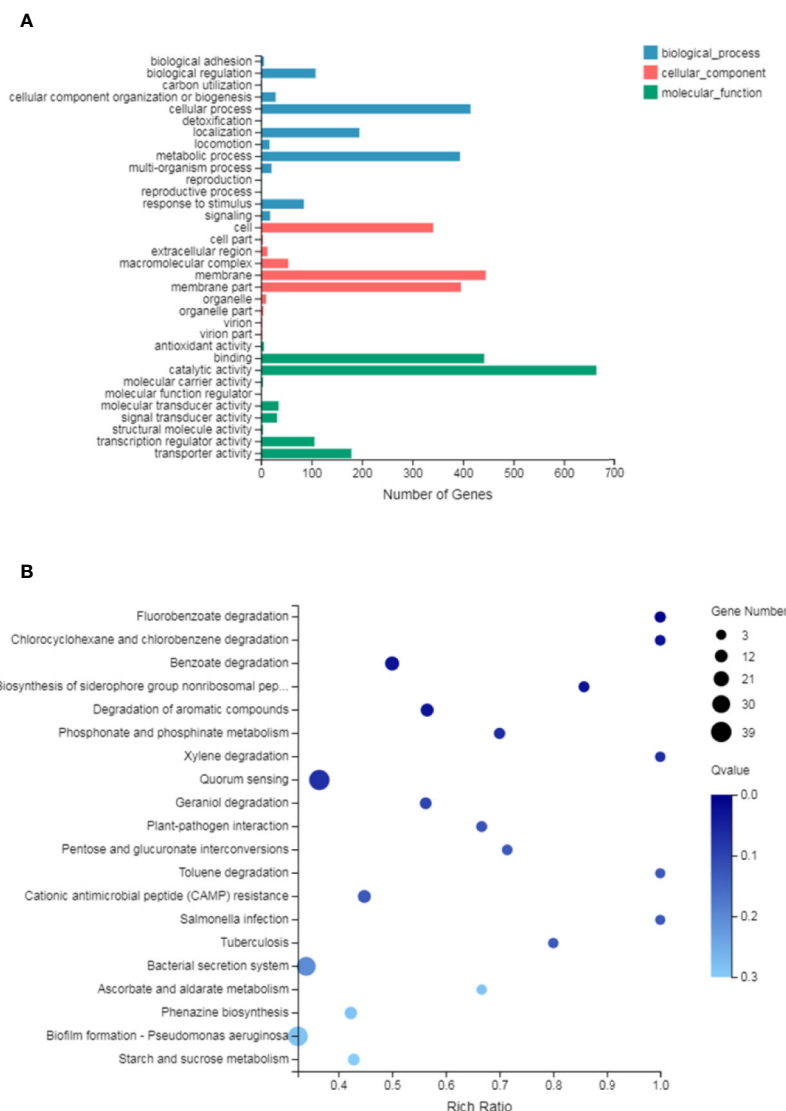


FIGURE 4 | (A) Differentially expressed genes (DEGs) of biological processes, cellular component and molecular function Gene Ontology (GO) terms. **(B)** Statistical enrichment of DEGs in Kyoto Encyclopedia of Genes and Genomes (KEGG) pathways.

Effect of SNH on *P. aeruginosa* DEGs

To better understand *P. aeruginosa* transcription changes under SNH treatment conditions, genes with expression differences were screened using GO and KEGG analyses. Expression genes involved in biofilm formation, the QS system, and phenazine biosynthesis were selected and examined further to reveal the effect of SNH on *P. aeruginosa*, and to classify their relative expression changes. The results show that among the 32 genes related to biofilm formation, QS system, and phenazine synthesis, 10 were up-regulated and 22 were down-regulated (Table 2), suggesting that SNH may have an inhibitory effect on the production of related virulence factors.

Effect of SNH on *P. aeruginosa* Virulence Factor

The total protease, LasA staphylococcus protease, LasB elastase, LecA lectin, and pyocyanin levels and swimming ability were assessed (Figure 5). Total protease, LasA staphylococcal protease, LasB elastase, LecA lectin, and pyocyanin production, along with swimming ability, were all inhibited. This inhibition was dose-dependent, and was significant for all measured values when compared with the blank control group ($p < 0.01$). These results indicate that SNH can inhibit the synthesis of total protease, LasA staphylococcal protease, LasB elastase, LecA lectin, and pyocyanin, and inhibit and swimming ability in *P.*

aeruginosa. Taken together, these results suggest that SNH may inhibit the activity of *P. aeruginosa* by inhibiting the expression of *P. aeruginosa* virulence factors.

Effect of SNH on *P. aeruginosa* Biofilm Formation

P. aeruginosa causes chronic infection because it can form a biofilm. Therefore, inhibiting *P. aeruginosa* biofilm formation may be an effective way to inhibit chronic infection of *P. aeruginosa*. To explain the effect of SNH on *P. aeruginosa* biofilm, we used an inverted SEM and crystal violet staining. At 24 h, *P. aeruginosa* had begun the initial adhesion state. Control group bacteria gathered together in large numbers and had a mucus layer that surrounded a large number of bacteria. The biofilm treated by SNH gradually dispersed with increasing SNH concentration and the number of bacteria decreased (Figure 6A). The amount of biofilm formed in the control group was the largest. The amount of biofilm formed gradually decreased as the SNH concentration increased, showing a dose-dependent characteristic, and a significant difference was observed when compared with the blank control group ($p <$

0.01) (Figure 6B). These results confirm that SNH can inhibit the formation of *P. aeruginosa* biofilm.

Effect of SNH on *P. aeruginosa* Gene Expression

RT-PCR and qRT-PCR analysis were performed to verify gene expression in bacteria. The virulence genes, biofilms, and related genes controlled by the QS system were selected as the RT-PCR and qRT-PCR analysis targets. RT-PCR results showed that *lasA*, *lasB*, *lecA*, *rhII*, *phzM*, *pqsA*, and *pilG* gene expression was down-regulated to different degrees after SNH treatment, and that the down regulation was dose dependent (Figure 7A). qRT-PCR results showed that increasing SNH concentration caused dose-dependent down regulation of the *lasA*, *lasB*, *lecA*, *rhII*, *phzM*, *pqsA*, and *pilG* genes (Figure 7B). Although there are some differences in the RT-PCR, qRT-PCR, and RNA-seq results, the expression trends are basically the same. These results indicate that SNH can inhibit the expression of some virulence genes, and biofilm related genes regulated by the QS system. Therefore, SNH may inhibit *P. aeruginosa* pathogenicity by inhibiting the expression of virulence genes, biofilm genes, and related genes regulated by the QS system.

TABLE 2 | Genes differentially expressed under sodium new houttuynate (SNH) and sodium houttuynate (SH) treatment.

Gene name	log2FoldChange		Category
	SNH	SH	
<i>phnA/trpE</i>	-2.32	-2.62	Biofilm
<i>phnB/trpG</i>	-1.43	-1.12	Biofilm
<i>pqsA</i>	-2.93	-3.78	Phenazine, Biofilm
<i>pqsB</i>	-3.34	-3.75	Phenazine, Biofilm
<i>pqsC</i>	-2.76	-3.15	Phenazine, Biofilm
<i>pqsD</i>	-2.91	-3.24	Phenazine, Biofilm
<i>pqsE</i>	-2.89	-3.05	Phenazine, Biofilm
<i>lasI</i>	/	-2.44	Biofilm
<i>rhII</i>	-1.11	-1.5	Biofilm
<i>rhIA</i>	-1.87	-3.05	Biofilm
<i>rhIB</i>	-1.15	-1.61	Biofilm
<i>rhIC</i>	-1.15	-1.16	Biofilm
<i>lecA</i>	-2.8	-4.02	Biofilm
<i>hsbR</i>	-1.85	-1.88	Biofilm
<i>hsbA</i>	-1.4	-1.26	Biofilm
<i>roeA</i>	-1.58	-1.02	Biofilm
<i>mucR</i>	-1.03	-1.53	Biofilm
<i>pslB</i>	1.02	1.72	Biofilm
<i>pslL</i>	1.19	1.66	Biofilm
<i>pslJ</i>	1.08	1.37	Biofilm
<i>pslI</i>	1.13	1.44	Biofilm
<i>pslH</i>	1.26	1.62	Biofilm
<i>pslG</i>	1.25	1.64	Biofilm
<i>pslF</i>	1.2	1.62	Biofilm
<i>pslE</i>	1.16	1.65	Biofilm
<i>pslD</i>	1.16	1.51	Biofilm
<i>rtbN</i>	1.04	1.23	Biofilm
<i>algA</i>	1.0	1.19	Biofilm
<i>alg44</i>	-1.3	-1.46	Biofilm
<i>phzI</i>	-1.1	/	Quorum Sensing
<i>lasB</i>	-1.6	/	Quorum Sensing
<i>GadC</i>	-1.14	/	Quorum Sensing
<i>LsrG</i>	-1.1	/	Quorum Sensing
<i>TofI</i>	-1.1	/	Quorum Sensing

In Vivo Evaluation of Efficacy of SNH Against *P. aeruginosa*

After pre-experiment study, we determined 10^4 CFU per one larvae as the applied concentration LD_{50} of *G. mellonella* larvae. As shown in Figure 8, we investigated the effects of SNH treatment at 24 h post-infection of *P. aeruginosa* against *G. mellonella*. The results show that the survival rate of the infection + PBS group was 0%, and the infection + SNH 512 μ g/mL group was 50%, and the infection + SNH 1024 μ g/mL group was 60%, and the infection + SNH 2048 μ g/mL group was 70%, and the infection + AZM 64 μ g/mL group was 70%, and the PBS group was 100% at 24 h. These results also indicate that compared with untreated larvae, infected larvae showed significantly higher survival rate in drug treatment groups, and the difference was statistically significant ($p < 0.01$). Hence, these results suggest that SNH can improve the survival rate of larvae infected by *P. aeruginosa*, thereby effectively inhibit *P. aeruginosa* infection *in vivo*.

DISCUSSION

SH may play an antibacterial role by regulating the *P. aeruginosa* QS system to inhibit the synthesis of the virulence factors LasA protease and pyocyanin. SNH is a new generation product of *Houttuynia cordata*. Compared with SH, SNH has higher safety and effectiveness, is less toxic, has fewer side effects, and has better clinical promotion value (Yefei and Meixian, 2016). It has been recently reported that some fatty acids as antibiofilm and antivirulence agents (Kumar et al., 2020) as *Houttuynia* controlled QS-dependent phenotypes. The structures of *Houttuynia* and SNH are similar to long-chain fatty acids.

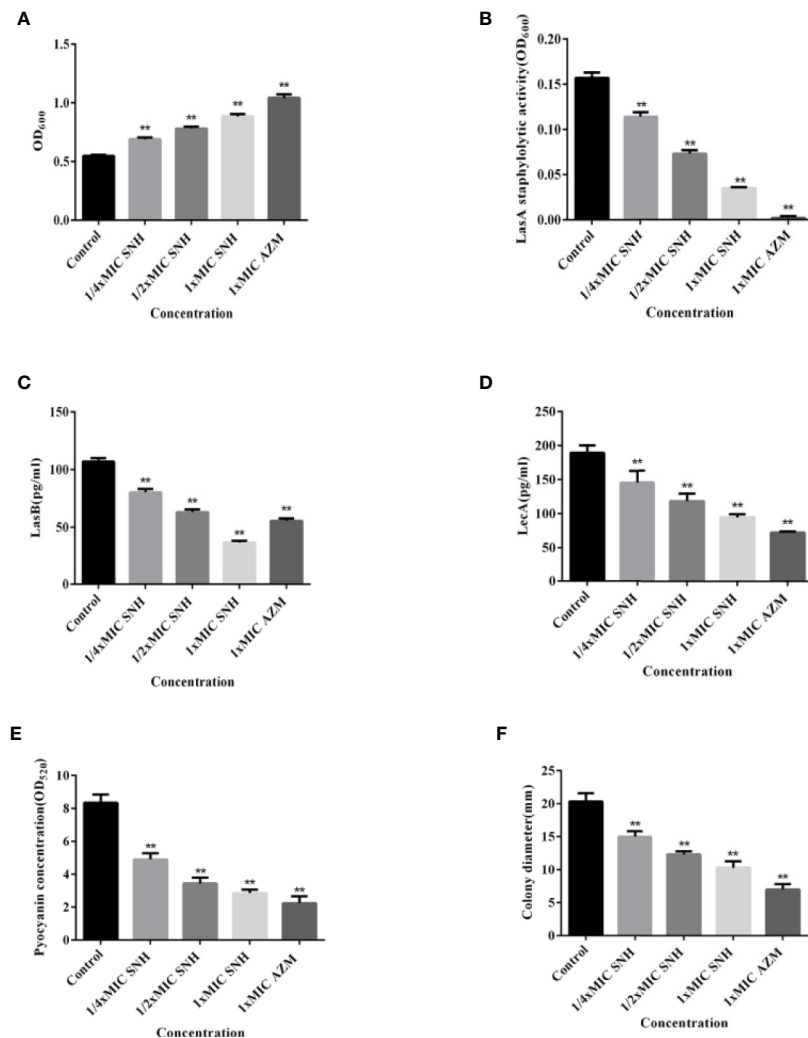


FIGURE 5 | Effect of sodium new houttuifonate (SNH) on virulence factor of *P. aeruginosa*. **(A)** Total protease. **(B)** LasA staphylococcal protease. **(C)** LasB elastase. **(D)** LecA lectin. **(E)** Pyocyanin. **(F)** Float swimming. The drug concentration of treatments was as follows: Control, 512 $\mu\text{g/ml}$ (1/4 MIC) SNH, 1024 $\mu\text{g/ml}$ (1/2 MIC) SNH, 2,048 $\mu\text{g/ml}$ (1x MIC) SNH, and 64 $\mu\text{g/ml}$ (1x MIC) azithromycin (AZM). Data represent the means \pm SD ($n=3$, ** $p < 0.01$ vs. control group).

Therefore, we speculate that SNH may also play an anti-*P. aeruginosa* effect based on QS-controlled signal transduction.

In order to determine the effect of SNH on the *P. aeruginosa* QS system and biofilm formation, we performed transcriptional analysis. Principle component analysis and correlation charts were used to evaluate the correlation between the blank control and SNH treatment groups (**Supplementary Material Figure 1**). Paired Pearson correlation coefficients for each group were higher than 0.7, proving that the samples were well correlated. Transcriptome analysis indicated that SNH may also play an antibacterial role by regulating the QS system of *P. aeruginosa*. Therefore, based on transcription analysis and experiments to examine the relationship between biofilm formation, the QS system, and pathogenicity, it may be possible to discover the mechanism of SNH action.

The virulence factors regulated by *P. aeruginosa* QS include protease, elastase, pyocyanin, lectin, rhamnolipid, toxin, and biofilm formation. These virulence factors can affect the formation and maintenance of biofilms and cluster movement. The mutual adjustment is complex, involving many internal and external environmental factors. Total protease can destroy the immunoglobulin that protects the mucous membrane, and destroy the tight junctions between host epithelial cells, which leads to invasion and injury of organism (Heras et al., 2014). Elastase is encoded by the *lasB* gene and plays an important role in *P. aeruginosa* infection, which can help bacteria damage host tissues and degrade immune proteins (Szamosvári et al., 2016). LecA is a galactose tetramer lectin produced by *P. aeruginosa*. It has affinity for extracellular polysaccharides, mediates the adhesion to host cells and infection and biofilm formation in

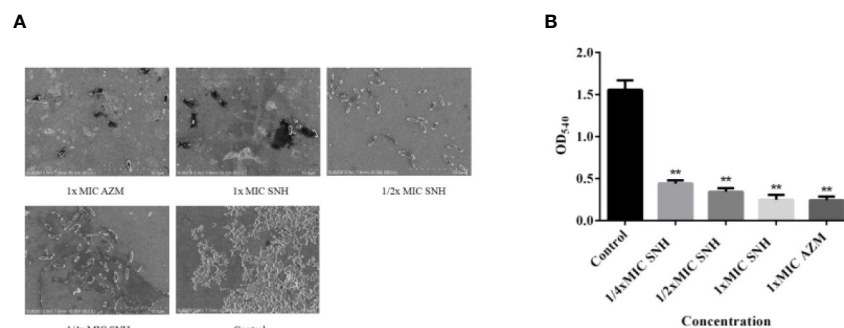


FIGURE 6 | Sodium new houttuifonate (SNH) effect on *P. aeruginosa* biofilm. **(A)** Morphology of ATCC 27853 biofilm under SEM (×5,000). **(B)** Effect of SNH on ATCC 27853 biofilm production. The drug concentration of treatments was as follows: Control, 512 μg/ml (1/4×MIC) SNH, 1,024 μg/ml (1/2×MIC) SNH, 2,048 μg/ml (1×MIC) SNH, and 64 μg/ml (1×MIC) azithromycin (AZM). Data represent the means ± SD (n=3, ***p* < 0.01 vs. control group).

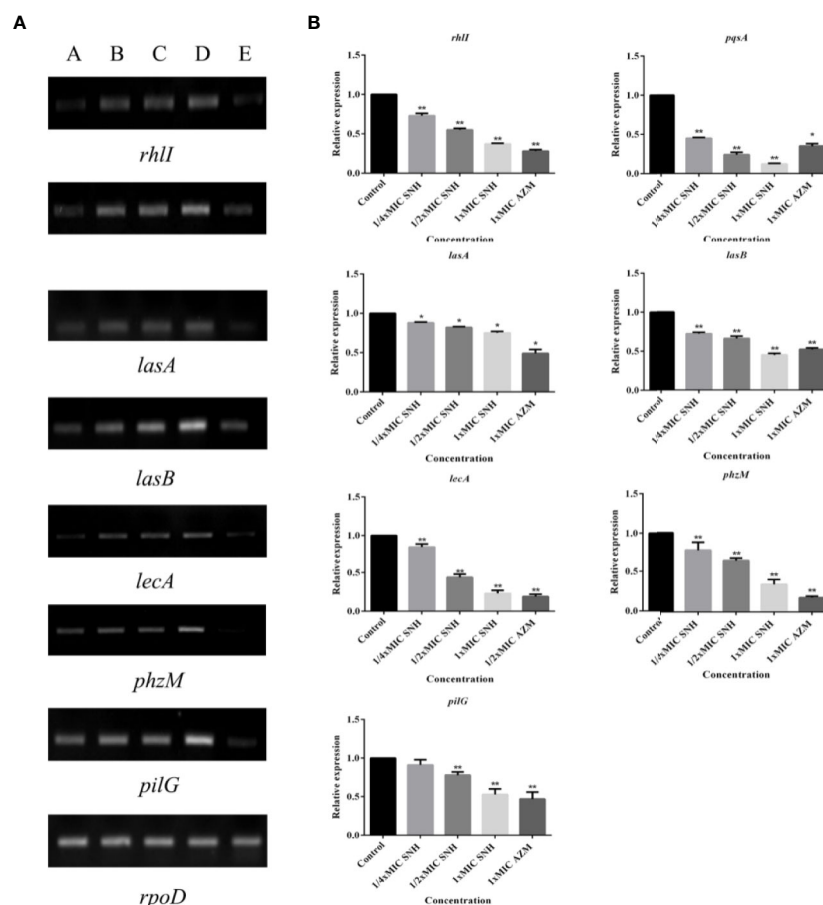
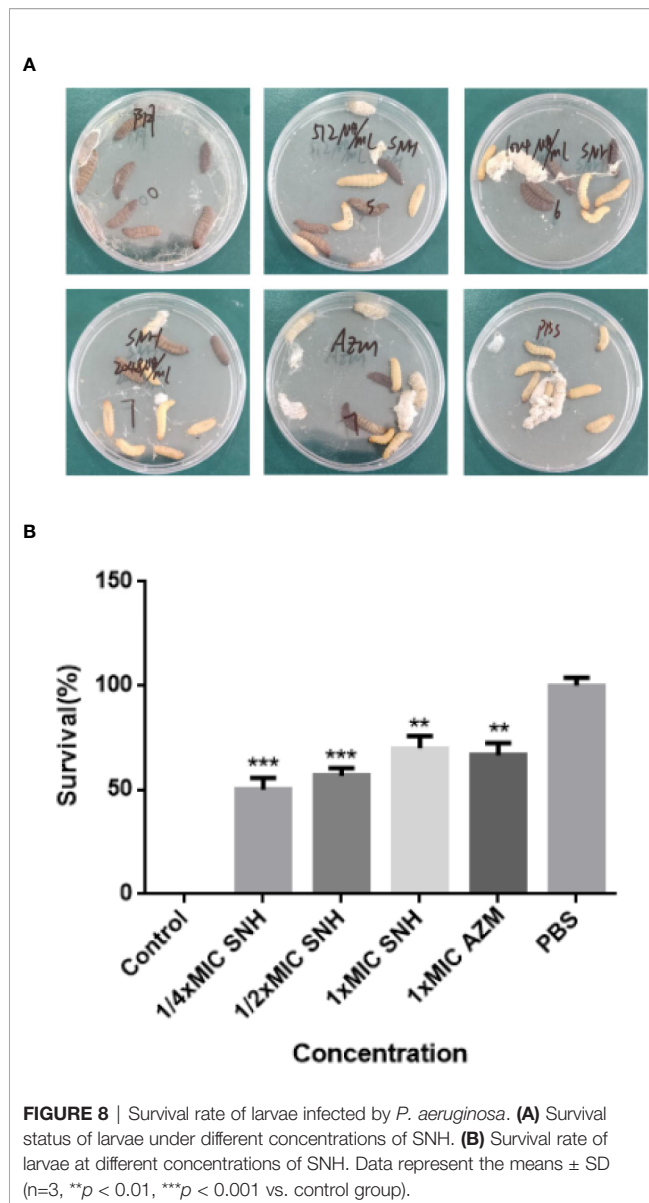


FIGURE 7 | (A) RT-PCR results of sodium new houttuifonate (SNH) inhibiting biofilm and related genes and virulence factors. The lanes from left to right were as follows: A: 2,048 μg/ml (1×MIC) SNH, B: 1,024 μg/ml (1/2×MIC) SNH, C: 512 μg/ml (1/4×MIC) SNH, D: Control, E: 1xMIC AZM. **(B)** qRT-PCR results of SNH inhibiting biofilm and related genes and virulence factors. Expression of the house-keeping gene, *rpoD*, was used as the internal control for each sample. The drug concentration of treatments was as follows: Control, 512 μg/ml (1/4×MIC) SNH, 1024 μg/ml (1/2×MIC) SNH, 2,048 μg/ml (1×MIC) SNH, and 64 μg/ml (1×MIC) azithromycin (AZM). Data represent the means ± SD (n=3, **p* < 0.05, ***p* < 0.01 vs. control group).



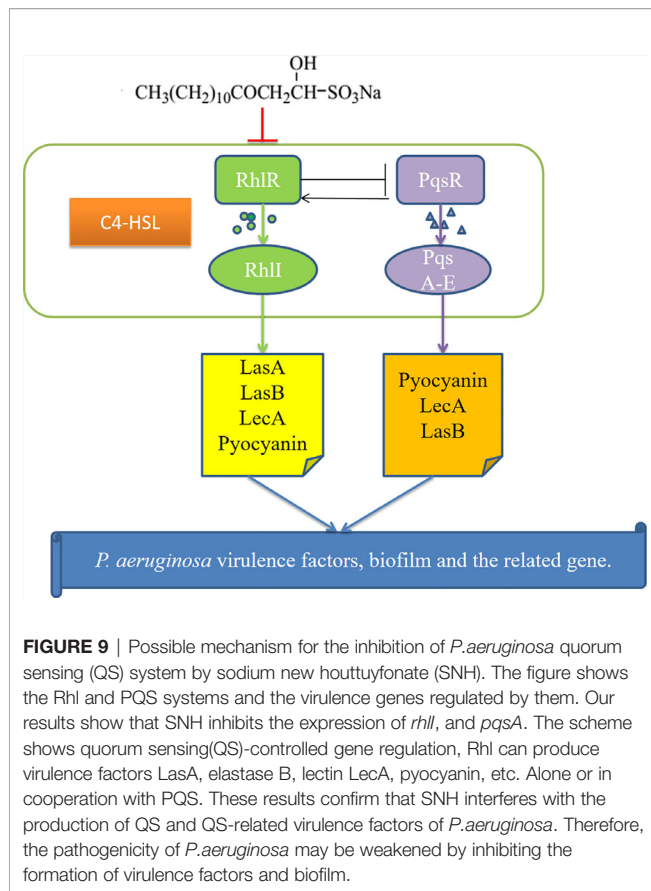
P. aeruginosa (Huang et al., 2018). Pyocyanin is a blue-green redox secondary metabolite produced by *P. aeruginosa*, which can induce host neutrophils to accelerate apoptosis and reduce local inflammatory reaction, thus providing advantages for the survival of bacteria in the host. In the presence of biofilms, pyocyanin can induce the deposition of extracellular DNA (eDNA), which is the main component of biofilm extracellular polysaccharides and is essential for the formation and stability of biofilms. We further analyzed the effect of SNH on its virulence factors and biofilm formation. In *P. aeruginosa* biofilm, SNH affects the expression of a large number of genes. SNH reduced the synthesis of total protease, LasA staphylococcal protease, LasB elastase, LecA lectin, pyocyanin, and biofilm in *P. aeruginosa*. RT-PCR and qRT-PCR revealed that expression of QS regulated genes *rhII*, *pqsA*, *lecA*, *lasA*, *lasB*, *phzM*, and *pilG* were down-regulated after SNH treatment.

In *P. aeruginosa*, SNH can inhibit the expression of some virulence factors and the formation of biofilms. Experimental results show that expression of these virulence genes, biofilms, and related genes is dose-dependent at concentrations of 1 x MIC SNH, 1/2 x MIC SNH and, 1/4 x MIC SNH. Additionally, analysis of virulence factor, biofilm, and related gene expression was consistent with transcriptome sequencing and PCR analysis, further supporting that SNH has an inhibitory effect on *P. aeruginosa*.

Larval model is an important tool to study the pathogenesis of *P. aeruginosa* infection *in vivo*. We simulated the larval model, which proved that SNH significantly reduced the mortality of larvae. The difference of virulence between the drug groups and the blank control group proved by previous growth and virulence testing experiments can be confirmed in the larval model, which proves that the larval model is a suitable model for *P. aeruginosa* infection. The larval model can be used to study the pathogenic mechanism of *P. aeruginosa*. Once the genome sequence of larvae is available, the model of larvae will become more valuable in the future.

The MIC of SNH to *P. aeruginosa* was 2,048 μ g/ml, which was four times higher than SH. This possible because our research group has been doing drug resistance tests on *P. aeruginosa* in recent years, which may gradually adapt to drugs and produce resistance. Previous studies found that SH could down-regulate *lasI* gene and up-regulate *rhII* gene after 72 h of treatment by our research group. However, through transcriptome sequencing data, it was found that *lasI*, *rhII*, and *pqsA* were down-regulated by 2.44, 1.5, and 3.78 times after SH treatment for 24 h in this study, while no change in *lasI* gene expression was detected after SNH treatment, and *rhII* gene was down-regulated by 1.11 times and *pqsA* was down-regulated by 2.93 times, which was inconsistent with the previous research results, possibly due to the different action time selected in the experiment (72 h was selected in the previous experiment, while the action time selected in this experiment was 24 h). And it can be seen that when the action time is 24 h, the ways of SH and SNH on inhibiting *P. aeruginosa* are not completely the same. SH works together by regulating the Las/Rhl and PQS system, in which Las system plays a major role, while SNH plays a regulatory role by regulating Rhl and PQS system. However, due to the limitations of transcriptome sequencing, we also suspect that the relevant data may not be detected because of the small change multiple of *lasI*.

Importantly, we found that the expression of virulence genes at the transcription level is regulated in different ways among SNH and SH. Although *LasR* is considered as the main regulator in *P. aeruginosa*, the cross-regulation between the Las and Rhl system was observed in this experiment. For example, low but detectable C4-HSL is produced without *LasR* (Wang et al., 2018). The specific reason the expression of *lasR* is not detected in SNH is still unclear, which may be caused by other highly interactive QS regulatory systems, such as Vfr, VqsR, MvaT, GacA, RpoN, RpoS, and RsmA (Balasubramanian et al., 2013). The existence of Rhl signal without Las signal in clinical isolates suggests that las-independent QS activity may play a role in maintaining *P. aeruginosa* infection (Feltner et al., 2016). There are researchers reported that *P. aeruginosa* may enhance some



virulence genes and reduce the expression of other genes as part of its survival strategy (Wang et al., 2018). We observed that the yield of total protease and lasB decreased in this experiment, which may be related to the high level of Psl. Therefore, exploring whether the presence of Psl levels in SNH is related to *P. aeruginosa* infection would be an interesting research direction in the future.

Our research shows that further study on QS system of *P. aeruginosa* may be helpful to understand its pathogenic mechanism. Nevertheless, there was no change of lasR gene in ATCC 27853 under the action of SNH, which indicated that Las system was not absolutely necessary for the establishment of *P. aeruginosa* infection. In addition, our study also questioned the previously recognized level understanding of the QS system, and the mechanism should be understood more comprehensively in many aspects and combination with specific situations i.e., different strains and hosts.

Combined with the above experiments, we infer that these virulence factors and biofilms are inhibited by SNH inhibiting the production of C4-HSL. The difference of action mechanism between SH and SNH on *P. aeruginosa* may lie in the number of C atoms in its structure, which is more than SH 2 C atoms in SNH, which may cause SNH not combining with 3-oxo-C12-HSL, combining with RhIR and C4-HSL complex to play an antibacterial role. SNH has replaced houttuynin, and to a large extent SH due to its improved chemical and pharmacological

properties, which has been used as an effective therapeutic agent for respiratory infections and inflammatory diseases such as acute or chronic bronchitis and pneumonia (Lu et al., 2013). Through the experimental study, it was found that SNH had a certain inhibitory effect on *P. aeruginosa*, but its MIC was high, which provided a certain basis for its structural modification and transformation in the future.

CONCLUSION

These results show that SNH may inhibit the *P. aeruginosa* QS system, reduce the synthesis of virulence factors and biofilms, and down-regulate the expression of key genes (Figure 9) to inhibit *P. aeruginosa* infection. Additionally, this study can be used as a basis for designing new QS-targeted drug candidates using SNH, while minimizing the chance of generating resistance (Rodolfo et al., 2013). These results are currently being expanded upon through research on animal infection models *in vivo* in our research group.

DATA AVAILABILITY STATEMENT

The original contributions presented in the study are included in the article/Supplementary Material; further inquiries can be directed to the corresponding author.

AUTHOR CONTRIBUTIONS

DW, GY, and CW conceived and designed the study. YZ and DW wrote the manuscript. JS and TW critically reviewed the manuscript and provided general advice. YZ, LM, YS, and JW performed the experiments and analyzed data. All authors contributed to the article and approved the submitted version.

FUNDING

This work was supported by the project funded by the China Postdoctoral Science Foundation under Grant No. 2019M662185, the key discipline of Anhui University of Chinese Medicine (DC18100042), the Outstanding Talent Support Program in University (Key project) of Anhui Province under Grant No. gxyqZD2020024, and the Natural Science Foundation (Key project) of Anhui University of Chinese Medicine under Grant No.2020zrzd07. The Funding is used to cover laboratory expenses, sample preparation and sequencing. These funding agencies have no role in research design, data collection, analysis of results, or manuscript writing.

ACKNOWLEDGMENTS

We thank the sequencing facilities of Huada Gene Cloud Platform for the preparation and sequencing of the library.

SUPPLEMENTARY MATERIAL

The Supplementary Material for this article can be found online at: <https://www.frontiersin.org/articles/10.3389/fphar.2020.572375/full#supplementary-material>

REFERENCES

- Asfahl, K. L., and Schuster, M. (2017). Additive effects of quorum sensing anti-activators on *Pseudomonas aeruginosa* virulence traits and transcriptome. *Front. Microbiol.* 8, 2654. doi: 10.3389/fmicb.2017.02654
- Balasubramanian, D., Schnepfer, L., Kumari, H., and Mathee, K. (2013). A dynamic and intricate regulatory network determines *Pseudomonas aeruginosa* virulence. *Nucleic Acids Res.* 41, 1–20. doi: 10.1093/nar/gks1039
- Bentzmann, S. D., and Patrick, P. (2011). The *Pseudomonas aeruginosa* opportunistic pathogen and human infections. *Environ. Microbiol.* 13, 1655–1665. doi: 10.1111/j.1462-2920.2011.02469.x
- Bolger, A. M., Lohse, M., and Usadel, B. (2014). Trimmomatic: a flexible trimmer for illumina sequence data. *Bioinf. (Oxford England)* 30 (15), 2114–2120. doi: 10.1093/bioinformatics/btu170
- Breidenstein, E. B., De La Fuente-Nunez, C., and Hancock, R. E. (2011). *Pseudomonas aeruginosa*: all roads lead to resistance. *Trends Microbiol.* 19, 419–426. doi: 10.1016/j.tim.2011.04.005
- Corral-Lugo, A., Daddaoua, A., Ortega, A., Espinosa-Urgel, M., and Krell, T. (2016). Rosmarinic acid is a homoserine lactone mimic produced by plants that activates a bacterial quorum-sensing regulator. *Sci. Signal.* 9, ra1–ra1. doi: 10.1126/scisignal.aaa8271
- Denning, G. M., Iyer, S. S., Reszka, K. J., O'Malley, Y., and Britigan, B. E. (2003). Phenazine-1-carboxylic acid, a secondary metabolite of *Pseudomonas aeruginosa*, alters expression of immunomodulatory proteins by human airway epithelial cells. *Am. J. Physiol. Lung Cell Mol. Physiol.* 285, 584–592. doi: 10.1152/ajplung.00086.2003
- Dewey, C. N., and Bo, L. (2011). RSEM: accurate transcript quantification from RNA-Seq data with or without a reference genome. *BMC Bioinform.* 12:323. doi: 10.1186/1471-2105-12-323
- El-Mowafy, S. A., Abd, E. G. K. H., El-Messery, S. M., and Shaaban, M. I. (2014). Aspirin is an efficient inhibitor of quorum sensing, virulence and toxins in *Pseudomonas aeruginosa*. *Microb. Pathog.* 74, 25–32. doi: 10.1016/j.micpath.2014.07.008
- Feltner, J. B., Wolter, D. J., Pope, C. E., Groleau, M. C., Smalley, N. E., Greenberg, E. P., et al. (2016). LasR variant cystic fibrosis isolates reveal an adaptable quorum-sensing hierarchy in *Pseudomonas aeruginosa*. *mBio* 7, 7 (5), e01513–e01516. doi: 10.1128/mBio.01513-16
- Gurunathan, S., Han, J. W., Kwon, D. N., and Kim, J. H. (2014). Enhanced antibacterial and anti-biofilm activities of silver nanoparticles against Gram-negative and Gram-positive bacteria. *Nanoscale Res. Lett.* 9, 1–17. doi: 10.1186/1556-276X-9-373
- Harding, C. R., Schroeder, G. N., Collins, J. W., and Frankel, G. (2013). Use of *Galleria mellonella* as a model organism to study *Legionella pneumophila* infection. *J. Vis. Exp.* 22 (81), e50964. doi: 10.3791/50964
- Heras, B., Scanlon, M. J., and Martin, J. L. (2014). Targeting virulence not viability in the search for future antibacterials. *Br. J. Clin. Pharmacol.* 79 (2), 208–215. doi: 10.1111/bcp.12356
- Hickey, C., Schaible, B., Nguyen, S., Hurley, D., Srikumar, S., Fanning, S., et al. (2018). Increased virulence of bloodstream over peripheral isolates of *P. aeruginosa* identified through post-transcriptional regulation of virulence factors. *Front. Cell Infect. Microbiol.* 8, 357. doi: 10.3389/fcimb.2018.00357
- Huang, S. F., Lin, C. H., Yu, L. T., Tsai, C. L., Cheng, T. J., R., and Wang, S. K. (2018). Development of *Pseudomonas aeruginosa* lectin LecA inhibitor by using bivalent galactosides supported on polyproline peptide scaffolds. *Chem. Asian J.* 13 (6), 686–700. doi: 10.1002/asia.201701724
- Juanjuan, H. (2009). Effect of sodium new houttuynonate injection combined with Interferon on children's autumn diarrhea. *Modern Chin. Drug Application* 1, 138–139. doi: 10.3969/j.issn.1673-9523.2009.01.114
- Kalia, M., Yadav, V. K., Singh, P. K., Sharma, D., Pandey, H., Narvi, S. S., et al. (2015). Effect of cinnamon oil on quorum sensing-controlled virulence factors and biofilm formation in *Pseudomonas aeruginosa*. *PLoS One* 10, e0135495. doi: 10.1371/journal.pone.0135495
- Kessler, E., Safran, M., Olson, J. C., and Ohman, D. E. (1993). Secreted LasA of *Pseudomonas aeruginosa* is a staphylolytic protease. *J. Biol. Chem.* 268, 7503–7508. doi: 10.1016/0014-5793(93)80087-B
- Kim, H. S., Lee, S. H., Byun, Y., and Park, H. D. (2015). 6-Gingerol reduces *Pseudomonas aeruginosa* biofilm formation and virulence via quorum sensing inhibition. *Sci. Rep.* 5, 8656. doi: 10.1038/srep08656
- Kong, K. F., Jayawardena, S. R., Indulkar, S. D., Del Puerto, A., Koh, C. L., Høiby, N., et al. (2005). *Pseudomonas aeruginosa* AmpR is a global transcriptional factor that regulates expression of AmpC and PoxB beta-lactamases, proteases, quorum sensing, and other virulence factors. *Antimicrob. Agents Chemother.* 49, 4567–4575. doi: 10.1128/AAC.49.11.4567-4575.2005
- Kumar, P., Lee, J. H., Beyenal, H., and Lee, J. (2020). Fatty Acids as Antibiofilm and Antivirulence Agents. *Trends Microbiol.* 28 (9), 753–768. doi: 10.1016/j.tim.2020.03.014
- Langmead, B., and Salzberg, S. L. (2012). Fast gapped-read alignment with Bowtie 2. *Nat. Methods* 9, 357–359. doi: 10.1038/nmeth.1923
- Lu, X., Yang, X., Li, X., Lu, Y., Ren, Z., Zhao, L., et al. (2013). In vitro activity of sodium new houttuynonate alone and in combination with oxacillin or netilmicin against methicillin-resistant *Staphylococcus aureus*. *PLoS One* 8, e68053. doi: 10.1371/journal.pone.0068053
- Ma, L., Liu, X., Liang, H., Che, Y., Chen, C., Dai, H., et al. (2012). Effects of 14-alpha-lipoyl andrographolide on quorum sensing in *Pseudomonas aeruginosa*. *Antimicrob. Agents Chemother.* 56, 6088–6094. doi: 10.1128/AAC.01119-12
- Nalca, Y., Jansch, L., Bredenbruch, F., Geffers, R., Buer, J., and Haussler, S. (2006). Quorum-sensing antagonistic activities of azithromycin in *Pseudomonas aeruginosa* PAO1: a global approach. *Antimicrob. Agents Chemother.* 50, 1680–1688. doi: 10.1128/AAC.50.5.1680-1688.2006
- Poluri, R. T. K., Beaparlant, C. J., Droit, A., and Etienne, A.-W. (2019). RNA sequencing data of human prostate cancer cells treated with androgens. *Data Brief.* 25:104372. doi: 10.1016/j.dib.2019.104372
- Rajkumari, J., Borkotoky, S., Murali, A., Suchiang, K., Mohanty, S. K., and Busi, S. (2018). Cinnamic acid attenuates quorum sensing associated virulence factors and biofilm formation in *Pseudomonas aeruginosa* PAO1. *Biotechnol. Lett.* 40, 1087–1100. doi: 10.1007/s10529-018-2557-9
- Ramsey, D. M., and Wozniak, D. J. (2005). Understanding the control of *Pseudomonas aeruginosa* alginate synthesis and the prospects for management of chronic infections in cystic fibrosis. *Mol. Microbiol.* 56, 309–322. doi: 10.1111/j.1365-2958.2005.04552.x
- Rashid, M. H., and Kornberg, A. (2000). Inorganic polyphosphate is needed for swimming, swarming, and twitching motilities of *Pseudomonas aeruginosa*. *Proc. Natl. Acad. Sci. U S A.* 97, 4885–4890. doi: 10.1073/pnas.060030097
- Rodolfo, G. C., Mariano, M. V., Norma, V. G., Alejandra, G., V., P., Takahiro, H., et al. (2013). Resistance to the quorum-quenching compounds brominated furanone C-30 and 5-fluorouracil in *Pseudomonas aeruginosa* clinical isolates. *Patho Dis.* 68 (1), 8–11. doi: 10.1111/2049-632X.12039
- Schuster, M., Sexton, D. J., Diggle, S. P., and Greenberg, E. P. (2013). Acyl-homoserine lactone quorum sensing: from evolution to application. *Annu. Rev. Microbiol.* 67, 43–63. doi: 10.1146/annurev-micro-092412-155635
- Shao, J., Cheng, H., Wang, C., and Wang, Y. (2012). A phytoanticipin derivative, sodium houttuynonate, induces in vitro synergistic effects with levofloxacin against biofilm formation by *Pseudomonas aeruginosa*. *Molecules* 17, 11242–11254. doi: 10.3390/molecules170911242
- Shao, J., Cheng, H., Wang, C., Wu, D., Zhu, X., Zhu, L., et al. (2013). Sodium houttuynonate, a potential phytoanticipin derivative of antibacterial agent, inhibits bacterial attachment and pyocyanine secretion of *Pseudomonas aeruginosa* by attenuating flagella-mediated swimming motility. *World J. Microbiol. Biotechnol.* 29, 2373–2378. doi: 10.1007/s11274-013-1405-2

- Sun, Q. L., Zhao, C. P., Wang, T. Y., Hao, X. B., Wang, X. Y., Zhang, X., et al. (2015). Expression profile analysis of long non-coding RNA associated with vincristine resistance in colon cancer cells by next-generation sequencing. *Gene* 572, 79–86. doi: 10.1016/j.gene.2015.06.087
- Sun, D., Zhang, W., Mou, Z., Chen, Y., Guo, F., Yang, E., et al. (2017). Transcriptome analysis reveals silver nanoparticle-decorated quercetin antibacterial molecular mechanism. *ACS Appl. Mater. Interfaces* 9, 10047–10060. doi: 10.1021/acsami.7b02380
- Szamosvári, D., Reichle, V. F., Jureschi, M., and Böttcher, T. (2016). Synthetic quinolone signal analogues inhibiting the virulence factor elastase of *Pseudomonas aeruginosa*. *Chem. Commun.* 52, 13440–13443. doi: 10.1039/c6cc06295d
- Van Delden, C., and Iglewski, B. H. (1998). Cell-to-cell signaling and *Pseudomonas aeruginosa* infections. *Emerg Infect. Dis.* 4, 551–560. doi: 10.3201/eid0404.980405
- Wang, L., Feng, Z., Wang, X., Wang, X., and Zhang, X. (2010). DEGseq: an R package for identifying differentially expressed genes from RNA-seq data. *Bioinformatics* 26, 136–138. doi: 10.1093/bioinformatics/btp612
- Wang, Y., Gao, L., Rao, X., Wang, J., Yu, H., Jiang, J., et al. (2018). Characterization of lasR-deficient clinical isolates of *Pseudomonas aeruginosa*. *Sci. Rep.* 8 (1), 13344. doi: 10.1038/s41598-018-30813-y
- Wiegand, I., Hilpert, K., and Hancock, R. E. (2008). Agar and broth dilution methods to determine the minimal inhibitory concentration (MIC) of antimicrobial substances. *Nat. Protoc.* 3, 163–175. doi: 10.1038/nprot.2007.521
- Williams, P., and Camara, M. (2009). Quorum sensing and environmental adaptation in *Pseudomonas aeruginosa*: a tale of regulatory networks and multifunctional signal molecules. *Curr. Opin. Microbiol.* 12, 182–191. doi: 10.1016/j.mib.2009.01.005
- Wu, D., Cheng, H., Huang, W., and Duan, Q. (2015). Sodium houttuynate in vitro inhibits the biofilm formation and alginate biosynthesis gene expression of *Pseudomonas aeruginosa* clinical strain. *Exp. Ther. Med.* 10, 753–758. doi: 10.3892/etm.2015.2562
- Wu, D., Huang, W., Duan, Q., Li, F., and Cheng, H. (2014). Sodium houttuynate affects production of N-acyl homoserine lactone and quorum sensing-regulated genes expression in *Pseudomonas aeruginosa*. *Front. Microbiol.* 5, 635. doi: 10.3389/fmicb.2014.00635
- Wu, J., Wu, D., Zhao, Y., Si, Y., Mei, L., Shao, J., et al. (2020). Sodium New Houttuynate Inhibits *Candida albicans* Biofilm Formation by Inhibiting the Ras1-cAMP-Efg1 Pathway Revealed by RNA-seq. *Front. Microbiol.* 11, 2075. doi: 10.3389/fmicb.2020.02075
- Xiaoming, Z., Jiaqing, Y., Changfeng, Z., and Huijuan, C. (2012). Huanglianjiadu decoction against *Pseudomonas aeruginosa* biofilm and its synergistic antibacterial effect with azithromycin. *Chin. J. Exp. Traditional Med. Formulae* 18, 155–158. doi: 10.13422/J.Cnki.Syfx.2012.11.051
- Yang, Z., Yefei, Z., and Meixian, Z. (2016). Effects of sodium new houttuynate on replication and antibody growth and decline of newcastle disease virus. *Heilongjiang Anim. Husbandry Veterinary Medicine* 10, P.150–P.152. doi: 10.13881/j.cnki.hljxmsy.2016.0895
- Yefei, Z., and Meixian, Z. (2016). Effect of sodium new houttuynate nanoemulsion adjuvant on immune function of broilers. *J. Northwest Agriculture* 11, 1591–1596. doi: 10.7606/j.issn.1004-1389.2016.11.001
- Yumei, L., Hong, H., Lu, H., and Lingli, Z. (2012). Spectrographic study on structural confirmation of sodium new houttuynate. *China Pharmacy* 23, 1777–1779. doi: CNKI:SUN:ZGYA.0.2012-19-027
- Yuxin, C., Yongsheng, C., Chunmei, S., Zhibo, H., Yong, Z., Shengkang, L., et al. (2018). SOAPnuke: a MapReduce acceleration-supported software for integrated quality control and preprocessing of high-throughput sequencing data. *GigaScience* 1, 1. doi: 10.1093/gigascience/gix120

Conflict of Interest: The authors declare that the research was conducted in the absence of any commercial or financial relationships that could be construed as a potential conflict of interest.

Copyright © 2020 Zhao, Mei, Si, Wu, Shao, Wang, Yan, Wang and Wu. This is an open-access article distributed under the terms of the Creative Commons Attribution License (CC BY). The use, distribution or reproduction in other forums is permitted, provided the original author(s) and the copyright owner(s) are credited and that the original publication in this journal is cited, in accordance with accepted academic practice. No use, distribution or reproduction is permitted which does not comply with these terms.



Discovery of a Novel Natural Allosteric Inhibitor That Targets NDM-1 Against *Escherichia coli*

Yanan Yang^{1†}, Yan Guo^{2†}, Yonglin Zhou², Yawen Gao¹, Xiyan Wang¹, Jianfeng Wang^{2*} and Xiaodi Niu^{1*}

¹ College of Food Science and Engineering, Jilin University, Changchun, China, ² Key Laboratory of Zoonosis Research, Ministry of Education, College of Veterinary Medicine, Institute of Zoonosis, Jilin University, Changchun, China

OPEN ACCESS

Edited by:

Jamshed Iqbal,
COMSATS University Islamabad,
Pakistan

Reviewed by:

Hasan Ejaz,
Al Jouf University, Saudi Arabia
Kewu Yang,
Northwest University, China

*Correspondence:

Xiaodi Niu
niuxd@jlu.edu.cn
Jianfeng Wang
wjf927@jlu.edu.cn

[†]These authors have contributed
equally to this work

Specialty section:

This article was submitted to
Experimental Pharmacology
and Drug Discovery,
a section of the journal
Frontiers in Pharmacology

Received: 07 July 2020

Accepted: 07 September 2020

Published: 02 October 2020

Citation:

Yang Y, Guo Y, Zhou Y, Gao Y,
Wang X, Wang J and Niu X (2020)
Discovery of a Novel Natural Allosteric
Inhibitor That Targets NDM-1
Against *Escherichia coli*.
Front. Pharmacol. 11:581001.
doi: 10.3389/fphar.2020.581001

At present, the resistance of New Delhi metallo- β -lactamase-1 (NDM-1) to carbapenems and cephalosporins, one of the mechanisms of bacterial resistance against β -lactam antibiotics, poses a threat to human health. In this work, based on the virtual ligand screen method, we found that carnosic acid¹ (CA), a natural compound, exhibited a significant inhibitory effect against NDM-1 ($IC_{50} = 27.07 \mu M$). Although carnosic acid did not display direct antibacterial activity, the combination of carnosic acid and meropenem still showed bactericidal activity after the loss of bactericidal effect of meropenem. The experimental results showed that carnosic acid can enhance the antibacterial activity of meropenem against *Escherichia coli* ZC-YN3. To explore the inhibitory mechanism of carnosic acid against NDM-1, we performed the molecular dynamics simulation and binding energy calculation for the NDM-1-CA complex system. Notably, the 3D structure of the complex obtained from molecular modeling indicates that the binding region of carnosic acid with NDM-1 was not situated in the active region of protein. Due to binding to the allosteric pocket of carnosic acid, the active region conformation of NDM-1 was observed to have been altered. The distance from the active center of the NDM-1-CA complex was larger than that of the free protein, leading to loss of activity. Then, the mutation experiments showed that carnosic acid had lower inhibitory activity against mutated protein than wild-type proteins. Fluorescence experiments verified the results reported above. Thus, our data indicate that carnosic acid is a potential NDM-1 inhibitor and is a promising drug for the treatment of NDM-1 producing pathogens.

Keywords: metallo- β -lactamases, carnosic acid, molecular modeling, allosteric inhibitor, *Escherichia coli*

INTRODUCTION

The inhibition of bacterial infection has important implications for human health (al Jalali and Zeitlinger, 2018; Li et al., 2018; Shamriz and Shoenfeld, 2018). At present, β -lactam antibiotics, including penicillins (Liu et al., 2018a), carbapenems (Edwards and Betts, 2000), and cephalosporins (Paterson et al., 2001), have been widely used to treat bacterial infections (Essack, 2001). However,

¹ CA is carnosic acid.

extensive use of antibiotics has led to the continued spread of drug-resistance (Khan et al., 2017a). Widespread resistance mechanisms of bacteria have lowered the effectiveness of antibiotics, leading to a health crisis (Khan et al., 2017b).

In 2008, the enzyme New Delhi metallo- β -lactamase-1 (NDM-1) was first reported (Groundwater et al., 2016). It was isolated from *Klebsiella pneumoniae* in India and belonged to the B1 subclass MBLs (Brem et al., 2016). Currently, bacteria containing the NDM-1 gene are found in many regions (Johnson and Woodford, 2013; Tran et al., 2015; Heinz et al., 2019). NDM-1 has been shown to be resistant to β -lactamase inhibitors mainly due to its ability to hydrolyze the amide bond of β -lactam ring (King et al., 2012). Moreover, the resistance of pathogenic bacteria has created a great challenge to the treatment of diseases (Ejaz et al., 2020). Therefore, NDM-1 can be targeted to inhibit the resistance of pathogenic bacteria.

At present, NDM-1 is often found in *Escherichia coli* (Zhang et al., 2017). Various pathogenic *E. coli* strains can cause diseases such as human diarrhea (Shah et al., 2015), urinary infections, and blood infections (Tuem et al., 2018). In recent years, *E. coli* resistance in the population has increased (Wang X. Q. et al., 2015). In addition, the resistance of bacteria to antibiotics increases medical costs and threatens human health (Yang et al., 2017). NDM-1 plays an important part in the resistance mechanism of bacteria (Du et al., 2017). At present, *E. coli* producing NDM-1 have been found in many countries (Erb et al., 2007) and has been known to continuously spread (Nordmann et al., 2012). At the same time, the plasmid with blaNDM-1 in the patient can spread among different *Enterobacteriaceae* species (Martino et al., 2019). Therefore, it is important to find an effective drug that inhibits the resistance of NDM-1 producing *E. coli*.

Recently, several inhibitors of NDM-1 have been discovered and synthesized. Among the currently found inhibitors, captopril and its analogs may be the desirable candidates. Among them, the IC₅₀ values of D- and L-captopril for inhibiting NDM-1 in the hydrolysis of imipenem were 7.9 and 202.0 μ M, respectively. However, they had no effect on bacteria carrying carbapenemases (Chiou et al., 2015). Jian Zhang et al. found that Aspergillomarasmine A derivatives can inhibit NDM-1 and overcome antibiotic resistance (Zhang et al., 2017). Scott J. Hecker et al. found that cyclic boronic acid QPX7728 showed effective activity on β -lactamases including NDM-1 (Hecker et al., 2020). It also showed similar pharmacokinetics to β -lactam antibiotics in rats and had good oral bioavailability. In addition, Chen Cheng et al. found that disulfiram is a promising candidate for the development of NDM-1 inhibitors, which can covalently bind to NDM-1 by forming an S-S bond with Cys208 residue at the active site (Chen et al., 2020b). At the same time, some metal complexes (cisplatin and Palladium(II) complexes) (Chen et al., 2020a) and DNA aptamers (Khan et al., 2019) have also been found to have inhibitory effects on NDM-1. Among them, the metal complexes inhibited MBLs through a new inhibition mode, which binds to the Cys208 residue in the active site, causing Zn²⁺ to be replaced by other ions. Moreover, scholars have also discovered some natural inhibitors. Xuequan Wang et al. purchased 44 compounds through

virtual screening and found three new NDM-1 inhibitors with smaller IC₅₀ values (Wang X. Q. et al., 2015). The most effective inhibitor displayed an IC₅₀ value of 29.6 \pm 1.3 μ M. However, in these previous literatures, most of these inhibitors may be competitive inhibitors, and their binding regions are all located in the active sites of NDM-1, which can easily lead to multiple drug resistance. Consequently, the demand for novel non-competitive inhibitors of NDM-1 is increasing.

In our work, a natural compound carnosic acid (CA) was identified as an effective inhibitor against the bioactivity of NDM-1 using virtual screening. Molecular dynamics simulations and binding free energy calculations further revealed that the bioactivity of NDM-1 was effectively inhibited due to the binding of carnosic acid with the allosteric pocket. Furthermore, it was identified that carnosic acid can significantly increase the antibacterial activity of meropenem. These results indicate that carnosic acid has the potential to become the novel NDM-1 inhibitor.

MATERIALS AND METHODS

Bacterial Strains and Chemicals

The isopropyl β -D-thiogalactoside (IPTG) and kanamycin were purchased from Dalian Meilun Company (Dalian, China). The carnosic acid (\geq 98% pure), meropenem (\geq 87% pure) and other chemicals were obtained from the National Institutes for Food and Drug Control (Beijing, China). Dimethyl sulfoxide (DMSO) was purchased from Sigma-Aldrich (St. Louis, MO, USA). The bacterial strains used in this study are showed in **Table 1**.

Plasmid Construction of blaNDM-1 and Its Mutant

The coding sequence of the NDM-1 gene were amplified from genomic DNA of *E. coli* and digested with BamHI and XhoI. Subsequently, it was cloned into pET28a to generate plasmid pET28a-NDM-1. Plasmids encoding F46A-NDM-1, L65A-NDM-1, and T94A-NDM-1 were constructed using a QuikChange site-directed mutagenesis kit. The ligation product was transformed into competent *E. coli* DH5 α cells. All constructed strains were verified by PCR and DNA sequencing (Ali et al., 2018). The primer pairs used in the work are listed in **Table 2**. The NDM-1 primer came from the literature (Teng et al., 2019), and the other primers were designed in this experiment.

Protein Expression and Purification

The pET28a-NDM-1 plasmid was introduced into *E. coli* BL21 cells. The cells were cultured in the LB medium with kanamycin (50 μ g/ml) at 37°C. When the cells were grown to OD₆₀₀ = 0.6, the cells were added IPTG (1 mM final concentration) to induce

TABLE 1 | The bacterial strains list.

Strain	Relevant genotype	Source or Reference
<i>E. coli</i> BL21	Expression strain	Invitrogen
<i>E. coli</i> ZC-YN3	producing NDM-1	(Liu et al., 2018b)

TABLE 2 | Oligonucleotide primers used in this study.

Primer name	Oligonucleotide (5'–3')
NDM-1-F	GCGCGGATCCGTGCTGGTGGTCGATAC
NDM-1-R	GCGCCTCGAGTCAGCGCAGCTTGTCG
F46A-F	GAAACTGGCGACCAACGGGCGGCGATCTGTTTCCG
F46A-R	CGGAAACCAGATCGCCCGCCGTTGGTCGCCAGTTTC
L65A-F	CACACTTCTATCGCGACATGCCGGGTTTC
L65A-R	GAAACCCGGCATGTCCGCATAGGAAGTGTG
T94A-F	GATACCGCTGGGCGCGATGACCAGAC
T94A-R	GTCTGGTCATCCGCCAGGCGGTATC

protein expression and cultured overnight at 16°C. The cells were harvested by centrifugation at 10,000 rpm for 5 min and resuspended. Subsequently, the cells were sonicated and centrifuged at 10000 rpm for 1 h. The supernatant was applied to a Ni-NTA column and the non-specific binding proteins were removed with buffer (20 mM imidazole, Tris-HCl, pH 7.4). The target protein was eluted with buffer (200 mM imidazole, Tris-HCl, pH 7.4). The purified protein was concentrated and desalted (Hinchliffe et al., 2016).

Enzyme Inhibition Assays

According to the methodology of Liu et al. the enzyme and nitrocefin were mixed and incubated at 37°C for 10 min. Consequently, absorbance was measured at 492 nm in a microplate reader. The specific calculation method was obtained from the literature (Liu et al., 2018b).

Determination of Minimum Inhibitory Concentration (MIC), Growth Curves, and Time-Killing Assays

The minimum inhibitory concentration (MIC) of carnosic acid to *E. coli* was determined by the broth microdilution method according to the Clinical and Laboratory Standards Institute (CLSI) guidelines (CLSI, 2019). Specifically, the strain was co-cultured with various concentrations of meropenem (0–128 μ g/ml) and carnosic acid (0–128 μ g/ml) at 37°C for 18 to 24 h. To plot the growth curves, overnight cultured *E. coli* was enlarged (1:50) into fresh BHI broth and incubated for different lengths of time at 37°C with or without carnosic acid. The absorbance was measured at OD₆₀₀ (Liu et al., 2018b). The potential bactericidal effect of carnosic acid was tested using the time-killing assay. According to the literature (Lagerback et al., 2016), the bacteria were diluted to 5×10^5 CFU/ml and incubated with carnosic acid and meropenem. Samples were taken at specific time to determine the bacterial count to plot the time consumption curves.

Virtual Screening

The virtual screening was performed based on compound docking to the NDM-1 via Autodock vina software (Hu et al., 2015). Notably, approximately 143,758 natural compounds are available on the ZINC database (Sterling and Irwin, 2015). The ligand structure files (.sdf) downloaded in batches in the ZINC database were converted into 3D structure files (.pdbqt). The 3D structure of NDM-1 came from Protein Data Bank (PDB ID is 5JQJ), which serves as the target structure for virtual screening.

The Auto Dock tools was used to add polar hydrogen atoms to NDM-1. Subsequently, a grid box was constructed as the ligand docking site (center_x = -17.96 Å, center_y = -17.588Å, and center_z = 12.27 Å; and size_x = 22 Å, size_y = 28 Å, and size_z = 20 Å). Virtual screening of the natural compounds from the ZINC database was performed via compound docking to NDM-1 using AutoDock Vina software. The entire virtual screening calculation process used the Lamarckian (LGA) algorithm. The target protein NDM-1 was always rigid, and all twisted bonds of the inhibitor can rotate freely. The docking results were then sorted and filtered to function as the basis for the experimental investigations. The docking score for the ligands is the binding energy of compounds with NDM-1.

Molecular Docking

The structure of NDM-1 was derived from the Protein Data Bank with PDB encoded as 5JQJ. The initial structure of the free protein was obtained using a molecular simulation of 100 ns and subsequently used for molecular docking with the ligands. The structure of carnosic acid was optimized by Gaussian 03 program. The standard docking procedures for NDM-1 and carnosic acid were performed using Auto Dock4 software. The Lamarckian genetic algorithm (LGA) was used for the docking calculations. A total of 150 independent runs were carried out with a maximum of 25,000,000 energy evaluations and a population size of 300. A grid box of dimensions (40×40×40) with a spacing of 1 Å was created and centered on the mass center of the NDM-1. The detailed docking process was referenced from previous studies (Niu et al., 2017).

Molecular Dynamics Simulation

The molecular modeling of the interaction between NDM-1 and carnosic acid was carried out after docking as described in the above experimental method (Niu et al., 2017; Nikitina et al., 2018). The system was simulated for 100 ns using the Amber 99sb force field (Sakkiah et al., 2018) and the TIP3P water model (Lim et al., 2019). The free binding energy between NDM-1 and the ligand was calculated by the Molecular Mechanics/Generalized Born Surface Area (MM-GBSA) method (Liu et al., 2018b; Zeb et al., 2019; Nie et al., 2020).

Fluorescence-Quenching Assay

The binding constant (K_A) of the binding site of carnosic acid to wild type NDM-1 (WT-NDM-1), F46A-NDM-1, L65A-NDM-1, and T94A-NDM-1 was measured using a fluorescence quenching method. The binding energy was calculated according to the equation: $r/D_f = nK - rK$. This method referred to the previous literature (Wang J. F. et al., 2015), using an excitation wavelength of 280 nm and an emission wavelength of 345 nm.

Determination of Enzyme Reaction Rate

The principle of the measurement is mainly by using nitrocefin as an indicator, and its color changes from yellow to red with the increase of hydrolysis. NDM-1 (250 ng/ml) was incubated with various concentrations of carnosic acid in phosphate buffered saline, and then 50 μ g/ml of nitrocefin was added to the mixture

(Teng et al., 2019). The reaction rate was determined by continuously measuring the absorbance at OD_{492 nm} at different times (Krupyanko, 2009).

Statistical Analysis

The statistical analysis of the results was performed using a two-tailed Student's t-test. The difference was considered to be statistically significant when the P was less than 0.05.

RESULTS

The Carnosic Acid Inhibits the Activity of NDM-1

Based on the virtual screening approach, 8 commercially available compounds were tested by the enzyme inhibition assays. The results showed that carnosic acid had a significant effect on the NDM-1 activity *in vitro* (IC₅₀ = 27.07 μ M) (Figure 1A). As is shown in Figure 1B, when 8 μ g/ml of carnosic acid were added, the activity of the protein was seen to decrease by 48.56%, indicating that the drug significantly inhibited the protein. The protein treated with 32 μ g/ml carnosic acid displayed the least activity (19.85%).

The Carnosic Acid Potentiates Inhibitory Activity of Meropenem Against *E. coli*

It was found by MIC experiments that carnosic acid can improve the antibacterial effect of meropenem. As shown in Table 3 and Figure 2C, the combination of meropenem and carnosic acid reduced the MIC of meropenem against *E. coli* ZC-YN3 (producing NDM-1) by a factor of 4 compared to meropenem alone. It was worth noting that neither an effective bacteriostatic effect (MIC > 32 μ g/ml) nor inhibitory effect on the growth of *E. coli* ZC-YN3 (Figures 2A, C) by carnosic acid was observed in our experimental conditions.

To verify the above conclusion, the time-kill curves were analyzed. The results showed that the combination of carnosic acid and meropenem was more effective than meropenem alone (Figure 2B). After 2 hours, the inhibitory effect of meropenem and carnosic acid on *E. coli* was stronger than that of meropenem

TABLE 3 | MIC (μ g/ml) of meropenem against *E. coli*.

Strain	Meropenem	Combination
<i>E. coli</i> ZC-YN3 (NDM-1)	16	4

alone. After 4 hours, the inhibitory effect of meropenem alone on *E. coli* was weakened, but meropenem and carnosic acid still had a strong inhibitory effect.

Determination of the Binding Mode of NDM-1 With Carnosic Acid

To explore the binding mechanism of NDM-1 and carnosic acid, the protein structure was docked with the drug using AutoDock 4.0 as the initial structure. The lowest energy conformation was chosen for further study. As shown in Figure 3, the stable binding sites of ligand with NDM-1 obtained from MD simulation were placed very near the binding position based on the molecular docking. During the 100 ns simulation, the 3D structure of NDM-1-CA was obtained (Figure 4A) and the root-mean-square deviation (RMSD) value of the protein backbone was calculated (Figure 4B). Figure 4B shows that the NDM-1-CA structure tended to be stable during the last 50 ns simulation. During the simulation, the main binding affinity of the carnosic acid binding to NDM-1 was hydrogen bonding and hydrophobic interactions. Specifically, the side chains of Phe46, Tyr64, Leu65, Asp66, and Thr94 can form the strong interactions with carnosic acid, as shown in the 3D structure of the complex (Figure 4A). Subsequently, an energy decomposition analysis was performed to confirm the above results.

The energy contribution of the selected residues was summarized in Figure 5A. Phe46 with a ΔE_{vdw} of less than -0.8 kcal/mol and the Tyr64 and Asp66 residues were observed to exhibit a strong Van der Waals interaction with carnosic acid, as these residues were proximate to the carnosic acid. In addition, Phe46 was seen to provide a significant electrostatic contribution ($\Delta E_{ele} \leq -1.0$ kcal/mol). At the same time, the residues Tyr64, Leu65, Asp66, and Asp94 also displayed strong Van der Waals interactions with carnosic acid (with the $\Delta E_{total} = -1.0, -0.53, -1.15, \text{ and } -1.05$ kcal/mol, respectively). In addition, the average distances between the carnosic acid and different

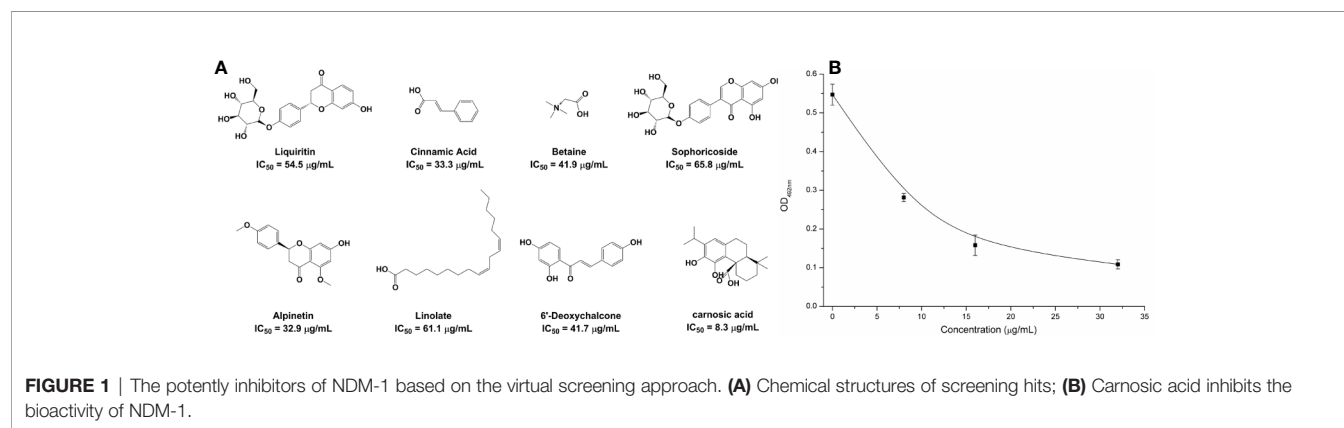


FIGURE 1 | The potentially inhibitors of NDM-1 based on the virtual screening approach. (A) Chemical structures of screening hits; (B) Carnosic acid inhibits the bioactivity of NDM-1.

residues of NDM-1 during the simulation were analyzed. As shown in **Figures 5B, C**, residues Phe46, Tyr64, Leu65, Asp66, and Thr94 were closer to carnosic acid than other residues, and the distance values < 0.2 nm (The distances between different groups are the distances between the center of mass of carnosic acid and the center of mass of residues of NDM-1 in this manuscript. The distances between the center of mass of different groups are not the real distances of different atoms.). These results indicated that residues of Phe46, Tyr64, Leu65,

Asp66, and Thr94 contributed to the major binding affinity for complex binding.

To detect the accuracy of the binding sites, the mutant complexes F46A-NDM-1, L65A-NDM-1, and T94A-NDM-1 as the initial structures were used in MD simulation. The MM-GBSA calculation predicted that the binding of F46A, L65A, and T94A to carnosic acid was weaker than WT-CA (F46A was -0.38 kcal/mol, L65A was -2.86 kcal/mol, and T94A was -1.77 kcal/mol), as shown in **Table 4**.

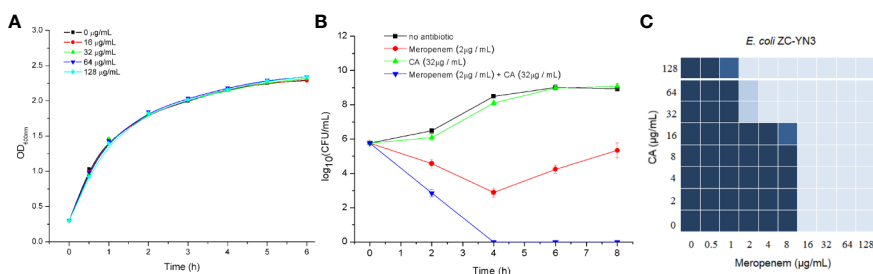


FIGURE 2 | The carnosic acid potentiates meropenem inhibitory activity against *E. coli*. **(A)** Growth curves of *E. coli* ZC-YN3 cultured with different concentrations of carnosic acid; **(B)** Time-kill curves of *E. coli* ZC-YN3 with the indicated treatment. These values are the average of three independent experiments; **(C)** The microdilution checkerboard analysis showed the combined effects of carnosic acid and meropenem on *E. coli* ZC-YN3. The data are the results of four independent experiments.

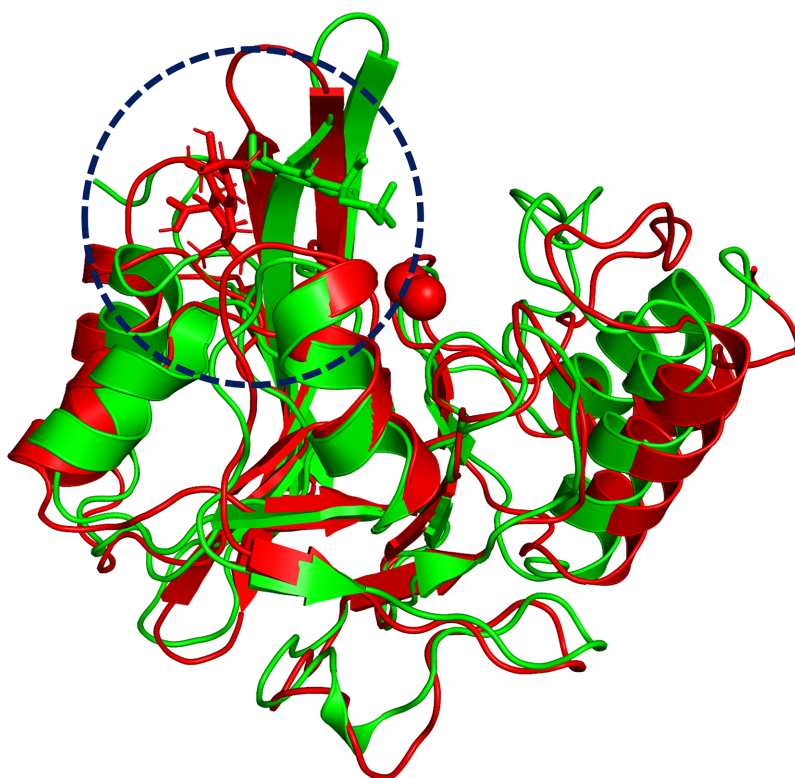


FIGURE 3 | The overlap structures of complex based on molecular docking (green molecule) and MD simulation (red molecule). The binding position of ligand obtained from molecular docking is very close to the binding region of ligand obtained from MD simulation. The binding regions of complexes is within the dashed line.

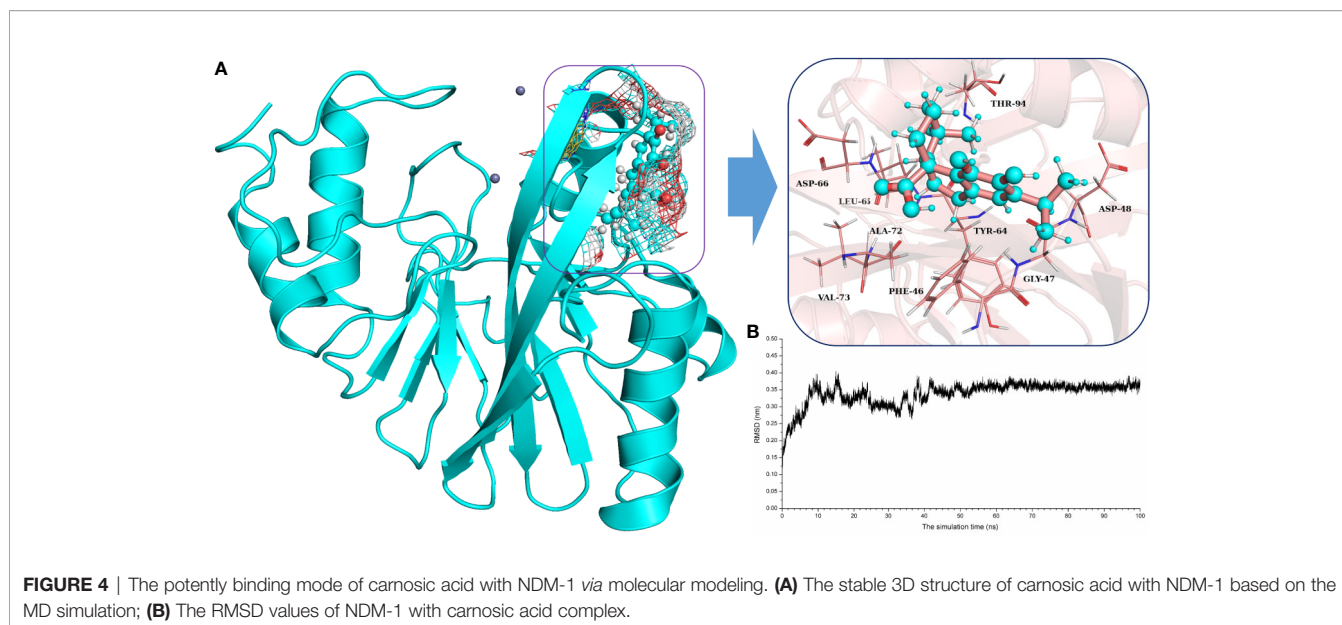


FIGURE 4 | The potentially binding mode of carnosic acid with NDM-1 via molecular modeling. **(A)** The stable 3D structure of carnosic acid with NDM-1 based on the MD simulation; **(B)** The RMSD values of NDM-1 with carnosic acid complex.

Furthermore, the interactions between carnosic acid and WT-NDM-1, F46A-NDM-1, L65A-NDM-1, and T94A-NDM-1 were investigated by fluorescence quenching. According to experimental results, the linear fitting plots of r/D_f vs. r between carnosic acid and WT-NDM-1, F46A-NDM-1, L65A-NDM-1, and T94A-NDM-1 can be made in **Figure 5D** and based on the plots the value of the binding constants, K , can be obtained and the binding constants were 0.45644, 0.12715, 0.33597, and 0.32911 $\text{ml} \cdot \mu\text{g}^{-1}$ for WT-NDM-1, F46A-NDM-1, L65A-NDM-1, and T94A-NDM-1. In **Table 4**, the binding constants of the interaction between carnosic acid and proteins decrease in the following order: WT > L65A > T94A > F46A at 300 K. It indicated that the binding of WT-NDM-1 with carnosic acid is stronger than those of mutants. The experimental results and theoretical results are in agreement (**Table 4**). Therefore, the residues of Phe46, Tyr64, Leu65, Asp66, and Thr94 played crucial roles in the binding of carnosic acid to NDM-1. Interestingly, residues of Phe46, Tyr64, Leu65, Asp66, and Thr94 are not located in the catalytic active region of NDM-1, which is binding sites of the substrate. This result implied that the inhibitory mechanism of carnosic acid against NDM-1 is not the competition with the substrate of NDM-1.

Subsequently, the inhibitory activity of carnosic acid against mutants was tested by the enzyme inhibition assays. In **Figure 5E**, the carnosic acid has no obvious effect on the activity of mutants. Moreover, the steady-state kinetics of the bioactivity of NDM-1 (wild type or mutants) treated with carnosic acid were shown in **Figure 5F**. As shown in **Figure 5F**, the reaction rates are 0.00742, 0.0225, 0.02164, and 0.02277 for WT-NDM-1, F46A, L65A, and T94A, respectively. These results shown that the bioactivity of mutants treated with carnosic acid has no obviously change compared with free WT-NDM-1, while the reaction rate of WT-NDM-1 decreased sharply when treated with carnosic acid. These results are consistent with the

thermodynamic results (**Figure 5E**), implying that carnosic acid has no obvious effect on the activity of mutants. The findings indicate that due to the mutation of residues, the binding affinity of carnosic acid with NDM-1 decreased, resulting in a loss of inhibitory activity. Therefore, the 3D structure of NDM-1-carnosic acid complex is reliable by MD simulation.

Meanwhile, the 100-ns molecular dynamics simulations were performed for the mutants. In **Figure 6A**, there was no significant change of the conformation between WT-protein and mutants through the molecular modeling. The binding sites of Zn^{2+} in the mutants were very similar to those of the WT-protein. In addition, the activities of WT-NDM-1 and its mutants were further determined using the same concentration. As expected, the mutated protein activity value deviation was within 10% compared with WT-NDM-1 (**Figure 6B**), suggesting that mutation of any of these residues did not affect the activity of NDM-1. In addition, the steady-state kinetics of WT-NDM-1 and mutants were provided. As shown in **Figure 6C**, the reaction rates are 0.01855, 0.0189, 0.01887, and 0.01891 for WT-NDM-1, F46A, L65A, and T94A, respectively. These results shown that the bioactivity of mutants has no obviously change compared with WT-NDM-1. Together, these results indicated that no significantly influence on structure or activity was observed for the site-directed mutation of F46A, L65A or T94A in NDM-1.

Analysis of Inhibition Mechanism

In the simulation, carnosic acid inhibited protein activity mainly by affecting the active region of NDM-1. Subsequently, the key movements of NDM-1 containing or not containing carnosic acid was explored by Principal Component Analysis (PCA) of the NDM-1-CA compound system. In **Figure 7A**, the active region was observed to have significant extensional motion to Zn^{2+} in the first element (PC1) and the second element (PC2) in

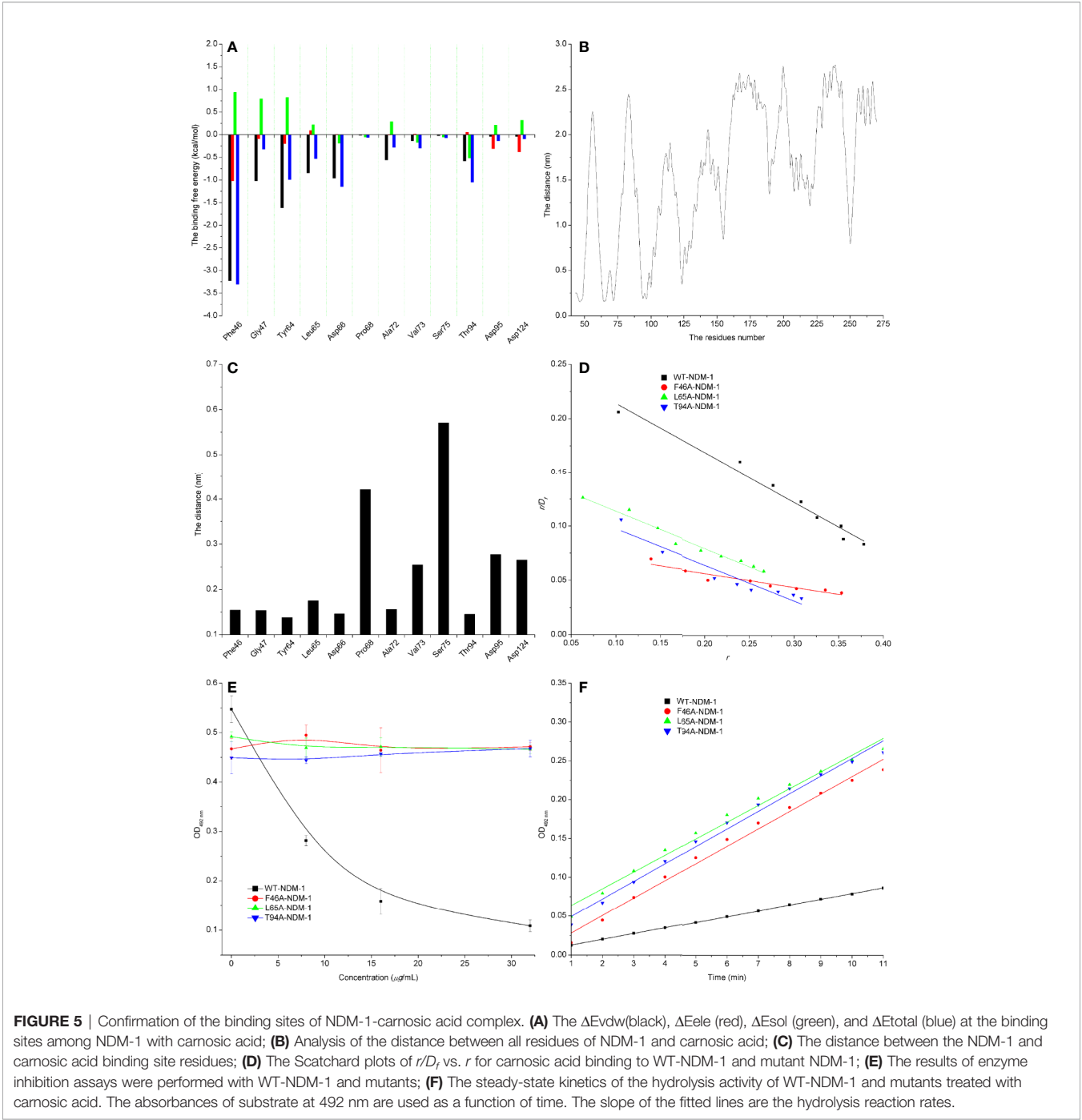


TABLE 4 | The binding free energy (kcal/mol) and binding constants of the WT-CA, F46A-CA, L65A-CA, and T94A-CA systems based on the fluorescence spectroscopy quenching method.

	WT-CA	F46A-CA	L65A-CA	T94A-CA
ΔG_{bind} (kcal/mol)	-12.16	-0.38	-2.86	-1.77
Binding constants K ml· μ g ⁻¹	0.45644	0.12715	0.33597	0.32911

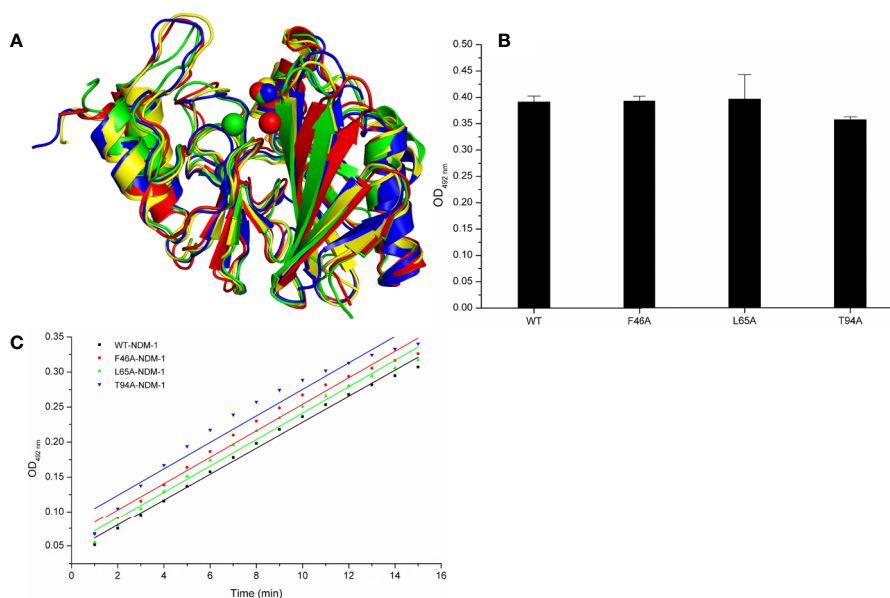


FIGURE 6 | The comparison of characterization between WT-protein and mutants. **(A)** The overlap stable structures of WT-protein (red), F46A (green), L65A (blue) and T94A (yellow); **(B)** The hydrolysis activities of WT-protein or mutants; **(C)** The steady-state kinetics of the hydrolysis activity of WT-NDM-1 and mutants.

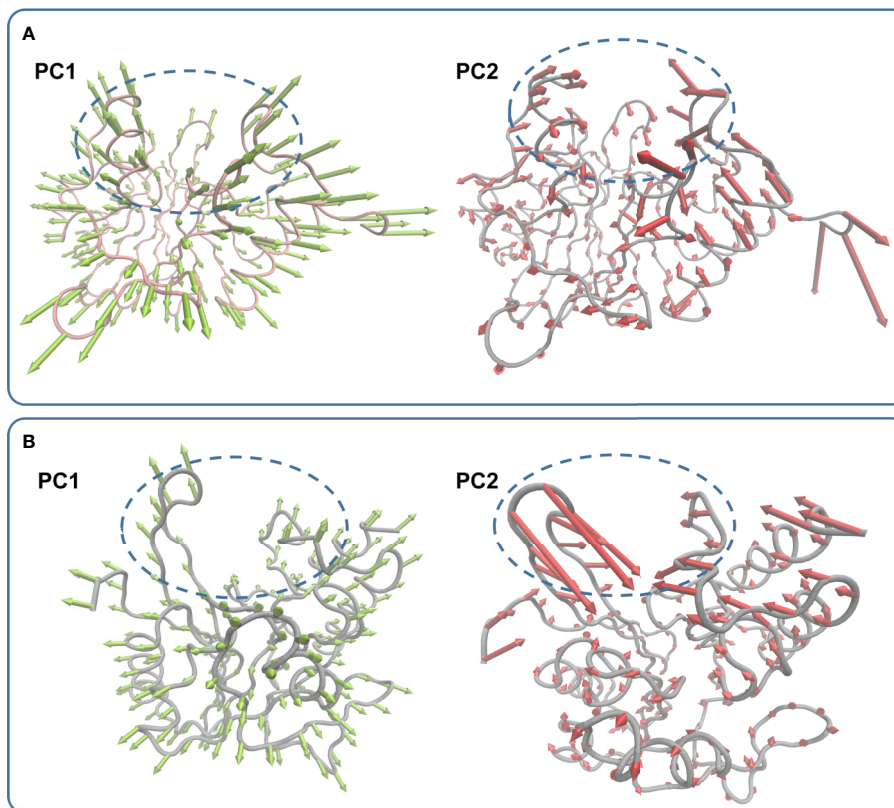


FIGURE 7 | Principal component analysis based on the simulation trajectory. The first and second principal components (PC1 and PC2) in the NDM-1-CA complex **(A)** and free NDM-1 **(B)** obtained by PCA are depicted as cones on the C α . The length of the cones represents the size of the movement.

the NDM-1-CA complex system. In addition, amino acid movement near the active region was obvious. Nevertheless, these two forms of motion were significantly impaired in PC1 and PC2 of free NDM-1 system in **Figure 7B**.

On the other hand, according to reports in literature (Guo et al., 2011), the NDM-1 active site was located in the loop region between Thr119-Met126 and Ser217-Asp225. Therefore, the change in the active region can be judged by calculating the loop region distance. As shown in **Figure 8**, the average distance from Thr119-Met126 to Ser217-Asp225 in the free NDM-1 system was 1.27 nm. However, in the complex system, the average distance of Thr119-Met126 to Ser217-Asp225 was 1.78 nm, respectively. Therefore, it was significantly different compared to the distance in the free system. This conformation changes of the active region of NDM-1 make the binding affinity of substrate with NDM-1 weaker, resulting in the catalytic activity loss of NDM-1. Thus, it can be seen residues of Phe46, Tyr64, Leu65, Asp66, and Thr94 are the allosteric sites of NDM-1, and carnosic acid is the novel allosteric inhibitor target NDM-1.

In 2013, Sohier et al. (2013) found that camelid nanobody can inhibit VIM metallo- β -lactamases. The inhibitor mainly bound to Loop 6 and the end of the $\alpha 2$ helix of VIM-4. The binding site of the complex was far from the active site, but it can change the substrate binding and catalytic properties of VIM-4. The residues of T107YVF110 contributed the major binding affinity for the ligand binding with the protein. In addition, DNA aptamer can be used as an allosteric inhibitor to bind Loop 4 and Loop 6 of 5/B/6 metallo- β -lactamase (Khan et al., 2019). In the complex, the binding sites of residues were Thr76, Lys78, Phe103, Lys104, Lys107, and Tyr208. In our work, the NDM-1-CA complex allosteric sites Phe46, Tyr64, Leu65, Asp66, and Thr94 were mainly located in L3 and $\alpha 1$ helix, which are obviously different with the results of the previous literatures (Sohier et al., 2013; Khan et al., 2019; **Supplementary Figure S1**). Therefore, we believed that the binding site of the NDM-1-CA complex is the novel allosteric site of NDM-1.

DISCUSSION

At present, the combination of antibiotics with β -lactamase inhibitors is an effective method for improving antibacterial activity (Everett et al., 2018). The inhibitors are comprised of chelates (Falconer et al., 2015), mildew products (Zhang et al., 2017), and analogs of chemicals (Yarlagadda et al., 2018). Venkateswarlu (Yarlagadda et al., 2018) established that vancomycin analogues restored meropenem activity against gram-negative pathogens. The inhibitor can penetrate the outer membrane of GNP and inactivate the enzyme by depleting metal ions (Zn^{2+}). However, many of these drugs are chemically synthesized and have not undergone clinical trials. Furthermore, these inhibitors are competitive inhibitors, which may contribute to the multidrug resistance. Therefore, the discovery of natural allosteric inhibitors that work against β -lactamase is the current need.

In this study, based on the virtual screening approach, we found that carnosic acid exhibited an inhibitory effect on NDM-1. Currently, carnosic acid has important applications in the fields of medicine, food, and cosmetics (Bauer et al., 2012). Scholars have revealed that the toxicity of carnosic acid is low. In the acute toxicity study, the oral lethal dose of mice was greater than 7000 mg/kg (Wang et al., 2012). It is noteworthy that food grade carnosic acid has appeared on the market (Masuda et al., 2002). At the same time, sources of carnosic acid are widely available, and it is convenient to manufacture (Birtic et al., 2015). Therefore, it has potential advantages as a clinical application inhibitor. It was established by MIC and time-killing assays that carnosic acid can restore the antibacterial activity of meropenem and inhibit NDM-1. We speculated that carnosic acid can improve the antibacterial ability of meropenem by inhibiting NDM-1. Contrary to other reported inhibitors, the results obtained from molecular modeling show that carnosic acid bound to NDM-1 *via* strong interaction with residues of Phe46, Tyr64, Leu65, Asp66, and Thr94. However, these residues are not in the active pocket of protein, implying that residues of Phe46, Tyr64, Leu65, Asp66, and Thr94 are the allosteric sites of NDM-1. Due to the binding of carnosic acid to the allosteric sites,

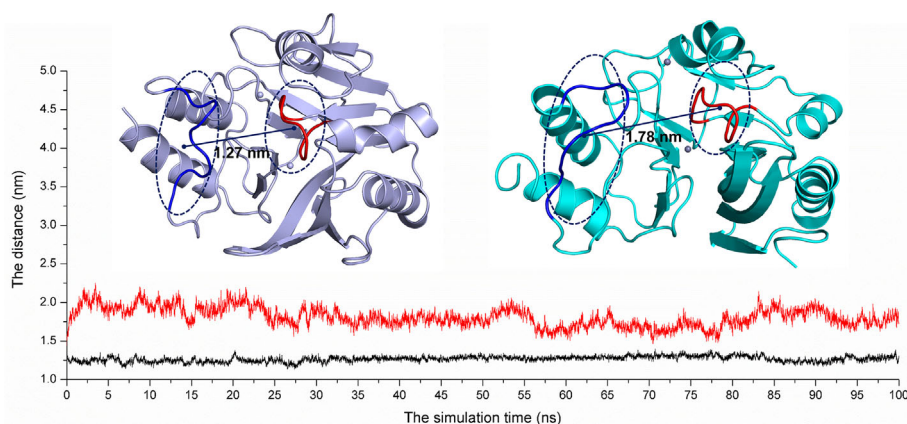


FIGURE 8 | The average distances from Thr119-Met126 to Ser217-Asp225 were calculated for the free NDM-1 system (black line) and the NDM-1-CA complex system (red line).

the conformation of the active sites of NDM-1 was altered, leading to the loss of bioactivity. Simultaneously, the fluorescence experiments confirmed this hypothesis. Therefore, these studies have contributed to the development and application of NDM-1 inhibitors.

DATA AVAILABILITY STATEMENT

The original contributions presented in the study are included in the article/**Supplementary Material**; further inquiries can be directed to the corresponding authors.

AUTHOR CONTRIBUTIONS

XN and JW designed the experiment. YY and YGu wrote the paper and conducted experiments. YZ and YGa assisted in the completion

of the experiment. XW conducted data collection. All authors contributed to the article and approved the submitted version.

FUNDING

The authors acknowledge the financial support from the National Nature Science Foundation of China [Grant no. 31872525 and 81861138046].

SUPPLEMENTARY MATERIAL

The Supplementary Material for this article can be found online at: <https://www.frontiersin.org/articles/10.3389/fphar.2020.581001/full#supplementary-material>

REFERENCES

- al Jalali, V., and Zeitlinger, M. (2018). Clinical Pharmacokinetics and Pharmacodynamics of Telavancin Compared with the Other Glycopeptides. *Clin. Pharmacokinet.* 57, 797–816.
- Ali, A., Azam, M. W., and Khan, A. U. (2018). Non-active site mutation (Q123A) in New Delhi metallo-beta-lactamase (NDM-1) enhanced its enzyme activity. *Int. J. Biol. Macromol.* 112, 1272–1277.
- Bauer, J., Kuehn, S., Rollinger, J. M., Scherer, O., Northoff, H., Stuppner, H., et al. (2012). Carnosol and Carnosic Acids from *Salvia officinalis* Inhibit Microsomal Prostaglandin E-2 Synthase-1. *J. Pharmacol. Exp. Ther.* 342, 169–176.
- Birtic, S., Dussort, P., Pierre, F. X., Bily, A. C., and Roller, M. (2015). Carnosic acid. *Phytochemistry* 115, 9–19.
- Brem, J., van Berkel, S. S., Zollman, D., Lee, S. Y., Gileadi, O., McHugh, P. J., et al. (2016). Structural Basis of Metallo-beta-Lactamase Inhibition by Captopril Stereoisomers. *Antimicrobial Agents Chemother.* 60, 142–150.
- Chen, C., Sun, L.-Y., Gao, H., Kang, P.-W., Li, J.-Q., Zhen, J.-B., et al. (2020a). Identification of Cisplatin and Palladium(II) Complexes as Potent Metallo- β -lactamase Inhibitors for Targeting Carbapenem-Resistant Enterobacteriaceae. *ACS Infect. Dis.* 6, 975–985.
- Chen, C., Yang, K.-W., Wu, L.-Y., Li, J.-Q., and Sun, L.-Y. (2020b). Disulfiram as a potent metallo-beta-lactamase inhibitor with dual functional mechanisms. *Chem. Commun.* 56, 2755–2758.
- Chiou, J., Wan, S., Chan, K.-F., So, P.-K., and He, D. (2015). Chan, E. W.-cEbselen as a potent covalent inhibitor of New Delhi metallo- β -lactamase (NDM-1). *Chem. Commun.* 51, 9543–9546.
- CLSI (2019). *M100. Performance Standards for Antimicrobial Susceptibility Testing*. 29th Edn (Wayne, PA: Clinical and Laboratory Standards Institute).
- Du, J., Li, B., Cao, J. M., Wu, Q., Chen, H. L., Hou, Y. B., et al. (2017). Molecular Characterization and Epidemiologic Study of NDM-1-Producing Extensively Drug-Resistant *Escherichia coli*. *Microbial Drug Resist.* 23, 272–279.
- Edwards, J. R., and Betts, M. J. (2000). Carbapenems: the pinnacle of the beta-lactam antibiotics or room for improvement? *J. Antimicrobial Chemother.* 45, 1–4.
- Ejaz, H., Alzahrani, B., Hamad, M. F. S., Abosalif, K. O. A., Junaid, K., Abdalla, A. E., et al. (2020). Molecular Analysis of the Antibiotic Resistant NDM-1 Gene in Clinical Isolates of Enterobacteriaceae. *Clin. Laboratory* 66, 409–417.
- Erb, A., Sturmer, T., Marre, R., and Brenner, H. (2007). Prevalence of antibiotic resistance in *Escherichia coli*: overview of geographical, temporal, and methodological variations. *Eur. J. Clin. Microbiol. Infect. Dis.* 26, 83–90.
- Essack, S. Y. (2001). The development of beta-lactam antibiotics in response to the evolution of beta-lactamases. *Pharm. Res.* 18, 1391–1399.
- Everett, M., Sprynski, N., Coelho, A., Castandet, J., Bayet, M., Bougnon, J., et al. (2018). Discovery of a Novel Metallo-beta-Lactamase Inhibitor That Potentiates Meropenem Activity against Carbapenem-Resistant Enterobacteriaceae. *Antimicrobial Agents Chemother.* 62, e00074–e00018.
- Falconer, S. B., Reid-Yu, S. A., King, A. M., Gehrke, S. S., Wang, W. L., Britten, J. F., et al. (2015). Zinc Chelation by a Small-Molecule Adjuvant Potentiates Meropenem Activity in Vivo against NDM-1-Producing *Klebsiella pneumoniae*. *ACS Infect. Dis.* 1, 533–543.
- Groundwater, P. W., Xu, S., Lai, F., Varadi, L., Tan, J., Perry, J. D., et al. (2016). New Delhi metallo-beta-lactamase-1: structure, inhibitors and detection of producers. *Future Med. Chem.* 8, 993–1012.
- Guo, Y., Wang, J., Niu, G., Shui, W., Sun, Y., Zhou, H., et al. (2011). A structural view of the antibiotic degradation enzyme NDM-1 from a superbug. *Protein Cell.* 2, 384–394.
- Hecker, S. J., Reddy, K. R., Lomovskaya, O., Griffith, D. C., Rubio-Aparicio, D., Nelson, K., et al. (2020). Discovery of Cyclic Boronic Acid QPX7728, an Ultrabroad-Spectrum Inhibitor of Serine and Metallo- β -lactamases. *J. Med. Chem.* 63, 7491–7507.
- Heinz, E., Ejaz, H., Bartholdson Scott, J., Wang, N., Gujran, S., Pickard, D., et al. (2019). Resistance mechanisms and population structure of highly drug resistant *Klebsiella* in Pakistan during the introduction of the carbapenemase NDM-1. *Sci. Rep.* 9, 2392–2944.
- Hinchliffe, P., Gonzalez, M. M., Mojica, M. F., Gonzalez, J. M., Castillo, V., Saiz, C., et al. (2016). Cross-class metallo-beta-lactamase inhibition by bisthiazolidines reveals multiple binding modes. *Proc. Natl. Acad. Sci. U. States A.* 113, E3745–E3754.
- Hu, B., Cui, F. C., Yin, F. P., Zeng, X. X., Sun, Y., and Li, Y. Q. (2015). Caffeoylquinic acids competitively inhibit pancreatic lipase through binding to the catalytic triad. *Int. J. Biol. Macromol.* 80, 529–535.
- Johnson, A. P., and Woodford, N. (2013). Global spread of antibiotic resistance: the example of New Delhi metallo-beta-lactamase (NDM)-mediated carbapenem resistance. *J. Med. Microbiol.* 62, 499–513.
- Khan, A. U., Ali, A., Danishuddin, S., Srivastava, G., and Sharma, A. (2017a). Potential inhibitors designed against NDM-1 type metallo-beta-lactamases: an attempt to enhance efficacies of antibiotics against multi-drug-resistant bacteria. *Sci. Rep.* 7, 9207–9220.
- Khan, A. U., Maryam, L., and Zarrilli, R. (2017b). Structure, Genetics and Worldwide Spread of New Delhi Metallo- β -lactamase (NDM): a threat to public health. *BMC Microbiol.* 17, 101–112.
- Khan, N. H., Bui, A. A., Xiao, Y., Sutton, R. B., Shaw, R. W., Wylie, B. J., et al. (2019). A DNA aptamer reveals an allosteric site for inhibition in metallo- β -lactamases. *PLoS One* 14, 1–19.
- King, D. T., Worrall, L. J., Gruninger, R., and Strynadka, N. C. J. (2012). New Delhi Metallo-beta-Lactamase: Structural Insights into beta-Lactam Recognition and Inhibition. *J. Am. Chem. Soc.* 134, 11362–11365.
- Krupyanko, V. I. (2009). Perspectives of Data Analysis of Enzyme Inhibition and Activation, Part 3: Equations for Calculation of the Initial Rates of Enzymatic Reactions. *J. Biochem. Mol. Toxicol.* 23, 108–118.
- Lagerback, P., Khine, W. W. T., Giske, C. G., and Tangden, T. (2016). Evaluation of antibacterial activities of colistin, rifampicin and meropenem combinations

- against NDM-1-producing *Klebsiella pneumoniae* in 24 h in vitro time-kill experiments. *J. Antimicrobial Chemother.* 71, 2321–2325.
- Li, X., Wu, B., Chen, H., Nan, K. H., Jin, Y. Y., Sun, L., et al. (2018). Recent developments in smart antibacterial surfaces to inhibit biofilm formation and bacterial infections. *J. Mater. Chem. B*, 6, 4274–4292.
- Lim, H., Jin, X., Kim, J., Hwang, S., Shin, K. B., Choi, J., et al. (2019). Investigation of Hot Spot Region in XIAP Inhibitor Binding Site by Fragment Molecular Orbital Method. *Comput. Struct. Biotechnol. J.* 17, 1217–1225.
- Liu, S., Jing, L., Yu, Z.-J., Wu, C., Zheng, Y., Zhang, E., et al. (2018a). ((S)-3-Mercapto-2-methylpropanamido)acetic acid derivatives as metallo-beta-lactamase inhibitors: Synthesis, kinetic and crystallographic studies. *Eur. J. Med. Chem.* 145, 649–660.
- Liu, S., Zhou, Y., Niu, X., Wang, T., Li, J., Liu, Z., et al. (2018b). Magnolol restores the activity of meropenem against NDM-1-producing *Escherichia coli* by inhibiting the activity of metallo-beta-lactamase. *Cell Death Discovery* 4, 28–35.
- Martino, F., Tijet, N., Melano, R., Petroni, A., Heinz, E., De Belder, D., et al. (2019). Isolation of five Enterobacteriaceae species harbouring blaNDM-1 and mcr-1 plasmids from a single paediatric patient. *PLoS One* 14, 1–13.
- Masuda, T., Inaba, Y., Maekawa, T., Takeda, Y., Tamura, H., and Yamaguchi, H. (2002). Recovery mechanism of the antioxidant activity from carnosic acid quinone, an oxidized sage and rosemary antioxidant. *J. Agric. Food Chem.* 50, 5863–5869.
- Nie, R. Z., Huo, Y. Q., Yu, B., Liu, C. J., Zhou, R., Bao, H. H., et al. (2020). Molecular insights into the inhibitory mechanisms of gallate moiety on the A beta(1-40) amyloid aggregation: A molecular dynamics simulation study. *Int. J. Biol. Macromol.* 156, 40–50.
- Nikitina, L. E., Kiselev, S. V., Startseva, V. A., Bodrov, A. V., Azizova, Z. R., Shipina, O. T., et al. (2018). Sulfur-Containing Monoterpenoids as Potential Antithrombotic Drugs: Research in the Molecular Mechanism of Coagulation Activity Using Pinanyl Sulfoxide as an Example. *Front. Pharmacol.* 9, 116–127.
- Niu, X. D., Yang, Y. N., Song, M., Wang, G. Z., Sun, L., Gao, Y. W., et al. (2017). Insight into the novel inhibition mechanism of apigenin to Pneumolysin by molecular modeling. *Chem. Phys. Lett.* 687, 85–90.
- Nordmann, P., Couard, J. P., Sansot, D., and Poirel, L. (2012). Emergence of an Autochthonous and Community-Acquired NDM-1-Producing *Klebsiella pneumoniae* in Europe. *Clin. Infect. Dis.* 54, 150–151.
- Paterson, D. L., Ko, W. C., Von Gottberg, A., Casellas, J. M., Mulazimoglu, L., Klugman, K. P., et al. (2001). Outcome of cephalosporin treatment for serious infections due to apparently susceptible organisms producing extended-spectrum beta-lactamases: Implications for the clinical microbiology laboratory. *J. Clin. Microbiol.* 39, 2206–2212.
- Sakkiah, S., Kusko, R., Pan, B. H., Guo, W. J., Ge, W. G., Tong, W. D., et al. (2018). Structural Changes Due to Antagonist Binding in Ligand Binding Pocket of Androgen Receptor Elucidated Through Molecular Dynamics Simulations. *Front. Pharmacol.* 9, 492–514.
- Shah, M. S., Eppinger, M., Ahmed, S., Shah, A. A., Hameed, A., and Hasan, F. (2015). Multidrug-resistant diarrheagenic E-coli pathotypes are associated with ready-to-eat salad and vegetables in Pakistan. *J. Korean Soc. Appl. Biol. Chem.* 58, 267–273.
- Shamriz, O., and Shoenfeld, Y. (2018). Infections: a double-edge sword in autoimmunity. *Curr. Opin. Rheumatol.* 30, 365–372.
- Sohier, J. S., Laurent, C., Chevigne, A., Pardon, E., Srinivasan, V., Wernery, U., et al. (2013). Allosteric inhibition of VIM metallo-beta-lactamases by a carnellid nanobody. *Biochem. J.* 450, 477–486.
- Sterling, T., and Irwin, J. J. (2015). ZINC 15-Ligand Discovery for Everyone. *J. Chem. Inf. Model.* 55, 2324–2337.
- Teng, Z., Guo, Y., Liu, X., Zhang, J., Niu, X., Yu, Q., et al. (2019). Theaflavin-3,3-digallate increases the antibacterial activity of beta-lactam antibiotics by inhibiting metallo-beta-lactamase activity. *J. Cell Mol. Med.* 23, 6955–6964.
- Tran, H. H., Ehsani, S., Shibayama, K., Matsui, M., Suzuki, S., Nguyen, M. B., et al. (2015). Common isolation of New Delhi metallo-beta-lactamase 1-producing Enterobacteriaceae in a large surgical hospital in Vietnam. *Eur. J. Clin. Microbiol. Infect. Dis.* 34, 1247–1254.
- Tuem, K. B., Gebre, A. K., Atey, T. M., Bitew, H., Yimer, E. M., and Berhe, D. F. (2018). Drug Resistance Patterns of *Escherichia coli* in Ethiopia: A Meta-Analysis. *BioMed. Res. Int.* 2018, 1–13.
- Wang, Q. L., Li, H., Li, X. X., Cui, C. Y., Wang, R., Yu, N. X., et al. (2012). Acute and 30-day oral toxicity studies of administered carnosic acid. *Food Chem. Toxicol.* 50, 4348–4355.
- Wang, J. F., Zhou, X., Liu, S., Li, G., Zhang, B., Deng, X. M., et al. (2015). Novel inhibitor discovery and the conformational analysis of inhibitors of listeriolysin O via protein-ligand modeling. *Sci. Rep.* 5, 8864–8870.
- Wang, X. Q., Lu, M. L., Shi, Y., Ou, Y., and Cheng, X. D. (2015). Discovery of Novel New Delhi Metallo-beta-Lactamases-1 Inhibitors by Multistep Virtual Screening. *PLoS One* 10, 1–17.
- Yang, S.-C., Lin, C.-H., Aljuffali, I. A., and Fang, J.-Y. (2017). Current pathogenic *Escherichia coli* foodborne outbreak cases and therapy development. *Arch. Microbiol.* 199, 811–825.
- Yarlagadda, V., Sarkar, P., Samaddar, S., Manjunath, G. B., Mitra, S. D., Paramanandham, K., et al. (2018). Vancomycin Analogue Restores Meropenem Activity against NDM-1 Gram-Negative Pathogens. *ACS Infect. Dis.* 4, 1093–1101.
- Zeb, A., Son, M., Yoon, S., Kim, J. H., Park, S. J., and Lee, K. W. (2019). Computational Simulations Identified Two Candidate Inhibitors of Cdk5/p25 to Abrogate Tau-associated Neurological Disorders. *Comput. Struct. Biotechnol. J.* 17, 579–590.
- Zhang, J., Wang, S. S., Wei, Q., Guo, Q. Q., Bai, Y. J., Yang, S. Q., et al. (2017). Synthesis and biological evaluation of Aspergillomarasmine A derivatives as novel NDM-1 inhibitor to overcome antibiotics resistance. *Bioorg. Med. Chem.* 25, 5133–5141.

Conflict of Interest: The authors declare that the research was conducted in the absence of any commercial or financial relationships that could be construed as a potential conflict of interest.

Copyright © 2020 Yang, Guo, Zhou, Gao, Wang, Wang and Niu. This is an open-access article distributed under the terms of the Creative Commons Attribution License (CC BY). The use, distribution or reproduction in other forums is permitted, provided the original author(s) and the copyright owner(s) are credited and that the original publication in this journal is cited, in accordance with accepted academic practice. No use, distribution or reproduction is permitted which does not comply with these terms.



Functionalized Oxoindolin Hydrazine Carbothioamide Derivatives as Highly Potent Inhibitors of Nucleoside Triphosphate Diphosphohydrolases

Saira Afzal¹, Mariya al-Rashida², Abdul Hameed¹, Julie Pelletier³, Jean Sévigny^{3,4} and Jamshed Iqbal^{1*}

¹Centre for Advanced Drug Research, COMSATS University Islamabad, Abbottabad Campus, Abbottabad, Pakistan,

²Department of Chemistry, Forman Christian College (A Chartered University), Lahore, Pakistan, ³Centre de Recherche du CHU de Québec–Université Laval, Québec City, QC, Canada, ⁴Département de Microbiologie-Infectiologie et d'Immunologie, Faculté de Médecine, Université Laval, Québec City, QC, Canada

OPEN ACCESS

Edited by:

Salvatore Salomone,
University of Catania, Italy

Reviewed by:

Dunja Drakulic,
University of Belgrade, Serbia
Terence L. Kirley,
University of Cincinnati, United States
Andreia Machado Cardoso,
Universidade Federal Da Fronteira Sul,
Brazil

*Correspondence:

Jamshed Iqbal
jamshediqb@googlemail.com

Specialty section:

This article was submitted to
Experimental Pharmacology and
Drug Discovery,
a section of the journal
Frontiers in Pharmacology

Received: 21 July 2020

Accepted: 13 October 2020

Published: 30 November 2020

Citation:

Afzal S, al-Rashida M, Hameed A,
Pelletier J, Sévigny J and Iqbal J (2020)
Functionalized Oxoindolin Hydrazine
Carbothioamide Derivatives as Highly
Potent Inhibitors of Nucleoside
Triphosphate Diphosphohydrolases.
Front. Phar. 11:585876.
doi: 10.3389/fphar.2020.585876

Ectonucleoside triphosphate diphosphohydrolases (NTPDases) are ectoenzymes that play an important role in the hydrolysis of nucleoside triphosphate and diphosphate to nucleoside monophosphate. NTPDase1, -2, -3 and -8 are the membrane bound members of this enzyme family that are responsible for regulating the levels of nucleotides in extracellular environment. However, the pathophysiological functions of these enzymes are not fully understood due to lack of potent and selective NTPDase inhibitors. Herein, a series of oxoindolin hydrazine carbothioamide derivatives is synthesized and screened for NTPDase inhibitory activity. Four compounds were identified as selective inhibitors of *h*-NTPDase1 having IC₅₀ values in lower micromolar range, these include compounds **8b** (IC₅₀ = 0.29 ± 0.02 μM), **8e** (IC₅₀ = 0.15 ± 0.009 μM), **8f** (IC₅₀ = 0.24 ± 0.01 μM) and **8i** (IC₅₀ = 0.30 ± 0.03 μM). Similarly, compound **8k** (IC₅₀ = 0.16 ± 0.01 μM) was found to be a selective *h*-NTPDase2 inhibitor. In case of *h*-NTPDase3, most potent inhibitors were compounds **8c** (IC₅₀ = 0.19 ± 0.02 μM) and **8m** (IC₅₀ = 0.38 ± 0.03 μM). Since NTPDase3 has been reported to be associated with the regulation of insulin secretion, we evaluated our synthesized NTPDase3 inhibitors for their ability to stimulate insulin secretion in isolated mice islets. Promising results were obtained showing that compound **8m** potently stimulated insulin secretion without affecting the NTPDase3 gene expression. Molecular docking studies of the most potent compounds were also carried out to rationalize binding site interactions. Hence, these compounds are useful tools to study the role of NTPDase3 in insulin secretion.

Keywords: carbothioamide, ectonucleotidases, nucleoside triphosphate diphosphohydrolase-3, oxoindolin hydrazine, molecular docking

INTRODUCTION

Glucose acts as a natural insulin secretagogue and maintains the blood glucose level. In response to an increase in blood glucose level, pancreatic beta cells release insulin to maintain glucose levels (Chen et al., 2018; Stuhlmann et al., 2018). However, this insulin secretion is not an isolated event, and is followed by release of other important components like peptides, Zn²⁺, adenosine triphosphate (ATP) and other related nucleotides (Tozzi et al., 2018; Vakilian et al., 2019).

Among them, ATP is an important signaling molecule that amplifies the glucose stimulated insulin secretion by activating purinergic (P2X and P2Y) receptors, present on the surface of β -cell membrane (Cieřlak and Cieřlak, 2017). P2X receptors are ionotropic receptors that are subdivided into seven types (P2X1 to P2X7). They have been associated with the transmembrane flow of cations such as Na^+ , Ca^{+2} , and K^+ ions (Kasuya et al., 2017a; Kasuya et al., 2017b; Giuliani et al., 2019). On the other hand, P2Y receptors are metabotropic receptors that are subdivided into eight types (P2Y₁, P2Y₂, P2Y₄, P2Y₆, P2Y₁₁, P2Y₁₂, P2Y₁₃, and P2Y₁₄) and have been linked to Ca^{+2} mobilization and generation or inhibition of cyclic adenosine monophosphate (cAMP) (Dou et al., 2018; Lu et al., 2019). In pancreatic β -cells, both receptor types have been reported to be involved in the regulation of insulin secretion; however, their mode of action is slightly different (Galicia-Garcia et al., 2020). In this regard, P2X receptor activation by ATP leads to Ca^{+2} flux that is believed to be responsible for P2X-mediated insulin secretion (Solini and Novak, 2019). Whereas, activation of P2Y receptors stimulates the inositol triphosphate, which in turn results in transient elevation of intracellular concentration of Ca^{+2} (Bartley et al., 2019).

The extracellular levels of ATP and related nucleotides are controlled by a cascade of enzymes known as ectonucleotidases. This enzymatic cascade is composed of four main families, including NTPDases (ectonucleoside triphosphate diphosphohydrolases), APs or ALPs (alkaline phosphatases), NPPs (nucleotide pyrophosphatases/phosphodiesterases) and e-5'-NT (ecto-5'-nucleotidase) (Lee et al., 2017; Lee and Müller, 2017; Tozzi and Novak, 2017; Grković et al., 2019; Nabinger et al., 2020). These are plasma membrane bound ecto-enzymes and regulate the availability of ligands (nucleotides and hydrolysis products thereof) for P1 and P2 receptors. Among them, NTPDase is an important member contributing to the hydrolysis of nucleoside tri- and diphosphates (Longhi et al., 2017; Bagatini et al., 2018). The NTPDase family comprises of eight members or isozymes (NTPDase1-8), these isozymes differ in their catalytic properties and show varying substrate preference (Allard et al., 2017; Zhong et al., 2017). NTPDase1, -2, -3, and -8 are membrane bound isoforms that play an important role in purinergic signaling (Castilhos et al., 2018; Bertoni et al., 2020) whereas NTPDase4, -5, -6, and -7 are expressed within intracellular organelles (Zhong et al., 2017; Paes-Vieira et al., 2018).

NTPDase3 is abundantly present in the pancreatic β -cells where it has been reported to play an important role in the regulation of insulin secretion (Bartley et al., 2019; Saunders et al., 2019). In this context, a study was conducted where 1-naphthol-3, 6-disulfonic acid (BG0136) and 8,8'-[Carbonylbis(imino-4,1-phenylenecarbonylimino-4,1-phenylenecarbonylimino)]bis-1, 3,5-naphthalenetrisulfonic acid (NF279) were used to explore the role of NTPDase3 in insulin secretion (Lavoie et al., 2010). Similarly, in another study 6-*N,N*-Diethyl-D- β - γ -dibromomethylene adenosine triphosphate (ARL67156) was used for this purpose and it was found that NTPDase3 was involved in the modulation of insulin release (Syed et al., 2013). These data highlight the potential (important) role of NTPDase3 in insulin secretion and necessitate

the need for further detailed investigations to support these claims. However, to the best of our knowledge, there is still a lack of studies focusing on this aspect of NTPDase3. Keeping in view this scarcity of data, we synthesized a class of oxoindolin hydrazine carbothioamide derivatives as NTPDase inhibitors. The NTPDase3 inhibitors were further analyzed for their effects on insulin secretion in mice pancreatic islets.

MATERIALS AND METHODS

Chemical Synthesis

General Comments

All reagents were obtained from commercial sources and used without further purification, unless stated otherwise. Reaction progress was monitored by thin layer chromatography, using aluminum sheets precoated with silica gel 60 F₂₅₄ (200 μm , Merck, Darmstadt, Germany). Melting points were determined on Weiss Gallenkamp melting point apparatus (Loughborough, England) and are uncorrected. IR spectra were recorded on Perkin Elmer BX-II spectrometer (Waltham, United States). ¹H and ¹³C spectra were obtained using Bruker AM-300 spectrophotometer (Billerica, United States). Chemical shifts were described in parts per million. Mass spectra were recorded on an Applied Biosystems API 2000 mass spectrometer (Darmstadt, Germany).

General Procedure for the Synthesis of Substituted Phenylhydrazine Carbothioamides (7a-m)

Excess of hydrazine hydrate was dissolved in ethanol and a solution of appropriate isothiocyanate (1 mMol) was prepared in ethanol. The isothiocyanate solution was added drop wise to hydrazine solution. The reaction was conducted on ice bath and stirred for half an hour. During the course of reaction, precipitates were formed which were filtered, washed and then dried.

General Procedure for the Synthesis of Oxoindolin-Ylidene Phenylhydrazine Carbothioamides (8a-m)

A solution of isatin (1 mMol, 0.147 g) was prepared in ethanol and few drops of acetic acid were added. Resulting solution was refluxed for 4 to 5 h with equimolar amount of an appropriate intermediate (7a-m), synthesized during last step. Progress of reaction was monitored by thin layer chromatography. At the end of reaction, the precipitated solid was filtered and washed with ethanol (Pervez et al., 2009).

(Z)-2-(2-oxoindolin-3-ylidene)-*N*-phenylhydrazine-1-carbothioamide (8a)

Obtained as yellow solid, Yield = 78%, mp = 245–247°C; IR (KBR): 3,280–3,172 (NH stretching), 1,691 (C = O), 1,603 (C = N), 1,560 (NH bending), 1,161 (C = S), cm^{-1} ; ¹H-NMR (300 MHz, DMSO-*d*₆): δ (ppm) 12.80 (s, 1H, N-H), 11.26 (s, 1H, N-H), 10.82 (s, 1H, N-H), 7.78 (d, *J* = 7.2, 1H, Ar-H), 7.61 (d, *J* = 7.8, 2H, Ar-H), 7.39 (m, 3H, Ar-H), 7.27 (t, *J* = 7.35, 1H, Ar-H) 7.11 (t, *J* = 7.5, 1H, Ar-H), 6.95 (d, *J* = 7.8, 1H, Ar-H); ¹³C-NMR (75 MHz, DMSO-*d*₆) δ (ppm): 175.60, 163.10, 146.23, 135.16, 132.88, 131.10, 128.06, 126.23, 125.45, 123.12, 122.18, 120.05, 111.67;

LC-MS (m/z): positive mode 297 $[M + H]^+$. Purity determined by HPLC-UV (254 nm)-ESI-MS: 97.26%

(*Z*)-*N*-(4-nitrophenyl)-2-(2-oxoindolin-3-ylidene)hydrazine-1-carbothioamide (8b)

Obtained as yellow solid, Yield = 86%, mp = 271–272°C; IR (KBR): 3,315–3,222 (NH stretching), 1,694 (C = O), 1,600 (C = N), 1,556 (NH bending), 1,168 (C = S), cm^{-1} ; **¹H-NMR** (300 MHz, DMSO-*d*₆): δ (ppm) 13.01 (s, 1H, N-H), 11.31 (s, 1H, N-H), 11.12 (s, 1H, N-H), 8.29 (m, 2H, Ar-H), 8.09 (m, 2H, Ar-H), 7.78 (d, J = 7.2, 1H, Ar-H), 7.40 (td, J = 7.8, 1.2 Hz, 1H, Ar-H), 7.13 (t, J = 7.5, 1H, Ar-H), 6.96 (d, J = 7.8, 1H, Ar-H); **¹³C-NMR** (75 MHz, DMSO-*d*₆) δ (ppm): 176.53, 163.20, 145.12, 144.60, 143.24, 133.79, 132.30, 125.24, 124.47, 122.93, 122.07, 120.15, 111.69; **LC-MS** (m/z): positive mode 342 $[M + H]^+$. Purity determined by HPLC-UV (254 nm)-ESI-MS: 97.18%

(*Z*)-*N*-(4-chlorophenyl)-2-(2-oxoindolin-3-ylidene)hydrazine-1-carbothioamide (8c)

Obtained as yellow solid, Yield = 85% mp = 240–244°C; IR (KBR): 3,315–3,210 (NH stretching), 1,692 (C = O), 1,591 (C = N), 1,527 (NH bending), 1,164 (C = S), cm^{-1} ; **¹H-NMR** (300 MHz, DMSO-*d*₆): δ (ppm) 12.84 (s, 1H, N-H), 11.27 (s, 1H, N-H), 10.86 (s, 1H, N-H), 7.76 (d, J = 7.2, 1H, Ar-H), 7.66 (m, 2H, Ar-H), 7.49 (m, 2H, Ar-H), 7.37 (td, J = 7.65, 1.1, 1H, Ar-H), 7.11 (td, J = 7.5, 0.7, 1H, Ar-H), 6.94 (d, J = 7.8, 1H, Ar-H); **¹³C-NMR** (75 MHz, DMSO-*d*₆) δ (ppm): 176.86, 163.17, 143.04, 137.92, 133.06, 132.01, 130.56, 128.79, 127.79, 122.86, 121.88, 120.30, 111.60; **LC-MS** (m/z): positive mode 331 $[M + H]^+$. Purity determined by HPLC-UV (254 nm)-ESI-MS: 95.63%

(*Z*)-*N*-(4-fluorophenyl)-2-(2-oxoindolin-3-ylidene)hydrazine-1-carbothioamide (8d)

Obtained as yellow solid, Yield = 87%, mp = 255–256°C; IR (KBR): 3,290–3,185 (NH stretching), 1,694 (C = O), 1,610 (C = N), 1,560 (NH bending), 1,166 (C = S), cm^{-1} ; **¹H-NMR** (300 MHz, DMSO-*d*₆): δ (ppm) 12.81 (s, 1H, N-H), 11.27 (s, 1H, N-H), 10.83 (s, 1H, N-H), 7.75 (d, J = 7.5, 1H, Ar-H), 7.60 (dd, J = 8.7, 5.1, 2H, Ar-H), 7.37 (t, J = 7.35, 1H, Ar-H), 7.26 (t, J = 8.85, 2H, Ar-H), 7.11 (t, J = 7.5, 1H, Ar-H), 6.94 (d, J = 7.8, 1H, Ar-H); **¹³C-NMR** (75 MHz, DMSO-*d*₆) δ (ppm): 177.20, 162.10, 158.88, 142.99, 135.26, 132.89, 131.95, 128.52, 122.86, 121.82, 120.35, 115.74, 111.58; **LC-MS** (m/z): positive mode 315 $[M + H]^+$. Purity determined by HPLC-UV (254 nm)-ESI-MS: 98.93%

(*Z*)-*N*-(3-methoxyphenyl)-2-(2-oxoindolin-3-ylidene)hydrazine-1-carbothioamide (8e)

Obtained as yellow solid, Yield = 80%, mp = 220–224°C; IR (KBR): 3,240–3,189 (NH stretching), 1,690 (C = O), 1,595 (C = N), 1,526 (NH bending), 1,161 (C = S), cm^{-1} ; **¹H-NMR** (300 MHz, DMSO-*d*₆): δ (ppm) 12.80 (s, 1H, N-H), 11.27 (s, 1H, N-H), 10.77 (s, 1H, N-H), 7.79 (d, J = 7.5, 1H, Ar-H), 7.35 (m, 3H, Ar-H), 7.24 (d, J = 7.2, 1H, Ar-H), 7.11 (t, J = 7.5, 2H, Ar-H), 6.94 (d, J = 7.8, 1H, Ar-H), 6.85 (dd, J = 8.1, 2.4, 1H, Ar-H); **¹³C-NMR** (75 MHz, DMSO-*d*₆) δ (ppm): 176.49, 163.17, 159.64, 142.97, 139.99, 132.77, 131.92, 129.59, 127.55, 122.83, 121.92, 120.35, 118.0, 112.0, 111.55, 55.69; **LC-MS** (m/z): positive mode 327 $[M + H]^+$. Purity determined by HPLC-UV (254 nm)-ESI-MS: 99.02%

(*Z*)-*N*-benzyl-2-(2-oxoindolin-3-ylidene)hydrazine-1-carbothioamide (8f)

Obtained as yellow solid, Yield = 84%, mp = 206–208°C; IR (KBR): 3,271–3,142 (NH stretching), 1,694 (C = O), 1,594 (C =

N), 1,535 (NH bending), 1,170 (C = S), cm^{-1} ; **¹H-NMR** (300 MHz, DMSO-*d*₆): δ (ppm) 12.66 (s, 1H, N-H), 11.22 (s, 1H, N-H), 9.82 (s, 1H, N-H), 7.65 (d, J = 7.5, 1H, Ar-H), 7.35 (m, 5H, Ar-H), 7.26 (m, 1H, Ar-H), 7.08 (d, J = 7.5, 1H, Ar-H), 6.93 (d, J = 7.8, 1H, Ar-H), 4.88 (d, J = 6, 2H, Alkyl H); **¹³C-NMR** (75 MHz, DMSO-*d*₆) δ (ppm): 178.17, 163.11, 142.82, 138.87, 132.53, 131.72, 128.75, 127.81, 127.48, 122.77, 121.37, 120.42, 111.55, 47.67; **LC-MS** (m/z): positive mode 311 $[M + H]^+$. Purity determined by HPLC-UV (254 nm)-ESI-MS: 97.81%

(*Z*)-*N*-(3-chlorophenyl)-2-(2-oxoindolin-3-ylidene)hydrazine-1-carbothioamide (8g)

Obtained as yellow solid, Yield = 74%, mp = 235–236°C; IR (KBR): 3,340–3,192 (NH stretching), 1,694 (C=O), 1,594 (C=N), 1,535 (NH bending), 1,170 (C=S), cm^{-1} ; **¹H-NMR** (300 MHz, DMSO-*d*₆): δ (ppm) 12.86 (s, 1H, N-H), 11.28 (s, 1H, N-H), 10.87 (s, 1H, N-H), 7.79 (t, J = 2.1, 1H, Ar-H), 7.76 (s, 1H, Ar-H), 7.65 (dq, J = 8.1, 1.2, 1H, Ar-H), 7.45 (t, J = 7.95, 1H, Ar-H), 7.35 (m, 2H, Ar-H), 7.12 (t, J = 7.35, 1H, Ar-H), 6.95 (d, J = 7.8, 1H, Ar-H); **¹³C-NMR** (75 MHz, DMSO-*d*₆) δ (ppm): 176.77, 163.18, 143.09, 140.40, 133.19, 132.91, 132.08, 130.44, 126.28, 125.53, 124.52, 122.87, 121.93, 120.28, 111.62; **LC-MS** (m/z): positive mode 331 $[M + H]^+$. Purity determined by HPLC-UV (254 nm)-ESI-MS: 98.38%

(*Z*)-2-(2-oxoindolin-3-ylidene)-*N*-(*p*-tolyl)hydrazine-1-carbothioamide (8h)

Obtained as yellow solid, Yield = 79%, mp = 240–242°C; IR (KBR): 3,260–3,130 (NH stretching), 1,698 (C = O), 1,608 (C = N), 1,530 (NH bending), 1,158 (C = S), cm^{-1} ; **¹H-NMR** (300 MHz, DMSO-*d*₆): δ (ppm) 12.77 (s, 1H, N-H), 11.25 (s, 1H, N-H), 10.75 (s, 1H, N-H), 7.77 (d, J = 7.2, 1H, Ar-H), 7.47 (d, J = 8.1, 2H, Ar-H), 7.37 (td, J = 7.8, 1.2, 1H, Ar-H), 7.22 (d, J = 8.4, 2H, Ar-H), 7.10 (dt, J = 7.65, 0.7, 1H, Ar-H), 6.94 (d, J = 7.8, 1H, Ar-H), 2.47 (s, 2H, Alkyl H); **¹³C-NMR** (75 MHz, DMSO-*d*₆) δ (ppm): 176.79, 163.17, 142.92, 136.36, 135.83, 132.61, 131.85, 129.31, 126.04, 122.82, 121.84, 120.41, 111.54, 21.0.

(*Z*)-*N*-(2,6-dimethylphenyl)-2-(2-oxoindolin-3-ylidene)hydrazine-1-carbothioamide (8i)

Obtained as yellow solid, Yield = 83%, mp = 250–252°C; IR (KBR): 3,250–3,155 (NH stretching), 1,688 (C = O), 1,619 (C = N), 1,520 (NH bending), 1,174 (C = S), cm^{-1} ; **¹H-NMR** (300 MHz, DMSO-*d*₆): δ (ppm) 12.76 (s, 1H, N-H), 11.23 (s, 1H, N-H), 10.61 (s, 1H, N-H), 7.73 (d, J = 7.5, 1H, Ar-H), 7.36 (t, J = 7.65, 1H, Ar-H), 7.17 (m, 3H, Ar-H), 7.09 (t, J = 7.5, 1H, Ar-H), 6.94 (d, J = 7.8, 1H, Ar-H), 2.20 (s, 6H, Alkyl H); **¹³C-NMR** (75 MHz, DMSO-*d*₆) δ (ppm): 177.43, 163.12, 142.92, 136.82, 136.52, 132.58, 131.77, 128.31, 127.89, 122.81, 121.71, 120.49, 111.51, 18.32; **LC-MS** (m/z): positive mode 325 $[M + H]^+$. Purity determined by HPLC-UV (254 nm)-ESI-MS: 98.27%

(*Z*)-*N*-(2,5-dimethoxyphenyl)-2-(2-oxoindolin-3-ylidene)hydrazine-1-carbothioamide (8j)

Obtained as yellow solid, Yield = 74%, mp = 245–248°C; IR (KBR): 3,285–3,170 (NH stretching), 1,690 (C = O), 1,606 (C = N), 1,545 (NH bending), 1,164 (C = S), cm^{-1} ; **¹H-NMR** (300 MHz, DMSO-*d*₆): δ (ppm) 12.81 (s, 1H, N-H), 11.27 (s, 1H, N-H), 10.43 (s, 1H, N-H), 7.77 (d, J = 2.7, 1H, Ar-H), 7.65 (d, J = 7.2, 1H, Ar-H), 7.38 (td, J = 7.65, 1.1, 1H, Ar-H), 7.09 (m, 2H, Ar-H), 6.95 (d, J = 7.8, 1H, Ar-H), 6.82 (dd, J = 9.0, 3.0, 1H, Ar-H), 3.84 (s, 3H,

Alkyl H), 3.72 (s, 3H, Ar-H); $^{13}\text{C-NMR}$ (75 MHz, DMSO-*d*₆) δ (ppm): 175.64, 163.17, 153.06, 146.68, 143.09, 132.87, 132.05, 128.06, 123.00, 121.41, 120.15, 112.78, 111.64, 111.53, 56.84, 55.95; **LC-MS** (*m/z*): positive mode 357 [M + H]⁺. Purity determined by HPLC-UV (254 nm)-ESI-MS: 95.39%

(*Z*)-*N*-(4-methoxyphenyl)-2-(2-oxoindolin-3-ylidene)hydrazine-1-carbothioamide (8k)

Obtained as yellow solid, Yield = 80%, mp = 255–260°C; IR (KBR): 3,270–3,160 (NH stretching), 1,692 (C = O), 1,623 (C = N), 1,546 (NH bending), 1,162 (C = S), cm⁻¹; $^1\text{H-NMR}$ (300 MHz, DMSO-*d*₆) δ (ppm): 12.75 (s, 1H, N-H), 11.25 (s, 1H, N-H), 10.73 (s, 1H, N-H), 7.76 (d, *J* = 7.5, 1H, Ar-H), 7.46 (d, *J* = 8.4, 2H, Ar-H), 7.37 (td, *J* = 7.8, 1.0, 1H, Ar-H), 7.10 (t, *J* = 7.2, 1H, Ar-H), 6.97 (t, *J* = 9.75, 3H, Ar-H), 3.78 (s, 3H, Alkyl-H); $^{13}\text{C-NMR}$ (75 MHz, DMSO-*d*₆) δ (ppm): 177.0, 163.16, 157.85, 142.89, 132.52, 131.80, 131.74, 127.73, 122.82, 121.79, 120.44, 114.03, 111.54, 55.75; **LC-MS** (*m/z*): positive mode 327 [M + H]⁺. Purity determined by HPLC-UV (254 nm)-ESI-MS: 98.73%

(*Z*)-*N*-(2,6-difluorophenyl)-2-(2-oxoindolin-3-ylidene)hydrazine-1-carbothioamide (8l)

Obtained as yellow solid, Yield = 75%, mp = 243–244°C; IR (KBR, cm⁻¹): 3,264–3,170 (NH stretching), 1,692 (C = O), 1,598 (C = N), 1,555 (NH bending), 1,170 (C = S), cm⁻¹; $^1\text{H-NMR}$ (300 MHz, DMSO-*d*₆) δ (ppm): 12.96 (s, 1H, N-H), 11.28 (s, 1H, N-H), 10.57 (s, 1H, N-H), 7.69 (d, *J* = 7.5, 1H, Ar-H), 7.49 (m, 1H, Ar-H), 7.39 (td, *J* = 7.65, 1.1, 1H, Ar-H), 7.26 (t, *J* = 9.9, 2H, Ar-H), 7.12 (t, *J* = 7.65, 1H, Ar-H), 6.95 (d, *J* = 7.5, 1H, Ar-H); $^{13}\text{C-NMR}$ (75 MHz, DMSO-*d*₆) δ (ppm): 179.09, 163.11, 157.42, 143.27, 133.83, 132.18, 130.15, 122.94, 121.72, 120.26, 116.56, 112.49, 111.67; **LC-MS** (*m/z*): positive mode 333 [M + H]⁺. Purity determined by HPLC-UV (254 nm)-ESI-MS: 97%

(*Z*)-*N*-ethyl-2-(2-oxoindolin-3-ylidene)hydrazine-1-carbothioamide (8m)

Obtained as yellow solid, Yield = 84%, mp = 190–194°C; IR (KBR): 3,315–3,281 (NH stretching), 1,686 (C = O), 1,619 (C = N), 1,541 (NH bending), 1,161 (C = S), cm⁻¹; $^1\text{H-NMR}$ (300 MHz, DMSO-*d*₆) δ (ppm): 12.96 (s, 1H, N-H), 11.28 (s, 1H, N-H), 10.57 (s, 1H, N-H), 7.65 (d, *J* = 7.2, 1H, Ar-H), 7.35 (td, *J* = 7.72, 1.1, 1H, Ar-H), 7.10 (td, *J* = 7.57, 0.7, 1H, Ar-H), 6.93 (d, *J* = 7.8, 1H, Ar-H), 3.64 (m, 2H, CH₂), 1.19 (t, *J* = 7.05, 3H, CH₃); $^{13}\text{C-NMR}$ (75 MHz, DMSO-*d*₆) δ (ppm): 177.08, 163.09, 142.71, 132.11, 131.61, 122.77, 121.27, 120.44, 111.52, 39.51, 14.52; **LC-MS** (*m/z*): positive mode 249 [M + H]⁺. Purity determined by HPLC-UV (254 nm)-ESI-MS: 98.56%

Biological Protocols

Cell Transfection and Protein Preparation

COS-7 cells were transfected with plasmids expressing human or mouse NTPDases1, -2, -3, and -8 as previously described (Levesque et al., 2007; Lecka et al., 2014). Briefly, the confluent cells were transferred to Dulbecco's Modified Eagle's Medium containing no fetal bovine serum. Then, these cells were incubated with plasmid DNA (6 μg) and Lipofectamine reagent (24 μl) at 37°C. After 5 h, transfection was terminated with the addition of an equal volume of DMEM/F-12

(supplemented with 20% FBS) and cells were collected by harvesting after 40–72 h.

To prepare protein extracts, transfected COS-7 cells were washed three times with tris-saline buffer while temperature was maintained at 4°C. Then cells were scraped and resuspended in harvesting buffer containing 95 mM NaCl, 45 mM tris and 0.1 mM phenylmethylsulfonyl fluoride (pH 7.5). Cells were again washed twice by centrifugation for 5 min at 300 \times g at 4°C and then resuspended in harvesting buffer (supplemented with 10 $\mu\text{g/ml}$ aprotinin). Following sonication, cellular debris was isolated by 10 min centrifugation at 300 g at 4°C. Subsequently, supernatant was removed very carefully and protein concentration was determined by using Bradford microplate assay while using the bovine serum albumin as a standard (Bradford, 1976).

Nucleoside Triphosphate Ddiphosphohydrolases Activity Assay

The inhibitory effects of synthesized compounds on *h*-NTPDase1, -2, -3, and -8 were determined as described previously, although with slight modifications (Martín-Satué et al., 2009). Assay was conducted in a reaction medium containing 50 mM tris-HCl and 5 mM CaCl₂ (pH 7.4). All the test compounds were dissolved in dimethyl sulfoxide (DMSO, 10%) and initially screened at a concentration of 100 μM . A reaction mixture containing 55 μl of assay buffer, 10 μl of test compound solution and 10 μl of *h*-NTPDase1 (58 ng/well) or *h*-NTPDase2 (79 ng/well) or *h*-NTPDase3 (163 ng/well) or *h*-NTPDase8 (66 ng/well) was incubated at 37°C for 10 min. Following the incubation, a 10 μl solution of adenosine triphosphate (ATP, 100 μM) was added as substrate and reaction mixture was again incubated for 15 min at 37°C. The reaction was stopped by adding malachite green reagent (15 μl) and placed at room temperature for 4 to 6 min. Finally, absorbance was measured at 630 nm by using Omega FLUOstar microplate reader (BMG Labtech, Ortenberg, Germany) and % inhibitions were calculated. For compounds showing more than 50% inhibition of any isozyme, dose response curves were generated and their IC₅₀ values were determined. Three separate enzyme inhibition assays were carried out in triplicate and dose-response curve were generated by using PRISM 5.0 (GraphPad, San Diego, United States).

Same procedure was adopted to determine the inhibitory effects of compounds on mouse NTPDases (*m*-NTPDases). However, the amount of protein used was as follows: *m*-NTPDase1 (82 ng/well), *m*-NTPDase2 (57 ng/well), *m*-NTPDase3 (110 ng/well) and *m*-NTPDase8 (79 ng/well)

Islets Isolation

Six to eight week old BALB/c mice, weighing 30–40 g, were used in the study. These mice were obtained from the animal house of COMSATS University Islamabad, Abbottabad Campus and placed under standard temperature (25 \pm 2°C) and humidity (50–55%) conditions with an alternate 12-h light/dark cycle. All the experimental animals were provided with a continuous supply of food and water. The

animals were handled according to internationally accepted guidelines of animal care and use. Moreover, this study was reviewed and approved by Research Ethics Committee, Department of Pharmacy, COMSATS University Islamabad, Abbottabad Campus. (Protocol number: PHM.Eth./CS-M01-020-1609)

The islets were isolated from mice pancreas as previously described, by a process involving collagenase digestion (Hameed et al., 2018). Briefly, mice were anesthetized with sodium thiopental (30 mg/kg) and sacrificed by cervical dislocation to block the flow of blood. Immediately, mice were transferred to biological hood and their abdominal cavity was opened completely by making an incision on abdomen. In order to stop the bile flow toward duodenum, ampulla was located and clamped under dissection microscope. Then, distention of pancreas was carried out by injecting 3 ml of collagenase solution (1 mg/ml) through common bile duct. The distended pancreas was removed as a whole, transferred to a 50 ml tube and digested in collagenase solution at 37°C. After 15 min, digestion was stopped by placing the tube on ice and 20 ml of Hank's Balanced Salt Solution (HBSS) was added to it. Thus the digested islets were washed with HBSS (two to three times) by centrifugation (1,000 rpm) for 1 min at 4°C. Finally, islets were purified by passing through a cell strainer (70 µm) and isolated manually (by hand picking) under stereomicroscope (Euromex, Arnhem, Netherlands). All the purification and isolation procedures were carried out in HBSS, containing no magnesium, calcium and phenol red.

Measurement of Insulin Secretion

Krebs-Ringer bicarbonate buffer (KRBB) was used as an incubation medium for islets and was composed of NaCl (118 mM), KCl (4.7 mM), CaCl₂ (1.9 mM), MgSO₄ (1.2 mM), NaHCO₃ (25 mM), 4-(2-hydroxyethyl)-1-piperazineethanesulfonic acid (HEPES, 10 mM) and bovine serum albumin (0.1%). The pH of KRBB was maintained at 7.4. The isolated islets were size-matched and pre-incubated (3 islets/tube) for 45 min at 37°C in KRBB, supplemented with 3 mM glucose. Thereafter, incubation medium was replaced with fresh KRBB (containing 16.7 mM glucose) and islets were incubated for 60 min at 37°C with or without test substance(s). After incubation, supernatant was collected and stored at -40°C until further use. Finally, collected samples were properly diluted and insulin secretion was estimated

with ultra-sensitive mouse insulin ELISA kit (Crystal Chem Inc., Downers Grove, United States) according to the manufacturer's instructions. The absorbance was measured at 450 nm and insulin secretion was normalized for number of islets used. (Hameed et al., 2018).

Ectonucleotidase Activity of Islets

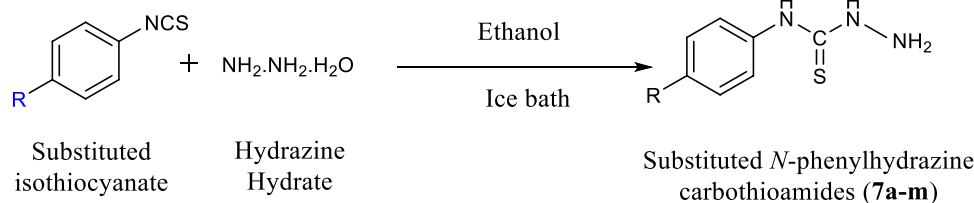
Preparation of Islet Homogenate

Islets were isolated and homogenized, according to the previously reported method (Hedekov and Capito, 1974). After isolation, islets were washed thrice with HBSS and suspended in an ice-cold buffer containing sucrose (0.25 M), ethylenediaminetetraacetic acid (EDTA, 1 mM) and tris-HCl (5 mM), maintained at pH 7.0. The resulting suspension was diluted with assay buffer, composed of tris-HCl (50 mM) and CaCl₂ (5 mM). Afterward, these islets were sonicated for 30 s leading to disruption of islets and formation of a homogenate. Cellular debris was removed by centrifugation at 15,000 rpm for 10 min (4°C). The supernatant was collected and stored on ice. Protein concentration was estimated by Bradford method, using bovine serum albumin as reference standard (Bradford, 1976).

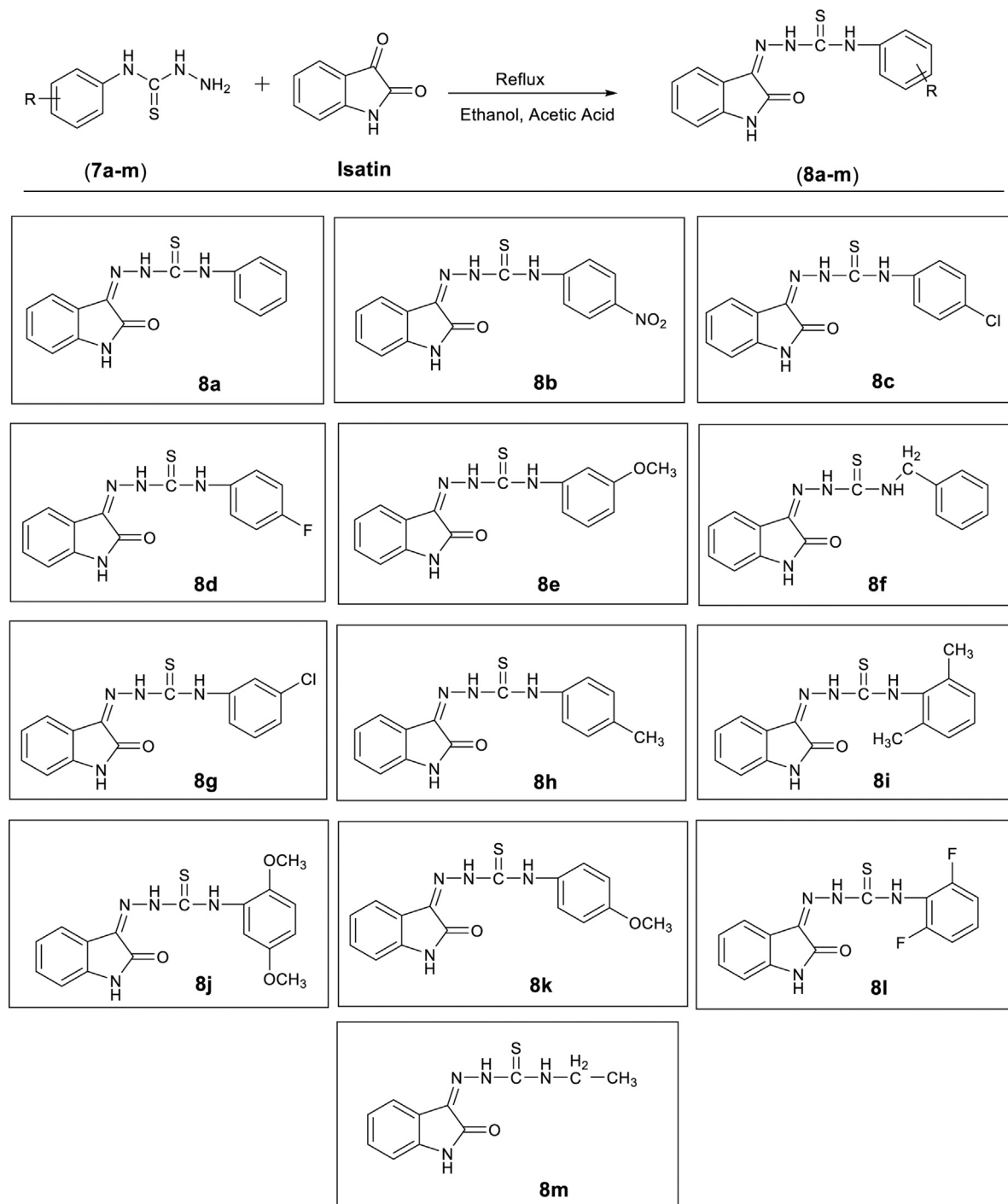
Ectonucleotidase Activity of Islet Homogenate

In order to determine the effect of compounds on ectonucleotidase activity in mice islets, standard curve based procedure was used where KH₂PO₄ was used as a standard. A stock solution of KH₂PO₄ (1 mM) was prepared in assay buffer that was used to prepare the working solutions of lower concentrations (0–100 µM). A standard curve was generated by incubating increasing concentration of KH₂PO₄ with buffer and malachite green reagent.

The assay was carried out in tris-buffer (pH 7.4) containing tris-HCl (50 mM) and CaCl₂ (5 mM), as previously described (Lavoie et al., 2010). Compounds were dissolved in DMSO (10%) and tested at a concentration of 100 µM. The assay was started by adding 10 µl of test compound solution to 56 µl of assay buffer, followed by the addition of 6 µl of homogenate (i.e., 3 µg of protein). The mixture was incubated at 37°C for 10 min and then 10 µl of ATP (100 µM) was added to start the reaction. Reaction mixture was again placed in incubator at 37°C for 15 min and then reaction was stopped by adding 100 µl of trichloroacetic acid (10%). These samples were placed on ice for 15 min. Finally, samples were mixed with malachite green reagent in an appropriate proportion and



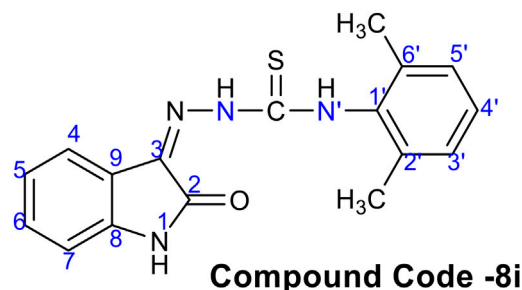
SCHEME 1 | Synthesis of substituted *N*-phenylhydrazine carbothioamides (7a-m).

TABLE 1 | Synthesis of compounds (**8a–pm**).

released Pi was determined by using standard curve. Moreover, test compounds were tested at different concentrations and dose response curves were generated indicating the amount of Pi released at corresponding dose. All the experiments were carried out in triplicate and enzyme activity was expressed as nm of Pi/min/mg of protein.

Real Time Quantitative Polymerase Chain Reaction *Treatment of Islets With Test Compound*

Freshly isolated mice islets were incubated in KRBB at 37°C with glucose (3 mM). After 45 min, these islets were treated with test compounds in KRBB at 37°C for 3 h, in the presence of stimulatory glucose concentration. Once the incubation was

TABLE 2 | ^1H NMR data of compound **8i**.

Atom No (N or C)	δ_{H}	δ_{C}	HSQC	HBMC
NH	12.77 (brs, 1H)	—	—	—
N'H	11.24 (brs, 1H)	—	—	—
NH	10.62 (brs, 1H)	—	—	—
CH-4	7.48 (d, $J = 7.5$ Hz, 1H)	121.7	C-4	C-6, C-8
CH-6	7.37 (t, $J = 7.5$ Hz, 1H)	131.8	C-6	C-4, C-8
CH-3'/4'/5'	7.20–7.46 (m, 3H)	128.3/127.9	C-3'/4'/5'	C-1'/5', C-2'/6', C-1'/3'
CH-5	7.09 (t, $J = 7.5$ Hz)	122.8	C-5	C-7, C-9
CH-7	6.94 (d, $J = 7.8$ Hz)	111.5	C-7	C-5, C-9
Ar(CH ₃) ₂	2.21 (s)	18.3	Ar(CH ₃) ₂	C-1', C-3', C-5'
C-1'	—	136.8	—	—
C-2'	—	136.5	—	—
C-5'	—	136.5	—	—
C-2	—	163.1	—	—
C-3	—	132.6	—	—
C-8	—	142.9	—	—
C-9	—	120.5	—	—
C=S	—	171.4	—	—

complete, supernatant was removed carefully, and RNA was extracted from these islets.

Total RNA Extraction and Real Time Quantitative Polymerase Chain Reaction

Total RNA was extracted using TRIzol reagent, according to manufacturer's instruction. The concentration of isolated RNA

was quantified by using Lvis plate method (FLUOstar Omega, BMG Labtech, Ortenberg, Germany). This RNA was then reverse transcribed to cDNA in a total reaction volume of 20 μl . Briefly, a reaction mixture containing RNA (1 μg) and oligo-dT (20 μM , 1 μl) was prepared and volume was adjusted to 12 μl with nuclease free water. The prepared mixture was incubated at 65°C for 5 min and then immediately chilled on ice. Afterward, 8 μl of master mix

TABLE 3 | Human NTPDase inhibitory data for compounds (**8a-m**).

Code	NTPDase1	NTPDase2	NTPDase3	NTPDase8	NTPDase1	NTPDase2	NTPDase3	NTPDase8
	IC_{50} (μM) \pm SEM ^a or %inhibition at 100 μM ^b				Ki (μM)			
8a	45% ^b	24% ^b	20% ^b	24% ^b	—	—	—	—
8b	0.29 \pm 0.02 ^a	19% ^b	20% ^b	24% ^b	0.04	—	—	—
8c	0.23 \pm 0.01 ^a	46% ^b	0.19 \pm 0.02 ^a	0.24 \pm 0.02 ^a	0.03	—	0.08	0.11
8d	49% ^b	48% ^b	46% ^b	33% ^b	—	—	—	—
8e	0.15 \pm 0.009 ^a	34% ^b	26% ^b	21% ^b	0.15	—	—	—
8f	0.24 \pm 0.01 ^a	38% ^b	27% ^b	31% ^b	0.03	—	—	—
8g	28% ^b	29% ^b	17% ^b	7% ^b	—	—	—	—
8h	49% ^b	17% ^b	26% ^b	22% ^b	—	—	—	—
8i	1.63 \pm 0.15 ^a	0.41 \pm 0.03 ^a	25% ^b	17% ^b	0.24	0.17	—	—
8j	0.15 \pm 0.01 ^a	0.11 \pm 0.08 ^a	34% ^b	19% ^b	0.02	0.04	—	—
8k	44% ^b	0.16 \pm 0.01 ^a	19% ^b	46% ^b	—	0.07	—	—
8l	0.30 \pm 0.03 ^a	45% ^b	22% ^b	32% ^b	0.04	—	—	—
8m	2.60 \pm 0.02 ^a	42% ^b	0.38 \pm 0.03 ^a	38% ^b	0.38	—	0.16	—
Suramin ³	16.1 \pm 1.02 ^a	24.1 \pm 3.01 ^a	4.31 \pm 0.41 ^a	>100 ^a	2.33	9.92	1.85	—

^a IC_{50} values are presented as mean \pm SEM of three independent experiments.

^bPercent inhibition determined at 100 μM .

TABLE 4 | Mouse NTPDase inhibitory data for compounds (**8a-m**).

Code	NTPDase1	NTPDase2	NTPDase3	NTPDase8	NTPDase1	NTPDase2	NTPDase3	NTPDase8
	IC ₅₀ (μM) ± SEM ^a or %inhibition at 100 μM ^b				K _i (μM)			
8a	38% ^b	42% ^b	31% ^b	28% ^b	—	—	—	—
8b	14% ^b	31% ^b	28% ^b	30% ^b	—	—	—	—
8c	28% ^b	36% ^b	27% ^b	36% ^b	—	—	—	—
8d	41% ^b	27% ^b	29% ^b	1.45 ± 0.12 ^a	—	—	—	0.17
8e	0.60 ± 0.03 ^a	29% ^b	0.70 ± 0.05 ^a	3.80 ± 0.21 ^a	0.006	—	0.07	0.44
8f	4.14 ± 0.13 ^a	34% ^b	32% ^b	38% ^b	0.04	—	—	—
8g	48% ^b	36% ^b	27% ^b	36% ^b	—	—	—	—
8h	29% ^b	31% ^b	31% ^b	28% ^b	—	—	—	—
8i	20% ^a	0.15 ± 0.01 ^a	32% ^b	26% ^b	—	0.04	—	—
8j	24% ^a	27% ^b	30% ^b	32% ^b	—	—	—	—
8k	42% ^b	29% ^b	36% ^b	24% ^b	—	—	—	—
8l	3.22 ± 0.19 ^a	0.20 ± 0.01 ^a	0.32 ± 0.04 ^a	13% ^b	0.03	0.05	0.03	—
8m	3.60 ± 0.02 ^a	1.50 ± 0.11 ^a	2.41 ± 0.15 ^a	35% ^b	0.04	0.41	0.24	—
Suramin ⁴	>100 ^a	21.0 ± 2.0 ^a	31.0 ± 2.0 ^a	>100 ^a	—	5.67	3.07	—

^aIC₅₀ values are presented as mean ± SEM of three independent experiments.

^bPercent inhibition determined at 100 μM

containing 5X reaction buffer (4 μl), rnaase inhibitor (1 μl), dNTPs mix (10 mM, 2 μl) and reverse transcriptase (1 μl) was added to above sample. After gentle pipetting, sample was run under following conditions: 25°C for 5 min, 42°C for 70 min and 70°C for 5 min. Once the cDNA was synthesized, real time quantitative PCR was conducted by using PikoReal 96 Real-Time PCR system (Thermo Scientific, Vantaa, Finland). For this purpose, a master mixture containing cDNA (1 μl), forward primer (0.25 μl), reverse primer (0.25 μl) and SYBER green master mix (10 μl) was prepared and total volume was adjusted to 20 μl with nuclease free water. Subsequently, thermal cycling conditions were set as follows: 95°C for 10 min and then 40 cycles at 95°C for 15 s and 55°C for 1 min. Relative expression was determined by normalization to β actin mRNA by ΔΔC_T method.

Molecular Docking Studies

Molecular docking analysis was carried out on the basis of results obtained in enzyme kinetics. Hence molecular docking was carried out for the most potent inhibitor of *h*-NTPDase2 (**8j**), *h*-NTPDase3 (**8c**) and *h*-NTPDase8 which showed a competitive

mode of inhibition. Compound **8e** revealed a non-competitive mechanism of inhibition against *h*-NTPDase1, therefore its docking was not performed. Since the crystal structures of human NTPDases are not yet available from the Protein Data Bank, their homology models were built according to our previously reported method (Iqbal and Shah, 2018). Docking studies were carried out using BioSolveIT's LeadIT software¹. Out of the top ten docked conformations obtained for each inhibitor, the one with the most favorable binding free energy was selected, using HYDE functionality of software. SeeSAR analysis of the inhibitors was also performed by BioSolveIT's SeeSAR².

Statistical Analysis

The data was presented as mean ± SEM and statistical analysis was performed using PRISM 5.0 (GraphPad, San Diego, United States). Statistical tests were performed by using student t test and one-way ANOVA. A *p* value < 0.05 was considered significant.

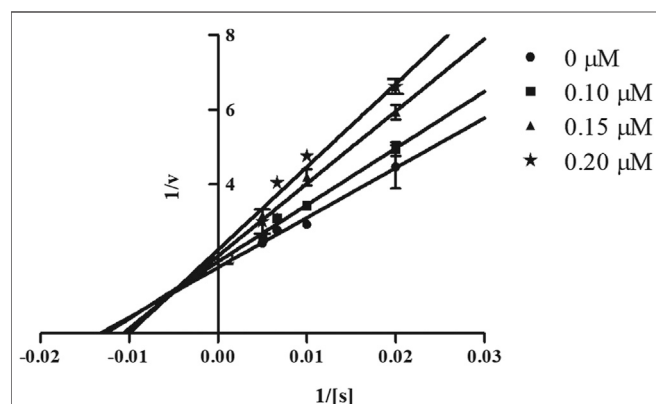


FIGURE 1 | Lineweaver-Burk Plot for *h*-NTPDase1 inhibitor (**8e**). S represents the substrate concentration (μM) and concentration of inhibitor (**8e**) are 0, 0.10, 0.15, and 0.20 μM.

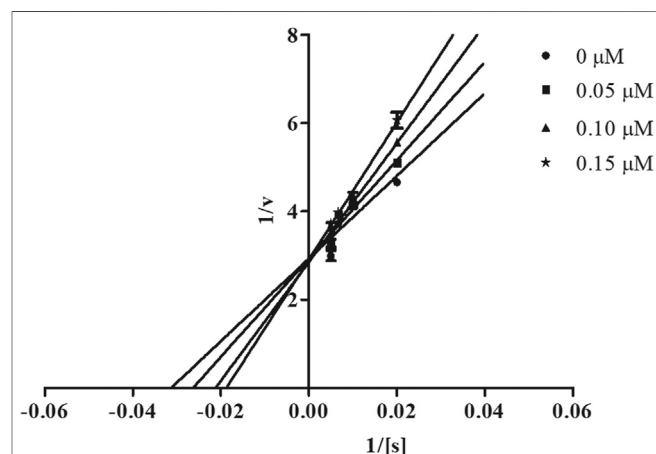


FIGURE 2 | Lineweaver-Burk Plot for *h*-NTPDase2 inhibitor (**8j**). S represents the substrate concentration (μM) and concentration of inhibitor (**8j**) are 0, 0.05, 0.10, and 0.15 μM.

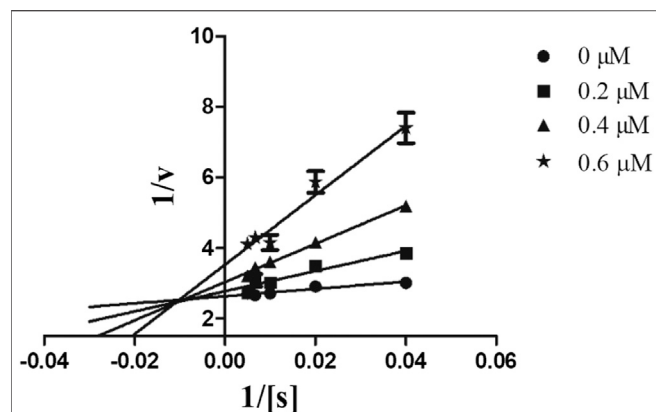


FIGURE 3 | Lineweaver-Burk Plot for *h*-NTPDase3 inhibitor (**8m**). S represents the substrate concentration (μM) and concentration of inhibitor (**8m**) are 0, 0.20, 0.4, and 0.6 μM .

RESULTS

Chemistry

A series of 13 hydrazine carbothioamide derivatives (**8a-m**) was synthesized as potential NTPDase inhibitors. Initially, substituted phenylhydrazine carbothioamides (**7a-m**) were prepared by dropwise addition of appropriate isothiocyanate to excess of hydrazine hydrate in ethanol as shown in **Scheme 1**. The target compounds (**8a-m**) were synthesized by refluxing the synthesized intermediates (**7a-m**) with isatin for 4 to 5 h (**Table 1**). After the reaction was completed, gradual evaporation of solvent at room temperature resulted in precipitate formation. These precipitates were filtered, washed with ethanol and then dried. The synthesized compounds (**8a-m**) were identified by different spectroscopic techniques including IR, LC/ESI-MS, ^1H -NMR and ^{13}C -NMR.

The IR spectra of synthesized compounds showed absorption bands in the region of $3,315\text{--}3,130\text{ cm}^{-1}$, resulting from NH

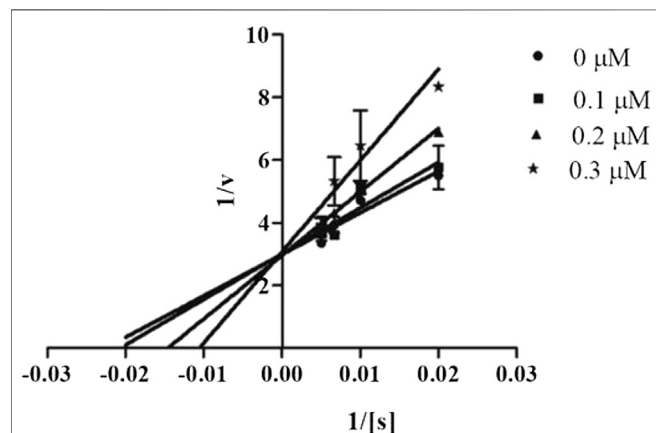


FIGURE 4 | Lineweaver-Burk Plot for *h*-NTPDase8 inhibitor (**8c**). S represents the substrate concentration (μM) and concentration of inhibitor (**8c**) are 0, 0.10, 0.20, and 0.30 μM .

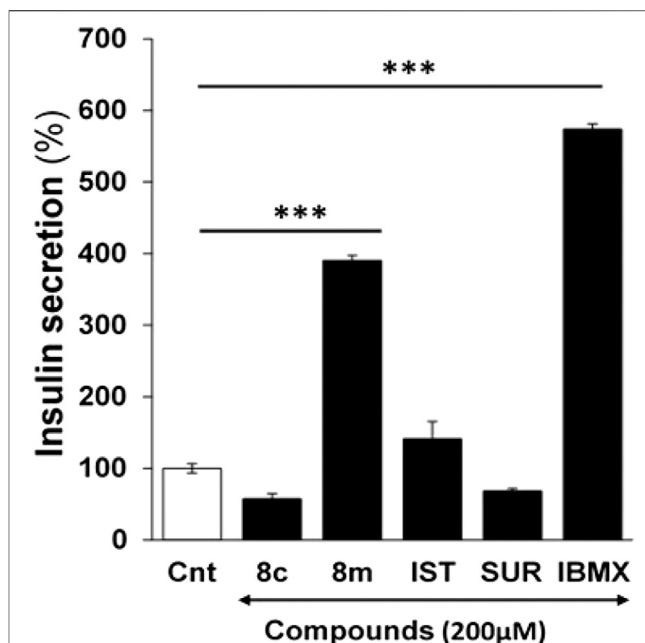


FIGURE 5 | Effect of compound **8c**, **8m**, suramin (SUR), isatin (IST) and isobutyl methyl xanthine (IBMX) on glucose stimulated insulin secretion in mice pancreatic islets at 200 μM . Group of size-matched islets were incubated at 37°C for 1 h in KRB buffer with 16.7 mM glucose supplemented with or without test compounds. Values are mean \pm S.E.M. from two to three independent experiments. Insulin secretion induced by 16.7 mM Glucose was considered 100%. *** $p < 0.0001$ vs. none. Cnt, insulin secretion induced by 16.7 mM glucose only.

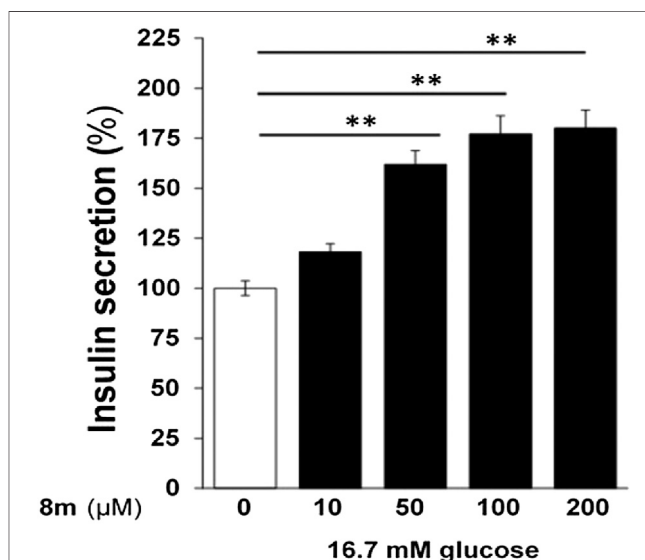
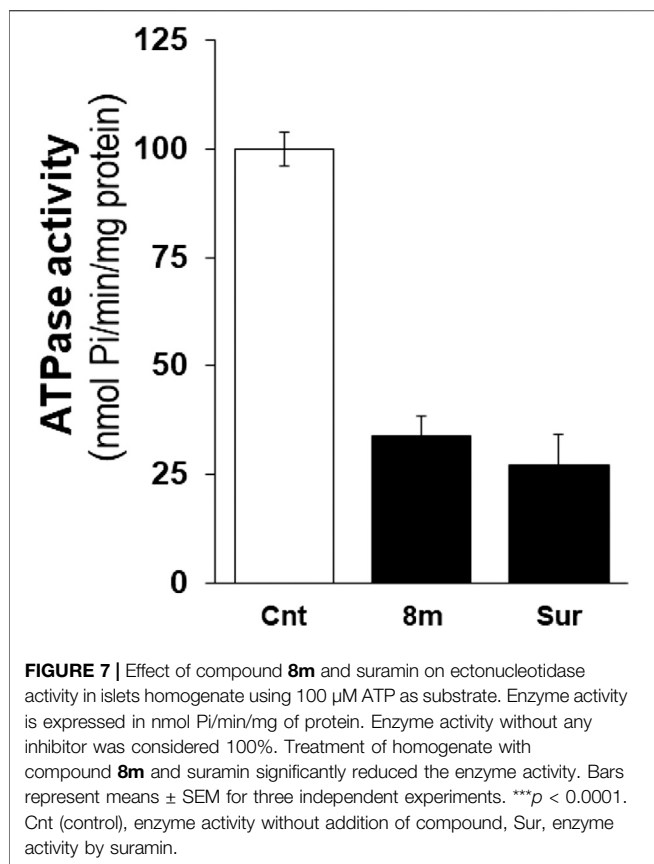


FIGURE 6 | Dose-dependent effect of compound **8m** on insulin secretion. Compound **8m** was employed at doses of 0, 10, 50, 100, and 200 μM concentration supplemented with 16.7 mM glucose. Group of size-matched islets were incubated at 37°C for 1 h in KRB buffer with 16.7 mM glucose supplemented with or without test compounds. Values are mean \pm S.E.M. from two to three independent experiments. ** $p < 0.001$.



stretching of indole and thioamide function. The absorption bands in the region of 1,698–1,686 (cm^{-1}) and 1,623–1,591 (cm^{-1}) can be assigned to the presence of C = O and C = N, respectively. Likewise, bands in the range of 1,560–1,541 (cm^{-1}) and 1,174–1,158 (cm^{-1}) reflect the presence of N-H and C = S, respectively. In case of ^1H -NMR, spectra showed three characteristic peaks (singlet) of NH in the range of δ 9.82–11.12 ppm, 11.22–11.31 ppm, 13.01–12.66 ppm, assigned to CS-NH, indole NH and -N-NH, respectively, confirming the synthesis of desired compounds. All the aromatic protons appeared (as expected) in the region of δ 8.29–6.82 ppm. The ^{13}C spectra showed thioamide carbon peak in the range δ 179.09–175.64 ppm, while carbonyl and imine carbon appeared in the range δ 163.20–163.09 ppm and δ 145.12–142.71 ppm, respectively (Pervez et al., 2009; Ali et al., 2014). Mass spectra of synthesized compound was recorded in positive mode, compounds showed molecular ions of varying intensity indicating molecular weights of the compounds. The information regarding ^1H and ^{13}C spectra of synthesized compounds was presented in **Supplementary Material**.

A typical structure of a hydrazine carbothioamide showed characteristic signals in 1D and 2D NMR spectra. The broad signals for NH groups appeared at δ_{H} 12.77, 11.24, and 10.62 ppm, respectively. The doublets of H-4 and H-7 appeared at δ_{H} 7.48 and 6.94 ppm, respectively. The carbon signals for δ_{C} C = O and C-S appeared at 163.1 and 171.4 ppm. The other characteristics signals of CH, C and CH_3 groups confirm the structure of compound **8i** and are presented in **Table 2**.

Effect of Compounds on Recombinant *h*-NTPDases

The synthesized compounds (**8a–m**) were investigated for their ability to inhibit *h*-NTPDases using the malachite green assay. Recombinant *h*-NTPDase1, -2, -3 and -8 were employed and initial screening was carried out at an initial concentration of 100 μM . In order to compare species difference, compounds were also tested against mouse NTPDases (*m*-NTPDases), including *m*-NTPDase1, -2, -3 and -8. Dose response curves were generated for compounds showing >50% inhibition of any isoform of enzyme. The inhibitory activity of these compounds against human and mouse NTPDases is presented in **Tables 3, 4**, respectively.

Structure Activity Relationship

Among thirteen derivatives, eight compounds inhibited *h*-NTPDases to a variable extent, however *h*-NTPDase1 was more susceptible as compared to other isozymes. Compound **8e** ($\text{IC}_{50} = 0.15 \pm 0.009 \mu\text{M}$) and **8j** ($\text{IC}_{50} = 0.15 \pm 0.01 \mu\text{M}$) revealed the most promising activity against *h*-NTPDase1. A structural comparison of these inhibitors showed that both compounds contained $-\text{OCH}_3$ group attached to phenyl ring, however, **8e** was mono substituted with $-\text{OCH}_3$ attached to phenyl ring whereas **8j** was substituted with two $-\text{OCH}_3$ groups. Hence, excellent activity of **8e** could be due this $-\text{OCH}_3$ group and incorporation of two $-\text{OCH}_3$ groups (**8j**) resulted in retention of activity.

Likewise, compounds containing $-\text{Cl}$ (**8c**, $\text{IC}_{50} = 0.23 \pm 0.01 \mu\text{M}$), $-\text{NO}_2$ (**8b**, $\text{IC}_{50} = 0.29 \pm 0.02 \mu\text{M}$) and $-(\text{F})_2$ (**8l**, $\text{IC}_{50} = 0.30 \pm 0.03 \mu\text{M}$) also showed promising activities. The lowest activity in the series was shown by compounds substituted with an alkyl group as indicated by IC_{50} values of **8i** ($\text{IC}_{50} = 1.63 \pm 0.15 \mu\text{M}$) and **8m** ($\text{IC}_{50} = 2.60 \pm 0.02 \mu\text{M}$), respectively.

The data suggest that position of substitution also plays an important role. For example, compound **8c** containing 4-Cl

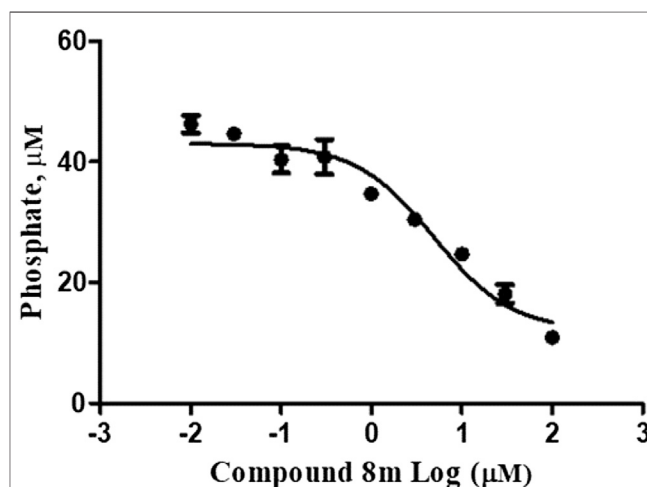


FIGURE 8 | Compound **8m** inhibits the ectonucleotidase activity in islet homogenate, measured as release of Pi from exogenously added ATP at a concentration of 100 μM ($n = 3$).

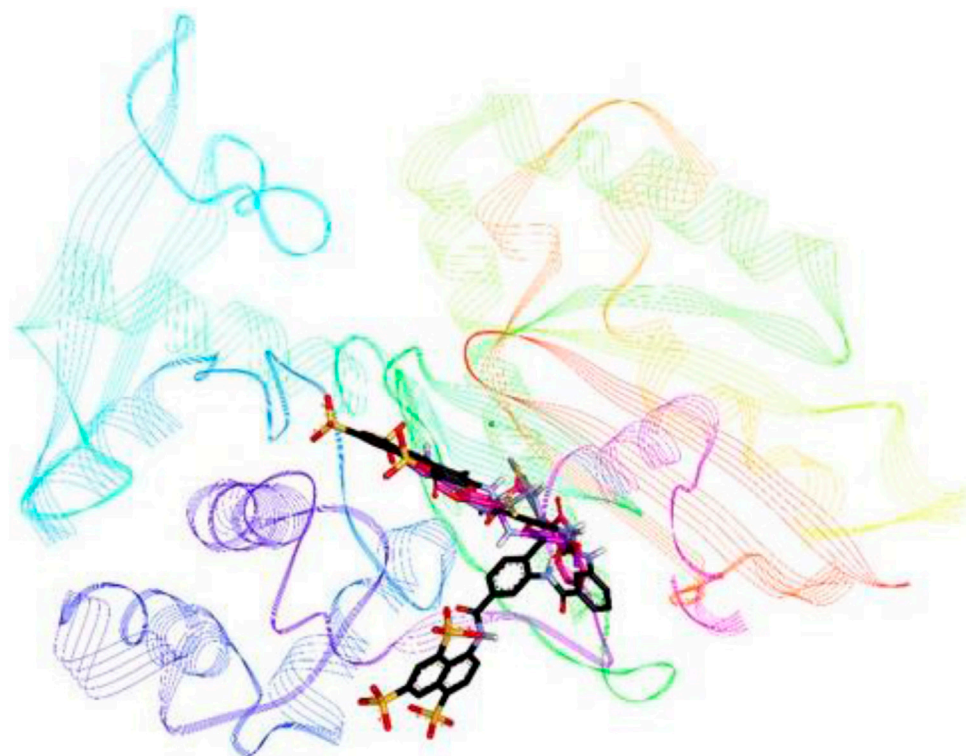


FIGURE 9 | Overlap of docked conformations of compounds **8i** (gray), **8j** (purple) and **8k** (pink) with standard inhibitor suramin (black), the protein backbone is represented in lined ribbon, the calcium ion is shown as green sphere.

substitution showed remarkable activity ($IC_{50} = 0.23 \pm 0.01 \mu M$); whereas, introduction of 3-Cl resulted in reduced activity of **8g** (28%). Similarly, position of substituent also contributed toward the activity of **8e** (containing 4- OCH_3 group) since introduction of 3- OCH_3 group lead to decreased activity of **8k** (44%).

Moreover, mono-substitution and di-substitution was another factor responsible for improved activity of derivatives. In this case, a comparison of **8d** (49.1%) vs. **8l** ($IC_{50} = 0.30 \pm 0.03 \mu M$) showed that di substitution was more favored than mono substitution. Same pattern of activity was observed for **8h** vs. **8i**. Above all, four compounds i.e. **8b**, **8e**, **8f** and **8l** selectively

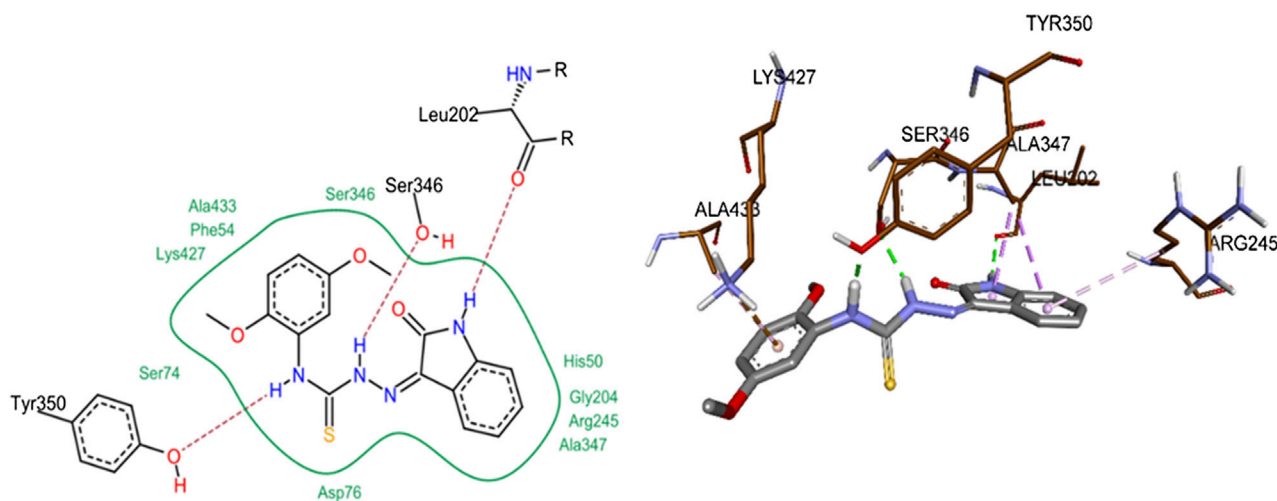


FIGURE 10 | 2D (left) and 3D (right) representation of docked conformations of *h*-NTPDase2 inhibitor **8j**.

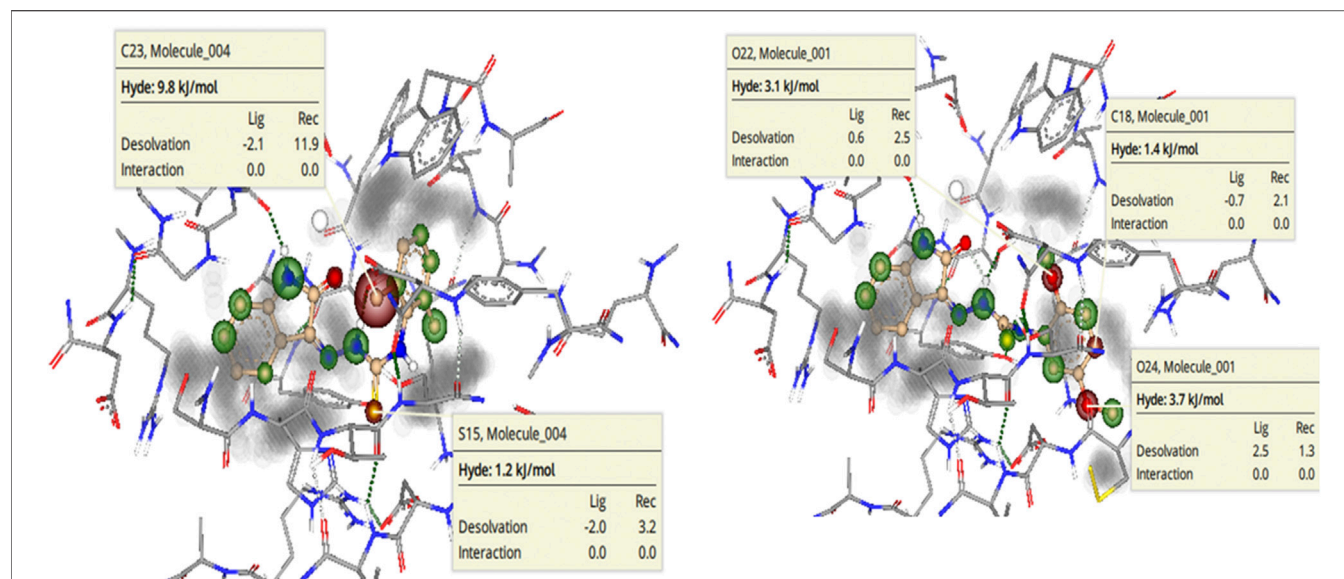


FIGURE 11 | See SAR Analysis (visual representation of contribution of each atom to overall binding affinity) of *h*-NTPDase2 inhibitors **8i** (left) and **8j** (right). The structural elements that are contributing favorably to the overall binding affinity are represented with green colored coronas, structural elements that with unfavorable contribution are represented with red colored coronas, neutral elements are not colored. Unoccupied space in the binding site is in gray color.

inhibited *h*-NTPDase1 and their %inhibition values for other isozymes was <50%.

In case of *h*-NTPDase2, three compounds could inhibit this isoform and IC_{50} values of these compounds were in sub-micro molar range. Compounds **8j** ($IC_{50} = 0.11 \pm 0.08 \mu M$) and **8k** ($IC_{50} = 0.16 \pm 0.01 \mu M$) shared almost comparable activity, indicating substitution with $-OCH_3$ was well tolerated, whether it was a mono substitution or a di substitution.

Compound **8i** ($IC_{50} = 0.41 \pm 0.03 \mu M$) also possessed good inhibitory activity and it incorporated two $-CH_3$ groups as a part of its structure. However, the activity of remaining derivatives was <50%.

There were only two hit compounds (**8c**, **8m**) which showed excellent inhibition of *h*-NTPDase3. A comparison of IC_{50} s showed that **8c** was 22 times more active than standard inhibitor i.e. suramin. Structure of **8c** contained 4-Cl attached to it and this activity appeared position dependent since introduction of 3-Cl resulted in loss of activity. Another inhibitor of *h*-NTPDase3 was **8m** and it also showed excellent inhibitory activity ($IC_{50} = 0.38 \pm 0.03 \mu M$). This compound contained an ethyl chain attached to $-NH$ of thioamide chain, indicating that alkyl chain was well tolerated. However, presence of other substituents like $-F$, $-CH_3$ and $-OCH_3$ did not show any remarkable activity toward *h*-NTPDase3.

Only one compound effectively inhibited *h*-NTPDase8 and that was **8c**. The IC_{50} of **8c** ($0.24 \pm 0.02 \mu M$) was 400 times than that of suramin. However, no other compound could inhibit *h*-NTPDase8 to an appreciable extent.

Mechanism of Inhibition of Candidate Compounds

In order to determine the mechanism of inhibition, kinetic studies of most potent inhibitors were performed against

respective isozymes. In this regard, compound **8e** revealed a non-competitive mode of inhibition for *h*-NTPDase1 (Figure 1). However, compound **8j** was found to be a competitive inhibitor of *h*-NTPDase2 since all the four lines (indicating different concentrations of inhibitor) were intersecting at y-axis (Figure 2). Compound **8m** showed a non-competitive mode of inhibition for *h*-NTPDase3 (Figure 3) whereas the Lineweaver-Burk plot for *h*-NTPDase8 with compound **8c** exhibited a competitive mechanism of inhibition (Figure 4).

Effect of NTPDase3 Inhibitors on Insulin Secretion

The ability of *h*-NTPDase3 inhibitors (**8c** and **8m**) to stimulate insulin secretion was determined by using freshly isolated mice islets. It was observed that compound **8m** produced a significant increase in glucose stimulated insulin secretion as compared to control and activity of this compound (**8m**) was comparable to that of isobutyl methyl xanthine (IBMX), used as positive control. The results are shown in Figure 5.

The compound **8m** was tested at different doses (10–200 μM) and it induced a dose dependent increase in insulin secretion (Figure 6). However, compound **8m** did not produce any significant effect at basal glucose level (3 mM).

Although compound **8c** was the most potent *h*-NTPDase3 inhibitor but it did not show any significant effect on insulin secretion. This discrepancy in the behavior of compound **8c** might be attributed to the species difference. Therefore, we tested all the compound on mouse NTPDases (*m*-NTPDases)

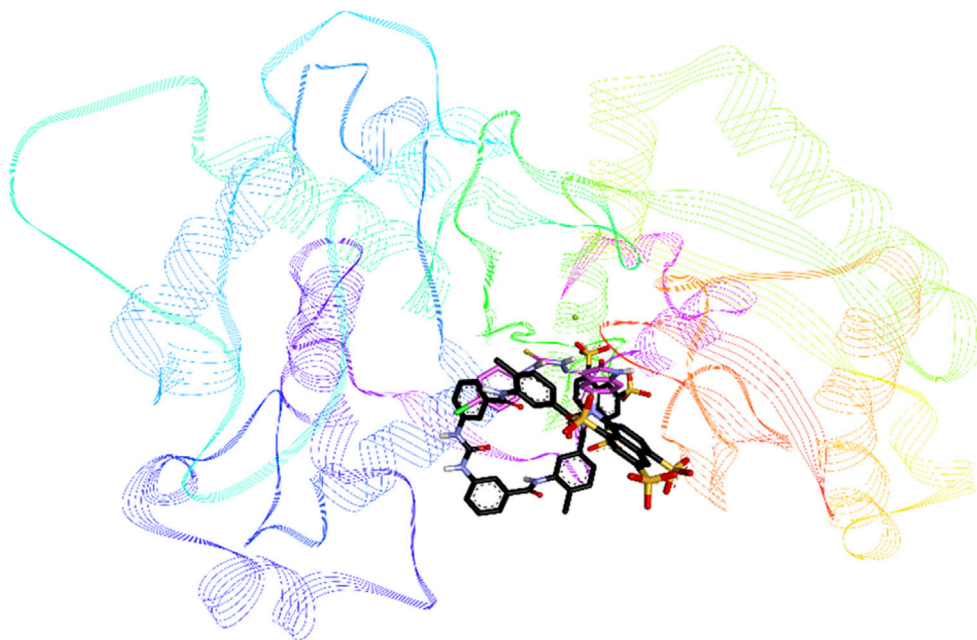


FIGURE 12 | Overlap of docked conformations of *h*-NTPDase3 inhibitor **8c** (gray) and standard inhibitor suramin (black), the protein backbone is represented in lined ribbon, the magnesium ion is shown as a green sphere.

and we found that compound **8c** was not an effective inhibitor of *m*-NTPDase3 (Table 4).

Suramin, used as positive control during enzyme inhibition studies, was tested for its insulin secretory activity. Isatin, used as a reactant during synthesis of target compounds, was also investigated for its ability to stimulate insulin secretion. Neither suramin nor isatin had any significant effect on insulin release (Figure 5).

Effect of **8m** on NTPDase3 Activity in Mice Pancreatic Islets

Given that compound **8m** was identified as an effective inhibitor of *h*-NTPDase3 as well as a regulator of the glucose-induced insulin secretion, we decided to determine the compound's effect on ectonucleotidase activity in isolated mice islets. A homogenate was prepared from the isolated islets which was treated with compound and then ectonucleotidase activity was

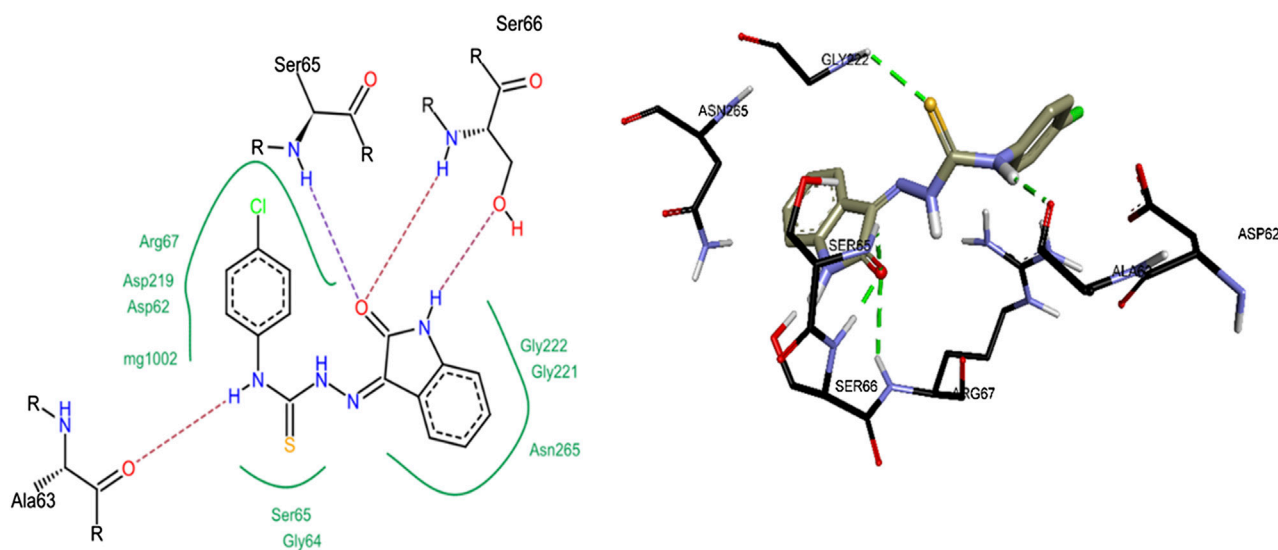
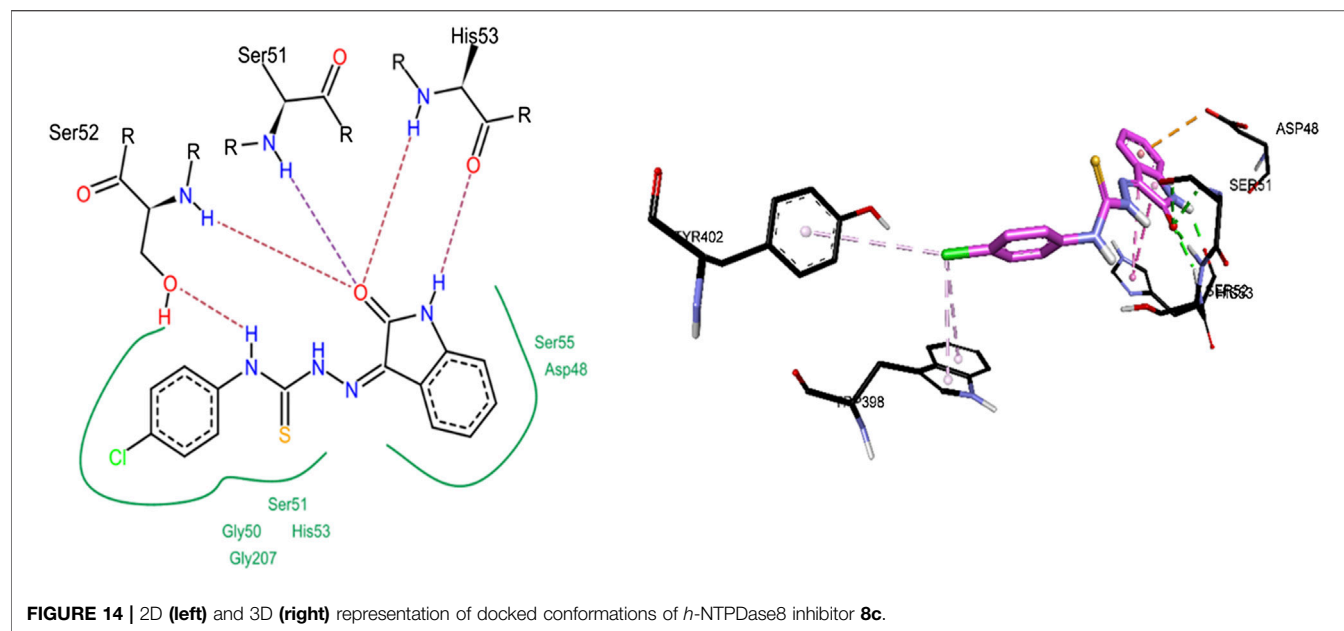


FIGURE 13 | 2D (left) and 3D (right) representation of docked conformations of *h*-NTPDase3 inhibitor **8c**.



determined by malachite green assay. At a concentration of 100 μ M, compound **8m** significantly decreased the ectonucleotidase activity as compared to control. The activity of test compound (**8m**) was comparable to that of suramin, a

standard inhibitor of NTPDase (Figure 7). Moreover, a dose response curve was generated for compound **8m** and it was found that compound **8m** produced a dose dependent decrease in enzyme activity (Figure 8).

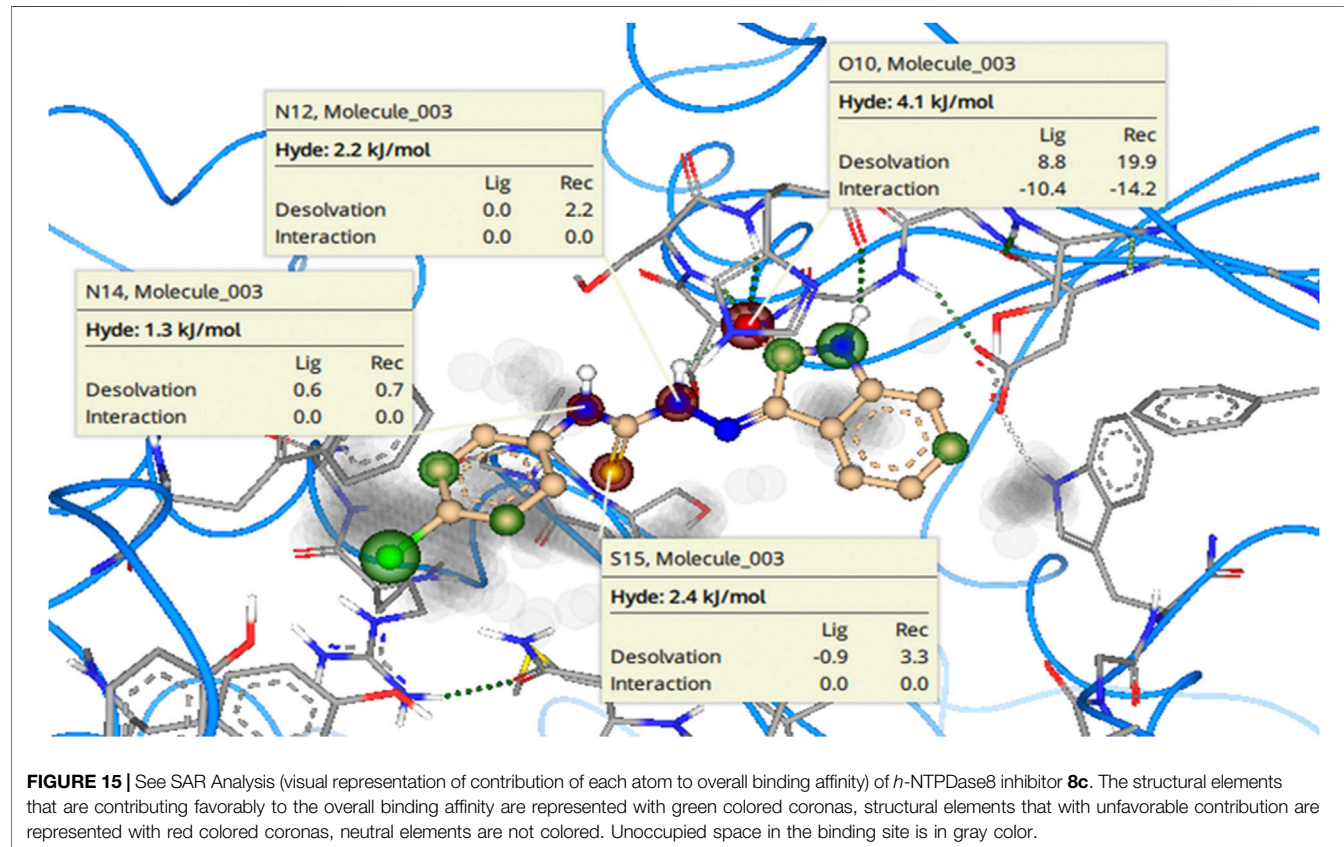


TABLE 5 | Summary of amino acids interacting with NTPDase inhibitors.

NTPDase inhibitors	Binding energy (kJ/mol)	Interacting amino acid residues	
		H-bond donors	H-bond acceptors
8i (NTPDase2)	–26	Nil	Leu202 (C=O), Ser346 (–OH), Ser52 (–OH)
8j (NTPDase2)	–29	Nil	Tyr350 (–OH), Ser346 (–OH), Leu202 (C=O)
8k (NTPDase2)	–29	Arg392 (NH(NH ₂)*NH ₂)	Ser346 (–OH), Ser52 (–OH)
8c (NTPDase3)	–27	Ser65 (–NH), Ser66 (–NH)	Ala63 (C=O), Ser66 (–OH)
8c (NTPDase8)	–27	Ser51 (–NH), Ser52 (–NH), His53 (–NH)	His53 (C=O), Ser52 (–OH)

Effect of 8m on NTPDase3 mRNA by Real Time Quantitative Polymerase Chain Reaction

To determine if the reduction in ectonucleotidase activity by compound **8m** in mice pancreatic islets was an outcome of downregulation of NTPDase3 mRNA, we analyzed the effect of this compound (**8m**) on NTPDase3 gene expression. Freshly isolated mice islets were incubated with test compound, total RNA was extracted and relative fold change in the NTPDase3 mRNA expression was determined by real time qPCR experiments. The results showed that test compound (**8m**) had no significant effect ($p > 0.05$) on the NTPDase3 gene expression in mice pancreatic islets as compared to control. Moreover, expression level of β -actin (housekeeping gene) was also not affected by compound **8m**.

Molecular Docking

Compounds **8i**, **8j** and **8k** were highly active against *h*-NTPDase2 and were therefore docked against this enzyme. For reference, docking of standard inhibitor suramin was also carried out. All compounds were found to bind in the same area of the active site, in the region that is also shared by suramin. **Figure 9** shows an overlap of docked conformations of inhibitors **8i**, **8j**, **8k** with suramin.

The most probable docked conformation of compound **8j**, the most active *h*-NTPDase2 inhibitor, is shown in **Figure 10**. As can be seen, the NH of the indole ring was making a hydrogen bond with Leu202. Likewise, one of the NH groups of thiourea moiety was making hydrogen bond with Ser346 whereas the other NH group was making hydrogen bond with Tyr350. The 2,5-dimethoxy phenyl ring was making a pi-cation interaction with Ala433, pi-sigma and pi-alkyl interactions were observed between the indole ring and the amino acids Ala347 and Arg245, respectively.

To further highlight the role of each structural element toward the overall binding affinity SeeSAR analysis was carried out.

BioSolveIT's SeeSAR is a tool that provides visual display of binding affinity. The information thus provided can be very helpful in logically modulating the structures of lead inhibitors, to synthesize even more potent inhibitors. The SeeSAR analysis of most active NTPDase inhibitors **8i** and **8j** is given in **Figure 11**. The structural features of the compound that are contributing positively to the overall binding affinity are indicated with green coronas; greater the contribution, larger is the size of the corona. Similarly, the structural elements that are not contributing favorably to the overall binding are indicated with red coronas, whereas the structural features with no contribution are not colored. As can be seen, most of the atoms in the molecule **8i** are contributing favorably to overall binding (indicated by green colored coronas), except two structural elements, i) one of the methyl carbon atoms of the 2,6-dimethyl substituted phenyl ring (labeled C23 in **Figure 11**, 9.8 kJ/mol), and ii) the sulfur atom (S15 in **Figure 11**, 1.2 kJ/mol) of thiourea (C = S) moiety. These unfavorable contributions are because of high desolvation energy which has not been compensated by any (favorable) non-bonded interaction. Based on the unoccupied space in the binding pocket (indicated in gray), the structure of the molecule can be changed/extended further to provide a more snug fit into the binding pocket. Similarly, for compound **8j**, unfavorable contribution to binding free energy is because of somewhat high desolvation energy of methoxy oxygen atoms (O22 and O24, 3.1 and 3.7 kJ/mol, respectively) and one of the phenyl ring carbon atoms (C18, 1.4 kJ/mol). Replacement of these atoms with some other suitable atoms/group is expected to result in even more active inhibitors.

Compound **8c** was the most active inhibitor of *h*-NTPDase3 and showed competitive mode of inhibition, hence its docking studies were carried out. For reference, suramin the standard inhibitor, was also docked. **Figure 12** shows overlap of docked conformation of **8c** with that of suramin. Docking studies of compound **8c** revealed a number of hydrogen bonded interactions, the indole NH was making a hydrogen bond with Ser66, while the carbonyl oxygen (of indole ring) was within hydrogen bond distance of Ser65 and Ser66. The NH group of thiourea moiety was making hydrogen bond with Ala63 (**Figure 13**).

Compound **8c** was the only inhibitor of *h*-NTPDase8 and showed competitive mode of inhibition, hence its docking studies were carried out. As shown in **Figure 14**, compound **8c** revealed a number of hydrogen bonded interactions, the indole NH was making a hydrogen bond with His53, while the carbonyl oxygen

TABLE 6 | Comparison of IC₅₀, Ki and binding energy of the most potent NTPDase inhibitors.

<i>h</i> -NTPDase inhibitor	IC ₅₀ (μM)	Ki (μM)	Binding energy (KJ/mol)
8i (NTPDase2)	0.41 ± 0.03	0.17	–26
8j (NTPDase2)	0.11 ± 0.08	0.04	–29
8k (NTPDase2)	0.16 ± 0.01	0.07	–29
8c (NTPDase3)	0.19 ± 0.02	0.08	–27
8c (NTPDase8)	0.24 ± 0.02	0.11	–27

(of indole ring) was within hydrogen bond distance of Ser52, Ser51 and His53. The NH group of thiourea moiety was making hydrogen bond with Ser52. Additionally, a pi-pi stacked interaction was also observed between the indole ring and His53. A pi-anion interaction was observed between indole phenyl ring and Asp48.

SeeSAR analysis of *h*-NTPDase8 inhibitor **8c** was also carried out as depicted in **Figure 15**. The structural elements with unfavorable contribution to the overall binding free energy are indicated in red coronas. These include the nitrogen atoms (N14, 1.3 kJ/mol; N12, 2.2 kJ/mol) and the sulfur atom (S15, 2.4 kJ/mol) of the thiourea moiety. This is because of high desolvation energy. The oxygen atom of the carbonyl group (O10 4.1 kJ/mol) also had high desolvation energy, although it was making a hydrogen bond, yet the compensation is not enough to fully compensate the penalty of (high) desolvation energy. It is suggested that replacement of these atoms with some other suitable atoms/group is expected to result in even more active inhibitors.

A summary of amino acids interacting with NTPDase inhibitors as well as binding energy associated with these inhibitors is presented in **Table 5**. These computed binding energies were compared with biological data in **Table 6**, where biological data is presented in the form of IC_{50} and K_i values. The binding energy values were in close agreement with the experimentally determined IC_{50}/K_i values. For instance, the most potent *h*-NTPDase2 inhibitor (**8j**, $IC_{50} = 0.11 \pm 0.08 \mu M$, $K_i = 0.04 \mu M$) had the best binding energy of -29 kJ/mol. Similarly, compounds **8c** with the binding energy of -27 kJ/mol was found to be the most potent inhibitor of *h*-NTPDase3 ($IC_{50} = 0.19 \pm 0.02 \mu M$, $K_i = 0.08$) and *h*-NTPDase8 ($IC_{50} = 0.24 \pm 0.02 \mu M$, $K_i = 0.11 \mu M$).

DISCUSSION

In this study, we have synthesized and evaluated a series of oxoindolin hydrazine carbothioamide derivatives as potential NTPDase inhibitors. Most of the compounds appeared to be more potent inhibitors of *h*-NTPDase1 than other NTPDases. Compound **8e** and **8j** were the most potent *h*-NTPDase1 inhibitors whereas compound **8j** was also the most potent inhibitor of *h*-NTPDase2. Both of these compounds contained an $-OCH_3$ group as a part of their structure, thus implying the importance of this $-OCH_3$ for *h*-NTPDase1 and -2 inhibitors. On the other hand, compound **8c** was found to be potent dual inhibitor of *h*-NTPDase3 and -8. Interestingly, compound **8b**, **8e**, **8f**, and **8i** were identified as selective inhibitors of *h*-NTPDase1 whereas compound **8k** selectively inhibited the *h*-NTPDase2. Furthermore, compound **8e**, **8j**, **8c**, and **8m** were studied in detail to establish their mechanism of inhibition. Compound **8e** inhibited *h*-NTPDase1 in a non-competitive manner whereas compound **8j** and **8c** revealed a competitive mode of inhibition against *h*-NTPDase2 and -8, respectively. Kinetics studies of compound **8m** revealed that it was inhibiting the *h*-NTPDase3 in a non-competitive manner.

In literature, different classes of compounds have been synthesized as NTPDase inhibitors, including nucleotide analogues, polyoxometalates (POMs) and anthraquinone

derivatives. Among them, POMs showed best inhibitory activity with K_i value as low as $0.0038 \mu M$ (Lee et al., 2015) whereas 8-Bus-ATP (nucleotide analogue) was found to be a selective inhibitor of *h*-NTPDase1 ($K_i = 0.8 \pm 0.2 \mu M$) (Lecka et al., 2013). The K_i values of our compounds against *h*-NTPDases were found to be in the range of 0.02 – $0.38 \mu M$. Thus, our compounds tend to be more potent than 8-Bus-ATP but their activity is low as compared to POMs. A recent study (Baqi et al., 2020) reported synthesis of anthraquinone derivatives as potent *h*-NTPDase inhibitors, showing selectivity against *h*-NTPDase2 and -3. The IC_{50} values of these compounds were found to be within the range of 0.39 – $15.3 \mu M$, while the IC_{50} values of our compounds were within the range of 0.11 – $2.60 \mu M$, indicating that our compounds are more active *h*-NTPDase inhibitors than anthraquinone derivatives.

NTPDase3 is the most prominent isoform in pancreatic islets where it has been reported to regulate the insulin secretion (Bartley et al., 2019; Saunders et al., 2019). Therefore, NTPDase3 inhibitors i.e. **8c** and **8m** were evaluated for their effects on insulin secretion in mice islets. Compound **8m** produced a dose dependent increase in insulin release, in the presence of high glucose concentration. At basal glucose level, compound **8m** has no effect on insulin secretion since glucose is the actual initiator of insulin release, whereas ATP can stimulate the insulin secretion only in the presence of high glucose concentration (Cieślak and Cieślak, 2017). On the other hand, compound **8c** had no significant effect on insulin secretion due to species difference, as the screening of compounds on *m*-NTPDases showed that compound **8c** exhibited $< 50\%$ inhibition against *m*-NTPDase3. Although compound **8m** was showing good inhibitory activity against *m*-NTPDase1, -2 and -3, it was the *m*-NTPDase3 inhibition that potentiated the insulin secretion since NTPDase3 is the predominant isoform expressed in mice islets. In this context, a study had reported that NTPDase3 was the most abundant isoform in mouse and human islets whereas least amounts of NTPDase1 and -2 were detected. They used a non-selective NTPDase inhibitor (ARL67156) and established that it was the NTPDase3 inhibition that potentiated insulin secretion. They also performed siRNA experiments and observed that the knockdown of NTPDase3 expression was producing the same effects on insulin secretion as those obtained with ARL67156, thus suggesting that it is NTPDase3 inhibition that is contributing to insulin secretion (Syed et al., 2013).

Furthermore, we also determined the inhibitory effect of compound (**8m**) in mice islets and it produced a significant reduction in ectonucleotidase activity, suggesting that compound (**8m**) is stimulating the insulin secretion via NTPDase3 inhibition. However, inhibition of NTPDase3 (by compound **8m**) was not occurring due to the downregulation of NTPDase3 mRNA since compound (**8m**) had not suppressed the gene expression of NTPDase3. Finally, molecular docking studies and SeeSAR analysis of the most potent inhibitors were also carried out and the calculated binding energies were in accordance with our experimental data. Taken together, our study demonstrates that **8m** is a potent inhibitor of NTPDase3 which is involved in the stimulation of glucose induced insulin secretion without suppressing the NTPDase3 gene.

CONCLUSION

In a series of oxoindolin hydrazine carbothioamide derivatives, only two compounds i.e. **8c** ($IC_{50} = 0.19 \mu M \pm 0.02$) and **8m** ($IC_{50} = 0.38 \pm 0.03$) showed excellent inhibition of *h*-NTPDase3. These inhibitors of *h*-NTPDase3 were investigated for their effects on insulin secretion and only compound **8m** was found as a lead regulator of insulin secretion. Further studies revealed that compound **8m** significantly reduced ectonucleotidase activity in mice pancreatic islets. In consistence with our *in vitro* data, docking studies displayed strong binding interaction of potent inhibitors within the active site of respective enzyme. In conclusion, we report compound **8m** as a potent inhibitor of *h*-NTPDase3, stimulating the glucose induced insulin secretion. Further study is needed to investigate **8m** as a potential drug candidate.

DATA AVAILABILITY STATEMENT

The raw data supporting the conclusions of this article will be made available by the authors, without undue reservation, to any qualified researcher.

REFERENCES

- Ali, A. Q., Teoh, S. G., Salhin, A., Eltayeb, N. E., Ahamed, M. B., and Majid, A. A. (2014). Synthesis of isatin thiosemicarbazones derivatives: in vitro anti-cancer, DNA binding and cleavage activities. *Spectrochim. Acta Mol. Biomol. Spectrosc.* 125, 440–448. doi:10.1016/j.saa.2014.01.086
- Allard, B., Longhi, M. S., Robson, S. C., and Stagg, J. (2017). The ectonucleotidases CD 39 and CD 73: novel checkpoint inhibitor targets. *Immunol. Rev.* 276, 121–144. doi:10.1111/imr.12528
- Bagatini, M. D., dos Santos, A. A., Cardoso, A. M., Mânica, A., Reschke, C. R., and Carvalho, F. B. (2018). The impact of purinergic system enzymes on noncommunicable, neurological, and degenerative diseases. *J. Immunol. Res.* 2018, 4892473. doi:10.1155/2018/4892473
- Baqi, Y., Rashed, M., Schäkel, L., Malik, E. M., Pelletier, J., Sévigny, J., et al. (2020). Development of anthraquinone derivatives as ectonucleoside triphosphate diphosphohydrolase (NTPDase) inhibitors with selectivity for NTPDase2 and NTPDase3. *Front. Pharmacol.* 11, 1282. doi:10.3389/fphar.2020.01282
- Bartley, C., Brun, T., Oberhauser, L., Grimaldi, M., Molica, F., Kwak, B. R., et al. (2019). Chronic fructose renders pancreatic β -cells hyper-responsive to glucose-stimulated insulin secretion through extracellular ATP signaling. *Am. J. Physiol. Endocrinol. Metab.* 317, E25–E41. doi:10.1152/ajpendo.00456.2018
- Bertoni, A. P., de Campos, R. P., Tamajusuku, A. S., Stefani, G. P., Braganhol, E., Battastini, A. M., et al. (2020). Biochemical analysis of ectonucleotidases on primary rat vascular smooth muscle cells and in silico investigation of their role in vascular diseases. *Life Sci.* 256, 117862. doi:10.1016/j.lfs.2020.117862
- Bradford, M. M. (1976). A rapid and sensitive method for the quantitation of microgram quantities of protein utilizing the principle of protein-dye binding. *Anal. Biochem.* 72, 248–254. doi:10.1016/0003-2697(76)90527-3
- Castilhos, L. G., Adefegha, S. A., Doleski, P. H., Bertoldo, T. M., Moritz, C. E., Casali, E. A., et al. (2018). NTPDase, 5'-nucleotidase and adenosine deaminase activities and purine levels in serum of sickle cell anemia patients. *J. Appl. Biomed.* 16, 208–213. doi:10.1016/j.jab.2017.12.004
- Chen, Z., Wang, J., Sun, W., Archibong, E., Kahkoska, A. R., Zhang, X., et al. (2018). Synthetic beta cells for fusion-mediated dynamic insulin secretion. *Nat. Chem. Biol.* 14, 86–93. doi:10.1038/nchembio.2511
- Cieślak, M., and Cieślak, M. (2017). Role of purinergic signalling and proinflammatory cytokines in diabetes. *Clin. Diabetol.* 6, 90–100. doi:10.5603/DK.2017.0015

ETHICS STATEMENT

This study was reviewed and approved by Research Ethics Committee, Department of Pharmacy, COMSATS University Islamabad, Abbottabad Campus.

AUTHOR CONTRIBUTIONS

SA carried out synthesis and enzyme assays, Mal-R Designed Synthesis of the derivatives, AH supervised the effect on glucose stimulated insulin secretion, JP and JS expressed the enzymes used in the study. JI designed the project and supervised the biological experiments.

SUPPLEMENTARY MATERIAL

The Supplementary Material for this article can be found online at: <https://www.frontiersin.org/articles/10.3389/fphar.2020.585876/full#supplementary-material>

- Dou, L., Chen, Y. F., Cowan, P. J., and Chen, X. P. (2018). Extracellular ATP signaling and clinical relevance. *Clin. Immunol.* 188, 67–73. doi:10.1016/j.clim.2017.12.006
- Galicía-García, U., Benito-Vicente, A., Jebari, S., Larrea-Sebal, A., Siddiqi, H., Uribe, K. B., et al. (2020). Pathophysiology of type 2 diabetes mellitus. *Int. J. Mol. Sci.* 21, 6275. doi:10.3390/ijms21176275
- Giuliani, A. L., Sarti, A. C., and Di Virgilio, F. (2019). Extracellular nucleotides and nucleosides as signalling molecules. *Immunol. Lett.* 205, 16–24. doi:10.1016/j.imlet.2018.11.006
- Grković, I., Drakulić, D., Martinović, J., and Mitrović, N. (2019). Role of ectonucleotidases in synapse formation during brain development: physiological and pathological implications. *Curr. Neuropharmacol.* 17, 84–98. doi:10.2174/1570159X15666170518151541
- Hameed, A., Hafizur, R. M., Hussain, N., Raza, S. A., Rehman, M., Ashraf, S., et al. (2018). Eriodictyol stimulates insulin secretion through cAMP/PKA signaling pathway in mice islets. *Eur. J. Pharmacol.* 820, 245–255. doi:10.1016/j.ejphar.2017.12.015
- Hedekso, C. J., and Capito, K. (1974). The effect of starvation on insulin secretion and glucose metabolism in mouse pancreatic islets. *Biochem. J.* 140, 423–433. doi:10.1042/bj1400423
- Iqbal, J., and Shah, S. J. A. (2018). Molecular dynamic simulations reveal structural insights into substrate and inhibitor binding modes and functionality of Ecto-Nucleoside Triphosphate Diphosphohydrolases. *Sci. Rep.* 8, 1–11. doi:10.1038/s41598-018-20971-4
- Kasuya, G., Fujiwara, Y., Tsukamoto, H., Morinaga, S., Ryu, S., Touhara, K., et al. (2017a). Structural insights into the nucleotide base specificity of P2X receptors. *Sci. Rep.* 7, 45208. doi:10.1038/srep45208
- Kasuya, G., Yamaura, T., Ma, X. B., Nakamura, R., Takemoto, M., Nagumo, H., et al. (2017b). Structural insights into the competitive inhibition of the ATP-gated P2X receptor channel. *Nat. Commun.* 8, 876. doi:10.1038/s41467-017-00887-9
- Lavoie, E. G., Fausther, M., Kauffenstein, G., Kukulski, F., Künzli, B. M., Friess, H., et al. (2010). Identification of the ectonucleotidases expressed in mouse, rat, and human Langerhans islets: potential role of NTPDase3 in insulin secretion. *Am. J. Physiol. Endocrinol. Metab.* 299, E647–E656. doi:10.1152/ajpendo.00126.2010
- Lecka, J., Fausther, M., Künzli, B., and Sévigny, J. (2014). Ticlopidine in its prodrug form is a selective inhibitor of human NTPDase1. *Mediat. Inflamm.* 2014, 547480. doi:10.1155/2014/547480
- Lecka, J., Gillerman, I., Fausther, M., Salem, M., Munkonda, M. N., Brosseau, J. P., et al. (2013). 8-BuS-ATP derivatives as specific NTPDase1 inhibitors. *Br. J. Pharmacol.* 169, 179–196. doi:10.1111/bph.12135

- Lee, S. Y., Fiene, A., Li, W., Hanck, T., Brylev, K. A., Fedorov, V. E., et al. (2015). Polyoxometalates—potent and selective ecto-nucleotidase inhibitors. *Biochem. Pharmacol.* 93, 171–181. doi:10.1016/j.bcp.2014.11.002
- Lee, S. Y., and Müller, C. E. (2017). Nucleotide pyrophosphatase/phosphodiesterase 1 (NPP1) and its inhibitors. *MedChemComm* 8, 823–840. doi:10.1039/C7MD00015D
- Lee, S. Y., Sarkar, S., Bhattacharai, S., Namasivayam, V., De Jonghe, S., Stephan, H., et al. (2017). Substrate-dependence of competitive nucleotide pyrophosphatase/phosphodiesterase1 (NPP1) inhibitors. *Front. Pharmacol.* 8, 54. doi:10.3389/fphar.2017.00054
- Levesque, S. A., Lavoie, É. G., Lecka, J., Bigonnesse, F., and Sévigny, J. (2007). Specificity of the ecto-ATPase inhibitor ARL 67156 on human and mouse ectonucleotidases. *Br. J. Pharmacol.* 152, 141–150. doi:10.1038/sj.bjp.0707361
- Longhi, M. S., Moss, A., Jiang, Z. G., and Robson, S. C. (2017). Purinergic signaling during intestinal inflammation. *J. Mol. Med.* 95, 915–925. doi:10.1007/s00109-017-1545-1
- Lu, R., Zhang, Z., and Jiang, C. (2019). Recent progress on the discovery of P2Y14 receptor antagonists. *Eur. J. Med. Chem.* 175, 34–39. doi:10.1016/j.ejmech.2019.04.068
- Martín-Satué, M., Lavoie, E. G., Pelletier, J., Fausther, M., Csizmadia, E., Guckelberger, O., et al. (2009). Localization of plasma membrane bound NTPDases in the murine reproductive tract. *Histochem. Cell Biol.* 131, 615–628. doi:10.1007/s00418-008-0551-3
- Nabinger, D. D., Altenhofen, S., and Bonan, C. D. (2020). Zebrafish models: gaining insight into purinergic signaling and neurological disorders. *Prog. Neurobiopharmacol. Biol. Psychiatry*. 98, 109770. doi:10.1016/j.pnpbp.2019.109770
- Paes-Vieira, L., Gomes-Vieira, A. L., and Meyer-Fernandes, J. R. (2018). NTPDase activities: possible roles on Leishmania spp infectivity and virulence. *Cell Biol. Int.* 42, 670–682. doi:10.1002/cbin.10944
- Pervez, H., Chohan, Z. H., Ramzan, M., Nasim, F. U. H., and Khan, K. M. (2009). Synthesis and biological evaluation of some new N4-substituted isatin-3-thiosemicarbazones. *J. Enzym. Inhib. Med. Chem.* 24, 437–446. doi:10.1080/14756360802188420
- Saunders, D. C., Brissova, M., Phillips, N., Shrestha, S., Walker, J. T., Aramandla, R., et al. (2019). Ectonucleoside triphosphate diphosphohydrolase-3 antibody targets adult human pancreatic β cells for *in vitro* and *in vivo* analysis. *Cell Metabol.* 29, 745–754. doi:10.1016/j.cmet.2018.10.007
- Solini, A., and Novak, I. (2019). Role of the P2X7 receptor in the pathogenesis of type 2 diabetes and its microvascular complications. *Curr. Opin. Pharmacol.* 47, 75–81. doi:10.1016/j.coph.2019.02.009
- Stuhlmann, T., Planells-Cases, R., and Jentsch, T. J. (2018). LRRC8/VRAC anion channels enhance β -cell glucose sensing and insulin secretion. *Nat. Commun.* 9, 1974. doi:10.1038/s41467-018-04353-y
- Syed, S. K., Kauffman, A. L., Beavers, L. S., Alston, J. T., Farb, T. B., Ficorilli, J., et al. (2013). Ectonucleotidase NTPDase3 is abundant in pancreatic β -cells and regulates glucose-induced insulin secretion. *Am. J. Physiol. Endocrinol. Metab.* 305, E1319–E1326. doi:10.1152/ajpendo.00328.2013
- Tozzi, M., Larsen, A. T., Lange, S. C., Giannuzzo, A., Andersen, M. N., and Novak, I. (2018). The P2X7 receptor and pannexin-1 are involved in glucose-induced autocrine regulation in β -cells. *Sci. Rep.* 8, 8926. doi:10.1038/s41598-018-27281-9
- Tozzi, M., and Novak, I. (2017). Purinergic receptors in adipose tissue as potential targets in metabolic disorders. *Front. Pharmacol.* 8, 878. doi:10.3389/fphar.2017.00878
- Vakilian, M., Tahamtani, Y., and Ghaedi, K. (2019). A review on insulin trafficking and exocytosis. *Gene* 706, 52–61. doi:10.1016/j.gene.2019.04.063
- Zhong, A. H., Jiang, Z. G., Cummings, R. D., and Robson, S. C. (2017). Various N-glycoforms differentially upregulate E-NTPDase activity of the NTPDase3/CD39L3 ecto-enzymatic domain. *Purinergic Signal.* 13, 601–609. doi:10.1007/s11302-017-9587-y

Conflict of Interest: The authors declare that the research was conducted in the absence of any commercial or financial relationships that could be construed as a potential conflict of interest.

Copyright © 2020 Iqbal, Afzal, al-Rashida, Hameed, Pelletier and Sévigny. This is an open-access article distributed under the terms of the Creative Commons Attribution License (CC BY). The use, distribution or reproduction in other forums is permitted, provided the original author(s) and the copyright owner(s) are credited and that the original publication in this journal is cited, in accordance with accepted academic practice. No use, distribution or reproduction is permitted which does not comply with these terms.



Biophysical Compatibility of a Heterotrimeric Tyrosinase-TYRP1-TYRP2 Metalloenzyme Complex

Olga Lavinda¹, Prashiela Manga², Seth J. Orlow² and Timothy Cardozo^{1*}

¹Department of Biochemistry and Molecular Pharmacology, NYU Grossman School of Medicine, New York, NY, United States,

²The Ronald O. Perleman Department of Dermatology, NYU Grossman School of Medicine, New York, NY, United States

OPEN ACCESS

Edited by:

Salvatore Salomone,
University of Catania, Italy

Reviewed by:

Yuri Sergeev,
National Institutes of Health (NIH),
United States
Montse Soler Lopez,
European Synchrotron Radiation
Facility, France

*Correspondence:

Timothy Cardozo
Timothy.Cardozo@nyulangone.org

Specialty section:

This article was submitted to
Experimental Pharmacology
and Drug Discovery,
a section of the journal
Frontiers in Pharmacology

Received: 02 September 2020

Accepted: 08 February 2021

Published: 28 April 2021

Citation:

Lavinda O, Manga P, Orlow SJ and
Cardozo T (2021) Biophysical
Compatibility of a Heterotrimeric
Tyrosinase-TYRP1-TYRP2
Metalloenzyme Complex.
Front. Pharmacol. 12:602206.
doi: 10.3389/fphar.2021.602206

Tyrosinase (TYR) is a copper-containing monooxygenase central to the function of melanocytes. Alterations in its expression or activity contribute to variations in skin, hair and eye color, and underlie a variety of pathogenic pigmentary phenotypes, including several forms of oculocutaneous albinism (OCA). Many of these phenotypes are linked to individual missense mutations causing single nucleotide variants and polymorphisms (SNVs) in *TYR*. We previously showed that two TYR homologues, TYRP1 and TYRP2, modulate TYR activity and stabilize the TYR protein. Accordingly, to investigate whether TYR, TYRP1, and TYRP2 are biophysically compatible with various heterocomplexes, we computationally docked a high-quality 3D model of TYR to the crystal structure of TYRP1 and to a high-quality 3D model of TYRP2. Remarkably, the resulting TYR-TYRP1 heterodimer was complementary in structure and energy with the TYR-TYRP2 heterodimer, with TYRP1 and TYRP2 docking to different adjacent surfaces on TYR that apposed a third realistic protein interface between TYRP1-TYRP2. Hence, the 3D models are compatible with a heterotrimeric TYR-TYRP1-TYRP2 complex. In addition, this heterotrimeric TYR-TYRP1-TYRP2 positioned the C-terminus of each folded enzymatic domain in an ideal position to allow their C-terminal transmembrane helices to form a putative membrane embedded three-helix bundle. Finally, pathogenic *TYR* mutations causing OCA1A, which also destabilize TYR biochemically, cluster on an unoccupied protein interface at the periphery of the heterotrimeric complex, suggesting that this may be a docking site for OCA2, an anion channel. Pathogenic OCA2 mutations result in similar phenotypes to those produced by OCA1A *TYR* mutations. While this complex may be difficult to detect *in vitro*, due to the complex environment of the vertebrate cellular membranous system, our results support the existence of a heterotrimeric complex in melanogenesis.

Keywords: tyrosinase, oculocutaneous albinism, computational molecular docking, protein-protein interface, melanosome, pigmentary disorders, molecular modeling

INTRODUCTION

Tyrosinase (TYR) catalyzes three reactions during melanin synthesis in mammalian skin, eyes, and other organs. Melanin biosynthesis requires TYR and is enhanced by expression of the TYR homologues, tyrosinase related proteins 1 and 2 (TYRP1 and TYRP2/Dopachrome Tautomerase). Efficient maturation of the TYR protein ensures stability, enzyme activity and delivery to melanosomes where melanin is produced and deposited. Impaired TYR maturation is common to several forms of the group of genetic disorders known as oculocutaneous albinism (OCA) in humans. Mutations in the *TYR* gene itself, many of which cause protein misfolding with attendant inability to exit the endoplasmic reticulum (ER) (Berson et al., 2000; Toyofuku et al., 2001a; Chaki et al., 2010), result in OCA type 1 (OCA1A). Less severe *TYR* mutations cause partial loss of function and reduced protein folding efficiency (OCA1B) (Toyofuku et al., 2001a). TYR is retained in the ER in OCA2 (Chen et al., 2002) [OCA2 gene mutations (Kedda et al., 1994)], OCA3 (Toyofuku et al., 2001b) [*TYRP1* mutations (Manga et al., 1997)] and OCA4 (Costin et al., 2003) [*SLC45A2* mutations (Newton et al., 2001)].

Trait-associated (non-pathogenic) *TYR* sequence variants (SNVs) that appear to exhibit maturation deficits are determinants of both skin (Shriver et al., 2003) and eye color (Sulem et al., 2007). Missense *TYR* SNVs that foster the production of autoantibodies against the protein correlate with reduced susceptibility to melanoma (Gerstenblith et al., 2010) and increased risk of the melanocyte-targeting autoimmune disorder vitiligo (Gerstenblith et al., 2007; Damico et al., 2009; Jin et al., 2010; Spritz, 2010). *TYR* SNVs are also genetically associated with susceptibility to cutaneous squamous cell carcinoma (SCC) (Asgari et al., 2016), the second most common cancer in the United States, and to its precursor, actinic keratosis (Jacobs et al., 2015). Interestingly, this association is independent of skin color (Jacobs et al., 2015; Asgari et al., 2016; Zhong et al., 2017). Over 100 *TYR* SNVs have been associated with disease phenotypes, while just a handful of variants are prevalent in the population at large. Thus, distinct phenotypes are caused by, or associated with, *TYR* amino acid variants/mutants.

TYR is a type I membrane protein, with a large intraluminal N-terminal folded domain followed by a short, flexible carboxy-terminus linker terminating in a C-terminal transmembrane helix. There are two copper binding sites required for catalytic activity, 7N-glycosylated asparagine residues and three cysteine-rich regions required for disulfide bond formation. Unlike many membrane proteins including TYRP1, TYR is retained for an unusually long period of time in the ER (Petrescu et al., 1997; Ujvari et al., 2001), which suggests that early TYR processing is highly regulated and/or complex.

The Tyrosinase family of genes is comprised of the ancestral gene *TYR* and two related genes *TYRP1* and *TYRP2*, which display a closer relationship to each other than that to *TYR* (Morrison et al., 1994). All three proteins in this family share both genetic sequence and structural similarities: all are type I membrane protein, with a large intraluminal N-terminal folded domain followed by a short, flexible linker terminating in a C-terminal transmembrane helix. In fact, TYRP1 is

hypothesized to have evolved from TYR by duplication, later giving rise to TYRP2 (Sturm et al., 1995).

A number of studies suggest that TYR and TYRPs may hetero-oligomerize. Biochemically (*in vitro*), immunopurified TYR was stabilized and more active with immunopurified TYRP1 and/or TYRP2 (Hearing et al., 1992; Kobayashi et al., 1994; Winder et al., 1994), and gel filtration chromatography experiments demonstrated that TYR and TYRP1 heterodimerize in solution (Jiménez-Cervantes et al., 1998). In cells, co-expression of TYRP1 or TYRP2 (TRPs) has been shown to improve TYR stability and pigmentation (Kobayashi et al., 1998; Manga et al., 2000), and chemical-crosslinking in cells suggests the association of TYRP1 with TYR (Kobayashi and Hearing, 2007). TRPs are also detected in large molecular complexes in melanocyte lysates (Orlow et al., 1994). Conversely, Lai et al. failed to detect oligomerization with *in vitro* with recombinant forms (Lai et al., 2017), and a study showed that TYR and TYRP1 may have a low propensity to form oligomeric complexes in *in vitro* conditions designed to mimic the *in vivo* environment of the melanosome (Dolinska et al., 2020). Thus, the question of whether TYR and the TRPs form physiologically relevant functional complexes in the ER or melanosome or both remains an unanswered question in the field.

3D structure often encodes specific, yet elusive, *in vivo* constraints. For example, the chemistry and shape of a direct protein interaction surface with a binding partner that is critical for organism fitness will be conserved through evolution, even if it is a transient association in a processing sequence or dependent on a large complex of allosteric cofactors, such as bridging proteins, cytoskeletal structures, membranes, carbohydrates etc. Thus, such an interaction may be difficult to reconstitute *in vitro* or even in cells, but will be evident by direct physics based complementarity between the 3D shapes of the binding partners, including for transient complexes (Medina et al., 2008). Thus, physiologically-relevant complexes may be evident in computational biophysical studies, such as computational molecular docking, that elude experimental biophysical experiments (e.g., crystallography, surface plasmon resonance) or experimental biochemical experiments (e.g., purified recombinant binding, chromatography, immunoprecipitation). We hypothesized that transient TYR complexes may be detectable by computational molecular docking, despite the difficulties of observing them biochemically. Mapping of TYR missense variants on TYR 3D structure in any suitable context suggested by the presence of its associated homologues TYRP1 and TYRP2 might validate such computational biophysical models and illuminate TYR function. While the 3D structure of human TYR has not been available, an X-ray crystallographic structure of closely related human TYRP1 was resolved (Lai et al., 2017). Accordingly, we built precise, full-length 3D structural models of human TYR and its homologue TYRP2, investigated how compatible, by computational molecular docking in physics-based force-fields, the 3D structural models of TYR, TYRP1, and TYRP2 were as heterocomplexes, and mapped the known phenotypic SNVs and pathogenic mutations onto the models to see if any physically realistic heterocomplexes were compatible with mutation locations. The results strongly suggest the

existence of a membrane-associated heterotrimeric TYR-TYRP1-TYRP2 complex, exhibiting an unoccupied protein surface decorated with OCA1A mutations.

MATERIALS AND METHODS

Previously Reported Mutations in TYR

Previously reported mutations in *TYR* were collected from the OMIM database: <https://www.omim.org>, dbSNP: <https://www.ncbi.nlm.nih.gov/snp>, UniProt: <https://www.uniprot.org>, and GWAS databases: <https://www.gwascentral.org>, and <https://www.genome.gov> databases.

Homology Models of TYR and TYRP2

The 2.35 Å crystallographic structure of TYRP1 (PDB: 5M8L) was used as a template for homology modeling (Lai et al., 2017). Maximally-accurate, full-length 3D homology models of TYR and TYRP2 were built as previously described (Cardozo et al., 1995; Martinez-Ortiz and Cardozo, 2018). Briefly, a sequence alignment between either the human TYR enzymatic domain amino acid sequence or the human TYRP2 enzymatic domain amino acid sequence and amino acid sequence of human TYRP1 from the template structure was generated using zero-end-gap global alignment, which is a variation of the original Needleman-Wunsch dynamic programming global alignment optimized for structural homology detection, and the *p*-value for statistical confidence/strength of this alignment was calculated (Abagyan and Batalov, 1997). The few TYR amino acid residue assignments predicted by the alignment to be at or in the vicinity of inserted or deleted residues relative to the two proteins were adjusted manually based on the 3D structural environment, as previously described (Cardozo et al., 1995), which resulted in significant conformational differences in these areas between our models and models generated previously by Lai et al. (e.g., **Supplementary Figure S1**). The conformations of non-identical side chains and loops containing insertions or deletions were then predicted *ab initio* using the Biased Probability Monte Carlo (BPMC) algorithm (Abagyan and Totrov, 1994). Energy-based refinement was carried out until minimal energy was reached, producing the most unclashed, stable, relaxed models possible for the purposes of protein-protein docking. As with the TYRP1 model used as a template modeling (Lai et al., 2017), glycans were not included in the models. Although some studies suggest that glycans are important for TYR stability, these studies used mutagenesis of glycosylated asparagines and did not prove that observed loss of stability was due to deglycosylation or the mutations themselves, which are historically far more deleterious to protein structure than deglycosylation (Cai et al., 2017; Dolinska and Sergeev, 2017). All modeling procedures were carried out using ICM-Pro/Homology software (Molsoft LLC, La Jolla, CA).

Prediction of Protein Interaction Sites on the Surface of TYR

Potential protein interfaces on TYR and TYRP2 were predicted using optimal docking area (ODA) (Fernandez-Recio et al.,

2005b). The same analysis was performed for the TYRP1 structure as part of the analysis of the complexes of TYR, TYRP1, and TYRP2.

Protein-Protein Docking

Docking to the TYR homology model (assigned as a receptor) using either the TYRP1 crystal structure or the TYRP2 homology model as rigid body search models/ligands was performed as previously described (Fernández-Recio et al., 2005a). Briefly, a set of soft receptor potentials were pre-calculated using the atom coordinates of the TYR model on a 0.5 Å grid from realistic solvent-corrected force-field energies, including improved implementations of de-solvation. A rotational and translational Monte-Carlo search with local minimization of the rigid all-atom model of either TYRP1 or TYRP2 within these potentials was then performed. This search finds the correct solution as the lowest energy conformation in almost 100% of test cases in which interfaces do not change on binding (Fernández-Recio et al., 2003; Fernandez-Recio et al., 2005a). The global optimization of the interface side-chains of up to 400 of the best solutions was then performed, in order to improve accuracy for cases where the interfaces change somewhat upon binding. Solutions were then ranked according to the energy terms, which include van der Waals, solvation electrostatics, hydrogen bonding and entropy. Once the heterodimers were identified and optimized, each heterodimer was then docked to the third protein in the Tyrosinase family, i.e., TYR-TYRP1 dimer was docked to TYRP2 and independently TYR-TYRP2 dimer was docked to TYRP1. This approach was taken to ensure reproducibility of the docking approach. If the heterotrimer complex obtained in the first docking procedure is valid, we expected it to be reproducible by docking using the second approach. Both docking protocols converged on the same lowest energy heterotrimer structure, within which the TYRP1 and TYRP2 conformations did not clash with each other despite being unaware of the other during docking.

Model of Transmembrane Helix Bundle and Linkers Between Transmembrane Helices and Enzymatic Domains

The template (HIV gp41 PDB 3F4Y) for modeling a parallel, transmembrane three-helix bundle formed by the three Tyrosinase family proteins in a complex was identified using the CC+ database (Testa et al., 2009). The sequences of the C-terminal transmembrane domain of TYR (amino acids 477-497: WLLGAAMVGAVLTALLAGLVS), TYRP1 (478-501: IIAIAVVGALLLVALIFGTASYL) and TYRP2 (473-493: LLVVMGTLVALVGLFVLLAFL) were modeled on the central parallel three helix bundle from the template using the same homology modeling approach as for the enzymatic domains. This 3-helix bundle was placed equidistant from the three C-termini of the three models in the heterotrimeric complex at a distance suitable for the shortest linker to reach between the two and the linkers were energy minimized.

45% pP=40.2		.FPR.C#...L...CCP.#S...P...CG..SGRG.C..#...#..PO#P#..G.DDRE.WP..F#NRTC.C.GNF.G#NCG.C+
HUMAN_TYR	1	HFPRACVSSKNLMEKECCPPWSGDRSE-----CGQLSGRGSCQNIILLSNAPLGPQFPFTGVDDRESWPSVFYNRTCQCSGNFMGFCNCK
HUMAN_TYRP1	1	QPPROCATVEALRSGMCCPDLSVPSGEGTDRCGSSSSSGRGCEAVTADSRPHSPQYPHDGRDREVWPLRFFNRTCHNGNFSGHNCGTGR
		#G#.G#.C..R.L#VRRN#DLS..EK..F#.#L.#AK.T...#VI#.....#...G.TP.F..I.IY.#FVW.HYY....#LG.G
HUMAN_TYR	87	FGWGPNCCTERRLLVRRNIFDLSAPEKDKFFAYLTLAKHTISSDYVIPIGTYGQM--KNGSTPMFNDINIXDLFVWMHYVVSMDALLG-G
HUMAN_TYRP1	91	PGWRGACDQRVLIIVRRNLLDLSKEKNHFRALDMARKRTTHPLFVIATRRSEEILGPDGNTBOENISITNYFVWTHYYSVKKTFLGVG
		.E.#.-#DF.HE.PAFL.WHR#LLR#E.-#Q.#...-F.#PYW.#.....CDICTD-#MG.....L#SP.S#FS.W.#VC..LE
HUMAN_TYR	174	SEIWRDIDFAHEAPAFLLPWHRLFLLRWEQEIQKLTDENFTIPYDWRDAEK-CDICTDEYMGQHPNPNLLSPASFSSQIVGSRLE
HUMAN_TYRP1	181	QESFGEVDFSEHGPAFLTWHRHLLRLLEKDMQEMLQEPSLSLPIYWNFATGKNVCDICTDMLGSRNSNFSTLISENSQWRVVCDSLE
		-Y.#..LCN.T.-GP#RRNP.GN#..+...R.LP...DV..CL.#..-#.....SFRNT#EG#..P.TG.#D#...S#HN#H##
HUMAN_TYR	263	EYNSHQSLCNGTPEGFLRRNP-GNHDKSRTPRLSSADVEFCLSLTQYESGSMDKAANFSFRNTLEGFASPLTGIDASQSSMHNALHIY
HUMAN_TYRP1	271	DYDTLGLTLCNSTEDGPIRRNEAGNVARPMVORLEPEQDVAQCLEVGLFDTPPFYSNSTNSFRNTVEGYSDE-TGKYDPAVRSLNLAHLF
		#NGT..Q...S#NDPIF#L#H.F.D.#F-.WLRR#.#...#P..NAPIGHNR...MVPF#P##.N.-#F#...D.LGY.Y.#...S.
HUMAN_TYR	352	MNGTMSQVQGSANDPIFLHHAFFVDSIEQWLRRHRPLQEVYEAANAPIGHNRRESYMVPEIPLRYRNGDFIISKDLGYDYSLYLDQSD
HUMAN_TYRP1	360	LNGTGGQTHLSPNDPIFVLLHFTTDAVEDEWLRRYNADISTFLENAPIGHNRQYNMVPFEPVTNTMTFVTAPDNLGYTYEIQWPS-

FIGURE 1 | Global Needleman and Wunsch sequence alignment between TYR and TYRP1 (PDB: 5m8n) showing 45% homology with a p -value ($p = -\log$ of p -value) of $10^{-40.2}$ for structural similarity. Residues highlighted in green represent conserved residues. Residues highlighted in yellow represent non-identical but homologous residues, which are expected to have little to no effect on the overall structure of the protein.

RESULTS AND DISCUSSION

Models of TYR-TYRP Heterocomplexes: Homology Models

In order to determine if TYR and the TRPs form molecular surfaces that are complementary to each other in pairs or trimers in terms of shape, electrostatics, and other physics-based properties (hydrophobic effect in water), we built maximally accurate, energy minimized models of TYR and TYRP2 based on their homology to the TYRP1 crystal structure (PDB: 5M8L; resolution 2.35 Å) (Lai et al., 2017). We recently demonstrated potential inaccuracies in models generated by the most commonly used homology modeling methods (Martinez-Ortiz and Cardozo, 2018). The state-of-the-art method requires the use of zero-end-gap global alignment with an associated p -value for structural similarity (Abagyan and Batalov, 1997) to identify the best possible starting target-template sequence alignment, which is then adjusted according to the structure. The sequence alignment between the TYR residues 1–510 and the corresponding intramelanosomal domain sequence from the crystallographic structure of TYRP1 (residues 25–471) was calculated to have highly significant 3D structural similarity [sequence identity 45%, $p = 10^{-40}$ (Abagyan and Batalov, 1997), **Figure 1**]. Based on prior studies, the quality of a homology model built from a sequence alignment of this strength is at least as good as an experimentally determined structure determined with NMR spectroscopy techniques or comparable to an X-ray crystallographic structure of moderate resolution (e.g., 3.5 Å) (Cardozo et al., 1995; Abagyan and Batalov, 1997; Abagyan and Totrov, 1997; Timothy et al., 2000). Accordingly, we built these maximally accurate homology models of TYR and of TYRP2 (residues 1–519), which also shares a high structural similarity with TYRP1 (sequence identity 54%, $p = 10^{-48}$).

Protein-Protein Docking

Because we were able to generate maximally accurate, low-energy 3D models of TYR, TYRP1 and TYRP2, we hypothesized that a computational molecular docking algorithm, which is customized

for docking of pairs of protein domains and have proven highly successful in the CAPRI blind prediction tests (Fernández-Recio et al., 2003; Fernandez-Recio et al., 2005a), could be used to dock the TYRP1 model with the structure of TYR. Eight energetically reasonable conformations were identified in the search. The lowest energy minimum conformation was separated by at least five energy units (approx. kcal/mol) from the other seven conformations, indicative of a highly energetically preferred conformation for the complex. This process was repeated to dock TYRP2 to TYR, and a similarly obvious result for a heterotrimer conformation was obtained.

Models of TYR-TYRP Heterocomplexes: TYR-TYRP1 Heterodimer

This docked model reveals an interaction surface between the TYR intramelanosomal domain and TYRP1 (**Figure 2**). 24 contact residues were identified on the surface of TYR exhibiting various strength of interactions. H256Y mutation associated with OCA1A disease also maps on the interaction surface between these two proteins (Farney et al., 2018). This SNV is predicted by PolyPhen2 to be destabilizing to the 3D structure (PolyPhen2 score 0.716); PolyPhen2 uses a machine-learned, probabilistic mathematical model to predict structurally destabilizing mutations on the basis of the evolutionary substitution pattern and the surface accessibility at that amino acid position (Adzhubei et al., 2010). The transmembrane domains of both proteins and the linkers between the transmembrane helices and the intramelanosomal domains were modeled onto this docked complex to test whether they were consistent with a transmembrane domain interaction as well.

TYR-TYRP2 Heterodimer

37 contact residues were identified on the surface of TYR exhibiting various strength of interactions with the surface of TYRP2 structure in a docked model of the TYR-TYRP2 heterodimer (**Figure 3**). Among these residues, we identified two glycosylation sites N111 and N230. Although we did not

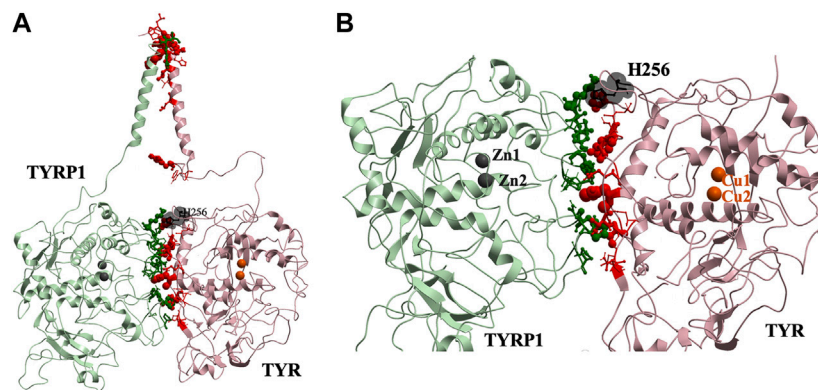


FIGURE 2 | Protein-protein interaction surface between TYR and TYRP1. Residues making key contacts are displayed in ball-and-stick (radius represents contribution size). **(A)**. Full size dimer with helix bundle. **(B)**. 24 contact residues highlighted at the interface of the two proteins. H256 residue where mutation associated with OCA1A occurs, is shown in black. Two Zn atoms in the active site of TYRP1 are shown in gray. Cu atoms in the active site of TYR are shown in orange.

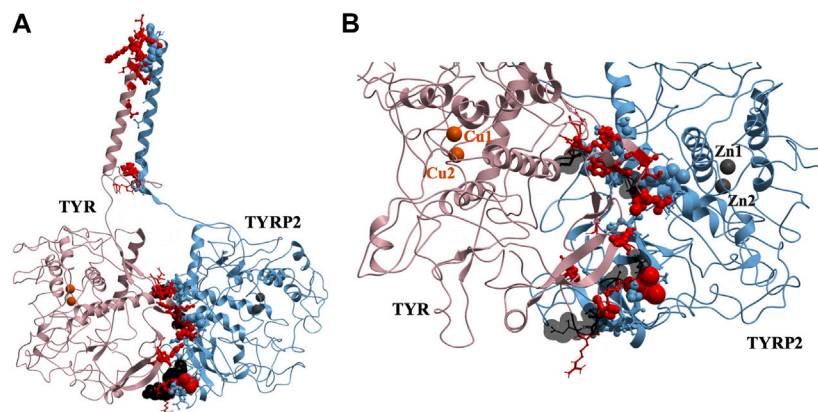


FIGURE 3 | Protein-protein interaction surface between TYR and TYRP2. Residues making key contacts are displayed in ball-and-stick (radius represents contribution size). **(A)**. Full size dimer with helix bundle. **(B)**. 37 contact residues highlighted at the interface of the two proteins. Residues where mutation associated with OCA1A occurs, is shown in black. Two Zn atoms in the active site of TYRP2 are shown in gray. Cu atoms in the active site of TYR are shown in orange.

model the effects of glycosylation, the presence of the sites on the surface and specifically to the interface of protein-protein interaction surface suggests a homing or chaperone function for these glycans. In addition, six mutation sites associated with OCA1A also map at the TYR-TYRP2 interaction surface. G227 is missing in OCA1A, which could disrupt the formation of the dimer. Two polymorphic residues S44 and G47, as well as S5, G19, and D42 which have documented single nucleotide polymorphisms are all linked to OCA1A and are located at the interface with TYRP2 (**Figure 3**) (Simeonov et al., 2013).

TYR-TYRP1-TYRP2 Heterotrimeric Complex

Remarkably, docking the TYRP2 structural model to the TYR-TYRP1 heterodimer and docking TYRP1 to the TYR-TYRP2 heterodimer resulted in convergence to the same conformation of

a heterotrimeric TYR-TYRP1-TYRP2 complex (**Figures 4A,B**). In addition, the heterotrimer model was independently consistent with a parallel three-helix, coiled-coil transmembrane helix bundle, as the C-termini of all three intramelanosomal domains were oriented in the same parallel direction by the docking. The heterotrimer placed TYR and TYRP1 active sites adjacent to each other (**Figure 4C**), while the TYRP2 active site was isolated facing away on the other side of the complex. The odds of this orientation occurring by random chance with an artificially docked conformation are very low as there are thousands of energetically reasonable conformations of unconstrained heterotrimer assembly of these three domains, and very few of them would be expected to place all of the C-terminal linkers pointing in the same direction and positioned so that the linker lengths could accommodate a helical bundle. All of the parallel 3-helix bundles found as templates for our model were from viruses and mediated membrane fusion, which may be

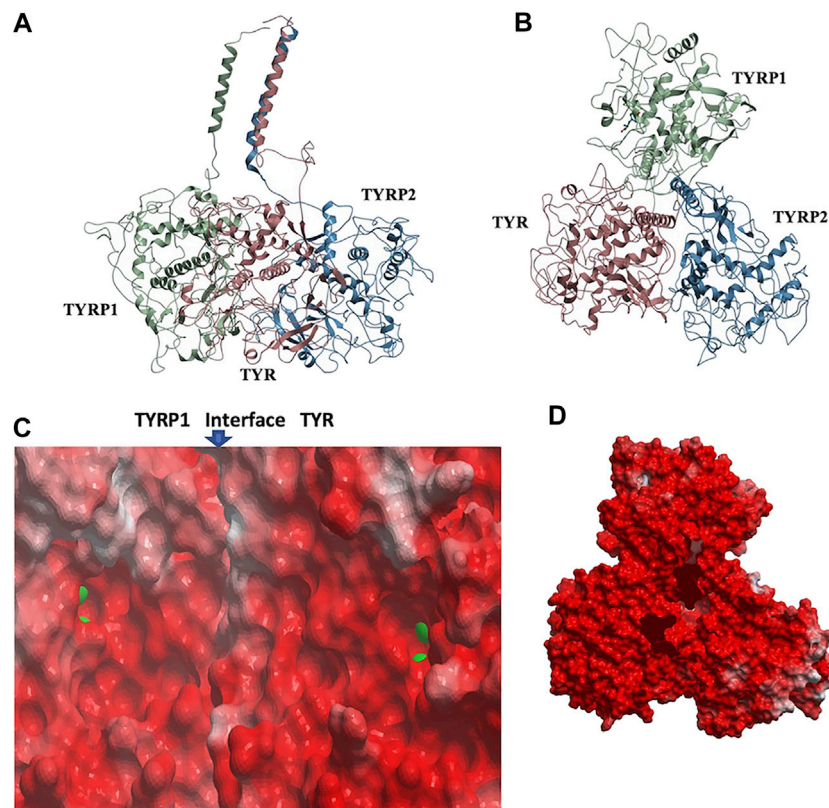


FIGURE 4 | TYR-TYRP1-TYRP2 heterotrimeric complex. **(A)** Side view, highlighting compatibility of the docked locations of the three N-terminii and their linker lengths between intramembranous domains and N-terminal TM-helices with formation of three-helix TM bundle. **(B)** Top view. **(C)** Electrostatic surfaces of the TYR-TYRP1 interface is shown, revealing continuity of active sites of TYR and TYRP1 in heterotrimer (zinc ions are green spheres marking active sites) **(D)** Electrostatic surface of heterotrimer surface facing the membrane (red = electronegative/acidic, blue = electropositive/basic).

significant in this case. In addition, the surface of the heterotrimer facing the membrane in the model is highly electronegative, which is consistent with the need for transmembrane anchors to oppose repulsion between this surface and the negatively charged phospholipid headgroups (**Figure 4D**).

The active site of TYR and its equivalent in the TYRP1 are connected by a contiguous channel, with a continuous pocket through which a substrate or a reactive metabolite may be easily shuttled between the active sites of the two enzymes (**Figure 4C**). Substrate/metabolite channeling has not been studied for human melanogenic proteins; however, it has been proposed to have a significant advantage for the human melanin synthesis cascade such as reduction of cellular toxicity and increase in substrate flux (Sugumaran et al., 2000; Sweetlove and Fernie, 2018). Tyrosinase family enzymes, just like many Cu and Zn containing metalloenzymes, produce highly reactive and unstable intermediates. Thus, metabolic intermediate shuttling, which prevents diffusion of the reactive metabolite into the bulk solution, can have important consequences on the melanin production cascade. Many metalloenzymes achieve substrate channeling by the formation of the multienzyme complexes. Tyrosinase produces o-benzoquinones as products of its enzymatic activity. Quinones are highly reactive electrophiles and can be toxic on cellular

environment due to their reactivity (O'Brien, 1991). Although metabolite channeling is a controversial topic, available evidence suggests that complex formation would be desirable for safe processing of quinone derivatives in the cellular environment. Our trimer complex model shows that metabolite channeling is possible between TYR and TYRP1 based on their interaction surface (**Table 1**). The orientation of the two proteins in the complex and location of the two active sites in close proximity to each other.

Interestingly, TYRP2 has a very different binding mode to TYR than TYRP1. The cys-rich subdomain (Lai et al., 2018) of TYR is involved in binding with TYRP2 in our model. The TYR-TYRP2 interaction has the larger contact area and number of residues involved (**Table 2**), suggestive of a higher affinity protein-protein interaction. Evidence for the evolutionary significance of the TYR-TYRP2 interaction is represented by the two glycosylation sites present in this domain.

OCA1 Pathogenic Mutations Associated With ER Retention Map Onto a Unique Surface of TYR

While mapping of common mutations of TYR onto a structural model was performed previously (Lai et al., 2018) and is

TABLE 1 | Residue contacts at the TYR-TYRP1 binding interface. Contact residues on TYR are ranked by decreasing strength of interactions, which is determined by a combination of the contact area, exposed area, the percentage of contact area compared to exposed (% buried) and closest distance to the atom on TYRP1.

TYR residue	Contact area	Exposed area	% Buried	Closest atom	Mutation	Disease
H143	95.2	144.3	66	TYRP1/pro/ca		
F268	69.9	125.1	56	TYRP1/pro/o		
P265	68.5	86.6	79	TYRP1/lys/ce		
I145	64.5	123.1	52	TYRP1/asn/od1		
R504	63.9	159.3	40	TYRP1/ala/o		
S271	60.0	79.4	76	TYRP1/asn/o		
T292	43.3	94.3	46	TYRP1/gln/o		
Q273	32.7	91.3	36	TYRP1/asn/nd2		
C500	26.2	67.3	39	TYRP1/arg/nh1		
N168	23.8	75.9	31	TYRP1/pro/cb		
H256	22.9	45.3	50	TYRP1/asp/od2	H to Y	OCA1A
S270	18.4	55.3	33	TYRP1/TYR/ce2		
G291	18.2	50.6	36	TYRP1/pro/cb		
L262	13.2	55.4	24	TYRP1/pro/cg		
D169	13.1	80.4	16	TYRP1/pro/cb		
N171	12.5	38.9	32	TYRP1/pro/cg		
P293	8.2	65.5	13	TYRP1/gln/cg		
P257	8.1	111.8	7	TYRP1/lys/nz		
I170	7.6	37.4	20	TYRP1/pro/cb		
A266	7.1	72.4	10	TYRP1/lys/cd		
T258	7.0	103.1	7	TYRP1/asp/od2		
L140	5.4	97.6	5	TYRP1/pro/cg		
T144	4.7	46.2	10	TYRP1/asn/nd2		
I153	3.1	62.8	5	TYRP1/pro/cb		

consistent with our model, we sought to examine mutations that have been linked to ER retention in OCA1A. Halaban et al. first demonstrated that human TYR substitutions T373K and R402Q resulted in the production of defective proteins and caused their ER retention (Halaban et al., 2000). In addition, the R402Q mutant showed temperature dependence for proper Golgi processing and transport. Toyofuku et al. expanded this list to include thermally sensitive variants P406L and R422Q (Toyofuku et al., 2001a). These mutants are functional at reduced temperatures, but lose catalytic activity at elevated temperatures, often resulting in the loss of pigmentation around warmer parts of the body. We mapped these mutations known to cause TYR retention in the ER onto the model. Mutations were color-coded to distinguish between the temperature-sensitive mutants of Tyrosinase and those that cause the ER retention but do not produce thermolabile TYR (Figure 5). The map suggests that mutations known to cause ER retention and thermal instability localize to a unique cluster on the surface of TYR.

In the past, it was postulated that these mutations result in loss of TYR catalytic activity by disrupting the copper B binding site. Yet, the R402Q and P406L variants were later shown to still be able to bind copper (Spritz et al., 1997) and as evident from the map in Figure 5, the surface localization of these mutations would make their direct effect on the active site unlikely.

Because these residues localize to a surface of the protein not predicted by our model to be an interface for the TYRPs, the mechanism by which they destabilize the protein remains unclear. However, the OCA1 mutations of these residues on

the surface of TYR do cause a change of net surface charge. One plausible explanation for the effect of these mutations is involvement in association with membrane phospholipids, or another currently unidentified protein partner, which would aid in the protein’s stability (Figure 6). Several binding partners for TYR have been identified, including TYRP1, TYRP2 (Orlow et al., 1994; Manga et al., 2000) as well as G Protein-Coupled Receptor 143 (De Filippo et al., 2017), while OCA4 mutations have been shown to result in reduced TYR maturation (Costin et al., 2003). Perhaps the most intriguing potential partner binding to this surface is OCA2, which is a putative anion channel. OCA2 mutations result in similar, albeit milder, pigmentary phenotypes as OCA1A and significant reduction in TYR maturation. The negative charge of the intramelanosomal heterotrimer surface suggests that the complex needs to be free to rotate and translate away from the membrane surface in order to dock this potential OCA2 surface into the membrane embedded OCA2, however such Brownian freedom would need to be constrained by the transmembrane domains. The transmembrane consistency of our heterotrimeric model thus suggests the possibility of a larger complex of this heterotrimer with OCA2, which, based on the phenotypes of mutations in the surface we have identified and the phenotype of OCA2 as preventing transit of TYR from the ER to the melanosome, may be required for transit of TYR out of the ER.

Validation

Although monomeric TYR has been reported in purely biochemical studies (Kus et al., 2018), our model suggests that

TABLE 2 | Residue contacts at the TYR-TYRP2 binding interface. Contact residues on TYR are ranked by decreasing strength of interactions, determined by a combination of contact area, exposed area, percentage of contact area compared to exposed (% buried) and closest distance to the atom on TYRP2.

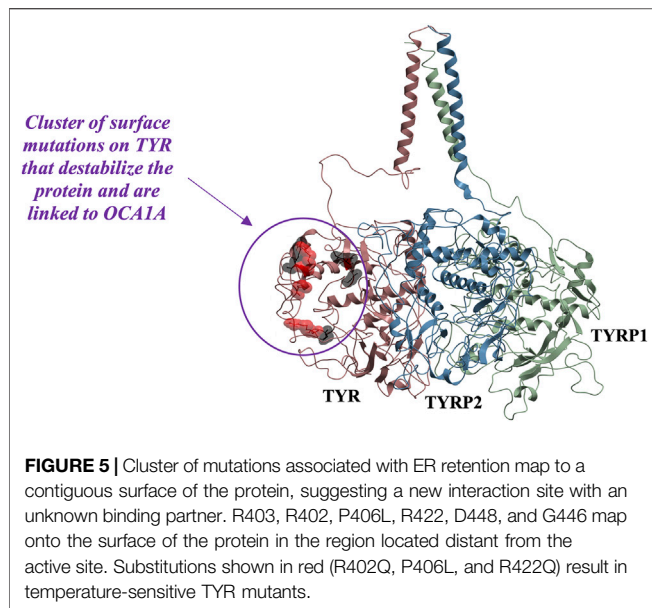
TYR residue	Contact area	Exposed area	% Buried	Closest atom	Mutation	Disease
L49	144.0	161.4	89	TYRP2/gln/c		
K503	107.3	120.4	89	TYRP2/phe/cd2		
P110	85.3	113.1	75	TYRP2/asn/o		
Q506	75.9	117.2	65	TYRP2/arg/cd		
R473	68.3	168.9	40	TYRP2/leu/cd2		
N111	67.3	100.2	67	TYRP2/thr/n	Glycosylation site	
P45	63.2	105.9	60	TYRP2/thr/o		
R52	54.4	121.9	45	TYRP2/asn/n		
L499	52.2	104.5	50	TYRP2/phe/ce2		
E229	49.7	67.9	73	TYRP2/lys/cb		
W108	48.9	141.4	35	TYRP2/lys/o		
R116	44.5	106.2	42	TYRP2/lys/cd		
W39	43.5	187.1	23	TYRP2/val/cg1		
E114	42.3	102.8	41	TYRP2/TYR/ce1		
L492	33.0	117.9	28	TYRP2/leu/cd2		
T113	30.1	98.1	31	TYRP2/TYR/ce1		
Q48	27.4	105.9	26	TYRP2/gln/ne2		
L507	26.9	162.7	17	TYRP2/arg/c		
G227	26.2	56.2	47	TYRP2/arg/nh2	Missing	OCA1A
S44	24.6	67.3	37	TYRP2/asp/od1	S to G, S to R	OCA1A
P508	22.2	80.7	27	TYRP2/TYR/c		
H502	22.1	109.6	20	TYRP2/arg/nh2		
S50	21.5	68.7	31	TYRP2/phe/o	S to L	OCA1A
R43	16.8	208.0	8	TYRP2/asp/od2		
N230	15.3	86.0	18	TYRP2/leu/cd2	Glycosylation site	
G101	14.0	47.2	30	TYRP2/asn/nd2		
V496	11.3	83.5	14	TYRP2/phe/ce2		
G47	11.2	49.7	23	TYRP2/pro/cd	G to V, G to D	OCA1A
D228	10.5	50.5	21	TYRP2/arg/nh2		
W477	10.2	115.0	9	TYRP2/trp/ch2		
K224	9.0	159.2	6	TYRP2/pro/cb		
G109	6.6	27.1	24	TYRP2/TYR/oh	G to R	OCA1A
D42	4.8	110.3	4	TYRP2/asp/od2	D to G	OCA1A
I474	4.1	51.6	8	TYRP2/trp/cz3		
T226	2.6	41.5	6	TYRP2/leu/o		
C112	0.8	20.8	4	TYRP2/TYR/oh		
E509	0.3	157.8	0	TYRP2/TYR/cb		

TYR and the TYRPs have evolved to form a membrane-anchored heterotrimeric TYR-TYRP1-TYRP2 complex *in vivo*. TYRP1 and TYRP2 docked unambiguously to their heterotrimeric conformations, constrained only by fundamental free energy terms, i.e., van der Waals, electrostatics, etc. If either the TYRP1-TYR or TYRP2-TYR docked conformation were artificial, clashing with the remaining TYRP docked conformation and failing to form a compatible inter-TYRP interface would be a virtual certainty. Similarly, even if an artificial docked conformation somehow survived the constraint of an independently docked counter-TYRP, the likelihood that the resulting docked conformation would also place the C-terminii of the intramembranous domains of all three proteins in the ideal positions to allow the linkers to form a transmembrane parallel 3-helix bundle (Figures 3–5) is very low. Finally, the consistency of all these constraints with ideal exposure of the ER retention surface in the heterotrimer (Figure 5) in the model belies an alternative molecular explanation.

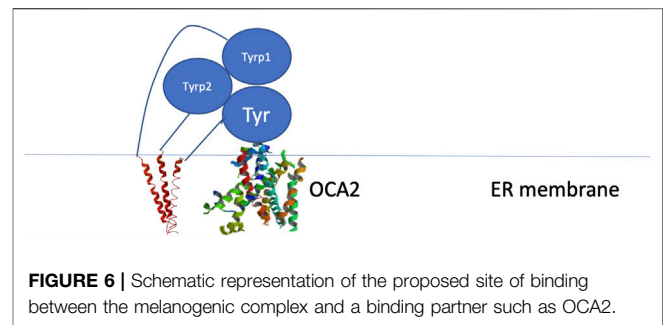
CONCLUSION

We built highly accurate 3D models of the structure of human Tyrosinase and TYRP2, based on the crystallographic structure of TYRP1 and comparable to experimentally determined atomic resolution structures by several informatics criteria. The models were sufficiently accurate to allow computational molecular docking to discover, using conformational search and free energy calculation alone, a model for a heterotrimeric TYR-TYRP1-TYRP2 complex that is independently consistent with voluminous independent data, including the active sites, cys-rich domain, linker and transmembrane domains of the proteins, Mendelian and pathogenic mutations and SNVs.

As noted in the Introduction, prior studies in the literature reveal a discrepancy as to whether TYR-TYRP1-TYRP2 heterocomplexes, including heterodimers of pairs of these, form. We suggest that this discrepancy derives from the inability to biochemically reconstitute the true intra-ER, transitional or intramembranous environment *in vitro*. The



demonstration that purified intramelanosomal domains of both TYRP1 and TYR elute as monomers on size-exclusion columns and that co-elution of TYRP1 and TYR showed no heterodimer (Lai et al., 2017) by no means equates with the conclusion that there is no formation of intramelanosomal TYR-TYRP1 heterodimer or the heterotrimer proposed in this report in cells. The term “intramelanosomal” has frequently been used in these prior studies to refer to the “intramelanosomal domain” of TYR/TYRP1 (Lai et al., 2017), so basically the soluble folded domain absent the transmembrane portion and the linker. This meaning would be no different biochemically than saying “luminal” or even “extracellular” TYR. Thus, this use of the term is somewhat misleading as these studies do not mimic the biochemical environment of the melanosome or the ER, within which physiologically relevant heterocomplex formation would take place. In addition, these studies use recombinant baculovirus expressed proteins with synthetic tags, in buffers optimized for monomer stability and crystallization, which may be very different from the *in vivo* environment. Our argument is that the *in vivo* environment is reflected more clearly in the evolution of these proteins, i.e., in their amino acid sequences. So, in our study, which relies only on this evolutionary signal, i.e., only on the biophysics of the amino acids, we see a heterotrimer. We conclude that this is evidence of the physiologically relevant *in vivo* complex, which may be hard to detect in its entirety by traditional *in vitro* biochemical means. We suspect that certain *in vitro* biochemical conditions (construct, cellular lysates, pH, concentration, temperature, etc) were ideal for heterodimer formation in the many studies leaning towards heterodimer formation and ideal for monomer formation in the conflicting studies, hence the discrepancy. The strong biophysical compatibility of evolved vertebrate TYR, TYRP1, and TYRP2 sequences, 3D structures and independent phenotype-genotype associations with a heterotrimer would be very unlikely by random chance and suggests *in vivo* relevance of the heterotrimer.



The model suggests the presence of a newly identified protein or membrane interaction surface that results in thermal instability when it is perturbed by mutation. We speculate that OCA2 may be an intriguing candidate as the binding partner for this surface and that its binding may be required for ER-melanosome transit. This model can account for the observation that TYR transit out of the ER is a “bottleneck” step of melanogenesis and requires TYRP1, TYRP2, and OCA2: the normal function of TYR that produces its baseline phenotype is highly dependent on the normal composition, architecture and sequence of ER environments, as well as ER-melanosome membrane events. The diverse pathological phenotypes associated with TYR may all have in common perturbation of this complex or of the ER environment it requires or of the membrane fusion events that transit this complex from the ER to the melanosome.

DATA AVAILABILITY STATEMENT

The original contributions presented in the study are included in the article/**Supplementary Material**, further inquiries can be directed to the corresponding author.

AUTHOR CONTRIBUTIONS

OL conceived the study, performed the computations, analyzed the data and wrote the manuscript. PM and SO contributed to the conception of the study, its interpretation and editing of the manuscript. TC conceived the study, analyzed the data and wrote the manuscript. TC also contributed some computations. All authors discussed the results and contributed to the final manuscript.

FUNDING

Research reported in this publication was supported in part by the National Institute of Arthritis and Musculoskeletal and Skin Diseases, part of the National Institutes of Health (NIH), under Award AR041880 (SO). The content is solely the responsibility of the authors and does not necessarily represent the official views of the NIH. Funding was also received from the New York University School of Medicine Biomedical Research Incentive Program (SO

and TC). OL received support from the Ruth L. Kirschstein National Research Service Award in Dermatology and Cutaneous Biology (T32 AR064184) and Ruth L. Kirschstein National Research Service Award in Molecular Oncology and Translational Immunology (T32 CA009161).

REFERENCES

- Abagyan, R., and Totrov, M. (1994). Biased probability Monte Carlo conformational searches and electrostatic calculations for peptides and proteins. *J. Mol. Biol.* 235 (3), 983–1002. doi:10.1006/jmbi.1994.1052
- Abagyan, R. A., and Batalov, S. (1997). Do aligned sequences share the same fold? *J. Mol. Biol.* 273 (1), 355–368. doi:10.1006/jmbi.1997.1287
- Abagyan, R. A., and Totrov, M. M. (1997). Contact area difference (CAD): a robust measure to evaluate accuracy of protein models. *J. Mol. Biol.* 268 (3), 678–685. doi:10.1006/jmbi.1997.0994
- Adzhubei, I. A., Schmidt, S., Peshkin, L., Ramensky, V. E., Gerasimova, A., Bork, P., et al. (2010). A method and server for predicting damaging missense mutations. *Nat. Methods* 7 (4), 248–249. doi:10.1038/nmeth0410-248
- Asgari, M. M., Wang, W., Ioannidis, N. M., Itnyre, J., Hoffmann, T., Jorgenson, E., et al. (2016). Identification of susceptibility loci for cutaneous squamous cell carcinoma. *J. Invest. Dermatol.* 136 (5), 930–937. doi:10.1016/j.jid.2016.01.013
- Berson, J. F., Frank, D. W., Calvo, P. A., Bieler, B. M., and Marks, M. S. (2000). A common temperature-sensitive allelic form of human tyrosinase is retained in the endoplasmic reticulum at the nonpermissive temperature. *J. Biol. Chem.* 275 (16), 12281–12289. doi:10.1074/jbc.275.16.12281
- Cai, X., Thinn, A. M. M., Wang, Z., Shan, H., and Zhu, J. (2017). The importance of N-glycosylation on β_3 integrin ligand binding and conformational regulation. *Sci. Rep.* 7 (1), 4656. doi:10.1038/s41598-017-04844-w
- Cardozo, T., Totrov, M., and Abagyan, R. (1995). Homology modeling by the ICM method. *Proteins* 23 (3), 403–414. doi:10.1002/prot.340230314
- Chaki, M., Sengupta, M., Mondal, M., Bhattacharya, A., Mallick, S., Bhadra, R., et al. (2010). Molecular and functional studies of tyrosinase variants among indian oculocutaneous albinism type 1 patients. *J. Invest. Dermatol.* 131, 260–262. doi:10.1038/jid.2010.274
- Chen, K., Manga, P., and Orlow, S. J. (2002). Pink-eyed dilution protein controls the processing of tyrosinase. *Mol. Bio. Cell* 13 (6), 1953–1964. doi:10.1091/mbc.02-02-0022
- Costin, G. E., Valencia, J. C., Vieira, W. D., Lamoreux, M. L., and Hearing, V. J. (2003). Tyrosinase processing and intracellular trafficking is disrupted in mouse primary melanocytes carrying the underwhite (uw) mutation. a model for oculocutaneous albinism (OCA) type 4. *J. Cell Sci.* 116 (Pt. 15), 3203–3212. doi:10.1242/jcs.00598
- Damico, F. M., Bezerra, F. T., Silva, G. C., Gasparin, F., and Yamamoto, J. H. (2009). New insights into vogt-koyanagi-harada disease. *Arq. Bras. Oftalmol.* 72 (3), 413–420. doi:10.1590/s0004-27492009000300028
- De Filippo, E., Schiedel, A. C., and Manga, P. (2017). Interaction between G protein-coupled receptor 143 and tyrosinase: implications for understanding ocular albinism type 1. *J. Invest. Dermatol.* 137 (2), 457–465. doi:10.1016/j.jid.2016.09.022
- Dolinska, M. B., and Sergeev, Y. V. (2017). The consequences of deglycosylation of recombinant intra-melanosomal domain of human tyrosinase. *Biol. Chem.* 399 (1), 73–77. doi:10.1515/hsz-2017-0178
- Dolinska, M. B., Young, K. L., 2nd, Kassouf, C., Dimitriadis, E. K., Wingfield, P. T., and Sergeev, Y. V. (2020). Protein stability and functional characterization of intra-melanosomal domain of human recombinant tyrosinase-related protein 1. *Int. J. Mol. Sci.* 21 (1), 331. doi:10.3390/ijms21010331
- Farney, S. K., Dolinska, M. B., and Sergeev, Y. V. (2018). Dynamic analysis of human tyrosinase intra-melanosomal domain and mutant variants to further understand oculocutaneous albinism type 1. *J. Anal. Pharm. Res.* 7 (6), 621–632. doi:10.15406/japlr.2018.07.00293
- Fernández-Recio, J., Abagyan, R., and Totrov, M. (2005a). Improving CAPRI predictions: optimized desolvation for rigid-body docking. *Proteins* 60 (2), 308–313. doi:10.1002/prot.20575
- Fernández-Recio, J., Totrov, M., and Abagyan, R. (2003). ICM-DISCO docking by global energy optimization with fully flexible side-chains. *Proteins* 52 (1), 113–117. doi:10.1002/prot.10383
- Fernandez-Recio, J., Totrov, M., Skorodumov, C., and Abagyan, R. (2005b). Optimal docking area: a new method for predicting protein-protein interaction sites. *Proteins* 58 (1), 134–143. doi:10.1002/prot.20285
- Gerstenblith, M. R., Goldstein, A. M., Tucker, M. A., and Fraser, M. C. (2007). Genetic testing for melanoma predisposition: current challenges. *Cancer Nurs.* 30 (6), 452–459. doi:10.1097/01.NCC.0000300165.98391.e7
- Gerstenblith, M. R., Shi, J., and Landi, M. T. (2010). Genome-wide association studies of pigmentation and skin cancer: a review and meta-analysis. *Pigment Cell Melanoma Res.* 23 (5), 587–606. doi:10.1111/j.1755-148X.2010.00730.x
- Halaban, R., Svedine, S., Cheng, E., Smicun, Y., Aron, R., and Hebert, D. N. (2000). Endoplasmic reticulum retention is a common defect associated with tyrosinase-negative albinism. *Proc. Natl. Acad. Sci. U.S.A.* 97 (11), 5889–5894. doi:10.1073/pnas.97.11.5889
- Hearing, V. J., Tsukamoto, K., Urabe, K., Kameyama, K., Montague, P. M., and Jackson, I. J. (1992). Functional properties of cloned melanogenic proteins. *Pigment Cell Res.* 5 (5), 264–270. doi:10.1111/j.1600-0749.1992.tb00547.x
- Jacobs, L. C., Liu, F., Pardo, L. M., Hofman, A., Uitterlinden, A. G., Kayser, M., et al. (2015). IRF4, MC1R and TYR genes are risk factors for actinic keratosis independent of skin color. *Hum. Mol. Genet.* 24 (11), 3296–3303. doi:10.1093/hmg/ddv076
- Jiménez-Cervantes, C., Martínez-Esparza, M., Solano, F., Lozano, J. A., and García-Borrón, J. C. (1998). Molecular interactions within the melanogenic complex: formation of heterodimers of tyrosinase and TRP1 from B16 mouse melanoma. *Biochem. Biophys. Res. Commun.* 253 (3), 761–767. doi:10.1006/bbrc.1998.9817
- Jin, Y., Birela, S. A., Fain, P. R., Gowan, K., Riccardi, S. L., Holland, P. J., et al. (2010). Variant of TYR and autoimmunity susceptibility loci in generalized vitiligo. *N. Engl. J. Med.* 362 (18), 1686–1697. doi:10.1056/NEJMoa0908547
- Kedda, M. A., Stevens, G., Manga, P., Viljoen, C., Jenkins, T., and Ramsay, M. (1994). The tyrosinase-positive oculocutaneous albinism gene shows locus homogeneity on chromosome 15q11-q13 and evidence of multiple mutations in southern African negroids. *Am. J. Hum. Genet.* 54 (6), 1078–1084.
- Kobayashi, T., and Hearing, V. J. (2007). Direct interaction of tyrosinase with Tyrp1 to form heterodimeric complexes *in vivo*. *J. Cell Sci.* 120 (Pt. 24), 4261–4268. doi:10.1242/jcs.017913
- Kobayashi, T., Imokawa, G., Bennett, D. C., and Hearing, V. J. (1998). Tyrosinase stabilization by Tyrp1 (the brown locus protein). *J. Biol. Chem.* 273 (48), 31801–31805. doi:10.1074/jbc.273.48.31801
- Kobayashi, T., Urabe, K., Winder, A., Tsukamoto, K., Brewington, T., Imokawa, G., et al. (1994). DHICA oxidase activity of TRP1 and interactions with other melanogenic enzymes. *Pigment Cell Res.* 7 (4), 227–234. doi:10.1111/j.1600-0749.1994.tb00054.x
- Kus, N. J., Dolinska, M. B., Young, K. L., Dimitriadis, E. K., Wingfield, P. T., and Sergeev, Y. V. (2018). Membrane-associated human tyrosinase is an enzymatically active monomeric glycoprotein. *PLoS One* 13 (6), e0198247. doi:10.1371/journal.pone.0198247
- Lai, X., Wichers, H. J., Soler-Lopez, M., and Dijkstra, B. W. (2017). Structure of human tyrosinase related protein 1 reveals a binuclear zinc active site important for melanogenesis. *Angew. Chem. Int. Ed. Engl.* 56 (33), 9812–9815. doi:10.1002/anie.201704616
- Lai, X., Wichers, H. J., Soler-Lopez, M., and Dijkstra, B. W. (2018). Structure and function of human tyrosinase and tyrosinase-related proteins. *Chem. Eur. J.* 24 (1), 47–55. doi:10.1002/chem.201704410
- Manga, P., Kromberg, J. G. R., Box, N. F., Sturm, R. A., Jenkins, T., and Ramsay, M. (1997). Rufous oculocutaneous albinism in Southern African blacks is caused by mutations in the TYRP1 gene. *Am. J. Hum. Genet.* 61 (5), 1095–1101. doi:10.1086/301603

SUPPLEMENTARY MATERIAL

The Supplementary Material for this article can be found online at: <https://www.frontiersin.org/articles/10.3389/fphar.2021.602206/full#supplementary-material>

- Manga, P., Sato, K., Ye, L., Beermann, F., Lamoreux, M. L., and Orlow, S. J. (2000). Mutational analysis of the modulation of tyrosinase by tyrosinase-related proteins 1 and 2 in vitro. *Pigment cell Res.* 13 (5), 364–374. doi:10.1034/j.1600-0749.2000.130510.x
- Martinez-Ortiz, W., and Cardozo, T. J. (2018). An improved method for modeling voltage-gated ion channels at atomic accuracy applied to human Ca_v channels. *Cell Rep.* 23 (5), 1399–1408. doi:10.1016/j.celrep.2018.04.024
- Medina, M., Abagyan, R., Gómez-Moreno, C., and Fernandez-Recio, J. (2008). Docking analysis of transient complexes: interaction of ferredoxin-NADP + reductase with ferredoxin and flavodoxin. *Proteins* 72 (3), 848–862. doi:10.1002/prot.21979
- Morrison, R., Mason, K., and Frost-Mason, S. (1994). A cladistic analysis of the evolutionary relationships of the members of the tyrosinase gene family using sequence data. *Pigment Cell Res.* 7 (6), 388–393. doi:10.1111/j.1600-0749.1994.tb00066.x
- Newton, J. M., Cohen-Barak, O., Hagiwara, N., Gardner, J. M., Davisson, M. T., King, R. A., et al. (2001). Mutations in the human orthologue of the mouse underwhite gene (*uw*) underlie a new form of oculocutaneous albinism, OCA4. *Am. J. Hum. Genet.* 69 (5), 981–988. doi:10.1086/324340
- O'Brien, P. J. (1991). Molecular mechanisms of quinone cytotoxicity. *Chem. Biol. Interact.* 80 (1), 1–41. doi:10.1016/0009-2797(91)90029-7
- Orlow, S. J., Zhou, B. K., Chakraborty, A. K., Drucker, M., Pifko-Hirst, S., and Pawelek, J. M. (1994). High-molecular weight forms of tyrosinase and the tyrosinase-related proteins: evidence for a melanogenic complex. *J. Invest. Dermatol.* 103 (2), 196–201. doi:10.1111/1523-1747.ep12392743
- Petrescu, A. J., Butters, T. D., Reinkensmeier, G., Petrescu, S., Platt, F. M., Dwek, R. A., et al. (1997). The solution NMR structure of glucosylated N-glycans involved in the early stages of glycoprotein biosynthesis and folding. *EMBO J.* 16 (14), 4302–4310. doi:10.1093/emboj/16.14.4302 Available at: http://www.ncbi.nlm.nih.gov/entrez/query.fcgi?cmd=Retrieve&db=PubMed&dopt=Citation&list_uids=9250674 (Accessed July 16, 1997).
- Shriver, M. D., Parra, E. J., Dios, S., Bonilla, C., Norton, H., Jovel, C., et al. (2003). Skin pigmentation, biogeographical ancestry and admixture mapping. *Hum. Genet.* 112 (4), 387–399. doi:10.1007/s00439-002-0896-y
- Simeonov, D. R., Wang, X., Wang, C., Sergeev, Y., Dolinska, M., Bower, M., et al. (2013). DNA variations in oculocutaneous albinism: an updated mutation list and current outstanding issues in molecular diagnostics. *Hum. Mutat.* 34 (6), 827–835. doi:10.1002/humu.22315
- Spritz, R. A., Ho, L., Furumura, M., and Hearing, V. J. (1997). Mutational analysis of copper binding by human tyrosinase. *J. Invest. Dermatol.* 109 (2), 207–212. doi:10.1111/1523-1747.ep12319351
- Spritz, R. A. (2010). The genetics of generalized vitiligo: autoimmune pathways and an inverse relationship with malignant melanoma. *Genome Med.* 2 (10), 78. doi:10.1186/gm199
- Sturm, R. A., O'Sullivan, B. J., Box, N. F., Smith, A. G., Smit, S. E., Puttick, E. R., et al. (1995). Chromosomal structure of the human TYRP1 and TYRP2 loci and comparison of the tyrosinase-related protein gene family. *Genomics* 29 (1), 24–34. doi:10.1006/geno.1995.1211
- Sugumaran, M., Nellaiappan, K., Amaratunga, C., Cardinale, S., and Scott, T. (2000). Insect melanogenesis: III. Metabolon formation in the melanogenic pathway—regulation of phenoloxidase activity by endogenous dopachrome isomerase (decarboxylating) from *Manduca sexta*. *Arch. Biochem. Biophys.* 378 (2), 393–403. doi:10.1006/abbi.2000.1848
- Sulem, P., Gudbjartsson, D. F., Stacey, S. N., Helgason, A., Rafnar, T., Magnusson, K. P., et al. (2007). Genetic determinants of hair, eye, and skin pigmentation in Europeans. *Nat. Genet.* 39 (12), 1443–1452. doi:10.1038/ng.2007.13
- Sweetlove, L. J., and Fernie, A. R. (2018). The role of dynamic enzyme assemblies and substrate channelling in metabolic regulation. *Nat. Commun.* 9 (1), 2136. doi:10.1038/s41467-018-04543-8
- Testa, O. D., Moutevelis, E., and Woolfson, D. N. (2009). CC+: a relational database of coiled-coil structures. *Nucleic Acids Res.* 37, D315–D322. doi:10.1093/nar/gkn675 Database issue.
- Timothy, C., Serge, B., and Ruben, A. (2000). Estimating local backbone structural deviation in homology models. *Comput. Chem.* 24 (1), 13–31. doi:10.1016/S0097-8485(99)00044-3
- Toyofuku, K., Wada, I., Spritz, R. A., and Hearing, V. J. (2001a). The molecular basis of oculocutaneous albinism type 1 (OCA1): sorting failure and degradation of mutant tyrosinases results in a lack of pigmentation. *Biochem. J.* 355 (Pt. 2), 259–269. doi:10.1042/0264-6021:3550259
- Toyofuku, K., Wada, I., Valencia, J. C., Kushimoto, T., Ferrans, V. J., and Hearing, V. J. (2001b). Oculocutaneous albinism types 1 and 3 are ER retention diseases: mutation of tyrosinase or Tyrp1 can affect the processing of both mutant and wild-type proteins. *FASEB J.* 15 (12), 2149–2161. doi:10.1096/fj.01-0216com
- Ujvari, A., Aron, R., Eisenhaure, T., Cheng, E., Parag, H. A., Smicun, Y., et al. (2001). Translation rate of human tyrosinase determines its N-linked glycosylation level. *J. Biol. Chem.* 276 (8), 5924–5931. doi:10.1074/jbc.m009203200
- Winder, A., Kobayashi, T., Tsukamoto, K., Urabe, K., Aroca, P., Kameyama, K., et al. (1994). The tyrosinase gene family—interactions of melanogenic proteins to regulate melanogenesis. *Cell Mol. Biol. Res.* 40 (7–8), 613–626.
- Zhong, K., Verkouteren, J. A., Jacobs, L. C., Uitterlinden, A. G., Hofman, A., Liu, F., et al. (2017). Pigmentation-Independent susceptibility loci for actinic keratosis highlighted by compound heterozygosity analysis. *J. Invest. Dermatol.* 137 (1), 77–84. doi:10.1016/j.jid.2016.09.007

Conflict of Interest: The authors declare that the research was conducted in the absence of any commercial or financial relationships that could be construed as a potential conflict of interest.

Copyright © 2021 Lavinda, Manga, Orlow and Cardozo. This is an open-access article distributed under the terms of the Creative Commons Attribution License (CC BY). The use, distribution or reproduction in other forums is permitted, provided the original author(s) and the copyright owner(s) are credited and that the original publication in this journal is cited, in accordance with accepted academic practice. No use, distribution or reproduction is permitted which does not comply with these terms.



Investigation of Angiogenesis and Wound Healing Potential Mechanisms of Zinc Oxide Nanorods

Amr Hassan^{1*}, Dalia Elebeedy², Emadeldin R. Matar³, Aly Fahmy Mohamed Elsayed⁴ and Ahmed I. Abd El Maksoud^{5,2}

¹Department of Bioinformatics, Genetic Engineering and Biotechnology Research Institute (GEBRI) University of Sadat City, Sadat, Egypt, ²College of Biotechnology, Misr University for Science and Technology, Giza, Egypt, ³Department of Pathology, Faculty of Medicine, Al-Azhar University, Cairo, Egypt, ⁴Holding Company for Vaccine and Sera Production (VACSERA), Giza, Egypt, ⁵Department of Industrial Biotechnology, Genetic Engineering and Biotechnology Research Institute (GEBRI) University of Sadat City, Sadat, Egypt

OPEN ACCESS

Edited by:

Salvatore Salomone,
University of Catania, Italy

Reviewed by:

Maria Paola Germanò,
University of Messina, Italy
Vittorio Calabrese,
University of Catania, Italy

*Correspondence:

Amr Hassan
amrhassan.nanotechnology@
gmail.com

Specialty section:

This article was submitted to
Experimental Pharmacology and Drug
Discovery,
a section of the journal
Frontiers in Pharmacology

Received: 30 January 2021

Accepted: 26 April 2021

Published: 11 October 2021

Citation:

Hassan A, Elebeedy D, Matar ER,
Fahmy Mohamed Elsayed A and
Abd El Maksoud AI (2021) Investigation
of Angiogenesis and Wound Healing
Potential Mechanisms of Zinc
Oxide Nanorods.
Front. Pharmacol. 12:661217.
doi: 10.3389/fphar.2021.661217

The angiogenesis process is an essential issue in tissue engineering. Zinc oxide nanorods are biocompatible metals capable of generating reactive oxygen species (ROS) that respond to induced angiogenesis through various mechanisms; however, released Zn (II) ions suppress the angiogenesis process. In this study, we fabricated green ZnO nanorods using albumin eggshell as a bio-template and investigate its angiogenic potential through chorioallantoic membrane assay and excision wound healing assay. This study demonstrated that angiogenesis and wound healing processes depend on pro-angiogenic factors as VEGF expression due to ZnO nanorods' exiting. Angiogenesis induced *via* zinc oxide nanorods may develop sophisticated materials to apply in the wound healing field.

Keywords: zinc oxide nanorods, angiogenesis, wound healing, VEGF, ROS

INTRODUCTION

Neovascularization is considered as an essential issue in regenerative medicine and tissue engineering (Ennett and Mooney, 2002). This issue has occurred *via* the microvascular process (Rouwkema et al., 2008). The angiogenesis process is the formation of novel capillary network to provide nutrients to cells (Folkman, 1984). Angiogenesis depends on factors like VEGF (Petrova et al., 1999), FGF (Ma, 2000), and angiopoietin activators of integrins (Suri et al., 1996). Although VEGF is an excellent, effective regulator to induce the angiogenesis process, there are enormous challenges to applying tissue engineering. The half-life of scaffolds is only a few minutes (Eliceiri and Cheresch, 1999). So, the presence of the material induces cells to produce VEGF, and FGF as a growth factor may help overcome these challenges. Previous studies reported that ROS functionalized in wound healing and cell proliferation throughout the activation of growth factors (Sen et al., 2002; Roy et al., 2006; Huo et al., 2009).

Abbreviations: VEGF, vascular endothelial growth factor.; ROS, reactive oxygen species; FT-IR, Fourier transformed infrared; XRD, X-ray diffraction; HRTEM, high-resolution transmission electron microscopy; HDF4, human dermal fibroblast cells; HDF4; CAM, chicken chorioallantoic membrane; ZnO-NRs, zinc oxide nanorods; ICP-AES, inductively coupled plasma-atomic emission spectroscopy; DMEM, Dulbecco's modified Eagle medium

Interestingly, ROS plays a prominent role in the angiogenesis process by activating key steps of cell proliferation, migration, and tube formation (Lelkes et al., 1998; Rhee, 2006; Xia et al., 2007; Augustine et al., 2014). H_2O_2 is considered as one of the ROS components, including in stages of angiogenesis. It contributes to the wound healing process by inducing VEGF expression in mice (Sen et al., 2002) and FGF in rat astrocyte cells (Pechan et al., 1992). Today, nanomedicine becomes one of the most important fields of nanotechnology and material science (Augustine et al., 2014). Over the past decade, there were many metal nanoparticle applications in biomedical applications such as diagnostic and therapeutic fields (quantum dots and semiconductors), anticancer therapy, antimicrobial therapy, and antiviral therapy. Zinc oxide (ZnO) is an inorganic material classified as an FDA-approved material based upon its stability, safety, and intrinsic potential to neutralize UV radiations (Zhang et al., 2013). It has wide applications. ZnO nanoparticle is a promising material in biomedical applications such as antimicrobial, antigen, gene, drug delivery (Rasmussen et al., 2010), biosensor, and tissue engineering applications. Furthermore, Ayan et al. reported that ZnO nanoflowers could be inducing angiogenesis through proliferation and migration of endothelial cells (Barui et al., 2012; Augustine et al., 2014). Also, they mention that ROS stimulates angiogenesis by europium hydroxide $[Eu(III)(OH)_3]$ nanorods (Patra et al., 2011).

MATERIALS AND METHODS

Chemicals

Zinc acetate hydrate was purchased from Sigma-Aldrich, United States, and albumin eggshells from Loba Chemical Co., Mumbai, India.

Animals and Experimental Design

We applied all the European Communities Council Directive (Directive 2010/63/EU of 22 September, 2010). According to the Institutional Animal Care and Use Committee at Cairo University, Egypt (IACUC, CU-II-F-10-19), we carried out the experimental procedure after the Animal Protocols Evaluation Committee's affirmative opinion. Sixty male albino Wister rats weighing approximately 170–200 g were brought from the Department of Veterinary Hygiene, Faculty of Veterinary Medicine, Sadat University, Egypt. According to the protocol, standard conditions for feeding, and living rats' before occurred experiments for ensuring animals in a healthy status.

Synthesis of ZnO Nanorods

Several routes synthesized ZnO nanorods, but one of the best methods is the sol-gel method with some modifications (Nouroozi and Farzaneh, 2011). In a typical synthesis, 1.1 gram of zinc acetate dihydrate $[Zn(CH_3COO)_2 \cdot 2H_2O]$ was added in 10 ml of ultrapure water (Milli-Q water, United States) (18 M Ω) containing 2 gm of albumin added gradually with 30 min stirring. The oven performed the calcination process at 300°C for 6 h, and

then, the precipitates were annealed slowly and characterized (**Supplementary Figure S1**).

Zinc Oxide Nanorod Characterization

A Fourier Transformed-Infrared spectrum (FT-IR) of the sample was recorded using the Nicolet 6700 apparatus (Thermo Scientific Inc., USA). The crystalline nature and grain size were studied by XRD patterns at 25–28°C with a D8 Advance X-ray diffractometer (Bruker, Germany). Shape and size of ZnO nanorods were determined using HRTEM, JSM-2100F, and JEOL Inc. (Tokyo, Japan) with a voltage of 15 Kv and 200 KeV.

Measurement of Released Zn (II) From Zinc Oxide Nanorods

The protocol of measurement of released Zn (II) from zinc oxide nanorods was determined as previously described (Tada-Oikawa et al., 2015). The suspension solutions were diluted to 15 ml of DMEM (GIBCO, United States) at 100 μ g/ml concentration of ZnO nanorods. All samples were incubated at 37°C in a 5% CO_2 incubator for 1, 3, 6, 12, 18, and 24 h, and then cold-centrifuged at 10,000 \times g for half an hour. Followed by which, the supernatant was aspirated and transferred into a test tube containing 0.5 ml of concentrated nitric acid (HNO_3 ; Merck Inc, Germany). The resultant solution was completed up to 50 ml with ultrapure water. So, the liberated Zn (II) was measured by ICP-AES-7500 (Perkin-Elmer, United States).

Angiogenesis Mechanism by Quantitative RT-PCR

Human dermal fibroblast cells (HDF₄) (ATCC PCS201012, United States) were harvested in six-well plates, and then exposed to 10 and 20 μ g/ml of suspended ZnO nanorods and Zn (II) ion (released from 100 mg/ml) for 24 h. Total RNA was isolated from cells posttreatment by using the RNeasy Mini Kit (Qiagen, Valencia CA, United States). The technical protocol for RNA extraction was according to the manufacturer's instructions (Pfaffl, 2001). The RNA concentration was measured through a Beckman dual spectrophotometer (United States). To quantify VEGF gene expression, the cDNA reverse transcriptase kit (Applied Biosystems, United States) was used to transfer the total RNA to cDNA. Then quantitative RT-PCR was carried out using the Syber Green I PCR Master Kit (Fermentas) (Applied Biosystems, USA); 2 μ l of template cDNA was then added to the final volume of 20 μ l of the reaction mixture. The procedures were carried out as the following enzyme activation for 10 min at 95°C, followed by forty cycles to denature for 15 s at 95°C, then annealing step for 20 s at 55°C and elongation step at 72°C for 20 s. We used specific sets of primers for the target gene VEGF: TGCAGATTATGCGGATCAAACC-3' (forward) and 5'-GCA TTCACATTTGTTGTGCTGTAG-3' (reverse), and VEGF gene was normalized with β -actin gene which was used as an internal control. RT-PCR experiments were repeated three independent times.

Reactive Oxygen Species Assay

Human Dermal Fibroblast Cells (HDF₄) (ATCC PCS201012, USA) were treated with ZnO nanorods at 10 μ g/ml, 20 μ g/ml,

and 50 µg/ml concentrations, and Zn (II) ions were released at 100 µg/ml concentration for 24 h. After treatment, the cells were washed and harvested in cold PBS (+4°C). Then lysis of the cell pellets was performed by using a cell lysis buffer. Then cell pellets were centrifuged at a speed of 15,000 g for 10 min at +4°C; the supernatant was maintained on ice until assayed for ROS assay. ROS was determined by using a ROS assay kit from Life Span Bioscience Inc. (Seattle WA, United States) following the manufacturer's instructions. Then 100 µl of the sample, standard, and blank was added to each well, followed by an incubation period of 90 min at a temperature of 37°C. All models were then aspirated, 100 µl of biotinylated detection antibody was added to the plate, and then the latter was incubated for 1 h at 37°C. After centrifugation (3,000 g), aspirate supernatants were washed in the plates three times by adding 100 µl of HRP conjugate incubated at 37°C for half an hour. Supernatants were removed, and then, plates were washed several times. Before adding 90 µl of TMB substrate solution and incubating at 37°C for 15 min. Then, a stopping reaction occurred by adding 50 µl of stop solution, followed which, the measurement of the absorbance at a wavelength of 450 nm was carried out *via* an ELISA plate reader, ELX-800 (Biotek, United States).

Antioxidant Stress Biomarker

Ellman's protocol was applied for evaluating a level of reduced glutathione (GSH) (Ellman, 1959). Measurement of glutathione was at 412 nm, and the unit of GSH protein is nmol/mg.

Chicken Chorioallantoic Membrane Assay

For fertilizing, chicken eggs were supplied from the poultry station (Giza, Egypt). Under the aseptic condition, eggs were cracked gently, and their yolks were put in sterile plastic dishes. We were soaking filter paper discs with ZnO nanorod suspension solution with different concentrations (10, 20, and 50 µg/ml), Zn (II) ions (released at 100 µg/ml concentration and incubated at a temperature of 37°C for 24 h), and 10 ng of VEGF that is known as a promoter of angiogenesis. It had worked as a positive control, while dimethyl sulphoxide (DMSO) worked as a negative control. We then placed all material (test, materials, and control (positive and negative)) on the egg yolks, and then incubated for 24 h. After 24 h of the explosion, we took images using an Olympus camera of 10 MP connected with a stereomicroscope. We used a manual method to count the new blood capillaries in a clockwise direction. The blood vessel branch was counted manually in a clockwise direction. Results were presented as the mean with standard deviation.

Histopathological Examination of Chicken Chorioallantoic Membrane Assay

On the second day after injection, the egg yolks were collected from each group (ZnO nanorods (10, 20, and 50 µg/ml), Zn (II) ions (released at 100 µg/ml), and 10 ng of VEGF) in PBS of pH 7.4 solutions, followed by a fixation step with 10% neutral-buffered formalin. The preparation of specimens for histological examination was according to Bancroft et al. (Velnar et al., 2009). The interpretation of results by a ranking score

indicated the degree of branching vessel and branching patterns. The specimen section photographs were taken and observed for angiogenesis (Ausprunk et al., 1975; Norrby, 2006). Repeat experiments were carried out with three independent experiments.

Wound Healing Study (Excision Wound Model)

Initially, the animals were anesthetized using ketamine (100 mg/ml) and xylazine (20 mg/ml) in a 3:1 v/v ratio, and subsequently, a piece of the skin (14 mm) was removed surgically from the dorsal region of each mouse. After skin excision, the wound was cleaned initially with diluted soap 50% in saline and rinsed with saline solution. Then wound groups (II and III) were treated with ZnO nanorods at concentration of 10 µg/200 µl and 20 µg/200 µl. Phenytoin (Pitiakoudis et al., 2004) was applied as a standard positive control for group IV. The mice's maintenance was followed in individual cages with total care under a warming lamp until its recovery from anesthesia. The total wound area was scaled daily for 14 days (the experiment time). Alternatively, the clinical condition of mice (Thomas, 1990) (e.g., total wound area and the healing process's progress) was recorded daily for 14 days (the experiment time). Skin images for photo documentation were acquired using an Olympus camera (Olympus, Tokyo, Japan) at a fixed distance of 30 cm perpendicular to the subject. The photographs were digitized, and the wound area was measured using Adobe Photoshop C5. After 14 days, acceptable euthanasia methods (decapitation method) were applied to sacrifice the mice (Clifford, 1984). Followed by excised skin tissue, skin sections of specimens from all groups were performed using a paraffin microtome (Shandon Finesse, Thermo Fisher Scientific, Cheshire, United Kingdom) and stained with hematoxylin and eosin stain kit (Atom Scientific, Cheshire, United Kingdom). Parameters such as inflammation and skin structure were estimated. The Walker equation evaluated the wound healing percentages after measurement of the wound area.

$$\text{Wound area} = \frac{\text{Wound area in the day X}}{\text{Wound area at the beginning}} \times 100.$$

STATISTICAL ANALYSIS

Statistical analysis was carried out using the variance (ANOVA) single factor test analysis with significance at $p < 0.05$.

RESULTS

Zinc Oxide Nanorod Characterization FT-IR Spectroscopy

FT-IR spectra of zinc oxide nanorods (ZnO-NRs) are shown in **Figure 1**. The wave band at 3415–3503 cm^{-1} indicated O–H stretching vibration that of Jong-hun et al. Borah et al. (2016) mentioned a band at 3503 cm^{-1} for O–H stretching vibration in the ZnO nanomaterials. Furthermore, hydroxyl groups' presence is due to a sharp band's appearance with intensity at 1136 cm^{-1} .

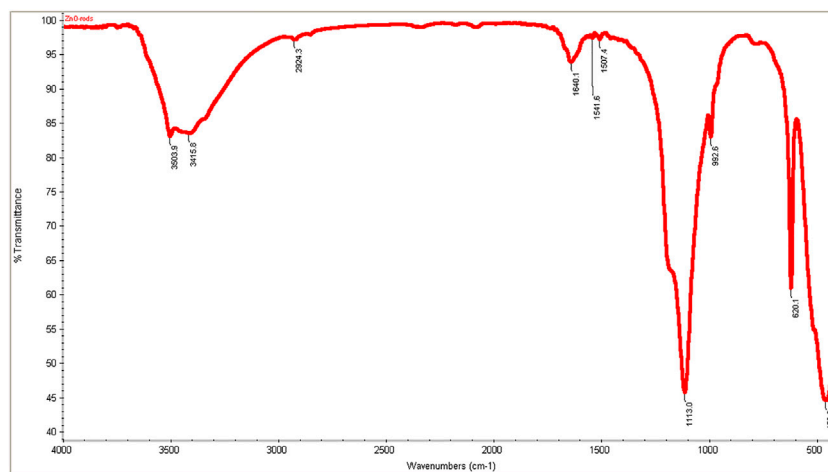


FIGURE 1 | FT-IR spectra ZnO nanorods (ZnO-NRs).

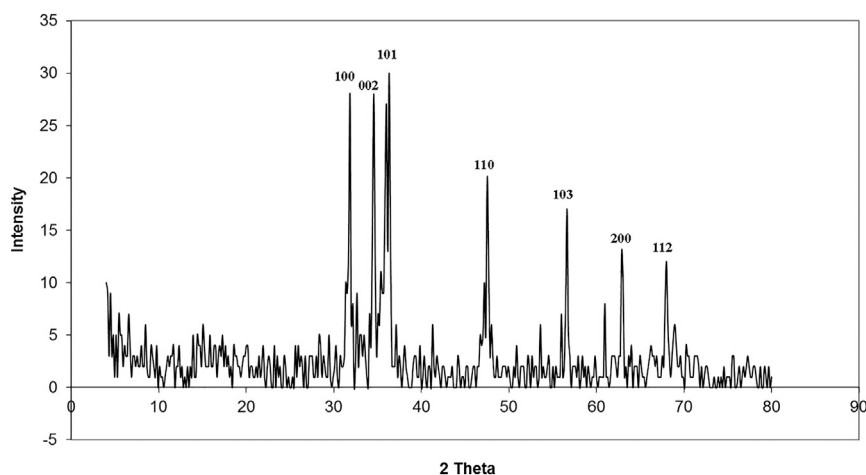


FIGURE 2 | XRD patterns of ZnO nanorods (ZnO-NRs).

This peak refers to O–H in-plane bending vibration. A strong band at 458 cm^{-1} was indicated or referred to as the Zn–O bond. The result supported that the appearance of hydroxo, oxo, or aqua species on the surface of zinc oxide nanorods was due to the existence of excess oxygen content in the nanomaterial (Silverstein and Bassler, 1962; Farmer, 1974).

X-Ray Diffraction

XRD patterns of ZnO nanorods are shown in **Figure 2**. The peaks at $2\theta = 31.746, 34.395, 36.226, 47.526, 56.549, 62.832, 67.893,$ and 69.028 were assigned to (100), (002), (101), (110), (103), (200), (112), and (201) of ZnO nanorods. All peaks indicated a hexagon wurtzite structure (Zincite, JCPDS no, 89–0510). The results indicated the high quality of ZnO nanorods. The average crystal sizes of ZnO-NRs obtained after calcination at 300°C for five hours have confirmed their rod shape with 285 nm

length and 84 nm diameter. Scherer's equation (Patterson, 1939; Cullity and Stock, 2001) evaluated the average crystallite size (4) of ZnO-NRs.

$$d = k\lambda/\beta \cos\theta,$$

where $k = 0.9$ is the shape factor, β is the measured FWHM, θ is the Bragg angle of the peak, and λ is the XRD wavelength.

Morphological Studies of ZnO-NRs

The identification of morphology, size, and diffraction lattice of zinc oxide nanorods was carried out using transmission electron microscopy. TEM analysis of ZnO-NRs confirmed their rod shape with the dimensions of 285 nm length and 84 nm diameter and diffraction index as shown in **Figures 3, 4; Supplementary Figure S2**. The obtained results are in total agreement with the results of the XRD data presented in **Figure 2**.

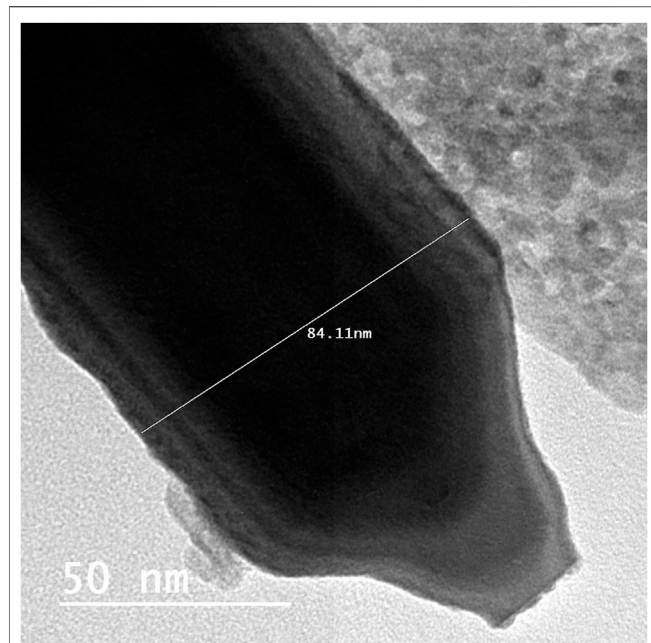


FIGURE 3 | Transmission electron microscopy of ZnO nanorods (ZnO-NRs).

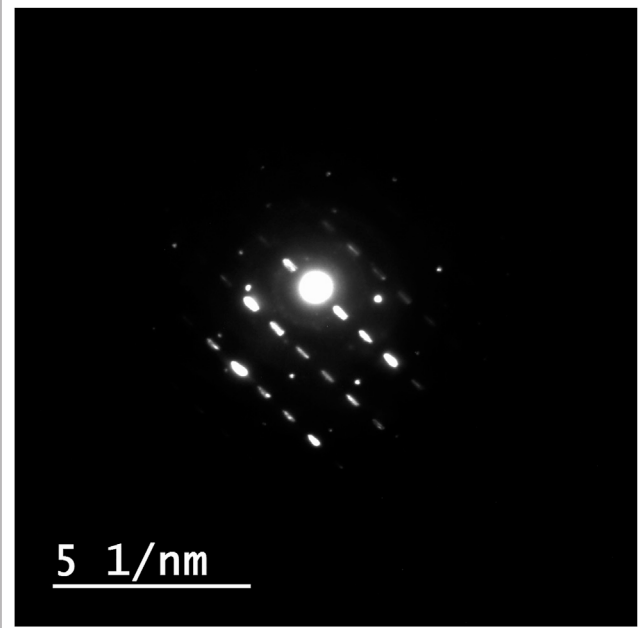


FIGURE 4 | Diffraction index of ZnO nanorods (ZnO-NRs).

Measurement of Released Zn (II) From Zinc Oxide Nanorods

ICP-AES was used to measure the quantity of Zn (II) ion liberated to the supernatant of the dispersed 100 µg of ZnO-NRs after 24 h. As shown in **Figure 5**, the Zn (II) ion's total amount was altered with different time intervals. The data also indicated that the amounts of Zn (II) ion released from ZnO-NRs were 23 ppm after 24 h, 18 ppm after 18 h, 15 ppm after 12 h, 11.5 ppm after 6 h, 6.5 ppm after 3 h, and 1.5 ppm at 1 h.

Quantitative RT-PCR

Real-time PCR was used to investigate the gene expression of VEGF. As shown in **Figure 6**, the VEGF gene was significantly upregulated with ZnO-NR concentrations (10 µg, 20 µg, and 50 µg), while the VEGF gene was significantly downregulated in the case of released Zn(II) ion ($p < 0.05$). The fold change of 10 µg of ZnO-NRs is double-fold superior to that of the non-treated control cells. Also, 20 µg of ZnO-NRs is fourfold superior to that of the non-treated control cells; also, 50 µg of ZnO-NRs is tenfold more remarkable than the control cells. VEGF expressions were increased relative to the increased ZnO-NRs. In contrast, the released Zn (II) ion was half of the value control cell, as shown in **Figure 6**.

Reactive Oxygen Species Assay

Figure 7 showed that ROS increased relatively to concentration of ZnO-NRs: 10 µg/ml (14%), 20 µg/ml (29%), and 50 µg/ml (49%) compared with the untreated cell control value. Released Zn (II) ion showed no positive effect, indicating that only ZnO-NRs induced reactive oxygen species, and Zn (II) ion released did not contribute to the angiogenesis process.

Antioxidant Stress Biomarker

Glutathione peroxidase enzyme favors the removal of hydrogen peroxide by catalyzing its reaction with reduced glutathione (GSH) according to the following reaction (Marklund s., 1982):

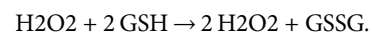


Figure 8 showed that glutathione of ZnO-NR concentrations of 10 µg/ml, 20 µg/ml, and 50 µg/ml treated with HDF4 cells increased compared to the untreated cell control. It indicated that ZnO-NRs behaved as an influential precursor of hydrogen peroxides. Due to GSH peroxidase with ZnO-NR-treated cells, glutathione decreased by 25%, 35%, and 40% compared to the untreated cell control, while released Zn (II) ion had no positive effect, indicating that ZnO-NRs contribute to producing H_2O_2 that promotes the angiogenesis process.

Chicken Chorioallantoic Membrane Assay

The chicken chorioallantoic membrane (CAM) assay considers a standard assay that measures the pro-angiogenic material potential. CAM assay has investigated the performance of ZnO-NRs to induce the microvascular process. After 24 h of remediation, the images were taken by Olympus camera. Interestingly, there was an increase in length, size, and junction as shown in **Figures 9,10A–D** that revealed ZnO-NRs with concentrations of 10 µg/ml and 20 µg/ml, and positive control VEGF (10 ng) increased the formation of matured vascular sprouting significantly as compared with a negative control. The percentages of increase in the length were 2.5, 3.5, and 4.5 fold. Also, the percentage of increase in size was 2.25, 3.25, and 3.75, and the injunction was 2, 2.5, and 4 fold for ZnO-NRs (10 µg/ml and 20 µg/ml) and VEGF (10 ng),

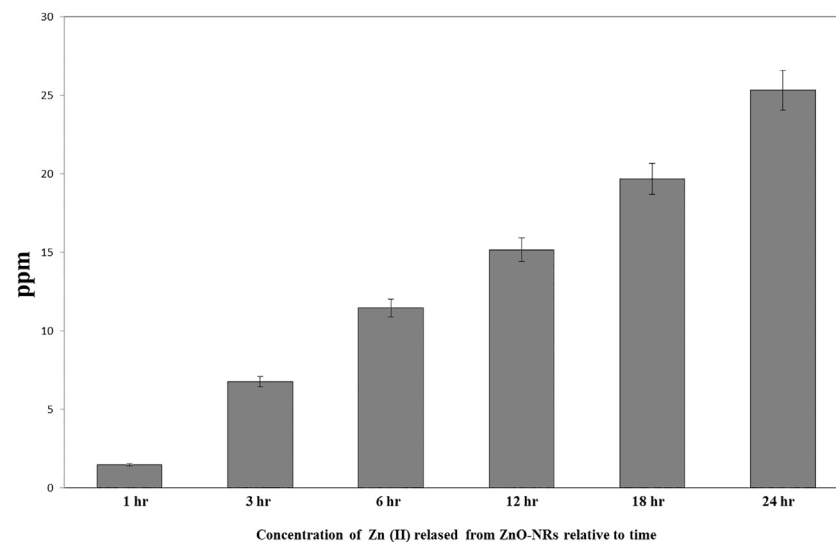


FIGURE 5 | Released zinc (II) ions from ZnO nanorods by ICP-AES.

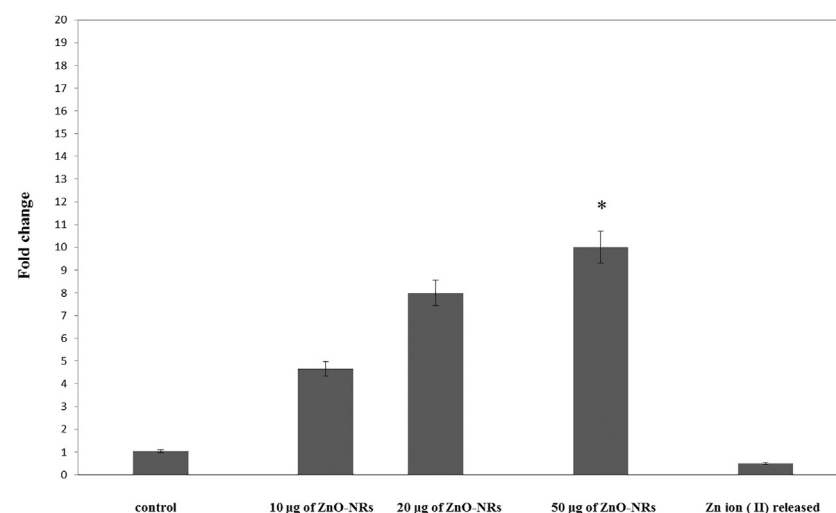


FIGURE 6 | Quantitative real-time PCR measures mRNA levels of the vascular endothelial growth factor gene (VEGF).

respectively, superior to that of the control. In contrast, **Figures 9,10E,F** demonstrated that ZnO-NRs 50 µg and liberated Zn (II) ions decreased vascular sprouting in length were 0.5 and 0.75, in sizes were 0.4 and 0.5, and junctions were 0.6 and 0.5. **Figures 9,10** displayed the effective influence of ZnO-NR concentrations with 10 µg/ml and 20 µg/ml on length and size, respectively, and junction as pro-angiogenic material potential.

CAM Histopathological Examination

The histopathological pattern of the chick embryo chorioallantoic membrane treated with ZnO-NRs, VEGF, and released Zn (II) ion investigates angiogenesis. Hematoxylin and eosin-stained CAM sections, as shown in **Figure 11C** revealed CAM exposed to ZnO-

NR concentration of 20 µg/ml showed well-developed neovascularization with a score of +3, which represented numerous branching patterns of blood vessels more than ZnO-NR concentration of 10 µg/ml with a score of +2 in **Figure 11B**. Both of ZnO-NR concentrations, 10 µg/ml and 20 µg/ml, had had better vascularization than the negative control (score 0), as shown in **Figure 11A**. Similarly, **Figure 11D** represented the CAM exposed to 10 ng of VEGF as a positive control with a score of +4. However, **Figure 11E** showed fewer vascular vessels due to exposure to released Zn (II) ions with a score of +1, and **Figure 11F** showed a minor vascular vessel due to exposure to 50 µg with a score of zero. **Table 1** interpreted the scores of the histological feature according to Ejaz et al. (2006) and Bao et al. (2012). The

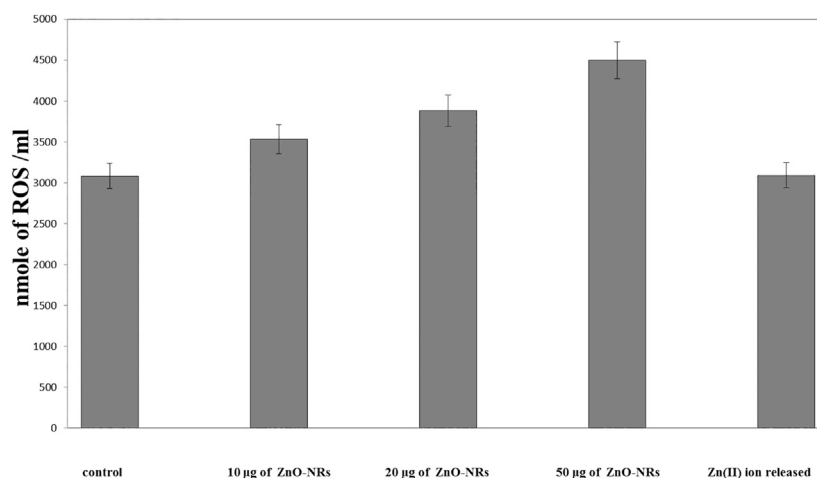


FIGURE 7 | Reactive oxygen species (ROS) of ZnO nanorods (ZnO-NRs) and released zinc (II) ions from ZnO nanorods (ZnO-NRs).

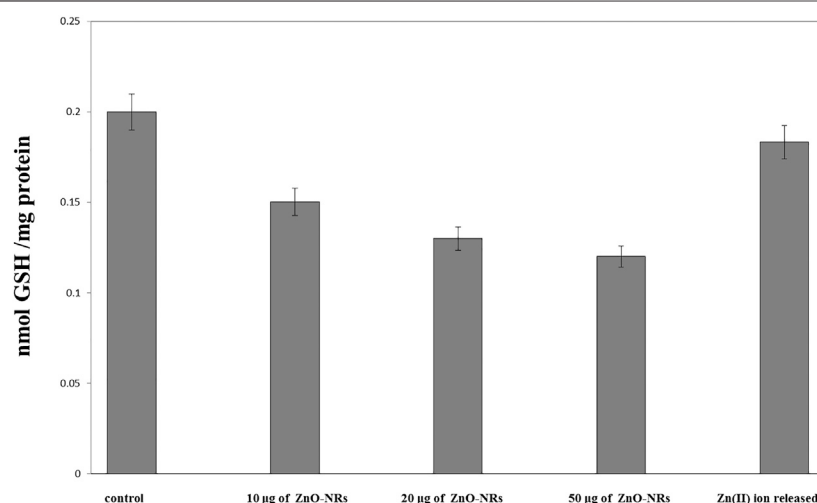


FIGURE 8 | Glutathione peroxidase enzyme of ZnO nanorods (ZnO-NRs) and released zinc (II) ions from ZnO nanorods (ZnO-NRs).

histological examination displayed those excess blood vessels with the highly branched network. These views support the angiogenesis activity induced by ZnO nanorods.

***In Vivo* Implantation Study (Morphology of Wound Healing)**

Based on the results of the *in vitro* assay and CAM assay studies, ZnO-NRs with concentrations of 10 µg/ml and 20 µg/ml and phenytoin (used as standard positive control) were selected for animal implantation studies to investigate *in vivo* angiogenesis. As shown in **Figure 12**, the initial skin wound appeared clearly with 14 mm. After 5 days, the wound healing percentage increased slightly compared with the non-treated control group (I). The percentages of wound healing using ZnO-NRs with concentrations of 10 µg/ml and 20 µg/ml were 20 and 28%, respectively, compared with 12% of the negative control (non-

treated). Similarly, the percentage of wound healing using phenytoin was 35%. After ten days, the percentages of wound healing increased to 46%, 59%, and 67% for ZnO-NRs with concentrations of 10 µg/ml and 20 µg/ml and phenytoin compared with the percentage of wound healing in negative control, which was 35%. After 14 days, the percentages of wound healing increased to 63%, 84%, and 93% for 10 µg/ml, 20 µg/ml, and phenytoin, respectively, compared with the negative control with a percentage of 55%. This result indicated that dressing with ZnO-NRs accelerates the healing of open-excision type wounds *in vivo*. **Figure 13** displayed the wound healing mechanism. After five days of treatment, **Figures 13E–H** demonstrated the thickening edematous and hotness of the epidermis at the injury edge. Interestingly, filling the wound gap with necrotic tissues and then filling the wound area with mature granulation tissues are shown in **Figures 13E–H**. Finally,

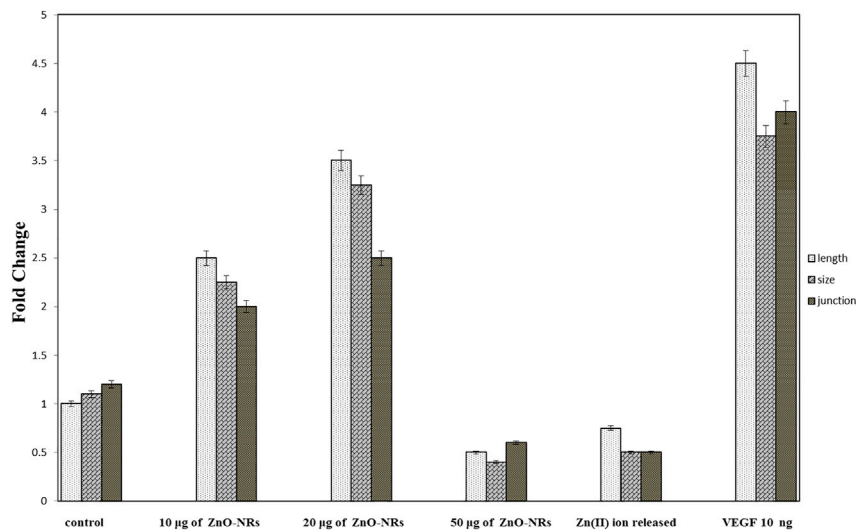


FIGURE 9 | Angiogenesis parameter quantitative of ZnO nanorods (ZnO-NRs) and released zinc (II) ions using chicken chorioallantoic membrane (CAM) assay.

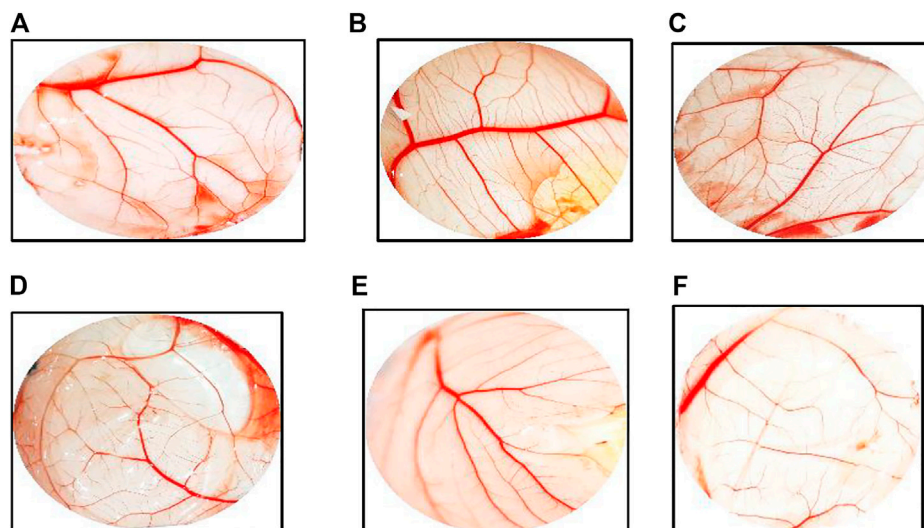


FIGURE 10 | Chicken chorioallantoic membrane (CAM) assay. **(A)** Negative control (non-treated). **(B)** CAM treated with 10 µg/ml of ZnO nanorods (ZnO-NRs). **(C)** CAM treated with 20 µg/ml of ZnO nanorods (ZnO-NRs). **(D)** CAM treated with 10 ng of positive control VEGF. **(E)** CAM treated with 50 µg/ml of ZnO nanorods (ZnO-NRs). **(F)** CAM treated with released Zn (II) ions.

Figures 13I–L displayed that wound gaps were shrinking due to the rate of epithelialization. As a result, ZnO-NR concentrations were found to show their contributory role in the accelerating epithelialization rate and required lesser time to complete the epithelialization process than the negative control.

Histological Explanation of Wound Healing

After three days of treatment with ZnO-NRs with concentrations of 10 µg/ml and 20 µg/ml and phenytoin as standard drugs, **Figures 14B–D** showed that the dermis near the excision was rich with inflammatory cells, mainly polymorphonuclear cells with an insufficient number of fibrosis in the outer skin near the

injury area. On the other side, a control skin tissue section (untreated skin tissue) shows cellular or rare endothelial cells with zero scores, as **Figure 14A** showed. As **Figures 14B–D** indicated, the healing process started and the neo-angiogenesis process begun with a score of +1. After five days of treatment with ZnO-NRs with concentrations of 10 µg/ml and 20 µg/ml and phenytoin as standard drugs, **Figures 14E–H** showed the fibrin net rich in inflammatory cells, mainly neutrophils, macrophages, and lymphocyte skin tissue of all groups (control, standard, and test material). Moreover, the reform of a cuticle was inhibited ultimately—also, observation of moderate propagation emigration of fibroblasts and mild new collagen. Control

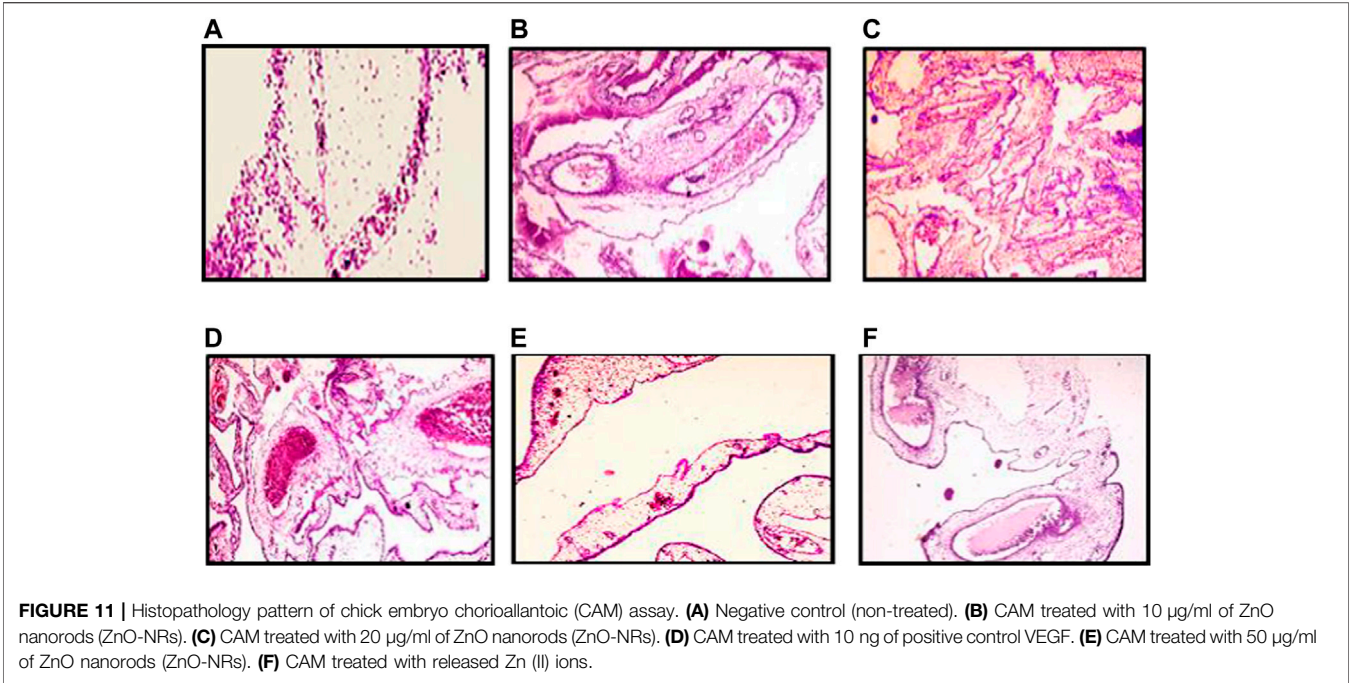
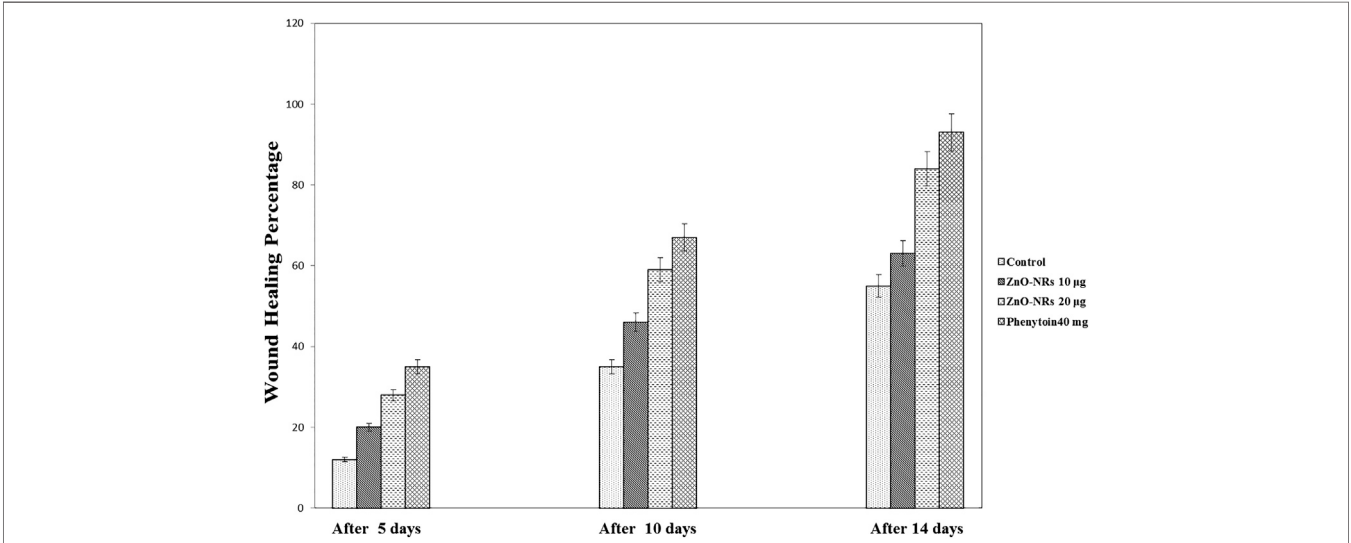


TABLE 1 | Angiogenesis score concerning histological feature

Score	Histological feature
0	It referred to cellular or rare endothelial cells
1	It illustrated that dispersed small aggregate endothelial cells without lumens
2	It indicated those endothelial cells in all parts of the section with some tube formation
3	It elucidates that readily identified capillary tube forming that includes RBCs and small amounts of collagen
4	It represented that those vast vessels have more than four red cells containing layers of collagen in vessel walls



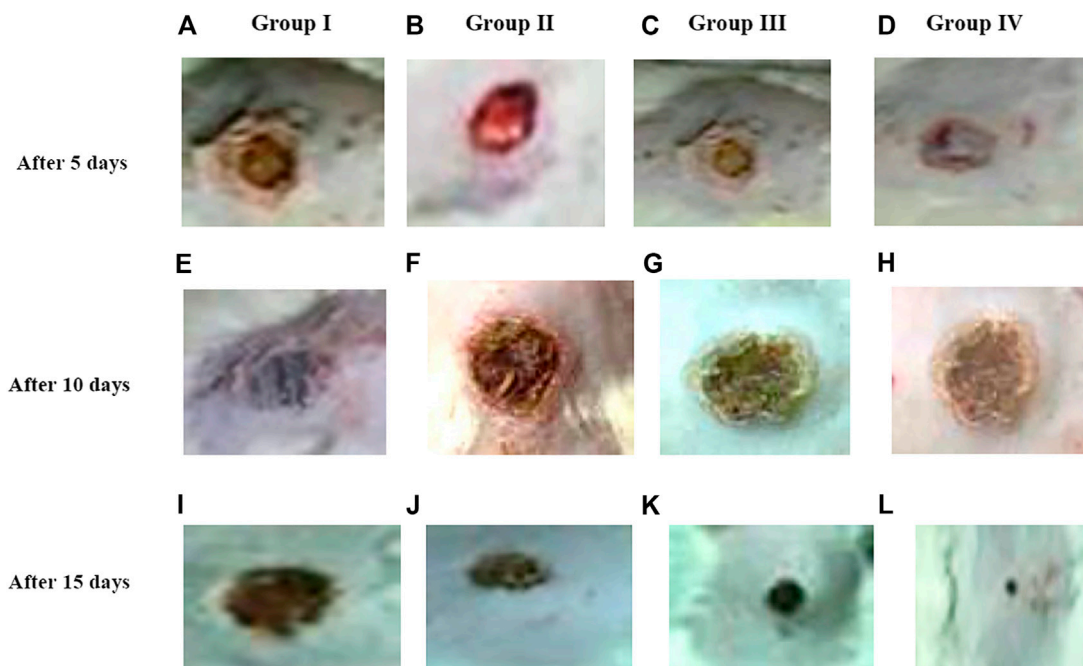


FIGURE 13 | Morphology of wound healing after exposure with ZnO nanorods (ZnO-NRs), phenytoin compared with control (non-treated). **(A)** Negative control (non-treated) after 5 days. **(B)** Wound healing after exposure with 10 $\mu\text{g/ml}$ of ZnO nanorods (ZnO-NRs) after 5 days. **(C)** Wound healing after exposure with 20 $\mu\text{g/ml}$ of ZnO nanorods (ZnO-NRs) after 5 days. **(D)** Wound healing after exposure with phenytoin as positive control after 5 days. **(E)** Negative control (non-treated) after 10 days. **(F)** Wound healing after exposure with 10 $\mu\text{g/ml}$ of ZnO nanorods (ZnO-NRs) after 10 days. **(G)** Wound healing after exposure with 20 $\mu\text{g/ml}$ of ZnO nanorods (ZnO-NRs) after 10 days. **(H)** Wound healing after exposure with phenytoin as positive control after 10 days. **(I)** Negative control (non-treated) after 15 days. **(J)** Wound healing after exposure with 10 $\mu\text{g/ml}$ of ZnO nanorods (ZnO-NRs) after 15 days. **(K)** Wound healing after exposure with 20 $\mu\text{g/ml}$ of ZnO nanorods (ZnO-NRs) after 15 days. **(L)** Wound healing after exposure with phenytoin as positive control after 15 days

animal groups reveal cellular or rare endothelial cells with a score of zero, as shown in **Figure 14E**. However, in **Figure 14** (F, G, and H), a dermal layer indicated the beginning of neo-angiogenesis with a score of +2 for ZnO-NRs with 20 $\mu\text{g/ml}$ phenytoin, characterized by prominent linear arrangements and some tube formation. The animal group treated with 10 $\mu\text{g/ml}$ of ZnO-NRs revealed dispersed small aggregate endothelial cells without lumens with a score of +1. Seven days after treatment, as **Figures 14I–L** (I, J, K, and L) revealed, wound tissues were filled with necrotic tissue and inflammatory neutrophils. The epidermis regeneration was significantly inhibited. Interestingly, new granulation tissues were created at the bottom of wounds in all animal groups, consisting of endothelial cells, fibroblast, and newly synthesized non-organized collagen. **Figure 14I** displayed that the control animal group has a score of +1 that revealed dispersed small aggregate endothelial cells without lumens. **Figures 14J,K** displayed the treated animal groups with ZnO-NR concentrations of 10 $\mu\text{g/ml}$ and 20 $\mu\text{g/ml}$, and phenytoin showed endothelial cells in all parts of the section with some tube formation with a score of +2.

Interestingly, endothelial cell proliferation was accompanied by a new vessel number. It was assigned for readily identified capillary tube forming that included RBCs and small amounts of collagen, especially in animals treated at concentration of 20 $\mu\text{g/ml}$ and had a score of +3. Ten days after treatment, control prominent linear arrangements and some tube formation (score 1) were observed, as

shown in **Figure 14M**. Otherwise, animal groups treated with phenytoin and ZnO-NR concentration of 20 $\mu\text{g/ml}$ showed capillary tube forming that includes RBCs and small amounts of collagen with a score of +3, as shown in **Figures 14O,P**, while ZnO-NR concentration of 10 $\mu\text{g/ml}$ had a score of +2, as shown in **Figure 14N**. Fourteen days after treatment, fibroblasts and endothelial cells decreased in granulation with an excess of collagen fibers in the negative control (non-treated) with a score +2, as shown in **Figure 14Q**. The negative control (untreated animals) and animal treated with 10 $\mu\text{g/ml}$ of ZnO-NR showed capillary tube formation which contained a red blood cell score of +3 as **Figure 14R** revealed. The animal group treated by ZnO-NR concentration of 20 $\mu\text{g/ml}$ and phenytoin showed vast vessels have more than four red cells containing layers of collagen in vessel walls with a score of four as **Figures 14S,T** showed. Finally, histological examination demonstrated that re-epithelization and new tissue formation in the treated groups' wound area.

DISCUSSION

Zinc oxide nanoparticles and their application in tissue engineering, as well as angiogenesis, were studied. Here in this study, we successfully fabricated green zinc oxide nanorods without complicated procedure or toxic chemicals to obtain a rod shape as other methods (Nouroozi and Farzaneh, 2011).

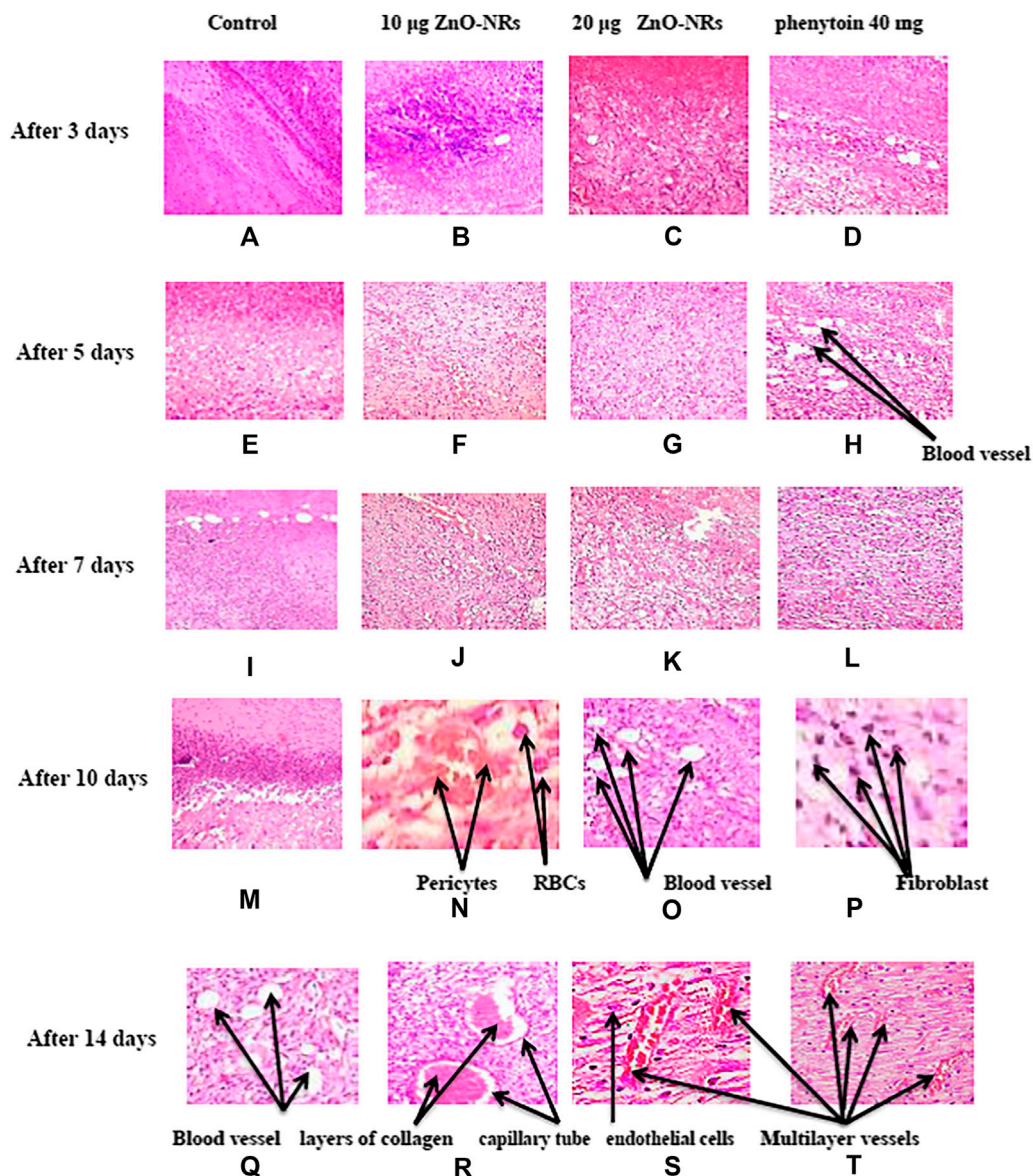


FIGURE 14 | Histopathology pattern of wound healing after treatment with ZnO nanorods (ZnO-NRs), phenytoin compared with control (non-treated). **(A)** Negative control (non-treated) after 3 days. **(B)** Wound healing after treatment with 10 µg/ml of ZnO nanorods (ZnO-NRs) after 3 days. **(C)** Wound healing after treatment with 20 µg/ml of ZnO nanorods (ZnO-NRs) after 3 days. **(D)** Wound healing after treatment with phenytoin as positive control after 3 days. **(E)** Negative control (non-treated) after 5 days. **(F)** Wound healing after treatment with 10 µg/ml of ZnO nanorods (ZnO-NRs) after 5 days. **(G)** Wound healing after treatment with 20 µg/ml of ZnO nanorods (ZnO-NRs) after 5 days. **(H)** Wound healing after treatment with phenytoin as positive control after 5 days. **(I)** Negative control (non-treated) after 7 days. **(J)** Wound healing after treatment with 10 µg/ml of ZnO nanorods (ZnO-NRs) after 7 days. **(K)** Wound healing after treatment with 20 µg/ml of ZnO nanorods (ZnO-NRs) after 7 days. **(L)** Wound healing after treatment with phenytoin as positive control after 7 days. **(M)** Negative control (non-treated) after 10 days. **(N)** Wound healing after treatment with 10 µg/ml of ZnO nanorods (ZnO-NRs) after 10 days. **(O)** Wound healing after treatment with 20 µg/ml of ZnO nanorods (ZnO-NRs) after 10 days. **(P)** Wound healing after treatment with phenytoin as positive control after 10 days. **(Q)** Negative control (non-treated) after 14 days. **(R)** Wound healing after treatment with 10 µg/ml of ZnO nanorods (ZnO-NRs) after 14 days. **(S)** Wound healing after treatment with 20 µg/ml of ZnO nanorods (ZnO-NRs) after 14 days. **(T)** Wound healing after treatment with phenytoin as positive control after 14 days.

FTIR, XRD, and HR-TEM results confirmed the fabrication of ZnO nanorods. The plausible mechanism of synthesis of zinc oxide nanorods (ZnO-NRs) was carried out according to Bao et al. (2012). They mentioned that ZnCl_2 dissolution to Zn^{2+} accumulated and oriented on the surface of the albumin template. The ions covered the albumin molecule, followed by thermal

treatment for calcination at 300°C for 5 h so that Zn ion after thermal treatment will reshape ZnO into a rod shape (Bao et al., 2012). Our ICP results reveal quantitative zinc ions released from zinc oxide nanorods after time intervals. According to Oikawa et al., the Zn released from zinc oxide nanorods is time dependent (Tada-Oikawa et al., 2015). This report successfully investigated

the effect of zinc oxide nanorods and Zn (II) ion released on angiogenesis markers using RT-PCR. The results of RT-PCR confirmed that Zn (II) ion released decreased VEGF gene expression. Hence, it suppresses the angiogenesis process. As Oikawa et al. mentioned, VEGF and its receptors can develop vascularization (Tada-Oikawa et al., 2015). On the other hand, upregulation of ZnO-NR expression is concentration dependent. Previous studies reported that zinc ions released from suspended zinc oxide nanoparticles and zinc chloride restricted the expression of receptors related to vascularization (Tada-Oikawa et al., 2015). Interestingly, many preclinical models of micro-blood vessels grown on VEGF-A were capable of inducing cells to invade the underlying matrix to form capillary-like tubules (Pepper et al., 1992). VEGF is considered as the most important angiogenic mediator characterized to date (Cisowski et al., 2005). Previous studies suggest that hydrogen peroxide can induce VEGF in many cells and organs such as human keratinocytes (Sen et al., 2002), retinal pigment epithelial cells (Cisowski et al., 2005), endothelial cells (Sanchez et al., 2013), murine fibroblasts (Pepper et al., 1992), and macrophages (Cho et al., 2001). Also, H_2O_2 enhanced the skin wound healing in mice by the expression of VEGF (Sen et al., 2002). Interestingly, ZnO-NRs contribute to making new blood vessels (neovascularization). As previously reported, reactive oxygen species (ROS) have a great role in the microvascular process due to stimulating all angiogenic stages such as migration, cell proliferation, tube formation, and redox signaling. Our results confirmed that ROS generation by ZnO-NRs is related to concentration. In contrast, Zn ions released showed no effect. Also, GSH is reduced with ZnO-NRs concentration increased relatively due to the presence of ROS and H_2O_2 . Also, the previous issue established that zinc oxide nanoparticles generate ROS components like H_2O_2 throughout photocatalysis (Hoffman et al., 1994). Both egg yolk and wound healing assay studies had displayed that ZnO nanorods were pro-angiogenic and mentioned that zinc oxide nanoflowers could make a new blood vessel. Patra et al. (2011) suggested that ROS activated angiogenesis by $[EuIII(OH)_3]$ nanorods (Patra et al., 2011; Makhluaf et al., 2008; Makhluaf et al., 2008; Bhattacharya et al., 2007). In CAM assay, the decreased angiogenic property of ZnO-NRs at higher concentration (50 μg) due to the higher level ROS induced cell damage. Also, the released Zn (II) ions decreased the angiogenic property due to a negative effect on the angiogenic factors. The wound healing assay had shown the presence of a broad blood vessel network throughout. Endothelial cells contributed to reform and reshape the inner wall of blood vessels surrounding basal lamina and pericytes. It extends to a large cytoplasmic process over the surface of the vessel tube. The presence of pericytes around the blood vessels indicated mature vessels. Wound healing is considered as a complicated process following harm to the skin of the whole body. It included coordinated interactions between diverse immunological and biological systems for restoring the damaged cellular structure to its original state (Clark, 1985). Wound healing mechanisms including the processes above involve (1) growth factors; (2) cell proliferation, migration, and differentiation; (3) epithelialization, fibroplasia, and

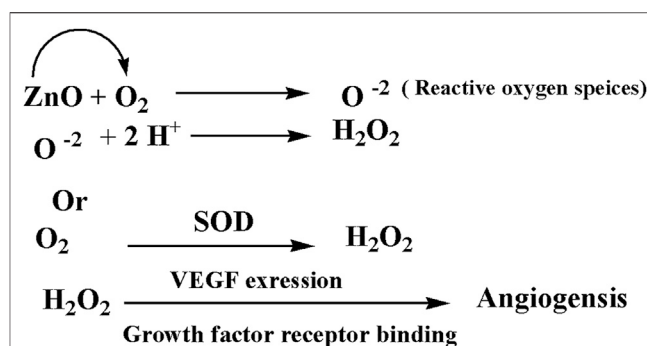


FIGURE 15 | A plausible mechanism of angiogenesis

angiogenesis; (4) wound contraction; and (5) remodeling (Velmar et al., 2009). Many mechanisms were accelerating injury healing, such as wound diminishing, epithelialization, and prevention of wound infection by bacteria that would delay and complicate the wound healing process (Lodhi and Singhai, 2013; Li et al., 2011). Zinc oxide nanomaterial has been known as an antibacterial agent (Jin et al., 2009). Collagen has a main role in extracellular protein in the granulation tissue of the wound healing process. Interestingly, it is a vital component that has a main role in incision solidity and impartiality of tissue matrix (Hassan et al., 2011). The wound healing process depends upon the controlled formation and deposition of novel collagens and their consequent maturation (Puratchikody et al., 2006). In our study, ZnO-NRs succeed in synthesizing a multilayer of collagen layers in vessel walls with red blood cells with a score of +4, which means large vascular contains more than four red cells and multilayered blood vessels, including layers of collagen in vessel walls. There was a plausible mechanism about zinc oxide nanorod methodology, as **Figure 15** displayed. We assumed that the ZnO nanorods could play an important role in ROS generation, especially H_2O_2 . There are enormous mechanisms able to generate hydrogen peroxide in the cells. One of these mechanisms is the direct production of O_2 and its interaction with water (Fridovich, 1975). Another one is converting superoxide to H_2O_2 through superoxide dismutase enzyme inside the cell generating H_2O_2 (Velmar et al., 2009; Bancroft et al., 2013). Hydrogen peroxide induces cells to express VEGF.

Interestingly, zinc oxide nanoparticles' exposure at a low dose (10 mg/l and 20 mg/l) does not have significant root growth inhibition for hormetic dose response for radish and ryegrass, respectively. Also, the hermetic phenomenon is evaluated by ATP measurement. The application of Zn-NPs on seed germination and root growth of radish and ryegrass showed a hermetic dose response. In contrast, the plant species' root growth was restricted at a high concentration up to 200 mg/l (Iavicoli et al., 2018). Furthermore, Calabrese et al. (2010) managed the hormetic responses of cells to a range of metabolic and oxidative stressors (Calabrese et al., 2010). The presence of high concentration of zinc oxide nanoparticle generated oxidative stress. However, hydrogen peroxide can generate

hydroxyl radical, a potent inducer of membrane lipid peroxidation (Calabrese et al., 2010).

Furthermore, endothelial cell proliferation, migration, and tube formation occurred due to the exiting of ZnO-NRs. Finally, the fabrication of ZnO-NRs could be applied in many tissue engineering applications such as skin tissue engineering, bone regeneration, and wound healing.

CONCLUSION

In this study, zinc oxide nanorods were fabricated and characterized. It has been synthesized *via* the green method using albumin eggshell. FTIR, XRD, and HR-TEM confirmed ZnO in a rod shape with a diameter of 84 nm and length of 281 nm. Also, ICP evidence the presence of Zn ions released from ZnO nanorods, and quantitative release of Zn ions is time dependent. Egg yolk assay investigates the performance of zinc oxide nanorods to induce angiogenesis. In the case of 20 µg/ml of ZnO nanorods, there is an increase in the length of the blood vessel and size and junction. However, excess of ZnO nanorods and released Zn ions had reverse results. In the *in vivo* wound study, the data emphasized ZnO nanorods' ability for vascularization and rapid rate to remodeling the skin to its original shape due to epithelialization. Gene expression study demonstrated that enhancement of ZnO nanorods is a key of the angiogenic factors such as VEGF. Therefore, this report confirmed the importance of ZnO nanorods in tissue engineering material due to their ability to induce angiogenesis.

DATA AVAILABILITY STATEMENT

The original contributions presented in the study are included in the article/**Supplementary Material**; further inquiries can be directed to the corresponding author.

REFERENCES

- Augustine, R., Dominic, E. A., Reju, I., Kaimal, B., Kalarikkal, N., and Thomas, S. (2014). Investigation of Angiogenesis and its Mechanism Using Zinc Oxide Nanoparticle-Loaded Electrospun Tissue Engineering Scaffolds. *RSC Advances* 93, 51528–51536. doi:10.1039/C4RA07361D
- Ausprunk, D. H., Knighton, D. R., and Folkman, J. (1975). Vascularization of Normal and Neoplastic Tissues Grafted to the Chick Chorioallantois. Role of Host and Preexisting Graft Blood Vessels. *Am. J. Pathol.*, 79 (3), 597, 618.
- Bancroft, J. D., Stevens, A., and Turner, D. R. (2013). *Theory and Practice of Histological Techniques*. 4th Ed. Edinburgh, London, Melbourne, New York: Churchill Livingstone.
- Bao, S.-J., Lei, C., Xu, M.-W., Cai, C.-J., and Jia, D.-Z. (2012). Environment-friendly Biomimetic Synthesis of TiO₂nanomaterials for Photocatalytic Application. *Nanotechnology*, 23 (20), 205601. doi:10.1088/0957-4484/23/20/205601
- Barui, A. K., Veeriah, V., Mukherjee, S., Manna, J., Patel, A. K., Patra, S., et al. (2012). Zinc Oxide Nanoflowers Make New Blood Vessels. *Nanoscale* 4 (24), 7861–7869. doi:10.1039/c2nr32369a

ETHICS STATEMENT

The experimental procedure was approved by the Institutional Animal Care and Use Committee at Cairo University, Egypt (IACUC, CU-II-F-10-19) after the affirmative opinion of the Animal Protocols Evaluation Committee.

AUTHOR CONTRIBUTIONS

Conceptualization: AH, AM, AE and EM; formal analysis: AM and DE; funding acquisition: AH, AM and DE; investigation: AH, AM, AE and EM; methodology: AH, AM, DE, AE and EM; project administration: AH, AM, DE; Resource: AM and DE; supervision: AH; Validation: AM and DE; visualization: AM and DE; writing original draft: AH, AM; writing -review edition. AH, AM and AE. All author approved the final version of the manuscript.

ACKNOWLEDGMENTS

The authors thank Genetic Engineering and Biotechnology Research Institute (GBRI), University of Sadat City, Egypt. Also, the authors wish to thank Professor Aly Fahmy Mohamed for his support and equipping the laboratory to carry out this research work. Also, the authors thank Dr. Ahmed Ibrahim Abd El Maksoud for his support especially in the Biological experiments.

SUPPLEMENTARY MATERIAL

The Supplementary Material for this article can be found online at: <https://www.frontiersin.org/articles/10.3389/fphar.2021.661217/full#supplementary-material>

Supplementary Figure 1 | The image of preparation Zinc oxide nanorod.

Supplementary Figure 2 | Another image of TEM of Zinc oxide nanorod.

- Bhattacharya, R., Patra, C. R., Verma, R., Kumar, S., Greipp, P. R., and Mukherjee, P. (2007). Gold Nanoparticles Inhibit the Proliferation of Multiple Myeloma Cells. *Adv. Mater.* 19 (5), 711–716. doi:10.1002/adma.200602098
- Borah, D., Baruah, M. K., Saikia, P. P., Senapoty, K. K., Barua, M., and Singha, R. (2016). Structural Characterization and Surface Environment of ZnOnanoflowers. *J. Mater. Environ. Sci.* 7, 310–315.
- Calabrese, V., Cornelius, C., Dinkova-Kostova, A. T., Calabrese, E. J., and Mattson, M. P. (2010). Cellular Stress Responses, the Hormesis Paradigm, and Vitagenes: Novel Targets for Therapeutic Intervention in Neurodegenerative Disorders. *Antioxid. Redox Signaling* 13 (11), 1763–1811. doi:10.1089/ars.2009.3074
- Cho, M., Hunt, T. K., and Hussain, M. Z. (2001). Hydrogen Peroxide Stimulates Macrophage Vascular Endothelial Growth Factor Release. *Am. J. physiology-heart circulatory Physiol.* 280 (5), H2357–H2363. doi:10.1152/ajpheart.2001.280.5.h2357
- Cisowski, J., Loboda, A., Józkowicz, A., Chen, S., Agarwal, A., and Dulak, J. (2005). Role of Heme Oxygenase-1 in Hydrogen Peroxide-Induced VEGF Synthesis: Effect of HO-1 Knockout. *Biochem. biophysical Res. Commun.* 326 (3), 670–676. doi:10.1016/j.bbrc.2004.11.083
- Clark, R. A. F. (1985). Cutaneous Tissue Repair: Basic Biologic Considerations. I. *J. Am. Acad. Dermatol.* 13 (5), 701–725. doi:10.1016/s0190-9622(85)70213-7

- Clifford, D. H. (1984). "Preanesthesia, Anesthesia, Analgesia, and Euthanasia," in *Laboratory Animal Medicine*. Editors J. G. Fox, B. J. Cohen, and F. M. Loew (Orlando, Florida: Academic Press), 527–562. doi:10.1016/b978-0-12-263620-2.50024-0
- Cullity, B. D., and Stock, S. R. (2001). *Elements of X-Ray Diffraction*, Prentice-Hall. Upper Saddle River, NJ, 388.
- Ejaz, S., Seok, K. B., and Woong Lim, C. (2006). A Novel Model of Image Acquisition and Processing for Holistic Quantification of Angiogenesis Disrupted by Application of Mainstream and Sidestream Cigarette Smoke Solutions. *Environ. Toxicol. Pharmacol.* 21 (1), 22–33. doi:10.1016/j.etap.2005.05.011
- Eliceiri, B. P., and Cheresch, D. A. (1999). The Role of α_v Integrins during Angiogenesis: Insights into Potential Mechanisms of Action and Clinical Development. *J. Clin. Invest.* 103 (9), 1227–1230. doi:10.1172/jci6869
- Ellman, G. L. (1959). Tissue Sulfhydryl Groups. *Arch. Biochem. Biophys.* 82 (1), 70–77. doi:10.1016/0003-9861(59)90090-6
- Ennett, A. B., and Mooney, D. J. (2002). Tissue Engineering Strategies for In Vivo Neovascularisation. *Expert Opin. Biol. Ther.* 2 (8), 805–818. doi:10.1517/14712598.2.8.805
- Farmer, V. C. (1974). *Infrared Spectra of Minerals*. Mineralogical society. Vol. 4, 331–363.
- Folkman, J. (1984). "Angiogenesis," in *Biology of Endothelial Cells* (Boston, MA: Springer), 412–428.
- Fridovich, I. (1975). Superoxide Dismutases. *Annu. Rev. Biochem.* 44 (1), 147–159. doi:10.1146/annurev.bi.44.070175.001051
- Hassan, S. W., Abubakar, M. G., Umar, R. A., Yakubu, A. S., Maishanu, H. M., and Ayeni, G. (2011). Pharmacological and Toxicological Properties of Leaf Extracts of *Kingelia Africana* (Bignoniaceae). *J. Pharmacol. Toxicol.* 6 (2), 124–132. doi:10.3923/jpt.2011.124.132
- Hoffman, A. J., Carraway, E. R., and Hoffmann, M. R. (1994). Photocatalytic Production of H₂O₂ and Organic Peroxides on Quantum-Sized Semiconductor Colloids. *Environ. Sci. Technol.* 28 (5), 776–785. doi:10.1021/es00054a006
- Huo, Y., Qiu, W.-Y., Pan, Q., Yao, Y.-F., Xing, K., and Lou, M. F. (2009). Reactive Oxygen Species (ROS) Are Essential Mediators in Epidermal Growth Factor (EGF)-stimulated Corneal Epithelial Cell Proliferation, Adhesion, Migration, and Wound Healing. *Exp. Eye Res.* 89 (6), 876–886. doi:10.1016/j.exer.2009.07.012
- Iavicoli, I., Leso, V., Fontana, L., and Calabrese, E. (2018). Nanoparticle Exposure and Hormetic Dose-Responses: An Update. *Ijms* 19 (3), 805. doi:10.3390/ijms19030805
- Jin, T., Sun, D., Su, J. Y., Zhang, H., and Sue, H.-J. (2009). Antimicrobial Efficacy of Zinc Oxide Quantum Dots against *Listeria Monocytogenes*, *Salmonella Enteritidis*, and *Escherichia coli* O157:H7. *J. Food Sci.* 74, M46–M52. doi:10.1111/j.1750-3841.2008.01013.x
- Lelkes, P. I., Hahn K., L., Sukovich, D. A., Karmiol, S., and Schmidt, D. H. (1998). "On the Possible Role of Reactive Oxygen Species in Angiogenesis," in *Oxygen Transport to Tissue XX* (Boston, MA: Springer), 454, 295–310. doi:10.1007/978-1-4615-4863-8_35
- Li, K., Diao, Y., Zhang, H., Wang, S., Zhang, Z., Yu, B., and Yang, H. (2011). Tannin Extracts from Immature Fruits of *Terminalia chebula* Fructus Retz. Promote Cutaneous Wound Healing in Rats. *BMC Complement. Altern. Med.* 11 (1), 1–9. doi:10.1186/1472-6882-11-86
- Lodhi, S., and Singhai, A. K. (2013). Wound Healing Effect of Flavonoid Rich Fraction and Luteolin Isolated from *Martynia Annua* Linn. On Streptozotocin Induced Diabetic Rats. *Asian Pac. J. Trop. Med.* 6 (4), 253–259. doi:10.1016/s1995-7645(13)60053-x
- Ma, N. (2000). Iozzo RV. Fibroblast Growth Factor-2. *Int. J. Biochem. Cel Biol* 32, 115–120.
- Makhluf, S. B.-D., Arnon, R., Patra, C. R., Mukhopadhyay, D., Gedanken, A., Mukherjee, P., et al. (2008). Labeling of Sperm Cells via the Spontaneous Penetration of Eu³⁺-Ions as Nanoparticles Complexed with PVA or PVP. *J. Phys. Chem. C* 112 (33), 12801–12807. doi:10.1021/jp804012b
- Marklund, S. L., Westman, N. G., Lundgren, E., and Roos, G. (1982). Copper- and Zinc-Containing Superoxide Dismutase, Manganese-Containing Superoxide Dismutase, Catalase, and Glutathione Peroxidase in Normal and Neoplastic Human Cell Lines and Normal Human Tissues. *Cancer Res.* 42 (5), 1955–1961.
- Norrbj, K. (2006). *In vivo* models of Angiogenesis. *J. Cell. Mol. Med.* 10 (3), 588–612. doi:10.1111/j.1582-4934.2006.tb00423.x
- Nouroozi, F., and Farzaneh, F. (2011). Synthesis and Characterization of Brush-like ZnO Nanorods Using Albumen as Biotemplate. *J. Braz. Chem. Soc.* 22 (3), 484–488. doi:10.1590/s0103-50532011000300011
- Patra, C. R., Kim, J.-H., Pramanik, K., d'Uscio, L. V., Patra, S., Pal, K., et al. (2011). Reactive Oxygen Species Driven Angiogenesis by Inorganic Nanorods. *Nano Lett.* 11 (11), 4932–4938. doi:10.1021/nl2028766
- Patterson, A. L. (1939). The Scherrer Formula for X-Ray Particle Size Determination. *Phys. Rev.* 56(10), 978, 982. doi:10.1103/physrev.56.978
- Pechan, P. A., Chowdhury, K., and Seifert, W. (1992). Free Radicals Induce Gene Expression of NGF and bFGF in Rat Astrocyte Culture. *Neuroreport* 3 (6), 469–472. doi:10.1097/00001756-199206000-00003
- Pepper, M. S., Ferrara, N., Orci, L., and Montesano, R. (1992). Potent Synergism between Vascular Endothelial Growth Factor and Basic Fibroblast Growth Factor in the Induction of Angiogenesis In Vitro. *Biochem. biophysical Res. Commun.* 189 (2), 824–831. doi:10.1016/0006-291x(92)92277-5
- Petrova, T. V., Makinen, T., and Alitalo, K. (1999). Signaling via Vascular Endothelial Growth Factor Receptors. *Exp. Cel. Res.* 253 (1), 117–130. doi:10.1006/excr.1999.4707
- Pfaffl, M. W. (2001). A New Mathematical Model for Relative Quantification in Real-Time RT-PCR. *Nucleic Acids Res.* 29 (9), e45. doi:10.1093/nar/29.9.e45
- Pitiakoudis, M., Giatromanolaki, A., Iliopoulos, I., Tzaroucha, A., Simopoulos, C., and Piperidou, C. (2004). Phenytoin-induced Lymphocytic Chemotaxis, Angiogenesis and Accelerated Healing of Decubitus Ulcer in a Patient with Stroke. *J. Int. Med. Res.* 32 (2), 201–205. doi:10.1177/147323000403200213
- Puratchikody, A., Devi, C., and Nagalakshmi, G. (2006). Wound Healing Activity of *Cyperus Rotundus* Linn. *Indian J. Pharm. Sci.* 68(1), 97. doi:10.4103/0250-474x.22976
- Rasmussen, J. W., Martinez, E., Louka, P., and Wingett, D. G. (2010). Zinc Oxide Nanoparticles for Selective Destruction of Tumor Cells and Potential for Drug Delivery Applications. *Expert Opin. Drug Deliv.* 7 (9), 1063–1077. doi:10.1517/17425247.2010.502560
- Rhee, S. G. (2006). CELL SIGNALING: H₂O₂, a Necessary Evil for Cell Signaling. *Science* 312 (5782), 1882–1883. doi:10.1126/science.1130481
- Rouwema, J., Rivron, N. C., and van Blitterswijk, C. A. (2008). Vascularization in Tissue Engineering. *Trends Biotechnol.* 26 (8), 434–441. doi:10.1016/j.tibtech.2008.04.009
- Roy, S., Khanna, S., Nallu, K., Hunt, T. K., and Sen, C. K. (2006). Dermal Wound Healing Is Subject to Redox Control. *Mol. Ther.* 13 (1), 211–220. doi:10.1016/j.ymthe.2005.07.684
- Sanchez, A., Tripathy, D., Luo, J., Yin, X., Martinez, J., and Grammas, P. (2013). Neurovascular Unit and the Effects of Dosage in VEGF Toxicity: Role for Oxidative Stress and Thrombin. *Jad* 34 (1), 281–291. doi:10.3233/jad-121636
- Sen, C. K., Khanna, S., Babior, B. M., Hunt, T. K., Ellison, E. C., and Roy, S. (2002). Oxidant-induced Vascular Endothelial Growth Factor Expression in Human Keratinocytes and Cutaneous Wound Healing. *J. Biol. Chem.* 277 (36), 33284–33290. doi:10.1074/jbc.m203391200
- Silverstein, R. M., and Bassler, G. C. (1962). Spectrometric Identification of Organic Compounds. *J. Chem. Educ.* 39(11), 546. doi:10.1021/ed039p546
- Suri, C., Jones, P. F., Patan, S., Bartunkova, S., Maisonnier, P. C., Davis, S., et al. (1996). Requisite Role of Angiopoietin-1, a Ligand for the TIE2 Receptor, during Embryonic Angiogenesis. *Cell* 87 (7), 1171–1180. doi:10.1016/s0092-8674(00)81813-9
- Tada-Oikawa, S., Ichihara, G., Suzuki, Y., Izuoka, K., Wu, W., Yamada, Y., et al. (2015). Zn(II) Released from Zinc Oxide Nano/micro Particles Suppresses Vasculogenesis in Human Endothelial Colony-Forming Cells. *Toxicol. Rep.* 2, 692–701. doi:10.1016/j.toxrep.2015.04.003
- Thomas, C. E. (1990). Ethylamine. *Wounds* 3, 95–101. doi:10.1016/b978-0-444-81316-9.50021-9

- Velnar, T., Bailey, T., and Smrkolj, V. (2009). The Wound Healing Process: an Overview of the Cellular and Molecular Mechanisms. *J. Int. Med. Res.* 37 (5), 1528–1542. doi:10.1177/147323000903700531
- Xia, C., Meng, Q., Liu, L.-Z., Rojanasakul, Y., Wang, X.-R., and Jiang, B.-H. (2007). Reactive Oxygen Species Regulate Angiogenesis and Tumor Growth through Vascular Endothelial Growth Factor. *Cancer Res.* 67 (22), 10823–10830. doi:10.1158/0008-5472.can-07-0783
- Zhang, Y., Nayak, T., Hong, H., and Cai, W. (2013). Biomedical Applications of Zinc Oxide Nanomaterials. *Cmm* 13 (10), 1633–1645. doi:10.2174/1566524013666131111130058

Conflict of Interest: The authors declare that the research was conducted in the absence of any commercial or financial relationships that could be construed as a potential conflict of interest.

Publisher's Note: All claims expressed in this article are solely those of the authors and do not necessarily represent those of their affiliated organizations, or those of the publisher, the editors and the reviewers. Any product that may be evaluated in this article, or claim that may be made by its manufacturer, is not guaranteed or endorsed by the publisher.

Copyright © 2021 Hassan, Elebeedy, Matar, Fahmy Mohamed Elsayed and Abd El Maksoud. This is an open-access article distributed under the terms of the Creative Commons Attribution License (CC BY). The use, distribution or reproduction in other forums is permitted, provided the original author(s) and the copyright owner(s) are credited and that the original publication in this journal is cited, in accordance with accepted academic practice. No use, distribution or reproduction is permitted which does not comply with these terms.

Advantages of publishing in Frontiers



OPEN ACCESS

Articles are free to read
for greatest visibility
and readership



FAST PUBLICATION

Around 90 days
from submission
to decision



HIGH QUALITY PEER-REVIEW

Rigorous, collaborative,
and constructive
peer-review



TRANSPARENT PEER-REVIEW

Editors and reviewers
acknowledged by name
on published articles

Frontiers

Avenue du Tribunal-Fédéral 34
1005 Lausanne | Switzerland

Visit us: www.frontiersin.org

Contact us: frontiersin.org/about/contact



REPRODUCIBILITY OF RESEARCH

Support open data
and methods to enhance
research reproducibility



DIGITAL PUBLISHING

Articles designed
for optimal readership
across devices



FOLLOW US

@frontiersin



IMPACT METRICS

Advanced article metrics
track visibility across
digital media



EXTENSIVE PROMOTION

Marketing
and promotion
of impactful research



LOOP RESEARCH NETWORK

Our network
increases your
article's readership